國立交通大學

電子物理系

博士論文

以高功率摻釹晶體雷射實現有效非線性轉換:
從人眼安全波段至紫外及深紫外波段

High-Power Nd-doped Crystal Lasers with Nonlinear Frequency Conversion from Eye-Safe to UV and DUV Regimes

學　　生：黃郁仁

指導老師：陳永富 教授

中 華 民 國 一 百 零 二 年 四 月

以高功率摻釹晶體雷射實現有效非線性轉換:
從人眼安全波段至紫外及深紫外波段

High-Power Nd-doped Crystal Lasers with Nonlinear Frequency Conversion from Eye-Safe to UV and DUV Regimes

研 究 生:黃郁仁　　Student:Yu-Jen Huang

指導老師:陳永富 教授　　Advisor:Prof. Yung-Fu Chen

國 立 交 通 大 學

電 子 物 理 系

博 士 論 文

A Dissertation

Submitted to Department of Electrophyscis

College of Science

National Chiao Tung University

in partial Fulfillment of the Requirements

for the Degree of

Doctor of Philosophy

in

Electrophysics

April 2013

Hsinchu, Taiwan, Republic of China

中華民國一百零二年四月

以高功率摻鈦晶體雷射實現有效非線性轉換:
從人眼安全波段至紫外及深紫外波段

學生：黃郁仁　　指導老師：陳永富 教授

國立交通大學電子物理學系博士班

摘　　要

本博士論文旨在以簡單的線性共振腔發展輕巧且穩定的高功率摻鈦晶體雷射，同時利用非線性轉換的技術進一步產生波長範圍涵蓋人眼安全至紫外以及深紫外波段的雷射光源。我們考慮了熱透鏡效應，被動式 Q 開關準則以及寄生雷射效應優化了被動式以及主動式 Q 開關摻鈦釩酸釔晶體雷射的輸出尖峰功率。我們也針對摻鈦氟化釔鋰晶體雷射提出了數個新穎且簡便的方法來實現高功率且高能量的被動式 Q 開關雷射。利用脈衝式激發以及聲光晶體，我們更進一步在摻鈦氟化釔鋰晶體雷射實現重複率可調的 Q 開關動作。

接著，我們設計了一個能夠針對腔內光學參數震盪器單獨優化且不影響基頻光光路的新穎共振腔，同時輔以被動式 Q 開關摻鈦釩酸釔晶體雷射作為基頻光來大幅提升人眼安全雷射的輸出特性。運用相同的設計理念，我們也以摻鈦氟化釔鋰晶體設計了輕巧且高效率的高能量人眼安全雷射；同時發現熱引起的雙折射效應是使等向性增益介質能夠實現有效腔內非線性轉換的主要機制。

利用優化過後的摻鈦晶體近紅外雷射搭配腔外諧波產生的技術，我們也進一步產生波長範圍落在綠光、紫外光、以及深紫外波段的雷射光源。在相同的環境條件下，我們比較了腔外以及腔內架構在產生二倍頻綠光時的轉換效率。我們接著以腔外三倍頻以及四倍頻的方法有效地產生瓦級的紫外以及深紫外波段的高功率光源。本論文所完成的高效率非線性轉換不只讓我們可以產生波長範圍涵蓋人

眼安全至紫外以及深紫外波段的雷射光源，同時並驗證了我們在優化高功率摻釹晶體雷射所設計的理念。

High-Power Nd-doped Crystal Lasers with Nonlinear Frequency Conversion from Eye-Safe to UV and DUV Regimes

Student：Yu-Jen Huang　　Advisor：Prof. Yung-Fu Chen

Department of Electrophysics
National Chiao Tung University

ABSTRACT

The aim of this thesis is focused on developing compact reliable Nd-doped crystal lasers near 1 μm based on linear cavity configuration, and these optimized near infrared lasers are subsequently applied for several nonlinear frequency conversions to effectively extend the spectrum from eye-safe to deep ultraviolet regimes. First of all, we take into account of the thermal-lensing effect, second threshold condition, and parasitic lasing effect to optimize high-peak-power Nd:YVO_4 lasers at 1064 nm in the passively and actively Q-switched operations. We also propose practical and unique methods to successfully accomplish power scale-up of high-energy passively Q-switched 1053-nm laser with either a-cut or c-cut Nd:YLF crystals. Pulsed operations with continuously adjustable pulse repetition rate are further realized with pulsed pumped passively Q-switched and continuously pumped actively Q-switched Nd:YLF lasers.

Then, we develop a separable monolithic cavity for intracavity optical parametric oscillator to remarkably improve the performance of the Nd:YVO_4/Cr^{4+}:YAG/KTP eye-safe laser at 1572 nm. The same design concept is also employed for achieving a compact and efficient high-energy Nd:YLF eye-safe laser at 1552 nm. Besides, we experimentally find that the thermally induced birefringence can lead the mutually orthogonal polarization states of the fundamental pulses to be effectively switched for accomplishing an efficient nonlinear frequency conversion without any additional polarization control.

Finally, the optimized Q-switched Nd-doped crystal lasers are employed to produce green, ultraviolet, and deep ultraviolet radiations via extracavity harmonic generations. We first compare the output performance between the extracavity and intracavity second harmonic generations at 532 nm under a similar operated condition. We further perform extracavity third and fourth harmonic generations to effectually produce ultraviolet waves at 355 and 351 nm as well as deep ultraviolet radiation at 266 nm with output powers up to several watts. Efficient nonlinear frequency conversions not only enable us to produce the emission wavelengths from eye-safe to deep ultraviolet regions, but also confirm the usefulness of our cavity design for Q-switched lasers at 1 μm.

誌謝

時光匆匆，還記得剛進實驗室就陸續在看過去實驗室學長姐的碩博士論文來學習東西，每次在翻他們的論文，總是會想多看看誌謝在寫些甚麼東西，沒想到，多年後的今天，我也開始在撰誌謝的稿要怎麼寫，哈哈。想當初，在高中畢業的時候其實對於大學科系不是那麼的了解，幾番考量後想要好好加強自己基礎學科的能力而進入了電物系，也在大一的普物課遇到了現在的指導老師陳永富教授。記得那時候只覺得陳老師每次都教蠻多東西的，因此上課我都要趕快去搶前面的座位來好好專心聽講，對於有些真的難以理解的內容有時也只能將疑惑擱在心裡，期待哪一天我能有天外飛來一筆的靈光飛進我腦海裡。隨著日子過去，上過許多老師的課程，感覺陳老師整體的學識風範著實令我著迷，再加上我本來就對光電科學有興趣，所以就在大三跟著陳老師做專題研究直到現在完成了博士學位。這麼多年過去了，心中一直很感謝陳老師願意擔任我的指導教授，親自帶著我做實驗、觀察每一個實驗現象、解決我課業研究上的疑惑、訂正我所寫的每一篇論文、願意分享他所經歷過的事情、以及待人處事之道等等。陳老師對於我，不只是帶著我做研究的指導教授，就某些層面來說，更像是我的爸爸，關心我的日常生活。我想，這份刻骨銘心的恩情是怎麼還也還不完的，不過還是要在這裡誠心的跟陳老師說一聲”謝謝您”！也要謝謝黃凱風老師，施宙聰老師，賴暎杰老師，蔡宗祐老師，林志平博士，陳彥宏老師，以及謝文峰老師撥空來擔任我的博士資格考以及畢業口試委員，並給予了我相當多的建議與寶貴意見。

能順利完成我的博士學位，也要感謝固態雷射實驗室眾多學長姐弟妹的幫忙。感謝蘇老大能幫忙解決許多我不是那麼清楚的研究問題；感謝建誠和興弛學長帶我踏入實驗室所研究的物理及固態雷射的世界，跟你們討論研究和一起打球總是非常的快樂愉悅；感謝依萍學姊這幾年來的照顧，在我們還不是那麼熟的時候願意幫我爭取到專班工讀生的打工機會，也願意一同討論並分享研究上的心得以及生活上的點點滴滴；感謝亭樺學姊、雅婷學姊、仕璋學長、哲彥學長、漢龍學長、鈺婷學姊以及彥廷學長所給予的照顧與幫忙；感謝今年一起畢業的威哲學長、毅帆學長、柏毅學長、文政學長、毓捷以及建至平常相互之間的切磋與鼓勵，尤其要封給威哲學長一個”實驗室最快的男人”稱號 XD；感謝易純、映舜、政猷、

必輝、俊佑、家翰、承曄、昱辰、啟平、國維、威霖、凱勝、茗婷、容辰、泰緯、昕翰、育廷、純甫等眾多學弟妹們的支持與愛戴，為我實驗室的生活添加了許多歡樂；感謝我所指導及認識的專班學生：榮輝、士瑋、瑋倫、昇晁、淑雅、玉楓、鳳蘭等等，我們之間的教學相長，也讓我受益良多；還要謝謝我求學路上所有給予我幫助的老師及朋友；當然更不能忘了總是在背後支持我的媽媽、姊姊以及阿姨等家人，感謝您們極大的寬容與細心的呵護，讓我能無憂無慮的完成我的博士學位；感謝懿萱這六年來的包容與照顧，讓我的身邊永遠都有一個人陪伴，接下來的日子裡，就換我照顧妳們嚕；我也要感謝一下我自己，能夠咬緊牙關克服許多大大小小的身心問題，不過也因為經歷了這些風風雨雨，讓我心智成熟了許多，但是身體卻要好好來保養照顧一下了，哈哈。

仔細回想起過去，說來也真奇妙，我高中時所做的專題題目就是"雷射"，而我現在的專長也恰好是固態"雷射"。會遇到甚麼樣的人、碰到怎麼樣的事，真的是很多都是冥冥中注定，回憶起來真的是不禁讓人莞爾而笑，呵。我想，拿到博士學位只是一個短暫的里程碑，未來還有許多值得我要去努力加油的地方，我會好好利用接下來三年研發替代役的時間繼續磨練自己，補強自己的不足，繼續燃燒我對學術研究的熱情，朝我的目標邁進，不辜負大家對我的期望與恩情！

Contents

List of Figures

Chapter 1

Chapter 2

Chapter 3

Chapter 4

List of Tables

Chapter 5

List of Abbreviations

IR	infrared
Nd	neodymium
UV	ultraviolet
SHG	second harmonic generation
THG	third harmonic generation
DUV	deep ultraviolet
PQS	passively Q-switched
AQS	actively Q-switched
IOPO	intracavity optical parametric oscillator
ESHG	extracavity second harmonic generation
ISHG	intracavity second harmonic generation
EFHG	extracavity fourth harmonic generation
ROC	radius of curvature
AR	antireflection
CW	continuous-wave
AO	acousto-optic
ETU	energy-transfer upconversion
FWHM	full width at half maximum
ETHG	extracavity third harmonic generation

List of Symbols

N	population inversion density inside the gain medium
r	pumping rate
c	light speed
σ	stimulated emission cross section of the gain medium
ϕ_p	intracavity photon density
τ	upper-state lifetime of the gain medium
l_{cry}	crystal length
L_{cav}	cavity length
Ω	fraction of spontaneous emission contributing to the laser emission
t_r	round trip time
t	time
τ_{cav}	decay time for photon in the resonator
R_{OC}	reflectivity of the output coupler
L_s	cavity loss
$\vec{P}$	induced polarization for a given optical material
$\vec{E}$	applied electric field
ε_0	permittivity of free space
$\chi^{(i)}$	ith-order nonlinearities
T_0	initial transmission of the saturable absorber
σ_{gsa}	ground-state absorption of the saturable absorber
A, A_s	laser mode area in the laser crystal and that in the saturable absorber
γ	population inversion reduction factor,
β	the ratio of the excite excited-state absorption cross section to the ground-state absorption cross section of the saturable absorber
g^*	equivalent g-parameters
L_{cav}^*	equivalent cavity length
f_{th}	effective thermal focal length
d_1, d_2	the optical path lengths from the center of the gain medium to the input mirror and output coupler
R_1, R_2	radius of curvature of the input mirror and output coupler

ξ	fraction of the incident pump power that results in heat
P_{in}	incident pump power
K_c	thermal conductivity
α	absorption coefficient
λ_p	pump wavelength
dn/dT	thermal-optic coefficient
n	refractive index
α_T	thermal expansion coefficient
M^2	pump beam quality factor
$\omega_p(z)$	variation of the pump radius
ω_{po}	pump beam waist
z_0	distance from the entrance of the laser crystal
ϕ_b	average photon density caused by parasitic lasing
θ_ω	wedged angle
ϕ_t	tilting angle
n_σ, n_π	refractive indices for the σ- and π-polarizations
ω_1, ω_2	cavity mode radii at the input mirror and at the output coupler
C	proportional constant representing the extent of the thermal-lensing effect
f	pulse repetition rate
$P_{horizontal}$, $P_{vertical}$	output power with the oscillated polarization to be parallel and perpendicular to the base of the AO Q-switch
R_s	reflectivity at signal wavelength
N	population inversion density inside the gain medium
r	pumping rate
c	light speed

Chapter 1

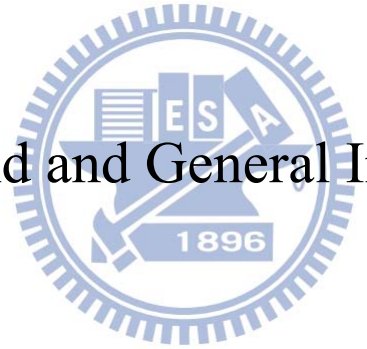

Background and General Introduction

1.1 Diode-Pumped Solid-State Laser

Diode-pumped solid-state laser is a laser made by pumping a solid gain medium with a semiconductor laser diode. The first experimental realization of diode-pumped solid-state laser was in 1964, where the U:CaF_2 crystal was pumped by the GaAs diode laser at a temperature of 4 K [1]. It was not until 1972 that the first diode-pumped solid-state laser at room temperature was achieved with the Nd:YAG crystal [2]. However, diode-pumped solid-state laser was still under relatively slow development until 1980-1990s, where the rapid advance and growing maturity of high-power, efficient, reliable laser diode and diode laser array lead to a renaissance of diode-pumped solid-state laser [3]. Since then, diode-pumped solid-state laser has made significant progress, and many excellent reviews have been given to comprehensively discuss the contemporary development and status of diode-pumped solid-state laser [4-14].

Compared with the traditionally lamp-pumped systems, the major advantages of the diode-pumping include:

1. Increased component lifetime (20000 hrs vs. 500 hrs or 10^9 shots vs. 10^7 shots).
2. Increased overall system efficiency (wall-plug efficiency: 10 % vs. 1 %).
3. Improved beam quality.
4. Enabling technology for compact, reliable, robust and versatile laser system.
5. Enabling technology for new laser materials.
6. Benign operating features of the laser diode such as good amplitude and spectral stability, low voltage operation, and so on.
7. Increased pulse repetition rate.

Although the laser diode can itself be used in a number of applications, the solid-state laser have several advantages over the laser diode. For example, the solid-state laser can operate in wavelength ranges via nonlinear frequency conversion where the laser diode neither is available nor has good performance. In addition, the radiation from high-power diode laser array is only partially coherent, while the output from the solid-state laser pumped by high-power laser diode can potentially achieve a nearly diffraction-limited beam with higher radiance and singly coherent emission. The

solid-state laser can store energy in the upper-state level to efficiently generate high-energy and high-peak-power giant pulses which can not be attained from the laser diode. The solid-state laser can also have a narrower linewidth than the laser diode with the same output power. Another feature is the insensitivity of output performance of solid-state laser to the temperature, while the laser diode has strong dependence (0.3 nm/K) between the emission wavelength and temperature.

The gain medium for diode-pumped solid-state laser consists of two parts, one is the host material, the other is the active ion [15]. To date, a large number of host materials have been investigated including glasses, oxides, sapphire, garnets, aluminate, oxysulfide, phosphates, silicates, tunstates, molybdates, vanadates, beryllates, fluorides, and ceramics etc. Generally speaking, the host material must have good optical, mechanical, and thermal properties to endure severe operating conditions for practical applications. On the other hand, the electron transition in the active ion determines the spectroscopic properties of the specific laser crystal, such as the output wavelength, upper-state lifetime, stimulated emission cross section, gain bandwidth and so on.

The rare earth ions are natural candidates to act as active ions in the solid-state laser because they exhibit a wealth of sharp fluorescent transitions covering the spectrum from visible to infrared (IR) regimes. Electronic structures of energy levels for various trivalent rare earth ions are illustrated in Fig. 1.1.1 [16]. Neodymium (Nd) is the first of the trivalent rare earth ions to be used in the solid-state laser [17], and it remains by far the most important element to achieve a highly efficient laser operation among all of active ions. The detailed energy level diagram for the Nd:YVO_4 crystal is depicted in Fig. 1.1.2 with indications of the possible excitation wavelengths as well as the potential emission lines. Note that the actual positions of individual Stark levels depend on the host materials due to different crystal field interactions. It can be found that the AlGaAs laser diodes with emission lines at 808 and 880 nm are suitable to be used as pump sources for the Nd-doped crystals, corresponding to the conventional pumping ($^4I_{9/2} \rightarrow {}^4F_{5/2}$) and direct in-band pumping ($^4I_{9/2} \rightarrow {}^4F_{3/2}$) [18-25]. On the other hand, the stimulated emission in the Nd-doped crystal can be categorized into three different groups with output wavelengths centered around 0.9, 1.06, and 1.3 μm, corresponding to the transition levels from $^4F_{3/2}$ to $^4I_{9/2}$, $^4I_{11/2}$, $^4I_{13/2}$, respectively. In this thesis, we will focus on the studies of two of widely used Nd-doped laser crystals; that is to say, the Nd:YVO_4 and Nd:YLF crystals.

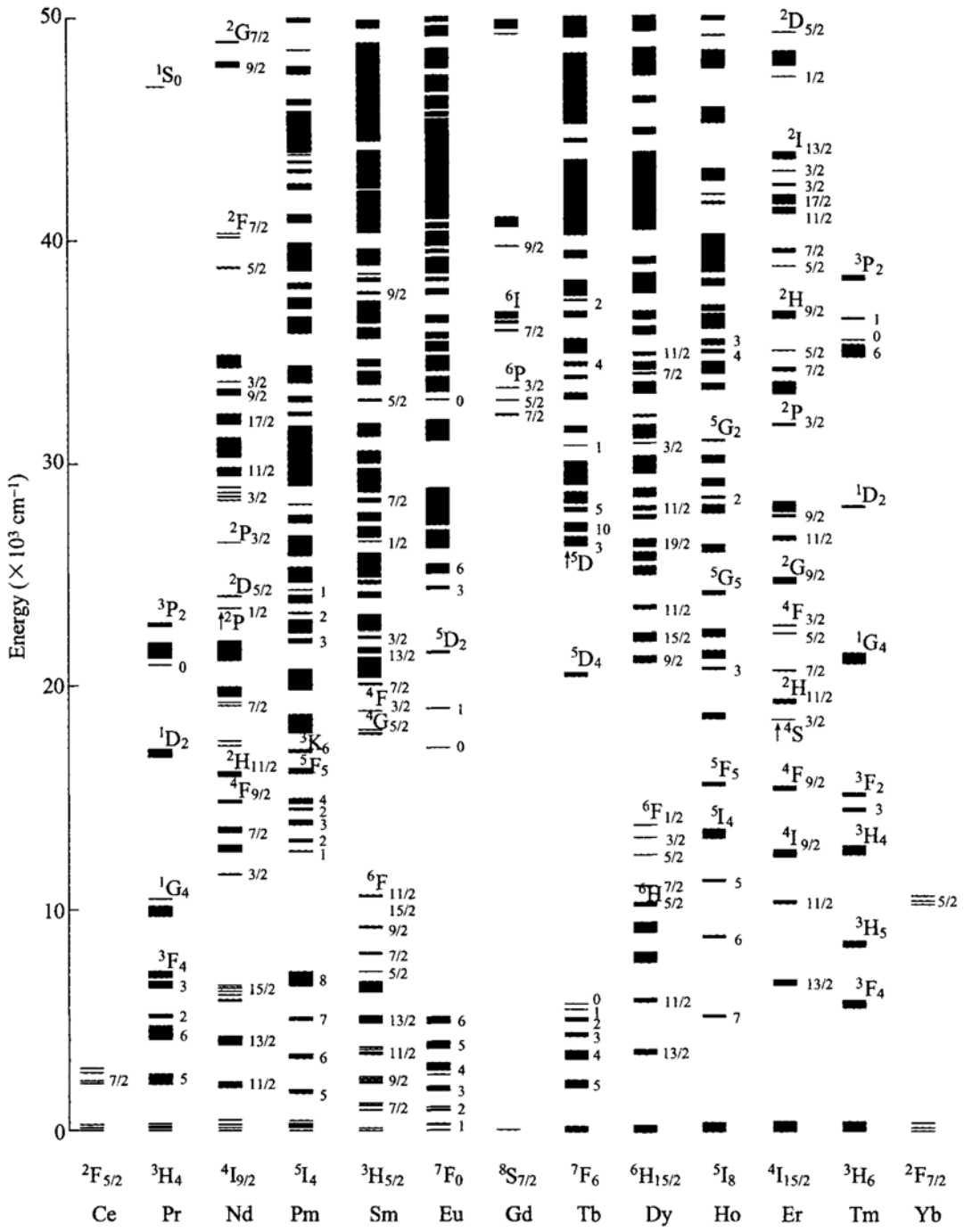

Fig. 1.1.1. Electronic structures of energy levels for various trivalent rare earth ions.

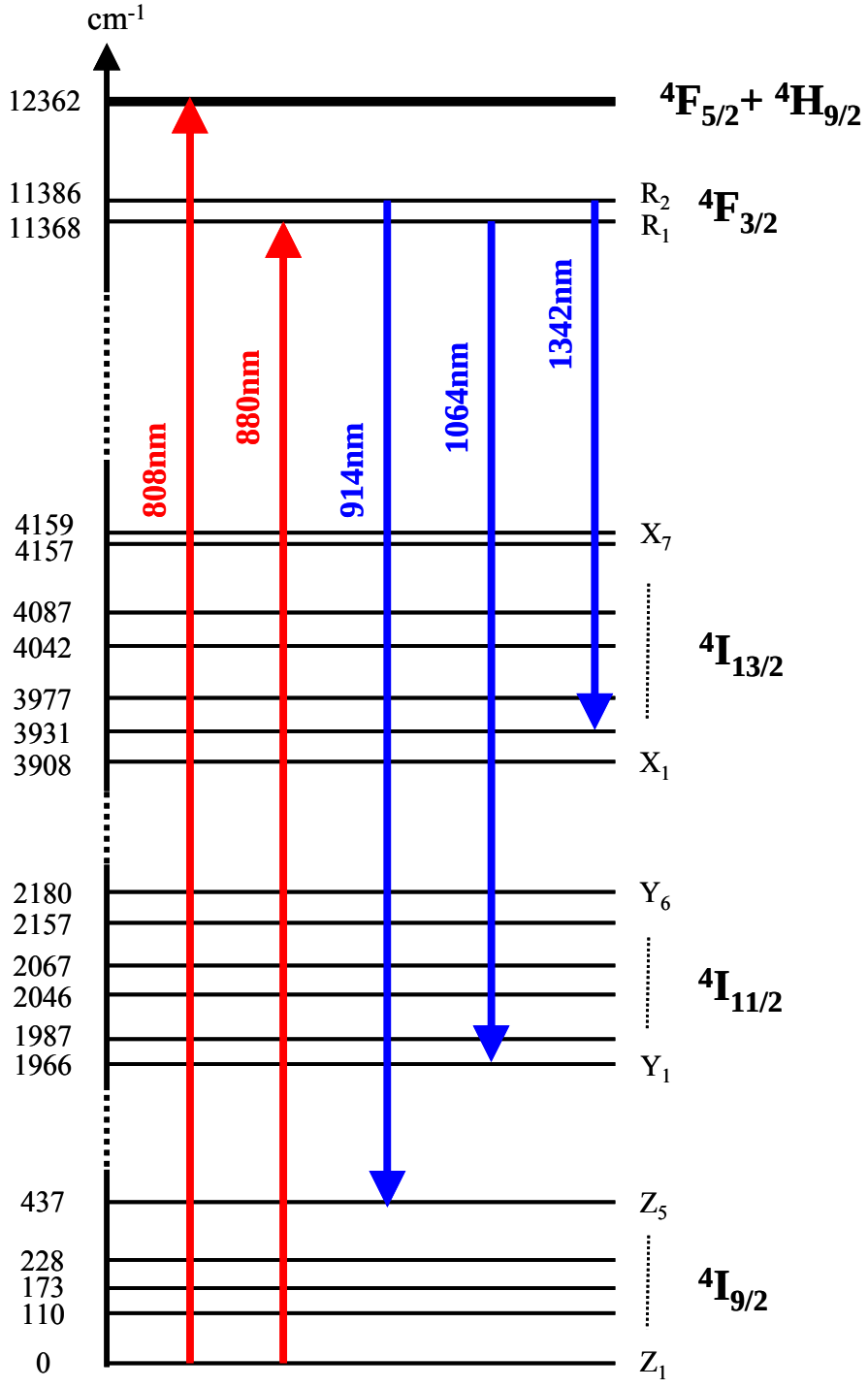

Fig. 1.1.2. Detailed energy level diagram for the Nd:YVO_4 crystal with indications of the possible excitation wavelengths as well as the potential emission lines.

1.2 Q-Switching

By periodically modulating the cavity loss, the generation of high-energy giant pulses with durations of a few nanoseconds can be achieved [26,27]. This method is called Q-switching. In the technique of Q-switching, the energy is initially stored in the gain medium with the prevention of laser emission by keeping the resonator loss high. That is, the cavity Q is maintained at a low value. Note that the word "Q" means the quality factor, which is defined as the ratio of the energy stored in the cavity to the energy loss per round trip. When the resonator loss is suddenly reduced, the accumulated gain is considerably higher than the threshold value. As a result, the stored energy is quickly released in the form of a very intense and short light pulse until the gain is saturated and the intracavity power decreases again. Figure 1.2.1(a) depicts the population inversion density, intracavity photon density, and resonator loss as a function of time during the development of a Q-switched laser pulse.

The temporal behaviors for the population inversion density, intracavity photon density, and resonator loss can be readily simulated with the conventional coupled rate equations as follows:

$$\frac{dN}{dt} = r - c\sigma N\phi_p - \frac{N}{\tau}, \tag{1.1}$$

$$\frac{d\phi_p}{dt} = c\sigma N\phi_p \frac{l_{cry}}{L_{cav}} - \frac{\phi_p}{\tau_{cav}} + \frac{N}{\tau}\Omega, \tag{1.2}$$

$$\tau_{cav} = \frac{t_r}{\ln\left(\frac{1}{R_{OC}}\right) + L_s}, \tag{1.3}$$

where N is the population inversion density inside the gain medium, t is the time, r is the pumping rate, c is the light speed, σ and τ are the stimulated emission cross section and upper-state lifetime of the gain medium, ϕ_p is the intracavity photon density, l_{cry} and L_{cav} are the crystal and cavity lengths, τ_{cav} is the decay time for photon in the resonator, t_r is the round trip time, R_{OC} is the reflectivity of the output coupler, L_s is the cavity loss, and Ω accounts for the fraction of spontaneous emission contributing to the laser emission. By numerically solving the Eqs. (1.1)-(1.3) with a periodically step function for the cavity loss, the temporal dynamics for the population inversion density and intracavity photon density during the continuously pumped, repetitively Q-switched

process can be sketched. Figure 1.2.1(a) illustrates the relationship among the population inversion density, intracavity photon density, resonator loss and time for the generation of a single Q-switched laser pulse, while a train of giant pulses is displayed in Fig. 1.2.1(b).

For producing large pulse energy, a high energy capability of the gain medium is highly desirable. One of the promising characteristics for the solid-state laser over other types of light sources is the long upper-state lifetimes for bulk crystals. Therefore, a solid-state laser can store the energy from the pump source for several hundred microseconds, and subsequently emits an intense pulse with a peak power nearly four orders of magnitude greater than the pump power. After the first demonstration of the Q-switched operation with the Ruby crystal [28], high-energy and high-peak-power Q-switched pulsed lasers with a large variety of solid-state crystals have been widely investigated and realized with active or passive approaches.

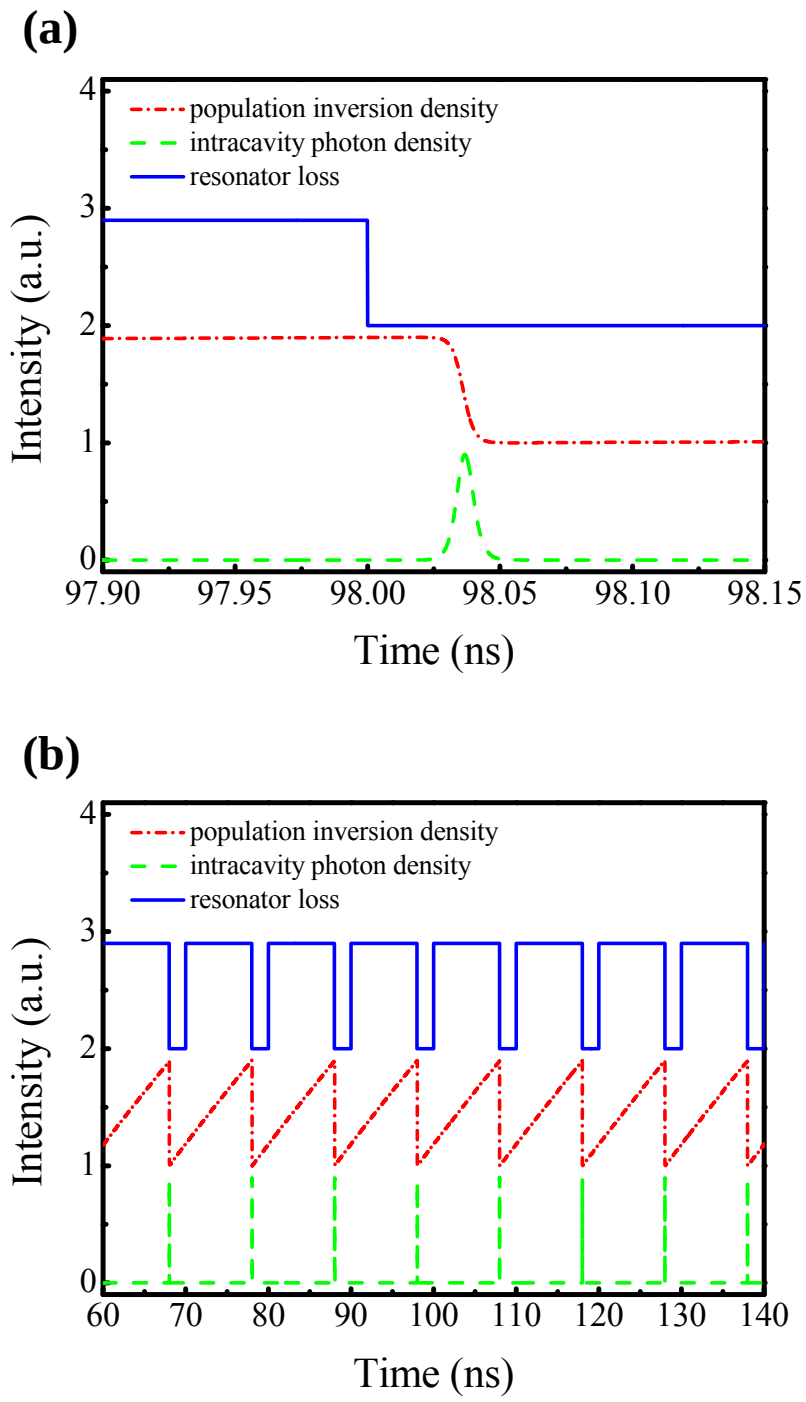

Fig. 1.2.1. Population inversion density, intracavity photon density, and resonator loss as a function of time for continuously pumped Q-switched operation.

1.3 Nonlinear Frequency Conversion

Since the unexpected ultraviolet (UV) light at twice the frequency of the Ruby laser was observed in 1961 [29], a large number of investigations on the nonlinear optical response of the optical medium have been extensively made. In general, the induced polarization $\vec{P}$ for a given optical material depends on the applied electric field $\vec{E}$, which can be expanded in a power series of electric field strength as [30,31]:

$$\vec{P} = \varepsilon_0 \chi^{(1)} \vec{E} + \varepsilon_0 \chi^{(2)} \vec{E}\vec{E} + \varepsilon_0 \chi^{(3)} \vec{E}\vec{E}\vec{E} + \cdots = \vec{P}^{(1)} + \vec{P}^{(2)} + \vec{P}^{(3)} + \cdots \quad (1.4)$$

where ε_0 is the permittivity of free space, $\chi^{(1)}$ is the linear susceptibility representing the linear response of the material, $\chi^{(2)}$ and $\chi^{(3)}$ are the second- and third-order nonlinearities accounting for the nonlinear responses of the material. From the wave equation, a time-varying polarization can act as the source of new components of the electric field:

$$\nabla^2 \vec{E} - \frac{1}{c^2}\frac{\partial \vec{E}^2}{\partial t^2} = \frac{1}{\varepsilon_0 c^2}\frac{\partial \vec{P}^2}{\partial t^2} \quad (1.5)$$

with the expression of Eq. (1.4), linear and several nonlinear responses can be described. For example, $\vec{P}^{(1)}$ describes the propagation of a wave in a linear medium rather than a vacuum. $\vec{P}^{(2)}$ is responsible for the optical rectification, second harmonic generation (SHG), sum and difference frequency generations, and optical parametric amplification. $\vec{P}^{(3)}$ explains the phenomena of third harmonic generation (THG), optical Kerr effect, stimulated Raman scattering, and stimulated Brillouin scattering.

Lasers with different wavelengths can find their unique usefulness in scientific research and industrial fields [32-36]. Nonlinear frequency conversion provides an useful means for extending the spectral range of available solid-state laser sources when the polarization state and the direction of the beam propagation are specifically designed to satisfy the phase matching condition. Figure 1.3.1 conceptually illustrates the feasible fundamental emissions and possible wavelength extensions for the Nd:YLF crystal via several nonlinear frequency conversion processes. With the improved quality of the nonlinear crystal as well as the great advance of the laser engineering, a number of light sources from eye-safe to UV and deep UV (DUV) regimes based on the combination of the nonlinear frequency conversion and diode-pumped solid-state laser are well developed and are becoming commercially available. For example, AVIA-series lasers manufactured by Coherent Inc. can supply the maximum output power of 45 W at 532

nm and 28 W at 355 nm with the pulse repetition rate ranging from 30 to 300 kHz [37]. Another well-known laser supplier, JDSU Inc., designs Q-series products for meeting a wide variety of industrial applications. Depending on the slightly different operating conditions, the Q-series products at 355 nm can work in the range 10-130 kHz with the maximum output power of 12 W, while the ones at 532 nm can operate in the range 5-60 kHz with the maximum output power of approximately 16 W [38].

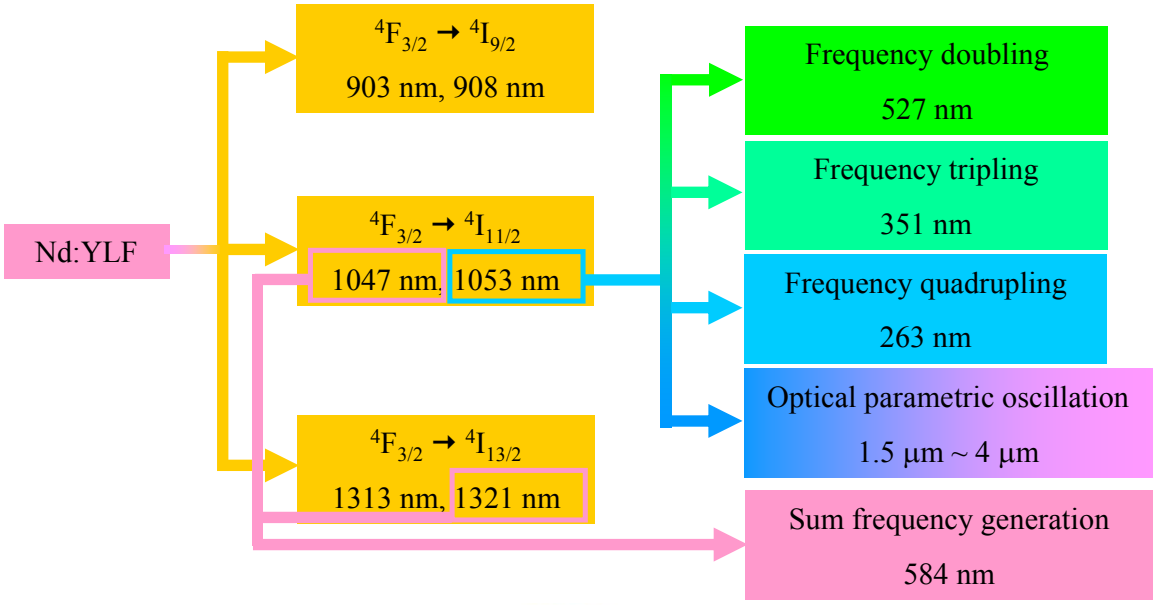

Fig. 1.3.1. Feasible fundamental emissions and possible wavelength extensions for the Nd:YLF crystal via several nonlinear frequency conversion processes.

1.4 Overview of Thesis

This thesis is organized as follows. Chapter 1 gives the general introduction to the property and development of diode-pumped solid-state laser. Operation principles for Q-switching and nonlinear frequency conversion are also addressed.

Then, the features of commonly used Nd:YVO_4 and Nd:YLF crystals are briefly discussed in 2.1 and 2.4, respectively. For the Nd:YVO_4 crystal, we take into account of the thermal-lensing effect and second threshold condition to design a high-peak-power passively Q-switched (PQS) laser at 1064 nm with the Cr^{4+}:YAG crystal as a saturable absorber. We also consider the parasitic lasing effect and thermal-lensing effect to optimize a high-peak-power actively Q-switched (AQS) Nd:YVO_4 laser at 1064 nm. As for the Nd:YLF crystal, a novel method is proposed to efficiently select the σ-polarization at 1053 nm in the a-cut crystal, and the PQS performance with the Cr^{4+}:YAG crystal is systematically investigated for various output couplings. We further present a practical tactic to scale up the pulse energy of the continuously pumped PQS laser at the $^4F_{3/2} \rightarrow {}^4I_{11/2}$ transition with the c-cut Nd:YLF crystal. Pulsed pumping is subsequently utilized to reduce the thermal effect and improve the timing jitter of a mJ- and ns-level PQS Nd:YLF/Cr^{4+}:YAG laser. AQS operation in the Nd:YLF crystal is also realized to provide a sequence of giant pulses with continuously adjustable pulse repetition rate. It is worthwhile to mention that all of above-mentioned achievements are optimized on the basis of extremely simple and compact linear cavity configurations.

In previous studies on the eye-safe radiations obtained from the Nd-doped crystal lasers, shared and coupled cavity configurations for intracavity optical parametric oscillator (IOPO) are adopted. However, the fundamental IR and eye-safe cavities can not be optimized independently, which in turn restricts the optical conversion efficiency and long-term stability. In Chap. 3, we develop a separable monolithic IOPO cavity to remarkably improve the performance of the PQS Nd:YVO_4/Cr^{4+}:YAG/KTP eye-safe laser at 1572 nm. With the same concept, we demonstrate a compact and efficient high-energy AQS Nd:YLF eye-safe laser at 1552 nm. In addition, it is found that the thermally induced birefringence can lead the mutually orthogonal polarization states of the fundamental IR pulses to be effectively switched for accomplishing an efficient IOPO operation without any extra polarization control.

In Chap. 4, the optimized Q-switched Nd-doped crystal lasers designed in Chap. 2 are employed to produce green, UV, and DUV radiations via extracavity harmonic generations. Firstly, the output performance between the extracavity and intracavity SHGs (ESHG and ISHG) at 532 nm under a similar operated condition is thoroughly explored with the type-I LBO crystal as a frequency doubler. Secondly, with the type-I and type-II LBO crystals as a frequency doubler and a frequency tripler, highly efficient UV emissions at 355 and 351 nm are obtained from the high-power Nd:YVO_4 lasers and high-energy Nd:YLF laser, respectively. Thirdly, the green lasers based on ESHG and ISHG are utilized as pump sources to make a comparison of the conversion efficiencies for producing 266-nm radiations, where the BBO crystal is exploited in the process of extracavity fourth harmonic generation (EFHG). Efficient nonlinear frequency conversions demonstrated in Chaps. 3 and 4 not only enable us to extend the emission lines from IR to eye-safe, green, UV, and DUV regimes, but also validate the usefulness of our cavity design for Q-switched IR lasers developed in Chap. 2.

Finally, a summary is given in Chap. 5 to conclude this thesis. Future plans and prospects are also described in this chapter with the aim for completing this doctoral thesis.

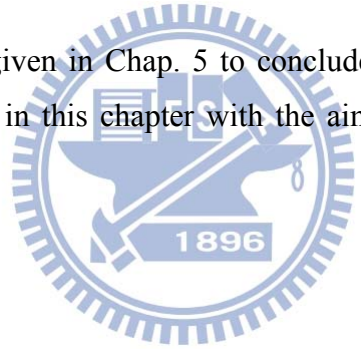

References

[1] R. L. Keyes and T. M. Quist, "Injection luminescent pumping of $CaF_2:U^{3+}$ with GaAs diode lasers," Appl. Phys. Lett. **4**, 50-52 (1964).

[2] H. G. Danielmeyer and F. W. Ostermayer, "Diode-pumped-modulated Nd:YAG laser," J. Appl. Phys. **43**, 2911-2913 (1972).

[3] W. Streifer, D. R. Scifres, G. L. Harnagel, D. F. Welch, J. Berger, and M. Sakamoto, "Advances in diode laser pumps," IEEE J. Quantum Electron. **24**, 883-894 (1988).

[4] R. L. Byer, "Diode laser-pumped solid-state lasers," Science **239**, 742-747 (1988).

[5] T. Y. Fan and R. L. Byer, "Diode laser-pumped solid-state lasers," IEEE J. Quantum Electron. **24**, 895-912 (1988).

[6] T. Y. Fan, "Diode-pumped solid state lasers," The Lincoln Laboratory Journal **3**, 413-426 (1990).

[7] B. D. Sinclair and M. H. Dunn, "All-solid-state lasers," Phys. Educ. **29**, 146-150 (1994).

[8] K. L. Schepler, "Trends in solid-state lasers," Opt. Photon. News **8**, 38-41 (1997).

[9] A. Leuzinger, "The evolution of diode-pumped solid-state lasers," Opt. Photon. News **10**, 37-40 (1999).

[10] Z. Jankiewicz and K. Kopczynski, "Diode-pumped solid-state lasers," Opto-Electron. Rev. **9**, 19-33 (2001).

[11] D. C. Brown and J. W. Kuper, "Solid-state lasers: steady progress through the decades," Opt. Photon. News **20**, 36-41 (2009).

[12] B. Davarcioglu, "An overview of diode pumped solid state (DPSS) lasers," Int. Arch. Appl. Sci. Technol. **1**, 1-12 (2010).

[13] G. Huber, C. Kränkel, and K. Petermann, "Solid-state lasers: status and future," J. Opt. Soc. Am. B **27**, B93-B105 (2010).

[14] W. Koechner, *Solid-State Laser Engineering*, 6th edn. (Springer, Berlin, 2006).

[15] W. Koechner, *Solid-State Laser Engineering*, 6th edn. (Springer, Berlin, 2006), Chap. 2.

[16] G. Liu, *Spectroscopic Properties of Rare Earths in Optical Materials*, (Springer,

Berlin, 2005), Chap. 1.

[17] J. E. Geusic, H. M. Marcos, and L. G. Van Uitert, "Laser oscillations in Nd-doped yttrium aluminum, yttrium gallium and gadolinium garnets," Appl. Phys. Lett. **4**, 182-184 (1964).

[18] V. Lupei, N. Pavel, and T. Taira, "Highly efficient laser emission in concentrated Nd:YVO_4 components under direct pumping into the emitting level," Opt. Commun. **201**, 431-435 (2002).

[19] Y. Sato, T. Taira, N. Pavel, and V. Lupei, "Laser operation with near quantum-defect slope efficiency in Nd:YVO_4 under direct pumping into the emitting level," Appl. Phys. Lett. **82**, 844-846 (2003).

[20] P. Zhu, D. Li, P. Hu, A. Schell, P. Shi, C. R. Haas, N. Wu, and K. Du, "High efficiency 165 W near-diffraction-limited Nd:YVO_4 slab oscillator pumped at 880 nm," Opt. Lett. **33**, 1930-1932 (2008).

[21] N. Pavel, T. Dascalu, N. Vasile, and V. Lupei, "Efficient 1.34-μm laser emission of Nd-doped vanadates under in-band pumping with diode lasers," Laser Phys. Lett. **6**, 38-43 (2009).

[22] X. Ding, R. Wang, H. Zhang, X. Y. Yu, W. Q. Wen, P. Wang, and J. Q. Yao, "High-efficiency Nd:YVO_4 laser emission under direct pumping at 880 nm," Opt. Commun. **282**, 981-984 (2009).

[23] J. Gao, X. Yu, B. Wei, and X. D. Wu, "Quasi-three-level Nd:YVO_4 laser operation at 914 nm under 879 nm diode laser pumping," Laser Phys. **20**, 1590-1593 (2010).

[24] Y. F. Lü, X. H. Zhang, X. D. Yin, J. Xia, A. F. Zhang, and J. Q. Lin, "Highly efficient continuous-wave intracavity frequency-doubled Nd:YVO_4-LBO laser at 457 nm under diode pumping into the emitting level $^4F_{3/2}$," Appl. Phys. B **99**, 115-119 (2010).

[25] L. Cui, H. L. Zhang, L. Xu, J. Li, Y. Yan, P. F. Sha, L. P. Fang, H. J. Zhang, J. L. He, and J. G. Xin, "880 nm laser-diode end-pumped Nd:YVO_4 slab laser at 1342 nm," Laser Phys. **21**, 105-107 (2011).

[26] W. Koechner, *Solid-State Laser Engineering*, 6th edn. (Springer, Berlin, 2006), Chap. 8.

[27] R. Paschotta, *Field Guide to Lasers*, (SPIE, Bellingham, Washington, 2007).

[28] F. J. McClung and R. W. Hellwarth, "Giant optical pulsations from Ruby," Appl. Opt. **1**, 103-105 (1962).

[29] P. A. Franken, A. E. Hill, C. W. Peters, and G. Weinreich, "Generation of optical harmonics," Phys. Rev. Lett. **7**, 118-119 (1961).

[30] W. Koechner, *Solid-State Laser Engineering*, 6th edn. (Springer, Berlin, 2006), Chap. 10.

[31] R. W. Boyd, *Nonlinear optics*, 3rd edn. (Elsevier, London, 2008).

[32] M. J. Weber, *Handbook of laser wavelengths*, (CRC, New York, 1999).

[33] http://en.wikipedia.org/wiki/List_of_laser_types

[34] http://www.laserfest.org/lasers/innovations.cfm

[35] http://www.rp-photonics.com/laser_applications.html

[36] http://www.photonics.com/LinearCharts/Default.aspx?ChartID=1

[37] http://www.coherent.com/Products/index.cfm?868/AVIA-Family-of-DPSS-Lasers

[38] http://www.jdsu.com/en-us/Lasers/Products/A-Z-Product-List/Pages/laser-solid-state-q-switched-355-532-q-series.aspx


E
S
A
1896


E S A
1896

Chapter 2

Fundamental IR Lasers with Nd-doped Crystals

2.1 Properties of Nd:YVO_4 Crystal

Nd-doped yttrium vanadate (Nd:YVO_4) is an important laser material which was first recognized in 1966 [1], and efficient diode-pumped Nd:YVO_4 laser was successfully demonstrated in 1987 [2]. Basic properties of the Nd:YVO_4 crystal are illustrated in Fig. 2.1.1, which is obtained from CASTECH [3]. The Nd:YVO_4 crystal belongs to the tetragonal group in crystal structure. The natural birefringence of this uniaxial crystal dominates the thermally induced birefringence, and subsequently the linearly polarized output can eliminate the undesirable thermal depolarization loss in the high-power operation, which is frequently observed in optically isotropic laser crystals such as the Nd:YAG crystal. Optical properties of the Nd:YVO_4 crystal are strongly polarization dependent, which can be classified as π-polarization (extraordinary beam) and σ-polarization (ordinary beam). The π- and σ-polarizations are defined as the oscillated polarizations of the light to be parallel and perpendicular to the crystallographic c axis, respectively. Unlike the Nd:YAG crystal, the Stark splitting in the Nd:YVO_4 crystal is small and the multiple transitions are more compact. These lead the Nd:YVO_4 crystal to possess the outstanding features over other Nd-doped crystals; that is, the large absorption coefficient around 808 nm and high stimulated emission cross section at 1064 nm. The former property allows the use of short crystal to efficiently absorb the incident pump light for the construction of a compact microchip laser, while the latter one is inherently suitable for developing a high-repetition-rate pulsed laser.

Crystal Structure: Cell Parameter:	Zircon Tetragonal, space group D_{4h}-I4/amd a=b=7.1193 Å, c=6.2892 Å
Density:	4.22g/cm^3
Atomic Density:	1.26x10^{20} atoms/cm^3 (Nd 1.0%)
Mohs Hardness:	4-5 (Glass-like)
Thermal Expansion Coefficient (300K):	α_a=4.43x10^{-6}/K α_c=11.37x10^{-6}/K
Thermal Conductivity Coefficient (300K):	//C: 0.0523W/cm/K ⊥C: 0.0510W/cm/K
Lasing wavelength:	1064nm, 1342nm
Thermal optical coefficient (300K):	dn_o/dT=8.5×10^{-6}/K dn_e/dT=2.9×10^{-6}/K
Stimulated emission cross-section:	25×10^{-19}cm^2 @1064nm
Fluorescent lifetime:	90μs (1% Nd doped)
Absorption coefficient:	31.4cm^{-1} @810nm
Intrinsic loss:	0.02cm^{-1} @1064nm
Gain bandwidth:	0.96nm @1064nm
Polarized laser emission:	π polarization; parallel to optical axis (c-axis)
Diode pumped optical to optical efficiency:	>60%
Sellmeier equations (λ in μm)	n_o^2=3.77834+0.069736/(λ ^{2}-0.04724)-0.010813 λ ^{2} n_e^2=4.59905 +0.110534/(λ ^{2}-0.04813)-0.012676 λ ^{2}

Fig. 2.1.1. Basic properties of the Nd:YVO_4 crystal.

2.2 Passively Q-Switched Nd:YVO_4 Laser at 1064 nm

I. Introduction

Passive Q-switching of a solid-state laser with a saturable absorber is a convenient way to provide a reliable pulsed operation with the benefits of high stability, inherent compactness, and low cost. As a promising saturable absorber near the IR region, the Cr^{4+}:YAG crystal has been widely investigated on the PQS performance thanks to its good chemical and mechanical stability, long lifetime, excellent optical quality, high damage threshold, high thermal conductivity, and large absorption cross section [4-12].

However, the stimulated emission cross section of the Nd:YVO_4 crystal at 1064 nm is too large to achieve a good PQS operation when the Cr^{4+}:YAG crystal is used as a saturable absorber. Several methods have been proposed to overcome the well-known condition for good passive Q-switching, including the intracavity focusing obtained from the three-element resonator [13-15] and the employment of a c-cut crystal as a gain medium [16-18]. Nevertheless, the peak powers with the above-mentioned reports are not high enough for some practical applications, especially for efficient extracavity nonlinear frequency conversion. Therefore, it is highly desirable to develop a high-peak-power PQS Nd:YVO_4 laser with the Cr^{4+}:YAG saturable absorber.

In this section, we take into account the second threshold and thermal-lensing effect to design and realize a compact reliable PQS Nd:YVO_4 laser with the Cr^{4+}:YAG crystal as a saturable absorber. At an incident pump power of 16.3 W, the output power at 1064 nm reaches 6.16 W with a pulse width of 7 ns and a pulse repetition rate of 56 kHz. The corresponding pulse energy and peak power are evaluated to be 111 μJ and 16 kW, respectively.

II. Cavity analysis

It is well known that the absorption saturation in the saturable absorber should occur before the gain saturation in the laser crystal for good PQS operation. The so-called second threshold condition has been analytically derived from the coupled rate equation, which can be mathematically expressed as [13,19]:

$$\frac{\ln(1/T_0^2)}{\ln(1/T_0^2)+\ln(1/R_{OC})+L_s}\frac{\sigma_{gsa}}{\sigma}\frac{A}{A_s}>\frac{\gamma}{1-\beta}, \tag{2.1}$$

where T_0 is the initial transmission of the saturable absorber, R_{OC} is the reflectivity of the output coupler, L_s is the nonsaturable round trip dissipative loss of the resonator, σ_{gsa} is the ground-state absorption of the saturable absorber, σ is the emission cross section of the laser crystal, A/A_s is the ratio of the laser mode area in the laser crystal to that in the saturable absorber, γ is the population inversion reduction factor, which is equal to one for the ideal four-level laser and two for the three-level laser, and $\beta = \sigma_{esa}/\sigma_{gsa}$ is the ratio of the excite excited-state absorption cross section to the ground-state absorption cross section of the saturable absorber. With the following parameters: $T_0 = 0.7$, $R_{OC} = 0.5$, $L_s = 0.03$, $\sigma_{gsa} = 2 \times 10^{-18}$ cm^2 [12], $\sigma = 2.5 \times 10^{-18}$ cm^2, $\gamma = 1$, and $\beta = 0.06$ [12], the second threshold condition can be deduced to be $A/A_s > 2.68$ in the case of the Nd:YVO_4 and Cr^{4+}:YAG crystals as a gain medium and a saturable absorber, respectively. As a consequence, the ratio of the laser mode radius in the laser crystal to that in the saturable absorber needs to be larger than 1.64 for achieving a high-quality PQS operation.

The configuration for a simple plano-concave resonator with the thermal-lensing effect is schematically shown in Fig. 2.2.1(a). In the present experiment, the laser crystal and saturable absorber are aimed to be as close as possible to the input concave mirror and flat output coupler, respectively. An optical resonator with an internal thermal lens between the resonator mirrors can be replaced by an empty cavity with the equivalent g-parameters g^* and the equivalent cavity length $L_{cav}{}^*$, which are given by [20]:

$$g_i^* = g_i - \frac{1}{f_{th}} d_j \left(1 - \frac{d_i}{R_i}\right), \tag{2.2}$$

$$g_i = 1 - \frac{d_1 + d_2}{R_i}, \tag{2.3}$$

$i, j = 1, 2;\ i \neq j,$

$$L_{cav}^{*} = d_1 + d_2 - \frac{1}{f_{th}} d_1 d_2 , \tag{2.4}$$

where f_{th} is the effective thermal focal length, d_1 and d_2 are the optical path lengths from the center of the gain medium to the input mirror and output coupler, R_1 and R_2 are the radius of curvature (ROC) of the input mirror and output coupler. In terms of the equivalent cavity parameters, the cavity mode radii at the input mirror (ω_1) and at the output coupler (ω_2) are given by [20]:

$$\omega_i = \sqrt{\frac{\lambda L_{cav}^{*}}{\pi}} \sqrt{\frac{g_j^{*}}{g_i^{*}(1 - g_1^{*} g_2^{*})}} , \ i, j = 1, 2;\ i \neq j, \tag{2.5}$$

As a result, we can calculate the variations of the cavity mode radius ω_1 and ω_2 with respect to the effective thermal focal length. The effective focal length of thermal lens in the end-pumped laser crystal can be estimated with the following equation [21]:

$$\frac{1}{f_{th}} = \frac{\xi P_{in}}{\pi K_c} \int_0^{l_{cry}} \frac{\alpha e^{-\alpha z}}{1 - e^{-\alpha l_{cry}}} \frac{1}{\omega_p^2(z)} \left[\frac{1}{2} \frac{dn}{dT} + (n-1)\alpha_T \frac{\omega_p(z)}{l_{cry}} \right] dz , \tag{2.6}$$

$$\omega_p(z) = \omega_{po} \sqrt{1 + \left[\frac{M^2 \lambda_p}{n \pi \omega_{po}^2} (z - z_0) \right]^2} , \tag{2.7}$$

where ξ is the fraction of the incident pump power that results in heat, P_{in} is the incident pump power, K_c is the thermal conductivity, α is the absorption coefficient at the pump wavelength λ_p, l_{cry} is the crystal length, dn/dT is the thermal-optic coefficient, n is the refractive index, and α_T is the thermal expansion coefficient, M^2 is the pump beam quality factor, and $\omega_p(z)$ is the variation of the pump radius, where the pump beam waist ω_{po} is assumed a distance z_0 from the entrance of the laser crystal. With the following parameters: $\xi = 0.24$, $K_c = 5.23$ W/m K, $\alpha = 0.2$ mm^{-1}, $\lambda_p = 808$ nm, $l_{cry} = 12$ mm, $dn/dT = 3 \times 10^{-6}$ K^{-1}, $n = 2.1652$, $\alpha_T = 4.43 \times 10^{-6}$ K^{-1}, $M^2 = 230$, $\omega_{po} = 300$ μm, and $z_0 = 1$ mm, the effective thermal focal length can be calculated as a function of the incident pump power. To be brief, the dependence of the ratio ω_1/ω_2 on the incident pump power can be generated to design and realize a high-quality PQS laser. Figure 2.2.1(b) depicts the calculated results for the cases of $L_{cav} = 90$, 80, 70, 60 and 50 mm, where the L_{cav} stands for the cavity length and the other parameters used in calculation are as follows: $R_1 = 100$ mm, $R_2 \rightarrow \infty$, $d_1 = 6$ mm, $d_2 = (L_{cav} - 6)$ mm. From the Fig. 2.2.1(b), it is obvious that the thermal lensing effect will make the cavity to be unstable when the cavity

length is too long; whereas the PQS laser can not well operate in a high-quality state when the cavity length is too short. Comparative speaking, we chose a resonator with L_{cav} = 70 mm to simultaneously satisfy the second threshold criterion and cavity stability condition to realize a compact reliable PQS laser.

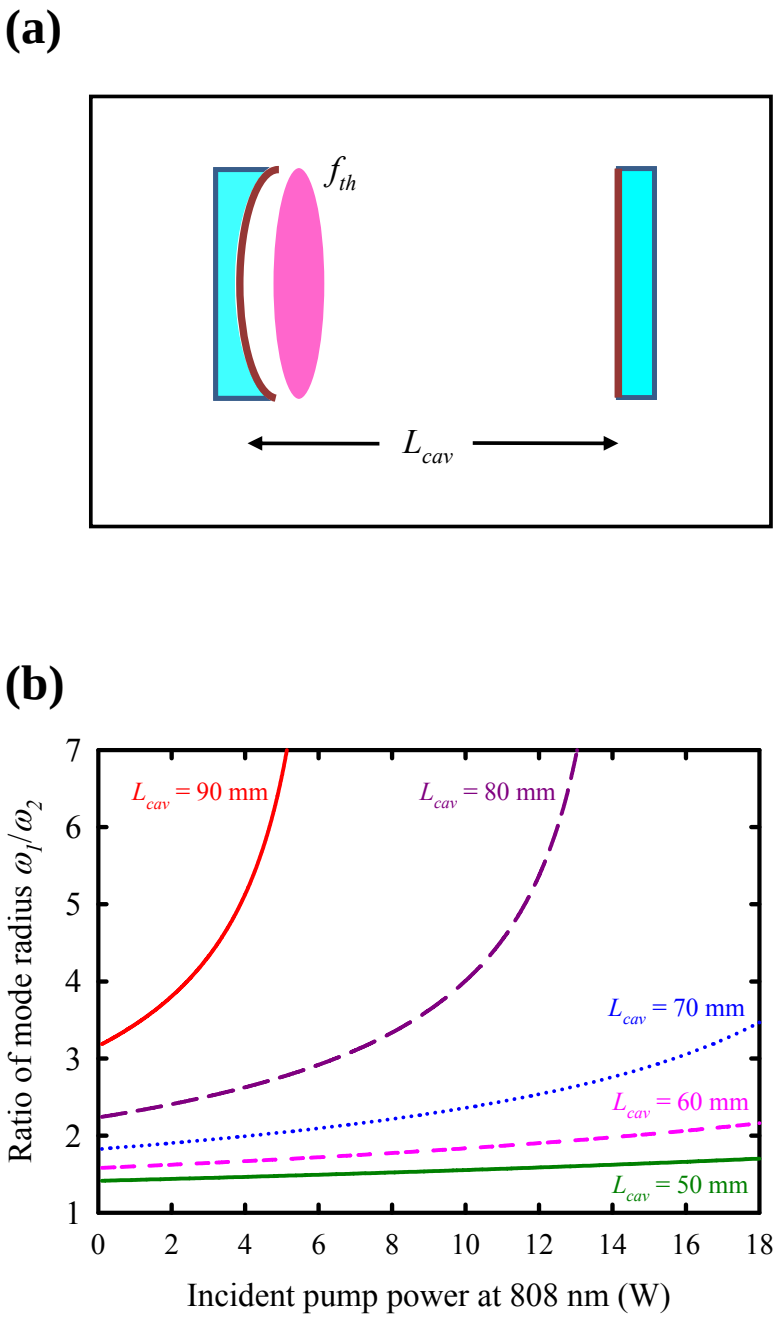

Fig. 2.2.1. (a) The configuration for a simple plano-concave cavity with the thermal lensing effect; (b) Calculated results for the ratio of the cavity mode size in the gain medium to that in the saturable absorber as a function of the incident pump power for the cases of L_{cav} = 90, 80, 70, 60, and 50 mm when the ROC of the input mirror is chosen to be R_1 = 100 mm.

III. Experimental setup

The experimental setup is schematically shown in Fig. 2.2.2. The input mirror was a concave mirror with the ROC of 100 mm. It was antireflection (AR) coated at 808 nm on the entrance face, and was coated at 808 nm for high transmission as well as 1064 nm for high reflection on the second surface. The gain medium was a 0.1 at. % a-cut Nd:YVO_4 crystal with dimensions of 3 × 3 × 12 mm^3, and it was placed as close as possible to the input mirror. Both facets of the laser crystal were AR coated at 808 and 1064 nm. The Cr^{4+}:YAG saturable absorber with an initial transmission of 70 % was AR coated at 1064 nm on both surfaces, and it was placed near to the output coupler. The laser crystal and saturable absorber were wrapped with indium foil and mounted in water-cooled copper heat sinks at 20 °C. The pump source was an 18-W 808-nm fiber-coupled laser diode with a core diameter of 600 μm and a numerical aperture of 0.2. The pump beam was reimaged into the laser crystal with a lens set that has a focal length of 25 mm with a magnification of unity and a coupling efficiency of 91 %. Therefore, the maximum incident pump power in our experiment was approximately 16.3 W. The flat output coupler with 50-% transmission was employed during the experiment. As designed in subsection II, the cavity length was set to be 70 mm for the construction of a compact high-power PQS laser. The pulse temporal behaviors were recorded by a LeCroy digital oscilloscope (Wavepro 7100, 10 G samples/s, 1 GHz bandwidth) with a fast Si photodiode.

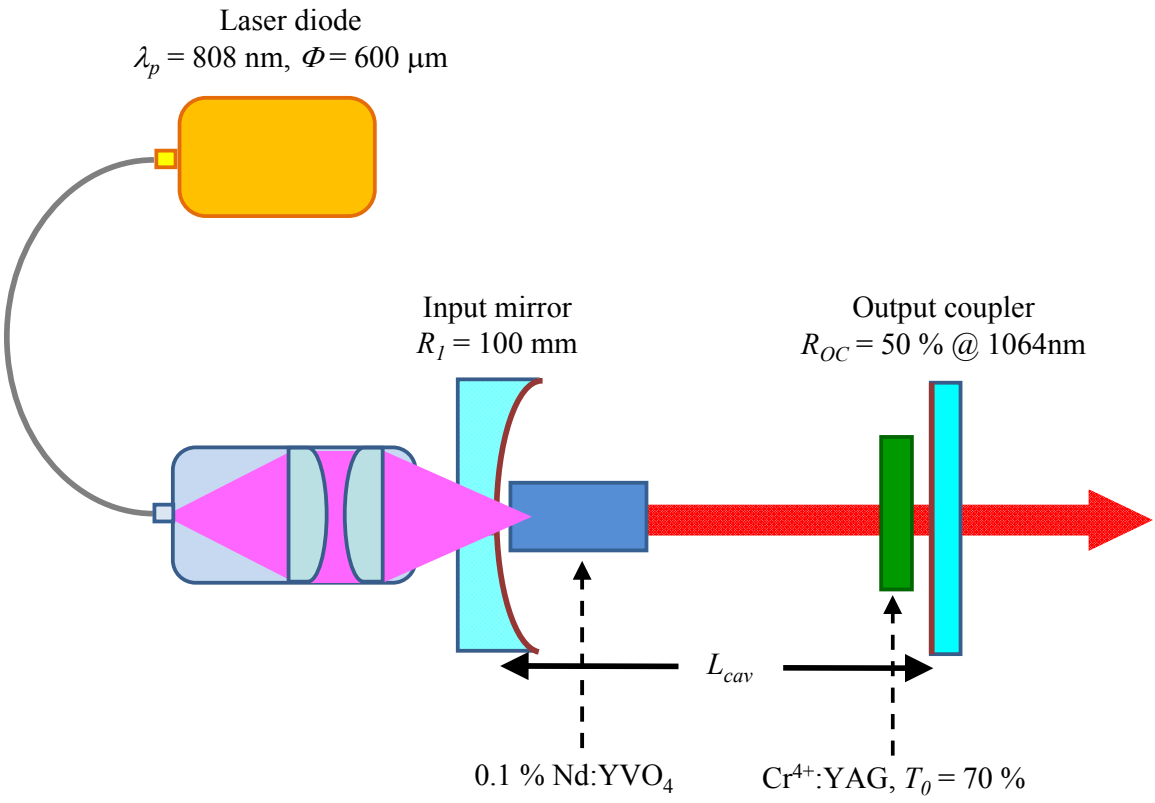

Fig. 2.2.2. Schematic of the cavity setup for a diode-pumped PQS Nd:YVO$_4$ laser with the Cr^{4+}:YAG saturable absorber.

IV. Performance of CW and PQS operations

First of all, the continuous-wave (CW) operation without the saturable absorber is studied. The output power as a function of the incident pump power is presented by the red curve in Fig. 2.2.3(a). The pump threshold and slope efficiency are determined to be 2.1 W and 62 %, respectively. At the maximum incident pump power of 16.3 W, the output power of 8.8 W is obtained, corresponding to the optical conversion efficiency from 808 to 1064 nm up to 54 %.

We then inserted the Cr^{4+}:YAG saturable absorber into the laser cavity to investigate the PQS performance in detail. The dependence of the output power on the incident pump power in the PQS operation is illustrated by the green curve in Fig. 2.2.3(a). The pump threshold and slope efficiency are found to be 3.3 W and 47.4 %, respectively. At the maximum incident pump power of 16.3 W, the output power as high as 6.16 W is obtained, corresponding to the optical conversion efficiency up to 37.8 %. Figures 2.2.3(b) and (c) show the pulse width, pulse repetition rate, pulse energy, and peak power as a function of the incident pump power. When the incident pump power increases from 5 to 16.3 W, the pulse repetition rate varies from 15.5 to 56 kHz and the pulse width changes from 20 to 7 ns, as shown in Fig. 2.2.3(b). Accordingly, it can be seen that the pulse energy increases from 27 to 111 μJ and the peak power increases from 1.3 to 16 kW by increasing the incident pump power from 5 to 16.3 W, as revealed in Fig. 2.2.3(c). Figures 2.2.4(a) and (b) show the typical oscilloscope traces of the output pulses at 1064 nm under an incident pump power of 16.3 W with the time span of 200 and 2 μs, respectively. Note that the appearance of the satellite pulses following the main Q-switched pulse was frequently observed in the past research [22-25]. This phenomenon inevitably degrades the Q-switched performance, leading to the restriction of the maximum achievable Q-switched pulse energy and peak power. However, we didn't observe any satellite pulses during the present experiment, indicating the validness of our cavity optimization.

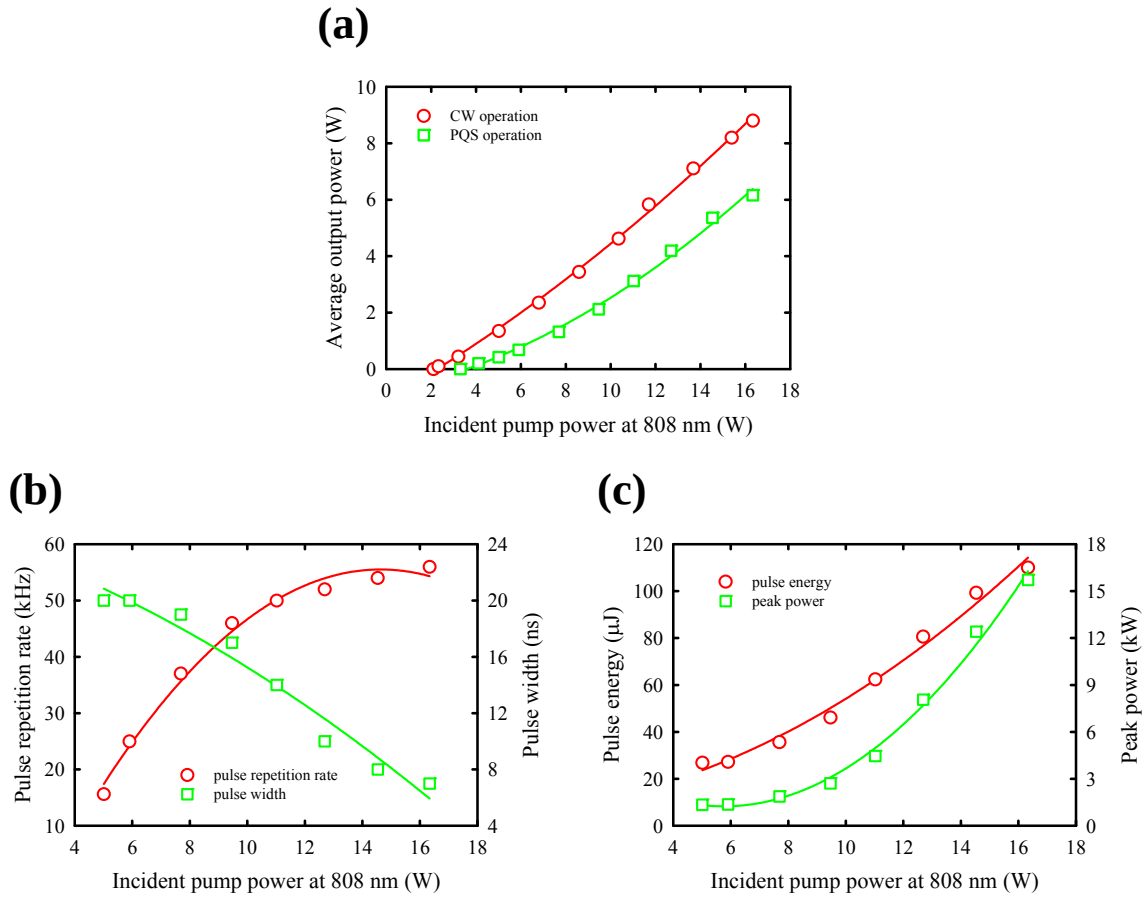

Fig. 2.2.3. (a) Output powers in CW (red curve) and PQS (green curve) operations as a function of the incident pump power; (b) Dependences of the pulse repetition rate (red curve) and pulse width (green curve) on the incident pump power; (c) Dependences of the pulse energy (red curve) and peak power (green curve) on the incident pump power.

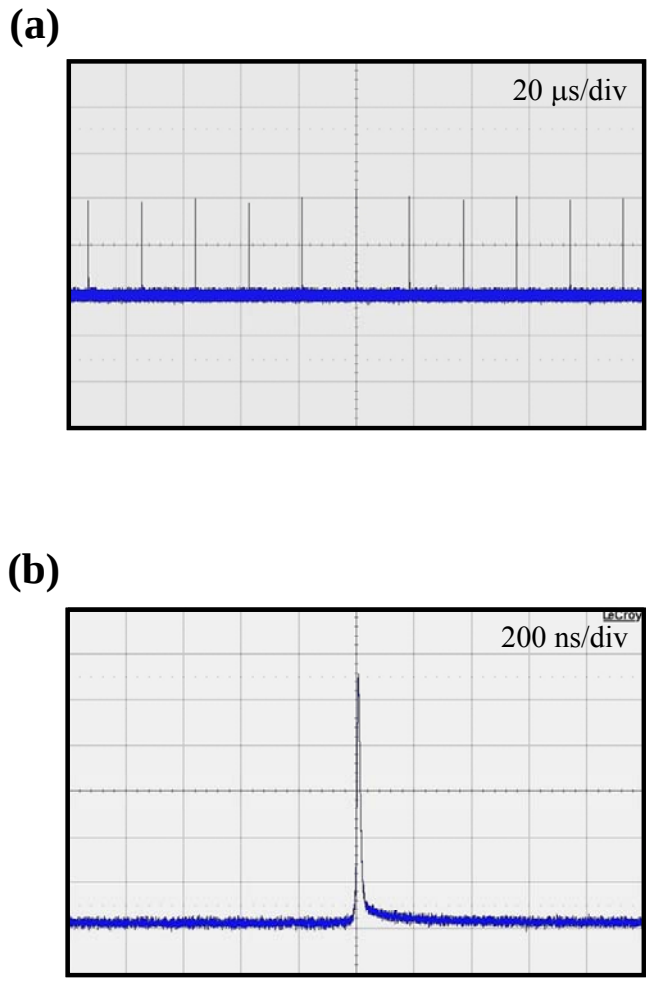

Fig. 2.2.4. Typical oscilloscope traces of the output pulses at 1064 nm under an incident pump power of 16.3 W with the time span of (a) 200 and (b) 2 μs.

2.3 Actively Q-Switched Nd:YVO_4 Laser at 1064 nm

I. Introduction

Compared with the PQS laser, AQS solid-state laser can provide a high-stability, low timing jitter and high-peak-power pulsed operation with a continuously adjustable pulse repetition rate. The acousto-optic (AO) Q-switch, which is characterized by its low-insertion loss, is one of promising methods to achieve AQS operation. It can exceptionally offer the convenience of converting from repetitively Q-switched to CW operations simply by removing the RF drive power [26-31].

Nevertheless, it is observed that the parasitic lasing effect is a critical issue for scaling up the output peak powers of the AQS lasers [26,32,33], and this detrimental effect usually leads to a significant reduction of the peak power of the AO Q-switched laser that inevitably deteriorates the performance of extracavity nonlinear frequency conversion. Note that the parasitic lasing means that there is residual lasing in the low-Q stage. Although lengthening the cavity length can effectively assist the diffraction loss of the AO device to suppress the parasitic lasing in the low-Q stage [34,35], a long cavity length usually needs an intricate design to obtain a stable resonator under the thermal lensing effect. More importantly, longer cavity lengths always lead to longer pulse widths that also reduce the output peak powers. Therefore, it is practically valuable to optimize the peak power by designing the shortest cavity length for the AO Q-switched laser without the parasitic lasing effect.

In this section, we investigate the parasitic lasing effect in the high-power AQS laser with a flat-flat resonator. The parasitic lasing effect in the low-Q stage is found to lead to long tails in the output pulses, corresponding to the peak-power reduction. We experimentally determine the shortest cavity length without the parasitic lasing effect to optimize the performance of the high-power AQS laser with a flat-flat cavity. At an incident pump power of 44 W, the maximum output power of 19.4 W at 100 kHz and the highest peak power of 81.5 kW at 20 kHz are accomplished, respectively.

II. Experimental setup

The experimental setup is schematically shown in Fig. 2.3.1. The flat input mirror was AR coated at 808 nm on the entrance face, and was coated at 808 nm for high transmission as well as 1064 nm for high reflection on the second surface for light with normal incidence. The flat folded mirror had the same coated characteristics as the flat input mirror except that the angle of the incident light was 45°. The gain medium was a 0.1 at. % Nd:YVO_4 crystal with dimensions of 3 × 3 × 14 mm^3. Both facets of the laser crystal were AR coated at 808 and 1064 nm. The laser crystal was wrapped with indium foil and mounted in a water-cooled copper heat sink at 20 °C. A 20-mm-long AO Q-switch (Gooch & Housego) with AR coating at 1064 nm on both faces was placed in the center of the cavity, and was driven at a central frequency of 41 MHz with a RF power of 25 W. The pump sources were two 25-W 808-nm fiber-coupled laser diodes with a core diameter of 800 μm and a numerical aperture of 0.16. The pump beam was reimaged into the laser crystal with a lens set that has a focal length of 25 mm with a magnification of unity and a coupling efficiency of 88 %. As a result, the maximum pump power in our experiment was approximately 44 W. The flat output coupler with 50 % transmission was employed during the experiment. The relatively low reflectivity of the output coupler is practically helpful for the effective hold-off in the low-Q stage. The pulse temporal behaviors were recorded by a LeCroy digital oscilloscope (Wavepro 7100, 10 G samples/s, 1 GHz bandwidth) with a fast Si photodiode.

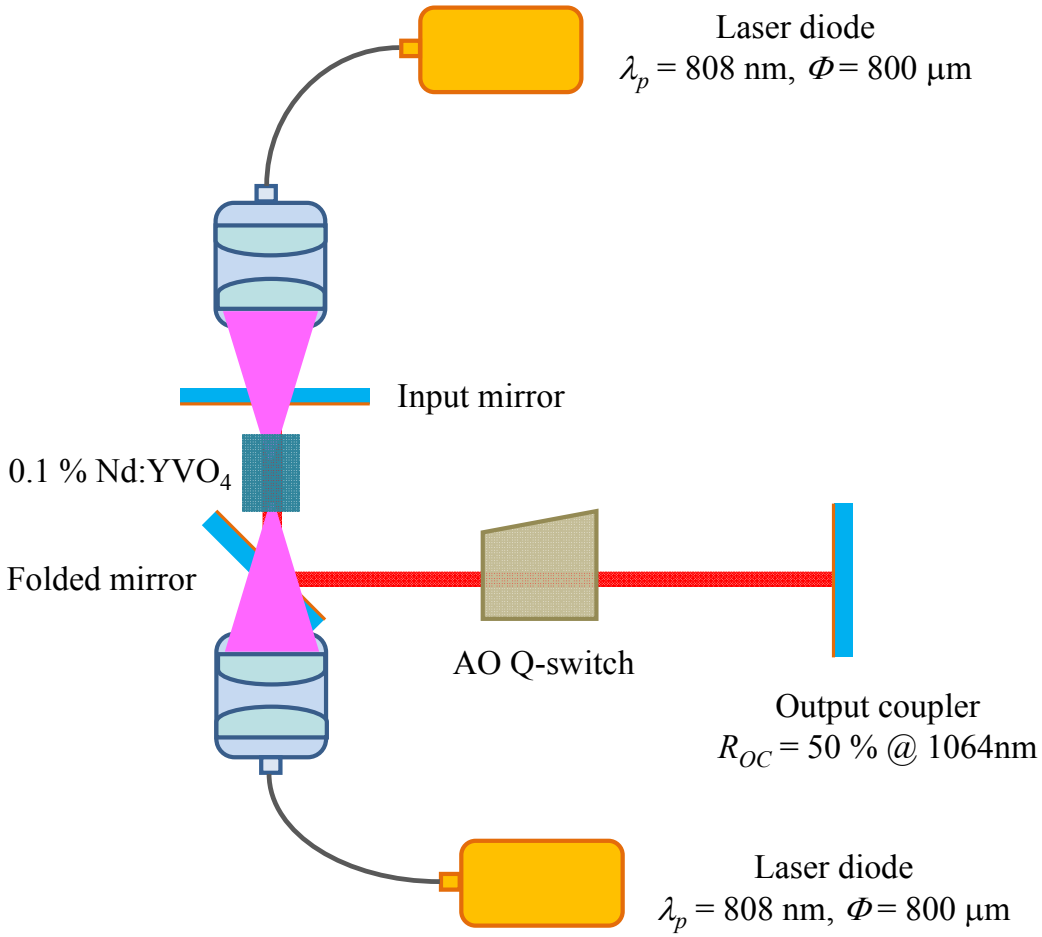

Fig. 2.3.1. Schematic of the cavity setup for a diode-pumped AO Q-switched Nd:YVO$_4$ laser.

III. Optimization in the flat-flat AO Q-switched laser

Since the parasitic lasing in the low-Q stage can be utterly suppressed with increasing the cavity length in a flat-flat cavity, we define the critical cavity length to be the shortest cavity length without parasitic lasing. Figure 2.3.2 depicts experimental results for the critical cavity length as a function of the pump power. The critical cavity length without parasitic lasing can be seen to increase with increasing the incident pump power. More importantly, we experimentally found that the parasitic lasing significantly affects the temporal shape of the Q-switched pulse. Figures 2.3.3(a) and (b) show the influence of parasitic lasing on the Q-switched pulse at the maximum pump power of 44 W for the cavity lengths of 16 and 18 cm, respectively. It can be seen that the Q-switched pulses are accompanied with a long tail or a satellite pulse. In contrast, the Q-switched pulse without parasitic lasing displays a short tail as well as no satellite pulse, as shown in Figs. 2.3.3(c) and (d) for the cavity lengths of 20 and 22 cm, respectively.

The long tail of Q-switched pulses induced by parasitic lasing imply the reduction of the peak power. The degree of the peak-power reduction can be simply analyzed with the rate equation. Assume the average photon density caused by parasitic lasing to be ϕ_b, the rate equation for the population inversion density N in the low-Q stage can be described as:

$$\frac{dN}{dt} = r - c\sigma N\phi_b - \frac{N}{\tau}, \tag{2.8}$$

where r is the rate of the pump density, τ is the upper-state lifetime of laser crystal, c is the speed of light, σ is the stimulated emission cross section. With $\tau_b = 1/c\sigma\phi_b$, Eq. (2.8) can be rewritten as:

$$\frac{dN}{dt} = r - \frac{N}{\tau_e}, \tag{2.9}$$

where $1/\tau_e = 1/\tau + 1/\tau_b$ and τ_e represents the effective upper-state lifetime with parasitic lasing. τ_e is clear to be smaller than τ. Since the amount of the maximum stored energy is proportional to the upper-state lifetime, the parasitic lasing can be comprehended to cause a reduction in the pulse energy and peak power. To be brief, the parasitic lasing scarcely affects the average output power but has a detrimental effect on the peak power.

As shown in Fig. 2.3.2, the critical cavity length is approximately 20 cm for the maximum pump power of 44 W. With the ABCD-matrix theory, it can be derived that the cavity length L_{cav} of a stable flat-flat resonator should be shorter than the thermal focal length f_{th}; namely, the criterion of $L_{cav} \leq f_{th}$ must be satisfied to maintain the cavity stable. Since the thermal focal length of the laser crystal can be verified to be inversely proportional to the dopant concentration, the criterion of $L_{cav} \leq f_{th}$ signifies the importance of using a Nd:YVO_4 crystal with extremely low dopant concentration. The effective focal length of thermal lens in the end-pumped laser crystal can be analyzed with the Eqs. (2.6) and (2.7). With the following parameters: $\xi = 0.24$, $K_c = 5.23$ W/m K, $\lambda_p = 808$ nm, $dn/dT = 3 \times 10^{-6}$ K^{-1}, $n = 2.1652$, $\alpha_T = 4.43 \times 10^{-6}$ K^{-1}, $M^2 = 250$, $\omega_{po} = 400$ μm, and $z_0 = 1$ mm, we calculated the effective thermal focal length f_{th} as a function of the Nd dopant concentration of laser crystal at the incident pump power of 44 W. In the present calculation, the crystal length l_{cry} is related to the absorption coefficient α with the condition of $\alpha l_{cry} = 4$ for pump absorption of 98 %. Note that the relation between the absorption coefficient α and the Nd dopant concentration of laser crystal for a pump wavelength of 808 nm is given by $\alpha = 2 \cdot N_d$ mm^{-1} [36], where N_d is the Nd dopant concentration in units of atomic %. Figure 2.3.4 depicts the calculated results ranging from $N_d = 0.05$ % to $N_d = 1$ % at a pump power of 44 W. It can be seen that the smaller the Nd dopant concentration, the longer the thermal focal length. Moreover, the Nd:YVO_4 crystal with dopant concentration greater than 0.2 at.% can not comply with the requirement of $L_{cav} \leq f_{th}$, where $L_{cav} = 20$ cm is employed to suppress the parasitic lasing at a pump power of 44 W. To sum up, using a Nd:YVO_4 crystal with extremely low dopant concentration is a promising way to simultaneously suppress the parasitic lasing and maintain a stable flat-flat resonator in high-power Q-switched lasers.

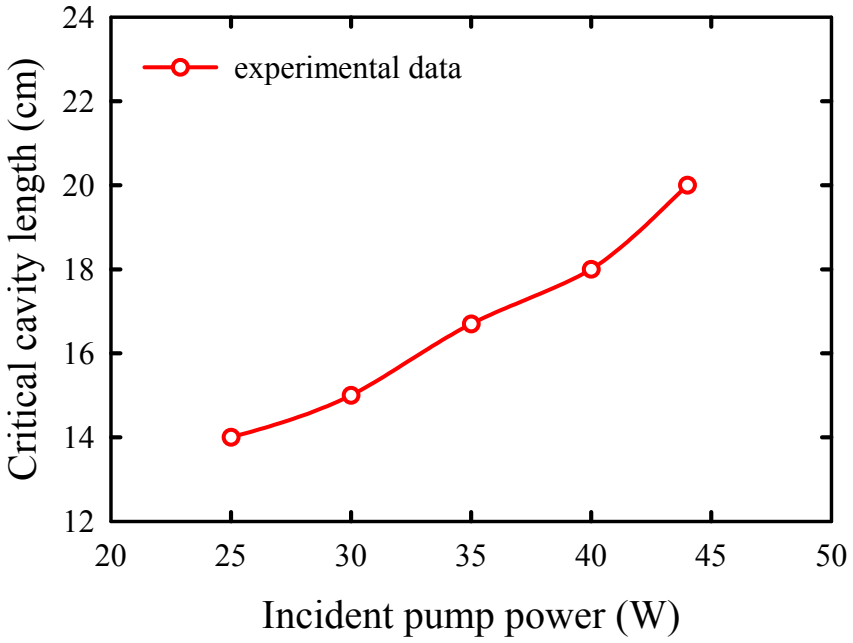

Fig. 2.3.2. Experimental results for the relationship between the critical cavity length and the incident pump power.

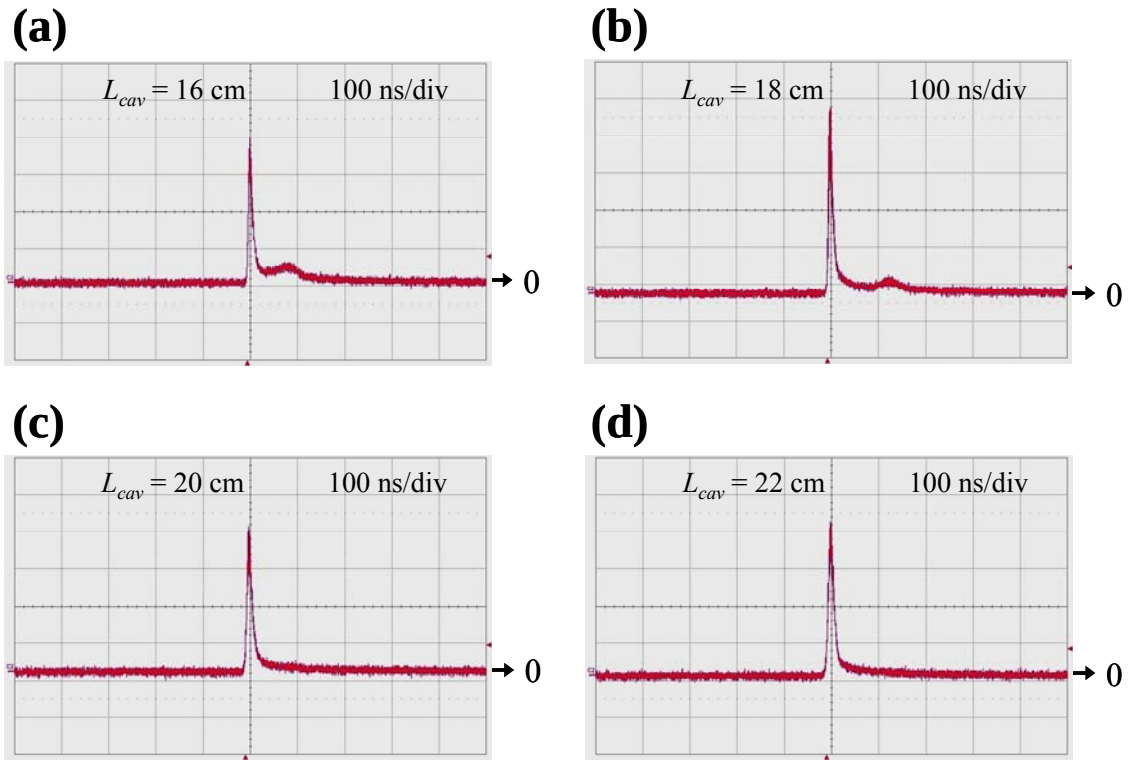

Fig. 2.3.3. Temporal behaviors of the Q-switched pulses with different cavity lengths L_{cav}: (a) L_{cav} = 16 cm; (b) L_{cav} = 18 cm; (c) L_{cav} = 20 cm; (d) L_{cav} = 22 cm.

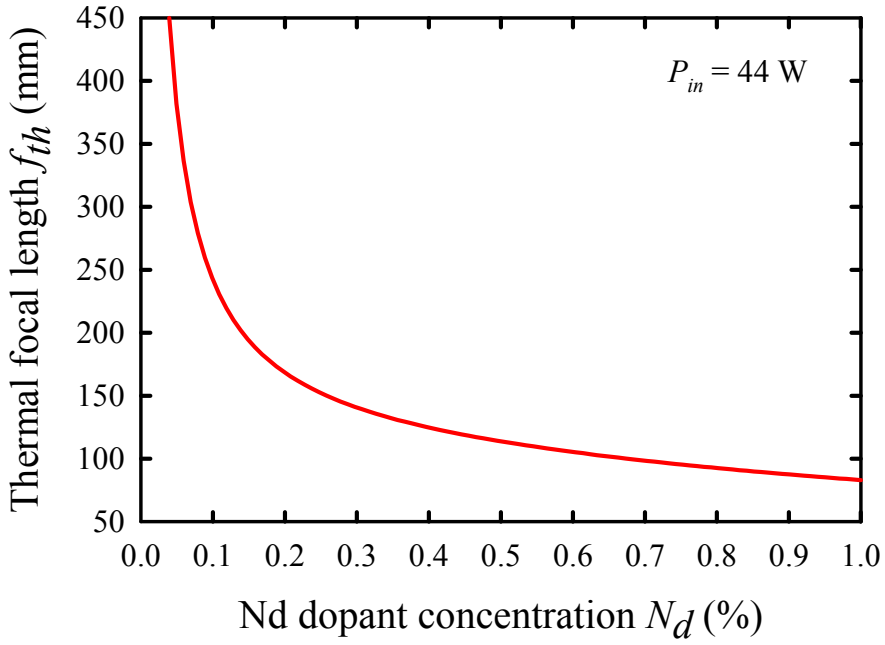

Fig. 2.3.4. Calculated results for the thermal focal length as a function of the Nd dopant concentration of laser crystal at a pump power of 44 W.

IV. Performance of AQS operation

With the cavity length of 20 cm, we make a thorough evaluation for the performance of Q-switched operation. Figure 2.3.5 shows the output power and pulse width as a function of the incident pump power at a pulse repetition rate of 40 kHz. At an incident pump power of 44 W, the output power of 17.5 W was obtained without any signature of output power saturation, indicating the cavity to remain in a stable region. When the incident pump power increases from 16 to 44 W, the pulse width can be seen to decrease from 36 to 12 ns. In the meanwhile, the pulse energy and peak power are found to increase from 60 to 435 μJ and from 1.6 to 36.3 kW by increasing the incident pump power from 16 to 44 W. Figures 2.3.6(a) and (b) illustrate the dependences of the output power, pulse width, pulse energy and peak power on the pulse repetition rate at an incident pump power of 44 W. It can be seen that by increasing the pulse repetition rate from 20 to 100 kHz, the output power increases from 13 to 19.4 W and the pulse duration smoothly varies from 8 to 24 ns. Accordingly, it can be found that when the pulse repetition rate increases from 20 to 100 kHz, the pulse energy changes from 650 to 194 μJ and the peak power varies from 81.5 to 8.1 kW, respectively.

In the future, the same concept of finding the shortest cavity length in a high-power AQS laser without the parasitic lasing effect can also be employed for optimizing the peak powers for the concave-plano or convex-plano cavities, respectively. Perhaps some interesting results would be observed unexpectedly.

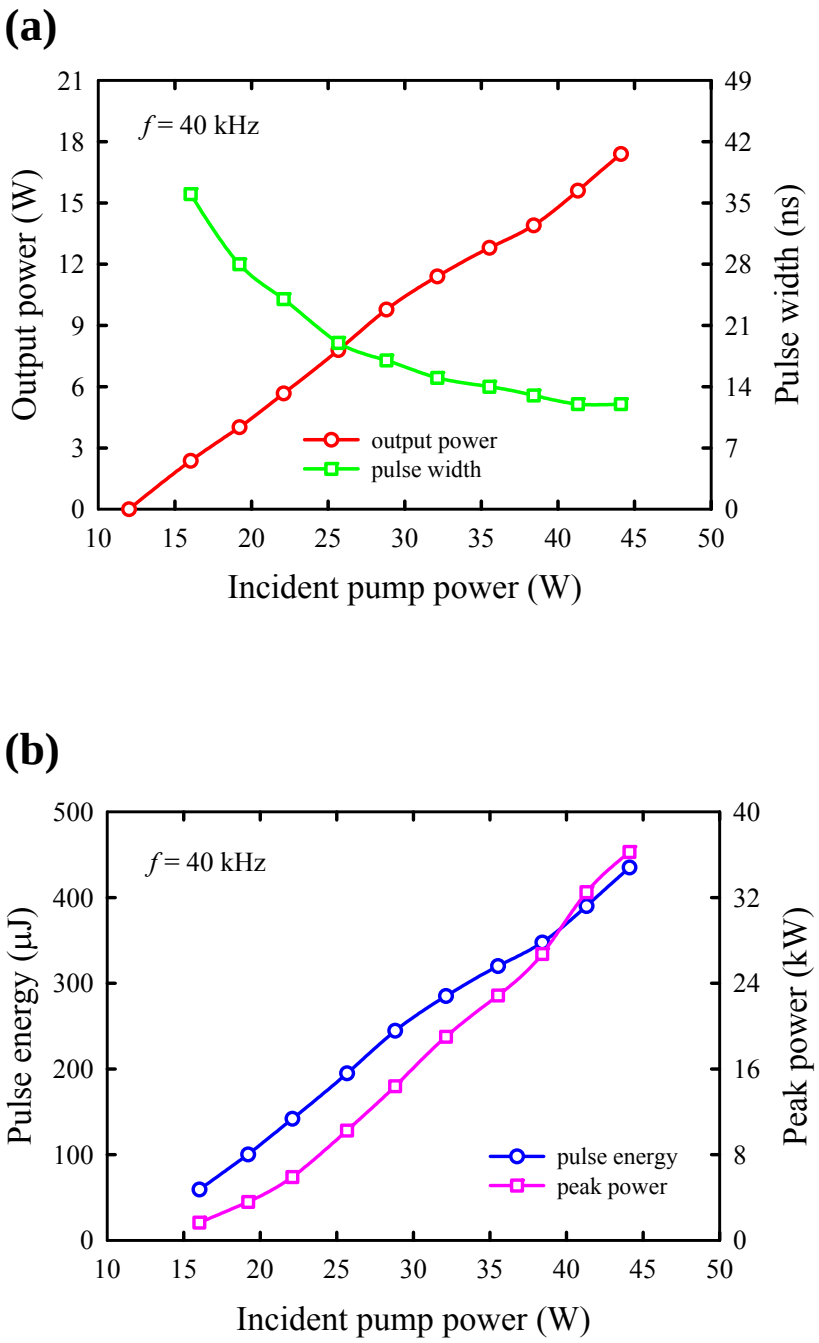

Fig. 2.3.5. Output power (red), pulse width (green), pulse energy (blue) and peak power (pink) versus the incident pump power at a pulse repetition rate of 40 kHz.

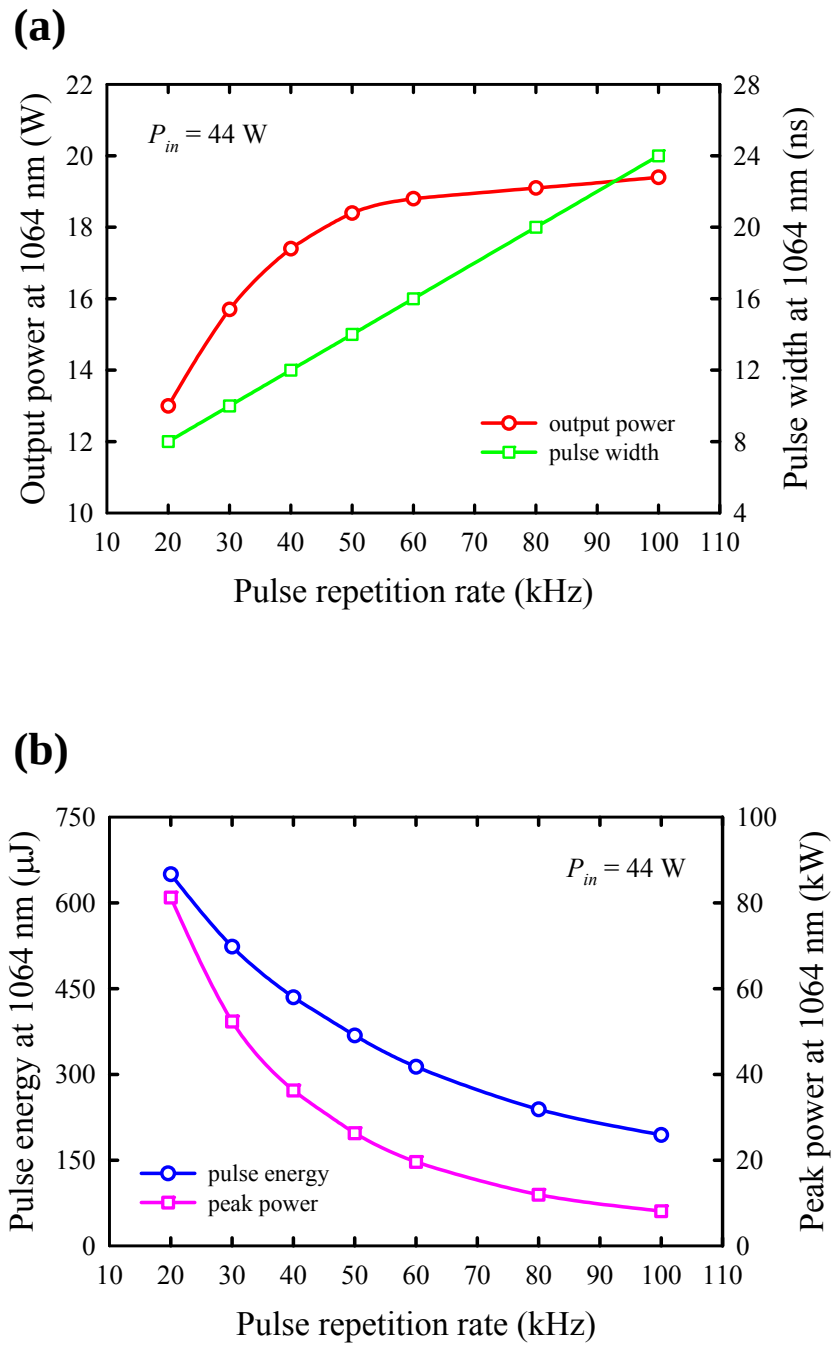

Fig. 2.3.6. (a) Dependences of the average output power (red) and the pulse width (green) on the pulse repetition rate at a pump power of 44 W; (b) Dependences of the pulse energy (blue) and the peak power (pink) on the pulse repetition rate at a pump power of 44 W.

2.4 Properties of Nd:YLF Crystal

Nd-doped yttrium lithium fluoride (Nd:YLF) is another important active medium in the field of solid-state lasers. Basic properties of the Nd:YLF crystal are illustrated in Fig. 2.4.1, which is also obtained from CASTECH [3]. Like the Nd:YVO_4 crystal, the Nd:YLF crystal belongs to the tetragonal group in crystal structure. Therefore, it can emit the linearly polarized output without the thermally induced birefringence as well as the thermal depolarization loss in the high-power operation. The Nd:YLF crystal is also highly desirable for generating high-energy pulses thanks to its long upper-state lifetime [37-39], where the fluorescent lifetime is around 500 μs. For comparison, the upper-state lifetimes in the Nd:YAG and Nd:YVO_4 crystals are roughly 230 and 100 μs, respectively. Note that the capability of the energy storage is directly proportional to the fluorescent time of the laser crystal. Another feature is the excellent spectral match between the emission line at 1053 nm and the gain peak of the Nd:phosphate glass, which makes the Nd:YLF crystal essentially favorable for constructing a high-energy master oscillator power amplifier [40].

Transparency Range:	180 - 6700 nm
Peak Stimulated Emission Cross Section	1.8×10^{-19}/cm^2(E ‖ c) at 1047nm 1.2×10^{-19}/cm^2(E ⊥ c) at 1053nm
Spontaneous Fluorescence Lifetime	485 μs for 1% Nd doping
Scatter Losses	<0.2%/cm
Peak Absorption Coefficient(for 1.2% Nd)	α = 10.8cm^{-1} (792.0 nm E ‖ c) α = 3.59cm^{-1} (797.0 nm E ⊥ c)
Laser Wavelength	1047nm (‖ c, a-cut crystal) 1053nm(⊥ c, a or c-cut crystal)
Chemical Formula	$LiY_{1.0-x}Nd_xF_4$
Space Group	$I4_1/a$
Nd atoms/cm^3	1.40 X 10^{20} atoms/cm^3 for 1% Nd doping
Modulus of Elasticity	85 GPa
Crystal Structure:	Tetragonal
Cell Parameters:	a=5.16 Å , c=10.85 Å
Melting Point:	819°C
Mohs Hardness:	4~5
Density:	3.99 g/cm^3
Thermal Conductivity	0.063 W/cm/K
Specific Heat	0.79 J/g/K
Thermal Expansion Coefficients	8.3×10^{-6}/k ‖c 13.3×10^{-6}/ k ⊥ c

Fig. 2.4.1. Basic properties of the Nd:YLF crystal.

2.5 Continuously Pumped Passively Q-Switched a-cut Nd:YLF Laser at 1053 nm

I. Introduction

Although it is generally convenient to employ the c-cut Nd:YLF crystal as a gain medium for generating an 1053-nm laser, the isotropic property in the transverse plane typically leads the polarization state not to be linearly polarized. The a-cut Nd:YLF crystal can alternatively be employed to obtain a linearly polarized output. However, the stimulated emission cross section at 1047 nm is higher than that at 1053 nm by a factor of 1.5 for the a-cut Nd:YLF crystal [41-45]. As a result, suppressing the π-polarized emission at 1047 nm turns into an important issue in designing a linearly-polarized 1053-nm laser with the a-cut Nd:YLF crystal. Notice that the Nd:YLF crystal is an uniaxially birefringent crystal that shows distinct emission characteristics for the π- and σ-polarizations, corresponding to the emission wavelengths of 1047 and 1053 nm, respectively. Furthermore, extra losses may be enhanced by the energy-transfer upconversion (ETU) effect, which causes a reduction in the effective upper laser level lifetime and an increase in fractional thermal loading [46-49]. Therefore, it is practically important to develop an approach without introducing considerable extra losses for achieving an efficient linearly polarized Nd:YLF 1053-nm pulsed laser.

In a previous study [50], it was demonstrated that the selection of the polarization in an a-cut Nd:YVO_4 laser could be attained by combining the birefringence of the laser crystal with the alignment sensitivity of the plano-plano resonator. Motivated by their work, in this section the natural birefringence of the Nd:YLF crystal is utilized to achieve a reliable TEM_{00}-mode linearly polarized laser at 1053 nm in a compact concave-plano resonator. The efficient selection of the polarization relies on the combined effect of the difference in diffraction angles for π- and σ-polarizations of a wedged laser crystal and the alignment sensitivity of an optical resonator. We further employ a Cr^{4+}:YAG saturable absorber to perform the PQS operation. At an incident pump power of 12 W, the maximum output power is up to 2.3 W with a pulse repetition rate of 8 kHz and a pulse width of 9 ns. The pulse energy and peak power are found to be 288 μJ and 32 kW, respectively.

II. Experimental setup

The experimental setup is schematically shown in Fig. 2.5.1. The input mirror was a concave mirror with the ROC of 500 mm. It was AR coated at 806 nm on the entrance face, and was coated for high transmission at 806 nm as well as for high reflection at 1053 nm on the second surface. The gain medium was a 0.8 at. % a-cut Nd:YLF crystal with dimensions of $3 \times 3 \times 20$ mm^3, and it was placed to be adjacent to the input mirror. Both facets of the laser crystal were AR coated at 806 and 1053 nm. The second surface of the laser crystal was wedged at an angle $\theta_w = 3^\circ$ with respect to the first surface, as indicated in Fig. 2.5.1. The Cr^{4+}:YAG saturable absorber with an initial transmission of 80 % was AR coated at 1053 nm on both surfaces, and it was placed near to the output coupler. The laser crystal and saturable absorber were wrapped with the indium foil and mounted in water-cooled copper heat sinks at 20 °C. The pump source was a 15-W fiber-coupled laser diode at 806 nm with a core diameter of 400 μm and a numerical aperture of 0.2. The pump beam was reimaged into the laser crystal with a lens set that has a focal length of 25 mm and a coupling efficiency of 90 %. The flat output couplers with the transmissions of 10, 20, 30, 36, and 50 % were utilized for systematic investigation on the laser characteristics during the experiment. The cavity length was set to be 50 mm for the construction of a compact laser. With the ABCD-matrix theory, the cavity mode radii inside the laser crystal and saturable absorber were estimated to be approximately 236 and 224 μm, respectively. The pulse temporal behaviors were recorded by a LeCroy digital oscilloscope (Wavepro 7100, 10 G samples/s, 1 GHz bandwidth) with a fast Si photodiode.

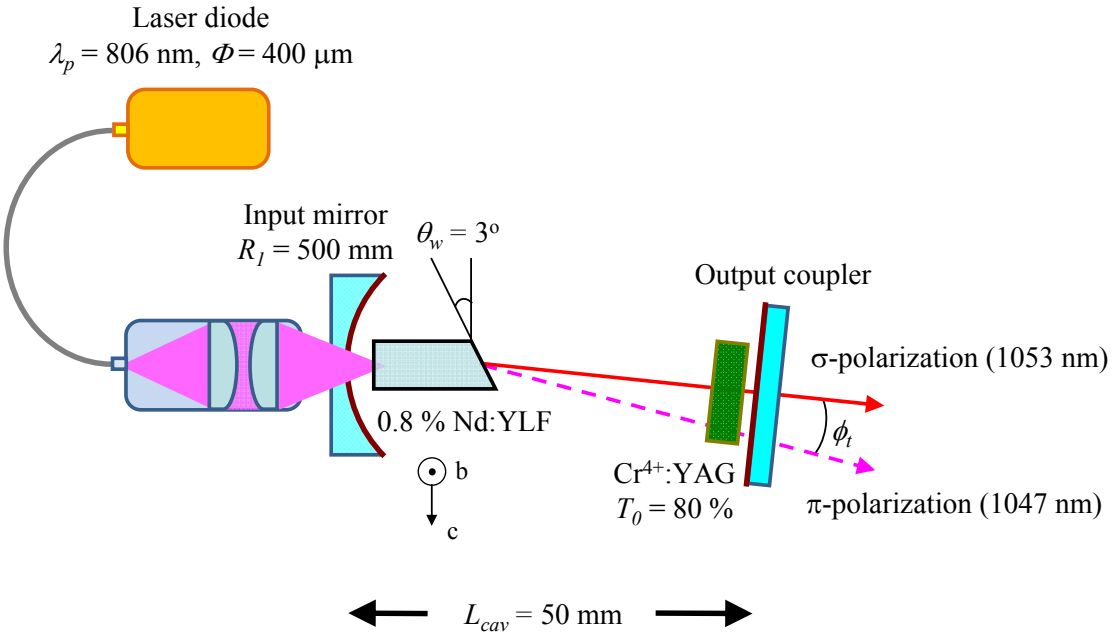

Fig. 2.5.1. Schematic of the cavity setup for a diode-pumped PQS Nd:YLF/Cr^{4+}:YAG laser.

III. Performance of CW and PQS operations

First of all, we explore the angle tuning characteristics of the Nd:YLF laser for the σ- and π-polarizations in the CW operation, where the Cr^{4+}:YAG saturable absorber was removed, the transmission of the output coupler was chosen to be 30 %, and the incident pump power was fixed to be 12 W to avoid the possibility of the thermal fracture in the laser crystal. As shown in Fig. 2.5.2(a), the output polarization state can be easily switched by simply tilting the orientation of the output coupler. Note that the tilting angle ϕ_t is defined as the included angle with respect to the orientation of the output coupler corresponding to the maximum output power at 1053 nm, as depicted in Fig. 2.5.1. The angular separation between the σ- and π-polarizations under the individual maximum output power is experimentally found to be around 1.153 mrad; that is, the angular separation between the point b and c indicated in Fig. 2.5.2(a) is approximately 1.153 mrad. On the other hand, the refractive indices for the σ- and π-polarizations in the a-cut Nd:YLF crystal are n_σ = 1.448 and n_π = 1.47, respectively. With the Snell's law under the small-angle approximation, we can theoretically derive an angular separation to be $(n_\pi - n_\sigma)\ \theta_w \sim 1.152$ mrad between the two polarizations external to the wedged crystal, which is in a good agreement with the experimental observations. The two-dimensional spatial distributions for the σ- and π-polarizations under the individual maximum output power are recorded with a digital camera, and both are found to display a near-diffraction-limited TEM_{00} transverse mode, as shown in Fig. 2.5.2(b) for the case of σ-polarization.

With the optimal alignment for 1053-nm emission, we made a thorough study on the output power with respect to the output coupling at an incident pump power of 12 W. Note that the polarization extinction ratio at 1053 nm is considerably larger than 100:1 once the cavity was aligned for the optimization at 1053 nm. The output power in the CW operation is experimentally found to decrease from 4.88 to 2.45 W by increasing the output coupling from 10 to 50 %, as revealed by the red curve in Fig. 2.5.3.

When the Cr^{4+}:YAG saturable absorber was inserted into the laser cavity, the dependence of the output power in the PQS operation on the output coupling is demonstrated by the green curve in Fig. 2.5.3. Experimental results reveal that at an incident pump power of 12 W, the maximum output power of 2.3 W is achieved with the output coupling of 30 % in the PQS operation. The optical conversion efficiency

from 806 to 1053 nm is thus evaluated to be 18.3 %. Figure 2.5.4 illustrates the pulse repetition rate and the pulse width versus the output coupling in the PQS operation. It is experimentally found that both the pulse repetition rate and the pulse width are insensitive to the change of the output coupling; namely, when the transmission of the output coupler is varied between 10-50 %, the pulse repetition rate and the pulse width are in the ranges 8-9 kHz and 9-10 ns, respectively. According to the experimental results illustrated in Figs. 2.5.3 and 2.5.4, the pulse energy and peak power are calculated as a function of the transmission of the output coupler, as depicted in Fig. 2.5.5. For the output coupler with the transmission of 30 %, the pulse energy and the peak power as high as 288 μJ and 32 kW are achieved at an incident pump power of 12 W.

Figures 2.5.6(a) and (b) show the typical oscilloscope traces of the output pulses at 1053 nm with the time span of 2 ms and 200 ns, respectively. The temporal behaviors were recorded with the output coupling of 30 % under an incident pump power of 12 W. The pulse-to-pulse amplitude fluctuation is found to be better than ±2 %. With a knife-edge method, the beam quality factors at 1053 nm for the orthogonal directions were measured to be $M_x^2 < 1.1$ and $M_y^2 < 1.15$, respectively.

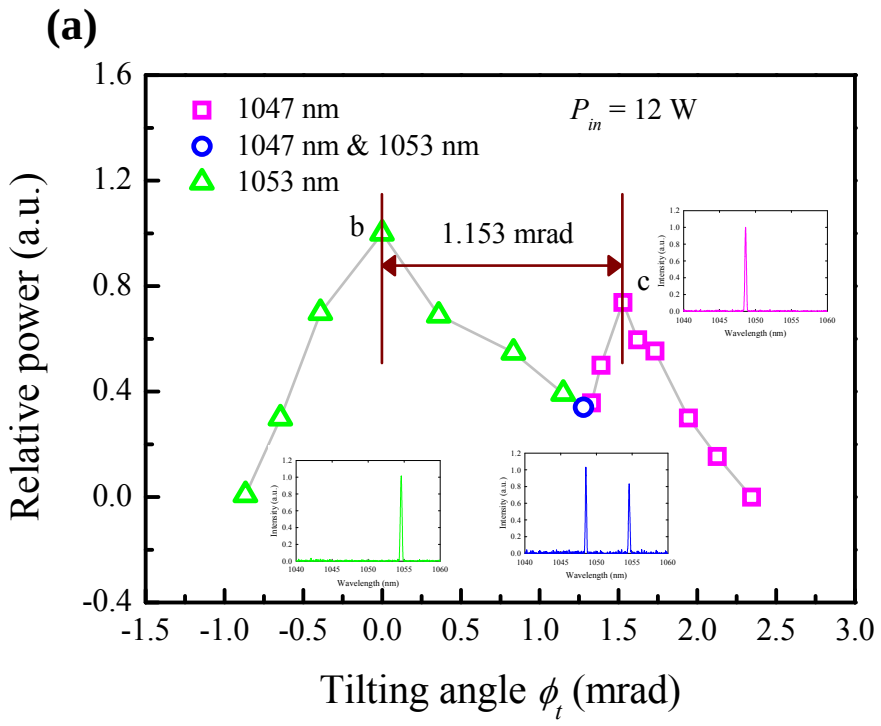

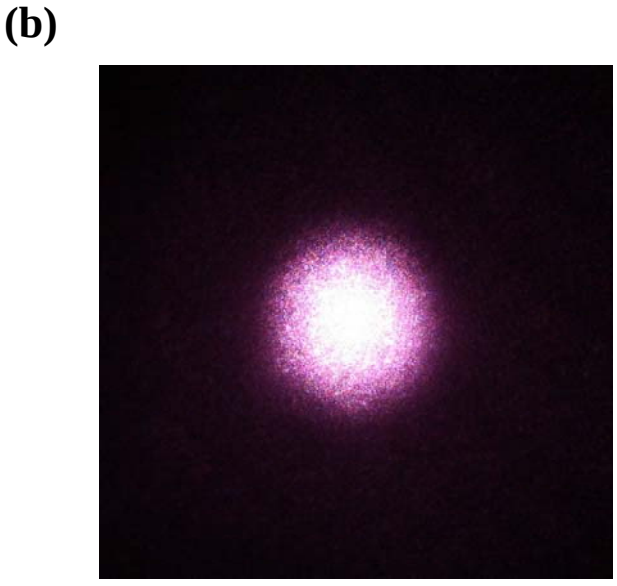

Fig. 2.5.2. (a) The angle tuning characteristics of the 3°-wedged a-cut Nd:YLF laser for the σ- and π-polarizations in the CW operation; (b) The two-dimensional spatial distributions for the σ-polarization under the maximum output power, indicating a near-diffraction-limited TEM_{00} transverse mode.

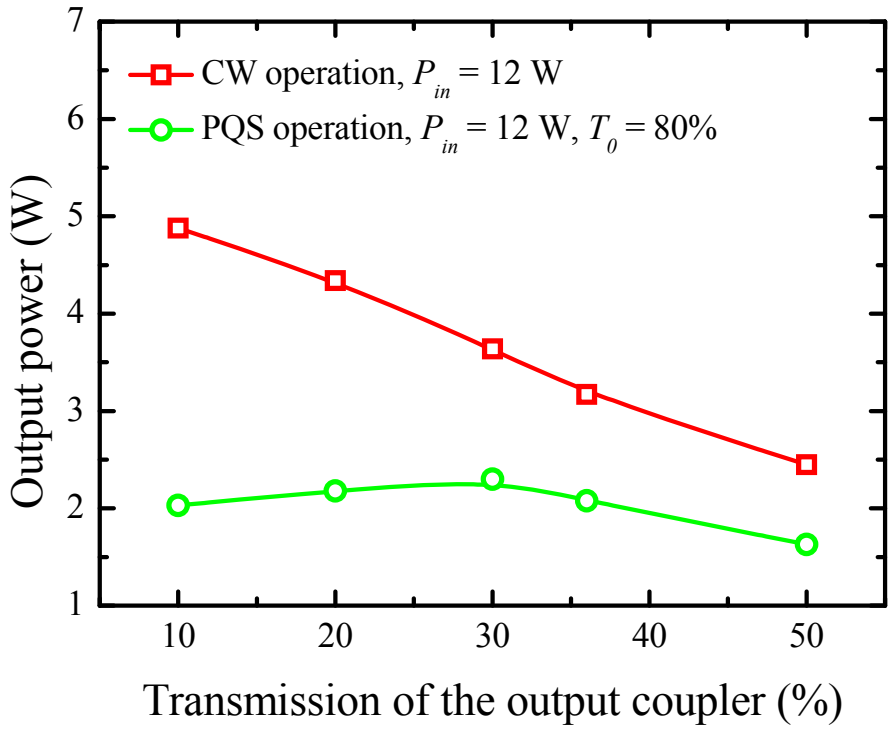

Fig. 2.5.3. The maximum output powers at 1053 nm in the CW and PQS operations as a function of the output coupling.

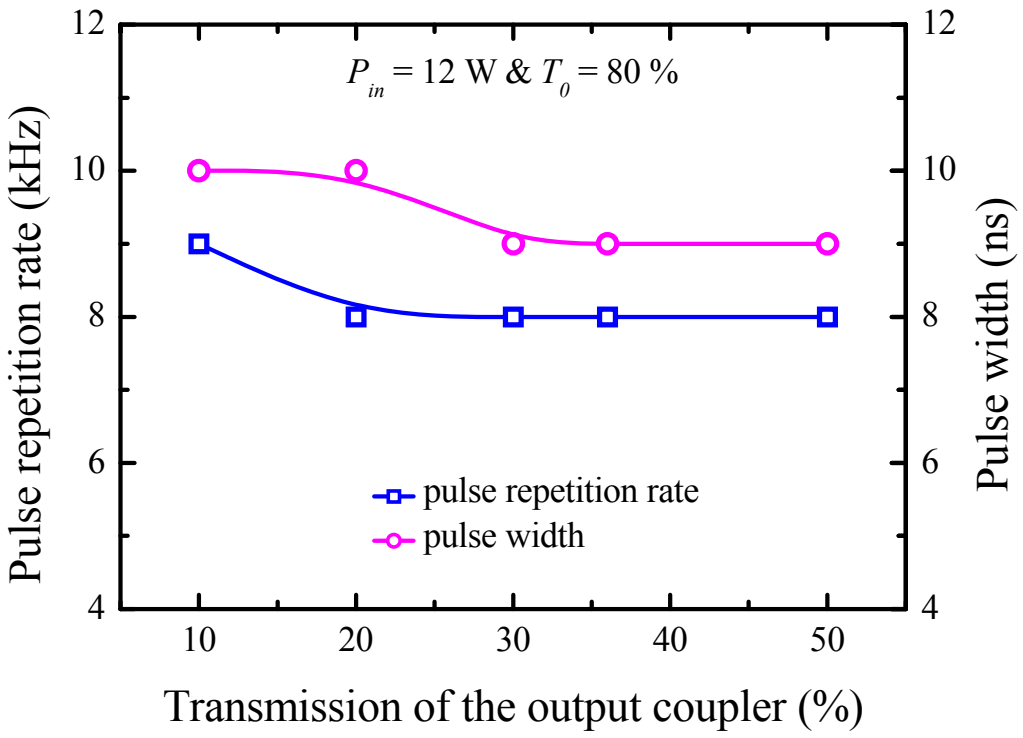

Fig. 2.5.4. Dependences of the pulse repetition rate and pulse width on the output coupling.

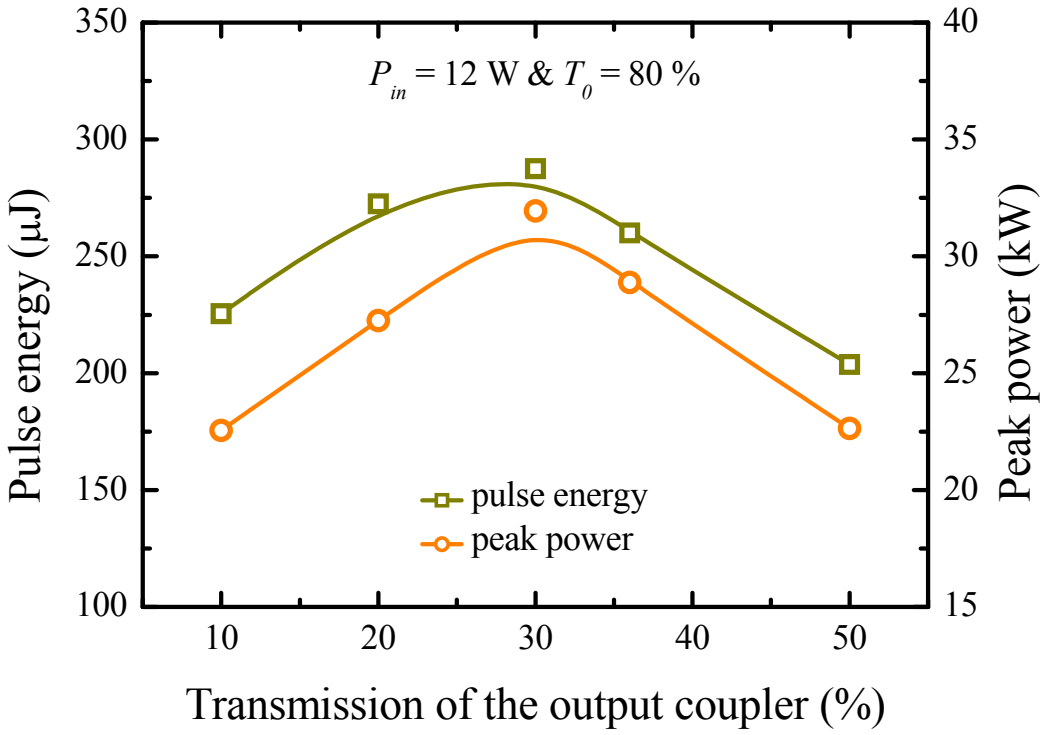

Fig. 2.5.5. Dependences of the pulse energy and peak power on the output coupling.

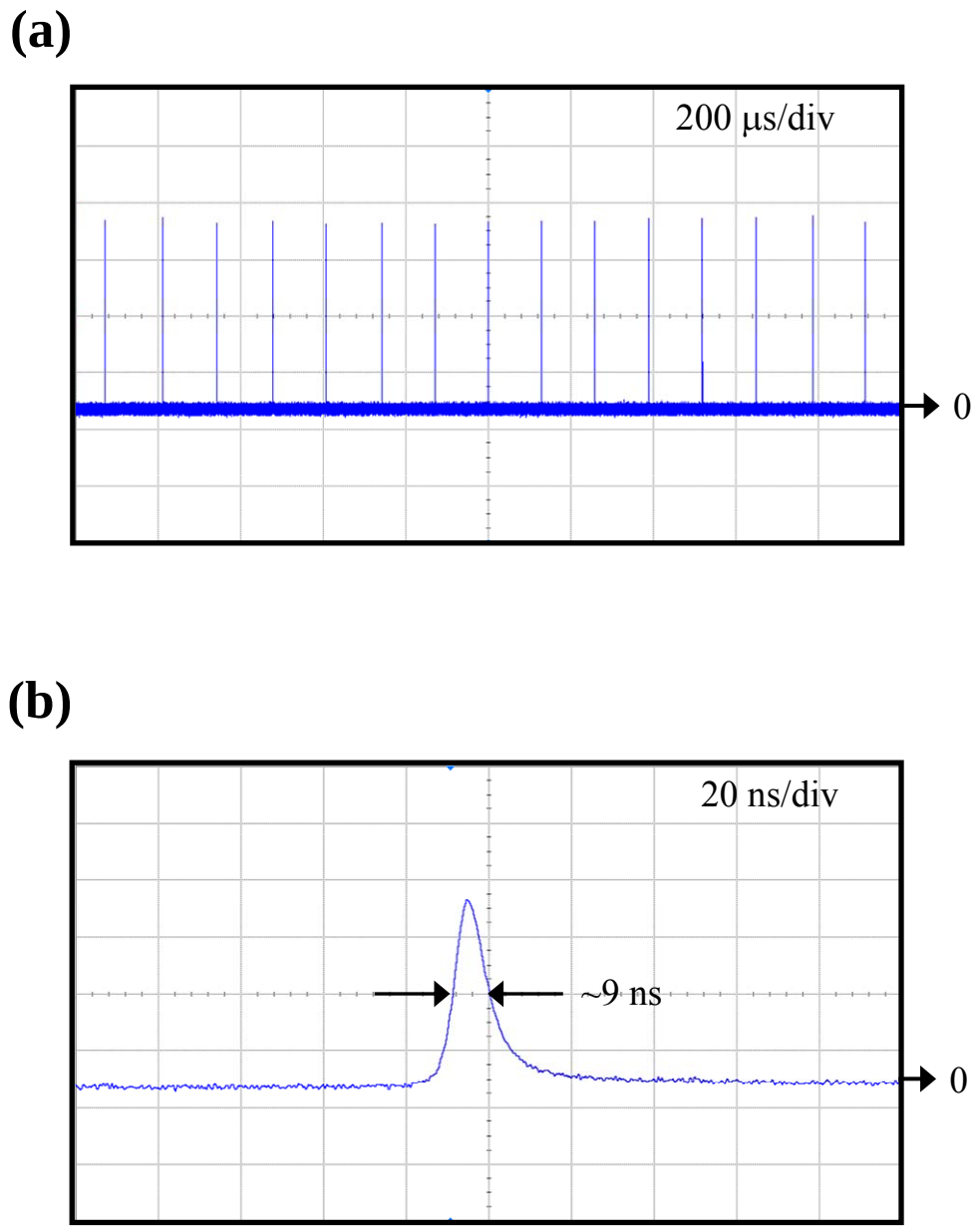

Fig. 2.5.6. Typical temporal behaviors at 1053 nm with: (a) time span of 2 ms, and (b) time span of 200 ns, which were recorded with the output coupling of 30 % under an incident pump power of 12 W.

2.6 Continuously Pumped Passively Q-Switched c-cut Nd:YLF Laser at 1053 nm

I. Introduction

If the polarization state of the output is not a critical issue, using the c-cut Nd:YLF crystal is a convenient way for generating the emission line at 1053 nm, because it can completely avoid the complexities required for the suppression of the unwanted laser transition at 1047 nm [51-53]. The fluorescent lifetime of 540 μs in the c-cut Nd:YLF crystal is also expected to be more suitable for producing high-energy pulses as compared with the 490 μs in the a-cut counterpart [54]. However, the implementation of high-pulse-energy PQS c-cut Nd:YLF lasers at 1053 nm has not been completely explored yet. The main reason is that the behavior of the thermal-lensing effect in the c-cut Nd:YLF crystal is significantly different from the ones in other popular gain media such as the Nd:YVO_4 and Nd:YAG crystals. The critical difference is that the negative dependence of the refractive index on the temperature (*dn/dT*) over the positive contribution from the end-face bulging of the gain medium leads the c-cut Nd:YLF crystal to behave a defocusing thermal lens. Furthermore, the ETU effect reduces the effective upper-state lifetime and increases the fractional thermal loading in the laser crystal, as discussed in Refs. [46-49]. The ETU effect inevitably causes the effective focal length of the thermal lens in the PQS operation to be considerably more negative than the one in the CW operation. As a result, a reliable and efficient tactic for designing continuously pumped high-pulse-energy PQS laser at 1053 nm is highly desirable to be developed.

In this section, we develop a practical method to extend the power scale-up for a laser in a concave-plano cavity to be influenced by a large negative thermal lens. With the developed method, we successfully scale up the output power of a compact high-pulse-energy PQS Nd:YLF laser at 1053 nm with the Cr^{4+}:YAG crystal as a saturable absorber. At an incident pump power of 12.6 W, the maximum output power under the optimum operation at 1053 nm reaches 2.61 W with a pulse width of 6 ns and a pulse repetition rate of 4.6 kHz. The corresponding pulse energy and peak power are estimated to be up to 570 μJ and 95 kW, respectively.

II. Numerical analysis

Previous studies have demonstrated that the mode-to-pump size ratio plays an important role for power scaling in diode-end-pumped solid-state lasers, in which the optimum mode-to-pump size ratio is practically found to be in the range 0.6-1 [36,55,56]. With the ABCD-matrix theory, here we take into account of the thermal-lensing effect to numerically calculate the mode-to-pump size ratio as a function of the thermal focal length for the cases of R_1 = 50, 100, 200, and 500 mm in a concave-plano cavity, where R_1 is the ROC of the input concave mirror. In the present analyses, the pump radius ω_{po} = 210 μm and the cavity length L_{cav} = 35 mm are used, and the thermally induced lens is set to be adjacent to the input concave mirror.

When the positive thermal lens is considered, we find that the mode-to-pump size ratios for all cases are well located between 0.6-1 in the large operated region, as depicted in Fig. 2.6.1(a). We also find that the magnitude of the thermal focal length $|f_{th}|$ should be larger than $(R_1L_{cav})/(R_1-L_{cav})$ to satisfy the stability criterion. Because the magnitude of the thermal focal length is inversely proportional to the incident pump power, the higher incident pump power can be allowed by using the concave mirror with larger ROC when the positive thermal lens is regarded.

On the other hand, we find that the ROC of the concave mirror needs to be small enough to fulfill the optimum mode-to-pump size ratio for the case of negative thermal-lensing effect, as shown in Fig. 2.6.1(b). At the same time, the magnitude of the thermal focal length $|f_{th}|$ is derived to need to be larger than R_1 to keep the cavity stable. On the whole, it is numerically found that decreasing the ROC of the concave mirror is favorable for simultaneously achieving good mode-to-pump size ratio as well as power scaling in a concave-plano cavity that is affected by a negative thermal lens.

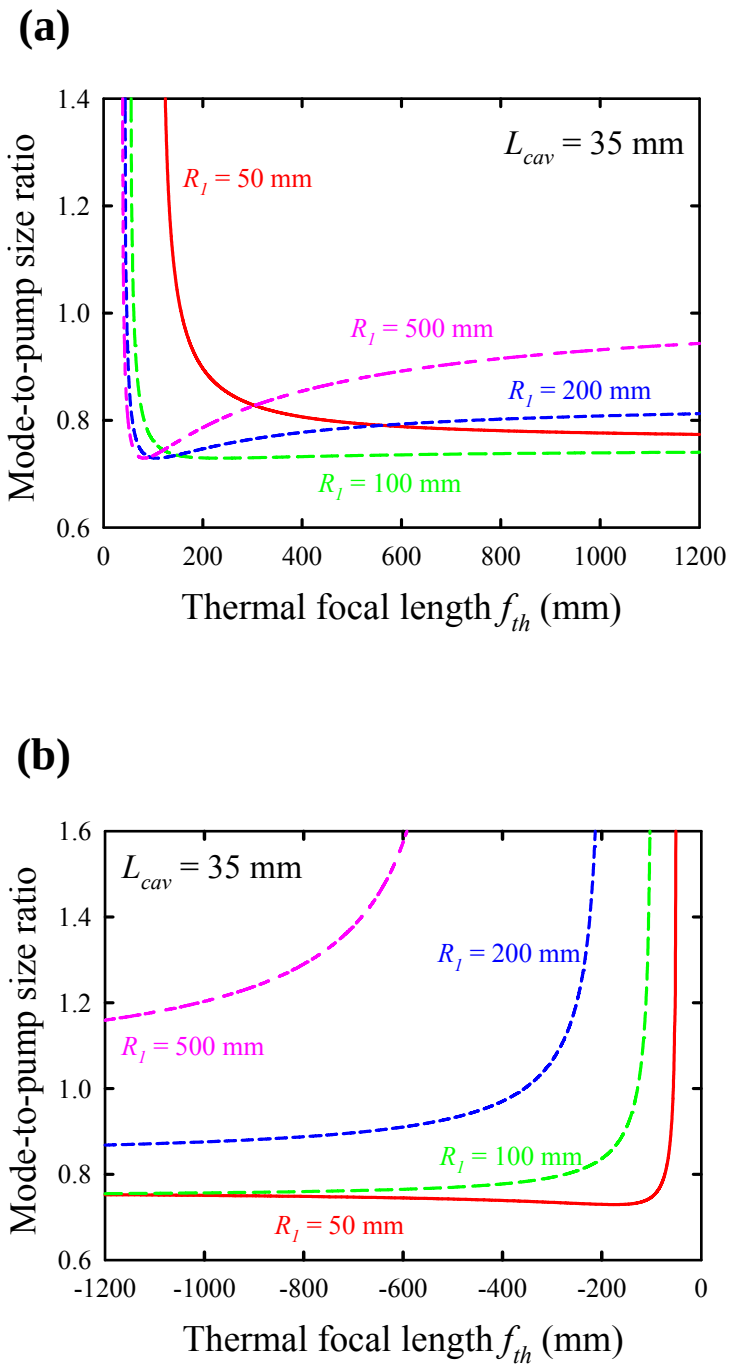

Fig. 2.6.1. Calculated results for the mode-to-pump size ratio as a function of the thermal focal length for the cases of R_1 = 50, 100, 200, and 500 mm: (a) positive thermal-lensing effect; (b) negative thermal-lensing effect.

III. Experimental setup

The experimental setup is schematically shown in Fig. 2.6.2. The input concave mirror was AR coated at 806 nm on the entrance face, and was coated for high transmission at 806 nm as well as for high reflection at 1053 nm on the second surface. The gain medium was a 0.8 at. % c-cut Nd:YLF crystal with the diameter of 4 mm and the length of 15 mm. The Nd:YLF crystal was placed adjacent to the input concave mirror. Both facets of the laser crystal were AR coated at 806 and 1053 nm. The Cr^{4+}:YAG saturable absorber with an initial transmission of 80 % was AR coated at 1053 nm on both surfaces, and it was placed near to the output coupler for achieving a high-quality PQS operation. The laser crystal and saturable absorber were wrapped with indium foil and mounted in water-cooled copper heat sinks at 16 °C. The pump source was a fiber-coupled laser diode at 806 nm with a core diameter of 400 μm and a numerical aperture of 0.14. The pump beam with the spot radius of 210 μm was reimaged inside the laser crystal with a lens set that has a focal length of 25 mm and a coupling efficiency of 90 %. The flat output coupler with a reflectivity of 74 % at 1053 nm was employed throughout the experiment. The cavity length was set to be 35 mm for the construction of a compact PQS laser. The pulse temporal behaviors were recorded by a LeCroy digital oscilloscope (Wavepro 7100, 10 G samples/s, 1 GHz bandwidth) with a fast InGaAs photodiode.

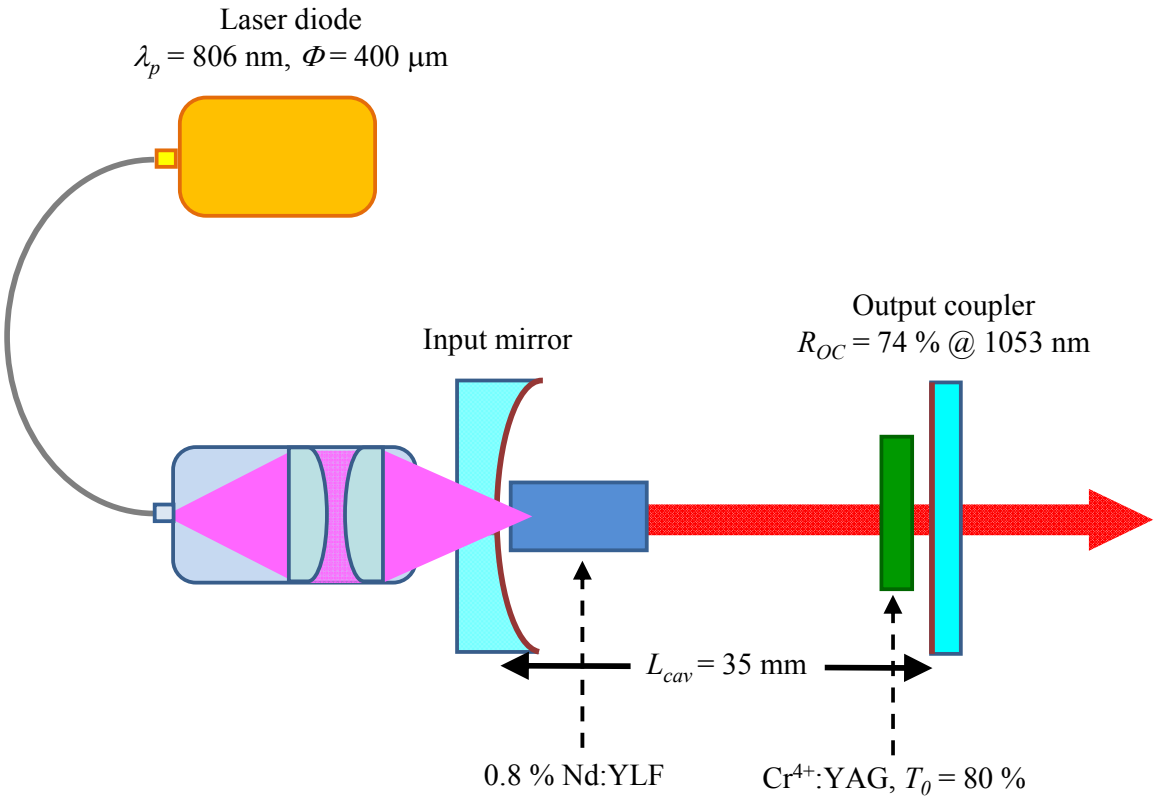

Fig. 2.6.2. Configuration of the cavity setup for a diode-pumped PQS Nd:YLF/Cr^{4+}:YAG laser.

IV. Performance of CW and PQS operations

First of all, the CW operation without the saturable absorber was studied. Figure 2.6.3(a) shows the output powers at 1053 nm as a function of the incident pump power at 806 nm for the cases of R_1 = 50, 100, 200, and 500 mm. It is obvious that although the pump thresholds for all cases are almost identical, the slope efficiency obtained with R_1 = 500 mm is remarkably lower than those obtained with other three cases. This observation is a result of the poorer mode-to-pump size ratio, as can be referred to Fig. 2.6.1(b) for R_1 = 500 mm case.

When the Cr^{4+}:YAG saturable absorber was inserted into the resonator, the degradations in the output power together with the roll-over phenomena for R_1 = 200 and 500 mm in the PQS operation further highlight the crucial importance of using small ROC of the concave mirror for power scale-up, as depicted in Fig. 2.6.3(b). During the early researches on the Nd:YLF crystal, many investigations indicated that power scaling in the Nd:YLF laser is practically hindered by the ETU effect [46-49]. The combined effect of the ETU effect and its subsequent multiphonon relaxation brings in the considerable enhancement of the thermal-lensing effect in the Nd:YLF laser. As a consequence, the increased thermal-lensing effect in the present PQS operation is believed to cause the deterioration in the output powers for R_1 = 200 and 500 mm. From the analysis of the coupled rate equation, the criterion for good PQS operation is given by Eq. (2.1). Since the σ_{gsa} value of the Cr^{4+}:YAG crystal (~(20 ± 5) × 10^{-19} cm^2) is remarkably larger than the σ value of the Nd:YLF crystal (1.2 × 10^{-19} cm^2), the criterion for good PQS operation is generally satisfied in the Nd:YLF/Cr^{4+}:YAG laser despite the ratio of the mode area A/A_s varies with the incident pump power and the ROC of the concave mirror. In other words, the influence of the changing mode area in the saturable absorber on the PQS performance can be neglected undoubtedly.

To further investigate the influence of the negative thermal lens on the Nd:YLF laser, we evaluate the effective focal length of the thermal lens with the help of Eqs. (2.6) and (2.7). With the following parameters: K_c = 6.3 W/m K, α = 0.18 mm^{-1}, λ_p = 806 nm, l_{cry} = 15 mm, dn/dT = -2 × 10^{-6} K^{-1}, n = 1.448, α_T = 8.3 × 10^{-6} K^{-1}, M^2 = 115, ω_{po} = 210 μm, and z_0 = 3.8 mm, the thermal focal length with respect to the incident pump power is plotted in Fig. 2.6.4. Numerical calculation for the CW case with ξ =

0.24 is found to be consistent with the previously published data, where the fractional thermal loading ξ is derived from the quantum defect value. According to the previous studies, the fractional thermal loading influenced by the ETU effect is usually magnified by a factor of ~3 as compared with the value in the CW operation. Therefore, we use ξ = 0.7 to calculate the PQS case, as revealed in Fig. 2.6.4. Numerical calculation for the PQS case is found to be in good agreement with the estimated results deduced from the experimental data shown in Fig. 2.6.3(b). The deduction is based on the fact that the ROC of the concave mirror needs to be smaller than the magnitude of the thermal focal length to satisfy the stability criterion, as analyzed in subsection II. To be brief, a concave mirror with the ROC significantly smaller than the thermal focal length can be effectively used to achieve the power scale-up for a laser influenced by a negative thermal lens with a plano-concave cavity. Moreover, due to the ETU effect, the suitable ROC of the concave mirror for the PQS case is considerably smaller than that for the CW case at the same incident pump power.

In Fig. 2.6.3(b), the resonator with R_1 = 100 mm is found to possess the highest maximum output power of 2.61 W at an incident pump power of 12.6 W. Therefore, we make a thorough study on the performance of the PQS Nd:YLF/Cr^{4+}:YAG laser with R_1 = 100 mm. Figures 2.6.5(a) and (b) illustrate the dependences of the pulse width, pulse repetition rate, pulse energy and peak power on the incident pump power. When the incident pump power increases from 5.17 to 12.6 W, the pulse width decreases from 14 to 6 ns and the pulse repetition rate varies from 1 to 4.6 kHz, as shown in Fig. 2.6.5(a). Accordingly, it can be seen that the pulse energy increases from 210 to 570 μJ and the peak power changes from 15 to 95 kW by increasing the incident pump power from 5.17 to 12.6 W, as revealed in Fig. 2.6.5(b). Typical temporal behaviors of the output pulses at an incident pump power of 12.6 W are shown in Figs. 2.6.6(a) and (b) with the time span of 2 ms and 100 ns, respectively. The pulse-to-pulse amplitude fluctuation is generally found to be within ± 3 %.

Finally, it is worthwhile to mention that so far the pulse energies obtained with the continuously pumped PQS Nd-doped crystal/Cr^{4+}:YAG lasers, such as the Nd:YAG, c-cut Nd:YLF, Nd-doped vanadate crystals and so on, are not more than ~300 μJ. That is to say, the pulse energy based on the $^4F_{3/2} \rightarrow {}^4I_{11/2}$ transition is significantly enhanced in our present work. This indicates that the c-cut Nd:YLF crystal is potentially favorable for the construction of high-pulse-energy lasers as long as the optical resonator is

intricately designed to compensate for the large negative thermal-lensing effect in the gain medium.

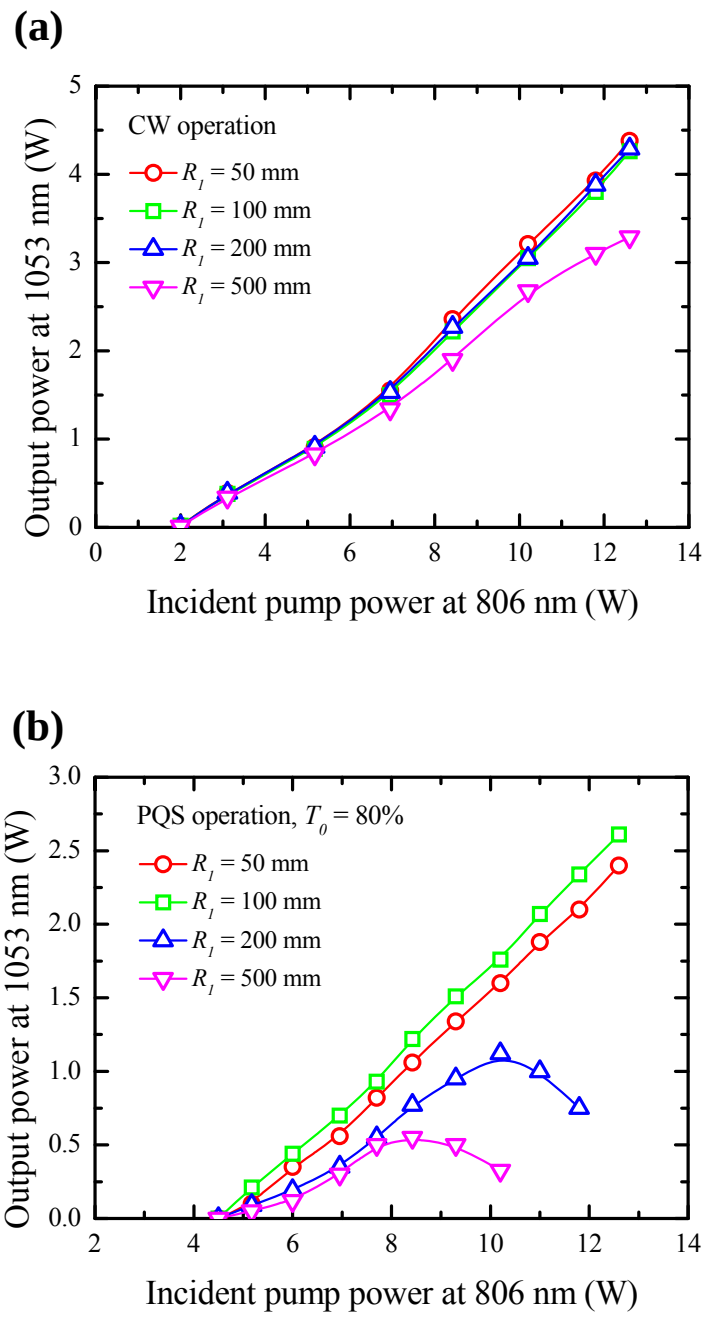

Fig. 2.6.3. Output power as a function of the incident pump power for the cases of R_1 = 50, 100, 200, and 500 mm: (a) in the CW operation; (b) in the PQS operation.

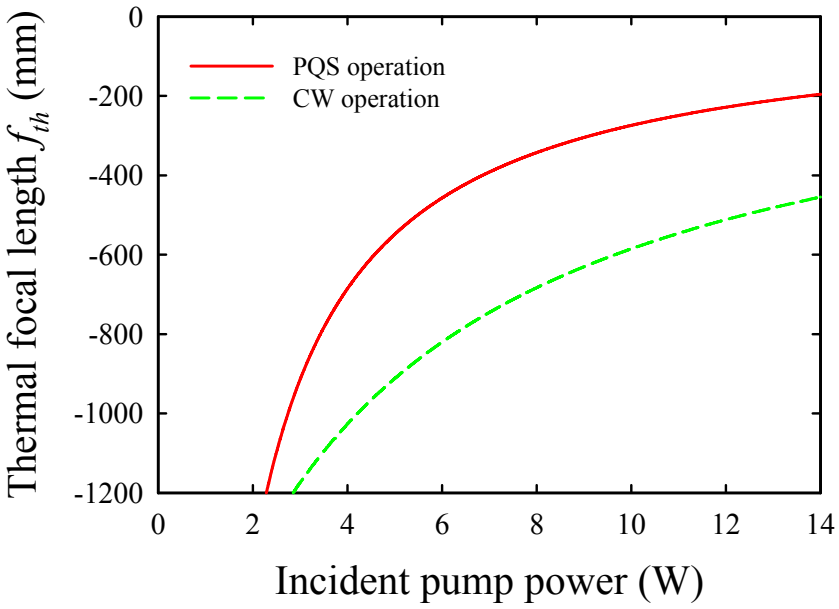

Fig. 2.6.4. Numerical calculations of the thermal focal length versus the incident pump power for the CW and PQS cases.

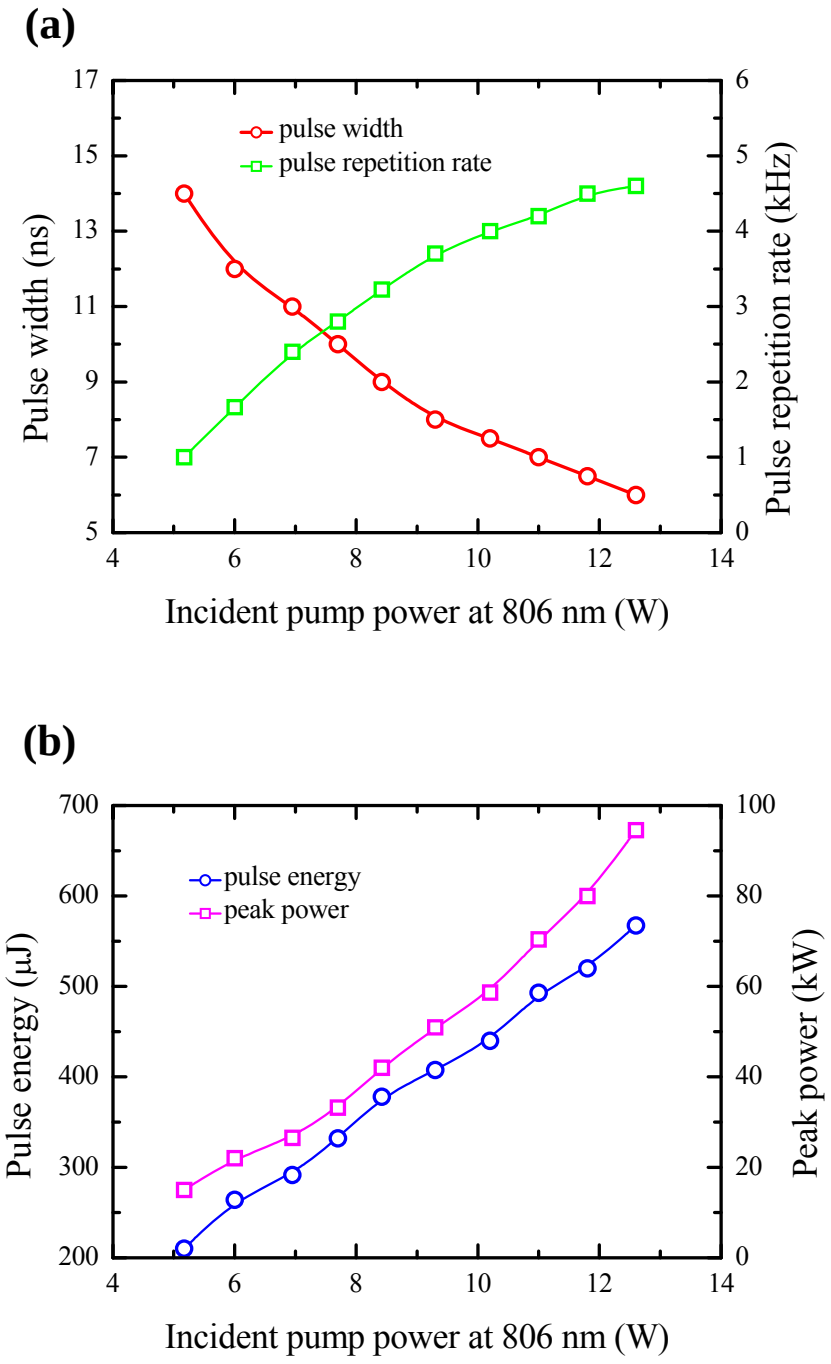

Fig. 2.6.5. Dependences of (a) the pulse width, pulse repetition rate, (b) pulse energy, and peak power on the incident pump power in the PQS operation with R_1 = 100 mm.

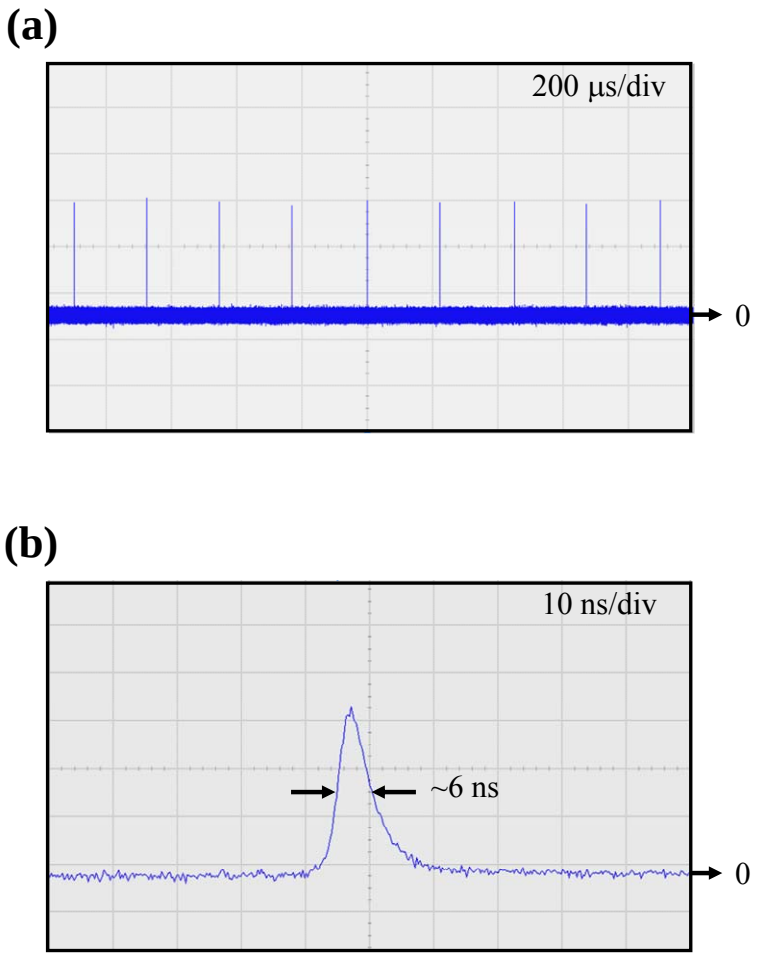

Fig. 2.6.6. Typical temporal behaviors at 1053 nm with: (a) time span of 2 ms, and (b) time span of 100 ns.

2.7 Pulsed Pumped Passively Q-Switched c-cut Nd:YLF Laser at 1053 nm

I. Introduction

As indicated in Sec. 2.6, the remarkable enhancement of the fractional thermal loading turns into a critical issue in designing the optical resonator under the continuously pumped PQS operation. Besides, the performance of the continuously pumped PQS laser can be noticeably degraded by the timing jitter as a result of the complex dynamic behavior inside the saturable absorber [57,58]. Practically, pulsed pumping and quasi-CW pumping are effective approaches capable of simultaneously reducing the heat generation inside the gain medium [59] and improving the instability of the pulse period [60,61].

In this section, we originally utilize a nearly hemispherical cavity to accomplish the energy scale-up for a mJ- and ns-level pulsed pumped Nd:YLF laser passively Q-switched by the Cr^{4+}:YAG saturable absorber. This compact laser is able to efficient generate pulse energy as large as 1.38 mJ and pulse width as short as 5 ns under a pulse repetition rate of 100 Hz.

II. Experimental setup

Figure 2.7.1 schematically depicts the experimental arrangement of our pulsed pumped PQS Nd:YLF laser. The input concave mirror was AR coated at 806 nm on the entrance face, and it was coated for high transmission at 806 nm as well as for high reflection at 1053 nm on the second surface. The gain medium was a 0.8 at. % c-cut Nd:YLF crystal with the dimensions of 4 mm in diameter and 15 mm in length. The Nd:YLF crystal was placed adjacent to the input mirror. Both facets of the laser crystal were AR coated at 806 and 1053 nm. The Cr^{4+}:YAG saturable absorber was with an initial transmission of 80 %, and it was AR coated at 1053 nm on both surfaces. The laser crystal and saturable absorber were wrapped with indium foil and mounted in water-cooled copper heat sinks at 16˚C. An intracavity Brewster plate was inserted inside the cavity to force linearly polarized operation. The pump source was a fiber-coupled laser diode at 806 nm with a core diameter of 400 μm and a numerical aperture of 0.14. A lens set having a focal length of 25 mm and a coupling efficiency of 90 % was used to reimage the pump beam inside the laser crystal with a magnification of unity. The output power of the laser diode was modulated by a train of pulses with a nearly rectangular shape. The pulse duration was set to be around 500 μs to match the upper-state lifetime of the Nd:YLF crystal. A flat mirror with a reflectivity of 60 % at 1053 nm was used as the output coupler during the experiment. The pulse temporal behaviors were recorded by a digital oscilloscope with the sampling interval of 0.1 ns and the bandwidth of 1 GHz together with a fast InGaAs photodiode. The pulse energy was measured with an energy meter (Thorlabs, PM100D).

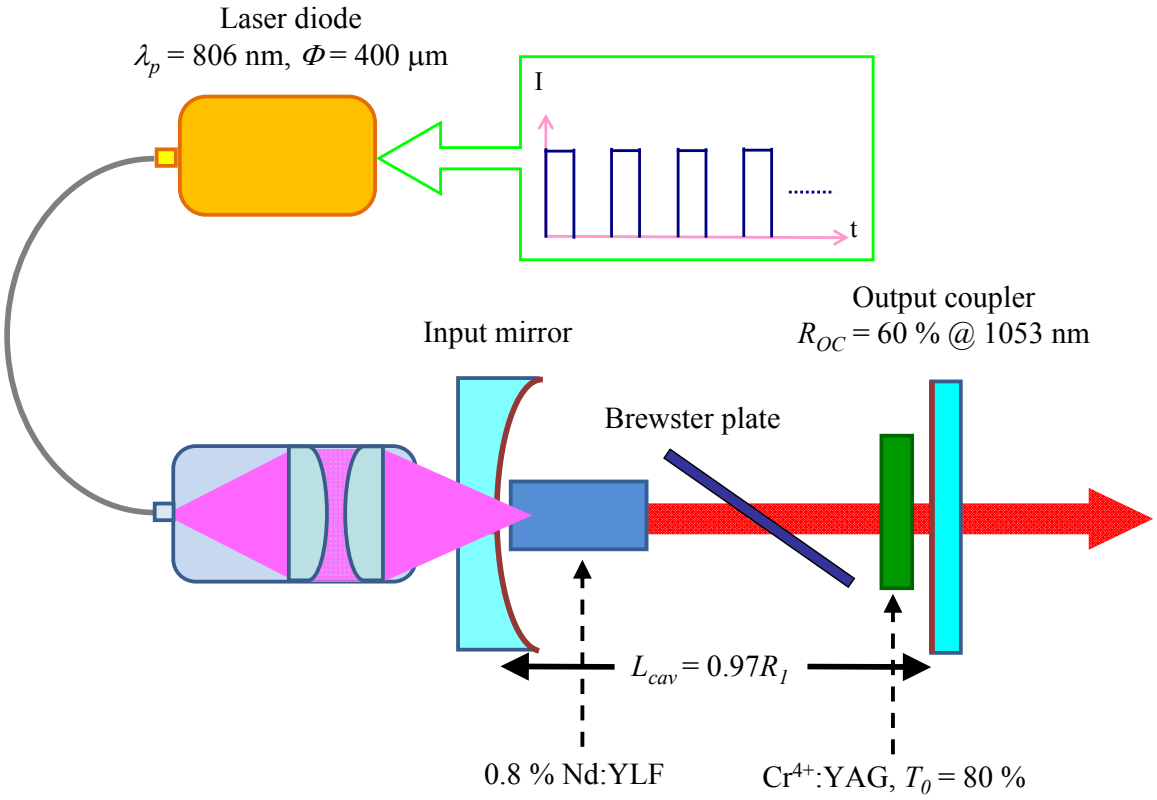

Fig. 2.7.1. Experimental arrangement of the pulsed pumped PQS Nd:YLF laser with the Cr^{4+}:YAG saturable absorber.

III. Cavity analysis

It is well known that the Q-switched pulse energy is linearly proportional to the square of the laser mode radius inside the gain medium. With the ABCD-matrix theory, Fig. 2.7.2 illustrates the numerical calculation of the dependences of the laser mode radius ω_1 inside the gain medium on the cavity length L_{cav} for the cases of R_1 = 50, 100, and 150 mm in a concave-plano cavity, where L_{cav} and R_1 stand for the cavity length and the ROC of the input mirror. Note that the thermal-lensing effect is not considered in this calculation, and including thermal lens is equivalent to the case of reducing the ROC of the input mirror. It can be seen that the laser mode radius increases with the cavity length until the resonator reaches the boundary of the stable region, i.e., $L_{cav} = R_1$. Practically, we choose the cavity length with the constraint $L_{cav} = 0.97R_1$ in the following discussions to realize the large laser mode radius and be insensitive to the environmental perturbation in the meantime. From Fig. 2.7.2, we also observe that increasing the ROC of the input mirror can further expand the laser mode radius to scale up the pulse energy of the Q-switched laser.

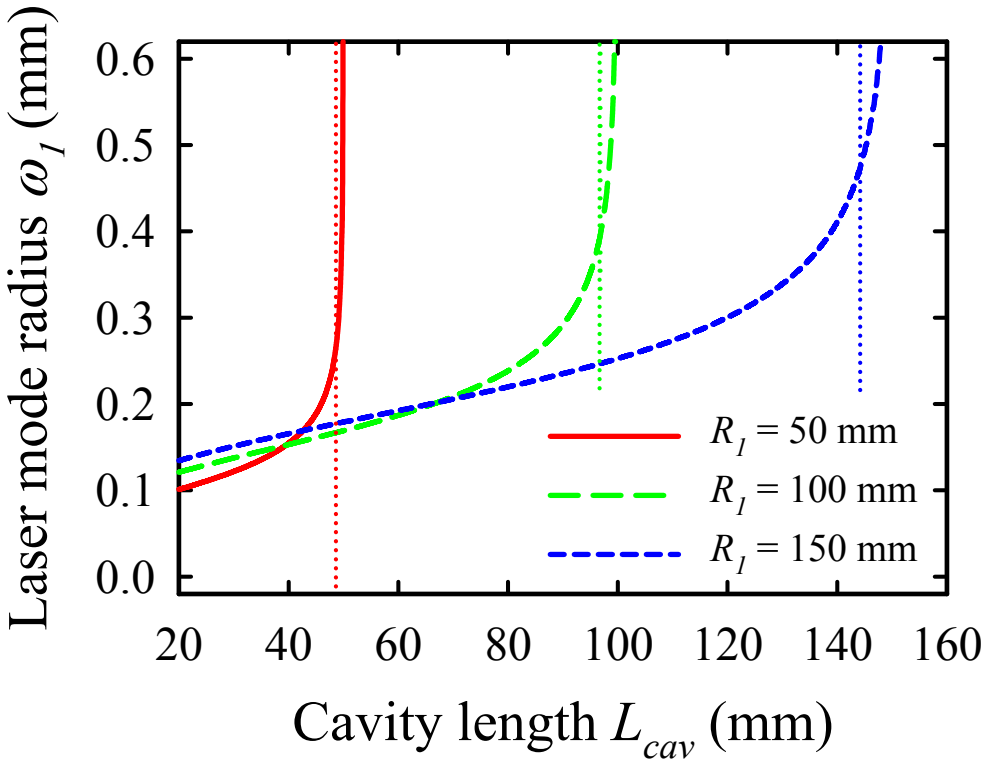

Fig. 2.7.2. Dependences of the laser mode radius inside the gain medium on the cavity length for R_1 = 50, 100, and 150 mm in a concave-plano cavity, where vertical dotted lines indicate the constraint of $L_{cav} = 0.97R_1$.

IV. Performance of PQS operation

During the experiment, the input mirrors with R_1 = 50, 100, and 150 mm were utilized for comparative investigation of the PQS performance. The pulse energies as a function of the pulse repetition rate are displayed in Fig. 2.7.3. The pulse energies were obtained by averaging the values of the multiple measurements. The pulse energies are found to increase from 0.44 to 0.57 mJ for R_1 = 50 mm, from 0.72 to 1.04 mJ for R_1 = 100 mm, and from 1 to 1.38 mJ for R_1 = 150 mm, when the pulse repetition rate is decreased from 1 kHz to 100 Hz. The threshold input energies are experimentally found to be 4.75-6 mJ for R_1 = 50 mm, 7-10.4 mJ for R_1 = 100 mm, and 8.67-14.1 mJ for R_1 = 150 mm, the real value depends on the pulse repetition rate. The experimentally obtained pulse energies are used to evaluate the laser mode radii with the fitted formula given by Eq. (26) from Ref. [19] in terms of the present cavity parameters. This equation is based on the fact that the pulse energy is proportional to the modulation loss of the saturable absorber and inversely proportional to the total cavity losses when the saturable absorber bleaches. The obtained radii are subsequently utilized to estimate the thermal focal lengths for the cavity to be influenced by a thermal lens with the condition $L_{cav} = 0.97R$. As a result, the relationship between the thermal focal length f_{th} and the average input power P_{in} can be built with the empirical formula $f_{th} = C / P_{in}$, where C is the proportional constant. The constant C for the present experiment is numerically determined to be -5.733 W m. For comparison, the proportional constant of -3.087 W m for the continuously pumped PQS case is estimated with a stability criterion by a separable experiment performed in Sec. 2.6. Note that the larger the magnitude of the constant $|C|$, the weaker the thermal-lensing effect. Therefore, the reduction of the thermal-lensing effect for the pulsed pumped PQS laser is manifestly verified in comparison with that for the continuously pumped counterpart. Besides, the shrinkage of the laser mode radius due to the relatively severe thermal-lensing effect explains why the pulse energy is smaller at higher pulse repetition rate for a specific ROC of the input mirror.

Typical temporal behavior at a pulse repetition rate of 500 Hz for R_1 = 100 mm is sketched in Fig. 2.7.4(a). The duration of the main pulse increases from 5 to 12 ns with the increase of the ROC of the input mirror from 50 to 150 mm. This trend is due to the fact that the Q-switched pulse duration is generally proportional to the cavity length. Moreover, it is experimentally found that the degree of the satellite pulse lessens with

the increase of the ROC of the input mirror. To discover the occurrence of the satellite pulse, the beam quality factors were measured with the 90/10 knife-edge method, as depicted in Fig. 2.7.4(b). It can be deduced that the improvement of the beam quality factors is consistent with the suppressing of the satellite pulse. This implies the repression of the excitation of few high-order transverse mode is of critical importance in obtaining a perfect Q-switched pulse without satellite pulse. With the numerical integration of the temporal pulse profile and the experimentally obtained pulse energy, the peak powers with respect to the pulse repetition rate are estimated. By increasing the pulse repetition rate from 100 Hz to 1 kHz, the peak powers are found to vary from 51.7 to 37.3 kW for R_1 = 50 mm, from 45.5 to 29.2 kW for R_1 = 100 mm, and from 47.4 to 29.6 kW for R_1 = 150 mm.

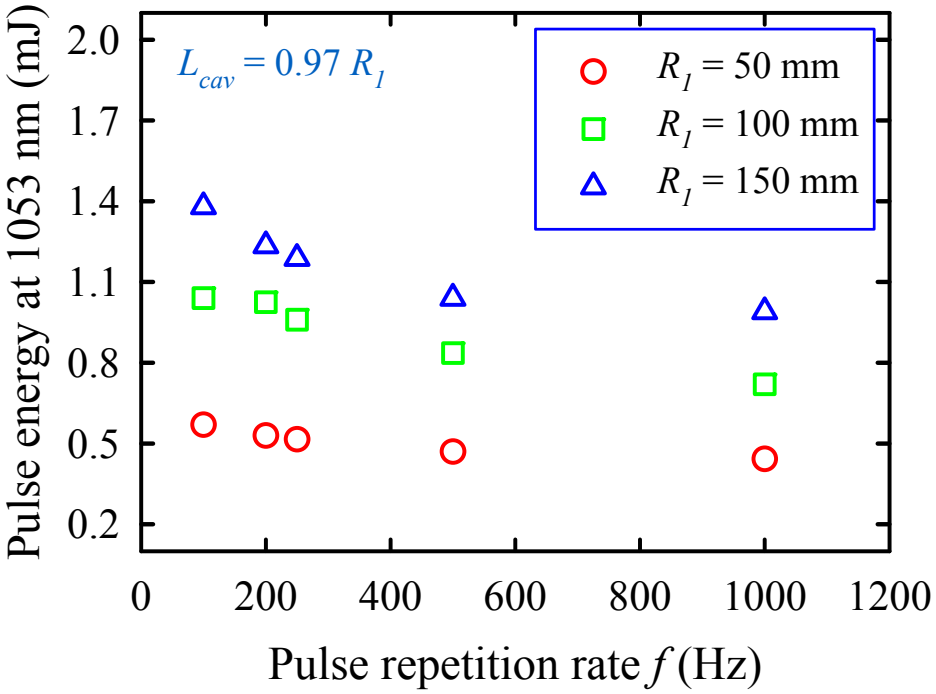

Fig. 2.7.3. Pulse energies at 1053 nm as a function of the pulse repetition rate.

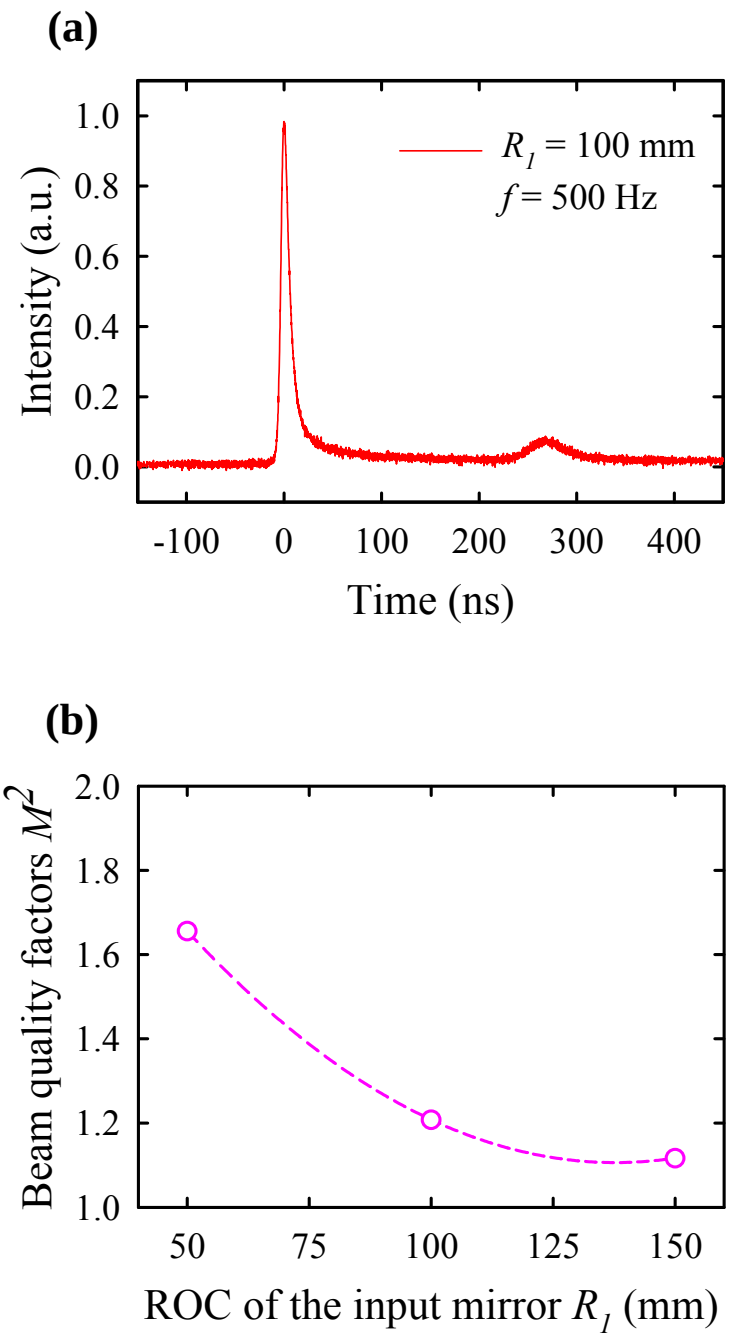

Fig. 2.7.4. (a) Typical temporal behavior at a pulse repetition rate of 500 Hz for R_1 = 100 mm; (b) Variation of the beam quality factors versus the ROC of the input mirror.

2.8 Actively Q-Switched Nd:YLF Laser at 1053 nm

I. Introduction

As discussed in Sec. 2.3, the AO Q-switch can offer the convenience of converting from CW to repetitively Q-switched operations simply by transmitting the RF drive power. In this section, we utilize the AO Q-switch to obtain a high-energy AQS Nd:YLF laser with the pulse repetition rate tunable from 5 to 40 kHz. We exhaustively explore the influences of the thermal effect and the anisotropic property of the AO Q-switch on the polarization characteristics of the c-cut Nd:YLF laser in the CW and Q-switched operation, respectively. Moreover, under an incident pump power of 12.7 W, the maximum output power of 4.5 W at 5 kHz and the largest pulse energy of 800 μJ at 40 kHz are accomplished, respectively.

II. Experimental setup

The experimental setup for the AQS Nd:YLF laser is schematically shown in Fig. 2.8.1. The input mirror was a concave mirror with the ROC of 300 mm. It was AR coated at 806 nm on the entrance face, and was coated at 806 nm for high transmission as well as 1053 nm for high reflection on the second surface. The gain medium was a 0.8 at. % c-cut Nd:YLF crystal (CASTECH) with the diameter of 4 mm and the length of 15 mm. Both facets of the laser crystal were AR coated at 806 and 1053 nm. Note that although it is an uniaxial crystal with the highly anisotropic property, the Nd:YLF crystal effectively exhibits the optically isotropic characteristics in the transverse plane when it is cut along the crystallographic c axis. The orientation of the rod axis of the present c-cut crystal to the crystallographic c axis was within 1 degree. The Nd:YLF crystals was wrapped with indium foil and mounted in a water-cooled copper heat sink at 18 °C. A 20-mm-long AO Q-switch (Gooch & Housego) was AR coated at 1053 nm on both surfaces. It was placed in the center of the laser cavity, and was driven at a central frequency of 41 MHz with a RF power of 25 W. A flat mirror with a reflectivity of 80 % at 1053 nm was utilized as the output coupler during the experiment. The pump source was an 806-nm fiber-coupled laser diode with a core diameter of 600 μm and a numerical aperture of 0.2, respectively. The polarization state emitted from the fiber-coupled laser diode was measured to be randomly polarized. The pump beam was reimaged into the laser crystal with a lens set that has a focal length of 25 mm with a magnification of unity and a coupling efficiency of 90 %. The cavity length was set to be L_{cav} = 115 mm for the construction of a compact AQS laser. The pulse temporal behaviors were recorded by a LeCroy digital oscilloscope (Wavepro 7100, 10 G samples/s, 1 GHz bandwidth) with a fast InGaAs photodiode.

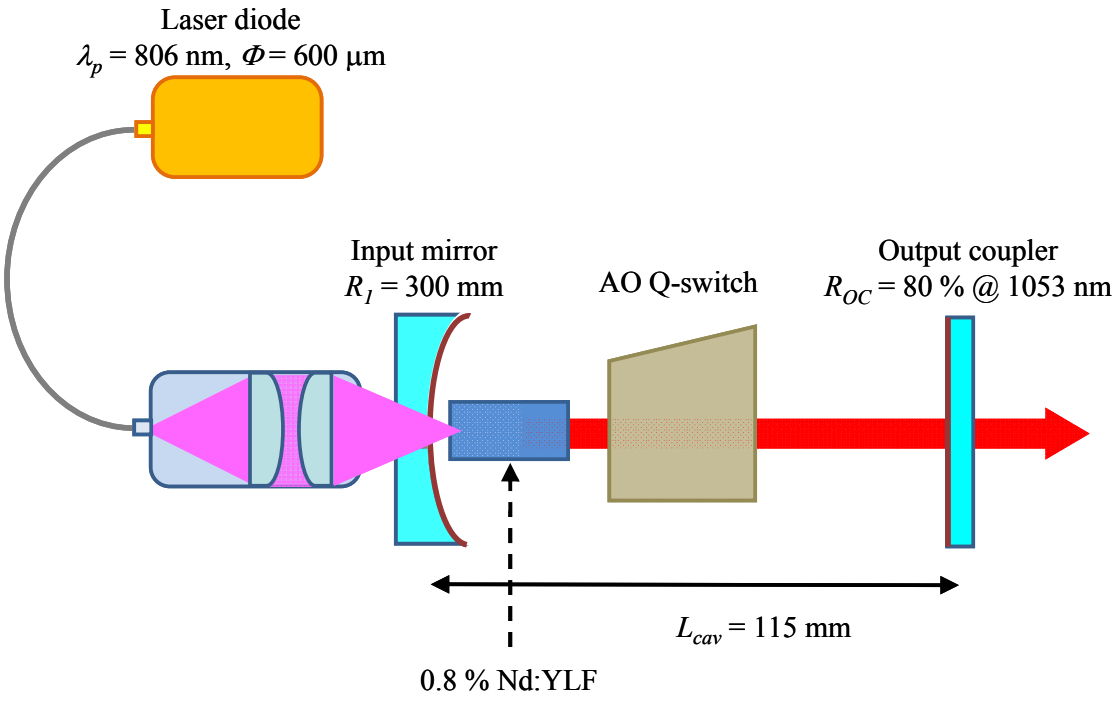

Fig. 2.8.1. Experimental setup for the AQS Nd:YLF laser.

III. Performance of CW and AQS operations

First of all, the AO Q-switch was removed from the laser cavity to investigate the CW performance of the c-cut Nd:YLF laser. We utilized an intracavity polarizer to make a comparative study of the output characteristics between the linearly and randomly polarized states, respectively. Figure 2.8.2(a) illustrates the output powers at 1053 nm with and without an intracavity polarizer versus the incident pump power at 806 nm. The maximum output power and slope efficiency without an intracavity polarizer are found to be up to 4.7 W and 43.1 %, respectively, as depicted by the red curve in Fig. 2.8.2(a). However, the output power and slope efficiency obtained with an intracavity polarizer are found to be remarkably lower than those obtained without an intracavity polarizer, as revealed by the green curve in Fig. 2.8.2(a). Moreover, the roll-over phenomenon in the linearly polarized state was experimentally observed at an incident pump power of 10.4 W. In the early researches on the solid-state laser, it was found that the thermally induced birefringence of the optically isotropic material brings in the coupling of the power between the mutually orthogonal polarization components. Consequently, the forbidden polarization state would be removed with the introduction of a polarizer inside the laser cavity [21]. This so-called thermal depolarization loss undoubtedly explains why substantially decreased output power and considerably poorer slope efficiency are obtained in the present linearly polarized c-cut Nd:YLF laser.

We then inserted the AO Q-switch into the laser cavity without an intracavity polarizer to explore the polarization characteristics of the c-cut Nd:YLF laser. Figure 2.8.2(b) describes the dependences of the polarization ratio $P_{horizontal}/P_{vertical}$ on the incident pump power at a pulse repetition rate of 5, 8, 10, 20, and 40 kHz, where $P_{horizontal}$ and $P_{vertical}$ stand for the output power with the oscillated polarization to be parallel and perpendicular to the base of the AO Q-switch, respectively. The polarization ratios for all cases are found to continuously decrease with the increase of the incident pump power. This observation is similar to the works reported in Refs. [62,63]. The diffractive efficiency of the AO Q-switch operated at the compressional mode is polarization dependent, in which the light with the oscillated polarization that is parallel to the propagation of the acoustic wave experiences lower diffractive loss. In the meantime, the randomly polarized pump beam leads the gain distribution in the c-cut Nd:YLF crystal to be isotropic; that is, the gains for the mutually orthogonal

polarization components of the laser beam are the same. As a consequence, the lower diffractive loss makes the horizontally polarized laser beam to own the larger net gain as compared with the vertically polarized one, which produces a high degree of the linearly polarized operation at a low incident pump power. However, the polarization ratio is experimentally found to decrease with increasing the incident pump power owing to the reduced difference of the net gain between the mutually orthogonal polarization components. Eventually, a nearly random polarization state was acquired at the maximum incident pump power of 12.7 W.

Figure 2.8.3 depicts the dependences of the output power, pulse width, pulse energy, and peak power on the pulse repetition rate at an incident pump power of 12.7 W. When the pulse repetition rate increases from 5 to 40 kHz, the output power varies from 4 to 4.5 W and the pulse width increases linearly from 25 to 180 ns, as shown in Fig. 2.8.3(a). Consequently, it can be found that the pulse energy changes from 800 to 113 μJ and the peak power decreases from 32 to 0.63 kW by increasing the pulse repetition rate from 5 to 40 kHz, as revealed in Fig. 2.8.3(b). Figures 2.8.4(a)-(d) illustrate the pulse trains of the AQS Nd:YLF laser at a pulse repetition rate of 5, 40, 50, and 100 kHz, respectively. It is experimentally found that the pulse-to-pulse amplitude stability is better than ± 8 % when the laser operates at 5-40 kHz, as exhibited in Figs. 2.8.4(a) and (b). Nevertheless, increasing the pulse repetition rate beyond 50 kHz results in an unstable Q-switched operation with the amplitude fluctuation larger than 20 %, as revealed in Fig. 2.8.4(c). Moreover, the phenomenon of the pulse missing shown in Fig. 2.8.4(d) is observed at a pulse repetition rate of 100 kHz owing to the lack of the gain for the Q-switched Nd:YLF laser operated at such high pulse repetition rate. Therefore, it is of crucial importance to design an intricate cavity for the stable pulsed operation if the Q-switched Nd:YLF laser with high pulse repetition rate is required [53].

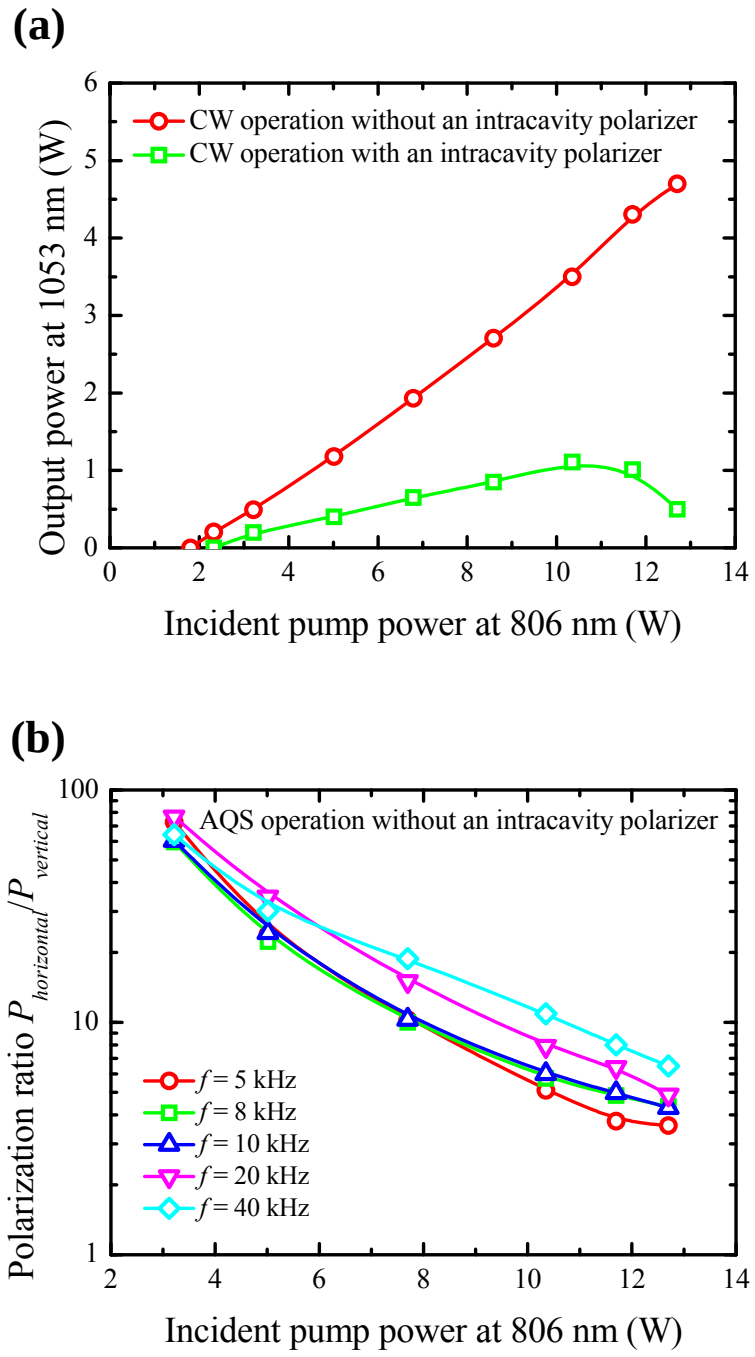

Fig. 2.8.2. (a) Output powers at 1053 nm with and without an intracavity polarizer versus the incident pump power at 806 nm in the CW operation; (b) The polarization ratios $P_{horizontal}/P_{vertical}$ with respect to the incident pump power at a pulse repetition rate of 5, 8, 10, 20, and 40 kHz, where $P_{horizontal}$ and $P_{vertical}$ represent the output powers with the oscillated polarization to be parallel and perpendicular to the base of the AO Q-switch, respectively.

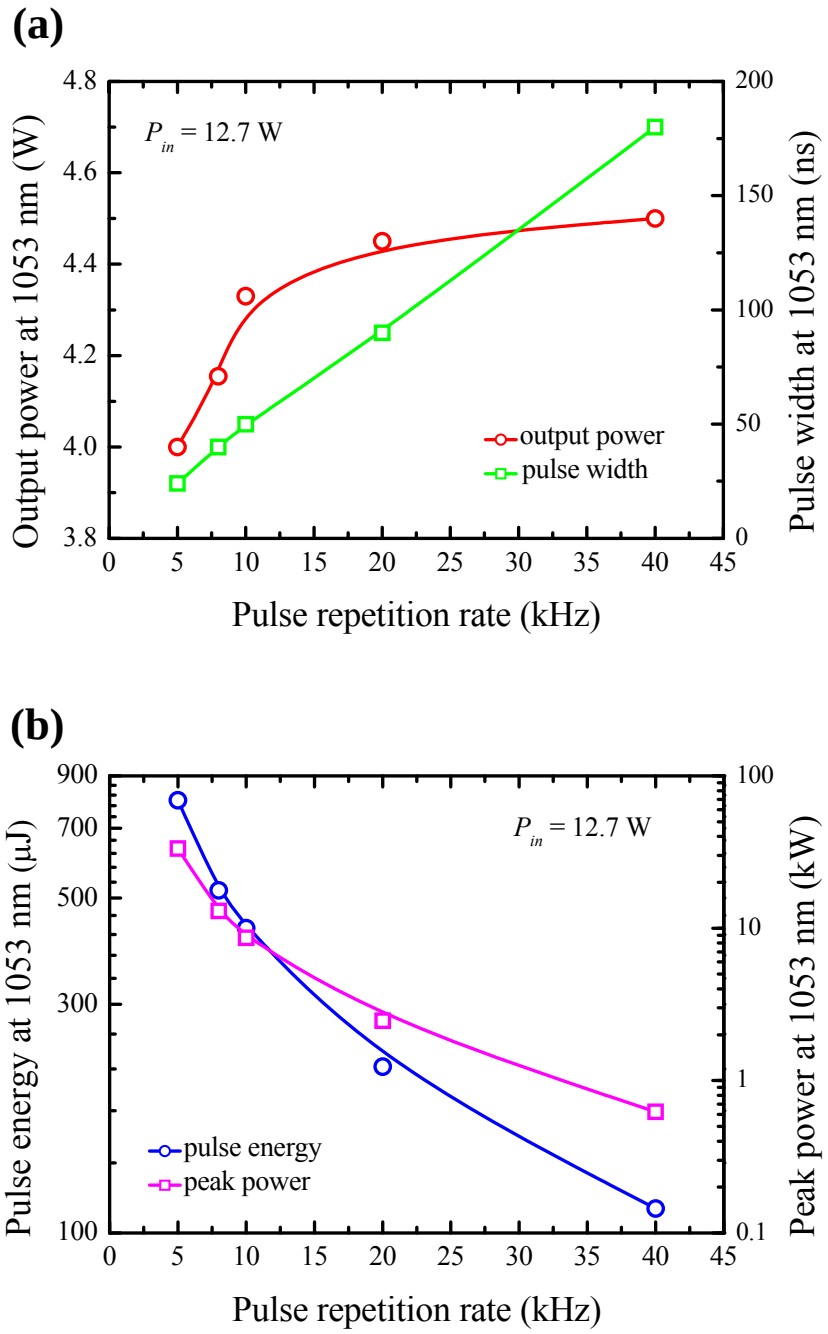

Fig. 2.8.3. Dependences of the (a) output power, pulse width, (b) pulse energy and peak power at 1053 nm on the pulse repetition rate at an incident pump power of 12.7 W.

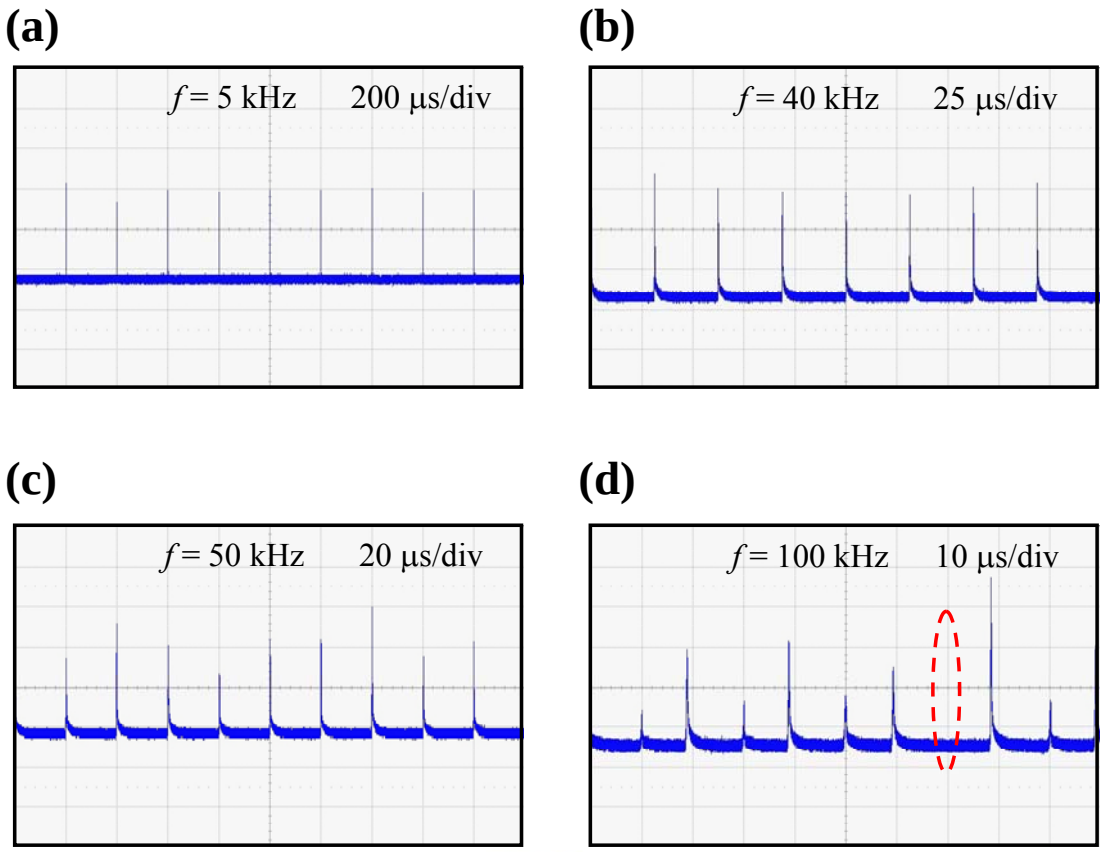

Fig. 2.8.4. Pulse trains of the Q-switched Nd:YLF laser at a pulse repetition rate of (a) 5 kHz, (b) 40 kHz, (c) 50 kHz, and (d) 100 kHz. The dashed circle in Fig. 4(d) indicates the phenomena of the pulse missing.

2.9 Conclusion

High-power Q-switched Nd:YVO_4 lasers at 1064 nm and high-energy Q-switched Nd:YLF lasers at 1053 nm have been optimized to exhibit excellent output performance. We have designed a high-peak-power PQS Nd:YVO_4 laser with the Cr^{4+}:YAG crystal as a saturable absorber. We theoretically analyze and experimentally realize a compact PQS laser by considering the second threshold condition and thermal-lensing effect. At an incident pump power of 16.3 W, the output power reaches 6.2 W with a pulse width of 7 ns and a pulse repetition rate of 56 kHz. The corresponding pulse energy and peak power are found to be up to 111 μJ and 16 kW, respectively.

In Sec. 2.3, we have firstly employed a Nd:YVO_4 crystal with dopant concentration as low as 0.1 at.% in an AQS laser to explore the parasitic lasing effect in a flat-flat resonator. Experimental results reveal that the parasitic lasing leads to a long tail in the Q-switched pulse. We experimentally determine the critical cavity length without the parasitic lasing effect as a function of incident pump power. We also confirm that the Nd:YVO_4 crystal with dopant concentration greater than 0.2 at.% is hardly serviceable in designing a high-power Q-switched laser without parasitic lasing. At an incident pump power of 44 W, the maximum output power of 19.4 W is obtained at 100 kHz, while the shortest pulse width of 8 ns, the largest pulse energy of 650 μJ, and the highest peak power of 81.5 kW are accomplished at 20 kHz.

In Sec. 2.5, we have exploited the birefringence of the a-cut Nd:YLF crystal to realize the selection of the polarization in a compact concave-plano resonator. We experimentally find that a reliable linearly polarized TEM_{00}-mode laser at 1053 nm can be achieved in a cavity as short as 5 cm by using an a-cut Nd:YLF crystal with a wedged angle of 3^o. We further use a Cr^{4+}:YAG saturable absorber with an initial transmission of 80 % to investigate the performance of the PQS operation for various output couplings. With an output coupling of 30 %, the maximum output power of 2.3 W is generated at an incident pump power of 12 W, where the pulse repetition rate and pulse width are 8 kHz and 9 ns, respectively. The corresponding pulse energy and peak power are calculated to be up to 288 μJ and 32 kW, respectively.

With c-cut Nd:YLF crystal, we have developed a straightforward method to implement the power scale-up of a compact high-pulse-energy PQS laser at 1053 nm

with the Cr^{4+}:YAG crystal as a saturable absorber in a concave-plano cavity. We numerically analyze the mode-to-pump size ratio as a function of the thermal focal length to verify that decreasing the ROC of the concave mirror can effectually extend the power scale-up for a laser in a concave-plano cavity to be influenced by a large negative thermal lens. With the developed method, we experimentally make a systematic comparison in the CW and PQS operations of the c-cut Nd:YLF laser to confirm the negative thermal-lensing effect enhanced by the ETU effect. At an incident pump power of 12.6 W, the optimum 1053-nm laser produces the maximum output power of 2.61 W with a pulse width of 6 ns and a pulse repetition rate of 4.6 kHz. The corresponding pulse energy and peak power are estimated to be up to 570 μJ and 95 kW, respectively.

Moreover, we have developed a compact mJ- and ns-level end-pumped PQS Nd:YLF/Cr^{4+}:YAG laser, where the pulse repetition rate can be easily controlled by the pulsed laser diode in the range from 100 Hz to 1 kHz. We theoretically analyze and experimentally realize that a nearly hemispherical resonator can effectively enlarge the laser mode area for energy scaling of the Q-switched laser. We also experimentally confirm that the reduction of the thermal-lensing effect with pulsed pumping as compared with CW pumping. The influences of the beam quality factors and the ROC of the input mirror on the performance of the PQS Nd:YLF laser are comparatively investigated. At a pulse repetition rate of 100 Hz, the pulse energy as large as 1.38 mJ and the pulse duration as short as 5 ns are efficiently produced with this compact pulsed laser.

Finally, the AO Q-switch has been utilized to achieve AQS operation in the c-cut Nd:YLF crystal with the pulse repetition rate ranging from 5 to 40 kHz. Under an incident pump power of 12.7 W, the maximum output power of 4.5 W is fulfilled at 5 kHz, whereas the shortest pulse duration of 25 ns, the largest pulse energy of 800 μJ, and the highest peak power of 32 kW are accomplished at 40 kHz. In addition, we have exhaustively explored the influences of the thermal effect and anisotropic property of the AO Q-switch on the polarization characteristics of the c-cut Nd:YLF laser in the CW and Q-switched operation for the first time.

References

[1] J. R. O'Connor, "Unusual crystal-field energy levels and efficient laser properties of YVO_4:Nd," Appl. Phys. Lett. **9**, 407-409 (1966).

[2] R. A. Fields, M. Birnbaum, and C. L. Fincher, "Highly efficient Nd:YVO_4 diode-laser end-pumped laser," Appl. Phys. Lett. **51**, 1885-1886 (1987).

[3] http://www.castech.com/download.html

[4] P. Yankov, "Cr^{4+}:YAG Q-switching of Nd:host laser oscillators," J. Phys. D **27**, 1118-1120 (1994).

[5] Y. Shimony, Y. Kalisky, and B. H. T. Chai, "Quantitative studies of Cr^{4+}:YAG as a saturable absorber for Nd:YAG laser," Opt. Mater. **4**, 547-551 (1995).

[6] Y. Shimony, Z. Burshtein, A. B. A. Baranga, Y. Kalisky, and M. Strauss, "Repetitive Q-switching of a CW Nd:YAG laser using Cr^{4+}:YAG saturable absorbers," IEEE J. Quantum Electron. **32**, 305-310 (1996).

[7] T. Dascalu, G. Philipps, and H. Weber, "Investigation of a Cr^{4+}:YAG passive Q-switch in CW pumped Nd:YAG lasers," Opt. Laser Technol. **29**, 145-149 (1997).

[8] X. Zhang, S. Zhao, Q. Wang, Q. Zhang, L. Sun, and S. Zhang, "Optimization of Cr^{4+}:doped saturable-absorber Q-switched lasers," IEEE J. Quantum Electron. **33**, 2286-2294 (1997).

[9] G. Xiao, J. H. Lim, S. Yang, E. V. Stryland, M. Bass, and L. Weichman, "Z-scan measurement of the ground and excited state absorption cross sections of Cr^{4+} in yttrium aluminum garnet," IEEE J. Quantum Electron. **35**, 1086-1091 (1999).

[10] A. Suda, A. Kadoi, K. Nagasaka, H. Tashiro, and K. Midorikawa, "Absorption and oscillation characteristics of a pulsed Cr^{4+}:YAG laser investigated by a double-pulse pumping technique," IEEE J. Quantum Electron. **35**, 1548-1553 (1999).

[11] A. G. Okhrimchuk and A. V. Shestakov, "Absorption saturation mechanism for YAG:Cr^{4+} crystals," Phys. Rev. B **61**, 988-995 (2000).

[12] A. Sennaroglu, U. Demirbas, S. Ozharar, and F. Yaman, "Accurate determination of saturation parameters for Cr^{4+}-doped solid-state saturable absorbers," J. Opt. Soc. Am. B **23**, 241-249 (2006).

[13] Y. Bai, N. Wu, J. Zhang, J. Li, S. Li, J. Xu, and P. Deng, "Passively Q-switched Nd:YVO_4 laser with a Cr^{4+}:YAG crystal saturable absorber," Appl. Opt. **36**, 2468-2472 (1997).

[14] C. Li, J. Song, D. Shen, N. S. Kim, J. Lu, and K. Ueda, "Diode-pumped passively Q-switched Nd:$GdVO_4$ lasers operating at 1.06 μm wavelength," Appl. Phys. B **70**, 471-474 (2000).

[15] C. Du, J. Liu, Z. Wang, G. Xu, X. Xu, K. Fu, X. Meng, and Z. Shao, "Continuous-wave and passively Q-switched Nd:$GdVO_4$ lasers at 1.06 μm end-pumped by laser-diode-array," Opt. Laser Technol. **34**, 699-702 (2002).

[16] Y. F. Chen and Y. P. Lan, "Comparison between c-cut and a-cut Nd:YVO_4 lasers passively Q-switched with a Cr^{4+}:YAG saturable absorber," Appl. Phys. B **74**, 415-418 (2002).

[17] J. Liu, J. Yang, and J. He, "Diode-pumped passively Q-switched c-cut Nd:$GdVO_4$ laser," Opt. Commun. **219**, 317-321 (2003).

[18] H. Yu, H. Zhang, Z. Wang, J. Wang, Z. Shao, and M. Jiang, "CW and Q-switched laser output of LD-end-pumped 1.06 μm c-cut Nd:$LuVO_4$ laser," Opt. Express **15**, 3206-3211 (2007).

[19] Y. F. Chen, Y. P. Lan, and H. L. Chang, "Analytical model for design criteria of passively Q-switched lasers," IEEE J. Quantum Electron. **37**, 462-468 (2001).

[20] N. Hodgson and H. Weber, *Laser Resonators and Beam Propagation*, 2nd edn. (Springer, Berlin, 2005), Chap. 8.

[21] W. Koechner, *Solid-State Laser Engineering*, 6th edn. (Springer, Berlin, 2005), Chap. 7.

[22] J. Bartschke, K. J. Boller, R. Wallenstein, I. V. Klimov, V. B. Tsvetkov, and I. A. Shcherbakov, "Diode-pumped passively Q-switched self-frequency-doubling Nd:YAB laser," J. Opt. Soc. Am. B **14**, 3452-3456 (1997).

[23] J. Liu, B. Ozygus, S. Yang, J. Erhard, U. Seelig, A. Ding, H. Weber, X. Meng, L. Zhu, L. Qin, C. Du, X. Xu, and Z. Shao, "Efficient passive Q-switching operation of a diode-pumped Nd:$GdVO_4$ laser with a Cr^{4+}:YAG saturable absorber," J. Opt. Soc. Am. B **20**, 652-661 (2003).

[24] S. P. Ng, D. Y. Tang, L. J. Qin, and X. L. Meng, "High power passively Q-switched Nd:$GdVO_4$ lasers," Opt. Commun. **229**, 331-336 (2004).

[25] S. P. Ng, D. Y. Tang, L. J. Qian, and L. J. Qin, "Satellite pulse generation in diode-pumped passively Q-switched Nd:$GdVO_4$ lasers," IEEE J. Quantum

Electron. **42**, 625-632 (2006).

[26] P. Maak, L. Jakab, P. Richter, H. J. Eichler, and B. Liu, "Efficient acousto-optic Q switching of Er:YSGG lasers at 2.79-μm wavelength," Appl. Opt. **39**, 3053-3059 (2000).

[27] J. Liu, C. Wang, C. Du, L. Zhu, H. Zhang, X. Meng, J. Wang, Z. Shao, and M. Jiang, "High-power actively Q-switched Nd:$GdVO_4$ laser end-pumped by a fiber-coupled diode-laser array," Opt. Commun. **188**, 155-162 (2001).

[28] J. H. García-López, V. Aboites, A. V. Kir'yanov, M. J. Damzen, and A. Minassian, "High repetition rate Q-switching of high power Nd:YVO_4 slab laser," Opt. Commun. **218**, 155-160 (2003).

[29] T. Ogawa, T. Imai, K. Onodera, H. Machida, M. Higuchi, Y. Urata, and S. Wada, "Efficient pulse operation of Nd:$GdVO_4$ laser with AO Q-switch," Appl. Phys. B **81**, 521-524 (2005).

[30] F. He, L. Huang, M. Gong, Q. Liu, and X. Yan, "Stable acousto-optics Q-switched Nd:YVO_4 laser at 500 kHz," Laser Phys. Lett. **4**, 511-514 (2007).

[31] X. Li, X. Yu, F. Chen, R. Yan, J. Gao, J. Yu, and D. Chen, "Comparison on performance of acousto-optically Q-switched Nd:$GdVO_4$ and Nd:YVO_4 lasers at high repetition rates under direct diode pumping of the emitting level," Opt. Express **17**, 9468-9476 (2009).

[32] M. E. Storm, "Controlled retroreflection: a technique for understanding and eliminating parasitic lasing," J. Opt. Soc. Am. B **9**, 1299-1304 (1992).

[33] Q. Liu, X. Yan, X. Fu, M. Gong, and D. Wang, "183 W TEM_{00} mode acoustic-optic Q-switched MOPA laser at 850 kHz," Opt. Express **17**, 5636-5644 (2009).

[34] A. G. Fox and T. Li, "Resonant modes in a maser interferometer," Bell Syst. Tech. J. **40**, 453-488 (1961).

[35] T. Li, "Diffraction loss and selection of modes in maser resonators with circular mirrors," Bell Syst. Tech. J. **40**, 917-932 (1965).

[36] Y. F. Chen, "Design criteria for concentration optimization in scaling diode end-pumped lasers to high powers: influence of thermal fracture," IEEE Quantum Electron. **35**, 234-239 (1999).

[37] S. Pan, L. Xue, X. Fan, H. Huang, and J. He, "Diode-pumped passively Q-switched mode-locked Nd:YLF laser with uncoated GaAs saturable absorber," Opt. Commun. **272**, 178-181 (2007).

[38] D. Li, Z. Ma, R. Haas, A. Schell, P. Zhu, P. Shi, and K. Du, "Diode-end-pumped double Nd:YLF slab laser with high energy, short pulse width, and diffraction-limited quality," Opt. Lett. **33**, 1708-1710 (2008).

[39] C. Bollig, C. Jacobs, M. J. D. Esser, E. H. Bernhardi, and H. M. V. Bergmann, "Power and energy scaling of a diode-end-pumped Nd:YLF laser through gain optimization," Opt. Express **18**, 13993-14003 (2010).

[40] A. V. Okishev and W. Seka, "Diode-pumped Nd:YLF master oscillator for the 30-kJ (UV), 60-beam OMEGA laser facility," IEEE J. Sel. Top. Quantum Electron. **3**, 59-63 (1997).

[41] T. M. Pollak, W. F. Wing, R. J. Grasso, E. P. Chicklis, and H. P. Jenssen, "CW laser operation of Nd:YLF," IEEE J. Quantum Electron. **18**, 159-163 (1982).

[42] J. E. Murray, "Pulsed gain and thermal lensing of Nd:$LiYF_4$," IEEE J. Quantum Electron. **19**, 488-491 (1983).

[43] G. Cerullo, S. D. Silvestri, and V. Magni, "High efficiency, 40 W cw Nd:YLF laser with large TEM_{00} mode," Opt. Commun. **93**, 77-81 (1992).

[44] B. Frei and J. E. Balmer, "1053-nm-wavelength selection in a diode-laser-pumped Nd:YLF laser," Appl. Opt. **33**, 6942-6946 (1994).

[45] W. A. Clarkson, P. J. Hardman, and D. C. Hanna, "High-power diode-bar end-pumped Nd:YLF laser at 1.053 μm," Opt. Lett. **23**, 1363-1365 (1998).

[46] M. Pollnau, P. J. Hardman, M. A. Kern, W. A. Clarkson, and D. C. Hanna, "Upconversion-induced heat generation and thermal lensing in Nd:YLF and Nd:YAG," Phys. Rev. B **58**, 16076-16092 (1998).

[47] P. J. Hardman, W. A. Clarkson, G. J. Friel, M. Pollnau, and D. C. Hanna, "Energy-transfer upconversion and thermal lensing in high-power end-pumped Nd:YLF laser crystals," IEEE J. Quantum Electron. **35**, 647-655 (1999).

[48] J. D. Zuegel and W. Seka, "Upconversion and reduced $^4F_{3/2}$ upper-state lifetime in intensely pumped Nd:YLF," Appl. Opt. **38**, 2714-2723 (1999).

[49] L. C. Courrol, E. P. Maldonado, L. Gomes, N. D. Vieira Jr, I. M. Ranieri, and S. P. Morato, "Diode pumping Nd-laser efficiency limitations due to up-conversion processes in Nd:YLF and Nd:GLF," Opt. Mater. **14**, 81-90 (2000).

[50] A. Agnesi and S. Dell'Acqua, "High-peak-power diode-pumped passively Q-switched Nd:YVO_4 laser," Appl. Phys. B **76**, 351-354 (2003).

[51] J. M. Auerbach and R. L. Schmitt, "Diode-laser-pumped monolithic Nd:YLF laser operating at 1.053 μm," Opt. Lett. **16**, 1171-1173 (1991).

[52] S. D. Pan, J. L. He, Y. E. Hou, Y. X. Fan, H. T. Wang, Y. G. Wang, and X. Y. Ma, "Diode-end-pumped passively CW mode-locked Nd:YLF laser by the LT-$In_{0.25}Ga_{0.75}As$ absorber," IEEE J. Quantum Electron. **42**, 1097-1100 (2006).

[53] Y. Sun, H. Zhang, Q. Liu, L. Huang, Y. Wang, and M. Gong, "High pulse repetition frequency all-solid-state 1053 nm Nd:YLF laser," Laser Phys. Lett. **7**, 722-725 (2010).

[54] S. Pan, K. Han, H. Wang, X. Fan, and J. He, "Diode-pumped passively Q-switched and mode-locked Nd:YLF laser with Cr^{4+}:YAG saturable absorber," Chin. Opt. Lett. **4**, 407-409 (2006).

[55] Y. F. Chen, T. M. Huang, C. C. Liao, Y. P. Lan, and S. C. Wang, "Efficient high-power diode-end-pumped TEM_{00} Nd:YVO_4 laser," IEEE Photon. Technol. Lett. **11**, 1241-1243 (1999).

[56] Y. F. Chen, Y. C. Chen, S. W. Chen, and Y. P. Lan, "High-power efficient diode-pumped passively Q-switched Nd:YVO_4/KTP/Cr^{4+}:YAG eye-safe laser," Opt. Commun. **234**, 337-342 (2004).

[57] D. Y. Tang, S. P. Ng, L. J. Qin, and X. L. Meng, "Deterministic chaos in a diode-pumped Nd:YAG laser passively Q switched by a Cr^{4+}:YAG crystal," Opt. Lett. **28**, 325 (2003).

[58] M. Kovalsky and A. Hnilo, "Chaos in the pulse spacing of passive Q-switched all-solid-state lasers," Opt. Lett. **35**, 3498 (2010).

[59] F. Hanson, "Efficient operation of a room-temperature Nd:YAG 946-nm laser pumped with multiple diode arrays," Opt. Lett. **20**, 148 (1995).

[60] J. B. Khurgin, F. Jin, G. Solyar, C. C. Wang, and S. Trivedi, "Cost-effective low timing jitter passively Q-switched diode-pumped solid-state laser with composite pumping pulses," Appl. Opt. **41**, 1095 (2002).

[61] K. Lee, Y. Kim, J. S. Gwag, J. H. Kwon, and J. Yi, "Comparison of CW pumping and Quasi-CW pumping for a passively Q-switched Nd:YAG laser," J. Korean Phys. Soc. **57**, 359 (2010).

[62] C. Lowrie, A. Zygmunt, A. Crout, Y. Liu, and J. R. Thompson, "Polarization control of a Q-switched, diode-pumped Nd:YAG laser," Appl. Opt. **34**, 4256-4260 (1995).

[63] T. Crawford, C. Lowrie, and J. R. Thompson, "Prelase stabilization of the polarization state and frequency of a Q-switched, diode-pumped, Nd:YAG laser," Appl. Opt. **35**, 5861-5869 (1996).


E S A
1896

Chapter 3

Nonlinear Frequency Conversion based on Optical Parametric Oscillations

3.1 Intracavity Optical Parametric Oscillator

Since the laser has become an indispensable component in many practical applications, laser safety attracts much attention, especially for the protection of eye hazards. Figure 3.1.1 shows the transmission of the human eye from the cornea to the retina and the absorption of the retina pigment epithelium as a function of the wavelength [1]. It can be seen that the radiation above 1400 nm would be strongly absorbed by the cornea and other tissues such as aqueous humor to considerably reduce the light intensity reaching the retina. As a consequence, the wavelength longer than 1400 nm is located in the so-called “eye-safe” regime, where higher pulse energy can be used without greatly damaging the human eyes.

High-peak-power eye-safe lasers have been rapidly developed since they are useful for a wide variety applications such as remote sensing, radar system, range finder, and biomedical research etc [2,3]. The OPO driven by the Q-switched Nd-doped crystal laser is one of the best methods for achieving nanosecond coherent radiation in the eye-safe region due to its high efficiency, high reliability, low threshold, and inherent robustness. Compared with the extracavity one, the IOPO intrinsically possesses the merits of lower pump threshold and higher conversion efficiency thanks to the multi-pass of the pump light through the nonlinear crystal in the fundamental laser cavity [4]. As a promising nonlinear crystal, the KTP crystal has the advantages of higher damage threshold, relatively wide acceptance angle, and larger nonlinear coefficient. Moreover, the KTP crystal with non-critical phase matching can maximize the effective nonlinear coefficient and eliminate the walk-off effect that is beneficial for efficient generation of the high-peak-power eye-safe lasers [5-10].

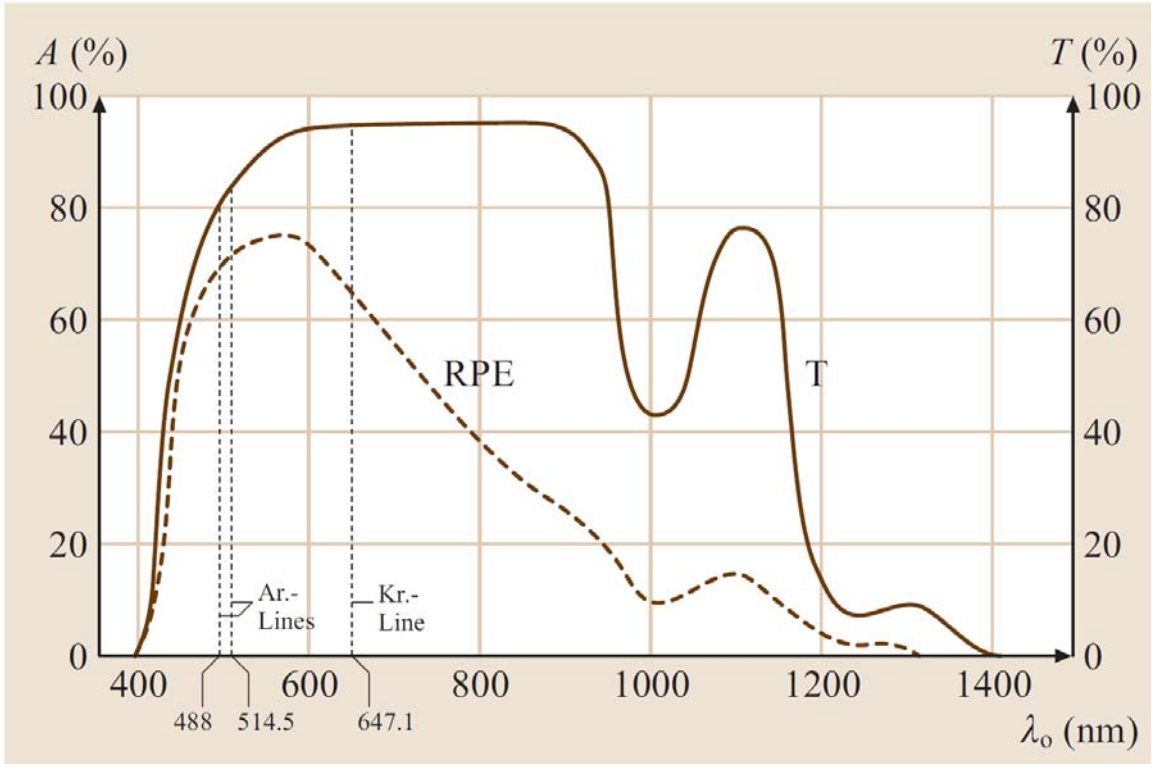

Fig. 3.1.1. Transmission of the human eye from the cornea to the retina and the absorption of the retina pigment epithelium as a function of the wavelength.

3.2 Q-Switched Nd:YVO_4 Eye-Safe Laser at 1572 nm

I. Introduction

To efficient generate the eye-safe radiation with the Nd-doped crystal laser, the IOPO cavity design is a crucial issue. We have reported that the scheme of the shared IOPO cavity [11] could achieve higher amplitude stability than the coupled cavity because more longitudinal modes could be simultaneously excited to reach OPO threshold. However, the shared cavity usually leads to lower conversion efficiency than the coupled cavity because of its longer cavity length. On the other hand, the configuration of the coupled IOPO cavity is usually designed to share the same output coupler with the fundamental cavity. Nevertheless, the amplitude stability of the signal output is severely dependent on the IOPO cavity alignment because the resonator length and the longitudinal-mode spacing are different for the fundamental and signal beams. It is not capable of aligning individually the IOPO cavity and the fundamental cavity for the coupled cavity. Consequently, the output power is very sensitive to the alignment of the shared output coupler and is difficult to optimize. From a review of previous studies, the power instability and the diode-to-signal conversion efficiency were 1.72 and 3.7 % for a Nd:YAG/KTA laser [12], 4 and 18 % for a Nd:YVO_4/KTA laser [13], and 1.2 and 6.5 % for a Nd:YAG/KTP/KTA laser [14]. It is practically important to improve the stability and attain high efficiency simultaneously in diode-pumped IOPOs.

In this section, we improve the performance of IOPO pumped by a diode-pumped Q-switched Nd:YVO_4/Cr^{4+}:YAG laser. The IOPO cavity is formed independently by a monolithic KTP crystal in which the mirrors are directly deposited on top of the nonlinear crystal. We study the performance of this IOPO cavity with different reflectivity of the output coupler at 1.5 μm (R_s) of 80 and 50 %. The output power at 1.5 μm is up to 3.3 W at the maximum incident pump power of 16.8 W, corresponding to the diode-to-signal conversion efficiency of up to 20 %, which is the highest one for IOPOs to our best knowledge. Moreover, the pulse amplitude fluctuations in standard deviation are greatly improved to be 2.6 % for R_s = 80 % and 4 % for R_s = 50 %, respectively.

II. Experimental setup

Figure 3.2.1 presents the schematic experimental setup, which is designed according to the guideline developed in Sec. 2.2. The 1064-nm resonator was formed by a plano-concave mirror with the ROC of 100 mm and a flat mirror. The input concave mirror was AR coated at 808 nm on the pump side, and was high reflection coated at 1064 nm and high transmission coated at 808 nm. The output coupler was coated to be highly reflective at 1064 nm and highly transmissive at 1.5 μm. The gain medium was a 12-mm-long a-cut 0.3 at.% Nd:YVO_4 crystal. Both end faces of the gain medium were AR coated at 1064 nm. The Cr^{4+}:YAG crystal with an initial transmission of 80 % was used for the PQS operation. Both end facets of the Cr^{4+}:YAG crystal were AR coated at 1064 nm and 1.5 μm. The gain medium and Cr^{4+}:YAG crystal were placed as close as possible to the input mirror and output coupler to achieve a high-quality PQS operation. Two KTP crystals with different coating characteristics were employed for comparison. Both of them were 20-mm-long and they were high transmission coated at 1064 nm and high reflection coated at 1.5 μm on one face. The remaining faces were coated for high transmission at 1064 nm together with R_s = 80 % and R_s = 50 % at 1.5 μm, respectively. The KTP crystals were used in a type-II non-critical phase matched configuration along the x-axis (θ = 90° and ϕ = 0°). The Nd:YVO_4, KTP, and Cr^{4+}:YAG crystals were wrapped with indium foil and mounted in water-cooled copper heat sinks. The water temperature was maintained at 20 °C. In comparison with our former work [15], we used a monolithic KTP crystal alone as the independent IOPO cavity and utilized another output coupler to form the fundamental cavity in this work. The pump source was an 18-W fiber-coupled laser diode at 808 nm. The fiber had an 800-μm core in diameter and a numerical aperture of 0.2. A focusing lens with a focal length of 25 mm and a coupling efficiency of 95 % was used to reimage the pump beam into the gain medium.

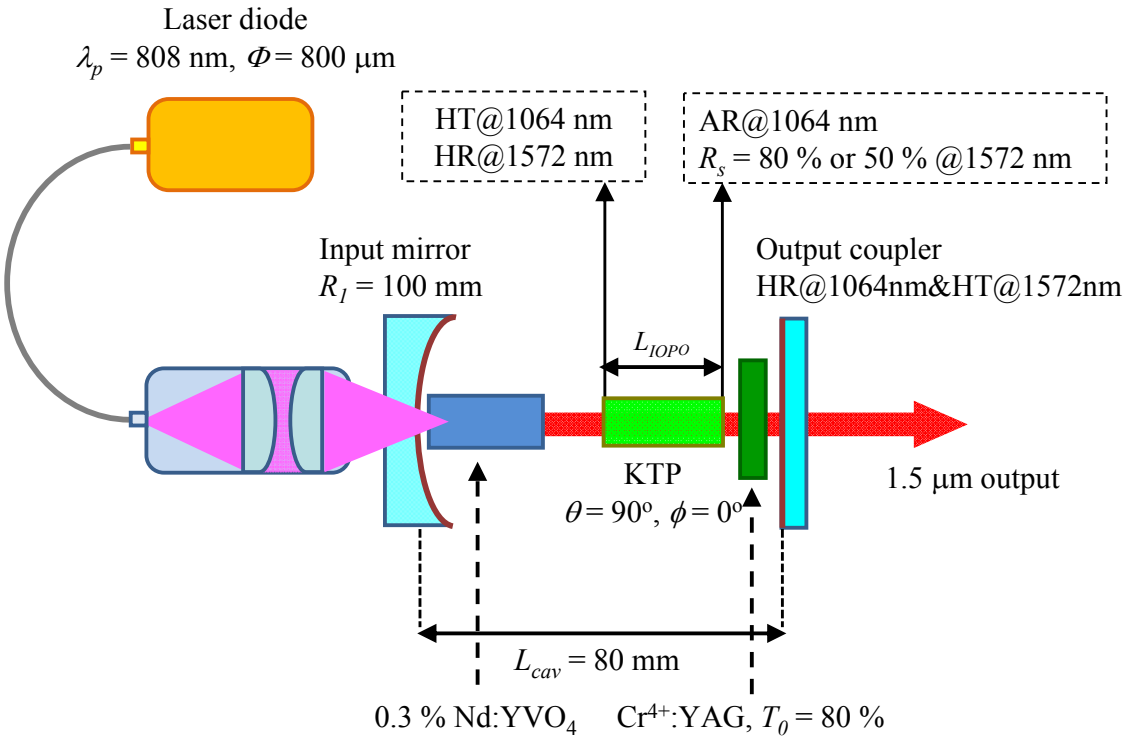

Fig. 3.2.1. Experimental setup for the diode-pumped Nd:YVO$_4$/Cr^{4+}:YAG/KTP eye-safe laser.

III. Performance of IOPO operation

Figure 3.2.2 shows the output powers at 1572 nm with respect to the incident pump power for R_s = 80 and 50 %, respectively. The pump thresholds and the maximum output powers for both cases are found to be almost the same, approximately 2 and 3.3 W. There are no obvious power roll-over phenomenon for both cases. The diode-to-signal conversion efficiencies are about 20 %, which are the highest conversion efficiencies among reported IOPOs performed with the Nd-doped crystal lasers to our knowledge. The improvement of output power as well as the conversion efficiency is very significant in comparison with our previous similar experiment [15]. Figure 3.2.3 depicts the pulse repetition rates with respect to the incident pump power for R_s = 80 and 50 %, respectively. The pulse repetition rates for both cases increase linearly with the incident pump power and reach 80 kHz for R_s = 80 % and 68 kHz for R_s = 50 % at the maximum incident pump power of 16.8 W. The pulse energies versus the incident pump power for R_s = 80 and 50 % are shown in Fig. 3.2.4. Both pulse energies increase with the incident pump power initially and start to saturate at about 40 and 45 μJ under an incident pump power of 9 W. The pulse energy saturation could be regarded as the satisfaction of the second threshold condition.

Figures 3.2.5 and 3.2.6 show the oscilloscope traces, which were recorded with a LeCroy digital oscilloscope (Wavepro 7100, 10 G samples/sec, 1 GHz bandwidth) with a fast InGaAs photodiode. Figure 3.2.5 illustrates the typical oscilloscope traces of the Q-switched pulse train for both cases at the maximum incident pump power. The amplitude fluctuations in standard deviation are 2.6 % for R_s = 80 % and 4 % for R_s = 50 %, respectively. Figure 3.2.6 presents the oscilloscope traces of a single pulse of the fundamental (1064 nm) and signal (1572 nm) waves at various incident pump powers for R_s = 80 and 50 %, respectively. For the case of R_s = 80 %, the number of satellite pulses in signal wave increases with the incident pump power. The ratio of the pulse energy of the major pulse to that of the entire pulses is calculated to be 10-15 % for the incident pump power higher than 12 W, where the pulse width of the major pulse is 2-3 ns. Hence the maximum peak power is estimated to be 1-2 kW. On the other hand, for the case of R_s = 50 %, the satellite pulse is not obvious for all pump powers because the conversion threshold is increased by reducing the reflectivity at signal wave [16,17]. The pulse duration is about 1.2 ns for all pump powers and the highest peak power is thus estimated to be 43 kW. To study the output power stability of the two cases, an

hour-long power fluctuation test was demonstrated. As shown in Fig. 3.2.7, the averaged output power is 3.34 W with a standard deviation of 6.9 mW for R_s = 80 % and the averaged output power is 3.3 W with a standard deviation of 35 mW for R_s = 50 %. The corresponding fluctuations in standard deviation are 0.2 and 1.0 % for R_s = 80 and 50 %, respectively.

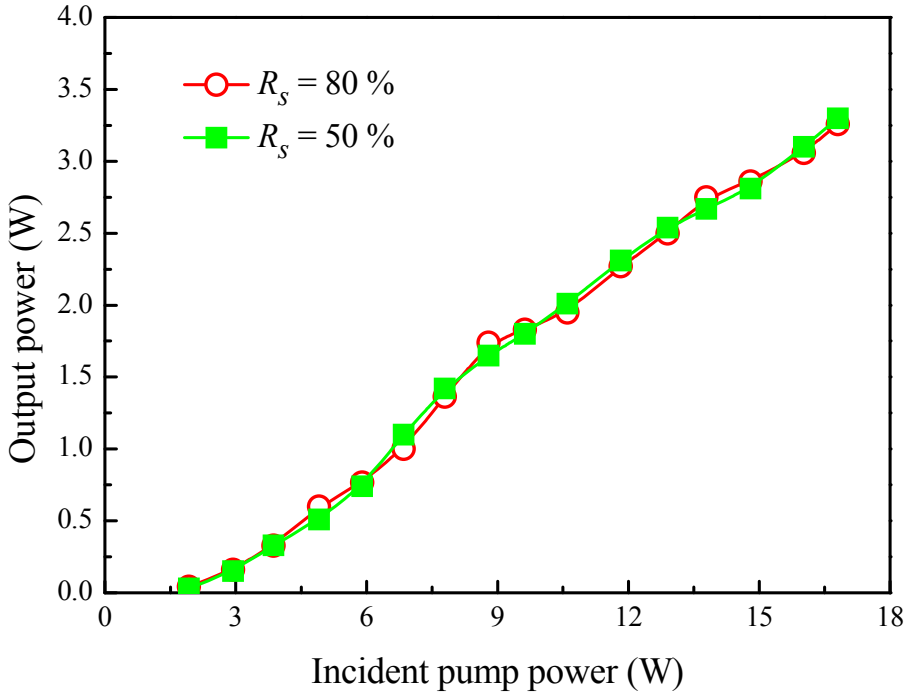

Fig. 3.2.2. Dependence of the output powers at 1572 nm on the incident pump power.

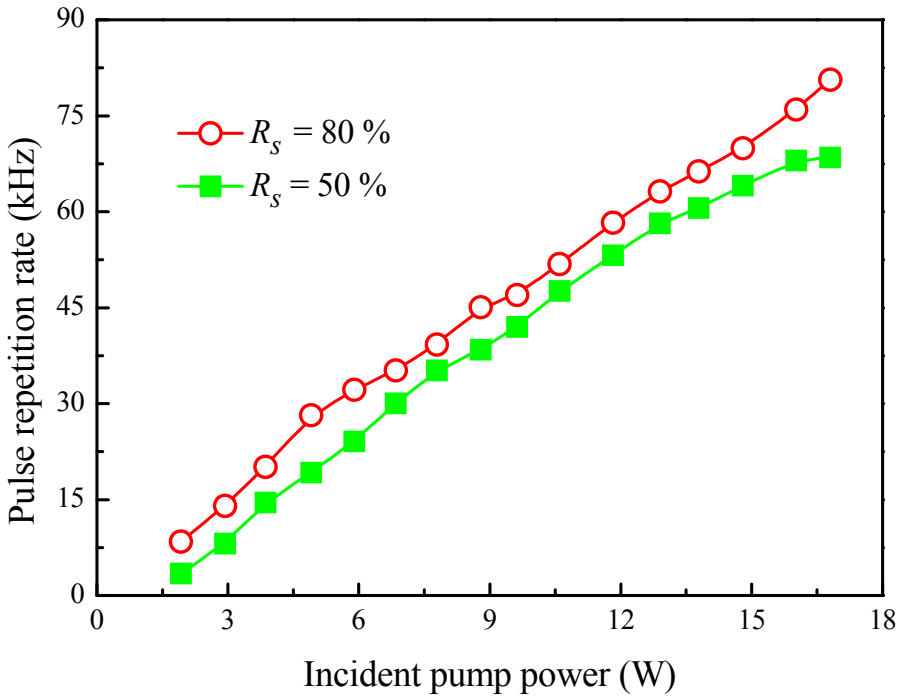

Fig. 3.2.3. Dependence of the pulse repetition rates at 1572 nm on the incident pump power.

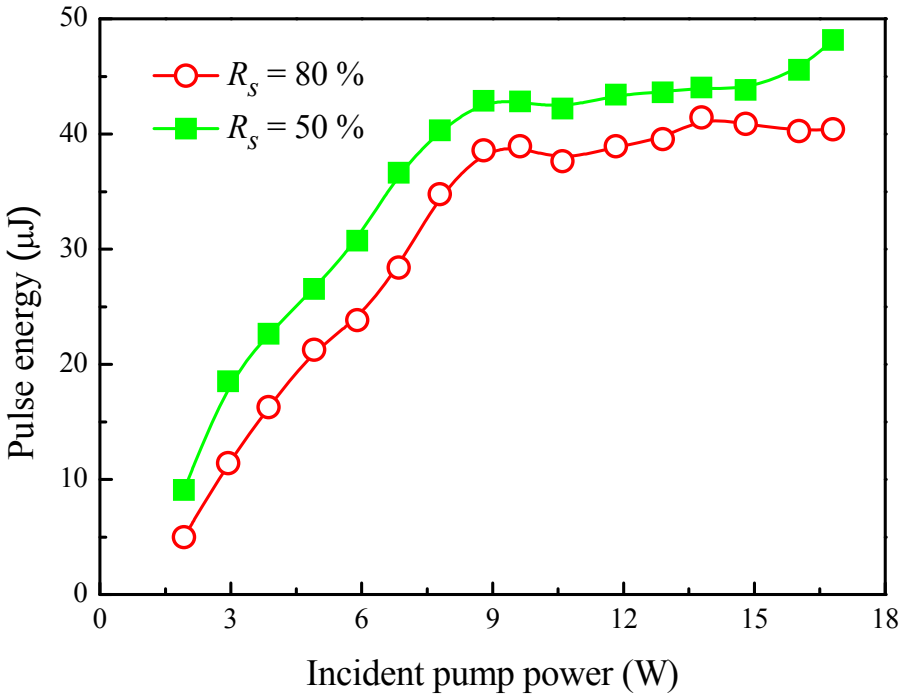

Fig. 3.2.4. Dependence of the pulse energies at 1572 nm on the incident pump power.

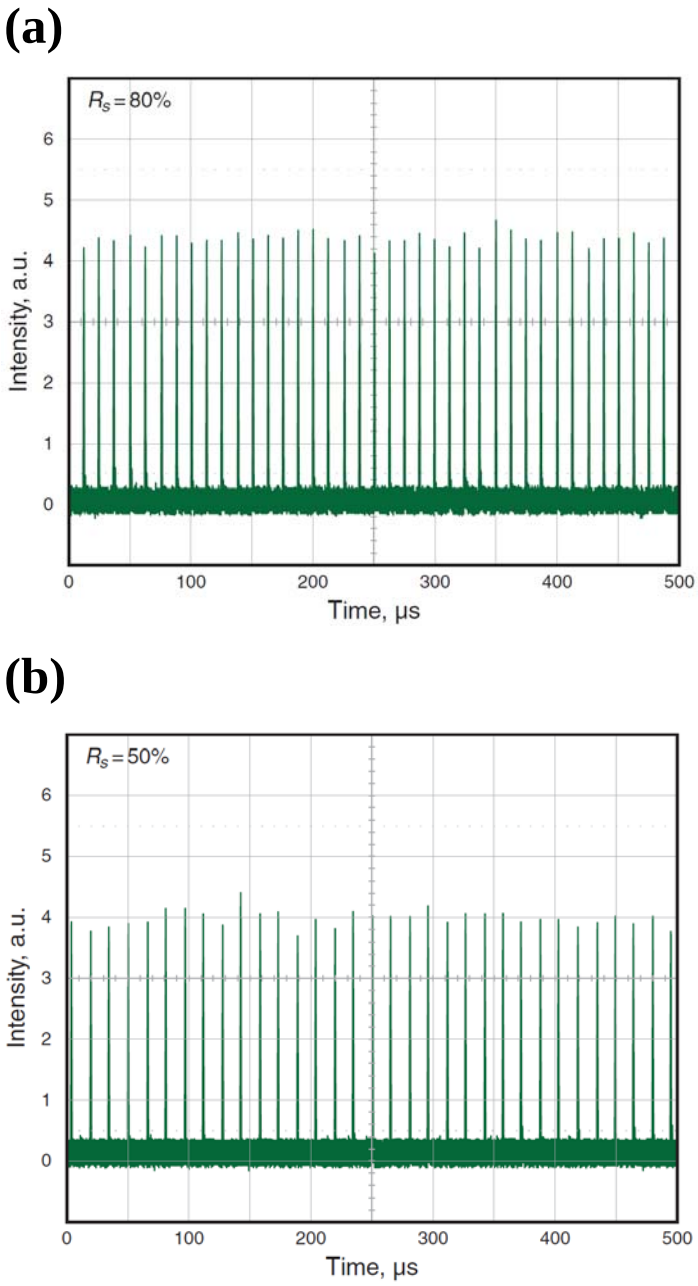

Fig. 3.2.5. Typical oscilloscope traces of the Q-switched pulse trains at 1572 nm.

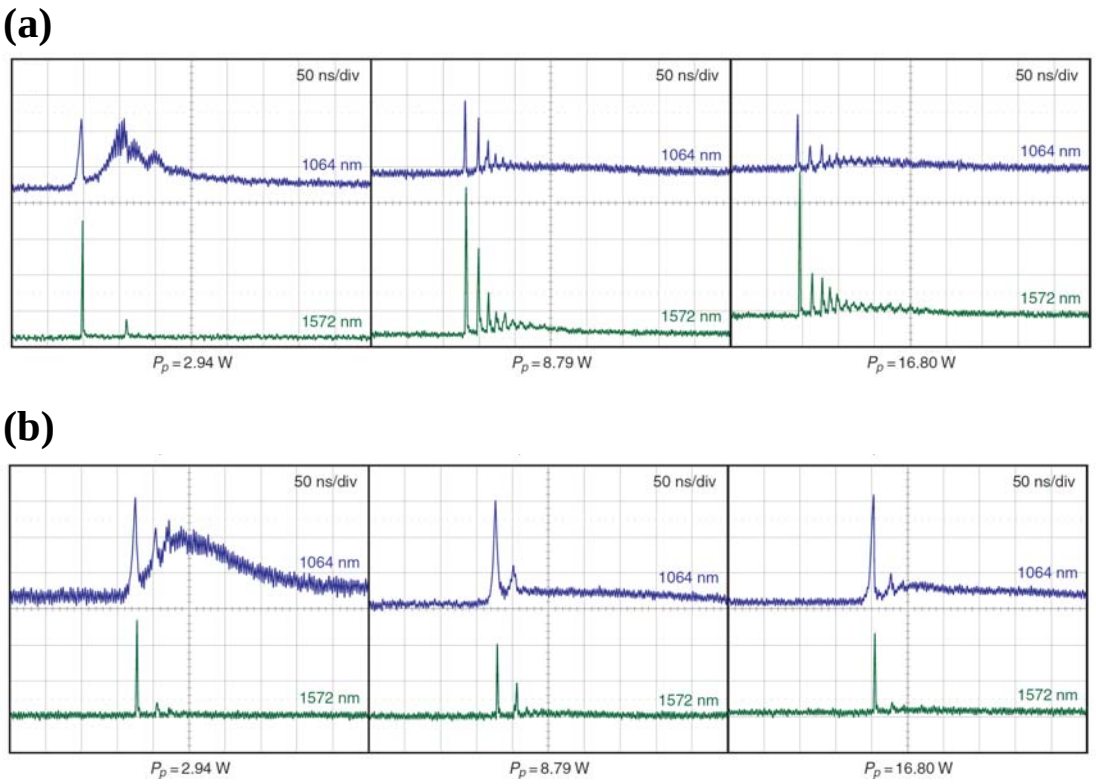

Fig. 3.2.6. Oscilloscope traces of a single pulse of fundamental (1064 nm) and signal (1572 nm) waves at various pump powers for (a) R_s = 80 % and (b) R_s = 50 %, respectively.

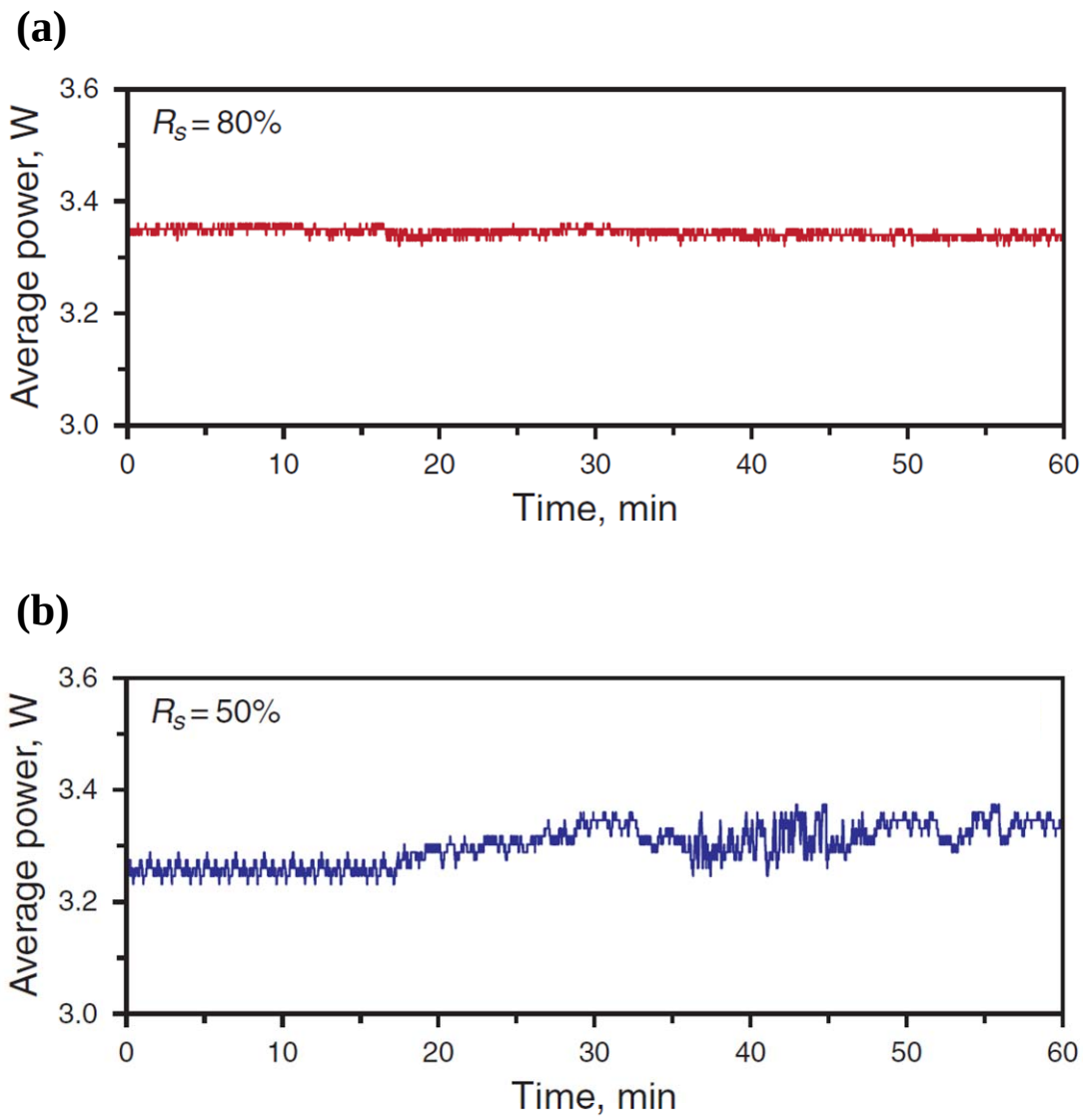

Fig. 3.2.7. Hour-long average power stabilities of the signal powers for R_s = 80 % and R_s = 50 % at the maximum incident pump power.

3.3 Q-Switched Nd:YLF Eye-Safe Laser at 1552 nm

I. Introduction

Nonlinear frequency conversion offers an useful method for extending the spectral range of available solid-state laser sources as long as the polarization state and the direction of the beam propagation are properly designed to meet the phase matching condition. Linearly polarized fundamental beam is usually adopted to perform an efficient extracavity nonlinear frequency conversion with a simple single-pass configuration. Compared with the extracavity method, the intracavity nonlinear frequency conversion takes the advantage of the multi-pass of the fundamental beam through the nonlinear crystal to effectively reduce the pump threshold and make the resonator more compact. Generally speaking, the multiple round trips can cause the polarization state of the fundamental beam to be changed by the birefringence in the laser cavity. The birefringence-induced polarization switching may be the main mechanism why efficient intracavity nonlinear frequency conversions, such as harmonic generations [18-21] and optical parametric oscillations [12,22-25], can be successfully realized by using the optically isotropic materials without any active polarization control in the optical resonator. For example, the output power as high as 36.9 W at 532 nm with the Nd:YAG crystal has been achieved by using an intracavity frequency doubling configuration [21], and the intracavity Nd:YAG/KTA OPO has efficiently generated the eye-safe radiation at 1.54 μm with the output power up to 12.7 W [25]. However, so far the effect of the birefringence-induced polarization switching in the process of intracavity nonlinear frequency conversion has not been experimentally manifested.

In this section, a high-pulse-energy eye-safe laser at 1552 nm is effectually generated by an intracavity Nd:YLF/KTP OPO with the help of the thermally induced polarization switching. We experimentally verify the thermally induced birefringence can lead to a polarization switching between the mutually orthogonal components of the fundamental pulses. Consequently, an efficient intracavity nonlinear frequency conversion can be achieved in an optically isotropic laser crystal without any additional polarization control. With this finding, the pulse energy and peak power of the compact Nd:YLF/KTP eye-safe laser under an incident pump power of 12.7 W and a pulse

repetition rate of 5 kHz are up to 306 μJ and 4 kW, respectively.

II. Experimental setup

The experimental setup for the Nd:YLF/KTP eye-safe laser is schematically shown in Fig. 3.3.1. The input mirror was a concave mirror with the ROC of 300 mm. It was AR coated at 806 nm on the entrance face, and was coated at 806 nm for high transmission as well as 1053 nm for high reflection on the second surface. The gain medium was a 0.8 at. % c-cut Nd:YLF crystal (CASTECH) with the diameter of 4 mm and the length of 15 mm. Both facets of the laser crystal were AR coated at 806 and 1053 nm. Note that although it is an uniaxial crystal with the highly anisotropic property, the Nd:YLF crystal effectively exhibits the optically isotropic characteristics in the transverse plane when it is cut along the crystallographic c axis. The orientation of the rod axis of the present c-cut crystal to the crystallographic c axis was within 1 degree. The KTP crystal with dimensions of $5 \times 5 \times 30$ mm^3 was x-cut at $\theta = 90°$, $\phi = 0°$ for the type-II non-critically phase-matched OPO operation. The pump face of the KTP crystal was high transmission coated at 1053 nm as well as high reflection coated at 1552 nm that acted as the front mirror of the IOPO cavity, while the other face of the KTP crystal was AR coated at 1053 nm and partially-reflection coated at 1552 nm with a reflectivity of 80 %. Both Nd:YLF and KTP crystals were wrapped with indium foil and mounted in water-cooled copper heat sinks at 18 °C. A 20-mm-long AO Q-switch (Gooch & Housego) was AR coated at 1053 nm on both surfaces. It was placed in the center of the laser cavity, and was driven at a central frequency of 41 MHz with a RF power of 25 W. A flat mirror that is high reflection coated at 1053 nm and high transmission coated at 1552 nm was utilized as the output coupler during the experiment. The pump source was an 806-nm fiber-coupled laser diode with a core diameter of 600 μm and a numerical aperture of 0.2, respectively. The polarization state emitted from the fiber-coupled laser diode was measured to be randomly polarized. The pump beam was reimaged into the laser crystal with a lens set that has a focal length of 25 mm with a magnification of unity and a coupling efficiency of 90 %. The length of the fundamental laser cavity was set to be L_{cav} = 115 mm for the construction of a compact AQS eye-safe laser. The pulse temporal behaviors were recorded by a LeCroy digital oscilloscope (Wavepro 7100, 10 G samples/s, 1 GHz bandwidth) with a fast InGaAs photodiode. The spectral information of the laser output was measured by an optical spectrum analyzer (Advantest 8381A) that is constructed with a diffraction monochromator with the resolution of 0.1 nm.

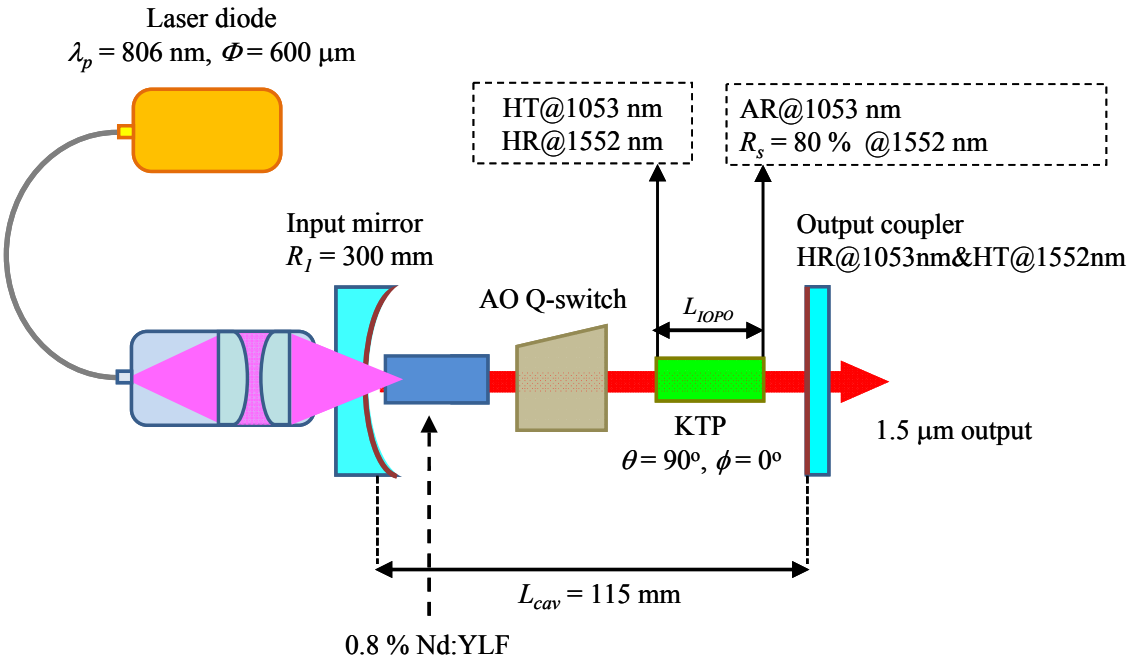

Fig. 3.3.1. Schematic of the cavity setup for a KTP-based IOPO pumped by an AO Q-switched c-cut Nd:YLF laser.

III. Performance of IOPO operation

The orientation of the y-axis of the KTP crystal was set to be parallel to the base of the AO Q-switch since the fundamental beam is partially polarized in the horizontal direction, as explored in Sec. 2.8. As a result, the oscillated polarization of the present eye-safe laser is horizontally polarized as derived from the type-II phase matching condition. Figure 3.3.2 displays the output powers at 1552 nm with respect to the incident pump power at 806 nm at a pulse repetition rate of 5, 8, 10, 20, and 40 kHz, while the inset of Fig. 3.3.2 shows the optical spectrum of the OPO signal wave with the central wavelength at 1552 nm. If the polarization state of the fundamental beam changes from linear to nearly random statuses with increasing the incident pump power as observed in Fig. 2.8.2(b), the saturation of the output powers at 1552 nm should be expected. However, it is apparent that the output powers at 1552 nm are almost linearly proportional to the incident pump power at 806 nm in the present situation. For the sake of discovering the interacted mechanism between the fundamental and OPO signal pulses, we used a polarization beam splitter to simultaneously monitor the temporal behaviors of the mutually orthogonal polarization components of the depleted fundamental pulses. Firstly, Fig. 3.3.3 describes the input fundamental pulses without the IOPO conversion at a pulse repetition rate of 5 kHz. It is obvious that the behaviors of the originally input fundamental pulses with mutually orthogonal polarizations are nearly the same. Figures 3.3.4(a)-(d) illustrate the characteristics of the depleted fundamental pulses with mutually orthogonal polarizations at a pulse repetition rate of 5 kHz when the incident pump power is increased. Note that the intensities for each case are normalized with respect to the peak of the originally input fundamental pulses. Initially, the 1552-nm pulses are mainly generated by the horizontally polarized fundamental pulses, which is consistent with the requirement of the type-II phase matching. However, it is experimentally found that the vertically polarized fundamental pulses can switch to the horizontally polarized state to participate in the IOPO conversion process. Further increasing the incident pump power, more and more parts of the vertically polarized fundamental pulses are contributed to the generation of the eye-safe radiation, as can be seen clearly in Figs. 3.3.4(a)-(d). Although the effect of the optically induced birefringence has been explored in the optically isotropic Nd:glass and Nd:YAG crystals [26,27], we infer that the thermally induced birefringence is the main mechanism that explains the polarization interaction and switching in the present IOPO

conversion process. The deduction is based on the degree of the polarization switching is increased with increasing the incident pump power. It is also worthwhile to mention that the polarization switching is consistent with the roll-over phenomena obtained with the linearly polarized c-cut Nd:YLF laser in Sec. 2.8, both observations are originated from the fact of the polarization state to be significantly influenced by the thermal effect in the laser crystal. To be brief, we first experimentally manifest that the thermally induced polarization switching plays a vital role in accomplishing an efficient intracavity conversion process in an optically isotropic crystal without any active polarization control. We believe that the observed phenomena can provide important insights into the laser physics in an intracavity nonlinear frequency conversion process.

Figures 3.3.5(a) and (b) demonstrate the typical temporal behaviors of the single pulse shape and pulse trains at 1552 nm under an incident pump power of 12.7 W and a pulse repetition rate of 5 kHz. The relatively long pulse with a remarkable tail depicted in Fig. 3.3.5(a) means that the eye-safe radiation is generated with several round trips inside the IOPO cavity. Consequently, the time-averaged effect as a result of this long pulse duration can alleviate the instability probably caused by the polarization switching of the fundamental pulses. The above-mentioned inspection can also be confirmed by referring to Fig. 3.3.5(b), where the peak-to-peak amplitude fluctuation is experimentally found to be within 10 % over an hour-long operation. According to Fig. 3.3.2, the maximum output power at 1552 nm is up to 1.56 W under an incident pump power of 12.7 W and a pulse repetition rate of 5 kHz, corresponding to the diode-to-signal conversion efficiency of 12.3 %. The optical conversion efficiency is comparable with those obtained with the eye-safe radiations driven by the linearly polarized fundamental lasers thanks to the assistance of the thermally induced polarization switching [5,7,28,29].

On the basis of Figs. 3.3.2 and 3.3.5, the pulse energy can be calculated to be as high as 306 μJ and the peak power can be numerically evaluated to be about 4 kW. In comparison with the reported KTP-based IOPOs pumped by the continuously diode-end-pumped Nd-doped crystal lasers, we have achieved the largest pulse energy of the eye-safe radiation by using the Nd:YLF crystal as a gain medium. This implies that the Nd:YLF crystal is potentially favorable to be employed for the construction of high-pulse-energy lasers.

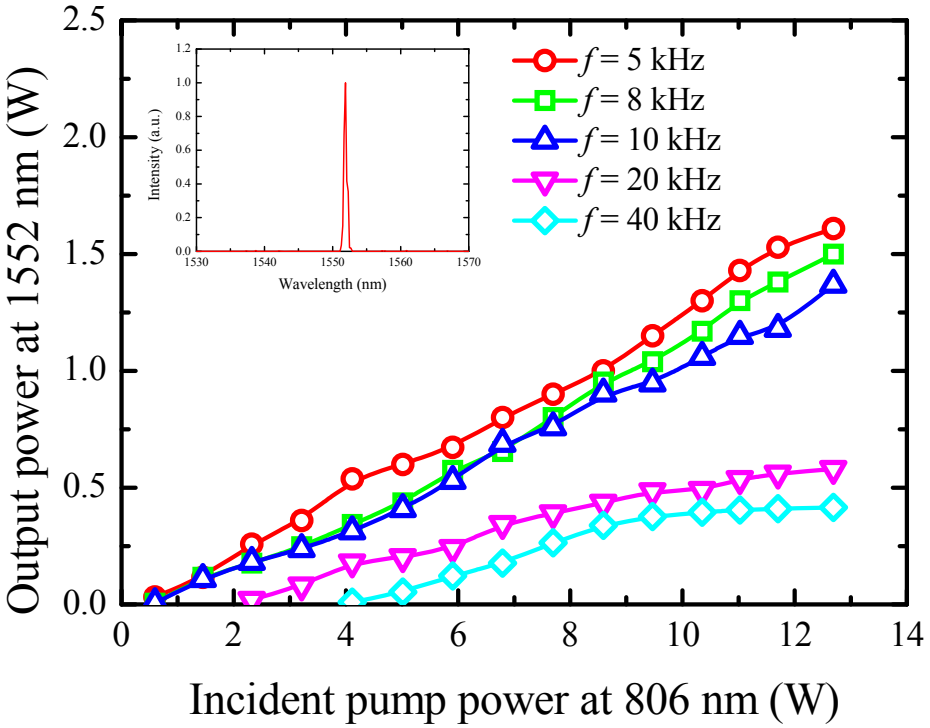

Fig. 3.3.2. Output powers at 1552 nm as a function of the incident pump power at 806 nm under a pulse repetition rate of 5, 8, 10, 20 and 40 kHz, respectively; Inset: Optical spectrum of the Nd:YLF/KTP eye-safe laser.

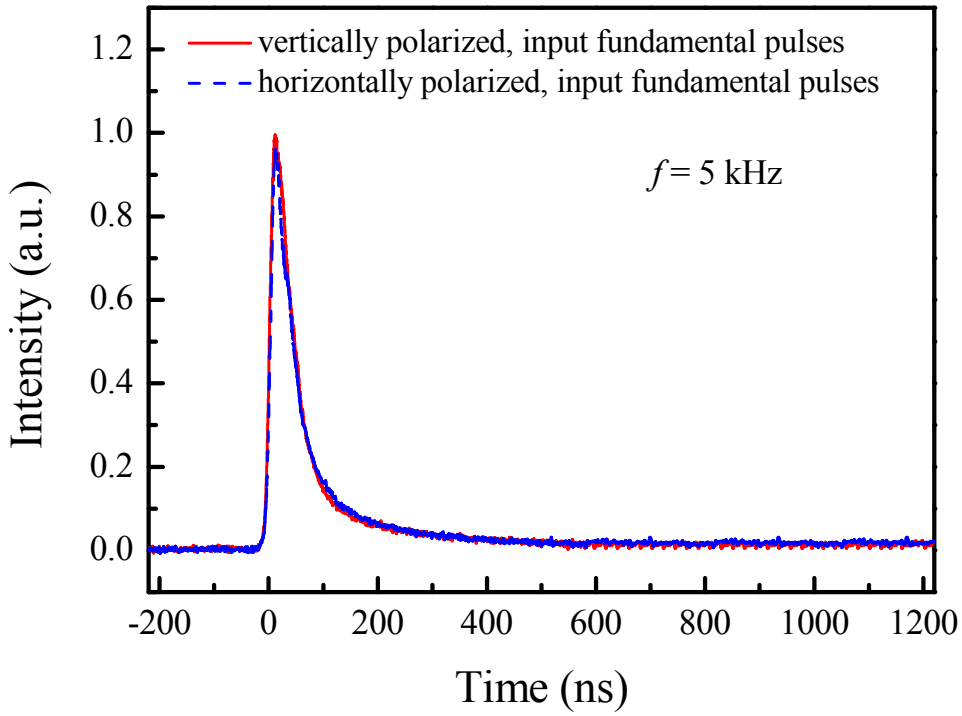

Fig. 3.3.3. Temporal behaviors of the originally input fundamental pulses with the mutually orthogonal polarizations at a pulse repetition rate of 5 kHz.

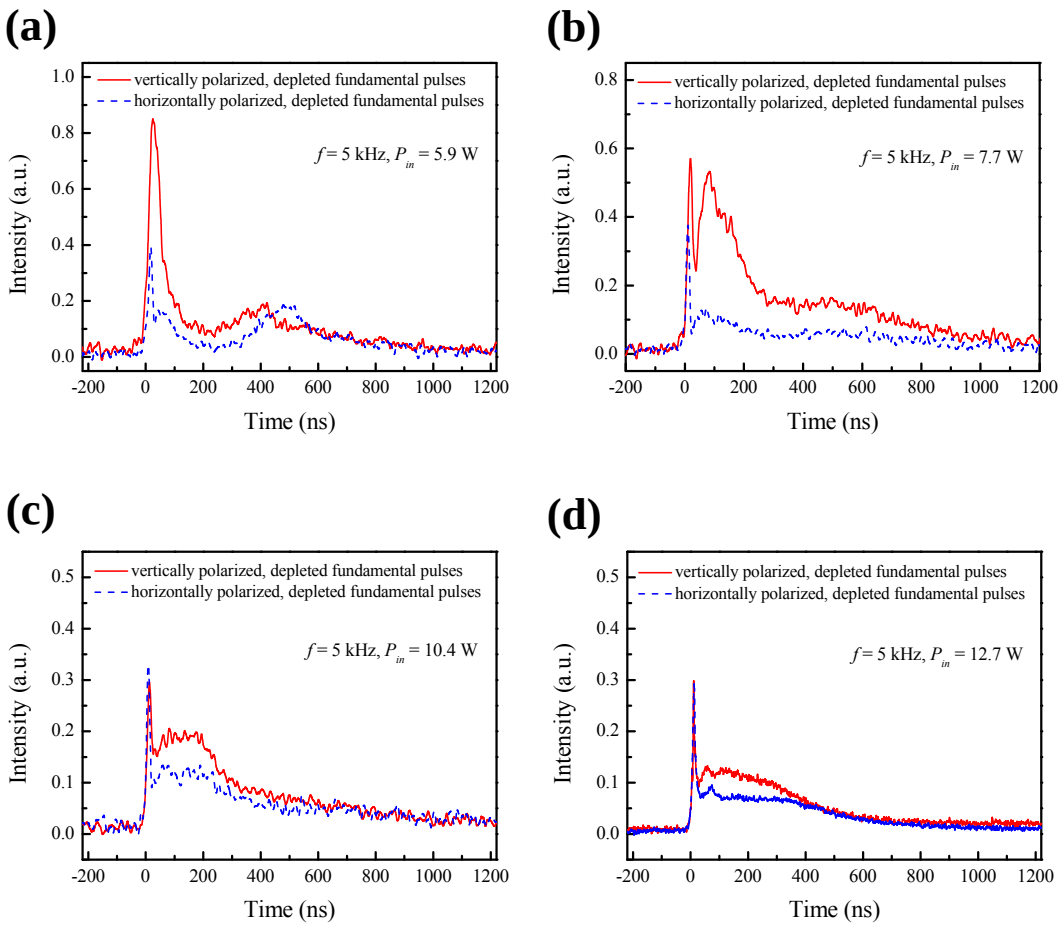

Fig. 3.3.4. Temporal behaviors of the mutually orthogonal polarization components of the depleted fundamental pulses at a pulse repetition rate of 5 kHz and an incident pump power of (a) 5.9 W, (b) 7.7 W, (c) 10.4 W, and (d) 12.7 W, respectively.

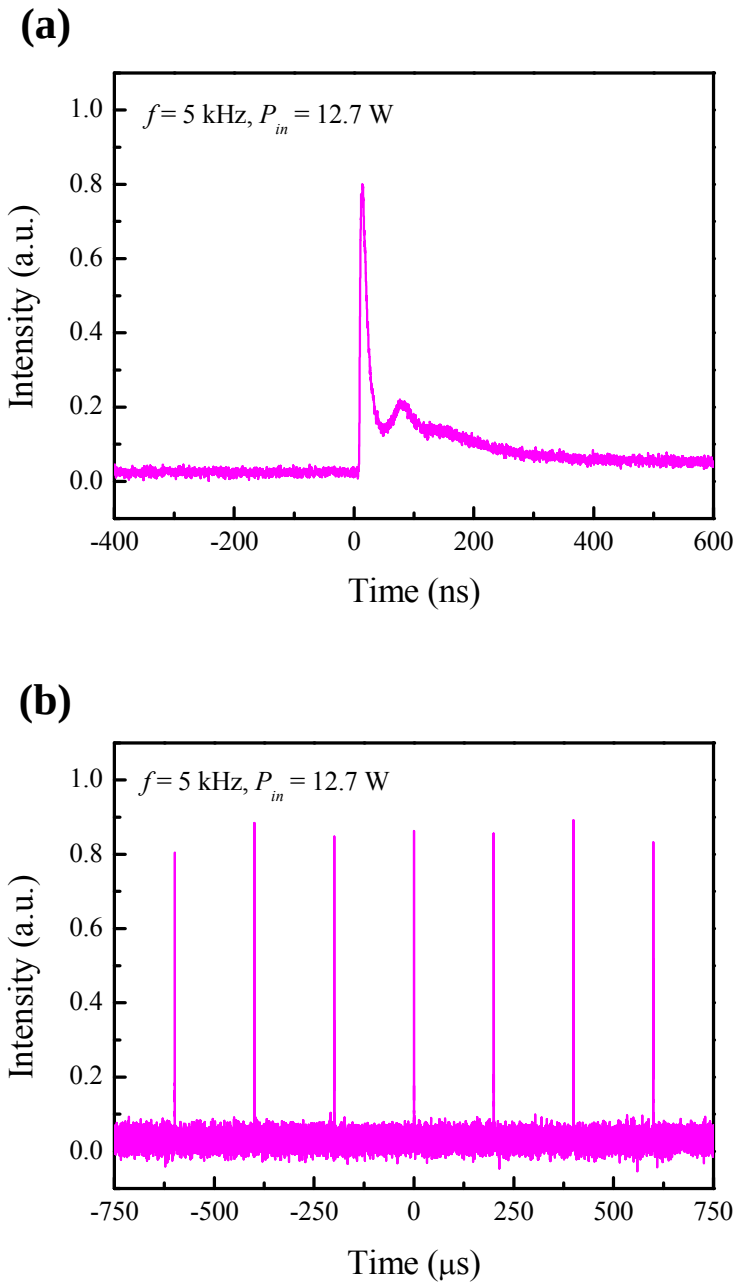

Fig. 3.3.5. Typical temporal behaviors of the eye-safe pulses at an incident pump power of 12.7 W and a pulse repetition rate of 5 kHz with: (a) the time span of 1 μs, and (b) the time span of 1.5 ms.

3.4 Conclusion

In this chapter, a novel concept of a separable monolithic IOPO cavity is originally proposed. With the developed approach, we have remarkably improved the stability and efficiency in a diode-pumped Q-switched Nd:YVO_4/Cr^{4+}:YAG IOPO laser with a type-II non-critical phase-matched KTP crystal. We study the performance of this IOPO cavity for R_s = 80 and 50 %. The output powers at 1552 nm are up to 3.3 W at the maximum incident pump power of 16.8 W for both cases with the instability of 0.2 % for R_s = 80 % and 1 % for R_s = 50 %, respectively. The diode-to-signal conversion efficiency that defined by the ratio of the output power at 1552 nm to that at 808 nm is up to 20 %, which is the highest one for IOPOs driven by Nd-doped crystal lasers to the best of our knowledge.

With the same design concept, we have realized an efficient high-pulse-energy eye-safe radiation in a KTP-based IOPO pumped by a c-cut Nd:YLF laser with the birefringence-induced polarization switching. The Q-switched Nd:YLF laser developed in Sec. 2.8 is utilized to intracavity pump a type-II non-critically phase-matched KTP crystal for the generation of the eye-safe radiation at 1552 nm. We properly measure the temporal behaviors of the depleted fundamental pulses to manifest that the thermally induced birefringence can lead the mutually orthogonal polarization states of the fundamental pulses to be effectively switched. This successive polarization switching is experimentally confirmed to be the key mechanism in achieving an efficient IOPO without any additional polarization control. With this finding, this compact Nd:YLF/KTP eye-safe laser effectually produces the pulse energy and peak power of up to 306 μJ and 4 kW under an incident pump power of 12.7 W and a pulse repetition rate of 5 kHz. To the best of our knowledge, this is the largest pulse energy ever reported among the continuously diode-end-pumped Nd-doped crystal/KTP eye-safe lasers.

References

[1] H. D. Reidenbach, *Springer Handbook of Lasers and Optics*, (Springer, Berlin, 2007), Chap. 21.

[2] R. Fischer and L. A. Kulevskii, "Optical parametric oscillators," Sov. J. Quantum Electron. **7**, 135-159 (1977).

[3] L. R. Marshall, A. D. Hays, J. Kasinski, and R. Burnham, "Highly efficient optical parametric oscillators," Proc. SPIE **1419**, 141-152 (1991).

[4] V. I. Dashkevich, A. I. Vodchits, V. A. Orlovich, N. S. Kazak, V. K. Pavlenko, V. I. Pokryshkin, I. P. Petrovich, and V. V. Rukhovets, "Comparative studies of eye-safe intracavity and extracavity optical parametric oscillators with an unstable telescopic cavity," J. Appl. Spectrosc. **73**, 604-612 (2006).

[5] Y. F. Chen, S. W. Chen, S. W. Tsai, and Y. P. Lan, "High-repetition-rate eye-safe optical parametric oscillator intracavity pumped by a diode-pumped Q-switched Nd:YVO_4 laser," Appl. Phys. B **76**, 263-266 (2003).

[6] Y. F. Chen, S. W. Chen, L. Y. Tsai, Y. C. Chen, and C. H. Chien, "Efficient sub-nanosecond intracavity optical parametric oscillator pumped with a passively Q-switched Nd:$GdVO_4$ laser," Appl. Phys. B **79**, 823-825 (2004).

[7] W. Żendzian, J. K. Jabczyński, P. Wachulak, and J. Kwiatkowski, "High-repetition-rate, intracavity-pumped KTP OPO at 1572 nm," Appl. Phys. B **80**, 329-332 (2005).

[8] J. Miao, J. Peng, B. Wang, H. Tan, and H. Bian, "Compact low threshold Cr:YAG passively Q-switched intracavity optical parametric oscillator," Opt. Commun. **281**, 2265-2270 (2008).

[9] Z. J. Liu, Q. P. Wang, X. Y. Zhang, Z. J. Liu, H. Wang, J. Chang, S. Z. Fan, F. S. Ma, and G. F. Jin, "Intracavity optical parametric oscillator pumped by an actively Q-switched Nd:YAG laser," Appl. Phys. B **90**, 439-443 (2008).

[10] F. Q. Liu, H. R. Xia, Y. Zhong, S. Q. Sun, Z. C. Ling, D. G. Ran, W. L. Gao, J. L. He, H. J. Zhang, and J. Y. Wang, "Intracavity optical parametric oscillator at 1.57 μm by a diode-pumped Q-switched Nd:$LuVO_4$ laser," Laser Phys. Lett. **5**, 585-588 (2008).

[11] Y. F. Chen and L. Y. Tsai, "Comparison between shared and coupled resonators for passively Q-switched Nd:$GdVO_4$ intracavity optical parametric oscillators,"

Appl. Phys. B **82**, 403-406 (2006).

[12] B. T. Zhang, X. L. Dong, J. L. He, H. T. Huang, K. J. Yang, C. H. Zuo, J. L. Xu, and S. Zhao, "High-power eye-safe intracavity KTA OPO driven by a diode-pumped Q-switched Nd:YAG laser," Laser Phys. Lett. **5**, 869-873 (2008).

[13] H. Zhu, G. Zhang, H. Chen, C. Huang, Y. Wei, Y. Duan, Y. Huang, H. Wang, and G. Qiu, "High-efficiency intracavity Nd:YVO_4\KTA optical parametric oscillator with 3.6 W output power at 1.53 μm," Opt. Express **17**, 20669-20674 (2009).

[14] H. T. Huang, J. L. He, S. D. Liu, F. Q. Liu, X. Q. Yang, H. W. Yang, Y. Yang, and H. Yang, "Synchronized generation of 1534 and 1572 nm by the mixed optical parameter oscillation," Laser Phys. Lett. **8**, 358-362 (2011).

[15] Y. F. Chen, Y. C. Chen, S. W. Chen, and Y. P. Lan, "High-power efficient diode-pumped passively Q-switched Nd:YVO_4/KTP/Cr^{4+}:YAG eye-safe laser," Opt. Commun. **234**, 337-342 (2004).

[16] A. Agnesi, S. Dell'Acqua, and G. Reali, "Diode-pumped quasi-cw intracavity optical parametric oscillator at 1.57 μm with efficient pulse shortening," Appl. Phys. B **70**, 751-753 (2000).

[17] Y. F. Chen, S. W. Chen, S. W. Tsai, and Y. P. Lan, "Output optimization of a high-repetition-rate diode-pumped Q-switched intracavity optical parametric oscillator at 1.57 μm," Appl. Phys. B **77**, 505-508 (2003).

[18] Y. Chen, W. Hou, H. Peng, H. Zhang, L. Guo, H. Zhang, D. Cui, and Z. Xu, "Intracavity frequency doubling of an actively Q-switched Nd:YAG laser with 2.25 W output power at 473 nm," Opt. Commun. **270**, 58-62 (2007).

[19] B. T. Zhang, J. F. Yang, J. L. He, H. T. Huang, X. L. Dong, J. L. Xu, C. H. Zuo, and K. J. Yang, "12-W red light generation by frequency-doubling Q-switched Nd:YAG laser," Laser Phys. **19**, 1389-1394 (2009).

[20] Z. Quan, Y. Yi, Q. Dapeng, Z. Kai, L. Yang, and Z. Ling, "All-solid-state 556 nm yellow-green laser generated by frequency doubling of a diode-pumped Nd:YAG laser," J. Opt. Soc. Am. B **26**, 1939-1943 (2009).

[21] B. Ji, X. S. Zheng, Z. P. Cai, H. Y. Xu, and F. Q. Jia, "Compact high conversion efficiency Nd:YAG/LBO green laser using unstable V cavity," Laser Phys. **22**, 406-410 (2012).

[22] A. Dubois, S. Victori, T. Lépine, P. Georges, and A. Brun, "High-repetition-rate eyesafe intracavity optical parametric oscillator," Appl. Phys. B **67**, 181-183

(1998).

[23] Z. Liu, Q. Wang, X. Zhang, Z. Liu, J. Chang, H. Wang, S. Fan, W. Sun, G. Jin, X. Tao, S. Zhang, and H. Zhang, "Efficient acousto-optically Q-switched intracavity Nd:YAG/$KTiOAsO_4$ optical parametric oscillator," Appl. Phys. B **92**, 37-41 (2008).

[24] Z. Liu, Q. Wang, X. Zhang, Z. Liu, J. Chang, H. Wang, S. Fan, S. Li, S. Huang, W. Sun, G. Jin, X. Tao, S. Zhang, and H. Zhang, "2.54 W 1535 nm $KTiOAsO_4$ optical parametric oscillator within a diode-side-pumped acousto-optically Q-switched Nd:YAG laser," J. Phys. D **41**, 135112 (2008).

[25] W. J. Sun, Q. P. Wang, Z. J. Liu, X. Y. Zhang, F. Bai, X. B. Wan, G. F. Jin, X. T. Tao, and Y. X. Sun, "High efficiency $KTiOAsO_4$ optical parametric oscillator within a diode-side-pumped two-rod Nd:YAG laser," Appl. Phys. B **104**, 87-91 (2011).

[26] Z. Blaszczak, "Optically induced birefringence of transparent media," Proc. SPIE **2202**, 469-480 (1995).

[27] P. Deb, K. C. Gupta, C. G. Murali, L. J. Dhareshwar, and B. K. Godwal, "Induced birefringence in optically isotropic glass by a short pulsed Nd:YAG laser," J. Opt. A **8**, 903-908 (2006).

[28] H. T. Huang, J. L. He, X. L. Dong, C. H. Zuo, B. T. Zhang, G. Qiu, and Z. K. Liu, "High-repetition-rate eye-safe intracavity KTA OPO driven by a diode-end-pumped Q-switched Nd:YVO_4 laser," Appl. Phys. B **90**, 43-45 (2008).

[29] H. Y. Zhu, Y. M. Duan, G. Zhang, C. H. Huang, Y. Wei, W. D. Chen, H. Y. Wang, and G. Qiu, "High-power LD end-pumped intra-cavity Nd:$YAlO_3$/$KTiOAsO_4$ optical parametric oscillator emitting at 1562 nm," Laser Phys. Lett. **7**, 703-706 (2010).


E S A
1896

Chapter 4

Nonlinear Frequency Conversion based on Harmonic Generations

4.1 Second Harmonic Generation at 532 nm

I. Introduction

With the improved quality of the nonlinear crystal as well as the great advance of the laser engineering, green lasers at 532 nm based on either ESHG or ISHG of the Q-switched Nd-doped crystal lasers at 1064 nm have been extensively studied in a variety of literatures and popularly applied in many commercial fields [1-8]. Employing the ISHG possesses the merit of the multi-pass of the fundamental IR beam through the nonlinear crystal inside the laser cavity, which can eliminate the need for focusing optics and make the resonator more compact, while the ESHG is characterized by the easy achievement of the high-power, high-repetition-rate, and high-beam-quality green laser emission. Although the difference of the temperature insensitivity between the two configurations was recently discussed [9], a thorough comparison between the output performance of the ESHG and ISHG under a similar operated circumstance has not been investigated to date.

In this section, we construct a reliable AQS Nd:YVO_4 laser to comparatively investigate the output performance of the SHG between the extracavity and intracavity configurations under a similar operated condition. It is experimentally found that the peak power at 532 nm obtained with the ESHG is remarkably higher than that obtained with the intracavity configuration, even though the higher output power and larger pulse energy can be acquired with the ISHG.

II. Experimental setup

Figures 4.1.1(a) and (b) schematically depict the experimental arrangements for the diode-pumped AQS Nd:YVO_4 lasers configured with the ESHG and ISHG, respectively. The gain medium was a 0.1 at. % a-cut Nd:YVO_4 crystal with the dimensions of 3 mm × 3 mm × 12 mm. The Nd:YVO_4 crystal was chosen because it is characterized by high stimulated emission cross section, good thermal and mechanical properties that is inherently favorable for constructing a high-power, high-repetition-rate Q-switched laser. The gain medium was placed adjacent to the input mirror for the convenience of the end-pumped scheme. Both facets of the laser crystal were AR coated at 808 and 1064 nm. The Nd:YVO_4 crystal was wrapped with indium foil and mounted in a water-cooled copper heat sink at 18 ˚C. The pump source was a fiber-coupled laser diode at 808 nm with a core diameter of 600 μm and a numerical aperture of 0.16. The pump beam with the spot radius of about 310 μm was reimaged inside the gain medium with a lens set that has a focal length of 25 mm and a coupling efficiency of 90 %. The input flat mirror was AR coated at 808 nm on the entrance face, and it was coated for high transmission at 808 nm as well as for high reflection at 1064 and 532 nm on the second surface. A 20-mm-long AO Q-switch (Gooch & Housego) was adopted to offer a high-stability and low timing jitter pulsed operation with a continuously adjustable pulse repetition rate. The AO Q-switch was located in the center of the laser cavity. It was driven at a modulated frequency of 41 MHz with a RF power of 25 W.

For the ESHG, the output coupler with a reflectivity of 50 % at 1064 nm was experimentally found to give the best performance in output power, while a flat mirror that is coated for high reflection at 1064 nm and for high transmission at 532 nm was utilized as the output coupler for the ISHG. It is worthwhile to mention that although the ISHG generally configures a folding mirror between the frequency doubler and laser crystal to couple out the green beam after double-passing the nonlinear crystal, the aim of the present investigation is concentrated on the comparison of the ESHG and ISHG on the basis of a compact linear plane-parallel resonator. Moreover, the coating with high reflection at 532 nm for the input mirror ensures the backward propagation of the green beam to be unidirectionally emitted through the output coupler. Also note that the current parameters and optical elements have been experimentally optimized.

As a frequency doubler, here we utilized the LBO crystal which is featured by high

damage threshold, large acceptance angle, moderate nonlinear coefficient, and small walk-off angle. The LBO crystal was with the dimensions of 3 × 3 × 20 mm^3, and it was cut at $\theta = 90^\circ$ and $\phi = 10.4^\circ$ for the type-I phase-matched SHG at a temperature of 47 ˚C. Both surfaces of the SHG crystal were AR coated at 1064 and 532 nm. The temperature of the LBO crystal was monitored by a thermo-electric controller with the precision of 0.1˚C. For the ESHG, a convex lens was employed to focus the fundamental beam into the SHG crystal. The convex lens had the focal length of 38 mm and it was AR coated at 1064 nm on both sides. For the ISHG, the LBO crystal was put near the output coupler where the mode radius inside the laser cavity is the smallest. The cavity lengths L_{cav} for both cases were optimized according to the criterion of suppressing the parasitic lasing effect introduced in Sec. 2.3, which were approximately 143 mm, to realize effective AO Q-switched operations. The pulse temporal behaviors were monitored with a fast Si photodetector, whose signal was analyzed by a digital oscilloscope (LeCroy, Wavepro 7100) with the sampling interval of 0.1 ns and the electrical bandwidth of 1 GHz.

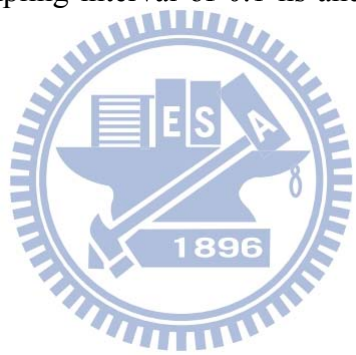

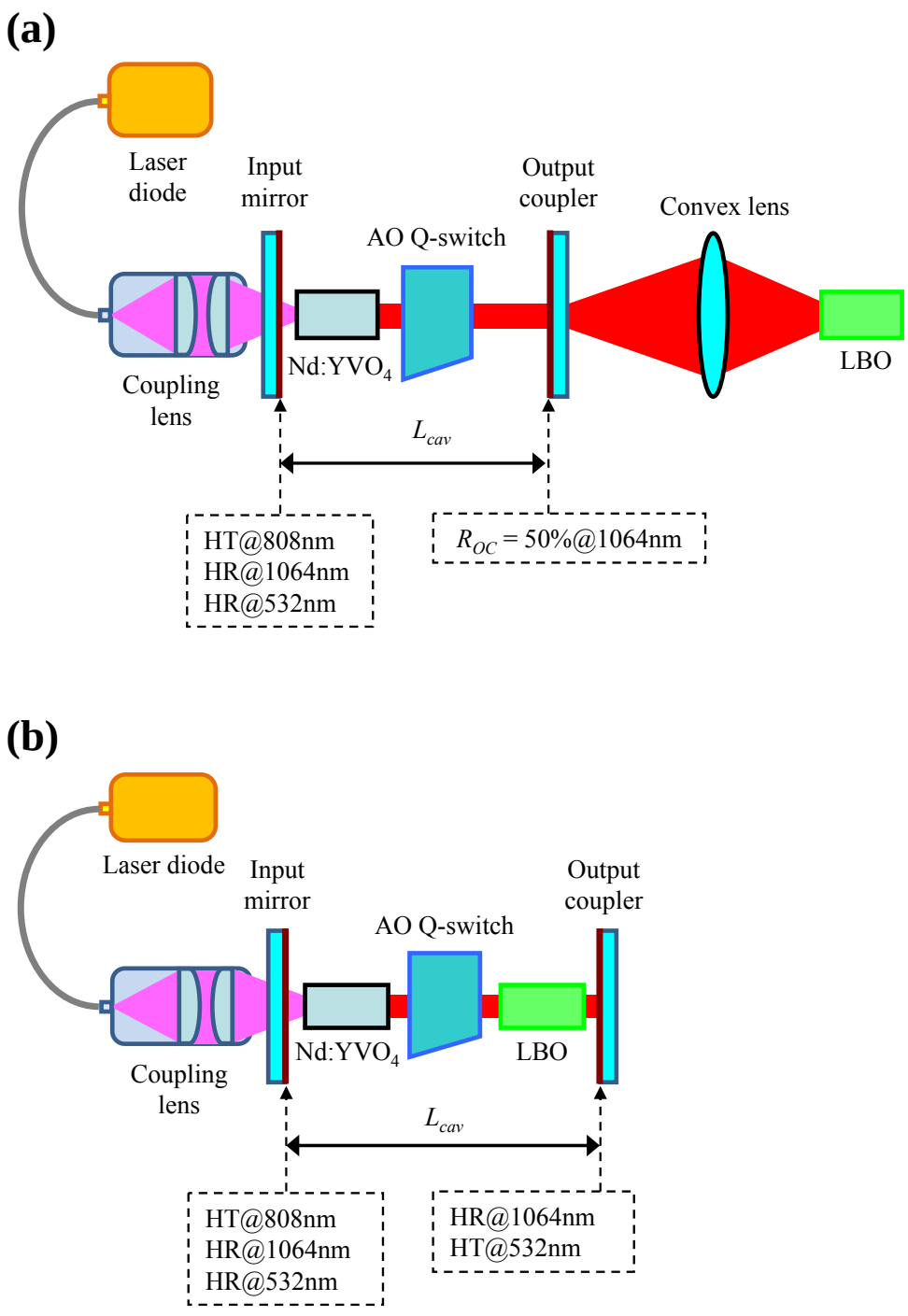

Fig. 4.1.1. Schemes of the cavity setup for the diode-pumped AQS Nd:YVO_4 lasers configured with the (a) ESHG and (b) ISHG.

III. Comparison of output performance between ESHG and ISHG

After optimizing the ESHG and ISHG individually, the output powers at 532 nm for the two configurations with respect to the pulse repetition rate were measured under an incident pump power of 26 W at 808 nm, as illustrated in Fig. 4.1.2(a). The output powers at 532 nm obtained with the ISHG are generally found to be 30-40 % higher than the results obtained with the ESHG, where the maximum output powers of 5.76 and 4.5 W for the ISHG and ESHG are achieved at a pulse repetition rate of 40 kHz, corresponding to the conversion efficiencies from 808 to 532 nm of 22.2 and 17.3 %, respectively. The increased interaction length thanks to the multi-pass of the fundamental beam through the LBO crystal undoubtedly explains why the higher conversion efficiency from 808 to 532 nm of the ISHG can be achieved as compared with that of the ESHG. Note that although the Nd:YVO_4 crystal slightly absorbs the radiation around 532 nm, it is experimentally found that the present ISHG shows a comparable conversion efficiency to the previous works [3-8], and it exhibits an excellent reliability over an hour-long operation. Figure 4.1.2(b) illustrates the dependences of the pulse energy at 532 nm on the pulse repetition rate for both cases. By increasing the pulse repetition rate from 30 to 100 kHz, the pulse energy changes from 177 to 42 μJ for the ISHG, and it varies from 133 to 29 μJ for the ESHG. The full width at half maximum (FWHM) of the envelop of the Q-switched pulse at 532 nm as a function of the pulse repetition rate is depicted in Fig. 4.1.2(c). When the pulse repetition rate increases from 30 to 100 kHz, the pulse durations for the ESHG and ISHG are found to change from 8 to 14 ns and 10 to 42 ns, respectively. The beam quality factors were experimentally measured to be $M_x^2 \sim 1.25$ and $M_y^2 \sim 1.35$ for the ESHG, while these values were $M_x^2 \sim 1.21$ and $M_y^2 \sim 1.24$ for the ISHG.

Typical temporal behaviors for the two configurations under an incident pump power of 26 W at 808 nm and a pulse repetition rate of 40 kHz are shown in Figs. 4.1.3(a) and (b), respectively. From the insets in Figs. 4.1.3(a) and (b), it is obvious that both pulses exhibit the modulation which probably comes from the frequency beating of adjacent longitudinal modes. It is also experimentally found that the Q-switched pulse for the ISHG has a relatively wide pulse duration and it is always accompanied with a long tail, which is resulted from the high finesse of the laser resonator. With the numerical integration of the temporal pulse profile and the experimentally obtained pulse energy, the peak powers for both cases are precisely evaluated, as displayed in Fig.

4.1.3(c). It is intriguing that the peak powers for the ESHG are significantly higher than those for the ISHG, even though the higher output powers and larger pulse energies are accomplished with the ISHG. The peak powers for the ESHG and ISHG are found to decrease from 30.4 to 3.7 kW and 11.6 to 1.4 kW with the increase of the pulse repetition rate from 30 to 100 kHz, respectively.

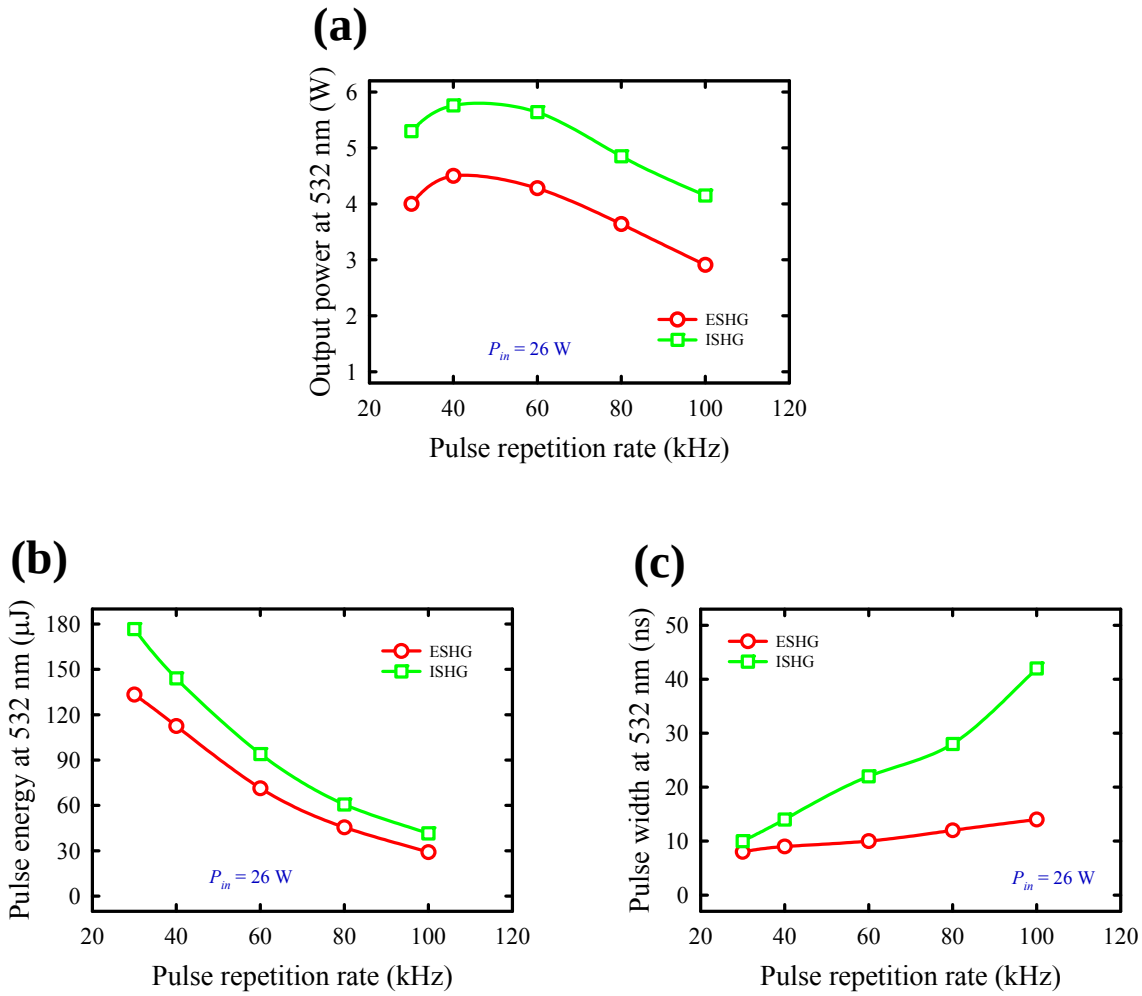

Fig. 4.1.2. Dependences of the (a) output power, (b) pulse energy, and (c) pulse width at 532 nm on the pulse repetition rate.

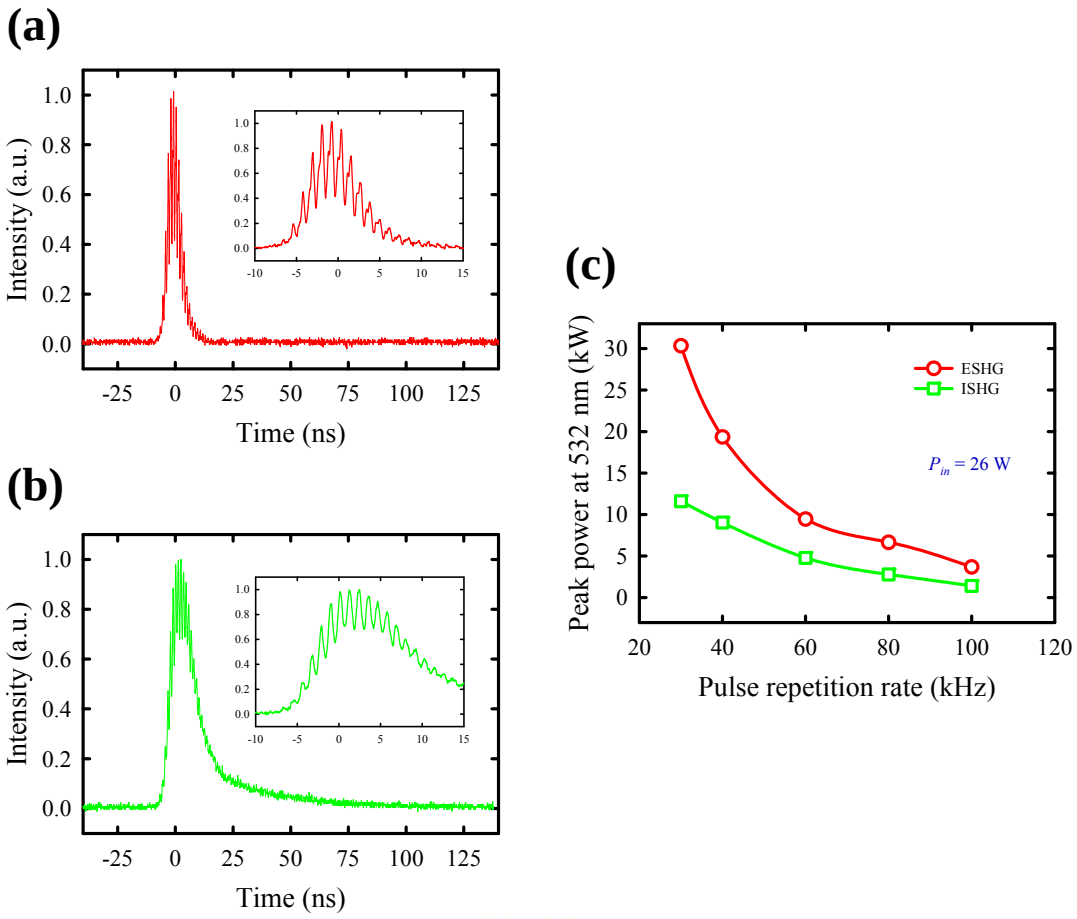

Fig. 4.1.3. Typical temporal behaviors for the (a) ESHG and (b) ISHG under an incident pump power of 26 W at 808 nm and a pulse repetition rate of 40 kHz; (c) Dependences of the peak power at 532 nm on the pulse repetition rate.

4.2 Third Harmonic Generation at 355 and 351 nm

I. Introduction

In recent years, UV light sources have been rapidly developed because they are useful in many applications such as rapid prototyping, laser printing, laser processing, spectroscopy, optical data storage, medical treatment and so on. Compared with other UV lasers, diode-pumped all-solid-state lasers with extracavity harmonic generations intrinsically possess advantages of smaller focused size, higher efficiency, longer life time, higher stability, easier implement and smaller system size etc [10-14].

Although utilizing third-order nonlinearity to directly perform THG exists in principle, typical values of third-order nonlinearity are generally smaller than that of second-order nonlinearity in nonlinear crystals. Practically, the THG of the Nd-doped crystal IR laser consists of two cascaded harmonic generations. The first stage is converting the fundamental IR beam to the visible green light by frequency doubling of the Nd-doped crystal laser at the $^4F_{3/2} \rightarrow {}^4I_{11/2}$ transition. The generated second harmonic radiation is subsequently mixed with the residual fundamental wave via sum frequency process to produce the UV laser near 0.35 μm.

During the early research on the extracavity THG (ETHG) of the all-solid-state laser, the KTP crystal was employed as the frequency doubler because of its large second-order nonlinearity for the SHG. However, the problems of gray tracking as well as low damage threshold make the KTP crystal unfavorable to be used in high-power and high-repetition-rate extracavity harmonic generation. Moreover, the type-II phase matching condition for the KTP crystal leads the polarizations for the fundamental and the second harmonic waves to be neither perpendicular nor parallel before performing sum frequency process. This means the beam manipulations for the fundamental and second harmonic waves before frequency tripler is needed. As a result, the conversion efficiency from 1064 to 355 nm and the UV output power obtained with the KTP crystal as the frequency doubler were quite low [15,16].

Currently, the most efficient way in obtaining the UV lasers near 0.35 μm is by frequency doubling with the type-I phase matching of a portion of the fundamental Nd-doped crystal laser near 1 μm and subsequently sum frequency generation with

type-II phase matching of the residual fundamental beam and the frequency doubled radiation. The easy implementation of the described scheme is due to the fact that the fundamental and frequency doubled beams after the first nonlinear crystal have mutually orthogonal polarizations, which are exactly what is required for type-II phase matching in the second nonlinear crystal. There is no need for beam manipulation between the nonlinear crystals except for possible requirement of focusing optics. Usually, LBO crystals are utilized for both processes thanks to high damage threshold, relatively large acceptance angle, low absorption in visible and UV ranges, and small walk-off angle etc [17-20].

In this section, the optimized Q-switched Nd:YVO_4 and Nd:YLF IR lasers developed in Chap. 2 are employed to generate green and UV radiations in the processes of ESHG and ETHG. For the PQS Nd:YVO_4 UV laser, the maximum output power at 355 nm is up to 1.62 W, corresponding to the optical conversion efficiency from 1064 to 355 nm of 26 %. For the AQS Nd:YVO_4 UV laser, the maximum output power of 6.65 W at 355 nm with the optical conversion efficiency from 1064 to 355 nm as high as 38.2 % is achieved. For the PQS Nd:YLF UV laser, the largest pulse energy of 360 μJ at 351 nm is efficiently obtained.

II. Passively Q-switched Nd:YVO_4 UV laser at 355 nm

Here LBO crystals are exploited as nonlinear frequency converters for SHG and THG of the PQS Nd:YVO_4 laser at 1064 nm developed in Sec. 2.2. One LBO crystal with dimensions of 3 × 3 × 15 mm^3 was cut at θ = 90°, ϕ = 10.4° for type-I phase-matched SHG at a temperature of 46.6 °C. Both facets of the SHG crystal were AR coated at 1064 and 532 nm. Another LBO crystal with dimensions of 3 × 3 × 10 mm^3 was cut at θ = 44°, ϕ = 90° for type-II phase-matched THG at a temperature of 48 °C. Both facets of the THG crystal were AR coated at 1064, 532, and 355 nm. The temperatures of the SHG and THG nonlinear crystals were monitored by thermoelectric controllers with the precision of 0.1 °C. Two convex lenses were used to focus the laser beams into the SHG and THG nonlinear crystals for achieving efficient harmonic generations. The former one with focal length of 38 mm was AR coated at 1064 nm on both sides, the latter one with focal length of 19 mm was AR coated at 1064 and 532 nm on both sides. The optimized geometrical distances of L_1, L_2, L_3 and L_4 indicated in Fig. 4.2.1 were experimentally determined to be approximately 100, 50, 40, and 20 mm, respectively.

After optimization in the extracavity harmonic generations, the dependences of the output powers at 532 and 355 nm on the incident pump power at 1064 nm are shown in Fig. 4.2.2. At the maximum incident pump power of 6.3 W at 1064 nm, the highest output powers at 532 and 355 nm reach 2.2 and 1.62 W with a pulse width as short as 5 ns and a pulse repetition rate of 56 kHz. Accordingly, the highest pulse energies at 532 and 355 nm are found to be 39 and 29 μJ. More importantly, the largest peak powers at 532 and 355 nm as high as 7.8 and 5.8 kW are achieved. The optical conversion efficiencies from 1064 to 355 nm and 808 to 355 nm are up to 26 and 10 %, respectively. With the knife-edge method, the beam quality factors at 355 nm for orthogonal directions were measured to be $M_x^2 < 1.2$ and $M_y^2 < 1.3$, respectively.

Finally, it is worthwhile to mention that although the intracavity focusing obtained from the three-element resonator can effectively enlarge the ratio of the laser mode area in the gain medium to that in the saturable absorber to meet the second threshold condition, it will not only add complexities to the overall laser cavity but also reduce the peak power that is detrimental for efficient extracavity harmonic generations. Employing a c-cut Nd:YVO_4 that has smaller stimulated emission cross section is

another suitable way to satisfy the second threshold condition; however, the non-polarized laser output is problematic in the processes of extracavity harmonic generations, in which the linearly polarized fundamental beam is usually required. Comparative speaking, using a simple concave-plano resonator to construct a compact high-power PQS Nd:YVO_4/Cr^{4+}:YAG laser with constantly linear polarization is a practical method to simultaneously satisfy the second threshold condition and provide adequate peak power for efficient extracavity harmonic generations.

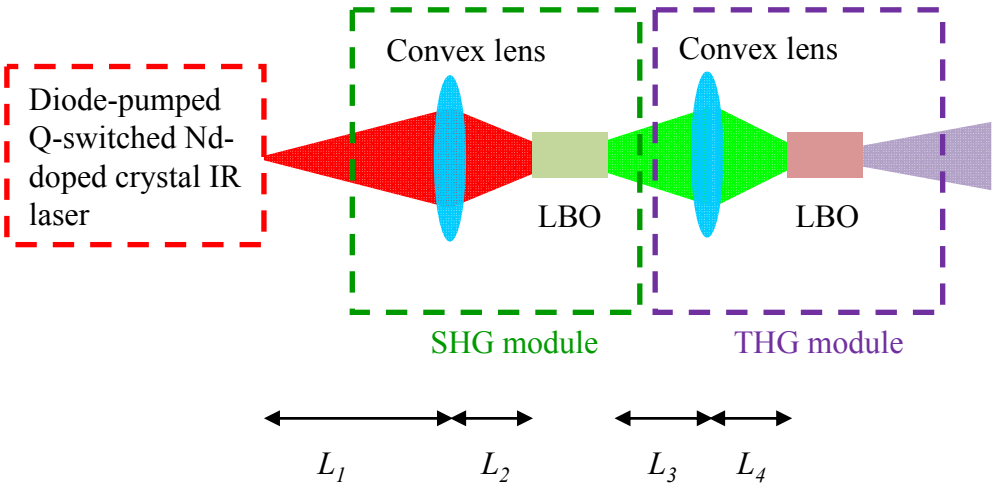

Fig. 4.2.1. Schematic of the experimental setup for the ESHG and ETHG.

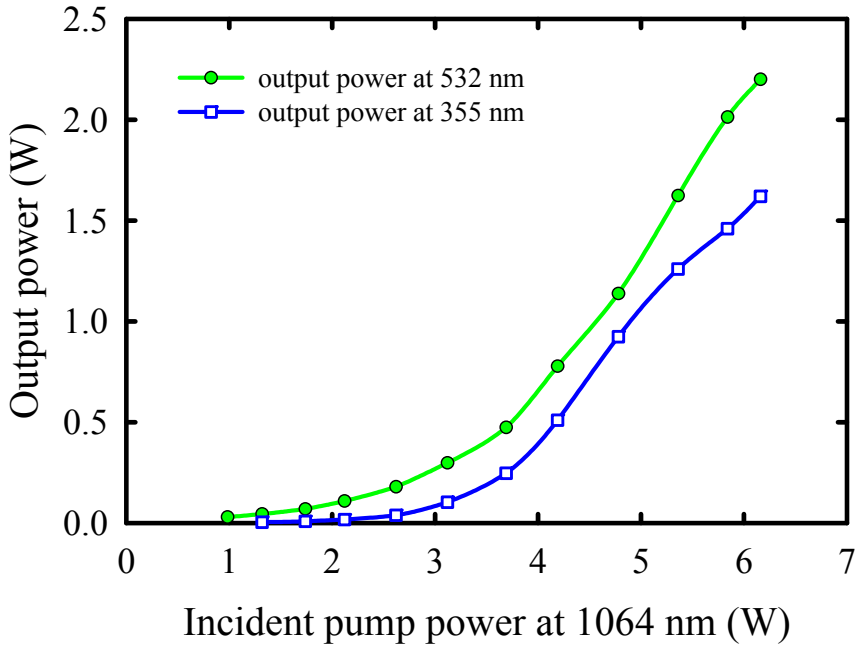

Fig. 4.2.2. Dependences of the output power at 532 nm (green curve) and 355 nm (blue curve) on the incident pump power at 1064 nm.

III. Actively Q-switched Nd:YVO_4 UV laser at 355 nm

The experimental setup for the SHG and THG of the AQS Nd:YVO_4 laser at 1064 nm developed in Sec. 2.3 is the same as that described in Fig. 4.2.1, except that the optimized geometrical distances of L_1, L_2, L_3 and L_4 were experimentally determined to be approximately 70, 43, 34, and 21 mm, respectively.

After optimization in the extracavity harmonic generations, the output power, the pulse energy, and the peak power at 532 and 355 nm versus the pulse repetition rate under an incident pump power of 44 W are shown in Figs. 4.2.3(a)-(c), respectively. Although the conversion efficiency of harmonic generations increases with decreasing the pulse repetition rate, the output power at 1064 nm is proportional to the pulse repetition rate in the range of 20-50 kHz. As a result, the highest output powers for ESHG and ETHG are found to be approximately at a pulse repetition rate of 40 kHz and their values at 532 and 355 nm are 8.38 and 6.65 W, respectively. The corresponding optical conversion efficiencies from 808 to 355 nm and 1064 to 355 nm are up to 15.1 % and 38.2 %, respectively. On the other hand, at a pulse repetition rate of 20 kHz, the largest pulse energy and the highest peak power at 532 nm are found to be 270 μJ and 30 kW, respectively. Similarly, at a pulse repetition rate of 20 kHz, the largest pulse energy and the highest peak power at 355 nm are found to be 200 μJ and 22 kW, respectively. With the knife-edge method, the beam quality factors at 355 nm for orthogonal directions were measured to be $M_x^2 < 1.2$ and $M_y^2 < 1.3$.

To manifest the influence of parasitic lasing on the extracavity harmonic generations discussed in Sec. 2.3, the Q-switched laser with L_{cav} = 16 cm was also employed to perform the process of SHG and THG. Experimental results reveal that even though the average output power at 1064 nm obtained with L_{cav} = 16 cm is nearly the same as that obtained with L_{cav} = 20 cm, the average output powers at SHG and THG obtained with L_{cav} = 16 cm were found to be 15-25 % lower than the results obtained with L_{cav} = 20 cm. The lower conversion efficiencies obtained with L_{cav} = 16 cm confirm that the parasitic lasing effect leads to the peak-power reduction in Q-switched lasers.

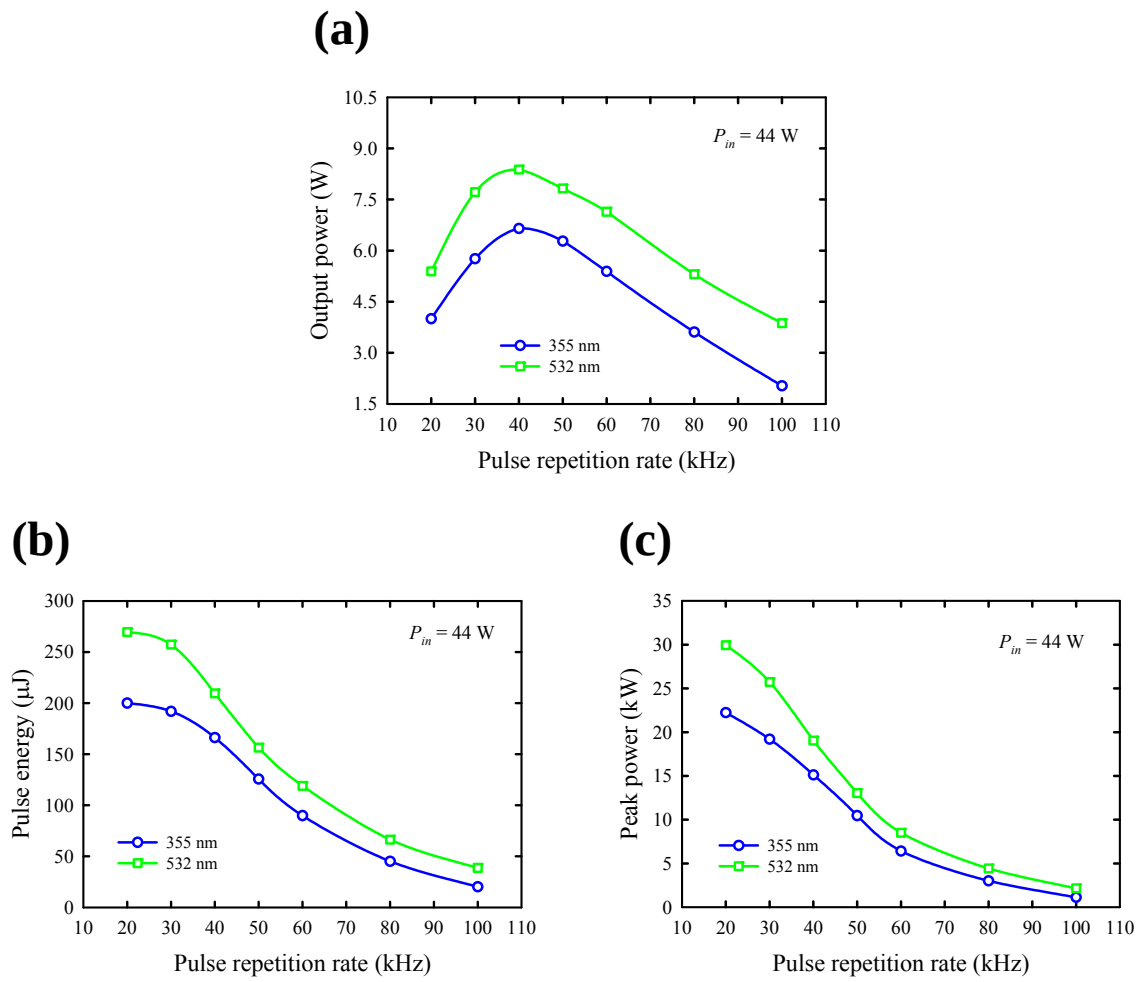

Fig. 4.2.3. Dependences of (a) the output powers, (b) the pulse energies, and (c) the peak powers at 532 and 355 nm on the pulse repetition rate at an incident pump power of 44 W.

IV. Passively Q-switched Nd:YLF UV laser at 351 nm

The experimental setup for the SHG and THG of the PQS Nd:YLF laser at 1053 nm developed in Sec. 2.7 is similar to that described in Fig. 4.2.1. The first LBO crystal with dimensions of 3 × 3 × 10 mm^3 was cut at θ = 90°, ϕ = 11.1° for type-I phase-matched SHG at a temperature of 47°C. Both facets of the SHG crystal were AR coated at 1053 and 527 nm. Another LBO crystal with dimensions of 3 × 3 × 10 mm^3 was cut at θ = 46.4°, ϕ = 90° for type-II phase-matched THG at a temperature of 48°C. Both surfaces of the THG crystal were AR coated at 1053, 527, and 351 nm. The thermoelectric controllers with a precision of 0.1 °C were utilized to monitor the temperatures of the SHG and THG nonlinear crystals. The laser beams were focused into the SHG and THG nonlinear crystals with two individual convex lenses for achieving efficient harmonic generations. The former one with focal length of 38 mm was AR coated at 1053 nm on both sides, the latter one with focal length of 19 mm was AR coated at 1053 and 527 nm on both facets. The optimized geometrical distances of L_1, L_2, L_3 and L_4 were experimentally determined to be approximately 76, 62, 31, and 29 mm, respectively.

Figures 4.2.4(a) and (b) show the pulse energies at 527 and 351 nm as a function of the pulse repetition rate. The pulse energy for the extracavity harmonic generation is determined by the combined effects of the spatial and temporal properties of the fundamental laser; that is, the beam quality factors and the peak power. Based on the present experimental circumstance, the largest pulse energies at 527 and 351 nm are achieved to be 490 and 360 μJ under a pulse repetition rate of 100 Hz, respectively. On the other hand, the pulse durations at 527 and 351 nm are experimentally found to be in the range 4-9 ns, depending on the ROC of the input mirror. In comparison with the studies in Refs. [21,22], we believe that the end-pumped scheme is a more feasible way to obtain a nearly diffraction-limited pulsed laser, and the efficient extracavity harmonic generations validate the applicability of our cavity design.

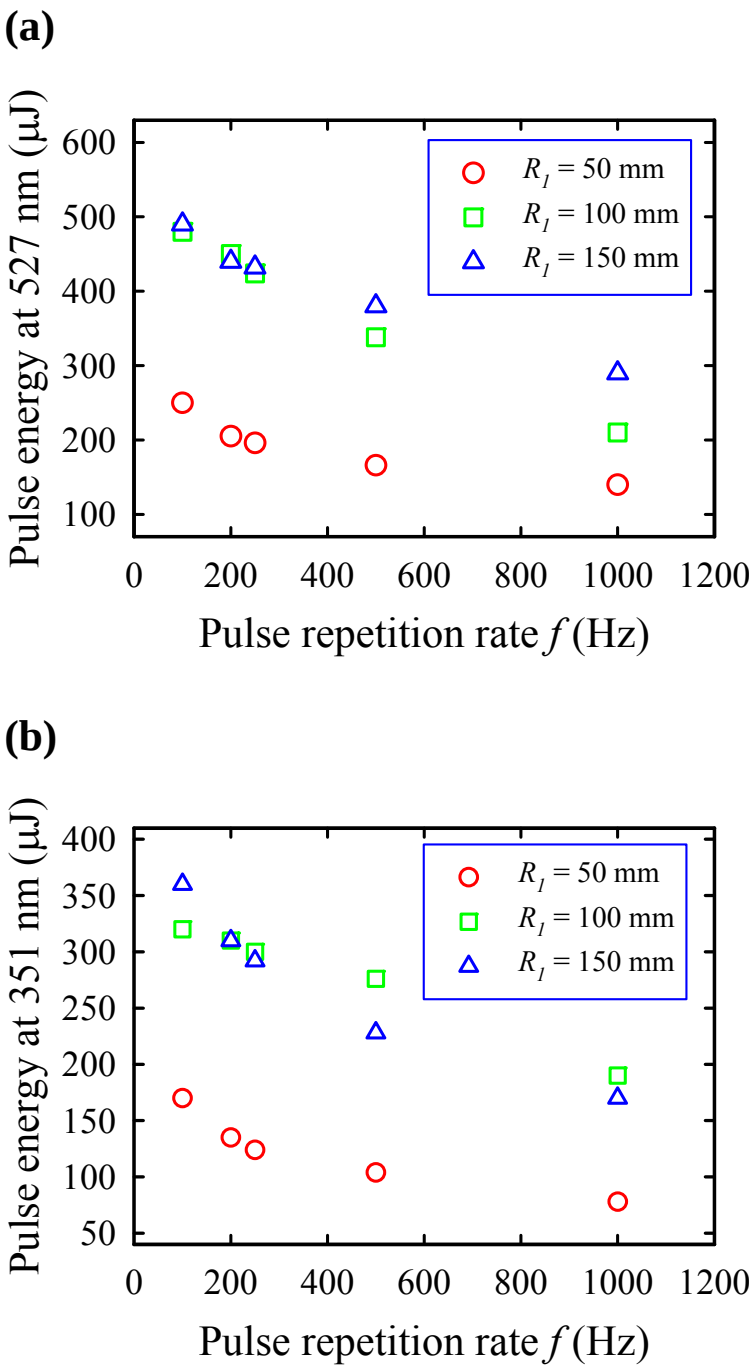

Fig. 4.2.4. Pulse energies as a function of the pulse repetition rate at (a) 527 nm and (b) 351 nm.

4.3 Fourth Harmonic Generation at 266 nm

I. Introduction

Recently, DUV light sources have also been rapidly developed because of their usefulness in a large number of industrial applications and scientific fields. Nowadays, the EFHG performed by the Nd-doped crystal laser at 1064 nm provides a convenient and reliable way to obtain the DUV radiation at 266 nm, which intrinsically takes the advantages of higher efficiency, longer lifetime, higher stability, easier implement, and smaller system size etc. The principle of the FHG with the widely used Nd-doped crystal at the $^4F_{3/2} \rightarrow {}^4I_{11/2}$ transition is based on the cascaded processes of the SHG. The first stage is converting the fundamental IR beam to the visible green light by frequency doubling of the Nd-doped crystal laser at 1064 nm, and one subsequently performs another SHG of the generated 532-nm radiation to acquire the DUV laser at 266 nm [23-28].

In this section, based on the green lasers discussed in Sec. 4.1, we perform the EFHG to verify that the ESHG is more advantageous in generating DUV laser at 266 nm than the intracavity one, where the conversion efficiencies from 532 to 266 nm for the two cases are 37.1 and 7.2 %, respectively. Moreover, the output power at 266 nm as high as 1.67 W is effectually generated with the combination of the ESHG and EFHG under an incident pump power of 26 W at 808 nm and a pulse repetition rate of 40 kHz, corresponding to the conversion efficiency from 808 to 266 nm of up to 6.4 %.

II. Experimental setup

Among several nonlinear crystals for realizing an efficient EFHG at 266 nm, we chose the BBO crystal because of its high nonlinear coefficient and low hygroscopic property. The dimensions of the BBO crystal were 3 × 3 × 10 mm^3, and it was used as the type-I phase-matched condition at room temperature along the direction at $\theta = 47.6^\circ$, $\phi = 0^\circ$. Both surfaces of the BBO crystal were AR coated at 1064, 532, and 266 nm. A convex lens with a focal length of 19 mm was employed to focus the green light into the BBO crystal for realizing an efficient EFHG operation. Both sides of the convex lens were AR coated at 1064 and 532 nm. Although the same optical components for the two configurations were exploited, the EFHG processes were individually optimized for the ESHG or ISHG. The geometrical distance of L_5 and L_6 indicated in Fig. 4.3.1 were 25 and 22 mm for the ESHG, while for the ISHG they were 16 and 30 mm.

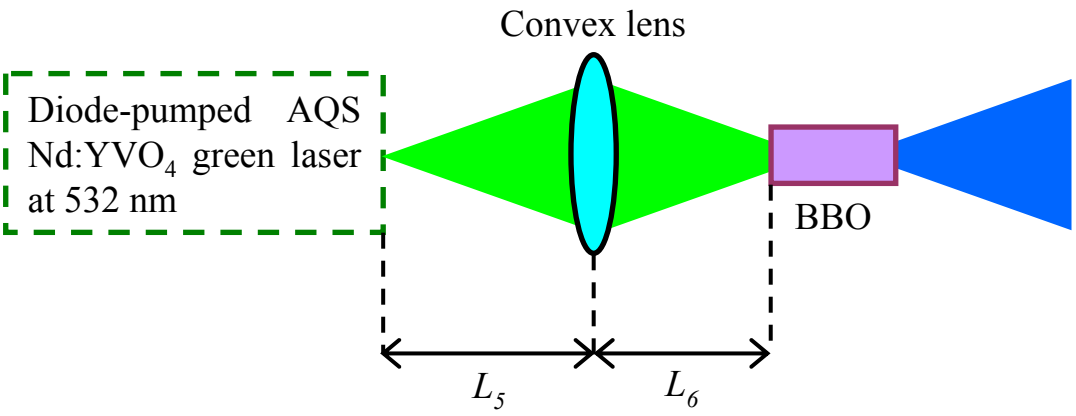

Fig. 4.3.1. Arrangement of the experimental setup for the EFHG.

III. Conversion efficiencies in the EFHG process with ESHG and ISHG

Figure 4.3.2 graphically summarizes the output characteristics at 266 nm by frequency doubling of the green lasers at 532 nm obtained with the ESHG and ISHG. Note that the incident powers at 532 nm for the ESHG are 30-40 % lower than those for the ISHG, as illustrated in Fig. 4.1.2(a). However, it is apparent that the conversion efficiencies in the EFHG process obtained with the ESHG are noticeably higher than the results obtained with the ISHG, as exhibited in Fig. 4.3.2(a). For the ESHG, the highest output power at 266 nm of 1.67 W is achieved under the maximum incident power of 4.5 W at 532 nm. The corresponding conversion efficiencies from 808 to 266 nm and from 532 to 266 nm are up to 6.4 and 37.1 %, respectively. Note that the conversion efficiencies from 808 to 266 nm and from 532 to 266 nm obtained with the previous studies on the DUV generation at 266 nm were not more than 3 and 20 % [25-28]. The high optical conversion efficiency achieved in this work is believed to come from the optimization of the AO Q-switched laser without the parasitic lasing effect as well as the use of the convex lens to focus the green light into the BBO crystal. On the other hand, the highest output power at 266 nm for the ISHG is only 0.46 W under the maximum incident power of 5.76 W at 532 nm. The corresponding optical conversion efficiencies from 808 to 266 nm and from 532 to 266 nm are 1.8 and 7.2 %, respectively. The more efficient DUV attainment obtained with the ESHG is definitely due to the fact that the considerably higher peak power greatly enhances the conversion efficiency in the EFHG process as compared with the ISHG.

The pulse energies at 266 nm versus the pulse repetition rate for both cases are illustrated in Fig. 4.3.2(b). The pulse energy at 266 nm decreases from 51 to 6.5 μJ for the ESHG and from 15 to 1 μJ for the ISHG by increasing the pulse repetition rate from 30 to 100 kHz. Figure 4.3.2(c) presents the dependences of the peak power at 266 nm on the pulse repetition rate for both cases. When the pulse repetition rate increases from 30 to 100 kHz, the peak powers for the ESHG and ISHG vary from 7.3 to 0.4 kW and from 1.2 to 0.1 kW, respectively. Owing to the combined effect of the large walk-off property of the BBO crystal and the tight-focusing scheme of the extracavity harmonic generation, the beam quality factors for the two cases are both found to be relatively poor; that is, $M_x^2 \sim 2$, and $M_y^2 \sim 1.5$. On the whole, we have experimentally manifested that using the ESHG to perform EFHG can provide a superior laser performance at 266 nm in output power, pulse energy, and peak power in comparison with the ISHG. We

believe that the comparison presented here can give important insights into the fields of the laser technology and the harmonic generation.

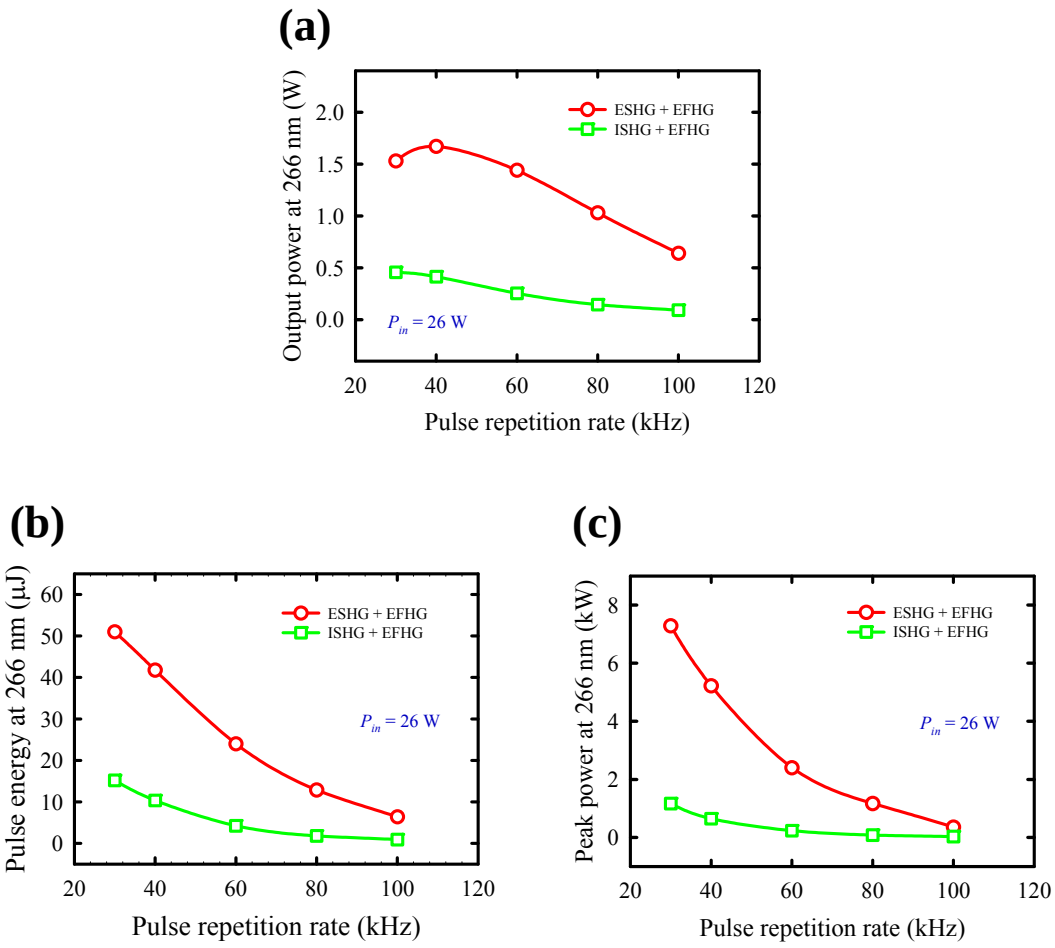

Fig. 4.3.2. Dependences of the (a) output power, (b) pulse energy, and (c) peak power at 266 nm on the pulse repetition rate.

4.4 Conclusion

Efficient extracavity harmonic generations performed with optimized Q-switched Nd-doped crystal IR lasers are successfully achieved. First of all, we properly design an efficient and reliable single-end-pumped AQS Nd:YVO_4 laser to make a systematic comparison of the output performance at 532 nm between the extracavity and intracavity configurations in the SHG process. Experimental investigations reveal that the output power and pulse energy obtained with the ISHG are higher than the results obtained with the ESHG under the same incident pump power and pulse repetition rate. Nevertheless, the relatively wide pulse duration accompanied with a long tail due to the high finesse of the laser cavity is experimentally found to lead the peak power obtained with the ISHG to be significantly lower than that obtained with the ESHG. Under an incident pump power of 26 W at 808 nm, the maximum output powers of 4.5 and 5.76 W and the largest pulse energies of 133 and 177 μJ are accomplished for ESHG and ISHG, whereas the highest peak powers obtained with ESHG and ISHG are found to be 30.4 and 11.6 kW, respectively.

In Sec. 4.2, utilizing the developed PQS Nd:YVO_4 laser to perform the ESHG and ETHG, the maximum output powers at 532 and 355 nm are found to be up to 2.2 and 1.62 W with a pulse width as short as 5 ns and a pulse repetition rate of 56 kHz. The largest pulse energy and the highest peak power at 355 nm are found to be 29 μJ and 5.8 kW, respectively. The optical conversion efficiencies from 1064 to 355 nm and 808 to 355 nm are up to 26 and 10 %, respectively. To our knowledge, this is the highest conversion efficiency for the 355-nm UV laser generated by the PQS Nd:YVO_4/Cr^{4+}:YAG laser.

We then employ the optimized AQS Nd:YVO_4 laser to achieve highly efficient extracavity harmonic generations. At an incident pump power of 44 W, the output powers at 532 and 355 nm under a pulse repetition rate of 40 kHz reach 8.38 and 6.65 W, respectively. In addition, at a pulse repetition rate of 20 kHz, the largest pulse energy and the highest peak power at 355 nm are found to be 200 μJ and 22 kW, respectively. The optical conversion efficiencies from 1064 to 355 nm and from 808 to 355 nm are found to be up to 38.2 and 15.1 %, respectively. This is the highest conversion efficiency for the 355-nm UV radiation based on the AO Q-switched laser

with a flat-flat cavity to date.

The PQS Nd:YLF laser developed in Sec. 2.7 is also successfully applied in the processes of the extracavity harmonic generations to produce green and UV radiations, where the largest pulse energies of 490 μJ at 527 nm and 360 μJ at 351 nm are efficiently generated with the shortest pulse width of 4 ns.

Finally, following the works in Sec. 4.1, we further verify that the higher peak power obtained with the ESHG is more helpful for the 266-nm generation via the EFHG process as compared with the ISHG, where the conversion efficiencies from 532 to 266 nm are 37.1 and 7.2 % for the ESHG and ISHG, respectively. In addition, under an incident pump power of 26 W at 808 nm and a pulse repetition rate of 40 kHz, the maximum output power of our Q-switched Nd:YVO_4 DUV laser at 266 nm based on the combination of the ESHG and EFHG arrangements reaches 1.67 W, corresponding to the conversion efficiency from 808 to 266 nm up to 6.4 %. To the best of our knowledge, this is the highest conversion efficiency at 266 nm ever reported among the continuously pumped Q-switched Nd-doped vanadate DUV oscillators with the same incident pump power at 808 nm.

References

[1] Q. Liu, X. Yan, M. Gong, X. Fu, and D. Wang, "103 W high beam quality green laser with an extra-cavity second harmonic generation," Opt. Express **16**, 14335-14340 (2008).

[2] R. Bhandari and T. Taira, "> 6 MW peak power at 532 nm from passively Q-switched Nd:YAG/Cr^{4+}:YAG microchip laser," Opt. Express **19**, 19135-19141 (2011).

[3] Y. Bo, A. Geng, Y. Bi, Z. Sun, X. Yang, Q. Peng, H. Li, R. Li, D. Cui, and Z. Xu, "High-power and high-quality, green-beam generation by employing a thermally near-unstable resonator design," Appl. Opt. **45**, 2499-2503 (2006).

[4] D. Xu, Y. Wang, H. Li, J. Yao, and Y. H. Tsang, "104 W high stability green laser generation by using diode laser pumped intracavity frequency-doubling Q-switched composite ceramic Nd:YAG laser," Opt. Express **15**, 3991-3997 (2007).

[5] S. Zhang, L. Guo, B. Xiong, Y. Liu, W. Hou, X. Lin, and J. Li, "High electro-to-optical efficiency 180 W Q-switched 532 nm laser with a pulsewidth of 70 ns," Appl. Phys. B **104**, 861-866 (2011).

[6] F. Hajiesmaeilbaigi, H. Razzaghi, M. Mahdizadeh, M. R. A. Moghaddam, and M. Ruzbehani, "Design and construction of a 110 W green laser for medical application," Opt. Laser Technol. **43**, 1428-1430 (2011).

[7] B. Ji, X. S. Zheng, Z. P. Cai, H. Y. Xu, and F. Q. Jia, "Compact high conversion efficiency Nd:YAG/LBO green laser using unstable V cavity," Laser Phys. **22**, 406-410 (2012).

[8] H. Bazyar, M. Aghaie, M. H. Daemi, and S. M. Bagherzadeh, "Compact 151 W green laser with U-type resonator for prostate surgery," Opt. Laser Technol. **47**, 237-241 (2013).

[9] H. Huang and J. He, "A new view on the temperature insensitivity of intracavity SHG configuration," Opt. Express **20**, 9079-9089 (2012).

[10] N. Hodgson, M. Li, A. Held, and A. Krueger, "Diode-pumped TEM_{00} mode solid state lasers and their micromachining applications," Proc. SPIE **4977**, 281-294 (2003).

[11] A. V. Hicks, C. X. Wang, and G. Y. Wang, "Advances in high power

diode-pumped ultraviolet lasers," Proc. SPIE **5332**, 120-133 (2004).

[12] C. X. Wang, G. Y. Wang, A. V. Hicks, D. R. Dudley, H. Y. Pang, and N. Hodgson, "High power Q-switched TEM_{00} mode diode-pumped solid state lasers with > 30 W output power at 355 nm," Proc. SPIE **6100**, 610019 (2006).

[13] D. R. Dudley, O. Mehl, G. Y. Wang, E. S. Allee, H. Y. Pang, and N. Hodgson, "Q-switched diode pumped Nd:YAG rod laser with output power of 420W at 532nm and 160W at 355nm," Proc. SPIE **7193**, 71930Z (2009).

[14] Q. Liu, X. Yan, H. Chen, L. Huang, and M. Gong, "New progress in high-power all-solid-state ultraviolet laser," Chin. J. Lasers **37**, 2289-2298 (2010).

[15] Y. L. Jia, J. L. He, H. T. Wang, S. N. Zhu, and Y. Y. Zhu, "Single pass third-harmonic generation of 310 mW of 355 nm with an all-solid-state laser," Chin. Phys. Lett. **18**, 1589-1591 (2001).

[16] G. Wang, J. Liu, S. Liu, M. Liu, S. Liu, and L. Li, "Short pulse duration of a 355-nm laser by extracavity sum-frequency mixing with a LiB_3O_5 (LBO) crystal," Laser Phys. Lett. **5**, 506-509 (2008).

[17] X. P. Yan, Q. Liu, M. Gong, D. S. Wang, and X. Fu, "Over 8 W high peak power UV laser with a high power Q-switched Nd:YVO_4 oscillator and the compact extra-cavity sum-frequency mixing," Laser Phys. Lett. **6**, 93-97 (2009).

[18] X. Ya, Q. Liu, M. Gong, X. Fu, and D. Wang, "High-repetition-rate high-beam-quality 43 W ultraviolet laser with extra-cavity third harmonic generation," Appl. Phys. B **95**, 323-328 (2009).

[19] X. Yan, Q. Liu, H. Chen, X. Fu, M. Gong, and D. Wang, "35.1 W all-solid-state 355 nm ultraviolet laser," Laser Phys. Lett. **7**, 563-568 (2010).

[20] H. Hong, Q. Liu, L. Huang, and M. Gong, "High-beam-quality all-solid-state 355 nm ultraviolet pulsed laser based on a master-oscillator power-amplifier system pumped at 888 nm," Appl. Phys. Express **5**, 092705 (2012).

[21] D. Li, Z. Ma, R. Haas, A. Schell, P. Zhu, P. Shi, and K. Du, "Diode-end-pumped double Nd:YLF slab laser with high energy, short pulse width, and diffraction-limited quality," Opt. Lett. **33**, 1708-1710 (2008).

[22] N. U. Wetter, E. C. Sousa, I. M. Ranieri, and S. L. Baldochi, "Compact, diode-side-pumped Nd^{3+}:$YLiF_4$ laser at 1053 nm with 45% efficiency and diffraction-limited quality by mode controlling," Opt. Lett. **34**, 292 (2009).

[23] T. Kojima, S. Konno, S. Fujikawa, K. Yasui, K. Yoshizawa, Y. Mori, T. Sasaki, M. Tanaka, and Y. Okada, "20-W ultraviolet-beam generation by

fourth-harmonic generation of an all-solid-state laser," Opt. Lett. **25**, 58-60 (2000).

[24] G. Wang, A. Geng, Y. Bo, H. Li, Z. Sun, Y. Bi, D. Cui, Z. Xu, X. Yuan, X. Wang, G. Shen, and D. Shen, "28.4 W 266 nm ultraviolet-beam generation by fourth-harmonic generation of an all-solid-state laser," Opt. Commun. **259**, 820-822 (2006).

[25] Q. Liu, X. P. Yan, X. Fu, M. Gong, and D. S. Wang, "High power all-solid-state fourth harmonic generation of 266 nm at the pulse repetition rate of 100 kHz," Laser Phys. Lett. **6**, 203-206 (2009).

[26] F. Chen, W. W. Wang, and J. Liu, "Diode single-end-pumped AO Q-switched Nd:$GdVO_4$ 266 nm laser," Laser Phys. **20**, 454-457 (2010).

[27] F. Zhuang, N. Ye, C. Huang, H. Zhu, Y. Wei, Z. Chen, H. Wang, and G. Zhang, "Multi-reflected enhancement of fourth harmonic DUV laser generation at 266 nm," Opt. Express **18**, 25339-25345 (2010).

[28] Q. Liu, X. Yan, M. Gong, H. Liu, G. Zhang, and N. Ye, "High-power 266 nm ultraviolet generation in yttrium aluminum borate," Opt. Lett. **36**, 2653-2655 (2011).

Chapter 5

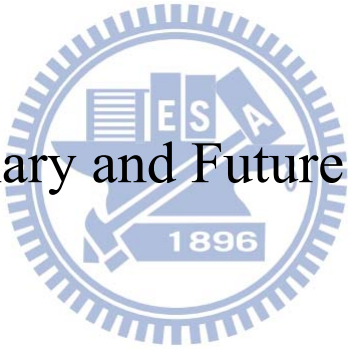

Summary and Future Works

5.1 Summary

High-power Q-switched Nd:YVO_4 lasers at 1064 nm and high-energy Q-switched Nd:YLF lasers at 1053 nm have been optimized to exhibit excellent output performance. We have considered the second threshold criterion and the thermal-lensing effect to design a high-peak-power PQS Nd:YVO_4 laser with the Cr^{4+}:YAG crystal as a saturable absorber. At an incident pump power of 16.3 W, the output power was found to reach 6.2 W with a pulse width of 7 ns and a pulse repetition rate of 56 kHz. The corresponding pulse energy and peak power were as high as 111 μJ and 16 kW, respectively.

In Sec. 2.3, we have explored the parasitic lasing effect in an AQS laser with a flat-flat resonator and a 0.1 at.% Nd:YVO_4 crystal. Experimental results revealed that the critical cavity length without parasitic lasing was proportional to the pump power. The parasitic lasing effect was also found to lead to a long tail in the Q-switched pulse, corresponding to a reduction in the peak power. We manifestly disclosed that the combined effects of the parasitic lasing and the thermal lens made Nd:YVO_4 crystals with dopant concentration greater than 0.2 at.% to be problematical in designing the high-power Q-switched laser with a flat-flat cavity. After optimizing the AQS laser, the maximum output power of 19.4 W was obtained at 100 kHz, while the shortest pulse width of 8 ns, the largest pulse energy of 650 μJ, and the highest peak power of 81.5 kW were accomplished at an incident pump power of 44 W.

In Sec. 2.5, we have successfully demonstrated a reliable TEM_{00}-mode linearly polarized laser at 1053 nm with the natural birefringence of a wedged Nd:YLF crystal in a compact concave-plano cavity. Using the Cr^{4+}:YAG saturable absorber to perform PQS operation, the maximum output power can be up to 2.3 W under an incident pump power of 12 W. Under this output condition, the pulse repetition rate and the pulse width were found to be 8 kHz and 9 ns, respectively. The corresponding pulse energy and the peak power were up to 288 μJ and 32 kW, respectively. We believe that the relatively compact configuration presented here is potentially useful for the generation of high-peak-power pulses in Q-switched Nd:YLF lasers at 1053 nm.

With c-cut Nd:YLF crystal, we have found that decreasing the ROC of the concave mirror can usefully extend the power scale-up for a laser in a concave-plano cavity to be

influenced by a large negative thermal lens. With this finding, we have developed a practical tactic to scale up the output power of a compact high-pulse-energy PQS Nd:YLF laser at 1053 nm with the Cr^{4+}:YAG crystal as a saturable absorber. At an incident pump power of 12.6 W, the optimum PQS laser at 1053 nm emitted the maximum output power of 2.61 W with a pulse width of 6 ns and a pulse repetition rate of 4.6 kHz. The corresponding pulse energy and peak power were up to 570 μJ and 95 kW, respectively. We further experimentally confirmed that the negative focal length of the thermal lens is considerably enhanced by the ETU effect in the PQS Nd:YLF laser.

Moreover, we have theoretically realized and experimentally designed a nearly hemispherical cavity to scale up the pulse energy of a nanosecond pulsed pumped PQS Nd:YLF/Cr^{4+}:YAG laser with the pulse repetition rate tunable from 100 Hz to 1 kHz. At a pulse repetition rate of 100 Hz, the largest pulse energy and the shortest pulse duration were achieved to be 1.38 mJ and 5 ns with this compact pulsed laser.

The AO Q-switch has been utilized to achieve AQS operation in the c-cut Nd:YLF crystal with the pulse repetition rate ranging from 5 to 40 kHz. Under an incident pump power of 12.7 W, the maximum output power of 4.5 W was fulfilled at 5 kHz, whereas the shortest pulse duration of 25 ns, the largest pulse energy of 800 μJ, and highest peak power of 32 kW were accomplished at 40 kHz. In addition, we have exhaustively explored the influences of the thermal effect and anisotropic property of the AO Q-switch on the polarization characteristics of the c-cut Nd:YLF laser in the CW and Q-switched operation for the first time.

In Chap. 3, a novel concept of a separable monolithic IOPO cavity was originally proposed. With the developed approach, we have remarkably improved the stability and efficiency of the IOPO driven by a diode-pumped Q-switched Nd:YVO_4/Cr^{4+}:YAG laser. The mirrors were directly deposited on the facets of the KTP crystal to form an independent monolithic IOPO cavity with high stability and high optical conversion efficiency. The performances of IOPO with R_s = 80 and 50 % have been investigated. The output powers at 1552 nm were up to 3.3 W at the maximum incident pump power of 16.8 W for both cases with the instability of 0.2 % for R_s = 80 % and 1 % for R_s = 50 %, respectively. The diode-to-signal conversion efficiency was up to 20 %, which is the highest one for IOPOs to our knowledge. At the maximum pump power, pulse energies were 40 μJ at a pulse repetition rate of 80 kHz for R_s = 80 % and 45 μJ at a pulse

repetition rate of 68 kHz for R_s = 50 %, respectively. The temporal domain showed that several satellite pulses were observed behind a major pulse for R_s = 80 %. Reducing the R_s to 50 %, satellite pulses could be suppressed effectively without energy loss. The pulse train amplitude fluctuation in standard deviation was slightly larger with the lower R_s. However, the peak power was remarkably enhanced by employing the KTP crystal with lower reflectivity of the output coupler at 1552 nm, which is advantageous to generate high-peak-power eye-safe light source.

With the same design concept, we have demonstrated an efficient high-pulse-energy eye-safe radiation in a Nd:YLF/KTP IOPO with the help of thermally induced polarization switching. We properly measured the temporal behaviors of the depleted fundamental pulses and manifestly found that the thermally induced birefringence can lead the mutually orthogonal polarization states of the fundamental pulses to be effectively switched for accomplishing an efficient IOPO operation without any extra polarization control. With this finding, the pulse energy as high as 306 μJ with the optical conversion efficiency up to 12.3 % was achieved in our compact Nd:YLF/KTP eye-safe laser under an incident pump power of 12.7 W and a pulse repetition rate of 5 kHz.

Efficient extracavity harmonic generations performed with optimized Q-switched Nd-doped crystal IR lasers were successfully achieved. First of all, a systematic comparison between the ESHG and ISHG with a diode-pumped AO Q-switched Nd:YVO_4 laser has been investigated. We have experimentally found that the output power and pulse energy at 532 nm for the ISHG were generally higher than the results obtained with the ESHG thanks to the increased interaction length of the fundamental beam through the nonlinear crystal. However, the high finesse of the laser cavity with the ISHG was observed to lead to a wider Q-switched pulse accompanied with a long tail, which significantly reduces the peak power at 532 nm. Under an incident pump power of 26 W at 808 nm, the maximum output powers of 4.5 and 5.76 W and the largest pulse energies of 133 and 177 μJ were accomplished for ESHG and ISHG, whereas the highest peak powers obtained with ESHG and ISHG were found to be 30.4 and 11.6 kW, respectively.

In Sec. 4.2, utilizing the developed PQS Nd:YVO_4 laser to perform the ESHG and ETHG, the maximum output powers at 532 and 355 nm were found to be up to 2.2 and

1.62 W with a pulse width as short as 5 ns and a pulse repetition rate of 56 kHz. The largest pulse energy and the highest peak power at 355 nm were found to be 29 μJ and 5.8 kW, respectively. The optical conversion efficiencies from 1064 to 355 nm and 808 to 355 nm were up to 26 and 10 %, respectively. To our knowledge, this is the highest conversion efficiency for the 355-nm UV laser generated by the PQS Nd:YVO_4/Cr^{4+}:YAG laser.

We then employed the optimized AQS Nd:YVO_4 laser to achieve highly efficient extracavity harmonic generations. At an incident pump power of 44 W, the output powers at 532 and 355 nm under a pulse repetition rate of 40 kHz reached 8.38 and 6.65 W, respectively. In addition, at a pulse repetition rate of 20 kHz, the largest pulse energy and the highest peak power at 355 nm were found to be 200 μJ and 22 kW, respectively. The optical conversion efficiencies from 1064 to 355 nm and from 808 to 355 nm were found to be up to 38.2 and 15.1 %, respectively. This is the highest conversion efficiency for the 355-nm UV radiation based on the AO Q-switched laser with a flat-flat cavity to date.

The PQS Nd:YLF laser developed in Sec. 2.7 was also successfully applied in the processes of the extracavity harmonic generations to produce green and UV radiations, where the largest pulse energies of 490 μJ at 527 nm and 360 μJ at 351 nm were efficiently generated with the shortest pulse width of 4 ns, respectively.

Finally, following the works in Sec. 4.1, we further verified that the higher peak power obtained with the ESHG is more helpful for the 266-nm generation via the EFHG process as compared with the ISHG, where the conversion efficiencies from 532 to 266 nm were 37.1 and 7.2 % for the ESHG and ISHG, respectively. In addition, under an incident pump power of 26 W at 808 nm and a pulse repetition rate of 40 kHz, the maximum output power of our Q-switched Nd:YVO_4 DUV laser at 266 nm based on the combination of the ESHG and EFHG arrangements reached 1.67 W, corresponding to the conversion efficiency from 808 to 266 nm up to 6.4 %. To the best of our knowledge, this is the highest conversion efficiency at 266 nm ever reported among the continuously pumped Q-switched Nd-doped vanadate DUV oscillators with the same incident pump power at 808 nm.

Table 5.1.1-5.1.3 summarize the achievements for the output performance of this thesis.

	PQS	AQS
a-cut Nd:YVO_4	6.16 W, 56 kHz, 7 ns, 111 μJ, 16 kW	13-19.4 W, 20-100 kHz, 8-24 ns, 194-650 μJ, 8.1-81.5 kW
a-cut Nd:YLF	2.3 W, 9 kHz, 8 ns, 288 μJ, 31.9 kW	future work
c-cut Nd:YLF	2.4 W, 4.6 kHz, 6 ns, 570 μJ, 95 kW	4-4.5 W, 5-40 kHz, 25-180 ns, 113-800 μJ, 0.63-32 kW
	100 Hz, 5 ns, 1.38 mJ, 51.7 kW	

Table 5.1.1. Summary for Q-switched Nd-doped crystal IR lasers.

	PQS eye-safe	AQS eye-safe
a-cut Nd:YVO_4	3.3 W, 80 kHz, 41 μJ, 2 kW	2.93 W, 80 kHz, 36.6 μJ, 9.6 kW
c-cut Nd:YLF	future work	1.56 W, 5 kHz, 306 μJ, 4 kW

Table 5.1.2. Summary for Q-switched Nd-doped crystal eye-safe lasers.

	AQS green	AQS UV	PQS green	PQS UV	AQS DUV
a-cut $Nd:YVO_4$	8.38 W, 270 μJ, 30 kW	6.65 W, 200 μJ, 22 kW	2.2 W, 56 kHz, 39 μJ, 7.8 kW	1.62 W, 56 kHz, 29 μJ, 5.8 kW	1.67 W, 51 μJ, 7.3 kW
c-cut Nd:YLF	future work	future work	490 μJ, 100 Hz, 53 kW	360 μJ, 100 Hz, 44.1 kW	future work

Table 5.1.3. Summary for harmonic generations performed by Q-switched Nd-doped crystal IR lasers.

5.2 Future Works

I. Long-term stability examination in the UV and DUV regimes

For our developed UV and DUV lasers to be used in commercial applications, a stable long-term operation is necessary. We have packaged a prototypical UV laser at 355 nm which can be operated at a pulse repetition rate of 30-100 kHz. Under a pulse repetition rate of 40 kHz, the maximum output power at 355 nm can be rated to be 2.5 W at an incident pump power of 22 W. We have performed some primary examinations and found that the key to accomplish a reliable long-term stability for the UV laser is that the avoidance of the humidity and airborne contamination. In addition, the high power density of the focused beams into the nonlinear crystal brings in a large risk of causing the surface damage of the crystal for the configuration of the extracavity harmonic generations. This would eventually render the crystal useless at the impact location, especially for the THG crystal. Such practical issue is also observed by the research group from Coherent Inc. They have proposed a solution that relies on the discrete motion to a fresh spot if significant degradation is seen on the old spot of the THG crystal, where the period of the movement is around 300 hours [1]. As a result, they expect the lifetime of their UV laser can be over 20000 hours with the guaranty of the laser performance to be comfortable within the specification. In the future, we will try to move the THG crystal continuously rather then the discrete motion and slightly alleviate the tight focusing inside the THG crystal to examine the reliability of our UV laser. With this prospect, long-term stability without considerable degradation at least 10000 hours can be expected. Similar consideration may also be usefully applied for the long-term operation of the 266-nm laser.

II. Improvement of transverse distribution at 266 nm

Although we have achieved a high-power DUV laser at 266 nm with the maximum output power of up to 1.67 W, the relatively large walk-off angle of the BBO crystal leads the output transverse distribution to behave a rice kernel shape. Recently, a multi-reflected cavity without tightly focusing was proposed to improve the output beam to be circular shape [2]. However, the conversion efficiency from 532 to 266 nm is only 11.9 %, which is significantly lower than our achievement where the conversion efficiency as high as 37.1 % is obtained. Comparative speaking, using the external optics to modify the astigmatism of the 266-nm beam in the EFHG configuration may be a more practical solution to fulfill the circular output profile while preserving the high conversion efficiency thanks to the tightly focused configuration. This idea will be attempted in the future.

To obtain the efficient DUV laser 266 nm via EFHG scheme, the CLBO crystal is another suitable candidate. Compared with the BBO crystal, it is featured by the relatively small walk-off angle, moderate nonlinear coefficient, large angular bandwidth, and high damage threshold. Nevertheless, the main drawback of the CLBO crystal is the highly hygroscopic property, which needs specially designed protected mechanism to be employed for the commercial product with a long-term stability. As long as the hygroscopic issue can be suitably treated, using the CLBO crystal to perform EFHG presents a promising way to obtain high-efficiency 266-nm laser with the circular output profile. This prospect is under preparation.

III. Power scaling with multi-segmented Nd:YVO_4 crystal

In this thesis, we have constructed a novel dual-end-pumped Nd:YVO_4 laser at 1064 nm to efficiently generate the UV radiation with the output power as high as 6.65 W. To further scale up the UV output power, more powerful fundamental IR laser is required. The critical issue for power scaling is the thermal management; that is, the thermally induced fracture is the main limiting factor for power scale-up in the end-pumped solid-state laser. Although the composite crystal, which means the active medium is thermally diffusion-bonded by an undoped part to reduce the thermal effect, was recently proposed [3-6], the exponential decay of the pump radiation due to the homogeneous dopant concentration of the active medium results in high temperature gradient and mechanical stress peaks restricting the maximum incident pump power. More recently, 407-W diode-end-pumped laser has been successfully demonstrated by applying multiple segments with increasing dopant concentrations for the Nd:YAG crystal [7,8]. This multi-segmented concept enable the power scaling of the end-pumped configuration comparable with the side-pumped systems while keeping the advantages of better beam quality factors and conversion efficiency.

The most promising property of the Nd:YVO_4 crystal over the Nd:YAG crystal is the constantly polarized emission due to the natural birefringence, which is essentially beneficial for efficient extracavity harmonic generations. To our knowledge, the multi-segmented Nd:YVO_4 crystal has not been realized and applied in the nonlinear frequency conversion. We have fabricated a set of the multi-segmented Nd:YVO_4 crystals that consist of undoped part, 0.1 at. % active region, and followed by 0.3 at. % active region. We have also prepared the high-power laser diode that can nominally deliver the maximum output power of 70 W around 808 nm. The large potential for power scaling with the multi-segmented Nd:YVO_4 crystal is highly expected and is under development.

IV. Energy scaling of Nd:YLF laser with unstable Cavity

As discussed in Sec. 2.7, the larger output energy can be obtained when the cavity mode area inside the gain medium is increased for a given laser crystal. Unstable cavity has been adopted in a number of literatures for the accomplishment of a good laser performance [9-14]. Recently, side-pumped ultra-low-magnification unstable resonators with the Nd:YLF and Nd:YAG crystals have been built in our group. Several tens of millijoule of output energy are accomplished and the developed lasers have been employed to efficiently pump a monolithic OPO for confirming the applicability in nonlinear frequency conversions. Consequently, the energy scaling in the end-pumped Nd:YLF laser with the nearly diffraction-limited output is greatly expected by using the configuration of the unstable cavity. This is another future work to be studied.

References

[1] C. X. Wang, G. Y. Wang, A. V. Hicks, D. R. Dudley, H. Y. Pang, and N. Hodgson, "High power Q-switched TEM_{00} mode diode-pumped solid state lasers with > 30 W output power at 355 nm," Proc. SPIE **6100**, 610019 (2006).

[2] F. Zhuang, N. Ye, C. Huang, H. Zhu, Y. Wei, Z. Chen, H. Wang, and G. Zhang, "Multi-reflected enhancement of fourth harmonic DUV laser generation at 266 nm," Opt. Express **18**, 25339-25345 (2010).

[3] F. Hanson, "Improved laser performance at 946 and 473 nm from a composite Nd:$Y_3Al_5O_{12}$ rod," Appl. Phys. Lett. **66**, 3549-3551 (1995).

[4] M. Tsunekane, N. Taguchi, T. Kasamastu, and H. Inaba, "Analytical and experimental studies on the characteristics of composite solid-state laser rods in diode-end-pumped geometry," IEEE J. Sel. Top. Quantum Electron. **3**, 9-18 (1997).

[5] Z. Zhuo, T. Li, X. Li, and H. Yang, "Investigation of Nd:YVO_4/YVO_4 composite crystal and its laser performance pumped by a fiber coupled diode laser," Opt. Commun. **274**, 176-181 (2007).

[6] Y. T. Chang, Y. P. Huang, K. W. Su, and Y. F. Chen, "Comparison of thermal lensing effects between single-end and double-end diffusion-bonded Nd:YVO_4 crystals for $^4F_{3/2}\rightarrow{}^4I_{11/2}$ and $^4F_{3/2}\rightarrow{}^4I1_{3/2}$ transitions," Opt. Express **16**, 21155-21160 (2008).

[7] D. Kracht, R. Wilhelm, and M. Frede, "407 W end-pumped multi-segmented Nd:YAG laser," Opt. Express **13**, 10140-10144 (2005).

[8] R. Wilhelm, M. Frede, and D. Kracht, "Power scaling of end-pumped solid-state rod lasers by longitudinal dopant concentration gradients," IEEE J. Quantum Electron. **44**, 232-244 (2008).

[9] R. L. Herbst, H. Komine, and R. L. Byer, "A 200 mJ unstable resonator Nd:YAG oscillator," Opt. Commun. **21**, 5-7 (1977).

[10] A. E. Siegman, "Unstable optical resonators," Appl. Opt. **13**, 353-367 (1974).

[11] V. Magni, G. Valentini, and S. De Silverstri, "Recent developments in laser resonator design," Opt. Quantum Electron. **23**, 1105-1134 (1991).

[12] T. Debuisschért, D. Mathieu, J. Raffy, L. Becouarn, E. Lallier, and J. P. Pocholle, "High beam quality unstable cavity infrared optical parametric

oscillator," Proc. SPIE **3267**, 170-180 (1998).

[13] M. Morin, "Graded reflectivity mirror unstable laser resonators," Opt. Quantum Electron. **29**, 819-866 (1997).

[14] E. Armandillo, C. Norrie, A. Cosentino, P. Laporta, P. Wazen, and P. Maine, "Diode-pumped high-efficiency high-brightness Q-switched Nd:YAG slab laser," Opt. Lett. **22**, 1168-1170 (1997).

Curriculum Vitae

Personal Data

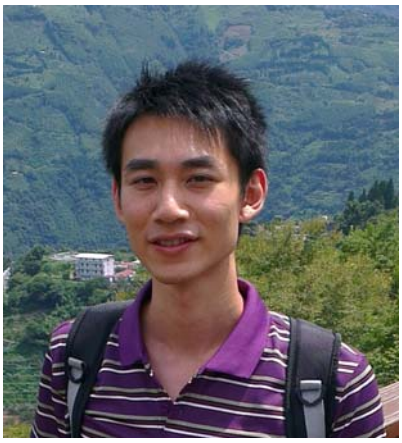

Name: Yu-Jen Huang

Nationality: Taiwan (R.O.C.)

Birthplace: Hualien

Sex: Male

Birthday: Mar. 11, 1987

Telephone (M): 886-910-535385

E-mail: shetogether2003@gmail.com

Education

2009~2013	Ph. D. in Department of Electrophysics, National Chiao Tung University, Hsinchu, Taiwan
2005~2009	B. S. in Department of Electrophysics, National Chiao Tung University, Hsinchu, Taiwan
2002~2005	National Hualien Senior High School, Hualien, Taiwan

Work Experience

2012~2013	Research Methods for Applied Science
2011~2012	Computer Simulation and Analysis (I) & (II)
2010~2011	Physics (I) & (II)
	Computer Simulation and Analysis (I) & (II)
	Research Methods for Applied Science
2009~2010	Physics (I) & (II)
	Computer Simulation and Analysis (I) & (II)

Specialty

Physics and technology of solid-state laser

Optical physcis

List of Publication

International journal paper:

[1] Y. P. Huang, ***Y. J. Huang***, C. Y. Cho and Y. F. Chen*, "Influence of output coupling on the performance of a passively Q-switched Nd:YAG laser with intracavity optical parametric oscillator," Opt. Express **21**, 7583-7589 (2013). (IF: 3.587)

[2] ***Y. J. Huang***, C. Y. Tang, Y. S. Tzeng, K. W. Su, and Y. F. Chen*, "Efficient high-energy passively Q-switched Nd:YLF/Cr^{4+}:YAG UV laser at 351 nm with pulsed pumping in a hemispherical cavity," Opt. Lett. **38**, 519-521 (2013). (IF: 3.399)

[3] C. Y. Cho, Y. P. Huang, ***Y. J. Huang***, Y. C. Chen, K. W. Su, and Y. F. Chen*, "Compact high-pulse-energy passively Q-switched Nd:YLF laser with an ultra-low-magnification unstable resonator: application for efficient optical parametric oscillator," Opt. Express **21**, 1489-1495 (2013). (IF: 3.587)

[4] ***Y. J. Huang***, C. Y. Tang, W. L. Lee, Y. P. Huang, S. C. Huang, and Y. F. Chen*, "Efficient passively Q-switched Nd:YLF TEM_{00}-mode laser at 1053 nm: selection of polarization with birefringence," Appl. Phys. B. **108**, 313-317 (2012). (IF: 2.189)

[5] ***Y. J. Huang***, Y. S. Tzeng, C. Y. Tang, Y. P. Huang, and Y. F. Chen*, "Tunable GHz pulse repetition rate operation in high-power TEM_{00}-mode Nd:YLF lasers at 1047 nm and 1053 nm with self mode locking," Opt. Express **20**, 18230-18237 (2012). (IF: 3.587)

[6] ***Y. J. Huang***, Y. P. Huang, P. Y. Chiang, H. C. Liang, K. W. Su, and Y. F. Chen*, "High-power passively Q-switched Nd:YVO_4 UV laser at 355 nm," Appl. Phys. B **106**, 893-898 (2012). (IF: 2.189)

[7] Y. P. Huang, C. Y. Cho, ***Y. J. Huang***, and Y. F. Chen*, "Orthogonally polarized dual-wavelength Nd:$LuVO_4$ laser at 1086 nm and 1089 nm," Opt. Express **20**, 5644-5651 (2012). (IF: 3.587)

[8] ***Y. J. Huang***, C. Y. Tang, Y. P. Huang, C. Y. Cho, K. W. Su, and Y. F. Chen*, "Efficient high-pulse-energy eye-safe laser generated by an intracavity Nd:YLF/KTP optical parametric oscillator: role of thermally induced polarization switching," Laser Phys. Lett. **9**, 709-715 (2012). (IF: 9.97)

[9] ***Y. J. Huang***, C. Y. Tang, Y. P. Huang, S. C. Huang, K. W. Su, and Y. F. Chen*, "Power scale-up of high-pulse-energy passively Q-switched Nd:YLF laser: influence of negative thermal lens enhanced by upconversion," Laser Phys. Lett. **9**, 625-630 (2012). (IF: 9.97)

[10] J. Y. Huang, W. Z. Zhuang, Y. P. Huang, ***Y. J. Huang***, K. W. Su, and Y. F. Chen*, "Improvement of stability and efficiency in diode-pumped passively Q-switched intracavity optical parametric oscillator with a monolithic cavity," Laser Phys. Lett. **9**, 485-490 (2012). (IF: 9.97)

[11] ***Y. J. Huang***, P. Y. Chiang, H. C. Liang, K. W. Su, and Y. F. Chen*, "Efficient high-power UV laser generated by an optimized flat-flat actively Q-switched laser with extra-cavity harmonic generations," Opt. Commun. **285**, 59-63 (2012). (IF: 1.486)

[12] ***Y. J. Huang***, P. Y. Chiang, H. C. Liang, K. W. Su, and Y. F. Chen*, "High-power Q-switched laser with high-order Laguerre-Gaussian modes: application for extra-cavity harmonic generations," Appl. Phys. B **105**, 385-390 (2011). (IF: 2.189)

[13] ***Y. J. Huang***, H. C. Liang, Y. F. Chen*, H. J. Zhang, J. Y. Wang, and M. H. Jiang, "High-power 10-GHz self-mode-locked Nd:$LuVO_4$ laser," Laser Phys. **21**, 1750-1754 (2011). (IF: 3.605)

[14] Y. T. Yu, ***Y. J. Huang***, P. Y. Chiang, Y. C. Lin, K. F. Huang, and Y. F. Chen*, "Non-paraxial contributions to the far-field pattern of surface-emitting lasers: a manifestation of the momentum-space wavefunctions of quantum billiards," J. Opt. **13**, 075705 (2011). (IF: 1.573)

[15] Y. F. Chen*, ***Y. J. Huang***, P. Y. Chiang, Y. C. Lin, and H. C. Liang, "Controlling number of lasing modes for designing short-cavity self-mode-locked Nd-doped vanadate lasers," Appl. Phys. B **103**, 841-846 (2011). (IF: 2.189)

[16] H. C. Liang, ***Y. J. Huang***, P. Y. Chiang, and Y. F. Chen*, "Highly efficient Nd:$Gd_{0.6}Y_{0.4}VO_4$ laser by direct in-band pumping at 914 nm and observation of self-mode-locked operation," Appl. Phys. B **103**, 637-641 (2011). (IF: 2.189)

[17] Y. P. Huang, P. Y. Chiang, ***Y. J. Huang***, K. W. Su, Y. F. Chen*, and K. F. Huang, "High-repetition-rate megawatt millijoule pulses from a Nd:YVO_4 laser passively Q-switched by a semiconductor saturable absorber," Appl. Phys. B **103**, 291-294 (2011). (IF: 2.189)

[18] H. C. Liang, P. Y. Chiang, ***Y. J. Huang***, Y. C. Lin, and Y. F. Chen*,

"Simultaneous self-mode-locking of $TEM_{0,0}$ and $TEM_{1,0}$ modes in a Nd:YVO_4 laser: application for measuring the thermal focal length," Laser Phys. **21**, 480-484 (2011). (IF: 3.605)

[19] Y. F. Chen*, Y. T. Yu, P. Y. Chiang, P. H. Tuan, ***Y. J. Huang***, H. C. Liang, and K. F. Huang, "Manifestation of quantum-billiard eigenvalue statistics from subthreshold emission of vertical-cavity surface-emitting lasers," Phys. Rev. E **83**, 016208 (2011). (IF: 2.255)

[20] Y. F. Chen*, Y. T. Yu, ***Y. J. Huang***, P. Y. Chiang, K. W. Su, and K. F. Huang, "Extracting photon periodic orbits from spontaneous emission spectra in laterally confined vertically emitted cavities," Opt. Lett. **35**, 2723-2725 (2010). (IF: 3.318)

[21] ***Y. J. Huang***, Y. P. Huang, H. C. Liang, K. W. Su, Y. F. Chen*, and K. F. Huang, "Comparative study between conventional and diffusion-bonded Nd-doped vanadate crystals in the passively mode-locked operation," Opt. Express **18**, 9518-9524 (2010). (IF: 3.753)

[22] T. H. Lu, Y. C. Lin, H. C. Liang, ***Y. J. Huang***, Y. F. Chen*, and K. F. Huang, "Observation of lasing modes with exotic localized wave patterns from astigmatic large-Fresnel-number cavities," Opt. Lett. **35**, 345-347 (2010). (IF: 3.318)

[23] H. C. Liang, ***Y. J. Huang***, W. C. Huang, K. W. Su, and Y. F. Chen*, "High-power, diode-end-pumped, multigigahertz self-mode-locked Nd:YVO_4 laser at 1342 nm," Opt. Lett. **35**, 4-6 (2010). (IF: 3.318)

[24] H. C. Liang, ***Y. J. Huang***, Y. C. Lin, T. H. Lu, Y. F. Chen*, and K. F. Huang, "Picosecond optical vortex converted from multigigahertz self-mode-locked high-order Hermite-Gaussian Nd:$GdVO_4$ lasers," Opt. Lett. **34**, 3842-3844 (2009). (IF: 3.059)

[25] R. C. C. Chen, Y. T. Yu, ***Y. J. Huang***, C. C. Chen, Y. F. Chen*, and K. F. Huang, "Exploring the origin of the directional emission from a microcavity with a large-aperture surface-emitting laser," Opt. Lett. **34**, 1810-1812 (2009). (IF: 3.059)

[26] Y. P. Huang, H. L. Chang, ***Y. J. Huang***, Y. T. Chang, K. W. Su, W. C. Yen, and Y. F. Chen*, "Subnanosecond mJ eye-safe laser with an intracavity optical parametric oscillator in a shared resonator," Opt. Express **17**, 1551-1556 (2009). (IF: 3.278)

[27] C. C. Chen, Y. T. Yu, R. C. C. Chen, ***Y. J. Huang***, K. W. Su, Y. F. Chen*, and K. F. Huang, "Transient dynamics of coherent waves released from quantum

billiards and analogous observation from free-space propagation of laser modes," Phys. Rev. Lett. **102**, 044101 (2009). (IF: 7.328)

[28] H. C. Liang, R. C. C. Chen, ***Y. J. Huang***, K. W. Su, and Y. F. Chen*, "Compact efficient multi-GHz Kerr-lens mode-locked diode-pumped Nd:YVO_4 laser," Opt. Express **16**, 21149-21154 (2008). (IF: 3.88)

Domestic journal paper:

[1] ***黃郁仁***, 唐政猷, 蘇冠暐, 陳永富,"高功率Q-開關紫外固態雷射的優化與製作," 科儀新知 **182**, 42-51 (2011). ***Y. J. Huang***, C. Y. Tang, K. W. Su, and Y. F. Chen, "Optimization and fabrication of high-power ultraviolet Q-switched solid-state laser," Instruments Today **182**, 42-51 (2011).

Conference paper:

[1] ***黃郁仁***, 唐政猷, 蘇冠暐, 陳永富, "Compact efficient high-energy high-repetition-rate pulsed pumped passively Q-switched Nd:YLF/Cr^{4+}:YAG UV laser at 351 nm with a nearly hemispherical cavity," 102 年度中華民國物理年會, 花蓮, 口頭論文發表. ***Y. J. Huang***, C. Y. Tang, K. W. Su, and Y. F. Chen, "Compact efficient high-energy high-repetition-rate pulsed pumped passively Q-switched Nd:YLF/Cr^{4+}/YAG UV laser at 351 nm with a nearly hemispherical cavity," Annual Meeting of the Physical Society of Republic of China, Hualien (2013) Oral presentation.

[2] 莊威哲, ***黃郁仁***, 蘇冠暐, 陳永富, "高功率固態光纖雷射關鍵技術開發研究," 101 年度國防科技學術合作計畫成果發表會, 論文集, 龍潭 (2012).

[3] K. W. Su, Y. F. Chen, H. C. Liang, ***Y. J. Huang***, Y. C. Lee, W. Z. Zhuang, G. W. Huang, Y. F. Chen, and Y. P. Huang, "Self-mode-locking of diode-pumped lasers," International Symposium on Physics and Applications of Laser Dynamics, Tainan (2012).

[4] 黃依萍, 卓俊佑, ***黃郁仁***, 蘇冠暐, 陳永富, "四十毫焦耳高能量脈衝雷射器之研究," 100 年度國防科技學術合作計畫成果發表會, 論文集, 龍潭 (2011).

[5] Y. P. Huang, ***Y. J. Huang***, Y. F. Chen, and K. F. Huang, "Multi-millijoule, high-repetition-rate Q-switched Nd:YVO_4 laser with an AlGaInAs quantum-well

saturable absorber," Photonics Global Conference (PGC), Singapore (2010).

[6] 梁興弛, ***黃郁仁***, 林毓捷, 陸亭樺, 陳永富, 黃凱風, "Picosecond optical vortex converted from multigigahertz self-mode-locked high-order Hermite-Gaussian Nd:$GdVO_4$ lasers," 99 年度中華民國物理年會, 台南, 壁報論文優勝. H. C. Liang, ***Y. J. Huang***, Y. C. Lin, T. H. Lu, Y. F. Chen, and K. F. Huang, "Picosecond optical vortex converted from multigigahertz self-mode-locked high-order Hermite-Gaussian Nd:$GdVO_4$ lasers," Annual Meeting of the Physical Society of Republic of China, Tainan (2010) Awarded poster.

[7] 陳建誠, 余彥廷, 陳建至, ***黃郁仁***, 蘇冠暐, 陳永富, 黃凱風, "Transient dynamics of coherent waves released from quantum billiards and analoguous observation from free-space propagation of laser modes," 98 年度中華民國物理年會, 彰化, 壁報論文優勝. C. C. Chen, Y. T. Yu, Ross C. C. Chen, ***Y. J. Huang***, K. W. Su, Y. F. Chen, and K. F. Huang, "Transient dynamics of coherent waves released from quantum billiards and analogous observation from free-space propagation of laser modes," Annual Meeting of the Physical Society of Republic of China, Changhua (2009) Awarded poster.

[8] 黃依萍, 張漢龍, ***黃郁仁***, 蘇冠暐, 陳永富, 閻偉中, "精巧與高能量的人眼安全腔內光參數震盪器雷射," 97 年度國防科技學術合作計畫成果發表會, 論文集, 龍潭 (2008).

Full Text of Journal Papers

Influence of output coupling on the performance of a passively Q-switched Nd:YAG laser with intracavity optical parametric oscillator

Y. P. Huang,[1,3] Y. J. Huang,[2] C. Y. Cho,[2] and Y. F. Chen[2,*]

[1]*Department of Physics, Soochow University, Shih Lin, Taipei, Taiwan*
[2]*Department of Electrophysics, National Chiao Tung University, Hsinchu, Taiwan*
[3]*yphuang@scu.edu.tw*
[*] *yfchen@cc.nctu.edu.tw*

Abstract: A singly-resonant intracavity optical parametric oscillator (OPO), pumped by a passively Q-switched Nd:YAG laser, is systematically investigated by means of a series of the output mirrors with various reflectivities for the fundamental wavelength at 1064 nm. Experimental results reveal that the output mirror with partial reflectivity instead of high reflection at 1064 nm not only is practicable to avoid the optical coatings damaged, but also enhances the dual-wavelength output efficiency for the OPO signal and fundamental laser waves. The overall optical-to-optical conversion efficiency is enhanced from 6.4% to 8.2% for the reflectivity decreasing from 99.8% to 90%.

OCIS codes: (140.3480) Lasers, diode-pumped; (140.3540) Lasers, Q-switched; (190.4410) Nonlinear optics, parametric processes; (140.3530) Lasers, neodymium.

References and links

1. B. W. Schilling, S. R. Chinn, A. D. Hays, L. Goldberg, and C. W. Trussell, "End-pumped 1.5 microm monoblock laser for broad temperature operation," Appl. Opt. **45**(25), 6607–6615 (2006).
2. Y. P. Huang, H. L. Chang, Y. J. Huang, Y. T. Chang, K. W. Su, W. C. Yen, and Y. F. Chen, "Subnanosecond mJ eye-safe laser with an intracavity optical parametric oscillator in a shared resonator," Opt. Express **17**(3), 1551–1556 (2009).
3. Y. Y. Wang, D. G. Xu, K. Zhong, P. Wang, and J. Q. Yao, "High-energy pulsed laser of twin wavelengths from KTP intracavity optical parametric oscillator," Appl. Phys. B **97**(2), 439–443 (2009).
4. Y. P. Huang, P. Y. Chiang, Y. F. Chen, and K. F. Huang, "Millijoule intracavity OPO driven by a passively Q-switched Nd:YVO_4 laser with AlGaInAs quantum-well saturable absorber," Appl. Phys. B **104**(3), 591–595 (2011).
5. R. Dabu, C. Fenic, and A. Stratan, "Intracavity pumped nanosecond optical parametric oscillator emitting in the eye-safe range," Appl. Opt. **40**(24), 4334–4340 (2001).
6. P. B. Phua, K. S. Lai, and R. F. Wu, "Multiwatt high-repetition-rate 2-μm output from an intracavity $KTiOPO_4$ optical parametric oscillator," Appl. Opt. **39**(9), 1435–1439 (2000).
7. H. Y. Zhu, G. Zhang, C. H. Huang, H. Y. Wang, Y. Wei, Y. F. Lin, L. X. Huang, G. Qiu, and Y. D. Huang, "Electro-optic Q-switched intracavity optical parametric oscillator at 1.53 μm based on $KTiOAsO_4$," Opt. Commun. **282**(4), 601–604 (2009).
8. Y. Y. Wang, D. G. Xu, K. Zhong, P. Wang, and J. Q. Yao, "High-energy pulsed laser of twin wavelengths from KTP intracavity optical parametric oscillator," Appl. Phys. B **97**(2), 439–443 (2009).
9. R. J. Beach, "Theory and optimization of lens ducts," Appl. Opt. **35**(12), 2005–2015 (1996).
10. R. Fu, G. Wang, Z. Wang, E. Ba, G. Mu, and X. H. Hu, "Design of efficient lens ducts," Appl. Opt. **37**(18), 4000–4003 (1998).
11. Y. F. Chen, J. L. Lee, H. D. Hsieh, and S. W. Tsai, "Analysis of passively Q-switched lasers with simultaneous modelocking," IEEE J. Quantum Electron. **38**(3), 312–317 (2002).
12. T. Debuisschert, J. Raffy, J. P. Pocholle, and M. Papuchon, "Intracavity optical parametric oscillator: study of the dynamics in pulsed regime," J. Opt. Soc. Am. B **13**(7), 1569–1587 (1996).
13. J. J. Degnan, D. B. Coyle, and R. B. Kay, "Effects of thermalization on Q-switched laser properties," IEEE J. Quantum Electron. **34**(5), 887–899 (1998).

1. Introduction

Nonlinear optical frequency conversions are quite attractive for wavelength extension of solid-state lasers. Optical parametric oscillators (OPOs), pumped with mature Nd-doped Q-

#185027 - $15.00 USD Received 6 Feb 2013; accepted 9 Mar 2013; published 19 Mar 2013

switched lasers, are commonly utilized for extending into the eye-safe region. Intracavity OPO takes the advantage of higher circulating intensity within the laser cavity, which allows lower pump threshold and higher conversion efficiency compared with the external configuration. With the advent of high-damage-threshold nonlinear crystals, many eye-safe intracavity OPO systems with high-power or high-energy outputs have been reported [1–4], and they are currently of great interest in military applications, particularly for the long-range laser finders. Traditionally, intracavity OPO exploits the output mirror with high-reflectivity coating for the fundamental pump wavelength. The high-power or high-energy intracavity OPOs, however, suffer from optical damage problems due to the extremely intense intracavity fluence for reaching the OPO threshold [5,6]. Recently, the output mirror with partial reflectivity for the fundamental wavelength was exploited in the actively Q-switched intracavity OPO for the reduction of a risk of optical damage [6–8]. Nevertheless, the influence of output coupling on the performance of a Q-switched laser with the intracavity OPO has not been thoroughly investigated so far.

In this work, we systematically explore the singly-resonant KTP-based intracavity OPO with a shared resonator, pumped by a passively Q-switched Nd:YAG/Cr^{4+}:YAG laser, by means of a series of output mirrors with different reflectivitives for the fundamental wavelength. The intracavity fluence is diminished one order of magnitude by the usage of an output mirror with a partial-reflectivity of 90%–98% instead of the highly reflective one of 99.8%. In addition, the partial-reflectivity output mirrors are experimentally practicable to avoid the optical damage. With the reflectivity of 99.8%, 98%, 94%, and 90%, the output pulse energies at 1572 nm are 10.8, 9.1, 7.7, and 6.6 mJ, respectively; the corresponding pulse energies at 1064 nm are 0.1, 1.9, 5.3, and 8.9 mJ, respectively. The overall optical-to-optical conversion efficiency is enhanced from 6.4% to 8.2% for the reflectivity decreasing from 99.8% to 90%. It is also found that lowering the reflectivity from 99.8% to 90% brings an increase in 1572-nm peak power from 580 to 820 kW, and the peak power at 1064 nm had a maximum value of 300 kW for the reflectivity of 90%.

2. Experimental setup

Figure 1 depicts the experimental scheme for an intracavity OPO driven by a diode-pumped passively Q-switched Nd:YAG / Cr^{4+}:YAG laser with a shared resonator. The structure of the shared resonator is that the OPO cavity completely overlaps with the fundamental laser cavity. The present fundamental laser cavity comprised a coated Nd:YAG crystal and an output coupler. The pump source was a quasi-cw high-power diode stack (Coherent G-stack package, Santa Clara, Calif., USA) which consisted of six 10-mm-long diode bars with a maximum output power of 120 W per bar at the central wavelength of 808 nm. The diode stack was constructed with 400 μm spacing between the diode bars and consequently the whole emission area was approximately 10 mm (slow axis) × 2.4 mm (fast axis). The full divergence angles in the fast and slow axes were approximately 35° and 10°, respectively. In the experiment, the diode stack was driven to emit optical pulse durations of 300 μs at a repetition rate less than 30 Hz with a maximum duty cycle of 1%. The pump radiation was delivered into the gain medium with a lens duct that was possessed of the advantages of simple fabrication, high coupling efficiency, and insensitivity to slight misalignment. The design parameters of a lens duct include r, L, H_1, H_2, and H_3, where r is the radius of the input surface, L is the length of the duct, H_1 is the width of the input surface, H_2 is the width of the output surface, and H_3 is the thickness of the duct [9,10]. In our experiment, the lens duct was manufactured with the parameters of r = 10 mm, L = 29 mm, H_1 = 12 mm, H_2 = 3.5 mm, and H_3 = 3.5 mm. The coupling efficiency of the lens duct was experimentally measured to be approximately 85%.

The gain medium was a 1.0 at. % Nd:YAG crystal with a diameter of 6 mm and a length of 20 mm. The entrance surface of the laser crystal was coated with high reflection at 1064 nm and 1572 nm (R>99.8%) and high transmission at 808 nm (T>90%); the other surface of the laser crystal was coated with antireflection at 1064 nm and 1572 nm (R<0.2%). The saturable absorber for the passively Q-switching was a Cr^{4+}:YAG crystal with a thickness of 2

#185027 - $15.00 USD Received 6 Feb 2013; accepted 9 Mar 2013; published 19 Mar 2013

mm and an initial transmission of 50% at 1064 nm. The nonlinear crystal for the OPO was a KTP crystal with a cross section of 4 mm × 4 mm and a length of 20 mm. The KTP crystal was *x*-cut (θ = 90°, and φ = 0°) for type II noncritical phase-matching to eliminate walk-off effect between the fundamental, signal, and idler beams. Both surfaces of the KTP and Cr^{4+}:YAG crystals were coated for anti-reflection at 1064 and 1572 nm. All crystals were wrapped with indium foil and mounted in conductively cooled copper blocks. Several output couplers with the reflectivity of 99.8%, 98%, 94%, and 90% at 1064 nm were used to investigate the influence of output coupling on the performance of a passively Q-switched Nd:YAG laser with an intracavity OPO. The reflectivities at 1572 nm for all output couplers were experimentally measured to be around 25%. Note that the optimal output reflectivity at the signal wavelength for the intracavity OPO has been previously verified to be approximately 10–30% [2]. The total cavity length was approximately 55 mm. The spectral information was monitored by an optical spectrum analyzer (Advantest Q8381A) that employs a diffraction grating monochromator to measure high-speed light pulses with the resolution of 0.1 nm. A LeCroy digital oscilloscope (Wavepro 7100; 10 G samples/sec; 1 GHz bandwidth) with two fast InGaAs photodiodes was used to record the pulse temporal behavior.

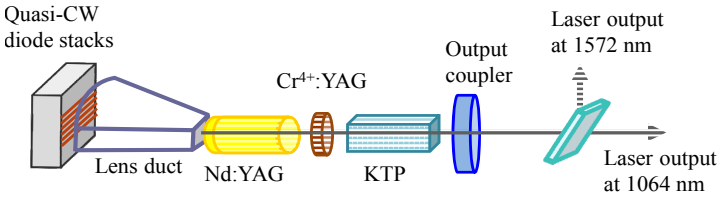

Fig. 1. Experimental setup for an intracavity OPO pumped by a diode-pumped passively Q-switched Nd:YAG / Cr^{4+}:YAG laser with a shared resonator.

3. Experimental results

Experimental results revealed that the pump threshold energies for the OPO were 170, 175, 182, and 188 mJ for the reflectivity of 99.8%, 98%, 94%, and 90% at 1064 nm, respectively. The pump threshold energy can be found to increase linearly with decreasing the output reflectivity. Note that the output coupler with a reflectivity below 90% was not employed in this experiment since the OPO threshold exceeded the available diode pump energy. The dependence of the pump threshold energy on the reflectivity can be calculated with [11]

$$E_{th} = \frac{1}{\eta_p}\frac{h\nu_p}{2\sigma}\left[\ln\left(1/T_o^2\right)+\ln\left(1/R\right)+L\right], \quad (1)$$

where η_p is the pump efficiency including the overlapping efficiency and the absorption efficiency, $h\nu_p$ is the pump photon energy, T_o is the initial transmission of the saturable absorber, L is the round-trip fundamental wave intensity loss in the cavity, and R is the output reflectivity at the fundamental laser wavelength. With the properties of the Nd:YAG and Cr^{4+}:YAG crystals and the typical cavity parameters: $\sigma = 2.8 \times 10^{-19}$ cm^2, $h\nu_p = 2.46 \times 10^{-19}$ J, $\eta_p = 0.54$, $A = 0.16$ cm^2, $T_o = 0.5$, and $L = 0.01$, the theoretical threshold energies were calculated to compare with the experimental results, as shown in Fig. 2. It can be seen that the experimental results agree very well with the theoretical values.

#185027 - $15.00 USD
Received 6 Feb 2013; accepted 9 Mar 2013; published 19 Mar 2013

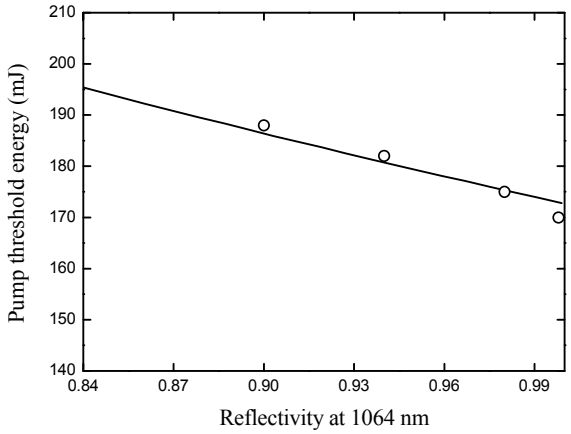

Fig. 2. The pump threshold energy with respect to the reflectivity at the fundamental laser wavelength of 1064 nm; solid lines: theoretical results; symbols: experimental values.

The experimental results for the output pulse energy with respect to the reflectivity at the fundamental wavelength of 1064 nm are shown in Fig. 3. Lowering the reflectivity at 1064 nm can be found to lead to a decrease in the signal output pulse energy at 1572 nm and a relative increase in the output pulse energy at 1064 nm. With the reflectivity of 99.8%, 98%, 94%, and 90%, the output pulse energies at 1572 nm were 10.8, 9.1, 7.7, and 6.6 mJ, respectively; the corresponding pulse energies at 1064 nm were 0.1, 1.9, 5.3, and 8.9 mJ, respectively. As a result, the total pulse energy of fundamental laser and OPO signal outputs increased from 10.9 mJ up to 15.5 mJ for the reflectivity decreasing from 99.8% to 90%. Divided by the pump threshold energy, the overall conversion efficiency was enhanced from 6.4% to 8.2% for the reflectivity decreasing from 99.8% to 90%. More importantly, the damage of the output coupler with the reflectivity of 99.8% was observed in this experiment, as illustrated in the insert of Fig. 3, but the output couplers with reflectivity of 90%–98% were not. In other words, the partial-reflectivity output coupler for the intracavity OPO not only is practicable to avoid the optical damage, but also enhances the overall output efficiency for the OPO signal and fundamental laser waves.

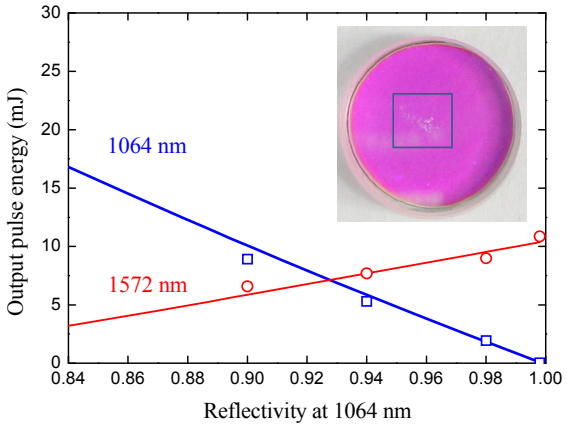

Fig. 3. Calculated and experimental results for the output pulse energy with respect to the reflectivity at the fundamental laser wavelength of 1064 nm; solid lines: theoretical results calculated from Eqs. (2)-(7); symbols: experimental results. Insert: a photograph for the damage of the output coupler with the reflectivity of 99.8%.

Based on the rate equation model for the passively Q-switched laser [12], the output pulse energies of the fundamental laser and OPO signal outputs for passively Q-switched

#185027 - $15.00 USD
Received 6 Feb 2013; accepted 9 Mar 2013; published 19 Mar 2013

intracavity OPOs with respect to the reflectivity at 1064 nm can be calculated. At first, the initial population of the passively Q-switched laser was employed in the rate equation model of Ref [12] to calculate the output pulse energies of the fundamental laser and OPO signal for passively Q-switched intracavity OPOs with a shared-resonator configuration. In a passively Q-switched laser, the initial population inversion density in the gain medium, $n(0) = n_i$, can be determined from the condition that the roundtrip gain is exactly equal to the roundtrip losses just before the Q-switch opens, i.e.

$$n_i = \frac{1}{2\sigma l}\left[\ln\left(1/T_o^2\right) + \ln\left(1/R\right) + L\right]. \tag{2}$$

Since only fundamental laser and signal waves were resonated in the shared resonator, the evolution equation of the idler wave was eliminated. The rate equations for the four-level Q switched laser with intracavity OPO are given by

$$\frac{dn}{dt} = -c\sigma\varphi_p n\ , \tag{3}$$

$$\frac{d\varphi_p}{dt} = \frac{l_{cr}}{l_{ca}} c\sigma n\left(\varphi_p + \Delta\varphi_p\right) - \frac{l_{nl}}{l_{ca}}\sigma_{opo}\varphi_s\varphi_p - \frac{\varphi_p}{t_r}\left[\ln\left(1/R\right) + L\right], \tag{4}$$

$$\frac{d\varphi_s}{dt} = \frac{l_{nl}}{l_{ca}} c\sigma_{opo}\varphi_p\left(\varphi_s + \Delta\varphi_s\right) - \frac{\varphi_s}{t_r}\left[\ln\left(1/R_s\right) + L_s\right], \tag{5}$$

where n is the inversion population density of the gain medium, σ is the stimulated emission cross section of the gain medium, c is the speed of light; φ_p is the fundamental laser photon density, φ_s is the OPO signal photon density, l_{ca} is the optical length of the laser cavity, l_{cr} is the length of the gain medium, l_{nl} is the length of the nonlinear crystal, σ_{opo} is the effective OPO conversion cross section, t_r is the round-trip time in the resonator cavity,$\otimes\Delta\varphi_p$ is the spontaneous emission intensity, $\Delta\varphi_s$ is the noise signal intensity, L_s is the round-trip signal wave intensity loss, and R_s is the output reflectivity at the OPO signal wavelength. The effective OPO cross section, σ_{opo}, is used to describe the conversion rate and derived from the parametric gain coefficient for small gains of the single resonator oscillator:

$$2\sigma_{opo} l_{nl} = \frac{8\omega_i\omega_s d_{eff}^2 l_{nl}^2}{n_i n_s n_p \varepsilon_o c^2}\frac{A_p}{A_s + A_p}, \tag{6}$$

where ω_i and ω_s are the idler and signal frequencies, respectively; n_1, n_2 and n_3 are the refractive indices at the idler, signal and fundamental laser wavelengths, respectively; d_{eff} is the effective nonlinear coefficient; ε_0 is the vacuum permittivity; A_s and A_p are the mode areas for the OPO signal and fundamental laser, respectively. The output pulse energy can be expressed as [13]

$$E_j = \frac{h\nu_j A_j}{2\sigma}\ln\left(1/R\right)\int\varphi_j(t)dt, \tag{7}$$

where $h\nu$ is the photon energy, A is the beam area and φ is the above-mentioned photon density. The subscripts $j = s, p$ represents the OPO signal and fundamental laser, respectively.

The solid lines in Fig. 3 depicts the calculated results for the output pulse energies for the dependence of reflectivity at 1064 nm with the properties of the Nd:YAG, KTP crystals and the typical cavity parameters: $h\nu_s = 1.26 \times 10^{-19}$ J, $h\nu_p = 1.86 \times 10^{-19}$ J, $\omega_i = 5.712 \times 10^{14}$ sec^{-1}, $\omega_s = 1.198 \times 10^{15}$ sec^{-1}, $l_{cr} = 2.0$ cm, $l_{nl} = 2.0$ cm, $d_{eff} = 3.64$ pm/V, $n_i = 1.771$, $n_s = 1.737$, $n_p = 1.748$, $\varepsilon_0 = 8.854$ pF/m, $A_s = 0.108$ cm^2, $A_p = 0.16$ cm^2, $l_{ca} = 5.5$ cm, $R_s = 0.25$, L

#185027 - $15.00 USD Received 6 Feb 2013; accepted 9 Mar 2013; published 19 Mar 2013

= L_s = 0.01, and $c = 3 \times 10^8$ m/s. The theoretical values agree very well with the experimental results. Moreover, it can be seen that the output energy of the OPO signal slightly decreases with decreasing the fundamental reflectivity, whereas the output energy of the fundamental laser considerably increases. Consequently, the dual-wavelength output efficiency for the OPO signal and fundamental laser waves was considerably greater than the output efficiency for only the OPO signal wave.

Typically temporal shapes for the OPO signal at 1572 nm were shown in Figs. 4(a)-4(d) for the reflectivity of 99.8%, 98%, 94%, and 90% at 1064 nm, respectively; the corresponding temporal shapes for the depleted fundamental laser at 1064 nm were simultaneously recorded. It can be seen that the OPO signal-pulse energy would be effectively concentrated in the first pulse for the reflectivity decreasing from 99.8% to 90%. As a result the peak power at 1572 nm increased from 580 to 820 kW as the reflectivity decreased from 99.8% to 90%, as shown in Fig. 5. The peak powers were precisely deduced by the numerical integration for the measured temporal pulse profiles to fit the experimental pulse energies. The peak power at 1064 nm had a maximum value of 300 kW for the reflectivity of 90%. We also employed the knife-edge method to evaluate the beam quality. The beam quality M^2 factor at 1572 nm was measured to be approximately 1.4.

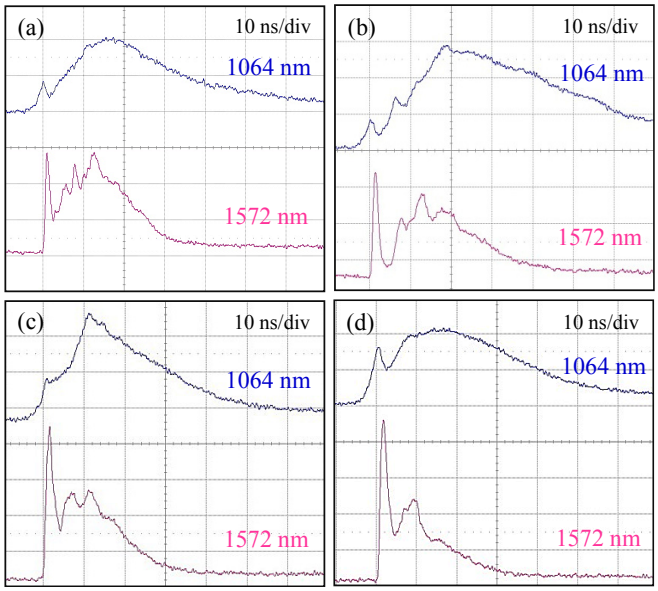

Fig. 4. Experimentally temporal shapes of the fundamental laser (1064 nm) and OPO signal (1572 nm) pulses for the reflectivity of (a) 0.998, (b) 0.98, (c) 0.94, and (d) 0.9.

#185027 - $15.00 USD
Received 6 Feb 2013; accepted 9 Mar 2013; published 19 Mar 2013

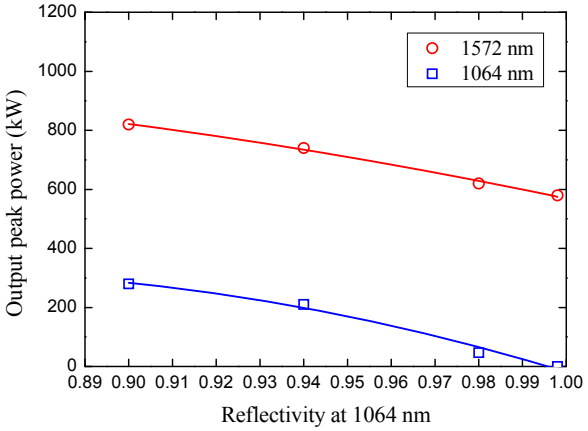

Fig. 5. The output peak power with respect to the reflectivity at the fundamental laser wavelength of 1064 nm.

4. Conclusion

We have systematically investigated the influence of output coupling on the performance of the singly-resonant intracavity OPO pumped by a passively Q-switched Nd:YAG/Cr^{4+}:YAG laser. Experimental results reveal that the output couplers with partial reflectivity for the fundamental laser wavelength at 1064 nm not only are practicable to avoid the optical coatings damaged, but also enhance the dual-wavelength output efficiency for the OPO signal wave at 1572 nm and fundamental laser wave at 1064 nm. The output pulse energies for OPO signal at 1572 nm were 10.8, 9.1, 7.7, and 6.6 mJ and the corresponding pulse energies for fundamental laser at 1064 nm were 0.1, 1.9, 5.3, and 8.9 mJ for the reflectivity of 99.8%, 98%, 94%, and 90% at 1064 nm, respectively. The overall optical-to-optical conversion efficiency was enhanced from 6.4% to 8.2% for the reflectivity decreasing from 99.8% to 90%.

Acknowledgments

The authors thank the National Science Council for the financial support of this research under Contract No. NSC100-2628-M-009-001-MY3.

#185027 - $15.00 USD Received 6 Feb 2013; accepted 9 Mar 2013; published 19 Mar 2013

Efficient high-energy passively Q-switched Nd:YLF/Cr^{4+}:YAG UV laser at 351 nm with pulsed pumping in a nearly hemispherical cavity

Y. J. Huang, C. Y. Tang, Y. S. Tzeng, K. W. Su, and Y. F. Chen*

Department of Electrophysics, National Chiao Tung University, Hsinchu 30010, Taiwan

**Corresponding author: yfchen@cc.nctu.edu.tw*

Received December 21, 2012; revised January 16, 2013; accepted January 16, 2013; posted January 16, 2013 (Doc. ID 182303); published February 12, 2013

We originally utilize a nearly hemispherical cavity to accomplish the energy scale-up for a high-repetition-rate nanosecond pulsed pumped Nd:YLF laser passively Q-switched by the Cr^{4+}:YAG saturable absorber. This compact laser is able to efficiently generate pulse energy as large as 1.38 mJ and pulse width as short as 5 ns under a pulse repetition rate of 100 Hz. Further employing the developed Nd:YLF laser to perform extracavity harmonic generations, the maximum pulse energies of 490 μJ at 527 nm and 360 μJ at 351 nm are achieved with the shortest pulse duration of 4 ns. © 2013 Optical Society of America

OCIS codes: 190.2620, 140.3480, 140.3540, 140.3530, 140.3580.

In recent years, diode-pumped all-solid-state ultraviolet (UV) lasers have been rapidly developed thanks to such advantages as high efficiency, long lifetime, high stability, and small overall system size [1–3]. The high-energy and high-repetition-rate solid-state UV laser with pulse duration on the order of several nanoseconds is one of the promising light sources for a great number of scientific studies as well as industrial fields, including military weapons, laser machining, and so on. The energy storage capability is directly proportional to the fluorescent lifetime of the laser crystal. As a result, the Nd:YLF crystal characterized by its relatively long upper-state lifetime is inherently suitable for generating large pulse energies among various Nd-doped laser crystals [4–6]. In addition, the excellent spectral match between the emission line at 1053 nm and the gain peak of the Nd:phosphate glass makes the Nd:YLF crystal essentially favorable for constructing a high-energy master oscillator power amplifier [7].

Passive Q-switching of a solid-state laser with a saturable absorber offers a convenient method to achieve a reliable pulsed operation with the merits of high stability, inherent compactness, simplicity, and low cost. However, the performance of the passively Q-switched (PQS) laser, which is frequently pumped by a continuous-wave (CW) laser diode, can be noticeably degraded by the timing jitter as a result of the complex dynamic behavior inside the saturable absorber [8,9]. Moreover, the fractional thermal loading would remarkably increase, which turns into a critical issue in designing the optical resonator under the continuously pumped PQS operation [10]. Pulsed pumping and quasi-CW pumping are effective approaches capable of simultaneously improving the instability of the pulse period [11,12] and reducing the heat generation inside the gain medium [13]. In this Letter, we report on a compact mJ- and ns-level end-pumped PQS Nd:YLF/Cr^{4+}:YAG laser, where the pulse repetition rate can be easily controlled by the pulsed laser diode in the range from 100 Hz to 1 kHz. We theoretically analyze and experimentally realize that a nearly hemispherical resonator can effectively enlarge the laser mode area for energy scaling of the Q-switched laser. We also experimentally confirm the reduction of the thermal-lensing effect with pulsed pumping as compared with CW pumping. The influences of the beam quality factors and the radius of curvature (ROC) of the input mirror on the performance of the PQS Nd:YLF laser are comparatively investigated. At a pulse repetition rate of 100 Hz, the pulse energy as large as 1.38 mJ and the pulse duration as short as 5 ns are efficiently produced with this compact pulsed laser. We further extend the emission lines into green and UV regimes via the extracavity harmonic generations. The pulse energies at 527 and 351 nm reach 490 and 360 μJ under a pulse repetition rate of 100 Hz, respectively.

Figure 1(a) schematically depicts the experimental arrangement of our pulsed pumped PQS Nd:YLF laser. The input concave mirror was antireflection (AR) coated at 806 nm on the entrance face, and it was coated for high transmission at 806 nm as well as for high reflection at 1053 nm on the second surface. The gain medium was a 0.8 at. % c-cut Nd:YLF crystal with dimensions of 4 mm in diameter and 15 mm in length. The Nd:YLF crystal was placed adjacent to the input mirror. Both facets of the laser crystal were AR coated at 806 and 1053 nm. The Cr^{4+}:YAG saturable absorber had an initial transmission of 80%, and it was AR coated at 1053 nm on both surfaces. The laser crystal and the saturable absorber were wrapped with indium foil and mounted in water-cooled

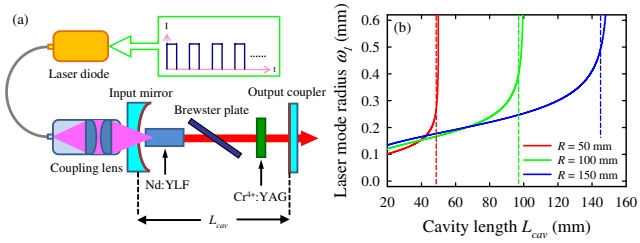

Fig. 1. (Color online) (a) Experimental arrangement of the pulsed pumped PQS Nd:YLF laser with the Cr^{4+}:YAG saturable absorber. (b) Dependences of the laser mode radius inside the gain medium on the cavity length for $R = 50$, 100, and 150 mm in a concave-plano cavity, where dashed lines indicate the constraint of $L_{cav} = 0.97R$.

copper heat sinks at 16°C. An intracavity Brewster plate was inserted inside the cavity to force linearly polarized operation. The pump source was a fiber-coupled laser diode at 806 nm with a core diameter of 400 μm and numerical aperture of 0.14. A lens set having a focal length of 25 mm and a coupling efficiency of 90% was used to reimage the pump beam inside the laser crystal with a magnification of unity. The output power of the laser diode was modulated by a train of pulses with a nearly rectangular shape. The pulse duration was set to be around 500 μs to match the upper-state lifetime of the Nd:YLF crystal. A flat mirror with a reflectivity of 60% at 1053 nm was used as the output coupler during the experiment. The pulse temporal behaviors were recorded by a digital oscilloscope with a sampling interval of 0.1 ns and bandwidth of 1 GHz together with a fast InGaAs photodiode. The pulse energy was measured with an energy meter (Thorlabs, PM100D).

It is well known that the Q-switched pulse energy is linearly proportional to the square of the laser mode radius inside the gain medium. With the ABCD-matrix theory, Fig. 1(b) illustrates the numerical calculation of the dependences of the laser mode radius ω_1 inside the gain medium on the cavity length L_{cav} for the cases of $R = 50$, 100, and 150 mm in a concave-plano cavity, where L_{cav} and R stand for the cavity length and the ROC of the input mirror. Note that the thermal-lensing effect is not considered in this calculation, and including thermal lens is equivalent to the case of reducing the ROC of the input mirror. It can be seen that the laser mode radius increases with the cavity length until the resonator reaches the boundary of the stable region, i.e., $L_{\mathrm{cav}} = R$. Practically, we choose the cavity length with the constraint $L_{\mathrm{cav}} = 0.97R$ in the following discussions to realize the large laser mode radius and be insensitive to the environmental perturbation in the meantime. From Fig. 1(b), we also observe that increasing the ROC of the input mirror can further expand the laser mode radius to scale up the pulse energy of the Q-switched laser.

During the experiment, the input mirrors with $R = 50$, 100, and 150 mm were utilized for comparative investigation of the PQS performance. The pulse energies as a function of the pulse repetition rate are displayed in Fig. 2. The pulse energies were obtained by averaging the values of the multiple measurements. The pulse energies are found to increase from 0.44 to 0.57 mJ for $R = 50$ mm, from 0.72 to 1.04 mJ for $R = 100$ mm, and from 1 to 1.38 mJ for $R = 150$ mm, when the pulse repetition rate is decreased from 1 kHz to 100 Hz. The threshold input energies are experimentally found to be 4.75–6 mJ for $R = 50$ mm, 7–10.4 mJ for $R = 100$ mm, and 8.67–14.1 mJ for $R = 150$ mm; the real value depends on the pulse repetition rate. The experimentally obtained pulse energies are used to evaluate the laser mode radii with the fitted formula given by Eq. (26) from [14] in terms of the present cavity parameters. This equation is based on the fact that the pulse energy is proportional to the modulation loss of the saturable absorber and inversely proportional to the total cavity losses when the saturable absorber bleaches. The obtained radii are subsequently utilized to estimate the thermal focal lengths for the cavity to be influenced by a thermal lens with the condition $L_{\mathrm{cav}} = 0.97R$. As a result, the relationship between the thermal focal length f_{th} and the average input power P_{in} can be built with the empirical formula $f_{\mathrm{th}} = C/P_{\mathrm{in}}$, where C is the proportional constant. The constant C for the present experiment is numerically determined to be −5.733 W/m. For comparison, the proportional constant of −3.087 W/m for the continuously pumped PQS case is estimated with a stability criterion by a separable experiment [10]. Note that the larger the magnitude of the constant $|C|$, the weaker the effect of the thermal-lensing effect. Therefore, the reduction of the thermal-lensing effect for the pulsed pumped PQS laser is manifestly verified in comparison with that for the continuously pumped counterpart. The shrinkage of the laser mode radius due to the relatively severe thermal-lensing effect explains why the pulse energy is smaller at a higher pulse repetition rate for a specific ROC of the input mirror.

Typical temporal behavior at a pulse repetition rate of 500 Hz for $R = 100$ mm is sketched in Fig. 3(a). The duration of the main pulse increases from 5 to 12 ns with the increase of the ROC of the input mirror from 50 to 150 mm. This trend is due to the fact that the Q-switched pulse duration is generally proportional to the cavity length. Moreover, it is experimentally found that the degree of the satellite pulse lessens with the increase of the ROC of the input mirror. To discover the occurrence of the satellite pulse, the beam quality factors are measured with the 90/10 knife-edge method, as depicted in Fig. 3(b). It can be deduced that the improvement of the beam quality factors is consistent with the suppressing of the satellite pulse. This implies the repression of the excitation of few high-order transverse mode is of critical importance in obtaining a perfect Q-switched pulse without satellite pulse. With the numerical integration of the

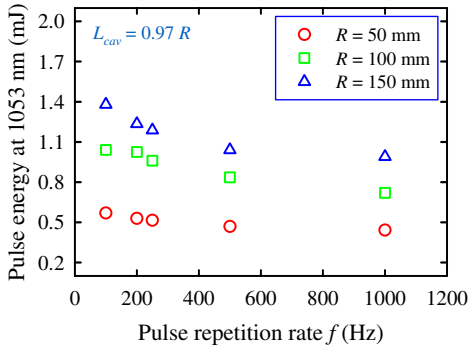

Fig. 2. (Color online) Pulse energies at 1053 nm as a function of the pulse repetition rate.

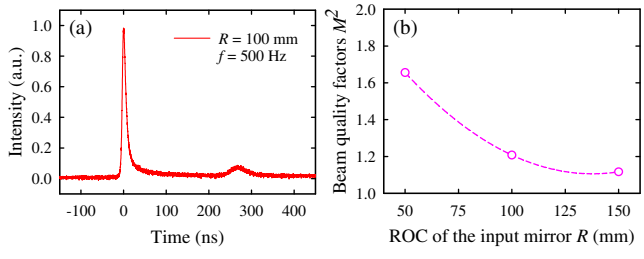

Fig. 3. (Color online) (a) Typical temporal behavior at a pulse repetition rate of 500 Hz for $R = 100$ mm. (b) Variation of the beam quality factors versus the ROC of the input mirror.

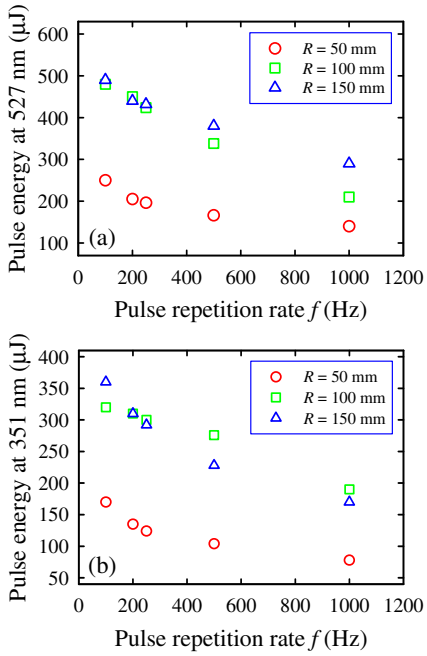

Fig. 4. (Color online) Pulse energies as a function of the pulse repetition rate at (a) 527 nm and (b) 351 nm.

temporal pulse profile and the experimentally obtained pulse energy, the peak powers with respect to the pulse repetition rate are estimated. By increasing the pulse repetition rate from 100 Hz to 1 kHz, the peak powers are found to vary from 51.7 to 37.3 kW for $R = 50$ mm, from 45.5 to 29.2 kW for $R = 100$ mm, and from 47.4 to 29.6 kW for $R = 150$ mm.

To obtain the output at 527 and 351 nm via the extracavity harmonic generations, LBO crystals were exploited as nonlinear frequency converters thanks to the benefits of high damage threshold, relatively large acceptance angle, and small walk-off angle. One LBO crystal with dimensions of $3\,\text{mm} \times 3\,\text{mm} \times 10$ was cut at $\theta = 90°$, $\phi = 11.1°$ for type-I phase-matched second harmonic generation (SHG) at a temperature of 47°C. Both facets of the SHG crystal were AR coated at 1053 and 527 nm. Another LBO crystal with dimensions of $3\,\text{mm} \times 3\,\text{mm} \times 10\,\text{mm}$ was cut at $\theta = 46.4°$, $\phi = 90°$ for type-II phase-matched third harmonic generation (THG) at a temperature of 48°C. Both surfaces of the THG crystal were AR coated at 1053, 527, and 351 nm. The thermoelectric controllers with a precision of 0.1°C were utilized to monitor the temperatures of the SHG and THG nonlinear crystals. The laser beams were focused into the SHG and THG nonlinear crystals with two individual convex lenses for achieving efficient harmonic generations. The former one with focal length of 38 mm was AR coated at 1053 nm on both sides, the latter one with focal length of 19 mm was AR coated at 1053 and 527 nm on both facets. Beam radii inside the two LBO crystals were calculated to be around 72 and 63 μm, respectively.

Figures 4(a) and 4(b) show the pulse energies at 527 and 351 nm as a function of the pulse repetition rate. The pulse energy for the extracavity harmonic generation is determined by the combined effects of the spatial and temporal properties of the fundamental laser; that is, the beam quality factors and the peak power. Based on the present experimental circumstance, the largest pulse energies at 527 and 351 nm are attained at 490 and 360 μJ under a pulse repetition rate of 100 Hz, respectively. On the other hand, the pulse durations at 527 and 351 nm are experimentally found to be in the range of 4–9 ns, depending on the ROC of the input mirror. In comparison with the studies in [5,15], we believe that the end-pumped scheme is a more feasible way to obtain a nearly diffraction-limited pulsed laser, and the efficient extracavity harmonic generations validate the applicability of our cavity design.

In summary, we have theoretically realized and experimentally designed a nearly hemispherical cavity to scale up the pulse energy of a nanosecond pulsed pumped PQS Nd:YLF/Cr^{4+}:YAG laser with the pulse repetition rate tunable from 100 Hz to 1 kHz. The largest pulse energy and shortest pulse duration are found to be 1.38 mJ and 5 ns, respectively. Moreover, the developed laser is successfully applied in the processes of the extracavity harmonic generations to produce green and UV radiations, where the largest pulse energies of 490 μJ at 527 nm and 360 μJ at 351 nm are efficiently generated with the shortest pulse width of 4 ns.

The authors thank the National Science Council for their financial support of this research under Contract No. NSC-100-2628-M-009-001-MY3.

References

1. D. R. Dudley, O. Mehl, G. Y. Wang, E. S. Allee, H. Y. Pang, and N. Hodgson, Proc. SPIE, **7193**, 71930Z (2009).
2. X. Ya, Q. Liu, M. Gong, X. Fu, and D. Wang, Appl. Phys. B **95**, 323 (2009).
3. Y. J. Huang, Y. P. Huang, P. Y. Chiang, H. C. Liang, K. W. Su, and Y. F. Chen, Appl. Phys. B **106**, 893 (2012).
4. W. A. Clarkson, P. J. Hardman, and D. C. Hanna, Opt. Lett. **23**, 1363 (1998).
5. D. Li, Z. Ma, R. Haas, A. Schell, P. Zhu, P. Shi, and K. Du, Opt. Lett. **33**, 1708 (2008).
6. C. Bollig, C. Jacobs, M. J. D. Esser, E. H. Bernhardi, and H. M. V. Bergmann, Opt. Express **18**, 13993 (2010).
7. A. V. Okishev and W. Seka, IEEE J. Sel. Top. Quantum Electron. **3**, 59 (1997).
8. D. Y. Tang, S. P. Ng, L. J. Qin, and X. L. Meng, Opt. Lett. **28**, 325 (2003).
9. M. Kovalsky and A. Hnilo, Opt. Lett. **35**, 3498 (2010).
10. Y. J. Huang, C. Y. Tang, Y. P. Huang, S. C. Huang, K. W. Su, and Y. F. Chen, Laser Phys. Lett. **9**, 625 (2012).
11. J. B. Khurgin, F. Jin, G. Solyar, C. C. Wang, and S. Trivedi, Appl. Opt. **41**, 1095 (2002).
12. K. Lee, Y. Kim, J. S. Gwag, J. H. Kwon, and J. Yi, J. Korean Phys. Soc. **57**, 1015 (2010).
13. F. Hanson, Opt. Lett. **20**, 148 (1995).
14. Y. F. Chen, Y. P. Lan, and H. L. Chang, IEEE J. Quantum Electron. **37**, 462 (2001).
15. N. U. Wetter, E. C. Sousa, I. M. Ranieri, and S. L. Baldochi, Opt. Lett. **34**, 292 (2009).

Compact high-pulse-energy passively Q-switched Nd:YLF laser with an ultra-low-magnification unstable resonator: application for efficient optical parametric oscillator

C. Y. Cho,[1] Y. P. Huang,[2] Y. J. Huang,[1] Y. C. Chen,[1] K. W. Su,[1] and Y. F. Chen[1,*]

[1]*Department of Electrophysics, National Chiao Tung University, Hsinchu, Taiwan*
[2]*Department of Physics, Soochow University, Shih Lin, Taipei, Taiwan*
[*]*yfchen@cc.nctu.edu.tw*

Abstract: We exploit an ultra-low-magnification unstable resonator to develop a high-pulse-energy side-pumped passively Q-switched Nd:YLF/Cr^{4+}:YAG laser with improving beam quality. A wedged laser crystal is employed in the cavity to control the emissions at 1047 nm and 1053 nm independently through the cavity alignment. The pulse energies at 1047 nm and 1053 nm are found to be 19 mJ and 23 mJ, respectively. The peak powers for both wavelengths are higher than 2 MW. Furthermore, the developed Nd:YLF lasers are employed to pump a monolithic optical parametric oscillator for confirming the applicability in nonlinear wavelength conversions.

OCIS codes: (140.3480) Lasers, diode-pumped; (140.3540) Lasers, Q-switched; (140.3530) Lasers, neodymium.

References and links

1. W. Krichbaumer, H. Herrmann, E. Nagel, R. Häring, J. Streicher, C. Werner, A. Mehnert, T. Halldorsson, S. Heinemann, P. Peuser, and N. P. Schmitt, "A diode-pumped Nd:YAG lidar for airborne cloud measurements," Opt. Laser Technol. **25**(5), 283–287 (1993).
2. D. J. Binks, P. S. Golding, and T. A. King, "Compact all-solid-state high repetition rate tunable ultraviolet source for airborne atmospheric gas sensing," J. Mod. Opt. **47**(11), 1899–1912 (2000).
3. D. Kracht, S. Hahn, R. Huss, J. Neumann, R. Wilhelm, M. Frede, and P. Peuser, "High efficiency, passively Q-switched Nd:YAG MOPA for spaceborne laser-altimetry," Proc. SPIE **6100**, 548–555 (2006).
4. P. Peuser, W. Platz, P. Zeller, T. Brand, M. Haag, and B. Köhler, "High-power, longitudinally fiber-pumped, passively Q-switched Nd:YAG oscillator-amplifier," Opt. Lett. **31**(13), 1991–1993 (2006).
5. C. Bollig, C. Jacobs, M. J. D. Esser, E. H. Bernhardi, and H. M. von Bergmann, "Power and energy scaling of a diode-end-pumped Nd:YLF laser through gain optimization," Opt. Express **18**(13), 13993–14003 (2010).
6. W. A. Clarkson, P. J. Hardman, and D. C. Hanna, "High-power diode-bar end-pumped Nd:YLF laser at 1.053 microm," Opt. Lett. **23**(17), 1363–1365 (1998).
7. Y. J. Huang, Y. S. Tzeng, C. Y. Tang, Y. P. Huang, and Y. F. Chen, "Tunable GHz pulse repetition rate operation in high-power TEM_{00}-mode Nd:YLF lasers at 1047 nm and 1053 nm with self mode locking," Opt. Express **20**(16), 18230–18237 (2012).
8. A. M. Deana, I. M. Ranieri, S. L. Baldochi, and N. U. Wetter, "Compact, diode-side-pumped and Q-switched Nd:$YLiF_4$ laser cavity operating at 1053 nm with diffraction limited beam quality," Appl. Phys. B **106**(4), 877–880 (2012).
9. Y. J. Huang, C. Y. Tang, W. L. Lee, Y. P. Huang, S. C. Huang, and Y. F. Chen, "Efficient passively Q-switched Nd:YLF TEM_{00}-mode laser at 1053 nm: selection of polarization with birefringence," Appl. Phys. B **108**(2), 313–317 (2012).
10. M. S. Ribeiro, D. F. Silva, E. P. Maldonado, W. de Rossi, and D. M. Zezell, "Effects of 1047-nm neodymium laser radiation on skin wound healing," J. Clin. Laser Med. Surg. **20**(1), 37–40 (2002).
11. A. V. Okishev and W. Seka, "Diode-pumped Nd:YLF master oscillator for the 30-kJ (UV), 60-beam OMEGA laser facility," IEEE J. Sel. Top. Quantum Electron. **3**(1), 59–63 (1997).
12. B. Frei and J. E. Balmer, "1053-nm-wavelength selection in a diode-laser-pumped Nd:YLF laser," Appl. Opt. **33**(30), 6942–6946 (1994).
13. H. Zbinden and J. E. Balmer, "Q-switched Nd:YLF laser end pumped by a diode-laser bar," Opt. Lett. **15**(18), 1014–1016 (1990).
14. T. Graf and J. E. Balmer, "High-power Nd:YLF laser end pumped by a diode-laser bar," Opt. Lett. **18**(16), 1317–1319 (1993).

#179633 - $15.00 USD Received 12 Nov 2012; revised 26 Dec 2012; accepted 7 Jan 2013; published 14 Jan 2013

15. C. F. Rae, J. A. C. Terry, B. D. Sinclair, M. H. Dunn, and W. Sibbett, "Single-frequency, end-pumped Nd:YLF laser excited by a 12-mJ diode-laser array," Opt. Lett. **17**(23), 1673–1675 (1992).
16. M. D. Selker, R. S. Afzal, and P. Reichert, "A pulse transmission mode Q-switched Nd:YLF laser pumped by cylindrical microlens-collimated diode bars," IEEE J. Quantum Electron. **30**(7), 1616–1622 (1994).
17. T. Debuisschért, D. Mathieu, J. Raffy, L. Becouarn, E. Lallier, and J.-P. Pocholle, "High beam quality unstable cavity infrared optical parametric oscillator," Proc. SPIE **3267**, 170–180 (1998).
18. R. Beach, J. Davin, S. Mitchell, W. Benett, B. Freitas, R. Solarz, and P. Avizonis, "Passively Q-switched transverse-diode-pumped Nd^{3+}:YLF laser oscillator," Opt. Lett. **17**(2), 124–126 (1992).
19. N. Hodgson and H. Weber, *Laser Resonators and Beam Propagation*, 2nd edn. (Springer, Berlin, 2005), Chap. 5–7.
20. J. E. Murray, "Pulsed Gain and Thermal Lensing of Nd:$LiYF_4$," IEEE J. Quantum Electron. **19**(4), 488–491 (1983).
21. Y. F. Chen, Y. P. Lan, and H. L. Chang, "Analytical Model for Design Criteria of Passively Q-Switched Lasers," IEEE J. Quantum Electron. **37**(3), 462–468 (2001).
22. S. Lee, Y. G. Kim, B. H. Cha, and Y. K. Kim, "A diode-pumped linear intracavity frequency doubled Nd:YAG rod laser with 40 ns pulse width and 73 W green output power," Opt. Laser Technol. **36**(4), 265–271 (2004).
23. Z. Sun, R. Li, Y. Bi, C. Hu, Y. Kong, G. Wang, H. Zhang, and Z. Xu, "Experimental study of high-power pulse side-pumped Nd:YAG laser," Opt. Laser Technol. **37**(2), 163–166 (2005).
24. S. K. Sharma, P. K. Mukhopadhyay, A. Singh, R. Kandasamy, and S. M. Oak, "A simple, compact, and efficient diode-side-pumped linear intracavity frequency doubled Nd:YAG rod laser with 50 ns pulse width and 124 W green output power," Rev. Sci. Instrum. **81**(7), 073104 (2010).

1. Introduction

High-pulse-energy all-solid-state lasers are widely used in scientific research and industrial applications, especially in military respect like airborne laser system, LIDAR and laser target designator, etc [1–4]. Compared to the mostly used Nd:YAG and Nd:YVO_4 crystals, the Nd:YLF crystal having the advantage of longer lifetime is more suitable for high-pulse-energy Q-switched lasers [5,6]. Furthermore, the uniaxial Nd:YLF crystal has two principal lasing transitions at 1047 nm (π) and at 1053 nm (σ), corresponding to the polarizations parallel and perpendicular to the crystal c-axis, respectively [7–9]. The 1047-nm and 1053-nm emissions are of great interest in the skin wound healing [10] and the Nd:glass amplification [11], respectively.

In addition to continuous-wave (CW) pumping, quasi-CW (QCW) diode stacks are often utilized to fulfill Q-switched Nd:YLF lasers with high pulse energies [12–16]. So far, the development of Nd:YLF lasers with energies of several millijoules and approximately 10-ns pulse durations is still highly desirable. Although the end-pumping scheme can permit excellent mode size matching to achieve good beam quality, the limited pump volume usually hinder the scale-up of the output pulse energy. In contrast, the side-pumping scheme can effectively enlarge the pump volume [17, 18]; however, this approach generally suffers from the degradation of beam quality. Therefore, it is practically valuable to develop a side-pumped Nd:YLF laser with improving beam quality.

The thermal lensing effect of the Nd:YLF crystal is identified to be relatively weak due to the compensation of negative temperature dependence of the refractive index and positive temperature dependence of the thermal expansion coefficient. In this work, we employ the property of the weak thermal lens with an ultra-low-magnification unstable resonator to develop a compact high-pulse-energy side-pumped passively Q-switched Nd:YLF/Cr^{4+}:YAG laser with improving beam quality. We also use the birefringent characteristics of an one-end-wedge a-cut Nd:YLF crystal to independently obtain the laser transitions at 1047 nm and 1053 nm through the cavity alignment. Using a Cr^{4+}:YAG crystal with initial transmission of 70% and at a repetition rate of 10 Hz, the pulse energies at 1053 nm and 1047 nm reach 23 mJ and 19 mJ, respectively. With the experimental pulse durations, the peak powers are calculated to be up to 2.3 MW and 2.7 MW at the emissions of 1053 nm and 1047 nm, respectively. The beam-quality factors M^2 are measured to be approximately 3.5 × 5.5 and 3.5 × 6.8 (vertical × horizontal) for the emissions at 1053 nm and 1047 nm, respectively. Furthermore, the developed Nd:YLF laser is employed to pump a monolithic optical parametric oscillator (OPO). The pulse energies generated in the external OPO are 10 mJ and 5.5 mJ for the wavelengths at 1552 nm and 1541 nm, respectively.

#179633 - $15.00 USD Received 12 Nov 2012; revised 26 Dec 2012; accepted 7 Jan 2013; published 14 Jan 2013

2. Cavity design and setup

For the cavity design, we first consider an optical resonator that consists of one laser crystal with thermally focal length f_{th} and two mirrors with radii of curvature ρ_1 and ρ_2 separated by an optical distance L. In term of the g^*-parameters, the beam radii ω_1 and ω_2 on the two mirrors can be expressed as [19]:

$$\omega_i = \sqrt{\frac{\lambda L^*}{\pi}} \sqrt{\frac{g_j^*}{g_i^*(1-g_1^* g_2^*)}}; i, j = 1,2; i \neq j, \tag{1}$$

where

$$g_i^* = g_i - \frac{d_j}{f_{th}}\left(1-\frac{d_i}{\rho_i}\right), \tag{2}$$

$$g_i = 1-\frac{d_1+d_2}{\rho_i}; i, j = 1,2; i \neq j, \tag{3}$$

$$L^* = d_1 + d_2 - \frac{d_1 d_2}{f_{th}}. \tag{4}$$

Here d_1 and d_2 are the optical path length between the cavity mirrors and the principal planes of the laser crystal. For the subsequent analysis, we specifically focus on the case of $d_1 = d_2 = L/2$. For the QCW pumping and the weak thermal lensing effect of the Nd:YLF crystal, the cavity length can be realistically designed to satisfy the condition of $L << f_{th}$. In order to obtain a large mode volume, we use an ultra-low-magnification positive-branch unstable cavity to design the resonator under the circumstance of $f_{th} \to \infty$. For the convenience of further discussion, we use the expression of $g_1 g_2 = 1 + \varepsilon$ with $0 < \varepsilon << 1$ to represent the cavity form.

With the conditions of $d_1 = d_2 = L/2$, $L << f_{th}$ and $g_1 g_2 = 1 + \varepsilon$, we can obtain that $g_1^* g_2^* \approx 1 - \Delta$, where

$$\Delta = \left(\frac{L}{f_{th}}\right)\left(\frac{g_1 + g_2 + 2g_1 g_2}{4}\right) - \varepsilon. \tag{5}$$

Equation (5) indicates that when the thermally focal length f_{th} of the gain medium makes the cavity to reach the condition of $\Delta \geq 0$ in the pumping stage, the laser resonator starts to be driven into the stable regime. As long as the factor Δ can satisfy the criterion of $0 < \Delta << 1$ in the lasing stage, the cavity mode sizes can be maintained fairly large, as indicated in Eq. (1).

We employ a convex-concave cavity to realize the criterion mentioned above. A convex mirror with the radius of curvature of 500 mm was used as the rear mirror of the cavity that was coated for high reflection (R>99.8%) in the range of 1040-1060 nm. A concave mirror with the radius curvature of 600 mm was used as the output coupler of the cavity that was coated for partial reflection in the range of 1040-1060 nm. We chose the effective cavity length L to be 90 mm. Consequently, the factor of $g_1 g_2$ can be calculated to be 1.003, i.e. $\varepsilon = 0.003$. In terms of the parameter ε, the magnification of the unstable resonator is given by $M \approx 1 + (2\varepsilon)^{0.5} + \varepsilon$. As a result, the magnification can be calculated to be approximately 1.08, corresponding to an ultra-low-magnification unstable resonator. It is worth to mention that for typical unstable resonators, larger magnification leads to a smaller misalignment sensitivity. Although the present cavity design is an unstable resonator with an ultra-low magnification, however, with appropriate thermal lensing effect in the laser crystal, it can step into the stable regime and possess a large mode volume. Therefore, the misalignment sensitivity is not rather critical. With Eq. (5), we can find that to step into the stable regime, the thermally focal

#179633 - $15.00 USD Received 12 Nov 2012; revised 26 Dec 2012; accepted 7 Jan 2013; published 14 Jan 2013

length f_{th} is approximately smaller than 30 m. This feature is quite appropriated for Nd:YLF crystal which has relatively weak thermal lensing effect [12, 20].

The experimental set-up for the Nd:YLF laser is schematically shown in Fig. 1. The laser crystal was a 1.0 at. % a-cut Nd:YLF crystal with dimension of 4 × 3 × 12 mm^3. The second end facet was cut with 3°-wedged to prevent the parasitic effect and to separate two wavelengths. Both end facets of the laser crystal were coated for anti-reflection (R<0.2%) at 1050 nm and its pump face was coated for anti-reflection (R<0.2%) at 808 nm. A Cr^{4+}:YAG crystal was applied for passively Q-switching as the saturable absorber. Both facets of the saturable absorber was coated for anti-reflection (R<0.2%) coating at 1050 nm. All crystals were wrapped with indium foil and mounted in conductively cooled copper blocks. The pump source was a high-power diode stacks (Coherent G-stack package, Santa Clara, Calif., USA), consisted of six 10-mm-long diode bars. Pitch between each diode bar was 0.4 mm, so the whole emission area was approximately 10 × 2.4 mm^2. The full divergence angles in the fast and slow axes were approximately 35° and 10°, respectively. The diode stack was placed close to the lateral surface of the laser crystal to receive good pump efficiency. In this work, pumping pulse width and pumping repetition rate of the diode stacks were all set to be 500 μs and 10 Hz. The pulse temporal behaviors were recorded by a LeCroy digital oscilloscope (Wavepro 7100, 10 G samples/s, 1 GHz bandwidth) with a fast InGaAs photodiode. The emission wavelengths were recorded by an ADVANTEST optical spectrum analyzer with resolution of 0.1 nm (Q89381A).

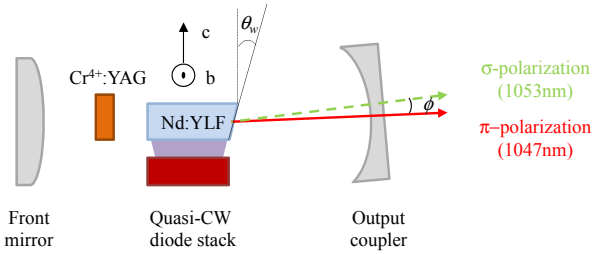

Fig. 1. Experimental set-up of Nd:YLF laser.

Before carrying on the experiment, we estimated the output performance of the passively Q-switched laser at two wavelengths to determine the parameters of the output coupler and the saturable absorber. We simply applied the analytical models in Ref. 21 for simulations. The reflectivity of the output coupler was chosen to be larger than 70% considering the higher pumping threshold at 1053 nm and the limitation of pumping source. In order to maintain the similar pulse energies at two wavelengths, the initial transmission of saturable absorber was chosen to be approximately 70%. Assuming the pumping mode radius was approximately 1.5 mm, the calculated output pulse energies at 1047 nm and 1053 nm were 17 mJ and 26 mJ.

3. Experimental results for laser performance

At first, we performed the QCW free-running without the Cr^{4+}:YAG crystal to confirm the reliability of the laser configuration and the quality of the laser crystal. We verified that tilting the orientation of the output coupler was able to switch the output wavelength of Nd:YLF laser. Figure 2 shows the curve of the laser output energies at 1047 nm and 1053 nm versus input energy of laser diode stacks under QCW free-running operation. The pump thresholds of 1047 nm and 1053 nm were 60 mJ and 96 mJ. With the pumping energy of 357 mJ, the output energies were 56 mJ and 48 mJ at 1047 nm and 1053 nm, respectively. The slope efficiency at 1047 nm and 1053 nm were both approximately 22%.

#179633 - $15.00 USD Received 12 Nov 2012; revised 26 Dec 2012; accepted 7 Jan 2013; published 14 Jan 2013

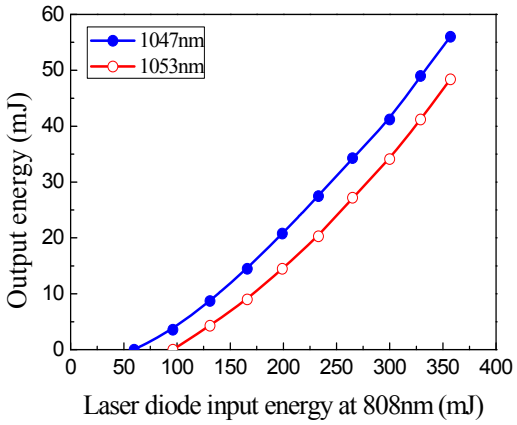

Fig. 2. Output energies under free-running operation with respected to the launched pump energies.

Then we inserted Cr^{4+}:YAG crystal to observe the performance of passively Q-switching at 1047 nm and 1053 nm, respectively. Since the threshold of Nd:YLF crystal at 1047 nm was lower than that at 1053 nm, we studied the performance at 1047 nm first. The pump threshold energy was measured to be 272 mJ with the output pulse energy about 19 mJ. The temporal shape of the passively Q-switched pulse at 1047 nm is depicted in Fig. 3 (a), which displays the frequency-beating modulation. The pulse width was approximately 9 ns. With the recorded data of pulse shape, the peak power was numerically calculated to be approximately 2.7 MW. We adjusted the output coupler to align the cavity for laser emission at 1053 nm. The output pulse energy was found to be 23 mJ in the passively Q-switched operation with the pump threshold energy of 357 mJ. Although the pump threshold energy at 1053 nm was higher than that at 1047 nm, which comes from the lower emission cross section, the output energy at 1053 nm was approximately 1.2 times higher than that at 1047 nm. The temporal shape of the passively Q-switched pulse at 1053 nm is depicted in Fig. 3(b). The pulse width was approximately 10 ns, and the peak power was numerically calculated to be approximately 2.3 MW.

Compared to the simulations, the experimental pulse energy at 1047 nm was larger, which was opposite at 1053 nm. We suspected that it was due to the different mode volumes in two wavelengths. According to previous works [12, 20], the thermal lensing effect in Nd:YLF crystal was relatively weak at 1047 nm than at 1053 nm, which contributed to a smaller thermally focusing length f_{th}. Furthermore, the higher threshold energy at 1053-nm transition increased the thermal lensing effect. Combining with Eq. (1), which implied that smaller f_{th} corresponds to a smaller mode radius, the cavity mode size at 1047-nm transition would be larger than that at 1053 nm. As a consequence, the experimental results should be modified considering the different mode areas.

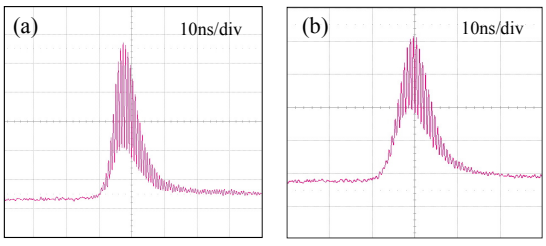

Fig. 3. Temporal shape for the laser pulses in the single pulse regime at (a) 1047 nm and (b) 1053 nm.

#179633 - $15.00 USD Received 12 Nov 2012; revised 26 Dec 2012; accepted 7 Jan 2013; published 14 Jan 2013

Figures 4(a) and 4(b) show the transverse mode distributions for the passively Q-switched lasers at 1047 nm and 1053 nm, respectively. It can be seen that the transverse pattern at 1053 nm is quite close to a Gaussian mode, whereas the mode structure at 1047 nm displays somewhat high-order modes. We employed the z-scan method to evaluate the beam quality. The beam quality factors M^2 at 1047 nm and 1053 nm were measured to be 3.5 × 6.8 and 3.5 × 5.5 (vertical × horizontal), respectively. As observed in the transverse patterns, the beam quality at 1053 nm is considerably better than that at 1047 nm in the horizontal direction. This result may arise from the fact that the temperature dependence of the refractive index for the 1053-nm emission is smaller than that for the 1047-nm emission. To compare the beam qualities, we simply replaced the convex rear mirror for a plane mirror, which allow the resonator to be in stable region. Through the experiment, we found that the beam quality factors $M_x \times M_y$ were measured to be larger than 30 × 10 at both wavelengths. Worse of all, the transverse patterns appeared to be both high-order modes. It is also worthwhile to mention that the beam quality factors obtained with the unstable cavity design are significantly improved as compared with the previous side-pumped solid-state lasers of the similar linear-cavity configuration [22–24]. In the following, we utilized the present Nd:YLF Q-switched lasers to pump an OPO cavity formed by a monolithic KTP crystal to confirm the application in nonlinear wavelength conversions.

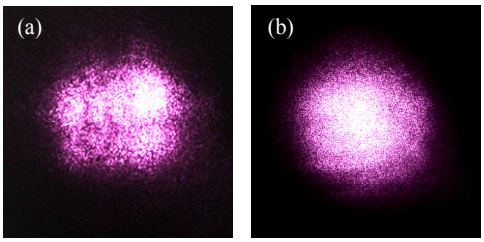

Fig. 4. Output transverse mode distributions at (a) 1047 nm and (b) 1053 nm.

The nonlinear crystal for the external OPO was an x-cut KTP with dimension of 4 × 4 × 20 mm^3. The first end facet was coated for high-transmission (T>95%) in the range of 1040-1060 nm and high-reflection (R>99.8%) in the range of 1540-1560 nm. The second end facet was coated for anti-reflection (R<0.2%) in the range of 1040-1060 nm and partial-reflection (R = 80%) within 1540-1560 nm. The KTP crystal was wrapped with indium foil and mounted in a conductively cooled copper block. An EOT isolator (1030 nm ~1080 nm) was used to prevent the depleted pump light getting back to the resonance. The effective transmission of the isolator was found to be approximately 92%.

After passing through the isolator, the pulse energies at 1053 nm and 1047 nm were 21.5 mJ and 17.5 mJ, operating at the same condition as the passively Q-switched laser. The output wavelength of external OPO pumped by the 1053 nm laser was found to be 1552 nm and the pulse energy was up to 10 mJ, corresponding to an optical-to-optical efficiency of 44%. With the temporal distribution, the peak power was numerically calculated to be 0.88 MW. On the other hand, the output wavelength of external OPO pumped by the 1047 nm laser was 1541 nm and the pulse energy was found to be 5.5 mJ, corresponding to an optical-to-optical efficiency of 28%. The peak power at 1541 nm was measured to be 0.63 MW. The higher conversion efficiency with 1053 nm laser is mainly due to the better beam quality. The oscilloscope traces are depicted in Fig. 5. It can be found that the mode-locking modulations in the temporal shapes of the fundamental light sources are effectively cleaned through the OPO process

#179633 - $15.00 USD Received 12 Nov 2012; revised 26 Dec 2012; accepted 7 Jan 2013; published 14 Jan 2013

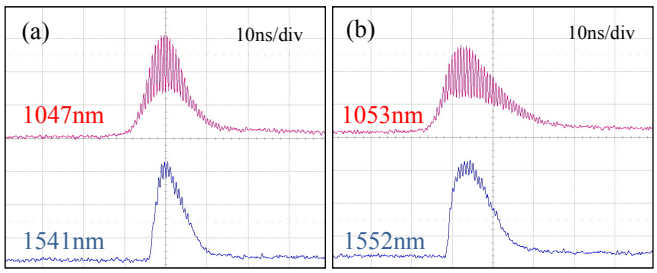

Fig. 5. Temporal shape for the pump pulses and signal pulses of external OPO at (a) 1047 nm and (b) 1053 nm.

4. Conclusion

An ultra-low-magnification unstable cavity has been used to develop a high-pulse-energy side-pumped Nd:YLF passively Q-switched laser with improving beam quality. With the birefringent property of a wedged gain medium, the laser cavity can be independently adjusted to obtain the emissions at 1047 nm and 1053 nm. With a Cr^{4+}:YAG crystal of initial transmission of 70%, the pulse energies at a repetition rate of 10 Hz are found to be 23 mJ and 19 mJ for the emissions at 1053 nm and 1047 nm, respectively. With the temporal pulse shapes, the peak powers for the emissions at 1053 nm and 1047 nm were evaluated to be up to 2.3 MW and 2.7 MW, respectively. With the z-scan method, the beam-quality factors M^2 are found to be 3.5 × 5.5 and 3.5 × 6.8 (vertical × horizontal) for the emissions at1053 nm and 1047 nm, respectively. Moreover, the developed Nd:YLF laser is used to pump a monolithic optical parametric oscillator (OPO) to generate the pulse energies of 10 mJ and 5.5 mJ for the wavelengths at 1552 nm and 1541 nm, respectively.

Acknowledgments

The authors thank the National Science Council for the financial support of this research under Contract No. NSC100-2628-M-009-001-MY3.

#179633 - $15.00 USD Received 12 Nov 2012; revised 26 Dec 2012; accepted 7 Jan 2013; published 14 Jan 2013

Appl Phys B (2012) 108:313–317
DOI 10.1007/s00340-012-4933-9

Applied Physics B
Lasers and Optics

Efficient passively Q-switched Nd:YLF TEM_{00}-mode laser at 1053 nm: selection of polarization with birefringence

Y.J. Huang · C.Y. Tang · W.L. Lee · Y.P. Huang · S.C. Huang · Y.F. Chen

Received: 11 November 2011 / Revised version: 19 December 2011 / Published online: 21 March 2012

Abstract The natural birefringence of the Nd:YLF crystal is utilized to achieve a reliable TEM_{00}-mode linearly polarized laser at 1053 nm in a compact concave-plano resonator. The efficient selection of the polarization relies on the combined effect of the difference in diffraction angle for σ- and π-polarization of a wedged laser crystal and the alignment sensitivity of an optical resonator. We further employ a Cr^{4+}:YAG saturable absorber to perform the passively Q-switched operation. At an incident pump power of 12 W, the maximum average output power is up to 2.3 W with a pulse repetition rate of 8 kHz and a pulse width of 9 ns. The pulse energy and peak power are found to be 288 μJ and 32 kW, respectively.

1 Introduction

Passive Q-switching has been widely exploited to accomplish compact diode-pumped all solid-state pulsed lasers [1–9]. A long upper-state lifetime of the gain medium is highly desirable for continuously pumped passively Q-switched (PQS) lasers to generate large amounts of pulse energies. As a consequence, the Nd:YLF crystal with a relatively long upper-state lifetime is usually expected to be appropriate for the construction of a high-pulse-energy laser with the Cr^{4+}:YAG crystal as a saturable absorber [10–12]. Another attractive feature of the Nd:YLF crystal is the emission line at 1053 nm, which makes it useful in developing the master oscillator for a Nd:glass power amplifier [13].

Y.J. Huang · C.Y. Tang · W.L. Lee · Y.P. Huang · S.C. Huang · Y.F. Chen (✉)
Department of Electrophysics, National Chiao Tung University, 1001 TA Hsueh Road, Hsinchu 30050, Taiwan
e-mail: yfchen@cc.nctu.edu.tw
Fax: +886-35-725230

Although it is generally convenient to employ the c-cut Nd:YLF crystal as a gain medium for generating a 1053-nm laser [14–16], the isotropic property in the transverse plane typically leads the polarization state not to be linearly polarized. The a-cut Nd:YLF crystal can alternatively be employed to obtain a linearly polarized output. However, the stimulated emission cross section at 1047 nm is higher than that at 1053 nm by a factor of 1.5 for the a-cut Nd:YLF crystal [17–22]. As a result, suppressing the π-polarized emission at 1047 nm turns into an important issue in designing a linearly-polarized 1053-nm laser with the a-cut Nd:YLF crystal. It has been shown that the effects of extra losses may be enhanced by the energy transfer upconversion (ETU) which causes a reduction in the effective upper laser level lifetime and an increase in fractional thermal loading [23, 24]. Therefore, it is practically important to develop an approach without introducing considerable extra losses for achieving an efficient linearly polarized Nd:YLF 1053-nm pulsed laser.

In a previous study [25], it was demonstrated that the selection of the polarization in an a-cut Nd:YVO_4 laser could be attained by combining the birefringence of the laser crystal with the alignment sensitivity of the plano-plano resonator. In this work, we exploit the birefringence of the a-cut Nd:YLF crystal to realize the selection of the polarization in a compact concave-plano resonator. Note that the plano-plano cavity is generally not appropriate for the Nd:YLF laser because the gain medium has a negative temperature coefficient for the refractive index, leading to a defocussing lens. We experimentally find that a reliable linearly polarized TEM_{00}-mode laser at 1053 nm can be achieved in a cavity as short as 5 cm by using an a-cut Nd:YLF crystal with a wedged angle of 3°. We further use a Cr^{4+}:YAG saturable absorber with an initial transmission of 80 % to investigate the performance of the PQS operation for vari-

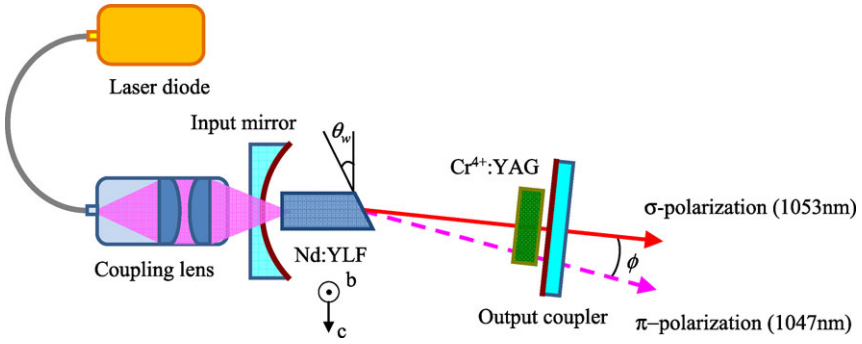

Fig. 1 Schematic of the cavity setup for a diode-pumped PQS Nd:YLF/Cr^{4+}:YAG laser

ous output couplings. With an output coupling of 30 %, the maximum output power of 2.3 W is generated at an incident pump power of 12 W, where the pulse repetition rate and pulse width are 8 kHz and 9 ns, respectively. The corresponding pulse energy and peak power are calculated to be up to 288 μJ and 32 kW, respectively. To the best of our knowledge, the pulse energy and peak power are the highest ever reported among the continuously diode-end-pumped PQS Nd-doped crystal lasers with the Cr^{4+}:YAG crystal of the same initial transmission.

2 Experimental setup

The experimental setup is schematically shown in Fig. 1. The input mirror was a concave mirror with the radius-of-curvature of 500 mm. It was antireflection (AR) coated at 806 nm on the entrance face, and was coated for high transmission at 806 nm as well as for high reflection at 1053 nm on the second surface. The gain medium was a 0.8 at% a-cut Nd:YLF crystal with dimensions of $3 \times 3 \times 20$ mm^3, and it was placed to be adjacent to the input mirror. Both facets of the laser crystal were AR coated at 806 nm and 1053 nm. The second surface of the laser crystal was wedged at an angle $\theta_w = 3°$ with respect to the first surface, as indicated in Fig. 1. The Cr^{4+}:YAG saturable absorber with the initial transmission of 80 % was AR coated at 1053 nm on both surfaces, and it was placed near to the output coupler. The laser crystal and the saturable absorber were wrapped with the indium foil and mounted in water-cooled copper heat sinks at 20 °C. The pump source was a 15-W fiber-coupled laser diode at 806 nm with a core diameter of 400 μm and a numerical aperture of 0.2. The pump beam was reimaged into the laser crystal with a lens set that has the focal length of 25 mm and the coupling efficiency of 90 %. The flat output couplers with the transmission of 10 %, 20 %, 30 %, 36 %, and 50 % were utilized for systematic investigations on the laser characteristics during the experiment. The cavity length was set to be 50 mm for the construction of a compact laser. With the ABCD-matrix theory, the cavity mode radii inside the laser crystal and the saturable absorber were estimated to be approximately 236 μm and 224 μm, respectively. The pulse temporal behaviors were recorded by a LeCroy digital oscilloscope (Wavepro 7100, 10 G samples/s, 1 GHz bandwidth) with a fast Si photodiode.

3 Performance of CW and PQS operations

First of all, we explore the angle tuning characteristics of the Nd:YLF laser for the σ- and π-polarization in the CW operation, where the Cr^{4+}:YAG saturable absorber was removed, the transmission of the output coupler was chosen to be 30 %, and the incident pump power was fixed to be 12 W to avoid the possibility of the thermal fracture in the laser crystal. As shown in Fig. 2(a), the output polarization state can be easily switched by simply tilting the orientation of the output coupler. Note that the tilting angle ϕ is defined as the included angle with respect to the orientation of the output coupler corresponding to the maximum output power at 1053 nm, as depicted in Fig. 1. The angular separation between the σ- and π-polarization under the individual maximum output power is experimentally found to be around 1.153 mrad; that is, the angular separation between the point b and c indicated in Fig. 2(a) is approximately 1.153 mrad. On the other hand, the refractive indices for the σ- and π-polarization in the a-cut Nd:YLF crystal are $n_\sigma = 1.448$ and $n_\pi = 1.47$, respectively. With the Snell's law under the small-angle approximation, we can theoretically derive an angular separation to be $(n_\pi - n_\sigma)\theta_w \sim 1.152$ mrad between the two polarizations external to the wedged crystal, which is in a good agreement with the experimental observations. The two-dimensional spatial distributions for the σ- and π-polarization under the individual maximum output power are recorded with a digital camera, and both are found to display a near-diffraction-limited TEM_{00} transverse mode, as shown in Fig. 2(b) for the case of σ-polarization.

With the optimal alignment for 1053-nm emission, we made a thorough study on the output power with respect to the output coupling at an incident pump power of 12 W. Note that the polarization extinction ratio at 1053 nm is considerably larger than 100:1 once the cavity was aligned for the

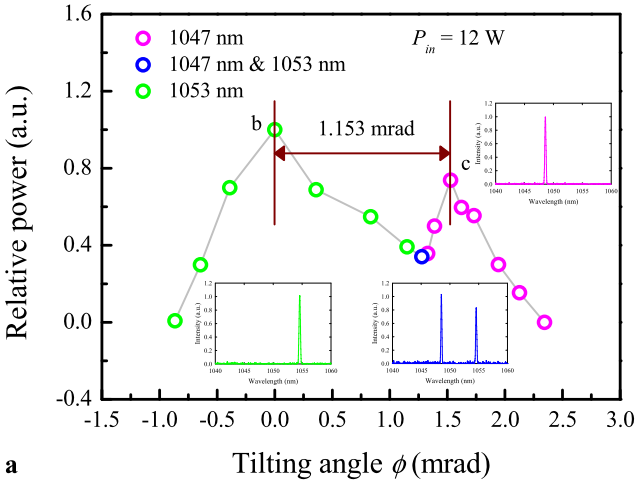

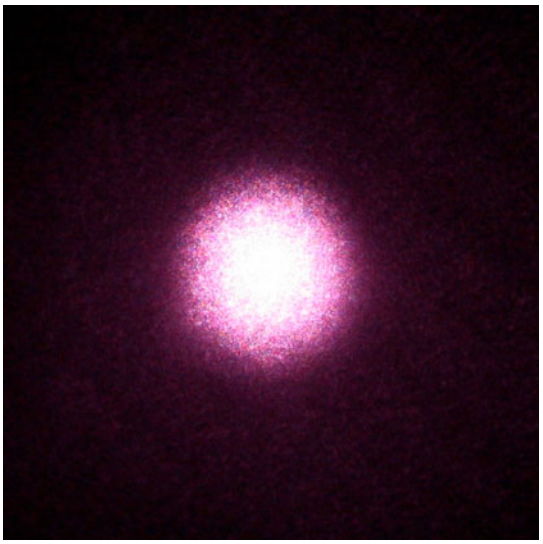

Fig. 2 (**a**) The angle tuning characteristics of the 3°-wedged a-cut Nd:YLF laser for the σ- and π-polarization in the CW operation; (**b**) The two-dimensional spatial distributions for the σ-polarization under the maximum output power, indicating a near-diffraction-limited TEM_{00} transverse mode

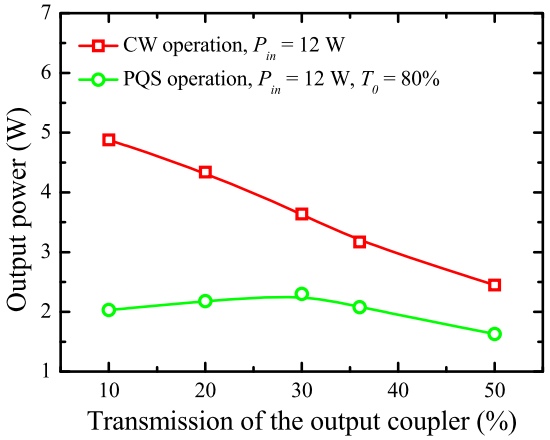

Fig. 3 The maximum output powers at 1053 nm in the CW and PQS operations as a function of the output coupling

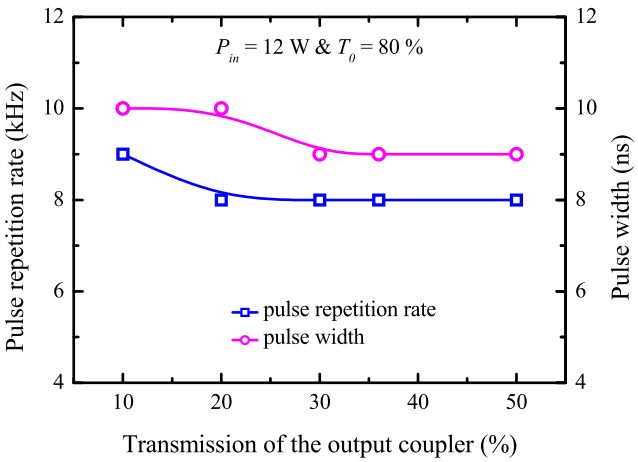

Fig. 4 Dependences of the pulse repetition rate and pulse width on the output coupling

optimization at 1053 nm. The output power in the CW operation is experimentally found to decrease from 4.88 W to 2.45 W with increasing the output coupling from 10 % to 50 %, as revealed by the red curve in Fig. 3.

When the Cr^{4+}:YAG saturable absorber was inserted into the laser cavity, the dependence of the output power in the PQS operation on the output coupling is demonstrated by the green curve in Fig. 3. Experimental results reveal that at an incident pump power of 12 W, the maximum output power of 2.3 W is achieved with the output coupling of 30 % in the PQS operation. The optical-to-optical conversion efficiency from 806 nm to 1053 nm is thus evaluated to be 18.3 %. Figure 4 illustrates the pulse repetition rate and the pulse width versus the output coupling in the PQS operation. It is experimentally found that both the pulse repetition rate and the pulse width are insensitive to the change of the output coupling; namely, when the transmission of the output coupler is varied between 10–50 %, the pulse repetition rate and the pulse width are in the ranges 8–9 kHz and 9–10 ns, respectively. According to the experimental results illustrated in Figs. 3 and 4, the pulse energy and peak power are calculated as a function of the transmission of the output coupler, as depicted in Fig. 5. For the output coupler with the transmission of 30 %, the pulse energy and the peak power as high as 288 μJ and 32 kW are achieved at an incident pump power of 12 W. It is worthwhile to mention that so far the pulse energies obtained with the continuously diode-end-pumped PQS Nd-doped crystal/Cr^{4+}:YAG lasers, such as the Nd:YAG [1, 3], c-cut Nd:YLF [7], Nd-doped vanadate crystals [1–6, 8, 9], are not more than ~210 μJ. That is to say, the pulse energy based on the $^4F_{3/2} \rightarrow {}^4I_{11/2}$ transition is greatly enhanced in our cavity design. Figures 6(a)–6(b) show the typical oscilloscope traces of the

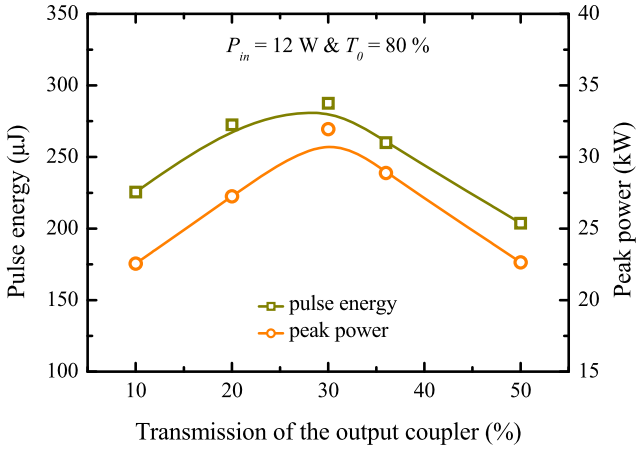

Fig. 5 Dependences of the pulse energy and peak power on the output coupling

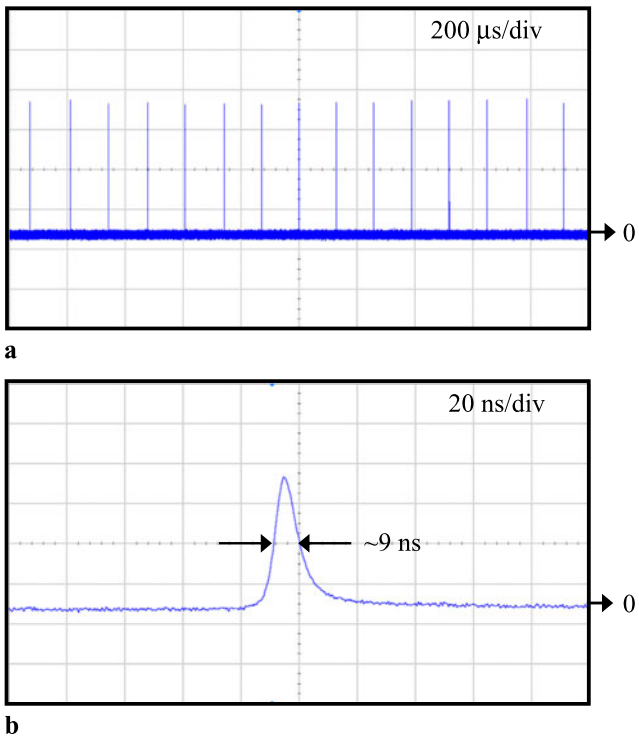

Fig. 6 Typical temporal behaviors at 1053 nm with: (**a**) time span of 2 ms, and (**b**) time span of 200 ns, which were recorded with the output coupling of 30 % under an incident pump power of 12 W

output pulses at 1053 nm with the time span of 2 ms and 200 ns, respectively. The temporal behaviors were recorded with the output coupling of 30 % under an incident pump power of 12 W. The pulse-to-pulse amplitude fluctuation is found to be better than ±2 %. With a knife-edge method, the beam quality factors at 1053 nm for the orthogonal directions were measured to be $M_x^2 < 1.1$ and $M_y^2 < 1.15$, respectively.

4 Conclusion

In summary, we have successfully demonstrated a reliable TEM_{00}-mode linearly polarized laser at 1053 nm with the natural birefringence of a wedged Nd:YLF crystal in a compact concave-plano cavity. Using the Cr^{4+}:YAG saturable absorber to perform PQS operation, the maximum output power can be up to 2.3 W under an incident pump power of 12 W. Under this output condition, the pulse repetition rate and the pulse width are found to be 8 kHz and 9 ns, respectively. The corresponding pulse energy and the peak power are up to 288 μJ and 32 kW, respectively. We believe that the relatively compact configuration presented here is potentially useful for the generation of high-peak-power pulses in Q-switched Nd:YLF lasers at 1053 nm.

Acknowledgements The authors thank the National Science Council for their financial support of this research under Contract No. NSC-100-2628-M-009-001-MY3.

References

1. A. Agnesi, S. Dell'Acqua, C. Morello, G. Piccinno, G.C. Reali, Z. Sun, IEEE J. Sel. Top. Quantum Electron. **3**, 45 (1997)
2. Y. Bai, N. Wu, J. Zhang, J. Li, S. Li, J. Xu, P. Deng, Appl. Opt. **36**, 2468 (1997)
3. A. Agnesi, S. Dell'Acqua, E. Piccinini, G. Reali, G. Piccinno, IEEE J. Quantum Electron. **34**, 1480 (1998)
4. C. Li, J. Song, D. Shen, N.S. Kim, J. Lu, K. Ueda, Appl. Phys. B **70**, 471 (2000)
5. J. Liu, Z. Wang, X. Meng, Z. Shao, B. Ozygus, A. Ding, H. Weber, Opt. Lett. **28**, 2330 (2003)
6. J. Liu, B. Ozygus, S. Yang, J. Erhard, U. Seelig, A. Ding, H. Weber, X. Meng, L. Zhu, L. Qin, C. Du, X. Xu, Z. Shao, J. Opt. Soc. Am. B **20**, 652 (2003)
7. S. Pan, K. Han, H. Wang, X. Fan, J. He, Chin. Opt. Lett. **4**, 407 (2006)
8. H. Yu, H. Zhang, Z. Wang, J. Wang, Y. Yu, Z. Shao, M. Jiang, Opt. Lett. **32**, 2152 (2007)
9. F.Q. Liu, H.R. Xia, S.D. Pan, W.L. Gao, D.G. Ran, S.Q. Sun, Z.C. Ling, H.J. Zhang, S.R. Zhao, J.Y. Wang, Opt. Laser Technol. **39**, 1449 (2007)
10. X. Peng, L. Xu, A. Asundi, IEEE J. Quantum Electron. **41**, 53 (2005)
11. D. Li, Z. Ma, R. Haas, A. Schell, P. Zhu, P. Shi, K. Du, Opt. Lett. **33**, 1708 (2008)
12. N.U. Wetter, E.C. Sousa, F.D.A. Camargo, I.M. Ranieri, S.L. Baldochi, J. Opt. A **10**, 104013 (2008)
13. A.V. Okishev, W. Seka, IEEE J. Sel. Top. Quantum Electron. **3**, 59 (1997)
14. J.M. Auerbach, R.L. Schmitt, Opt. Lett. **16**, 1171 (1991)
15. S.D. Pan, J.L. He, Y.E. Hou, Y.X. Fan, H.T. Wang, Y.G. Wang, X.Y. Ma, IEEE J. Quantum Electron. **42**, 1097 (2006)
16. Y. Sun, H. Zhang, Q. Liu, L. Huang, Y. Wang, M. Gong, Laser Phys. Lett. **7**, 722 (2010)
17. T.M. Pollak, W.F. Wing, R.J. Grasso, E.P. Chicklis, H.P. Jenssen, IEEE J. Quantum Electron. **18**, 159 (1982)
18. J.E. Murray, IEEE J. Quantum Electron. **19**, 488 (1983)
19. G. Cerullo, S.D. Silvestri, V. Magni, Opt. Commun. **93**, 77 (1992)

20. B. Frei, J.E. Balmer, Appl. Opt. **33**, 6942 (1994)
21. W.A. Clarkson, P.J. Hardman, D.C. Hanna, Opt. Lett. **23**, 1363 (1998)
22. C. Bollig, C. Jacobs, M.J.D. Esser, E.H. Bernhardi, H.M.V. Bergmann, Opt. Express **18**, 13993 (2010)
23. P.J. Hardman, W.A. Clarkson, G.J. Friel, M. Pollnau, D.C. Hanna, IEEE J. Quantum Electron. **35**, 647 (1999)
24. L.C. Courrol, E.P. Maldonado, L. Gomes, N.D. Vieira Jr, I.M. Ranieri, S.P. Morato, Opt. Mater. **14**, 81 (2000)
25. A. Agnesi, S. Dell'Acqua, Appl. Phys. B **76**, 351 (2003)

Tunable GHz pulse repetition rate operation in high-power TEM_{00}-mode Nd:YLF lasers at 1047 nm and 1053 nm with self mode locking

Y. J. Huang, Y. S. Tzeng, C. Y. Tang, Y. P. Huang, and Y. F. Chen*

Department of Electrophysics, National Chiao Tung University, Hsinchu, Taiwan
yfchen@cc.nctu.edu.tw

Abstract: We report on a high-power diode-pumped self-mode-locked Nd:YLF laser with the pulse repetition rate up to several GHz. A novel tactic is developed to efficiently select the output polarization state for achieving the stable TEM_{00}-mode self-mode-locked operations at 1053 nm and 1047 nm, respectively. At an incident pump power of 6.93 W and a pulse repetition rate of 2.717 GHz, output powers as high as 2.15 W and 1.35 W are generated for the σ- and π-polarization, respectively. We experimentally find that decreasing the separation between the gain medium and the input mirror not only brings in the pulse shortening thanks to the enhanced effect of the spatial hole burning, but also effectively introduces the effect of the spectral filtering to lead the Nd:YLF laser to be in a second harmonic mode-locked status. Consequently, pulse durations as short as 8 ps and 8.5 ps are obtained at 1053 nm and 1047 nm with a pulse repetition rate of 5.434 GHz.

OCIS codes: (140.3480) Lasers, diode-pumped; (140.3530) Lasers, neodymium; (140.3580) Lasers, solid-state; (140.4050) Mode-locked lasers.

References and links

1. U. Keller, "Recent developments in compact ultrafast lasers," Nature **424**(6950), 831–838 (2003).
2. K. J. Weingarten, D. C. Shannon, R. W. Wallace, and U. Keller, "Two-gigahertz repetition-rate, diode-pumped, mode-locked Nd:YLF laser," Opt. Lett. **15**(17), 962–964 (1990).
3. G. P. A. Malcolm, P. F. Curley, and A. I. Ferguson, "Additive-pulse mode locking of a diode-pumped Nd:YLF laser," Opt. Lett. **15**(22), 1303–1305 (1990).
4. T. Juhasz, S. T. Lai, and M. A. Pessot, "Efficient short-pulse generation from a diode-pumped Nd:YLF laser with a piezoelectrically induced diffraction modulator," Opt. Lett. **15**(24), 1458–1460 (1990).
5. K. J. Weingarten, U. Keller, T. H. Chiu, and J. F. Ferguson, "Passively mode-locked diode-pumped solid-state-lasers that use an antiresonant Fabry - Perot saturable absorber," Opt. Lett. **18**(8), 640–642 (1993).
6. M. B. Danailov, G. Cerullo, V. Magni, D. Segala, and S. De Silvestri, "Nonlinear mirror mode locking of a cw Nd:YLF laser," Opt. Lett. **19**(11), 792–794 (1994).
7. S. D. Pan, J. L. He, Y. E. Hou, Y. X. Fan, H. T. Wang, Y. G. Wang, and X. Y. Ma, "Diode-end-pumped passively CW mode-locked Nd:YLF laser by the LT-$In_{0.25}Ga_{0.75}As$ absorber," IEEE J. Quantum Electron. **42**(10), 1097–1100 (2006).
8. S. D. Pan and Y. G. Wang, "Diode end-pumped passively mode-locked Nd:YLF laser at 1047 nm using single-wall carbon nanotubes based saturable absorber," Laser Phys. **21**(8), 1353–1357 (2011).
9. U. Keller, K. J. Weingarten, F. X. Kärtner, D. Kopf, B. Braun, I. D. Jung, R. Fluck, C. Hönninger, N. Matuschek, and J. A. D. Au, "Semiconductor saturable absorber mirrors (SESAM's) for femtosecond to nanosecond pulse generation in solid-state lasers," IEEE J. Sel. Top. Quantum Electron. **2**(3), 435–453 (1996).
10. S. Tsuda, W. H. Knox, S. T. Cundiff, W. Y. Jan, and J. E. Cunningham, "Mode-locking ultrafast solid-state lasers with saturable Bragg reflectors," IEEE J. Sel. Top. Quantum Electron. **2**(3), 454–464 (1996).
11. C. Hönninger, R. Paschotta, F. Morier-Genoud, M. Moser, and U. Keller, "Q-switching stability limits of continuous-wave passive mode locking," J. Opt. Soc. Am. B **16**(1), 46–56 (1999).
12. H. C. Liang, R. C. C. Chen, Y. J. Huang, K. W. Su, and Y. F. Chen, "Compact efficient multi-GHz Kerr-lens mode-locked diode-pumped Nd:YVO_4 laser," Opt. Express **16**(25), 21149–21154 (2008).
13. H. C. Liang, Y. J. Huang, W. C. Huang, K. W. Su, and Y. F. Chen, "High-power, diode-end-pumped, multigigahertz self-mode-locked Nd:YVO_4 laser at 1342 nm," Opt. Lett. **35**(1), 4–6 (2010).

#171067 - $15.00 USD Received 22 Jun 2012; revised 19 Jul 2012; accepted 19 Jul 2012; published 24 Jul 2012

14. H. C. Liang, Y. J. Huang, P. Y. Chiang, and Y. F. Chen, "Highly efficient Nd:$Gd_{0.6}Y_{0.4}VO_4$ laser by direct in-band pumping at 914 nm and observation of self-mode-locked operation," Appl. Phys. B **103**(3), 637–641 (2011).
15. A. V. Okishev and W. Seka, "Diode-pumped Nd:YLF master oscillator for the 30-kJ (UV), 60-beam OMEGA laser facility," IEEE J. Sel. Top. Quantum Electron. **3**(1), 59–63 (1997).
16. M. S. Ribeiro, D. F. Silva, E. P. Maldonado, W. de Rossi, and D. M. Zezell, "Effects of 1047-nm neodymium laser radiation on skin wound healing," J. Clin. Laser Med. Surg. **20**(1), 37–40 (2002).
17. Y. J. Huang, C. Y. Tang, W. L. Lee, Y. P. Huang, S. C. Huang, and Y. F. Chen, "Efficient passively Q-switched Nd:YLF TEM_{00}-mode laser at 1053 nm: selection of polarization with birefringence," Appl. Phys. B, doi:10.1007/s00340-012-4933-9.
18. G. Q. Xie, D. Y. Tang, L. M. Zhao, L. J. Qian, and K. Ueda, "High-power self-mode-locked Yb:Y_2O_3 ceramic laser," Opt. Lett. **32**(18), 2741–2743 (2007).
19. B. Braun, K. J. Weingarten, F. X. Kärtner, and U. Keller, "Continuous-wave mode-locked solid-state lasers with enhanced spatial hole burning: Part I," Appl. Phys. B **61**(5), 429–437 (1995).
F. X. Kärtner, B. Braun, and U. Keller, "Continuous-wave mode-locked solid-state lasers with enhanced spatial hole burning: Part II," Appl. Phys. B **61**(6), 569–579 (1995).
20. Y. J. Huang, Y. P. Huang, H. C. Liang, K. W. Su, Y. F. Chen, and K. F. Huang, "Comparative study between conventional and diffusion-bonded Nd-doped vanadate crystals in the passively mode-locked operation," Opt. Express **18**(9), 9518–9524 (2010).
21. Y. F. Chen, Y. J. Huang, P. Y. Chiang, Y. C. Lin, and H. C. Liang, "Controlling number of lasing modes for designing short-cavity self-mode-locked Nd-doped vanadate lasers," Appl. Phys. B **103**(4), 841–846 (2011).

1. Introduction

High-power mode-locked solid-state lasers with multi-GHz pulse repetition rate are attractive in a great number of applications including high-speed optical sampling, optical clocking, ultrafast spectroscopy, high-capacity telecommunication, and so on [1]. The Nd:YLF crystal is specifically characterized by the negative dependence of the refractive index on the temperature, which can partly compensate for the positive contribution from the end-face bulging of the gain medium to exhibit a relatively weak thermal-lensing effect. As a consequence, the Nd:YLF crystal is recognized as one of the most competitive candidates for constructing high-power lasers with excellent output beam quality. In addition, the natural birefringence enables the Nd:YLF crystal to easily emit a linearly polarized beam and completely eliminate the possibility of the thermal depolarization under the high-power operation. More importantly, the Nd:YLF crystal has a gain bandwidth wider than 1 nm at the transition line of $^4F_{3/2} \rightarrow {}^4I_{11/2}$, which is more favorable for generating short-duration mode-locked pulses as compared with other Nd-doped laser crystal. Over the past years, continuous-wave (CW) mode-locked operation in the Nd:YLF crystal has been successfully realized with various methods [2–8]. However, high-power mode-locked Nd:YLF lasers with the pulse repetition rate up to several GHz have been scarcely demonstrated so far.

Passive mode locking with the semiconductor saturable absorber mirror (SESAM) is by far the most powerful technique to obtain the ultrashort pulses with the pulse repetition rate in the several hundred MHz range [9, 10]. To further increase the pulse repetition rate into the GHz region for the passively mode-locked laser, the main challenge is to overcome the tendency of the Q-switched mode locking, where the pulse train is modulated by the Q-switched envelop [11]. As a result, the SESAM usually needs to be intricately designed to have very small modulation depth (typically, below 1%) and low saturation fluence for achieving a multi-GHz passively mode-locked laser without the Q-switching instability, which undoubtedly increases the difficulties and costs in fabricating the SESAM. The extremely small modulation depth and low saturation fluence make it possible to utilize the nonlinear effect of the laser crystal itself as an alternative means for fulfilling a high-repetition-rate mode-locked laser. In fact, it was recently found that the third-order nonlinearity of the gain medium could be used to achieve a fairly stable multi-GHz operation in Nd-doped vanadate crystals with the mechanism of the self mode locking [12–14]. Such self-mode-locked mechanism relies on the fact that the number of the oscillated longitudinal modes in a multi-GHz mode-locked laser with the Nd-doped laser crystals to be characterized by the narrow gain bandwidth is not large, which is generally less than about 20 modes.

#171067 - $15.00 USD Received 22 Jun 2012; revised 19 Jul 2012; accepted 19 Jul 2012; published 24 Jul 2012

Consequently, the third-order nonlinearity of the gain medium could offer enough locking strength to lock several tens of the oscillated longitudinal modes in a short cavity for accomplishing a high-repetition-rate mode-locked laser without any additional modulation elements except the gain medium inside the laser cavity, which is experimentally verified with our previous works [12–14]. It is worthwhile to point out that the previously reported high-repetition-rate self-mode-locked lasers were mainly focused on the performance at 1064 nm and 1342 nm. One of the attractive features of the Nd:YLF crystal is the emission lines at 1053 nm and 1047 nm. The 1053-nm line is inherently useful in developing a master oscillator for the Nd:glass power amplifier [15], while the 1047-nm line is found to play an important role in the skin wound healing [16]. Therefore, high-power high-repetition-rate mode-locked Nd:YLF lasers at 1053 nm and 1047 nm are highly desirable to be developed.

In this work, we report our experimental observations on a diode-pumped self-mode-locked Nd:YLF laser with multi-GHz pulse repetition rate for the first time. A novel approach that bases on the natural birefringence of a wedged Nd:YLF crystal and the alignment sensitivity of an optical resonator is utilized for efficient selection of the output polarization state. With the developed method, stable self-mode-locked operations with TEM_{00} transverse mode are accomplished for the σ- and π-polarization, respectively. At an incident pump power of 6.93 W, this compact pulsed laser produces output powers up to 2.15 W and 1.15 W at 1053 nm and 1047 nm under a pulse repetition rate of 2.717 GHz. We find that decreasing the separation between the gain medium and the input mirror brings in the pulse shortening thanks to the enhanced effect of the spatial hole burning (SHB), where the shortest pulse widths of 8 ps and 8.5 ps are obtained for the σ- and π-polarization, respectively. Furthermore, the occurrence of the second harmonic mode locking rather than the fundamental mode locking is experimentally observed when the gain medium is closely adjacent to the input mirror.

2. Experimental setup

The experimental setup for the diode-pumped self-mode-locked Nd:YLF laser is schematically sketched in Fig. 1. The input mirror was a concave mirror with the radius of curvature of 500 mm. It was antireflection (AR) coated at 806 nm on the entrance face, and was coated for high transmission at 806 nm as well as for high reflection at 1053 nm on the second surface. The gain medium was a 0.8 at. % a-cut Nd:YLF crystal with dimensions of 3 × 3 × 20 mm^3. Both facets of the laser crystal were AR coated at 806 nm and 1053 nm. Besides, the second surface of the gain medium was wedged at an angle $\theta_w = 3^\circ$ with respect to the first surface for efficient selection of the output polarization state as well as absolute elimination of the etalon effect. The laser crystal was wrapped with indium foil and mounted in a water-cooled copper heat sink with the temperature of 16°C. The pump source was an 806-nm fiber-coupled laser diode with the core diameter of 400 μm and the numerical aperture of 0.14. The pump beam with the spot radius of approximately 200 μm was re-imaged inside the laser crystal with a lens set that has the focal length of 25 mm and the coupling efficiency of 90%. A flat wedged mirror with the reflectivity of 90% in the range of 1040-1060 nm was used as the output coupler during the experiment, which is experimentally found to allow for the maximum output power under the CW mode-locked circumstance and provide sufficient intracavity energy for stable self mode locking simultaneously. The optical cavity length was set to be about 55 mm, which corresponds to the free spectral range of 2.717 GHz. By using the ABCD-matrix theory, the cavity mode radius inside the laser crystal was calculated to be 230 μm. It should be mentioned that the stable self-mode-locked operation could be realized with the optical cavity length ranging from 45 mm to 100 mm, corresponding to the free spectral range of 1.5-3 GHz.

The real-time temporal behaviors of the mode-locked pulses were received by a high-speed InGaAs photodetector with the rise time of 35 ps, and the recorded signal was connected to a digital oscilloscope (Agilent, DSO 80000) with the electrical bandwidth of 12

#171067 - $15.00 USD Received 22 Jun 2012; revised 19 Jul 2012; accepted 19 Jul 2012; published 24 Jul 2012

GHz and the maximum sampling interval of 25 ps. The output signal of the photodetector was also delivered to a radio frequency (RF) spectrum analyzer (Advantest, R3256A) with the bandwidth of 8 GHz. The fine structure of the mode-locked pulses was measured with the help of a commercial autocorrelator (APE pulse check, Angewandte Physik and Elektronik GmbH). A Fourier optical spectrum analyzer (Advantest, Q8347), which is constructed with a Michelson interferometer, was employed to monitor the spectral information with the resolution of 0.003 nm.

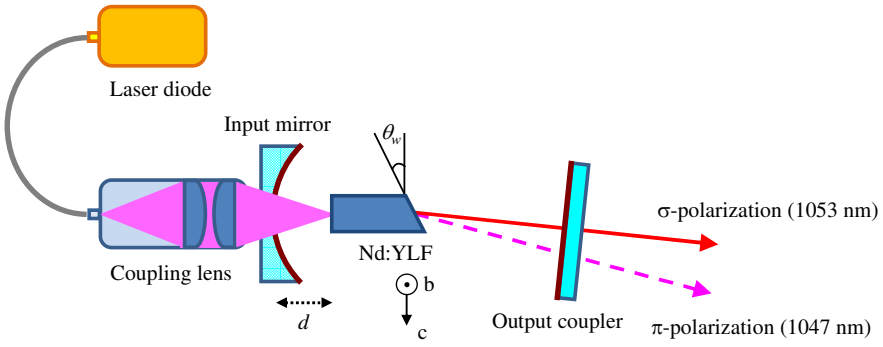

Fig. 1. Configuration of the cavity setup for the diode-pumped self-mode-locked Nd:YLF laser.

3. Performance of the self-mode-locked Nd:YLF laser

On the basis of the combined effect of the different deflection angle for the σ- and π-polarization due to the natural birefringence of a wedged laser crystal and the alignment sensitivity of an optical resonator, we experimentally verify that the output polarization state of the Nd:YLF laser could be switched simply by tilting the orientation of the output coupler [17]. Note that the σ- and π-polarization in the Nd:YLF crystal correspond to the emission lines at 1053 nm and 1047 nm, respectively. Then the Nd:YLF laser was finely adjusted to be in a steady CW mode-locked state by monitoring the real-time oscilloscope traces. The separation d between the laser crystal and the input mirror was initially set to be around 8 mm. At a pulse repetition rate of 2.717 GHz, the output powers for the CW mode locking at 1053 nm and 1047 nm as a function of the incident pump power at 806 nm are illustrated in Fig. 2. Note that the stable CW self-mode-locked operation could always be achieved as long as the incident pump power reaches the threshold. Meanwhile, the laser beam radius of 230 μm is larger than the pump beam radius of 200 μm in the present setup, which leads to a relatively large diffraction loss induced by the thermal lens aberration. Based on the assumption of a Gaussian-like pump profile and following the analysis in Ref [18], here we find that the combined effect of the mode size change in the laser crystal due to the Kerr self-focusing and the thermally induced diffraction loss could result in the nonlinear diffraction loss modulation on the order of 10^{-4}. This nonlinear loss modulation of the so-called thermo-Kerr mode locking is experimentally confirmed to be sufficient for the self-starting of the present self-mode-locked laser, where the required nonlinear loss modulation is numerically estimated to be around 10^{-5} [18]. Refer to the Fig. 2, the threshold pump powers at 1053 nm and 1047 nm are found to be almost the same. The maximum output power as high as 2.15 W is achieved for the σ-polarization, while the maximum output power for the π-polarization is 1.15 W. The two-dimensional spatial distributions at 1053 nm and 1047 nm under an incident pump power of 6.93 W were recorded with a digital camera, and both are found to display a near-diffraction-limited TEM_{00} transverse mode, as revealed in the inset of Fig. 2 for the case of the σ-polarization.

#171067 - $15.00 USD Received 22 Jun 2012; revised 19 Jul 2012; accepted 19 Jul 2012; published 24 Jul 2012

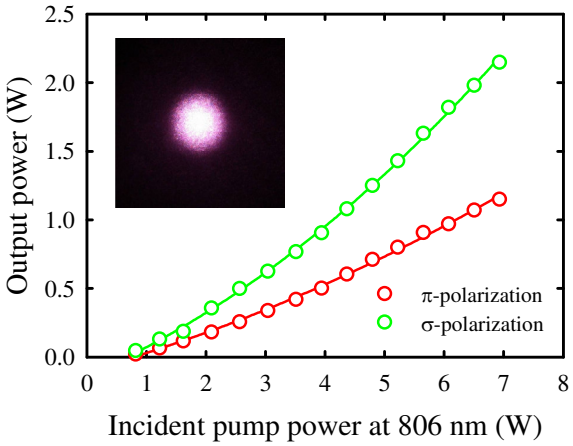

Fig. 2. Output powers for the CW mode locking at 1053 nm and 1047 nm as a function of the incident pump power at 806 nm, where the pulse repetition rate is 2.717 GHz. Inset: two-dimensional spatial distribution of the TEM_{00} transverse mode for the case of the σ-polarization.

Typical oscilloscope traces of the mode-locked pulses at 1053 nm are illustrated in Figs. 3(a)-3(b) with the time span of 1 μs and 5 ns, respectively. The amplitude fluctuation is experimentally found to be better than 2%. Moreover, the full modulation of the pulse trains without any CW background indicates that the complete mode locking is achieved in the current configuration. It is also worthwhile to mention that the Q-switched mode locking is not experimentally observed in the self-mode-locked Nd:YLF laser. For Q-switched mode locking, the period between the Q-switched envelops ranges from several hundreds of microsecond to several millisecond. However, the pulse train in millisecond time scale is not presented here because the temporal behavior could not be properly resolved with such wide time span owing to the reduction of the sampling rate. Therefore, we measure the RF spectrum to confirm the stability of the present self-mode-locked Nd:YLF laser, which is displayed in Figs. 3(c)-3(d). It can be seen clearly that the peak of the fundamental harmonic is 35 dBc above the background level, and the relaxation oscillation sidebands are negligibly observable. The stability of the laser is examined by the relative frequency deviation of the fundamental harmonic $\Delta v/v$, where v is the central frequency and Δv is the full width at half maximum (FWHM) of the fundamental harmonic, respectively. The relative frequency deviation of the fundamental harmonic is experimentally found to be around 10^{-5} over the day-long operation, which implies a nice long term stability.

On the other hand, Fig. 3(e) reveals the autocorrelation trace at 1053 nm. Assuming the temporal intensity to follow the Gaussian-shaped profile, the pulse width could be evaluated as 28.5 ps. Figure 3(f) depicts the corresponding optical spectrum with the central wavelength of 1053.34 nm and the FWHM of approximately 0.05 nm. As a result, the time-bandwidth product is estimated to be 0.424, which indicates the present pulses to be frequency chirped. Note that the mode spacing of 0.01 nm between the adjacent longitudinal modes is consistent with the fundamental harmonic of 2.717 GHz, as indicated in Fig. 3(f).

#171067 - $15.00 USD Received 22 Jun 2012; revised 19 Jul 2012; accepted 19 Jul 2012; published 24 Jul 2012

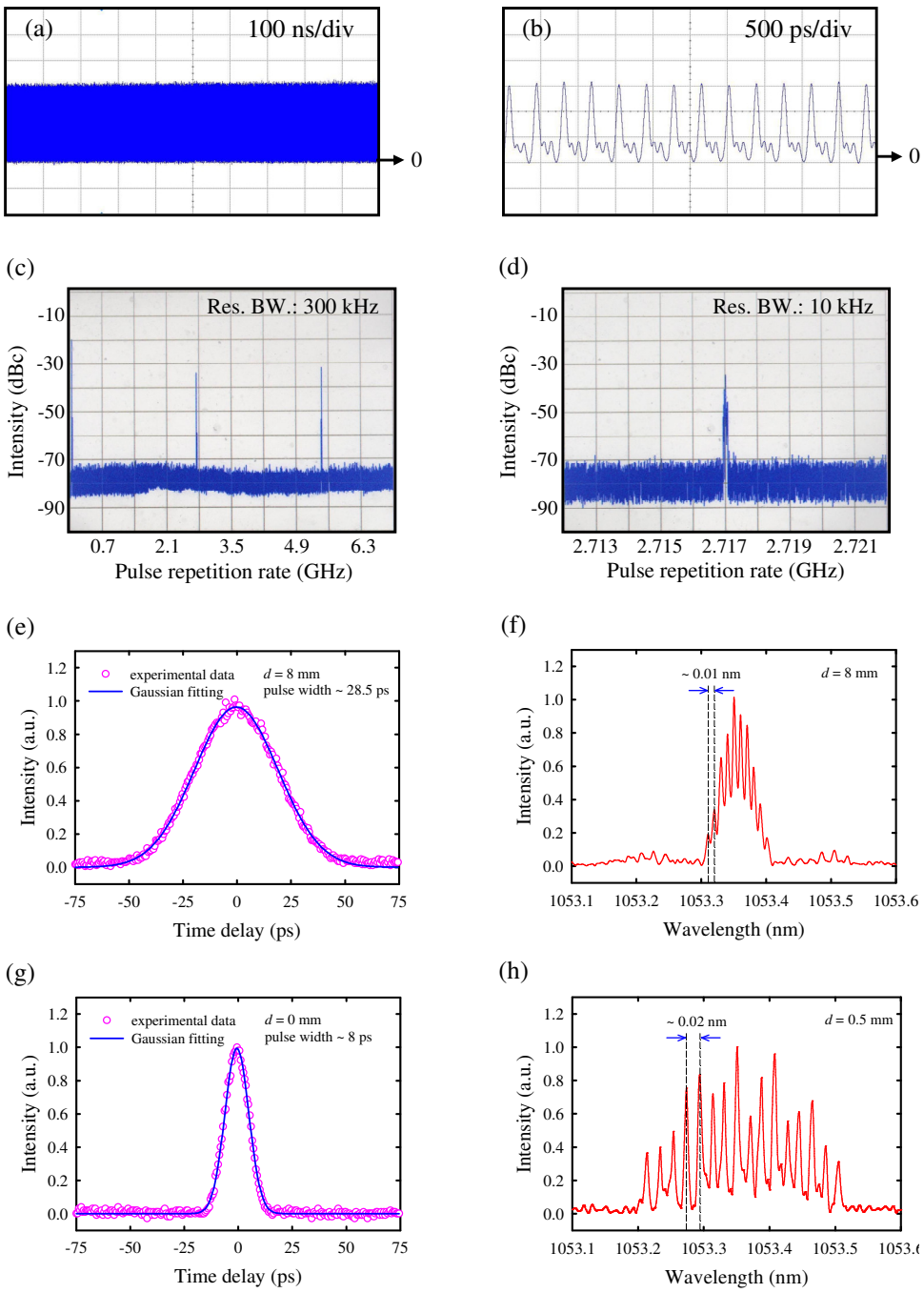

Fig. 3. Performance of the self-mode-locked Nd:YLF laser at 1053 nm: oscilloscope traces with the time span of (a) 1 μs and (b) 5 ns; RF spectrum with the frequency span of (c) 7 GHz and (d) 10 MHz; (e) autocorrelation trace for $d = 8$ mm; (f) optical spectrum for $d = 8$ mm; (g) autocorrelation trace for $d = 0.5$ mm; (h) optical spectrum for $d = 0.5$ mm.

#171067 - $15.00 USD Received 22 Jun 2012; revised 19 Jul 2012; accepted 19 Jul 2012; published 24 Jul 2012

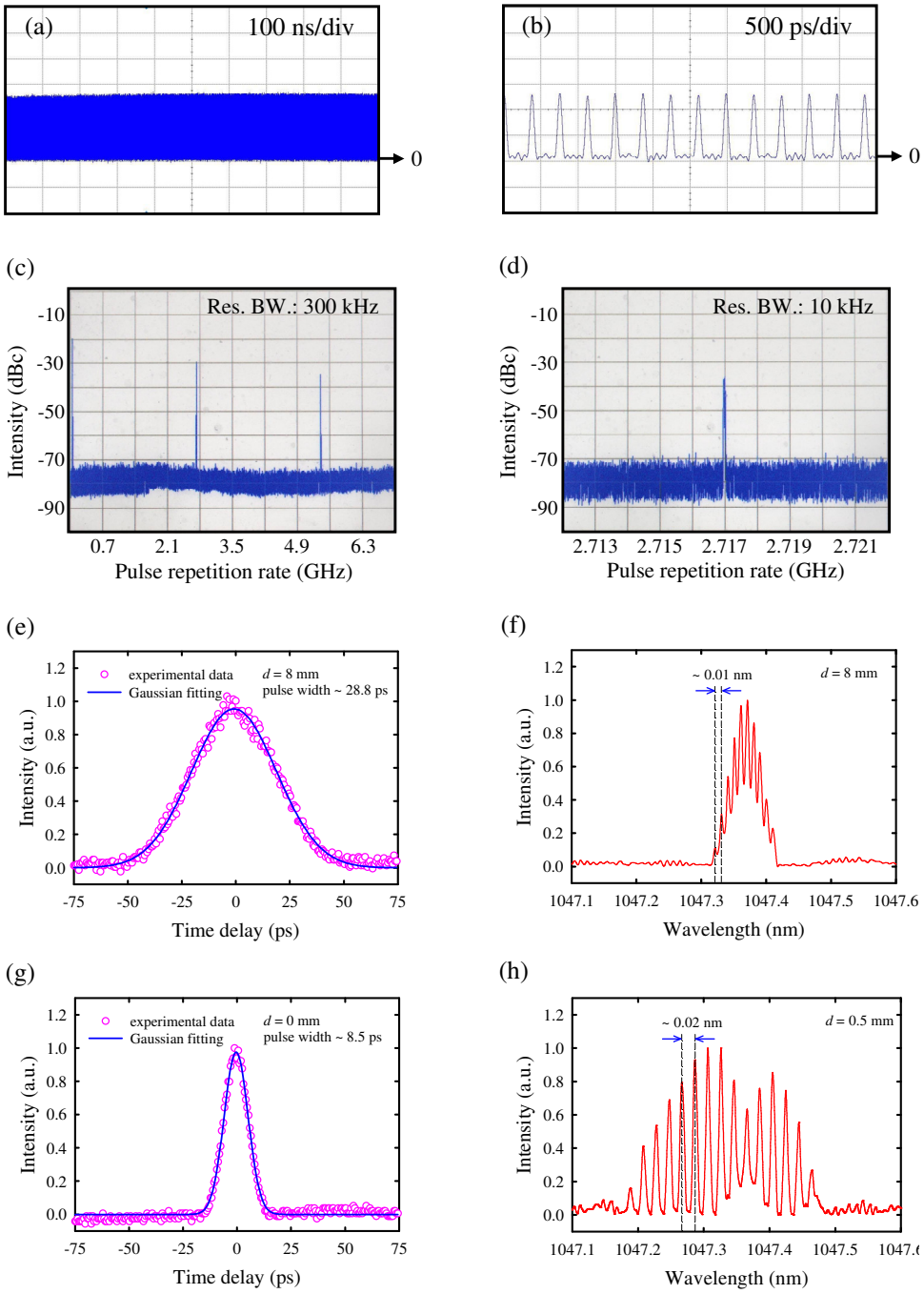

Fig. 4. Performance of the self-mode-locked Nd:YLF laser at 1047 nm: oscilloscope traces with the time span of (a) 1 μs and (b) 5 ns; RF spectrum with the frequency span of (c) 7 GHz and (d) 10 MHz; (e) autocorrelation trace for d = 8 mm; (f) optical spectrum for d = 8 mm; (g) autocorrelation trace for d = 0.5 mm; (h) optical spectrum for d = 0.5 mm.

Previous studies have theoretically analyzed and experimentally realized that decreasing the separation between the gain medium and the input mirror allows more longitudinal modes to oscillate in a standing-wave cavity [19–21]. Consequently, the SHB effect would be enhanced to lead the duration of the mode-locked pulse to be effectually shortened. In the

#171067 - $15.00 USD Received 22 Jun 2012; revised 19 Jul 2012; accepted 19 Jul 2012; published 24 Jul 2012

present configuration, the pulse width of the mode-locked Nd:YLF laser is found to reduce continuously with decreasing the separation d between the gain medium and the input mirror. When the laser crystal is intimately next to the input mirror, i.e., d = 0.5 mm, the shortest pulse width of 8 ps is obtained at 1053 nm, as shown in Fig. 3(g). Figure 3(h) demonstrates the corresponding optical spectrum for d = 0.5 mm. It is obvious that the pulse shortening is accompanied with the spectral broadening due to the enhancement of the SHB effect. More intriguingly, the mode spacing between the adjacent longitudinal modes for d = 0.5 mm is found to be two times wider than that for d = 8 mm. The mode spacing of 0.02 nm corresponds to the pulse repetition rate of 5.434 GHz, which implies that the Nd:YLF laser changes the mode-locked status from the fundamental mode locking to the second harmonic mode locking. This observation might come from the fact that the locking strength due to the third-order nonlinearity is not strong enough to lock the phases of all lasing longitudinal modes with the mode spacing of 0.01 nm for d = 0.5 mm, in which the number of the oscillated longitudinal modes is estimated to be approximately 30 modes. In order to keep a stable self-mode-locked state within the large gain bandwidth supported by the enhanced SHB effect, it is experimentally found that the number of longitudinal modes would reduce by half with the longitudinal mode spacing to be doubled. This effectively introduces the effect of the spectral filtering to lead the Nd:YLF laser to operate at the second harmonic mode locking rather than the fundamental mode locking. This experimental result is never observed in our previous studies on the self-mode-locked lasers owing to the relatively narrow gain bandwidth in the Nd-doped vanadate crystals as compared with the Nd:YLF crystal [12–14].

Finally, the overall characteristics for the self-mode-locked Nd:YLF laser at 1047 nm are graphically summarized in Fig. 4. Generally speaking, the mode-locked performance for the π-polarization is found to be similar to the results obtained with the σ-polarization.

4. Conclusion

In summary, we have developed a novel technique that relies on the natural birefringence of a wedged laser crystal and the alignment sensitivity of an optical resonator to realize the reliable TEM_{00}-mode self-mode-locked lasers in the Nd:YLF crystal at 1053 nm and 1047 nm, respectively. It is experimentally found that the fundamental mode locking of the Nd:YLF laser could be reliably obtained with the tunable pulse repetition rate in the range of 1.5-3 GHz. At an incident pump power of 6.93 W and a pulse repetition rate of 2.717 GHz, this compact mode-locked laser produces the output powers up to 2.15 W and 1.35 W for the σ- and π-polarization, respectively. Furthermore, we have found that decreasing the separation between the laser crystal and the input mirror not only brings in the pulse shortening due to the enhancement of the SHB effect, where the shortest pulse durations at 1053 nm and 1047 nm are 8 ps and 8.5 ps, but also effectively introduces the effect of the spectral filtering to cause the Nd:YLF laser to operate at the second harmonic mode locking instead of the fundamental mode locking.

Acknowledgments

The authors thank the National Science Council for their financial support of this research under Contract No. NSC-100-2628-M-009-001-MY3.

#171067 - $15.00 USD Received 22 Jun 2012; revised 19 Jul 2012; accepted 19 Jul 2012; published 24 Jul 2012

Appl Phys B (2012) 106:893–898
DOI 10.1007/s00340-011-4758-y

Applied Physics B
Lasers and Optics

High-power passively Q-switched Nd:YVO_4 UV laser at 355 nm

Y.J. Huang · Y.P. Huang · P.Y. Chiang · H.C. Liang · K.W. Su · Y.-F. Chen

Received: 17 June 2011 / Revised version: 18 August 2011 / Published online: 11 October 2011

Abstract We report on an efficient high-power passively Q-switched UV laser at 355 nm. We take into account the second threshold criterion and the thermal-lensing effect to design and realize a compact reliable passively Q-switched Nd:YVO_4 laser with Cr^{4+}:YAG as a saturable absorber. At an incident pump power of 16.3 W, the average output power at 1064 nm reaches 6.2 W with a pulse width of 7 ns and a pulse repetition rate of 56 kHz. Employing the developed passively Q-switched laser to perform the extra-cavity harmonic generations, the maximum average output powers at 532 nm and 355 nm are up to 2.2 W and 1.62 W, respectively.

1 Introduction

In recent years, ultraviolet (UV) light sources have been rapidly developed because they are useful in many scientific research and industrial applications. Compared with other UV lasers, diode-pumped all-solid-state pulsed lasers with extra-cavity harmonic generations intrinsically possess advantages of smaller focused size, higher efficiency, longer life time, higher stability, easier implement and smaller system size etc. [1, 2]. Passively Q-switching of the solid-state laser with a saturable absorber can provide a reliable pulsed operation with the benefits of high stability, inherent compactness, and low cost. As a promising saturable absorber near the infrared region, Cr^{4+}:YAG crystal has been widely investigated on the passively Q-switched performance thanks to its good chemical and mechanical stability, long lifetime, excellent optical quality, high damage threshold, high thermal conductivity, and large absorption cross section [3–11].

Nd-doped vanadate crystals are characterized by their high absorption coefficients for diode pumping, large stimulated emission cross sections, and moderate thermal conductivities that are suitable for achieving excellent laser performance. Unfortunately, their stimulated emission cross sections at 1064 nm are too large to achieve the good passively Q-switched operations when the Cr^{4+}:YAG is used as a saturable absorber. Several methods have been proposed to overcome the second threshold of the passive Q-switching, including the intra-cavity focusing obtained from the three-element resonator [12–14] and the employment of a c-cut crystal as a gain medium [15–17]. However, the peak powers did not reach a critical level for efficient extra-cavity second and third harmonic generations (SHG and THG). As a result, high-power UV lasers at 355 nm based on passively Q-switched Nd:YVO_4/Cr^{4+}:YAG laser at 1064 nm have not been performed so far.

In this work, we design a high-peak-power passively Q-switched Nd:YVO_4 laser with Cr^{4+}:YAG as a saturable absorber for generating a high-power UV laser at 355 nm. We theoretically analyze and experimentally realize a compact passively Q-switched laser by considering the second threshold condition and the thermal-lensing effect. At an incident pump power of 16.3 W, the average output power reaches 6.2 W with a pulse width of 7 ns and a pulse repetition rate of 56 kHz. The corresponding pulse energy and peak power are found to be as high as 111 μJ and 16 kW, respectively. With the developed passively Q-switched laser to perform the extra-cavity SHG and THG, the maximum average output powers at 532 nm and 355 nm are found to

Y.J. Huang · Y.P. Huang · P.Y. Chiang · H.C. Liang · K.W. Su · Y.-F. Chen (✉)
Department of Electrophysics, National Chiao Tung University, 1001 TA Hsueh Road, Hsinchu, 30050 Taiwan
e-mail: yfchen@cc.nctu.edu.tw
Fax: +886-35-725230

be up to 2.2 W and 1.62 W, respectively. The optical-to-optical conversion efficiencies from 1064 nm to 355 nm and 808 nm to 355 nm are up to 26% and 10%, respectively. To our knowledge, this is the highest conversion efficiency for the 355-nm UV laser generated by the passively Q-switched Nd:YVO_4/Cr^{4+}:YAG laser.

2 Cavity analysis

It is well known that the absorption saturation in the saturable absorber should occur earlier than the gain saturation in the laser crystal for good passively Q-switched operation. The so-called second threshold condition has been analytically derived from the coupled rate equation, which can be mathematically expressed as [12, 18]

$$\frac{\ln(1/T_0^2)}{\ln(1/T_0^2)+\ln(1/R_{\mathrm{OC}})+L}\frac{\sigma_{\mathrm{gsa}}}{\sigma}\frac{A}{A_{\mathrm{s}}} > \frac{\gamma}{1-\beta}, \tag{1}$$

where T_0 is the initial transmission of the saturable absorber, R_{OC} is the reflectivity of the output coupler, L is the nonsaturable round-trip dissipative loss of the resonator, σ_{gsa} is the ground-state absorption of the saturable absorber, σ is the emission cross section of the laser crystal, A/A_{s} is the ratio of the laser mode area in the laser crystal to that in the saturable absorber, γ is the population inversion reduction factor, which is equals to one for the ideal four-level laser and two for the three-level laser, and $\beta = \sigma_{\mathrm{esa}}/\sigma_{\mathrm{gsa}}$ is the ratio of the excite excited-state absorption cross section to the ground-state absorption cross section of the saturable absorber. With the following parameters: $T_0 = 0.7$, $R = 0.5$, $L = 0.03$, $\sigma_{\mathrm{gsa}} = 2 \times 10^{-18}$ cm^2 [11], $\sigma = 25 \times 10^{-18}$ cm^2, $\gamma = 1$, and $\beta = 0.06$ [11], the second threshold condition can be deduced to be $A/A_{\mathrm{s}} > 2.68$ in the case of Nd:YVO_4 and Cr^{4+}:YAG as a gain medium and a saturable absorber, respectively. As a consequence, the ratio of the laser mode radius in the laser crystal to that in the saturable absorber needs to be larger than 1.64 for achieving a high-quality passively Q-switched operation.

The configuration for a simple plano-concave resonator with the thermal-lensing effect is schematically shown in Fig. 1(a). In the present experiment, the laser crystal and the saturable absorber are aimed to be as close as possible to the input concave mirror and the flat output coupler, respectively. An optical resonator with an internal thermal lens between the resonator mirrors can be replaced by an empty cavity with the equivalent g-parameters g^* and the equivalent cavity length L^*, which are given by [19]

$$g_i^* = g_i - \frac{1}{f_{\mathrm{th}}} d_j \left(1 - \frac{d_i}{R_i}\right), \tag{2}$$

$$g_i = 1 - \frac{d_1 + d_2}{R_i}, \tag{3}$$

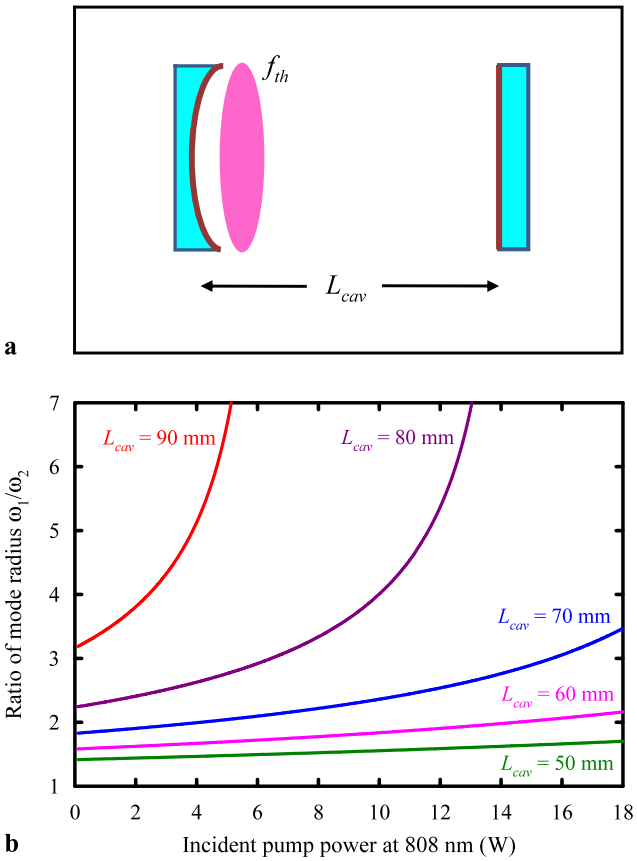

Fig. 1 (**a**) The configuration for a simple plano-concave cavity with the thermal-lensing effect; (**b**) calculated results for the ratio of the cavity mode size in the gain medium to that in the saturable absorber as a function of the incident pump power for the cases of $L_{\mathrm{cav}} = 90$ mm, 80 mm, 70 mm, 60 mm, and 50 mm when the radius-of-curvature of the input mirror is chosen to be $R = 100$ mm

$$i, j = 1, 2; \quad i \neq j,$$

$$L^* = d_1 + d_2 - \frac{1}{f_{\mathrm{th}}} d_1 d_2, \tag{4}$$

where f_{th} is the effective thermal focal length, d_1 and d_2 are the optical path length from the center of the gain medium to the input mirror and output coupler, R_1 and R_2 are the radius of curvature of the input mirror and output coupler. In terms of the equivalent cavity parameters, the cavity mode radius at the input mirror (ω_1) and at the output coupler (ω_2) are given by [19]

$$\omega_i = \sqrt{\frac{\lambda L^*}{\pi}\sqrt{\frac{g_j^*}{g_i^*(1 - g_1^* g_2^*)}}}, \quad i,\ j = 1, 2;\ i \neq j. \tag{5}$$

As a result, we can calculate the variations of the cavity mode radius ω_1 and ω_2 with respect to the effective thermal focal length. The effective focal length of thermal lens in the end-pumped laser crystal can be estimated with the

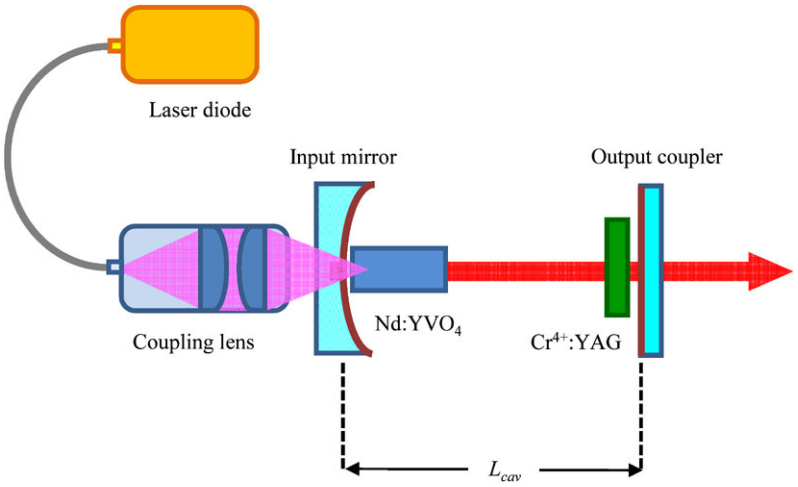

Fig. 2 Schematic of the cavity setup for a diode-pumped passively Q-switched Nd:YVO_4/Cr^{4+}:YAG laser

following equation [20]:

$$\frac{1}{f_{\text{th}}} = \frac{\xi P}{\pi K_c} \int_0^l \frac{\alpha e^{-\alpha z}}{1 - e^{-\alpha l}} \times \frac{1}{\omega_p^2(z)} \left[\frac{1}{2} \frac{dn}{dT} + (n-1)\alpha_T \frac{\omega_p(z)}{l} \right] dz, \tag{6}$$

where ξ is the fraction of the incident pump power that results in heat, P is the incident pump power, K_c is the thermal conductivity, α is the absorption coefficient, l is the crystal length, $\omega_p(z)$ is the variation of the pump radius, dn/dT is the thermal-optic coefficient, n is the refractive index, and α_T is the thermal expansion coefficient. With the following parameters: $\xi = 0.24$, $K_c = 5.23$ W/m K, $\alpha = 0.2$ mm^{-1}, $l = 12$ mm, $\omega_{po} = 300$ μm, $dn/dT = 3 \times 10^{-6}$ K^{-1}, $n = 2.1652$, and $\alpha_T = 4.43 \times 10^{-6}$ K^{-1}, the effective thermal focal length can be calculated as a function of the incident pump power. To be brief, the dependence of the ratio ω_1/ω_2 on the incident pump power can be generated to design and realize a high-quality passively Q-switched laser. Figure 1(b) depicts the calculated results for the cases of $L_{\text{cav}} = 90$ mm, 80 mm, 70 mm, 60 mm and 50 mm, where the L_{cav} stands for the cavity length and the other parameters used in calculation are as follows: $R_1 = 100$ mm, $R_2 \to \infty$, $d_1 = 6$ mm, $d_2 = (L_{\text{cav}} - 6)$ mm. From the Fig. 1(b), it is obvious that the thermal-lensing effect will make the cavity to be unstable when the cavity length is too long; whereas the passively Q-switched laser cannot well operate in a high-quality state when the cavity length is too short. Comparative speaking, we chose a resonator with $L_{\text{cav}} = 70$ mm to simultaneously satisfy the second threshold criterion and cavity-stability condition to realize a compact reliable passively Q-switched laser.

3 Experimental setup and results

The experimental setup is schematically shown in Fig. 2. The input mirror was a concave mirror with the radius-of-curvature of 100 mm. It was antireflection (AR) coated at 808 nm on the entrance face, and was coated at 808 nm for high transmission as well as 1064 nm for high reflection on the second surface. The gain medium was a 0.1 at.% a-cut Nd:YVO_4 crystal with dimensions of $3 \times 3 \times 12$ mm^3, and it was placed as close as possible to the input mirror. Both facets of the laser crystal were AR coated at 808 nm and 1064 nm. The Cr^{4+}:YAG saturable absorber with an initial transmission of 70% was AR coated at 1064 nm on both surfaces, and it was placed near to the output coupler. The laser crystal and the saturable absorber were wrapped with indium foils and mounted in water-cooled copper heat sinks at 20°C. The pump source was a 18-W 808-nm fiber-coupled laser diode with a core diameter of 600 μm and a numerical aperture of 0.2. The pump beam was re-imaged into the laser crystal with a lens set that has the focal length of 25 mm with a magnification of unity and the coupling efficiency of 91%. Therefore, the maximum incident pump power in our experiment is approximately 16.3 W. The flat output coupler with 50% transmission was employed during the experiment. As designed in Sect. 2, the cavity length was set to be 70 mm for the construction of the compact high-power passively Q-switched laser. The pulse temporal behaviors were recorded by a LeCroy digital oscilloscope (Wavepro 7100, 10 G samples/s, 1 GHz bandwidth) with a fast Si photodiode.

First of all, the continuous-wave operation without the saturable absorber is studied. The average output power as a function of the incident pump power is presented by the red curve in Fig. 3(a). The pump threshold and the slope efficiency are determined to be 2.1 W and 62%, respectively. At the maximum incident pump power of 16.3 W, the average output power of 8.8 W is obtained, corresponding to

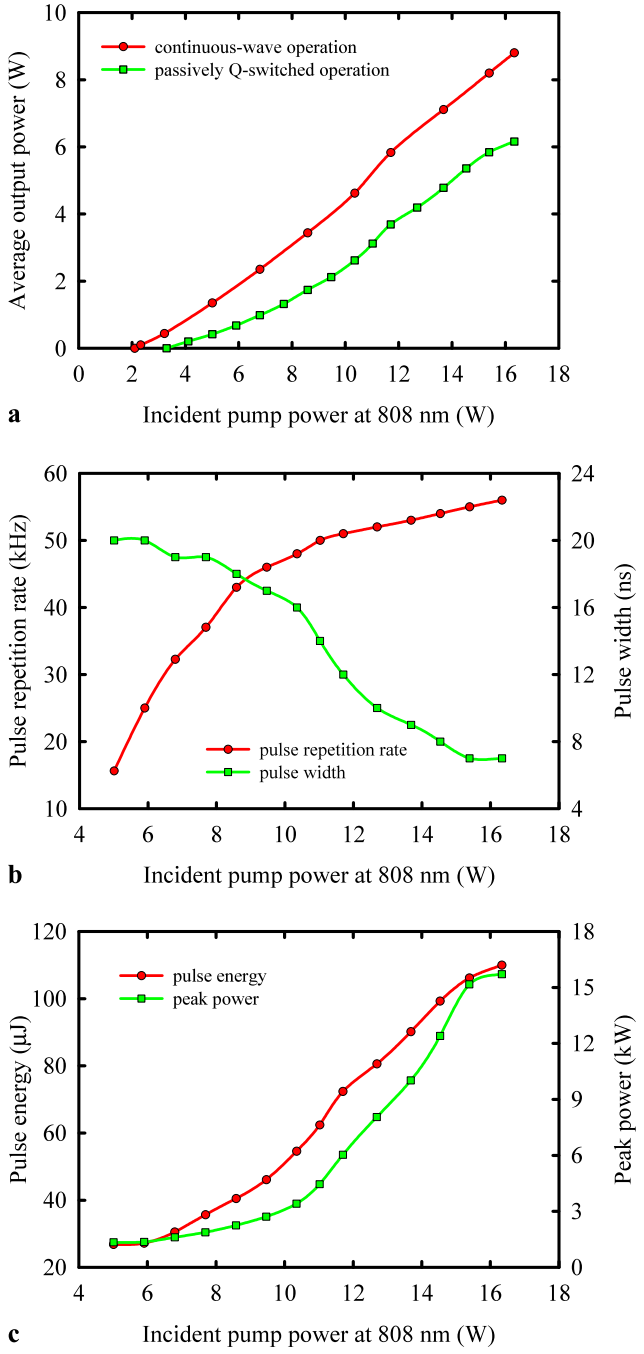

Fig. 3 (**a**) Average output powers in continuous-wave (*red curve*) and passively Q-switched (*green curve*) operations as a function of the incident pump power; (**b**) dependences of the pulse repetition rate (*red curve*) and pulse width (*green curve*) on the incident pump power; (**c**) dependences of the pulse energy (*red curve*) and peak power (*green curve*) on the incident pump power

the optical-to-optical conversion efficiency up to 54%. We then inserted the Cr^{4+}:YAG saturable absorber into the laser cavity to investigate the passively Q-switched performance in detail. The dependence of the average output power on the incident pump power in the passively Q-switched operation is illustrated by the green curve in Fig. 3(a). The pump threshold and the slope efficiency are found to be 3.3 W and 47.4%, respectively. At the maximum incident pump power of 16.3 W, the average output power as high as 6.16 W is obtained, corresponding to the optical-to-optical conversion efficiency up to 37.8%. Figures 3(b)–(c) show the pulse width, pulse repetition rate, pulse energy, and peak power as a function of the incident pump power. For the incident pump power increases from 5 W to 16.3 W, the pulse repetition rate varies from 15.5 kHz to 56 kHz and the pulse width changes from 20 ns to 7 ns, as shown in Fig. 3(b). Accordingly, it can be seen that the pulse energy increases from 27 μJ to 111 μJ and the peak power increases from 1.3 kW to 16 kW when the incident pump power increases from 5 W to 16.3 W, as revealed in Fig. 3(c). Note that the appearance of the satellite pulses following the main Q-switched pulse was frequently observed in the past research [21–24]. This phenomenon inevitably degrades the Q-switched performance, leading to the restriction of the maximum achievable Q-switched pulse energy and peak power. However, we did not observe any satellite pulses during the present experiment, indicating the validness of our cavity optimization. In the following section, we will employ this compact reliable high-power passively Q-switched laser to explore the performance in the processes of the extra-cavity SHG and THG.

4 Conversion efficiencies of extra-cavity harmonic generations

Here lithium triborate (LBO) crystals are exploited as nonlinear frequency converters for SHG and THG since they have the advantages of high damage threshold, relatively large acceptance angle, and small walk-off angle. One LBO crystal with dimensions of $3 \times 3 \times 15$ mm^3 was cut at $\theta = 90°, \phi = 10.4°$ for type-I phase-matched SHG at temperature of 46.6°C. Both facets of the SHG crystal were AR coated at 1064 nm and 532 nm. Another LBO crystal with dimensions of $3 \times 3 \times 10$ mm^3 was cut at $\theta = 44°, \phi = 90°$ for type-II phase-matched THG at temperature of 48°C. Both facets of the THG crystal were AR coated at 1064 nm, 532 nm, and 355 nm. The temperatures of the SHG and THG nonlinear crystals were monitored by thermoelectric controllers with the precision of 0.1°C. Two convex lenses were used to focus the laser beams into the SHG and THG nonlinear crystals for achieving efficient harmonic generations. The former one with focal length of 38 mm was AR coated at 1064 nm on both sides, the latter one with focal length of 19 mm was AR coated at 1064 nm and 532 nm on both sides. The optimized geometrical distances of L_1, L_2, L_3 and L_4 indicated in Fig. 4 were experimentally determined to be approximately 100 mm, 50 mm, 40 mm, and 20 mm,

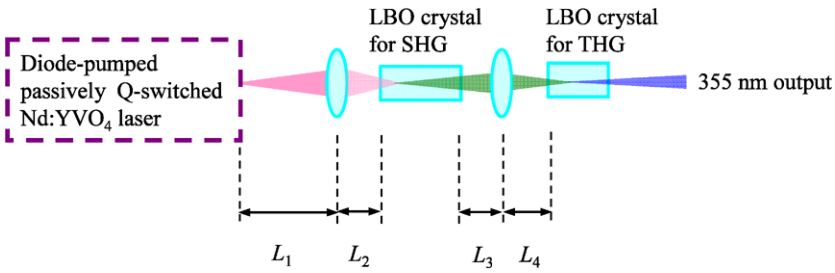

Fig. 4 Schematic of the experimental setup for the extra-cavity SHG and THG

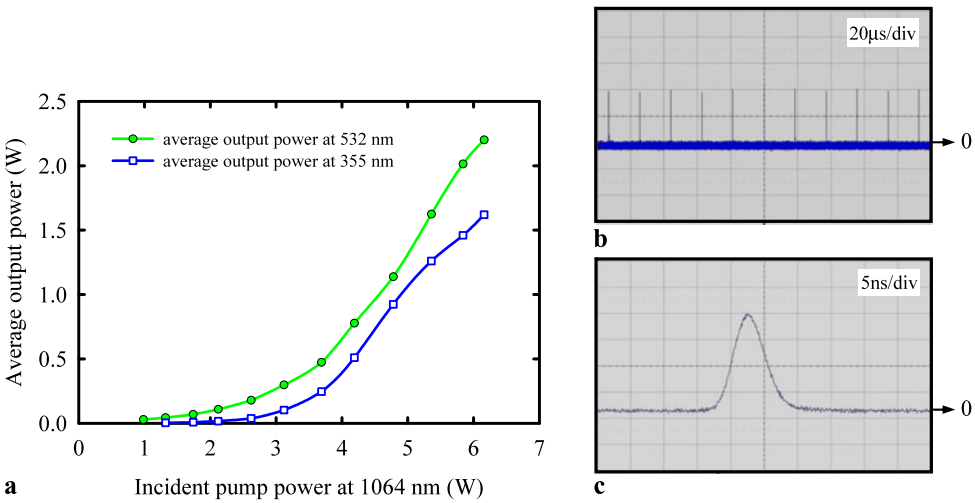

Fig. 5 (**a**) Dependences of the average output power at 532 nm (*green curve*) and 355 nm (*blue curve*) on the incident pump power at 1064 nm; typical temporal behaviors at 355 nm with: (**b**) time span of 200 μs, and (**c**) time span of 50 ns

respectively. The spot radii inside the SHG and THG nonlinear crystals were estimated to be about 71 μm and 38 μm, respectively.

The dependences of the average output powers at 532 nm and 355 nm on the incident pump power at 1064 nm are shown in Fig. 5(a). At the maximum incident pump power of 6.3 W at 1064 nm, the highest average output powers at 532 nm and 355 nm reach 2.2 W and 1.62 W with a pulse width as short as 5 ns and a pulse repetition rate of 56 kHz. Accordingly, the highest pulse energies at 532 nm and 355 nm are found to be 39 μJ and 29 μJ. More importantly, the largest peak powers at 532 nm and 355 nm as high as 7.8 kW and 5.8 kW are achieved. The optical-to-optical conversion efficiencies from 1064 to 355 nm and 808 nm to 355 nm are up to 26% and 10%, respectively. With a knife-edge method, the beam quality factors at 355 nm for orthogonal direction were measured to be $M_x^2 < 1.2$ and $M_y^2 < 1.3$, respectively. Typical temporal behaviors of the output pulses at 355 nm are shown in Figs. 5(b)–(c) with time span of 200 μs and 50 ns, respectively. The pulse-to-pulse amplitude fluctuation is found to be better than ±3%.

Finally, it is worthwhile to mention that although the intra-cavity focusing obtained from the three-element resonator can effectively enlarge the ratio of the laser mode area in the gain medium to that in the saturable absorber to meet the second threshold condition, it will not only add complexities to the overall laser cavity but also reduce the peak power that is detrimental for efficient extra-cavity harmonic generations. Employing a c-cut Nd:YVO_4 that has smaller stimulated emission cross section is another suitable way to satisfy the second threshold condition; however, the non-polarized laser output is problematic in the processes of harmonic generations, in which the linearly polarized fundamental beam is usually required. Comparative speaking, using a simple plano-concave resonator to construct a compact high-power passively Q-switched Nd:YVO_4/Cr^{4+}:YAG laser with constantly linear polarization is a practical method to simultaneously satisfy the second threshold condition and provide adequate peak power for efficient extra-cavity harmonic generations.

5 Conclusion

In summary, we have considered the second threshold criterion and the thermal-lensing effect to design a high-peak-power passively Q-switched Nd:YVO_4 laser with Cr^{4+}:YAG as a saturable absorber. At an incident pump power of 16.3 W, the average output power was found to reach 6.2 W with a pulse width of 7 ns and a pulse repetition rate of 56 kHz. The corresponding pulse energy and peak power were as high as 111 μJ and 16 kW, respectively. We further employed the developed passively Q-switched laser to perform the extra-cavity SHG and THG. At an incident pump power of 16.3 W, the average output powers

at 532 nm and 355 nm were found to be up to 2.2 W and 1.62 W, respectively. The optical-to-optical conversion efficiencies from 1064 nm to 355 nm and 808 nm to 355 nm were 26% and 10%, respectively. The excellent conversion efficiency in the generation of UV light confirms the theoretical analysis of the cavity design.

The authors thank the National Science Council for their financial support of this research under Contract No. NSC-97-2112-M-009-016-MY3.

References

1. A.V. Hicks, C.X. Wang, G.Y. Wang, Proc. SPIE **5332**, 120 (2004)
2. C.X. Wang, G.Y. Wang, A.V. Hicks, D.R. Dudley, H.Y. Pang, N. Hodgson, Proc. SPIE **6100**, 610019 (2006)
3. P. Yankov, J. Phys. D, Appl. Phys. **27**, 1118 (1994)
4. Y. Shimony, Y. Kalisky, B.H.T. Chai, Opt. Mater. **4**, 547 (1995)
5. Y. Shimony, Z. Burshtein, A.B.A. Baranga, Y. Kalisky, M. Strauss, IEEE J. Quantum Electron. **32**, 305 (1996)
6. T. Dascalu, G. Philipps, H. Weber, Opt. Laser Technol. **29**, 145 (1997)
7. X. Zhang, S. Zhao, Q. Wang, Q. Zhang, L. Sun, S. Zhang, IEEE J. Quantum Electron. **33**, 2286 (1997)
8. G. Xiao, J.H. Lim, S. Yang, E.V. Stryland, M. Bass, L. Weichman, IEEE J. Quantum Electron. **35**, 1086 (1999)
9. A. Suda, A. Kadoi, K. Nagasaka, H. Tashiro, K. Midorikawa, IEEE J. Quantum Electron. **35**, 1548 (1999)
10. A.G. Okhrimchuk, A.V. Shestakov, Phys. Rev. B **61**, 988 (2000)
11. A. Sennaroglu, U. Demirbas, S. Ozharar, F. Yaman, J. Opt. Soc. Am. B **23**, 241 (2006)
12. Y. Bai, N. Wu, J. Zhang, J. Li, S. Li, J. Xu, P. Deng, Appl. Opt. **36**, 2468 (1997)
13. C. Li, J. Song, D. Shen, N.S. Kim, J. Lu, K. Ueda, Appl. Phys. B **70**, 471 (2000)
14. C. Du, J. Liu, Z. Wang, G. Xu, X. Xu, K. Fu, X. Meng, Z. Shao, Opt. Laser Technol. **34**, 699 (2002)
15. Y.F. Chen, Y.P. Lan, Appl. Phys. B **74**, 415 (2002)
16. J. Liu, J. Yang, J. He, Opt. Commun. **219**, 317 (2003)
17. H. Yu, H. Zhang, Z. Wang, J. Wang, Z. Shao, M. Jiang, Opt. Express **15**, 3206 (2007)
18. Y.F. Chen, Y.P. Lan, H.L. Chang, IEEE J. Quantum Electron. **37**, 462 (2001)
19. N. Hodgson, H. Weber, *Laser Resonators and Beam Propagation*, 2nd edn. (Springer, Berlin, 2005), Chap. 8
20. W. Koechner, *Solid-State Laser Engineering*, 6th edn. (Springer, Berlin, 2005), Chap. 7
21. J. Bartschke, K.-J. Boller, R. Wallenstein, I.V. Klimov, V.B. Tsvetkov, I.A. Shcherbakov, J. Opt. Soc. Am. B **14**, 3452 (1997)
22. J. Liu, B. Ozygus, S. Yang, J. Erhard, U. Seelig, A. Ding, H. Weber, X. Meng, L. Zhu, L. Qin, C. Du, X. Xu, Z. Shao, J. Opt. Soc. Am. B **20**, 652 (2003)
23. S.P. Ng, D.Y. Tang, L.J. Qin, X.L. Meng, Opt. Commun. **229**, 331 (2004)
24. S.P. Ng, D.Y. Tang, L.J. Qian, L.J. Qin, IEEE J. Quantum Electron. **42**, 625 (2006)

Orthogonally polarized dual-wavelength Nd:$LuVO_4$ laser at 1086 nm and 1089 nm

Y. P. Huang, C. Y. Cho, Y. J. Huang, and Y. F. Chen*

Department of Electrophysics, National Chiao Tung University, 1001 TA Hsueh Road,Hsinchu, Taiwan
yfchen@cc.nctu.edu.tw

Abstract: A comparison between the fluorescence spectra of the Nd-doped vanadate crystals (Nd:YVO_4, Nd:$GdVO_4$, Nd:$LuVO_4$) for the ${}^4F_{3/2} \rightarrow {}^4I_{11/2}$ transition is studied. We numerically analyze the condition of gain-to-loss balance via an uncoated intracavity etalon to achieve the dual-wavelength operation. We further experimentally demonstrate the orthogonally polarized dual-wavelength laser with a single Nd:$LuVO_4$ crystal. The simultaneous dual-wavelength Nd:$LuVO_4$ laser at 1085.7 nm in σ polarization and 1088.5 nm in π polarization is realized. At an incident pump power of 12 W, the average output power obtained at 1085.7 nm and 1088.5 nm is 0.4 W and 1.7 W, respectively.

OCIS codes: (140.3410) Laser resonators; (140.3580) Lasers, solid-state.

References and links

1. F. Weigl, "A generalized technique of two-wavelength, nondiffuse holographic interferometry," Appl. Opt. **10**(1), 187–192 (1971).
2. N. G. Basov, M. A. Gubin, V. V. Nikitin, A. V. Nikuchin, V. N. Petrovskii, E. D. Protsenko, and D. A. Tyurikov, "Highly-sensitive method of narrow spectral-line separations, based on the detection of frequency resonances of a 2-mode gas-laser with non-linear absorption," Izv. Akad. Nauk SSSR, Ser. Fiz. **46**, 1573–1583 (1982).
3. R. W. Farley and P. D. Dao, "Development of an intracavity-summed multiple-wavelength Nd:YAG laser for a rugged, solid-state sodium lidar system," Appl. Opt. **34**(21), 4269–4273 (1995).
4. Y. F. Chen, Y. S. Chen, and S. W. Tsai, "Diode-pumped Q-switched laser with intracavity sum frequency mixing in periodically poled KTP," Appl. Phys. B **79**(2), 207–210 (2004).
5. S. N. Son, J. J. Song, J. U. Kang, and C. S. Kim, "Simultaneous second harmonic generation of multiple wavelength laser outputs for medical sensing," Sensors (Basel) **11**(6), 6125–6130 (2011).
6. Y. Lu, B. G. Zhang, E. B. Li, D. G. Xu, R. Zhou, X. Zhao, F. Ji, T. L. Zhang, P. Wang, and J. Q. Yao, "High-power simultaneous dual-wavelength emission of an end-pumped Nd:YAG laser using the quasi-three-level and the four-level transition," Opt. Commun. **262**(2), 241–245 (2006).
7. K. Lünstedt, N. Pavel, K. Petermann, and G. Huber, "Continuous-wave simultaneous dual-wavelength operation at 912 and 1063 nm in Nd:$GdVO_4$," Appl. Phys. B **86**(1), 65–70 (2007).
8. H. Y. Shen, R. R. Zeng, Y. P. Zhou, G. F. Yu, C. H. Huang, Z. D. Zeng, W. J. Zhang, and Q. J. Ye, "Simultaneous multiple wavelength laser action in various Neodymium host crystals," IEEE J. Quantum Electron. **27**(10), 2315–2318 (1991).
9. Y. F. Chen, "CW dual-wavelength operation of a diode-end-pumped Nd:YVO_4 laser," Appl. Phys. B **70**(4), 475–478 (2000).
10. X. Yu, C. L. Li, G. C. Sun, B. Z. Li, X. Y. Chen, M. Zhao, J. B. Wang, X. H. Zhang, and G. Y. Jin, "Continuous-wave dual-wavelength operation of a diode-end-pumped Nd:$LuVO_4$ laser," Laser Phys. **21**(6), 1039–1041 (2011).
11. H. H. Yu, H. J. Zhang, Z. P. Wang, J. Y. Wang, Y. G. Yu, Z. B. Shi, X. Y. Zhang, and M. H. Jiang, "High-power dual-wavelength laser with disordered Nd:CNGG crystals," Opt. Lett. **34**(2), 151–153 (2009).
12. H. H. Yu, H. J. Zhang, Z. P. Wang, J. Y. Wang, Y. G. Yu, X. Y. Zhang, R. J. Lan, and M. H. Jiang, "Dual-wavelength neodymium-doped yttrium aluminum garnet laser with chromium-doped yttrium aluminum garnet as frequency selector," Appl. Phys. Lett. **94**(4), 041126 (2009).
13. R. Zhou, B. G. Zhang, X. Ding, Z. Q. Cai, W. Q. Wen, P. Wang, and J. Q. Yao, "Continuous-wave operation at 1386 nm in a diode-end-pumped Nd:YVO_4 laser," Opt. Express **13**(15), 5818–5824 (2005).
14. H. Y. Zhu, G. Zhang, C. H. Huang, Y. Wei, L. X. Huang, A. H. Li, and Z. Q. Chen, "1318.8 nm/1338.2 nm simultaneous dual-wavelength Q-switched Nd:YAG laser," Appl. Phys. B **90**(3-4), 451–454 (2008).
15. Y. F. Chen, M. L. Ku, and K. W. Su, "High-power efficient tunable Nd:$GdVO_4$ laser at 1083 nm," Opt. Lett. **30**(16), 2107–2109 (2005).
16. W. Shi, Y. J. Ding, N. Fernelius, and K. Vodopyanov, "Efficient, tunable, and coherent 0.18-5.27-THz source based on GaSe crystal," Opt. Lett. **27**(16), 1454–1456 (2002).

#161858 - $15.00 USD Received 19 Jan 2012; revised 13 Feb 2012; accepted 13 Feb 2012; published 22 Feb 2012

17. J. F. Federici, B. Schulkin, F. Huang, D. Gary, R. Barat, F. Oliveira, and D. Zimdars, "THz imaging and sensing for security applications—explosives, weapons and drugs," Semicond. Sci. Technol. **20**(7), S266–S280 (2005).
18. J. B. Baxter and G. W. Guglietta, "Terahertz spectroscopy," Anal. Chem. **83**(12), 4342–4368 (2011).
19. C. B. Reid, E. Pickwell-MacPherson, J. G. Laufer, A. P. Gibson, J. C. Hebden, and V. P. Wallace, "Accuracy and resolution of THz reflection spectroscopy for medical imaging," Phys. Med. Biol. **55**(16), 4825–4838 (2010).
20. L. G. Fei and S. L. Zhang, "The discovery of nanometer fringes in laser self-mixing interference," Opt. Commun. **273**(1), 226–230 (2007).
21. S. L. Zhang, Y. D. Tan, and Y. Li, "Orthogonally polarized dual frequency lasers and applications in self-sensing metrology," Meas. Sci. Technol. **21**(5), 054016 (2010).
22. C. Ren and S. L. Zhang, "Diode-pumped dual-frequency microchip Nd:YAG laser with tunable frequency difference," J. Phys. D Appl. Phys. **42**(15), 155107 (2009).
23. X. P. Yan, Q. Liu, H. L. Chen, F. Xing, M. L. Gong, and D. S. Wang, "A novel orthogonally linearly polarized Nd:YVO_4 laser," Chin. Phys. B **19**(8), 084202 (2010).
24. B. Wu, P. P. Jiang, D. Z. Yang, T. Chen, J. Kong, and Y. H. Shen, "Compact dual-wavelength Nd:$GdVO_4$ laser working at 1063 and 1065 nm," Opt. Express **17**(8), 6004–6009 (2009).
25. C. Maunier, J. L. Doualan, R. Moncorge, A. Speghini, M. Bettinelli, and E. Cavalli, "Growth, spectroscopic characterization, and laser performance of Nd:$LuVO_4$, a new infrared laser material that is suitable for diode pumping," J. Opt. Soc. Am. B **19**(8), 1794–1800 (2002).
26. Y. F. Chen, "cw dual-wavelength operation of a diode-pumped Nd:YVO_4 laser," Appl. Phys. B **70**(4), 475–478 (2000).
27. C. A. Bennett, *Principles of Physical Optics* (Wiley, 2008).

1. Introduction

Simultaneous dual-wavelength laser has been of great interest for many applications such as medical instrumentation, precision laser spectroscopy, holography, lidar, and scientific research of nonlinear optical mixers [1–5]. Rare-earth-doped laser media possessing many sharp fluorescent lines, especially in the $^4F_{3/2} \rightarrow {}^4I_{11/2}$ transition, are natural candidates to realize the simultaneous dual-wavelength solid-state lasers. Neodymium (Nd) lasers, because of their high gains and the good thermal and mechanical properties, are by far the most important solid-state lasers. The realized simultaneous dual-wavelength lasers in Nd host crystals can be classified into three main types. The first type involving two different laser transitions from $^4F_{3/2} \rightarrow {}^4I_{11/2}$, $^4F_{3/2} \rightarrow {}^4I_{13/2}$, or $^4F_{3/2} \rightarrow {}^4I_{9/2}$ gives a large wavelength separation with a single polarization [6–10]. The second type is the laser operated in the same laser transition with a smaller wavelength separation and a single polarization [11–15], which is very attractive for coherent terahertz (THz) generation by nonlinear difference frequency mixing [16]. Coherent THz waves, traditionally defined in the frequency range of 0.1–3 THz, have great potential for THz imaging, sensing and THz spectroscopy applications [17–19]. The dual-wavelength lasers with orthogonal polarizations, classifying as the third type, are desirable for the applications of laser interferometry and precision metrology [20,21]. Nd:YAG, Nd:YVO_4, and Nd:$GdVO_4$ lasers have been demonstrated recently to achieve the simultaneous emissions of two orthogonally polarized wavelengths, in which an additional birefringent element or second gain medium was employed for obtaining orthogonal linear polarizations [22–24]. It will be more practically desirable and convenient to develop a compact orthogonally polarized dual-wavelength laser with a single gain medium in a simple cavity.

In this work, we first make a comparison between the fluorescence spectra of Nd:YVO_4, Nd:$GdVO_4$ and Nd:$LuVO_4$ crystals for the $^4F_{3/2} \rightarrow {}^4I_{11/2}$ transition. It is found that the spontaneous emission spectra of Nd:$LuVO_4$ crystals in the range of 1080 nm and 1090 nm display comparable radiation strengths in π and σ polarizations. Comparing to the properties of Nd:YVO_4 and Nd:$GdVO_4$ crystals, the Nd:$LuVO_4$ crystal possesses a wider separation between the fluorescence peak positions of π and σ polarizations near 1080–1090 nm. With these superior properties, we numerically analyze the condition of gain-to-loss balance via an uncoated intracavity etalon to achieve the dual-wavelength operation in a Nd:$LuVO_4$ laser. Finally, we experimentally accomplish a diode-end-pumped dual-wavelength Nd:$LuVO_4$ laser with orthogonal σ and π polarizations at 1085.7 nm and 1088.5 nm, respectively. At an incident pump power of 12 W, the output powers of 0.4 W at 1085.7 nm and of 1.7 W and 1088.5 nm are simultaneously obtained.

#161858 - $15.00 USD Received 19 Jan 2012; revised 13 Feb 2012; accepted 13 Feb 2012; published 22 Feb 2012

2. Fluorescence spectra of Nd:YVO_4, Nd:$GdVO_4$ and Nd:$LuVO_4$ crystals

Vanadate family crystals doped with Nd^{3+} ions, such as Nd:YVO_4, Nd:$GdVO_4$ and Nd:$LuVO_4$, have been recognized as the excellent active media for diode-pumped solid-state lasers due to their broad absorption bands, large absorption and emission cross sections. Nd-doped vanadate crystals, however, are characterized by their polarization-dependent gains. We experimentally study the fluorescence properties of Nd:YVO_4, Nd:$GdVO_4$ and Nd:$LuVO_4$ crystals with doping concentrations of 0.25%, 0.5%, and 0.5%, respectively. Three crystals were cut along the *a* axis with dimensions of 3 × 3 × 8 mm^3 in size. Both end faces of the crystals were antireflection coated at 808 nm for diode pumping. Figure 1 displays the room-temperature polarized fluorescence spectra of the Nd:YVO_4, Nd:$GdVO_4$ and Nd:$LuVO_4$ crystals for the ${}^4F_{3/2} \rightarrow {}^4I_{11/2}$ laser transition which are relative emission-line intensities measurements for the respective crystals. The spectral information was monitored by an optical spectrum analyzer (Advantest Q8381A) that employs a diffraction grating monochromator with the resolution of 0.1 nm. The blue and red curves represent the π and σ polarizations, respectively. As shown in Fig. 1(a), the strongest emission lines of three laser materials are typically near 1060 nm in π polarization, about several times higher than that in σ polarization. Unfortunately, it is considerably difficult to realize an orthogonal-polarization dual-wavelength laser with a single laser crystal near 1060 nm due to the extremely intense gain competition between two polarizations. It is obviously seen that all three crystals exhibit the significant secondary emission lines in the range of 1080–1090 nm with comparable emission intensity in π and σ polarizations. However, the spectral characteristics are extremely different in the three crystals, as shown in Fig. 1(b). The spectrum of Nd:$GdVO_4$ crystal reveals a large overlap between the emission distributions in π and σ polarizations. On the other hand, the separation between the fluorescence peak positions of π and σ polarizations in the Nd:$LuVO_4$ crystal is considerably wider than that in the Nd:YVO_4 crystal. As a consequence, the Nd:$LuVO_4$ crystal is superior to the Nd:YVO_4 and Nd:$GdVO_4$ media for achieving an orthogonally polarized dual-wavelength laser near 1080–1090 nm, which can be used as a light source to generate the THz-frequency radiation.

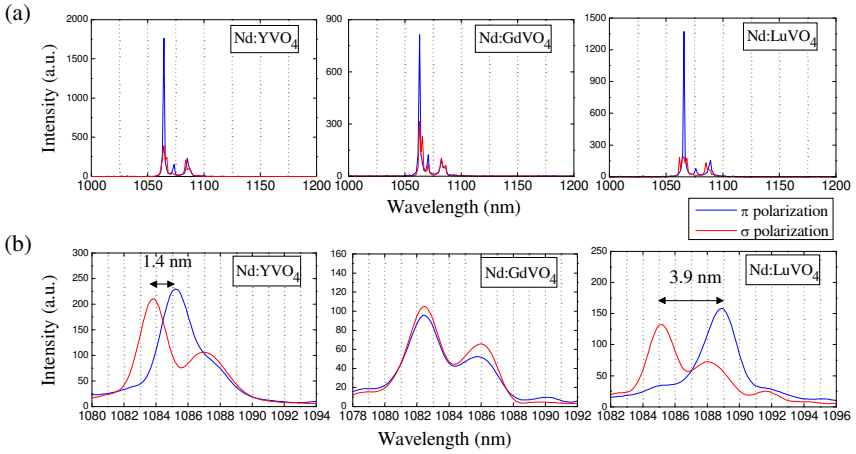

Fig. 1. (a) Fluorescence emission spectra for the ${}^4F_{3/2} \rightarrow {}^4I_{11/2}$ laser transition in the Nd:YVO_4, Nd:$GdVO_4$ and Nd:$LuVO_4$ crystals at room temperature; (b) fragments of the room-temperature fluorescence spectra near 1080 and 1090 nm.

3. Numerical analysis for dual-wavelength operation

We analyze the dual-wavelength operation with the Nd:$LuVO_4$ crystal in the range of 1080-1090 nm under the circumstance of suppressing the strongest emission line near 1060 nm. As shown in the fluorescence spectrum, the Nd:$LuVO_4$ crystal has the comparable emission cross sections in σ and π polarizations that are respectively near 1086 nm (~18 × 10^{-20} cm^2) and

#161858 - $15.00 USD Received 19 Jan 2012; revised 13 Feb 2012; accepted 13 Feb 2012; published 22 Feb 2012

1089 nm (~20 × 10^{-20} cm^2) [25]. The threshold condition for each transition wavelength in a simultaneous dual-wavelength operation is given by [26]

$$P_{\mathrm{th},i} = \frac{\ln(1/R_i) + L_i}{2l\eta_i} \frac{h\upsilon_{\mathrm{p}}}{\sigma_i \tau_i} \frac{1}{\iiint s_i(r,z) r_{\mathrm{p}}(r,z) dv}, \quad i = 1,2, \tag{1}$$

where R_i, L_i, η_i, σ_i, and τ_i are, respectively, the reflectivity, the cavity round-trip loss, the quantum efficiency, the stimulated emission cross section, and the fluorescence lifetime at the upper level for the corresponding transition wavelength. Parameters of $h\nu_{\mathrm{p}}$, l, $s_i(r,z)$, and $r_{\mathrm{p}}(r,z)$ are the pump photon energy, the length of gain medium, the normalized cavity mode intensity distribution for the corresponding transition wavelength, and the normalized pump intensity distribution in the laser cavity. Here i = 1, 2 represents the two wavelengths of 1086 nm and 1089 nm, respectively. Since the two nearly close wavelengths transmitting from the same upper and lower level in the same cavity, the parameters of η_i, τ_i, $s_i(r,z)$, and $r_{\mathrm{p}}(r,z)$ can be reasonably considered to be equal. Therefore, the ratio of laser thresholds for 1089 nm and 1086 nm can be expressed as:

$$\gamma = \frac{P_{th,2}}{P_{th,1}} = \frac{\ln(1/R_2) + L_2}{\ln(1/R_1) + L_1} \frac{\sigma_1}{\sigma_2}. \tag{2}$$

Since $\sigma_1 < \sigma_2$ and the values of the reflectivity at 1086 nm and 1089 nm are usually nearly equal, i.e. $R_1 \cong R_2$, the ratio γ is less than one without introducing the deliberate difference for losses L_1 and L_2. The result of $\gamma < 1$ indicates that the laser will be dominated at 1089 nm because this emission line has a lower threshold and a higher stimulated cross section. For obtaining a dual-wavelength operation, an appropriate difference for losses L_1 and L_2 needs to be introduced to reach the condition of $\gamma > 1$. The result of $\gamma > 1$ means that the laser will first emit the radiation at the weaker line at 1086 nm and then simultaneously emit the radiation at 1089 nm under a higher pump power.

Next we numerically verify that a uncoated intracavity etalon can be utilized to adjust the difference for losses L_1 and L_2 based on the dependence of Fresnel reflection upon the incident angle as well as the electric field polarization. The c axis of Nd:$LuVO_4$ crystal is set to be placed in the vertical direction, and the angle of inclination of the etalon is relative to the optical axis of the resonator, which the plane of incidence is in the horizontal direction. As a result, the π and σ polarized waves are perpendicularly and parallel to the plane of incidence, corresponding to the S and P waves respectively. The inclined angle of the etalon is equal to the incident angle of light. In terms of incident angle θ, the losses caused by the Fresnel reflection for S and P waves can be given by [27]

$$L_S = R_S(n,\theta) + \left[1 - R_S(n,\theta)\right] \cdot R_S(1/n, \sin^{-1}(\sin\theta / n)) \tag{3}$$

and

$$L_P = R_P(n,\theta) + \left[1 - R_P(n,\theta)\right] \cdot R_P(1/n, \sin^{-1}(\sin\theta / n)), \tag{4}$$

where

$$R_S(n,\theta) = \left| \frac{\cos\theta - \sqrt{n^2 - \sin^2\theta}}{\cos\theta + \sqrt{n^2 - \sin^2\theta}} \right|^2, \quad R_P(n,\theta) = \left| \frac{\sqrt{n^2 - \sin^2\theta} - n^2\cos\theta}{\sqrt{n^2 - \sin^2\theta} + n^2\cos\theta} \right|^2, \tag{5}$$

and n is the ratio of the refractive indices for the etalon and air. With Eqs. (2)-(5) and the parameters in the experiment: σ_1 = 18 × 10^{-20} cm^2, σ_2 = 20 × 10^{-20} cm^2, n = 1.5, $R_1 = R_2$ = 0.92, the losses for S and P waves and the ratio of laser thresholds γ are calculated as a function of incident angle θ. It can be seen in Fig. 2(a) that the overlapping curves for the losses L_S and L_P at the small incident angle, and then gradually separate. As shown in Fig.

#161858 - $15.00 USD Received 19 Jan 2012; revised 13 Feb 2012; accepted 13 Feb 2012; published 22 Feb 2012

2(b), the ratio of laser thresholds γ increases with the incident angle, reaches a maximum, and then falls with further increase in the incident angle. In experiment, we will control the incident angle θ to be approximately 30 degrees to obtain a ratio of γ = 1.5 for achieving a dual-wavelength operation.

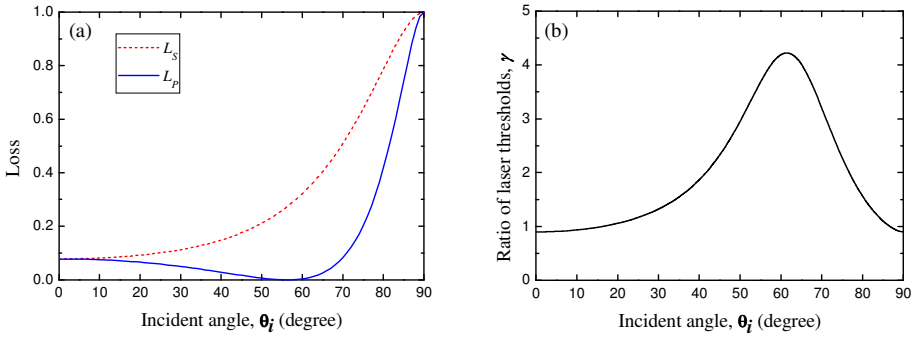

Fig. 2. Calculated results for the dependence of (a) the losses for S and P waves and (b) the ratio of laser thresholds on the incident angle for dual-wavelength operation.

4. Experimental results and discussions

A sketch of the experimental scheme for a cw simultaneous dual-wavelength generation with orthogonal polarizations is presented in Fig. 3. The gain medium was 0.5 at. % Nd:$LuVO_4$ crystal with a length of 8 mm cut along the *a* axis. Both facets of the laser crystal were antireflection-coated at 808 nm and 1080–1100 nm (R <0.2%). The pump source was a 12-W 808-nm fiber-coupled laser diode with a 600-μm fiber core diameter and a numerical aperture of 0.16, reimaged into the laser crystal through a pair of focusing lenses with a focal length of 5 mm and 90% coupling efficiency. The pump spot radius was approximately 200 μm. The input mirror was a 100-cm radius-of-curvature concave mirror with antireflection coating at 808 nm (R <0.2%) on the entrance face and with high-reflectance coating at 1000-1100 nm (R >99.8%) and high-transmittance coating at 808 nm (T >85%) on the second surface. The output coupler was a flat mirror with transmission of 7% near 1090 nm and high transmission at 1064 nm (T >85%) for suppressing the gain oscillation at 1064 nm. The measured transmittance curve for the output coupler is inserted in Fig. 3. An uncoated glass etalon with a thickness of 0.155 mm was used to nearly fit the wavelength separation between two fluorescence peak positions of π and σ polarizations near 1080-1090 nm in Nd:$LuVO_4$ crystal. The laser crystal was wrapped with indium foil and mounted in a water-cooled copper heat sink at 20°C. The cavity length was approximately 17 mm.

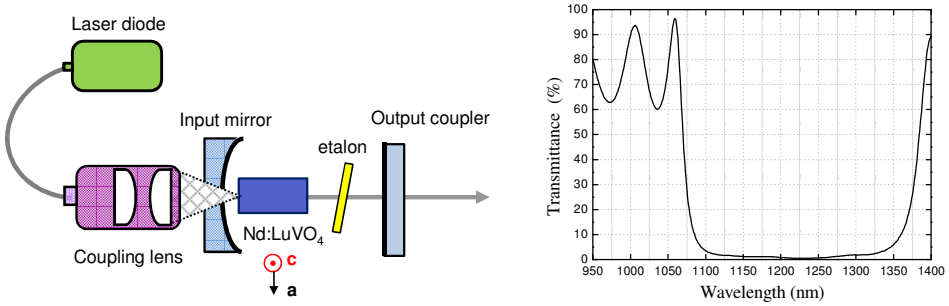

Fig. 3. Schematic of the experimental setup for the dual-wavelength Nd:$LuVO_4$ laser. Right: Measured transmittance curve for the output coupler.

#161858 - $15.00 USD Received 19 Jan 2012; revised 13 Feb 2012; accepted 13 Feb 2012; published 22 Feb 2012

First of all, the cw laser operation without an etalon was performed to study the Nd:$LuVO_4$ laser characteristics. Figure 4 presents the dependence of the average output power on the incident pump power for the single-wavelength Nd:$LuVO_4$ laser at 1089.5 nm. The pump threshold is 0.63 W. The average output power reaches 3.6 W at 12 W of incident pump power. The corresponding optical-to-optical conversion efficiency is 30% with a slope efficiency of approximately 35%. The measured optical spectrum at the maximum output power is depicted in the inset of Fig. 4. The spectral linewidth (FWHM) is about 0.4 nm with the central wavelength at 1089.5 nm. Note that the present laser output is linearly polarized along the π direction.

For achieving the dual-wavelength operation, an uncoated glass etalon was inserted in the laser cavity. By adjusting the inclination of the etalon relative to the optical axis of the resonator, we realized the simultaneous dual-wavelength lasing regime. At an inclined angle near 30 degrees, the dual-wavelength emission at 1086 nm and 1089 nm with orthogonal polarizations was achieved. The dual-wavelength laser was separated into two orthogonally polarized beams with a polarizing beam splitter (PBS), and the average output power for individual wavelengths were measured simultaneously. Figure 5 shows the average output power at each lasing wavelength with respect to the incident pump power at 808 nm. It can be found that the 1086 nm (σ polarization) is lasing prior to the 1089 nm (π polarization) light due to the initial suppression of π polarization by the inclined etalon. The threshold pump power is 4.1 W for 1086 nm, and 5.7 W for 1089 nm, which accords with the calculated result in Fig. 2(b). The output power of 1086-nm line first increases linearly with the pump power, reaches its maximum power of 0.84 W at the pump power of 7.5 W, and then rises monotonically. On the other hand, the output power of 1089-nm line increases linearly as the pump power increases, reaches the intersection of the 1089-nm and 1086-nm curves with an equal power of 0.73 W at the pump power of 8.8 W, and then generates 1.7 W at 12 W of pump power. We believe that the gain competition between 1086-nm and 1089-nm lines leads to the output power of 1086 nm decreases over 7.5 W of pump power. The cw laser operation has good temporal stability without power competition between the two wavelengths. It is worthwhile to mention that the equal power operation of 1086-nm and 1089-nm lines at higher pump power can be promoted by re-angling the etalon.

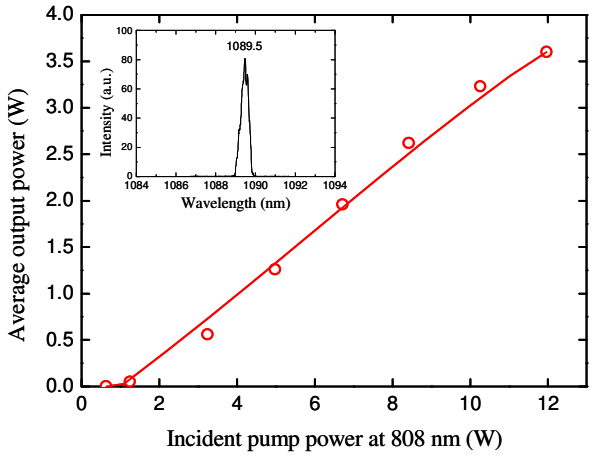

Fig. 4. Average output power versus the incident pump power for single-wavelength operation. Inset, optical spectrum of single-wavelength operation at the maximum output power.

#161858 - $15.00 USD Received 19 Jan 2012; revised 13 Feb 2012; accepted 13 Feb 2012; published 22 Feb 2012

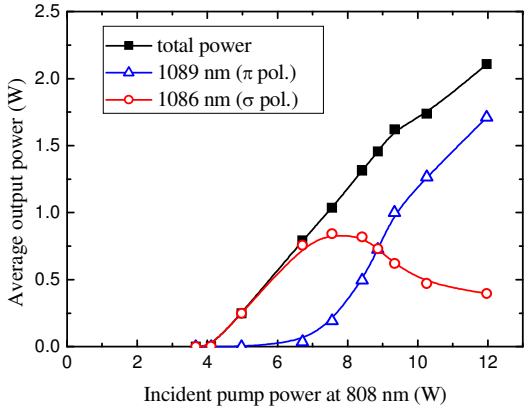

Fig. 5. Average output powers versus the incident pump power for dual-wavelength operation.

The laser beams of both the two polarizations were observed at different pump powers. The M^2 factor of σ polarization is estimated to be approximately 1.1 near threshold, and then increases to be 2.5 at pump power greater than 6 W. On the other hand, the π polarization maintains the beam quality factor M^2 less than 1.3 over the full range of pump powers. It can be deduced that the spatial distribution of σ-polarized component is influenced by the presence of π polarization. The balance the beam quality between two polarized components is currently under further development. Figure 6 shows the measured optical spectrum for the simultaneous dual-wavelength laser at the output power intersection of the two wavelengths. The central wavelengths are 1085.7 nm (σ polarization) and 1088.5 nm (π polarization), in accord with the maximum transmission of the tilted etalon, with the spectral linewidths (FWHM) of 0.1 nm and 0.3 nm, respectively. The wavelength separation of 2.8 nm is equivalent to a frequency difference of 0.7 THz, which is significant for terahertz generation. The simultaneous dual-wavelength Nd:$LuVO_4$ laser is desirable for scientific and practical applications, especially for the development of terahertz sources. Compared with our previously published work [15], the dual-wavelength operation at 1083 nm and 1086 nm in Nd:$GdVO_4$ crystal was achieved with an almost identical experimental setup. However, both the two wavelengths were with the same polarization. Note that it is impossible to generate the dual-wavelength Nd:$GdVO_4$ laser with orthogonal polarizations in the range of 1080–1090 nm owing to the overlap between the emission distributions in π and σ polarizations.

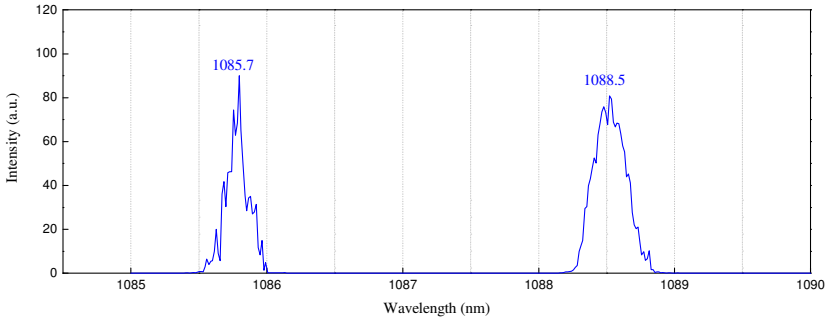

Fig. 6. Optical spectrum of dual-wavelength operation at the output power intersection.

#161858 - $15.00 USD Received 19 Jan 2012; revised 13 Feb 2012; accepted 13 Feb 2012; published 22 Feb 2012

5. Conclusion

The fluorescence propeties of of Nd:YVO_4, Nd:$GdVO_4$ and Nd:$LuVO_4$ crystals for the $^4F_{3/2} \rightarrow {}^4I_{11/2}$ transition have been studied and compared. It shows that the Nd-doped vanadate crystals have the comparable radiation strengths in σ and π polarizations in the range of 1080–1090 nm. In addition, Nd:$LuVO_4$ crystal specifically possesses the wider wavelength separation between the fluorescence peak positions of π and σ polarizations. Based on the superior properties of Nd:$LuVO_4$ crystal, we have numerically analyzed the condition of gain-to-loss balance via an uncoated intracavity etalon for achieving the orthogonally polarized dual-wavelength operation. A diode-pumped dual-wavelength Nd:$LuVO_4$ laser with orthogonal polarizations in the range of 1080–1090 nm has been experimentally demonstrated. The lasing wavelengths are 1085.7 nm and 1088.5 nm belonging to the σ and π polarizations, respectively. At 12 W of incident pump power, the cw output power obtained at 1085.7 nm and 1088.5 nm was 0.4 W and 1.7 W, respectively. We believed that the insertion of an etalon to control the cavity losses of two orthogonal polarizations is a simple and potential method for the low-gain line with a broad-gain bandwidth to realize the simultaneous dual-wavelength laser with orthogonal polarizations.

Acknowledgments

The authors thank the National Science Council for the financial support of this research under Contract No. NSC-100-2628-M-009-001-MY3.

#161858 - $15.00 USD Received 19 Jan 2012; revised 13 Feb 2012; accepted 13 Feb 2012; published 22 Feb 2012

Abstract: A high-pulse-energy eye-safe laser at 1552 nm is effectually generated by an intracavity Nd:YLF/KTP optical parametric oscillator (OPO) with the help of the thermally induced polarization switching. The polarization characteristics of the c-cut Nd:YLF laser at 1053 nm in the continuous-wave (CW) and Q-switched operation are comprehensively investigated. We experimentally verify the thermally induced birefringence can lead to a polarization switching between the mutually orthogonal components of the fundamental pulses. Consequently, an efficient intracavity nonlinear frequency conversion can be achieved in an optically isotropic laser crystal without any additional polarization control. With this finding, the pulse energy and peak power of the compact Nd:YLF/KTP eye-safe laser under an incident pump power of 12.7 W and a pulse repetition rate of 5 kHz are up to 306 μJ and 4 kW, respectively.

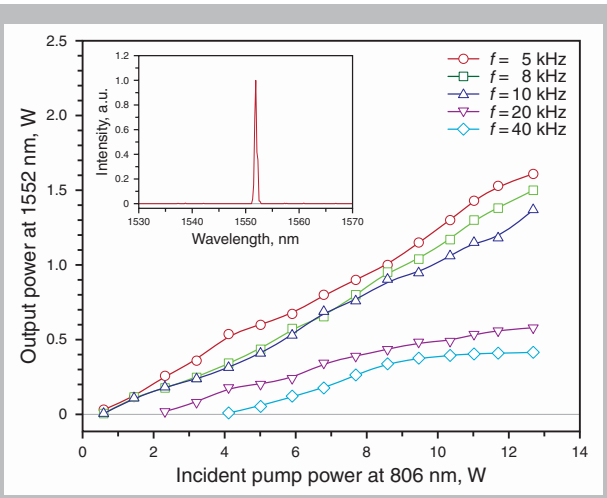

Output powers at 1552 nm as a function of the incident pump power at 806 nm under a pulse repetition rate of 5, 8, 10, 20 and 40 kHz, respectively. Inset – optical spectrum of the Nd:YLF/KTP eye-safe laser

Efficient high-pulse-energy eye-safe laser generated by an intracavity Nd:YLF/KTP optical parametric oscillator: role of thermally induced polarization switching

Y.J. Huang, C.Y. Tang, Y.P. Huang, C.Y. Cho, K.W. Su, and Y.F. Chen *

Department of Electrophysics, National Chiao Tung University, Hsinchu, Taiwan

Received: 19 March 2012, Revised: 22 May 2012, Accepted: 1 June 2012
Published online: 24 August 2012

Key words: Nd:YLF; intracavity OPO; thermal effects; polarization switching

1. Introduction

Among various Nd-doped laser crystals, the negative temperature dependence of the refractive index in the Nd:YLF crystal can partly compensate for the positive contribution of the end-face bulging to exhibit a relatively weak thermal-lensing effect [1–3], which is inherently beneficial for designing high-power solid-state lasers. The Nd:YLF crystal is also highly desirable for generating high-energy pulses thanks to its long upper-state lifetime [4–7]. The fluorescence lifetime of 540 μs at 1053 nm in the c-cut Nd:YLF crystal is expected to be more suitable for constructing high-pulse-energy lasers as compared with that of 490 μs at 1047 nm in the a-cut counterpart [8]. Unfortunately, the transversely isotropic property characterized by the c-cut Nd:YLF crystal leads the polarization state not to be linearly polarized. Note that the Nd:YLF crystal is an uniaxial birefringent crystal that shows distinct emission characteristics between the σ- and π-polarization, where the σ- and π-polarization are defined as the oscillated polarization of the light to be perpendicular and parallel to the crystallographic c axis, respectively. As a result, ef-

* Corresponding author: e-mail: yfchen@cc.nctu.edu.tw

ficient extracavity nonlinear frequency conversions have been scarcely reported with the c-cut Nd:YLF crystal to date because of its randomly polarized emission property.

Nonlinear frequency conversion provides a useful means for extending the spectral range of available solid-state laser sources when the polarization state and the direction of the beam propagation are specifically designed to satisfy the phase matching condition. Linearly polarized fundamental beam is usually adopted to perform an efficient extracavity nonlinear frequency conversion with a simple single-pass configuration. Compared with the extracavity method, the intracavity nonlinear frequency conversion takes the advantage of the multi-pass of the fundamental beam through the nonlinear crystal to effectively reduce the pump threshold and make the resonator more compact. Generally speaking, the multiple round trips can cause the polarization state of the fundamental beam to be changed by the birefringence in the laser cavity. The birefringence-induced polarization switching may be the main mechanism why efficient intracavity nonlinear frequency conversions, such as harmonic generations [9–12] and optical parametric oscillations [13–17], can be successfully realized by using the optically isotropic materials without any active polarization control in the optical resonator. For example, the output power as high as 36.9 W at 532 nm with the Nd:YAG crystal has been achieved by using an intracavity frequency doubling configuration [12], and the intracavity Nd:YAG/KTA optical parametric oscillator (OPO) has efficiently generated the eye-safe radiation at 1.54 μm with the output power up to 12.7 W [17]. However, so far the effect of the birefringence-induced polarization switching in the process of intracavity nonlinear frequency conversion has not been experimentally manifested.

In this Letter, we report on an efficient high-pulse-energy eye-safe radiation in a $KTiOPO_4$ (KTP) based intracavity optical parametric oscillator (IOPO) pumped by a c-cut Nd:YLF laser with the birefringence-induced polarization switching. We exhaustively explore the influences of the thermal effect and the anisotropic property of the acousto-optic (AO) Q-switch on the polarization characteristics of the c-cut Nd:YLF laser in the continuous-wave (CW) and Q-switched operation, respectively. The Q-switched Nd:YLF laser is subsequently utilized to intracavity pump a type-II non-critically phase-matched KTP crystal for the generation of the eye-safe radiation at 1552 nm. We properly measure the temporal behaviors of the depleted fundamental pulses to manifest that the thermally induced birefringence can lead the mutually orthogonal polarization states of the fundamental pulses to be effectively switched. This successive polarization switching is experimentally confirmed to be the key mechanism in achieving an efficient IOPO without any additional polarization control. With this finding, this compact Nd:YLF/KTP eye-safe laser effectually produces the pulse energy and peak power up to 306 μJ and 4 kW under an incident pump power of 12.7 W and a pulse repetition rate of 5 kHz. To the best of our knowledge, this is the largest pulse energy ever reported among the continuously diode-end-pumped Nd-doped crystal/KTP eye-safe lasers.

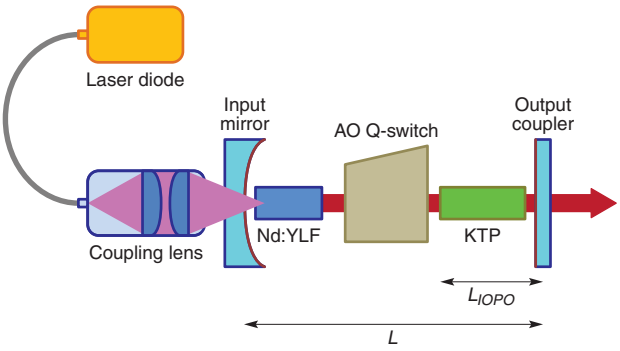

Figure 1 (online color at www.lasphys.com) Schematic of the cavity setup for a KTP-based optical parametric oscillator intracavity pumped by an AO Q-switched c-cut Nd:YLF laser

2. Experimental setup

The experimental setup for the Nd:YLF/KTP eye-safe laser is schematically shown in Fig. 1. The input mirror was a concave mirror with the radius of curvature of 300 mm. It was antireflection (AR) coated at 806 nm on the entrance face, and was coated at 806 nm for high transmission (HT) as well as 1053 nm for high reflection (HR) on the second surface. The gain medium was a 0.8 at.% c-cut Nd:YLF crystal (CASTECH Inc.) with the diameter of 4 mm and the length of 15 mm. Both facets of the laser crystal were AR coated at 806 and 1053 nm. Note that although it is an uniaxial crystal with the highly anisotropic property, the Nd:YLF crystal effectively exhibits the optically isotropic characteristics in the transverse plane when it is cut along the crystallographic c axis. The orientation of the rod axis of the present c-cut crystal to the crystallographic c axis is within 1 degree. The KTP crystal with dimensions of $5\times5\times30$ mm^3 was x-cut at $\theta=90°$, $\phi=0°$ for the type-II non-critically phase-matched OPO operation, which maximizes the effective nonlinear coefficient and eliminates the walk-off effect. The pump face of the KTP crystal was HT coated at 1053 nm as well as HR coated at 1552 nm that acted as the front mirror of the IOPO cavity, while the other face of the KTP crystal was AR coated at 1053 and 1552 nm. Both Nd:YLF and KTP crystals were wrapped with indium foil and mounted in water-cooled copper heat sinks at 18°C. A 20-mm-long AO Q-switch (NEOS technologies) was AR coated at 1053 nm on both surfaces. It was placed in the center of the laser cavity, and was driven at a central frequency of 41 MHz with the radio-frequency (RF) power of 25 W. A flat mirror that is HR coated at 1053 nm and partially-reflection coated at 1552 nm with the reflectance

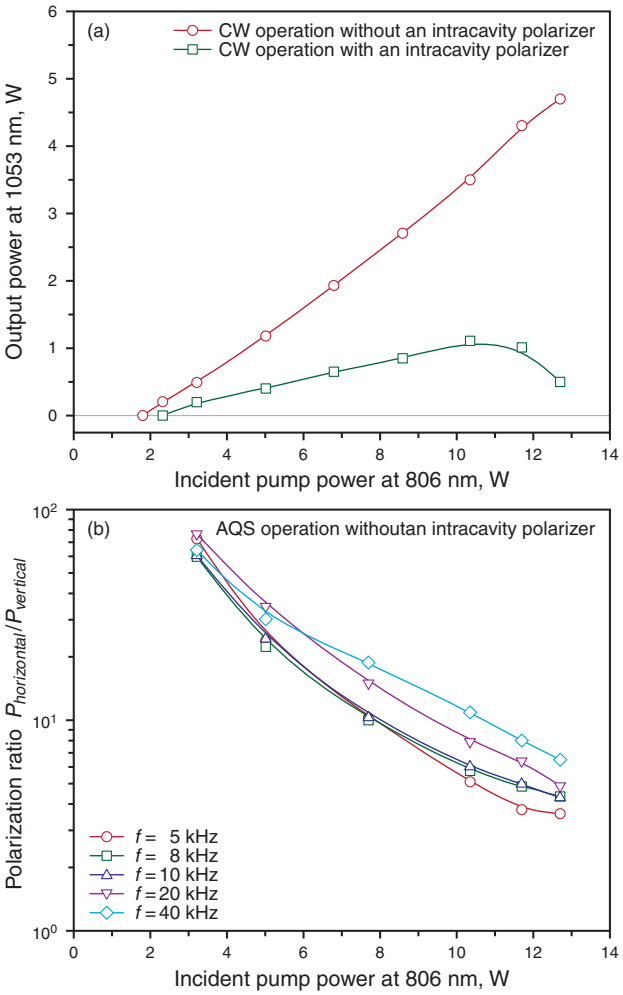

Figure 2 (online color at www.lasphys.com) (a) – output powers at 1053 nm with and without an intracavity polarizer *versus* the incident pump power at 806 nm in the CW operation and (b) – the polarization ratios $P_{horizontal}/P_{vertical}$ with respect to the incident pump power at a pulse repetition rate of 5, 8, 10, 20, and 40 kHz, where $P_{horizontal}$ and $P_{vertical}$ represent the output power with the oscillated polarization to be parallel and perpendicular to the base of the AO Q-switch, respectively

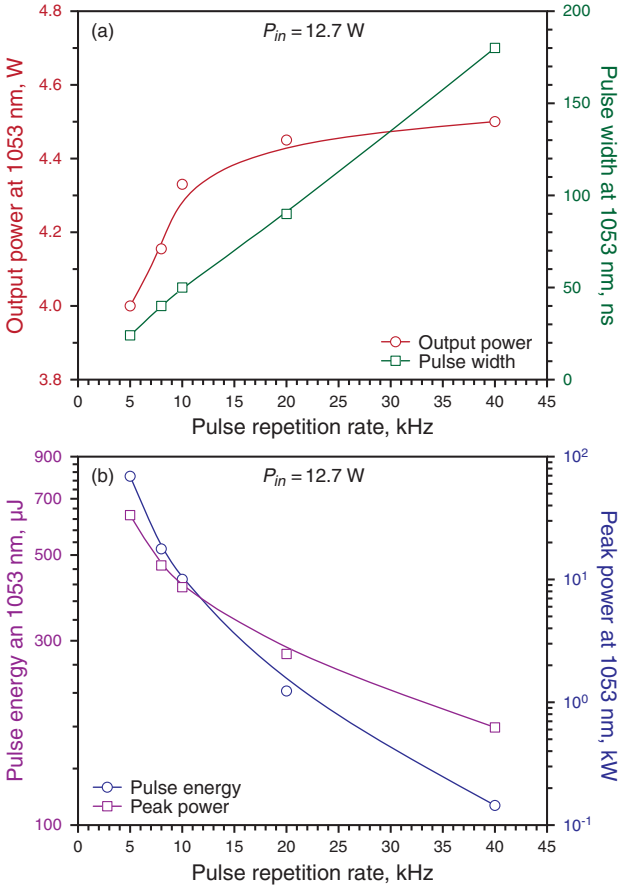

Figure 3 (online color at www.lasphys.com) Dependences of the (a) – output power and pulse width and (b) – pulse energy and peak power at 1053 nm on the pulse repetition rate at an incident pump power of 12.7 W

of 80% was utilized as the output coupler during the experiment. The pump source was an 806-nm fiber-coupled laser diode with the core diameter of 600 μm and the numerical aperture of 0.2, respectively. The polarization state emitted from the fiber-coupled laser diode was measured to be randomly polarized. The pump beam was re-imaged into the laser crystal with a lens set that has the focal length of 25 mm with the magnification of unity and the coupling efficiency of 90%. The lengths of the fundamental laser cavity and the IOPO cavity were set to be $L = 115$ mm and $L_{IOPO} = 32$ mm for the construction of a compact actively Q-switched (AQS) eye-safe laser. The pulse temporal behaviors were recorded by a LeCroy digital oscilloscope (Wavepro 7100, 10 G samples/s, 1 GHz bandwidth) with a fast InGaAs photodiode. The spectral information of the laser output was measured by an optical spectrum analyzer (Advantest 8381A) that is constructed with a diffraction monochromator with the resolution of 0.1 nm.

3. Performance of CW and AQS operation at 1053 nm

First of all, the AO Q-switch and the KTP crystal were removed from the laser cavity to investigate the CW performance of the c-cut Nd:YLF laser, where the output coupler with the reflectance of 80% at 1053 nm was exploited. We utilized an intracavity polarizer to make a comparative study of the output characteristics between the linearly and randomly polarized state, respectively. Fig. 2a illustrates the output powers at 1053 nm with and without an intracavity polarizer *versus* the incident pump power

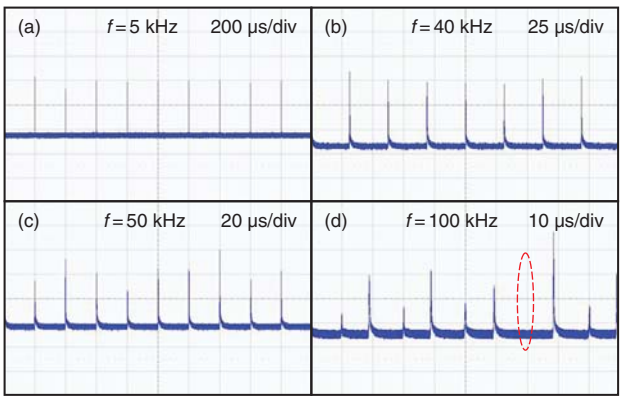

Figure 4 (online color at www.lasphys.com) Pulse trains of the Q-switched Nd:YLF laser at a pulse repetition rate of (a) 5 kHz, (b) 40 kHz, (c) 50 kHz, and (d) 100 kHz. The dashed circle in Fig. 4d indicates the phenomena of the pulse missing

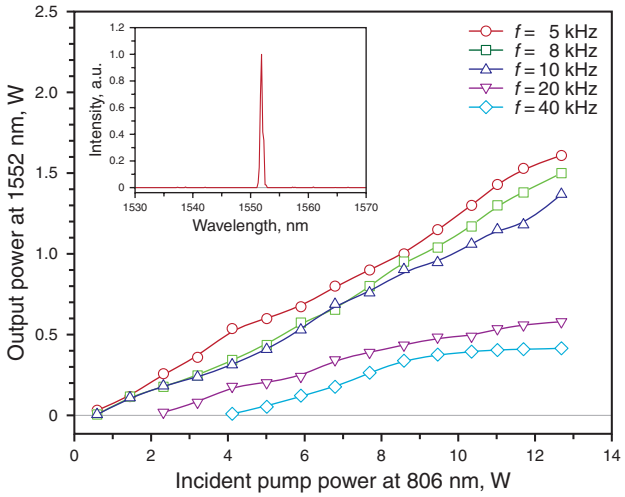

Figure 5 (online color at www.lasphys.com) Output powers at 1552 nm as a function of the incident pump power at 806 nm under a pulse repetition rate of 5, 8, 10, 20 and 40 kHz, respectively. Inset – optical spectrum of the Nd:YLF/KTP eye-safe laser

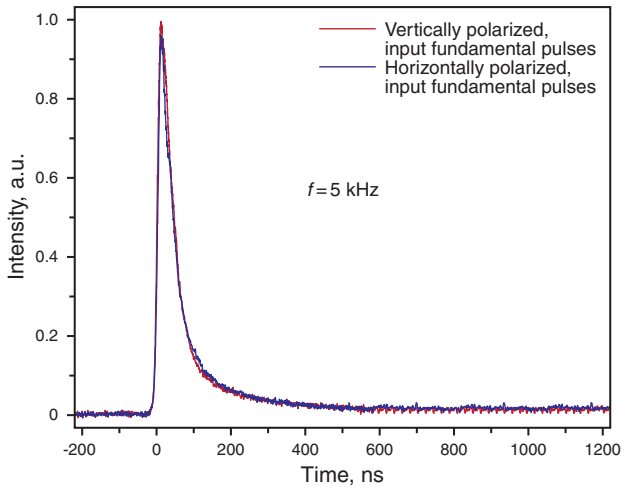

Figure 6 (online color at www.lasphys.com) Temporal behaviors of the originally input fundamental pulses with the mutually orthogonal polarizations at a pulse repetition rate of 5 kHz

at 806 nm. The maximum output power and slope efficiency without an intracavity polarizer are found to be up to 4.7 W and 43.1%, respectively, as depicted by the red curve in Fig. 2a. However, the output power and slope efficiency obtained with an intracavity polarizer are found to be remarkably lower than those obtained without an intracavity polarizer, as revealed by the green curve in Fig. 2a. Moreover, the roll-over phenomena in the linearly polarized state is experimentally observed at an incident pump power of 10.4 W. In the early researches on the solid-state laser, it was found that the thermally induced birefringence of the optically isotropic material brings in the coupling of the power between the mutually orthogonal polarization components. Consequently, the forbidden polarization state would be removed with the introduction of a polarizer inside the laser cavity [18]. This so-called thermal depolarization loss undoubtedly explains why substantially decreased output power and considerably poorer slope efficiency are obtained in the present linearly polarized c-cut Nd:YLF laser.

We then inserted the AO Q-switch into the laser cavity without an intracavity polarizer to explore the polarization characteristics of the c-cut Nd:YLF laser. Figure 2(b) describes the dependences of the polarization ratio $P_{horizontal}/P_{vertical}$ on the incident pump power at a pulse repetition rate of 5, 8, 10, 20, and 40 kHz, where $P_{horizontal}$ and $P_{vertical}$ stand for the output power with the oscillated polarization to be parallel and perpendicular to the base of the AO Q-switch, respectively. The polarization ratios for all cases are found to continuously decrease with the increase of the incident pump power. This observation is similar to the works reported in Refs. [19,20]. The diffractive efficiency of the AO Q-switch operated at the compressional mode is polarization dependent, in which the light with the oscillated polarization that is parallel to the propagation of the acoustic wave experiences lower diffractive loss. In the meantime, the randomly polarized pump beam leads the gain distribution in the c-cut Nd:YLF crystal to be isotropic; that is, the gain for the mutually orthogonal polarization components of the laser beam are the same. As a consequence, the lower diffractive loss makes the horizontally polarized laser beam to own the larger net gain as compared with the vertically polarized one, which produces a high degree of the linearly polarized operation at a low incident pump power. However, the polarization ratio is experimentally found to decrease with increasing the incident pump power owing to the reduced difference

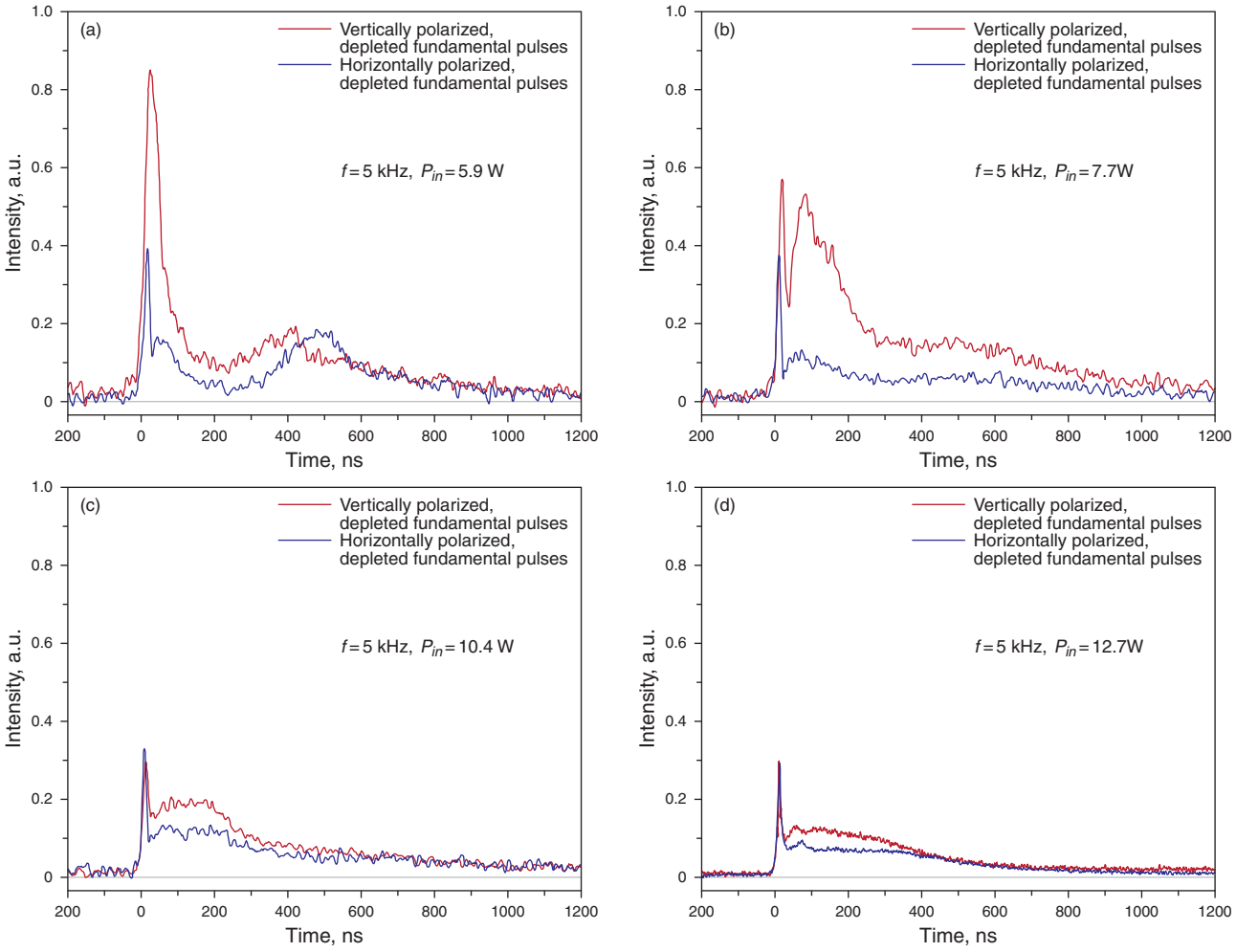

Figure 7 (online color at www.lasphys.com) Temporal behaviors of the mutually orthogonal polarization components of the depleted fundamental pulses at a pulse repetition rate of 5 kHz and an incident pump power of (a) 5.9 W, (b) 7.7 W, (c) 10.4 W, and (d) 12.7 W, respectively

of the net gain between the mutually orthogonal polarization components. Eventually, a nearly random polarization state was acquired at the maximum incident pump power of 12.7 W. Before examining the IOPO conversion efficiency with the KTP crystal, we make a thorough study of the output performance of this AQS Nd:YLF laser.

Fig. 3 depicts the dependences of the output power, pulse width, pulse energy, and peak power on the pulse repetition rate at an incident pump power of 12.7 W. When the pulse repetition rate increases from 5 to 40 kHz, the output power varies from 4.0 to 4.5 W and the pulse width increases linearly from 25 to 180 ns, as shown in Fig. 3a. Consequently, it can be found that the pulse energy changes from 800 to 113 μJ and the peak power decreases from 32 to 0.63 kW with increasing the pulse repetition rate from 5 to 40 kHz, as revealed in Fig. 3b. Fig. 4a – Fig. 4d illustrate the pulse trains of the AQS Nd:YLF laser at a pulse repetition rate of 5, 40, 50, and 100 kHz, respectively. It is experimentally found that the pulse-to-pulse amplitude stability is better than $\pm 8\%$ when the laser operates at 5 – 40 kHz, as exhibited in Fig. 4a and Fig. 4b. Nevertheless, increasing the pulse repetition rate beyond 50 kHz results in an unstable Q-switched operation with the amplitude fluctuation larger than 20%, as revealed in Fig. 4c. Moreover, the phenomena of the pulse missing shown in Fig. 4d is observed at a pulse repetition rate of 100 kHz owing to the lack of the gain for the Q-switched Nd:YLF laser operated at such high pulse repetition rate. Therefore, it is of crucial importance to design an intricate cavity for the stable pulsed operation if the Q-switched Nd:YLF laser with high pulse repetition rate is required [21].

4. Performance of IOPO operation at 1552 nm

When the KTP crystal was inserted into the Q-switched laser cavity and the original IOPO output coupler was employed, the eye-safe pulsed radiation was achieved. The orientation of the y-axis of the KTP crystal is set to be parallel to the base of the AO Q-switch since the fundamental beam is partially polarized in the horizontal direction. As a result, the oscillated polarization of the present eye-safe laser is horizontally polarized as derived from the type II phase matching condition. Fig. 5 displays the output powers at 1552 nm with respect to the incident pump power at 806 nm at a pulse repetition rate of 5, 8, 10, 20, and 40 kHz, while the inset of Fig. 5 shows the optical spectrum of the OPO signal pulses with the central wavelength at 1552 nm. If the polarization state of the fundamental beam changes from linear to nearly random status with increasing the incident pump power as observed in Fig. 2b, the saturation of the output powers at 1552 nm should be expected. However, it is apparent that the output powers at 1552 nm are almost linearly proportional to the incident pump power at 806 nm in the present situation. For the sake of discovering the interacted mechanism between the fundamental and OPO signal pulses, we used a polarization beam splitter to simultaneously monitor the temporal behaviors of the mutually orthogonal polarization components of the depleted fundamental pulses. Firstly, figure 6 describes the input fundamental pulses without the IOPO conversion at a pulse repetition rate of 5 kHz. It is obvious that the behaviors of the originally input fundamental pulses with mutually orthogonal polarizations are nearly the same. Fig. 7a – Fig. 7d illustrate the characteristics of the depleted fundamental pulses with mutually orthogonal polarizations at a pulse repetition rate of 5 kHz when the incident pump power is increased. Note that the intensities for each case are normalized with respect to the peak of the originally input fundamental pulses. Initially, the 1552-nm pulses are mainly generated by the horizontally polarized fundamental pulses, which is consistent with the requirement of the type-II phase matching. However, it is experimentally found that the vertically polarized fundamental pulses can switch to the horizontally polarized state to participate in the IOPO conversion process. Further increasing the incident pump power, more and more parts of the vertically polarized fundamental pulses are contributed to the generation of the eye-safe radiation, as can be seen clearly in Fig. 7a – Fig. 7d. Although the effect of the optically induced birefringence has been explored in the optically isotropic Nd:Glass and Nd:YAG crystals [22,23], we infer that the thermally induced birefringence is the main mechanism that explains the polarization interaction and switching in the present IOPO conversion process. The deduction is based on the degree of the polarization switching is increased with increasing the incident pump power. It is also worthwhile to mention that the polarization switching is consistent with the roll-over phenomena obtained with the linearly polarized c-cut Nd:YLF laser in Sec. 3, both observations are originated from the fact of the polarization state to be significantly influenced by the thermal effect in the laser crystal. To be brief, we first experimentally manifest that the thermally induced polarization switching plays a vital role in accomplishing an efficient intracavity conversion process in an optically isotropic crystal without any active polarization control. We believe that the observed phenomena can provide important insights into the laser physics in an intracavity nonlinear frequency conversion process.

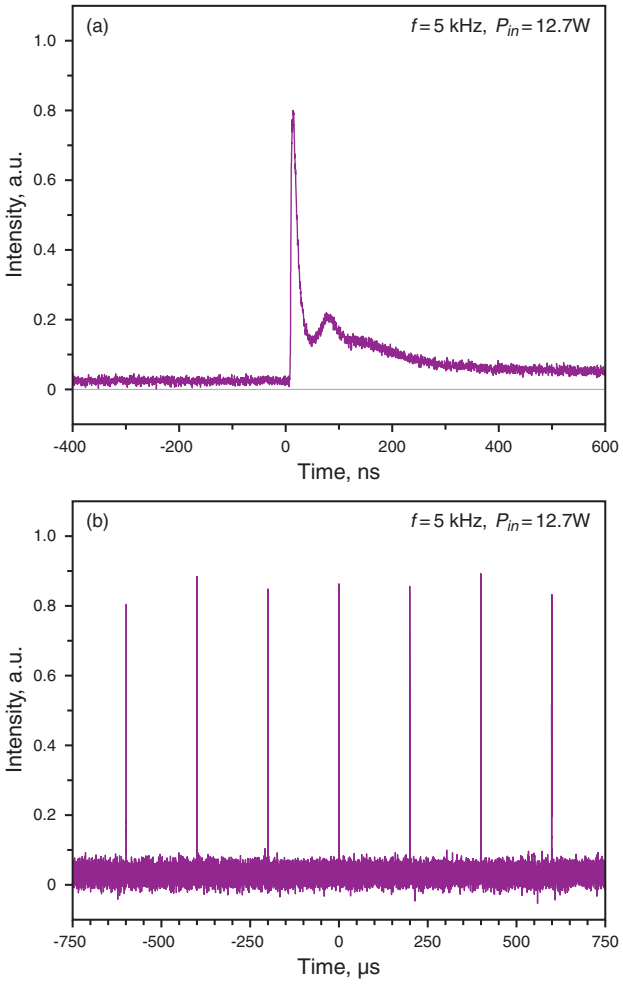

Figure 8 (online color at www.lasphys.com) Typical temporal behaviors of the eye-safe pulses at an incident pump power of 12.7 W and a pulse repetition rate of 5 kHz with: (a) the time span of 1 μs and (b) the time span of 1.5 ms

Fig. 8a and Fig. 8b demonstrate the typical temporal behaviors of the single pulse shape and pulse trains at 1552 nm under an incident pump power of 12.7 W and a pulse repetition rate of 5 kHz. The relatively long pulse with a remarkable tail depicted in Fig. 8a means that the eye-safe radiation is generated with several round trips inside the IOPO cavity. Consequently, the time-averaged ef-

fect as a result of this long pulse duration can alleviate the instability probably caused by the polarization switching of the fundamental pulses. The above-mentioned inspection can also be confirmed by referring to Fig. 8b, where the peak-to-peak amplitude fluctuation is experimentally found to be within 10% over an hour-long operation. According to Fig. 5, the maximum output power at 1552 nm is up to 1.56 W under an incident pump power of 12.7 W and a pulse repetition rate of 5 kHz, corresponding to the diode-to-signal conversion efficiency of 12.3%. The optical conversion efficiency is comparable with those obtained with the eye-safe lasers driven by the linearly polarized fundamental pulses thanks to the assistance of the thermally induced polarization switching [24–27]. On the basis of the Fig. 5 and Fig. 8, the pulse energy can be calculated to be as high as 312 μJ and the peak power can be numerically evaluated to be about 4 kW. In comparison with the reported KTP-based IOPOs pumped by the continuously diode-end-pumped Nd-doped crystal lasers, we have achieved the largest pulse energy of the eye-safe radiation by using the Nd:YLF crystal as a gain medium. This implies that the Nd:YLF crystal is potentially favorable to be employed for the construction of high-pulse-energy lasers.

5. Conclusion

In summary, we have demonstrated an efficient high-pulse-energy eye-safe radiation in a Nd:YLF/KTP IOPO with the help of thermally induced polarization switching. The polarization characteristics of the c-cut Nd:YLF laser in the CW and AQS operation are comprehensively investigated and discussed. We properly measure the temporal behaviors of the depleted fundamental pulses and manifestly find that the thermally induced birefringence can lead the mutually orthogonal polarization states of the fundamental pulses to be effectively switched for accomplishing an efficient IOPO operation without any extra polarization control. With this finding, the pulse energy as high as 306 μJ with the optical conversion efficiency up to 12.3% is achieved in our compact Nd:YLF/KTP eye-safe laser under an incident pump power of 12.7 W and a pulse repetition rate of 5 kHz.

Acknowledgements The authors thank the National Science Council for their financial support of this research under Contract No. NSC-97-2112-M-009-016-MY3.

References

[1] C. Pfistner, R. Weber, H.P. Weber, S. Merazzi, and R. Gruber, IEEE J. Quantum Electron. **30**, 1605–1615 (1994).
[2] W.A. Clarkson, P.J. Hardman, and D.C. Hanna, Opt. Lett. **23**, 1363–1365 (1998).
[3] P.J. Hardman, W.A. Clarkson, G.J. Friel, M. Pollnau, and D.C. Hanna, IEEE Quantum Electron. **35**, 647–655 (1999).
[4] S.D. Pan, L. Xue, X.W. Fan, H.T. Huang, and J.L. He, Opt. Commun. **272**, 178–181 (2007).
[5] D.J. Li, Z. Ma, R. Haas, A. Schell, P. Zhu, P. Shi, and K.M. Du, Opt. Lett. **33**, 1708–1710 (2008).
[6] C. Bollig, C. Jacobs, M.J.D. Esser, E.H. Bernhardi, and H.M. von Bergmann, Opt. Express **18**, 13993–14003 (2010).
[7] K. Zhong, J.Q. Yao, Y.Y. Wang, D.G. Xu, and P. Wang, Opt. Laser Technol. **43**, 636–641 (2011).
[8] S.D. Pan, K.Z. Han, H.M. Wang, X.W. Fan, and J.L. He, Chin. Opt. Lett. **4**, 407–409 (2006).
[9] Y.H. Chen, W. Hou, H.B. Peng, H.L. Zhang, L. Guo, H.B. Zhang, D.F. Cui, and Z.Y. Xu, Opt. Commun. **270**, 58–62 (2007).
[10] B.-T. Zhang, J.-F. Yang, J.-L. He, H.-T. Huang, X.-L. Dong, J.-L. Xu, C.-H. Zuo, and K.-J. Yang, Laser Phys. **19**, 1389–1394 (2009).
[11] Q. Zheng, Y. Yao, D.P. Qu, K. Zhou, Y. Liu, and L. Zhao, J. Opt. Soc. Am. B **26**, 1939–1943 (2009).
[12] B. Ji, X.S. Zheng, Z.P. Cai, H.Y. Xu, and F.Q. Jia, Laser Phys. **22**, 406–410 (2012).
[13] A. Dubois, S. Victori, T. Lépine, P. Georges, and A. Brun, Appl. Phys. B **67**, 181–183 (1998).
[14] Z. Liu, Q. Wang, X. Zhang, Z. Liu, J. Chang, H. Wang, S. Fan, W. Sun, G. Jin, X. Tao, S. Zhang, and H. Zhang, Appl. Phys. B **92**, 37–41 (2008).
[15] B.T. Zhang, X.L. Dong, J.L. He, H.T. Huang, K.J. Yang, C.H. Zuo, J.L. Xu, and S. Zhao, Laser Phys. Lett. **5**, 869–873 (2008).
[16] Z.J. Liu, Q.P. Wang, X.Y. Zhang, Z.J. Liu, J. Chang, H. Wang, S.Z. Fan, S.T. Li, S.S. Huang, W.J. Sun, G.F. Jin, X.T. Tao, S.J. Zhang, and H.J. Zhang, J. Phys. D **41**, 135112 (2008).
[17] W.J. Sun, Q.P. Wang, Z.J. Liu, X.Y. Zhang, F. Bai, X.B. Wan, G.F. Jin, X.T. Tao, and Y.X. Sun, Appl. Phys. B **104**, 87–91 (2011).
[18] W. Koechner, Solid–State Laser Engineering, 6th ed. (Springer, Berlin, 2005), chap. 7.
[19] C. Lowrie, A. Zygmunt, A. Crout, Y.S. Liu, and J.R. Thompson, Appl. Opt. **34**, 4256–4260 (1995).
[20] T. Crawford, C. Lowrie, and J.R. Thompson, Appl. Opt. **35**, 5861–5869 (1996).
[21] Y. Sun, H. Zhang, Q. Liu, L. Huang, Y. Wang, and M. Gong, Laser Phys. Lett. **7**, 722–725 (2010).
[22] Z. Blaszczak, Proc. SPIE **2202**, 469–480 (1995).
[23] P. Deb, K.C. Gupta, C.G. Murali, L.J. Dhareshwar, and B.K. Godwal, J. Opt. A **8**, 903–908 (2006).
[24] Y.F. Chen, S.W. Chen, S.W. Tsai, and Y.P. Lan, Appl. Phys. B **76**, 263–266 (2003).
[25] W. Żendzian, J.K. Jabczyński, P. Wachulak, and J. Kwiatkowski, Appl. Phys. B **80**, 329–332 (2005).
[26] H.T. Huang, J.L. He, X.L. Dong, C.H. Zuo, B.T. Zhang, G. Qiu, and Z.K. Liu, Appl. Phys. B **90**, 43–45 (2008).
[27] H.Y. Zhu, Y.M. Duan, G. Zhang, C.H. Huang, Y. Wei, W.D. Chen, H.Y. Wang, and G. Qiu, Laser Phys. Lett. **7**, 703–706 (2010).

Abstract: We develop a practical method to extend the power scale-up for a laser in a concave-plano cavity to be influenced by a large negative thermal lens. With the developed method, we successfully scale up the output power of a compact high-pulse-energy passively Q-switched Nd:YLF laser at 1053 nm with the Cr^{4+}:YAG crystal as a saturable absorber. At an incident pump power of 12.6 W, the maximum output power under the optimum operation at 1053 nm reaches 2.61 W with a pulse width of 6 ns and a pulse repetition rate of 4.6 kHz. More importantly, we experimentally verify that the energy-transfer upconversion significantly enhances the negative focal length of thermal lens in the passively Q-switched Nd:YLF laser.

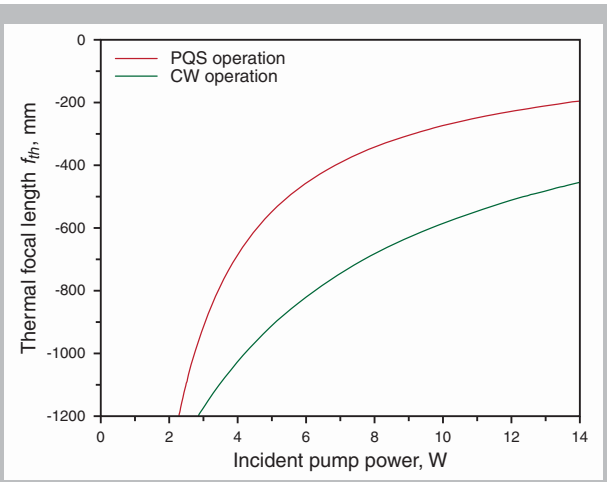

Numerical calculations of the thermal focal length *versus* the incident pump power for the CW and PQS cases

Power scale-up of high-pulse-energy passively Q-switched Nd:YLF laser: influence of negative thermal lens enhanced by upconversion

Y.J. Huang, C.Y. Tang, Y.P. Huang, S.C. Huang, K.W. Su, and Y.F. Chen *

Department of Electrophysics, National Chiao Tung University, Hsinchu, Taiwan

Received: 13 February 2012, Revised: 25 February 2012, Accepted: 1 March 2012
Published online: 12 June 2012

Key words: passive Q-switching; thermal lens; energy-transfer upconversion; Nd:YLF

1. Introduction

Diode-pumped solid-state lasers are useful in a great number of industrial applications and scientific researches. Passive Q-switching of the solid-state laser with a saturable absorber provides a reliable pulsed operation that takes the advantages of high stability, inherent compactness, and low cost [1–3]. The laser crystal with long fluorescence lifetime is highly desirable for continuously pumped passively Q-switched (PQS) laser to generate high-energy pulses. Consequently, the Nd:YLF crystal that is characterized by relatively long upper-state lifetime has large potential for developing a high-pulse-energy pulsed laser with the Cr^{4+}:YAG saturable absorber. Moreover, the Nd:YLF laser is inherently beneficial to be a master oscillator for the Nd:Glass power amplifier due to the excellent spectral overlap between the 1053-nm emission line and the gain peak of the Nd:Glass laser [4].

Practically, using the c-cut Nd:YLF crystal is a convenient way for generating the emission line at 1053 nm, because it can completely avoid the complexities required for the suppression of the unwanted laser transition at 1047 nm. The fluorescence lifetime of 540 μs at 1053 nm in the c-cut Nd:YLF crystal is also expected to be more suitable for producing high-energy pulses as compared with that of 490 μs at 1047 nm in the a-cut counterpart [3].

* Corresponding author: e-mail: yfchen@cc.nctu.edu.tw

However, the implementation of high-pulse-energy PQS Nd:YLF lasers at 1053 nm has not been completely explored yet. The main reason is that the behavior of the thermal-lensing effect in the c-cut Nd:YLF crystal is significantly different from the ones in other popular gain media such as Nd:YVO_4 and Nd:YAG crystals. The critical difference is that the negative dependence of the refractive index on the temperature (*dn/dT*) over the positive contribution from the end-face bulging of the gain medium leads the c-cut Nd:YLF crystal to behave a defocusing thermal lens. Furthermore, the effect of the energy-transfer upconversion (ETU) reduces the effective upper-state lifetime and increases the fractional thermal loading in the laser crystal [5–8]. The ETU effect inevitably causes the effective focal length of the thermal lens in the PQS operation to be considerably more negative than the one in the continuous wave (CW) operation. As a result, a reliable and efficient tactic for designing continuously pumped high-pulse-energy PQS laser at 1053 nm is highly desirable to be developed.

In this work, we develop a straightforward method to implement the power scale-up of a compact high-pulse-energy PQS Nd:YLF laser at 1053 nm with the Cr^{4+}:YAG crystal as a saturable absorber in a concave-plano cavity. We numerically analyze the mode-to-pump size ratio as a function of the thermal focal length to verify that decreasing the radius of curvature (ROC) of the concave mirror can effectually extend the power scale-up for a laser in a concave-plano cavity to be influenced by a large negative thermal lens. With the developed method, we experimentally make a systematic comparison between the CW and PQS operations of the c-cut Nd:YLF laser to confirm the negative thermal-lensing effect enhanced by the ETU effect. At an incident pump power of 12.6 W, the optimum 1053-nm laser produces the maximum output power of 2.61 W with a pulse width of 6 ns and a pulse repetition rate of 4.6 kHz. The corresponding pulse energy and peak power are estimated to be up to 570 μJ and 95 kW, respectively. To the best of our knowledge, these are the largest pulse energy and highest peak power ever reported among continuously pumped PQS Nd-doped crystal/Cr^{4+}:YAG lasers with the same initial transmission.

2. Numerical analyses

Previous studies have demonstrated that the mode-to-pump size ratio plays an important role for power scaling in diode-end-pumped solid-state lasers, in which the optimum mode-to-pump size ratio is practically found to be in the range 0.6 – 1.0 [9–11]. With the ABCD-matrix theory, here we take into account of the thermal-lensing effect to numerically calculate the mode-to-pump size ratio as a function of the thermal focal length for the cases of R = 50 mm, 100 mm, 200 mm, and 500 mm in a concave-plano cavity, where R is the ROC of the input concave mirror. In the present analyses, the pump radius ω_{p0} = 210 μm and the cavity length L_{cav} = 35 mm are used, and the thermally induced lens is set to be adjacent to the input concave mirror.

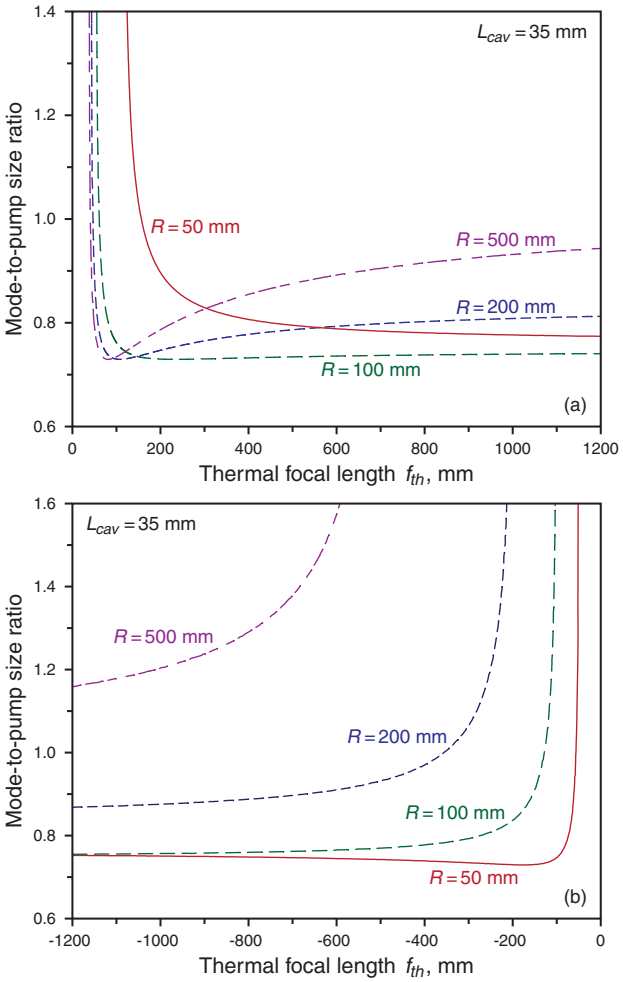

Figure 1 (online color at www.lasphys.com) Calculated results for the mode-to-pump size ratio as a function of the thermal focal length for the cases of R=50 mm, 100 mm, 200 mm, and 500 mm. (a) – positive thermal-lensing effect and (b) – negative thermal-lensing effect

When the positive thermal lens is considered, we find that the mode-to-pump size ratios for all cases are well located between 0.6 – 1.0 in the large operated region, as depicted in Fig. 1a. We also find that the magnitude of the thermal focal length $|f_{th}|$ should be larger than $(RL)/(R-L)$ to satisfy the stability criterion. Because the magnitude of the thermal focal length is inversely proportional to the incident pump power, the higher incident pump power can be allowed by using the concave mirror with larger ROC when the positive thermal lens is regarded.

On the other hand, we find that the ROC of the concave mirror needs to be small enough to fulfill the optimum mode-to-pump size ratio for the case of negative thermal-

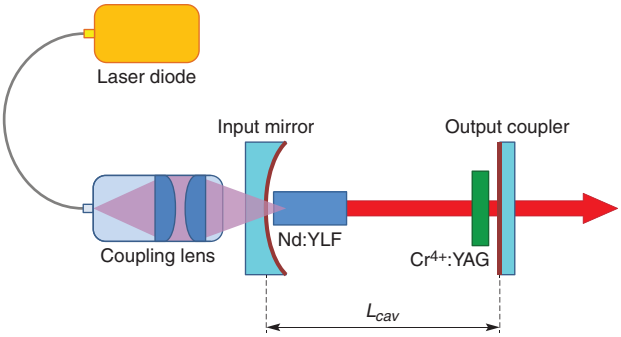

Figure 2 (online color at www.lasphys.com) Configuration of the cavity setup for a diode-pumped PQS Nd:YLF/Cr^{4+}:YAG laser

lensing effect, as shown in Fig. 1b. At the same time, the magnitude of the thermal focal length $|f_{th}|$ is derived to need to be larger than R to keep the cavity stable. On the whole, it is numerically found that decreasing the ROC of the concave mirror is favorable for simultaneously achieving good mode-to-pump size ratio as well as power scaling in a concave-plano cavity that is affected by a negative thermal lens.

3. Experimental setup

The experimental setup is schematically shown in Fig. 2. The input concave mirror was antireflection (AR) coated at 806 nm on the entrance face, and was coated for high transmission at 806 nm as well as for high reflection at 1053 nm on the second surface. The gain medium was a 0.8 at.% c-cut Nd:YLF crystal with the diameter of 4 mm and the length of 15 mm. The Nd:YLF crystal was placed adjacent to the input concave mirror. Both facets of the laser crystal were AR coated at 806 and 1053 nm. The Cr^{4+}:YAG saturable absorber with an initial transmission of 80% was AR coated at 1053 nm on both surfaces, and it was placed near to the output coupler for achieving a high-quality PQS operation. The laser crystal and the saturable absorber were wrapped with indium foil and mounted in water-cooled copper heat sinks at 16°C. The pump source was a fiber-coupled laser diode at 806 nm with a core diameter of 400 μm and a numerical aperture of 0.14. The pump beam with the spot radius of 210 μm was re-imaged inside the laser crystal with a lens set that has the focal length of 25 mm and the coupling efficiency of 90%. The flat output coupler with the reflectivity of 74% at 1053 nm was employed throughout the experiment. The cavity length was set to be 35 mm for the construction of a compact PQS laser. The pulse temporal behaviors were recorded by a LeCroy digital oscilloscope (Wavepro 7100, 10 G samples/s, 1 GHz bandwidth) with a fast InGaAs photodiode.

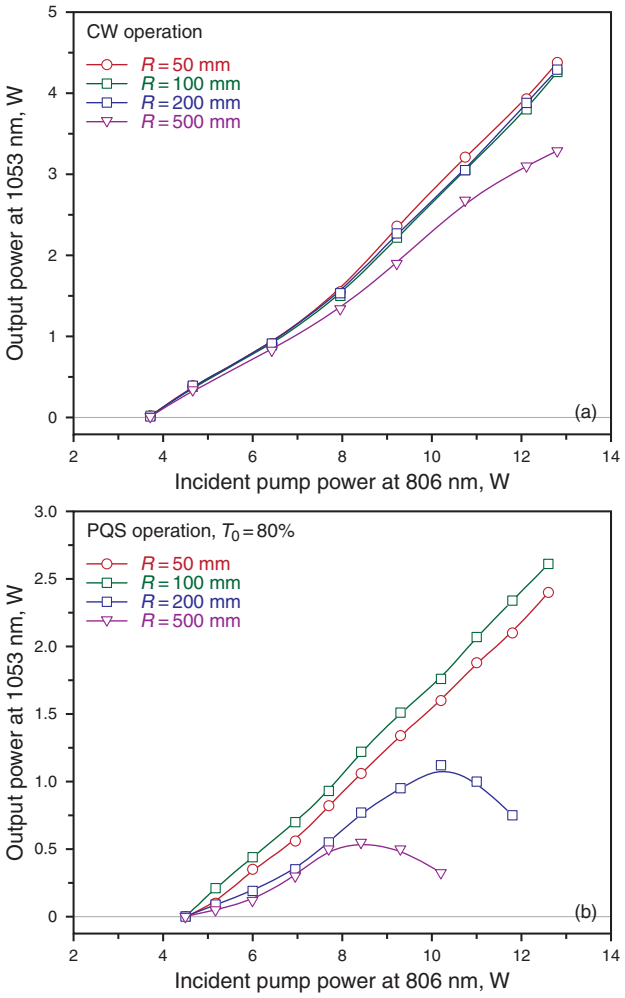

Figure 3 (online color at www.lasphys.com) Output power as a function of the incident pump power for the cases of $R = 50$ mm, 100 mm, 200 mm, and 500 mm. (a) – in the CW operation and (b) – in the PQS operation

4. Performance of CW and PQS operations

First of all, the CW operation without the saturable absorber was studied. Fig. 3a shows the output power at 1053 nm as a function of the incident pump power at 806 nm for the cases of $R = 50$ mm, 100 mm, 200 mm, and 500 mm. It is obvious that although the pump thresholds for all cases are almost identical, the slope efficiency obtained with $R = 500$ mm is remarkably lower than those obtained with other three cases. This observation is a result of the poorer mode-to-pump size ratio, as can be referred to Fig. 1b for $R = 500$ mm case.

When the Cr^{4+}:YAG saturable absorber was inserted into the resonator, the degradation in the output power together with the roll-over phenomena for R=200 mm and 500 mm in the PQS operation further highlight the crucial importance of using small ROC of the concave mirror for

power scale-up, as depicted in Fig. 3b. During the early researches on the Nd:YLF crystal, many investigations indicated that power scaling in the Nd:YLF laser is practically hindered by the ETU effect [5–8]. The combined effect of the ETU effect and its subsequent multiphonon relaxation brings in the considerable enhancement of the thermal-lensing effect in the Nd:YLF laser. As a consequence, the increased thermal-lensing effect in the present PQS operation is believed to cause the deterioration in the output powers for $R = 200$ mm and 500 mm. From the analyses of the coupled rate equation, the criterion for good PQS operation is given by [12]:

$$\frac{\ln\left(\frac{1}{T_0^2}\right)}{\ln\left(\frac{1}{T_0^2}\right)+\ln\left(\frac{1}{R_{OC}}\right)}\frac{\sigma_{gs}}{\sigma}\frac{A}{A_s} \gg \frac{\gamma}{1-\beta}\,, \tag{1}$$

where T_0 is the initial transmission of the saturable absorber, R_{OC} is the reflectivity of the output coupler, L is the nonsaturable loss, σ_{gs} is the ground-state absorption cross section of the saturable absorber, σ is the stimulated emission cross section of the gain medium, A/A_s is the ratio of the mode area in the gain medium and in the saturable absorber, γ is the inversion reduction factor, and β is the ratio of the excited-state absorption cross section to the ground-state absorption cross section in the saturable absorber. Since the σ_{gs} value of the Cr^{4+}:YAG crystal ($\sim(20\pm5)\times10^{-19}$ cm^2) is remarkably larger than the σ value of the Nd:YLF crystal (1.2×10^{-19} cm^2), the criterion for good PQS operation is generally satisfied in the Nd:YLF/Cr^{4+}:YAG laser despite the ratio of the mode area A/A_s varies with the incident pump power and the ROC of the concave mirror. In other words, the influence of the changing mode area in the saturable absorber on the PQS performance can be neglected undoubtedly.

To further investigate the influence of the negative thermal lens on the Nd:YLF laser, we evaluate the effective focal length of the thermal lens with the following equation [13,14]:

$$\frac{1}{f_{th}} = \tag{2}$$

$$=\frac{\xi P_{in}}{\pi K_c}\int_0^l \frac{\alpha e^{-\alpha z}}{1-e^{-\alpha z}}\frac{1}{\omega_p^2(z)}\left[\frac{1}{2}\frac{dn}{dt}+(n-1)\alpha_T\frac{\omega_P(z)}{l}\right]dz\,,$$

$$\omega_p(z)=\omega_{p0}\sqrt{1+\left[\frac{M^2\lambda_p}{n\pi\omega_{p0}^2}(z-z_0)\right]^2}\,, \tag{3}$$

where ξ is the fractional thermal loading, P_{in} is the incident pump power, K_c is the thermal conductivity of the laser crystal, l is the length of the laser crystal, α is the absorption coefficient at the pump wavelength λ_p, dn/dT is the temperature dependence of the refractive index, n is the refractive index, α_T is the coefficient of the thermal expansion, M^2 is the pump beam quality factor, and

Figure 4 (online color at www.lasphys.com) Numerical calculations of the thermal focal length *versus* the incident pump power for the CW and PQS cases

$\omega_p(z)$ is the variation of the pump radius, where the pump beam waist ω_{p0} is assumed a distance z_0 from the entrance of the laser crystal. With the following parameters: $K_c = 6.3$ W/m K, $l = 15$ mm, $\alpha = 0.18$ mm^{-1}, $\lambda_p = 806$ nm, $dn/dT = -2\times10^{-6}$ K^{-1}, $n = 1.448$, $\alpha_T = 8.3\times10^{-6}$ K^{-1}, $M^2 = 115$, $\omega_{p0} = 210$ μm, and $z_0 = 3.8$ mm, the thermal focal length with respect to the incident pump power is plotted in Fig. 4. Numerical calculations for the CW case with $\xi = 0.24$ are found to be consistent with the previously published data, where the fractional thermal loading ξ is derived from the quantum defect value. According to the previous studies, the fractional thermal loading influenced by the ETU effect is usually magnified by a factor of ~ 3 as compared with the value in the CW operation. Therefore, we use $\xi = 0.7$ to calculate the PQS case, as revealed in Fig. 4. Numerical calculations for the PQS case are found to be in good agreement with the estimated results deduced from the experimental data shown in Fig. 3b. The deduction is based on the fact that the ROC of the concave mirror needs to be smaller than the magnitude of the thermal focal length to satisfy the stability criterion, as analyzed in Sec. 2. To be brief, a concave mirror with the ROC significantly smaller than the thermal focal length can be effectively used to achieve the power scale-up for a laser influenced by a negative thermal lens with a plano-concave cavity. Moreover, due to the ETU effect, the suitable ROC of the concave mirror for the PQS case is considerably smaller than that for the CW case at the same incident pump power.

In Fig. 3b, the resonator with $R = 100$ mm is found to possess the highest maximum output power of 2.61 W at an incident pump power of 12.6 W. Therefore, we make a thorough study on the performance of the PQS Nd:YLF/Cr^{4+}:YAG laser with $R = 100$ mm. Fig. 5a and Fig. 5b illustrate the dependences of the pulse width, pulse

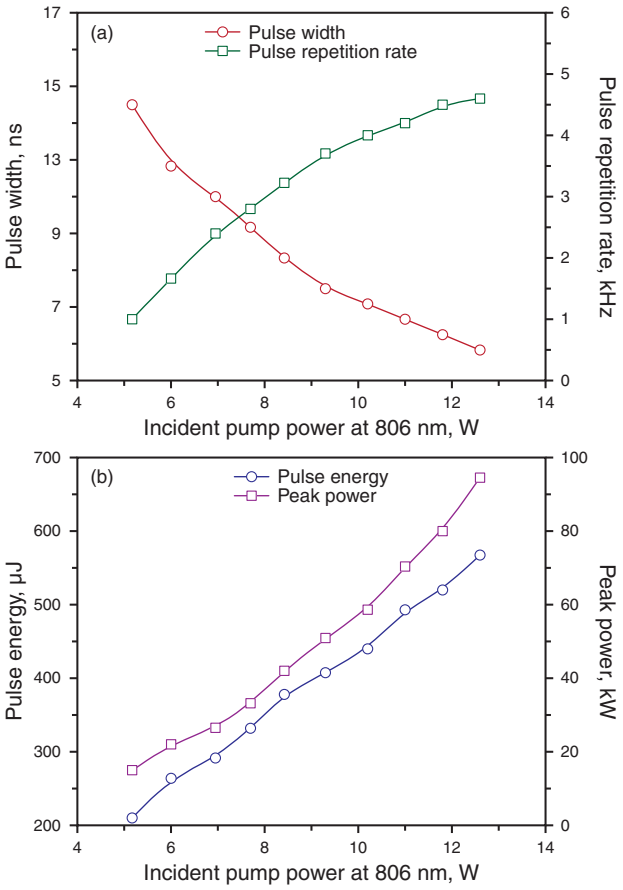

Figure 5 (online color at www.lasphys.com) Dependences of (a) the pulse width, pulse repetition rate and (b) pulse energy, peak power on the incident pump power in the PQS operation with $R = 100$ mm

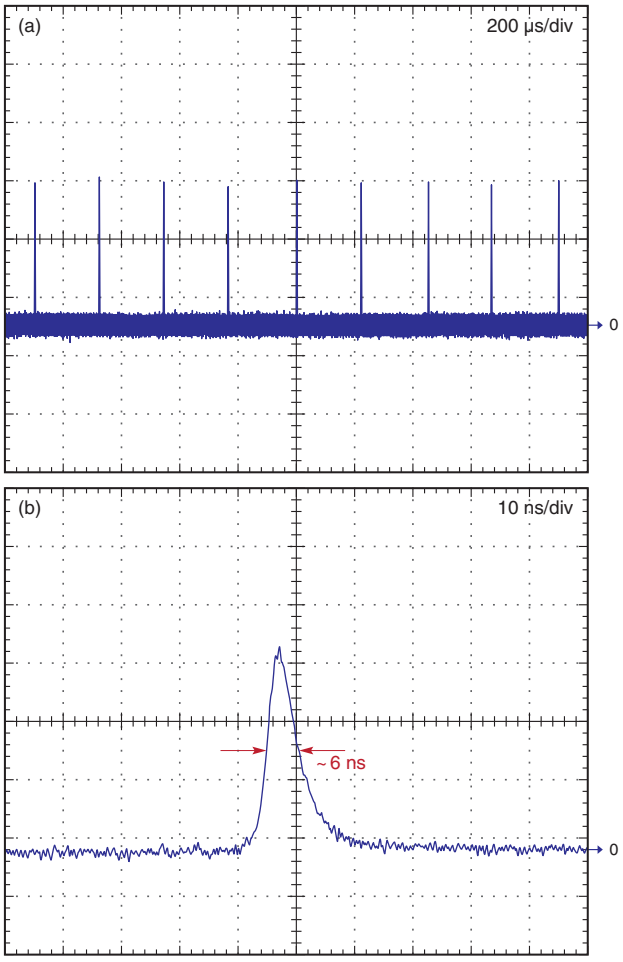

Figure 6 (online color at www.lasphys.com) Typical temporal behaviors at 1053 nm with (a) – time span of 2 ms and (b) – time span of 100 ns

repetition rate, pulse energy and peak power on the incident pump power. When the incident pump power increases from 5.17 to 12.6 W, the pulse width decreases from 14s to 6 ns and the pulse repetition rate varies from 1.0 to 4.6 kHz, as shown in Fig. 5a. Accordingly, it can be seen that the pulse energy increases from 210 to 570 μJ and the peak power changes from 15 to 95 kW with increasing the incident pump power from 5.17 to 12.60 W, as revealed in Fig. 5b. Typical temporal behaviors of the output pulses at an incident pump power of 12.6 W are shown in Fig. 6a and Fig. 6b with the time span of 2 ms and 100 ns, respectively. The pulse-to-pulse amplitude fluctuation is generally found to be within $\pm 3\%$.

Finally, it is worthwhile to mention that so far the pulse energies obtained with the continuously pumped PQS Nd-doped crystal/Cr^{4+}:YAG lasers, such as the Nd:YAG [1,2], c-cut Nd:YLF [3], Nd-doped vanadate crystals [1], and so on, are not more than ~ 300 μJ. That is to say, the pulse energy based on the $^4F_{3/2} \rightarrow {}^4I_{11/2}$ transition is significantly enhanced in our present work. This indicates that the c-cut Nd:YLF crystal is potentially favorable for the construction of high-pulse-energy lasers as long as the optical resonator is intricately designed to compensate for the large negative thermal-lensing effect in the gain medium.

5. Conclusion

In summary, we have found that decreasing the ROC of the concave mirror can usefully extend the power scale-up for a laser in a concave-plano cavity to be influenced by a large negative thermal lens. With this finding, we have developed a practical tactic to scale up the output power of a compact high-pulse-energy PQS Nd:YLF laser at 1053 nm with the Cr^{4+}:YAG crystal as a saturable absorber. At an incident pump power of 12.6 W, the optimum PQS laser at 1053 nm emits the maximum output power of 2.61 W with a pulse width of 6 ns and a pulse repetition rate of 4.6 kHz. The corresponding pulse energy and peak power are up to

570 μJ and 95 kW, respectively. We further experimentally confirmed that the negative focal length of the thermal lens is considerably enhanced by the ETU effect in the PQS Nd:YLF laser.

Acknowledgements The authors thank the National Science Council for their financial support of this research under Contract No. NSC-100-2628-M-009-001-MY3.

References

[1] A. Agnesi, S. Dell'Acqua, C. Morello, G. Piccinno, G.C. Reali, and Z.Y. Sun, IEEE J. Sel. Top. Quantum Electron. **3**, 45–52 (1997).
[2] N. Pavel, J. Saikawa, S. Kurimura, and T. Taira, Jpn. J. Appl. Phys. **40**, 1253–1259 (2001).
[3] S.D. Pan, K.Z. Han, H.M. Wang, X.W. Fan, and J.L. He, Chin. Opt. Lett. **4**, 407–409 (2006).
[4] A.V. Okishev and W. Seka, IEEE J. Sel. Top. Quantum Electron. **3**, 59–63 (1997).
[5] M. Pollnau, P.J. Hardman, M.A. Kern, W.A. Clarkson, and D.C. Hanna, Phys. Rev. B **58**, 16076–16092 (1998).
[6] P.J. Hardman, W.A. Clarkson, G.J. Friel, M. Pollnau, and D.C. Hanna, IEEE J. Quantum Electron. **35**, 647–655 (1999).
[7] J.D. Zuegel and W. Seka, Appl. Opt. **38**, 2714–2723 (1999).
[8] L.C. Courrol, E.P. Maldonado, L. Gomes, N.D. Vieira, Jr., I.M. Ranieri, and S.P. Morato, Opt. Mater. **14**, 81–90 (2000).
[9] Y.F. Chen, T.M. Huang, C.F. Kao, C.L. Wang, and S.C. Wang, IEEE J. Quantum Electron. **33**, 1424–1429 (1997).
[10] Y.F. Chen, T.M. Huang, C.C. Liao, Y.P. Lan, and S.C. Wang, IEEE Photon. Technol. Lett. **11**, 1241–1243 (1999).
[11] Y.F. Chen, Y.C. Chen, S.W. Chen, and Y.P. Lan, Opt. Commun. **234**, 337–342 (2004).
[12] Y.F. Chen, Y.P. Lan, and H.L. Chang, IEEE J. Quantum Electron. **37**, 462–468 (2001).
[13] W. Koechner, Solid-State Laser Engineering, 6th ed. (Springer, Berlin, 2005), chapter 7.
[14] Y.J. Huang, P.Y. Chiang, H.C. Liang, K.W. Su, and Y.F. Chen, Opt. Commun. **285**, 59–63 (2012).

Abstract: We improve the performance of intracavity optical parametric oscillator (IOPO) pumped by a diode-pumped Q-switched Nd:YVO_4/Cr^{4+}:YAG laser. The IOPO cavity is formed independently by a monolithic KTP crystal that the mirrors are directly deposited on top of the nonlinear crystal. We study the performances of this IOPO cavity with different reflectivity of the output coupler at 1.5 μm (R_s) of 80 and 50%. The average power of 1.5 μm is up to 3.3 W at the maximum pump power of 16.8 W for both cases. The diode-to-signal conversion efficiency is up to 20%, which is the highest one for IOPOs to our best knowledge. At the maximum pump power, the pulse energies are 41 μJ with the pulse width of 3 ns at a pulse repetition rate (PRR) of 80 kHz for $R_s = 80\%$ and 51 μJ with the pulse width of 1.2 ns at a PRR of 65 kHz for $R_s = 50\%$, respectively. The pulse amplitude fluctuations in standard deviation are 2.6% for $R_s = 80\%$ and 4% for $R_s = 50\%$, respectively.

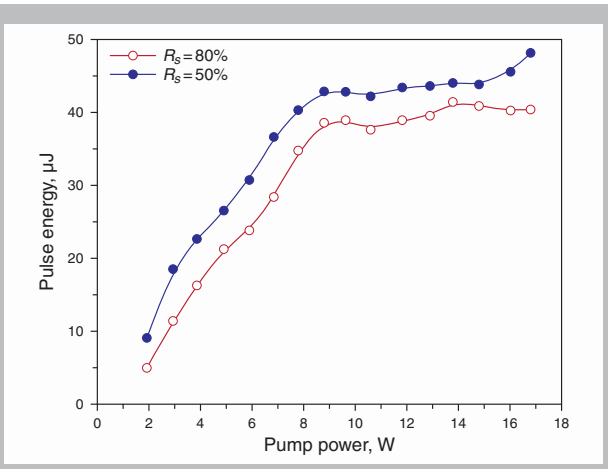

Dependence of the pulse repetition rate at 1572 nm on the pump power for different KTPs with $R_s = 80\%$ (open symbol) and $R_s = 50\%$ (filled symbol)

Improvement of stability and efficiency in diode-pumped passively Q-switched intracavity optical parametric oscillator with a monolithic cavity

J.Y. Huang, W.Z. Zhuang, Y.P. Huang, Y.J. Huang, K.W. Su, and Y.F. Chen *

Department of Electrophysics, National Chiao Tung University, Hsinchu, Taiwan

Received: 13 February 2012, Revised: 1 March 2012, Accepted: 7 March 2012
Published online: 17 April 2012

Key words: diode-pumped; passively Q-switched;intracavity optical parametric oscillator

1. Introduction

Eye-safe nanosecond 1.5 – 1.6 μm pulsed lasers have a great interest for applications such as remote sensing, range finder, and lidar systems. The optical parametric oscillator is one of the promising and efficient approaches to obtain such light sources. Compared with extracavity optical parametric oscillators (EOPOs), intracavity optical parametric oscillators (IOPOs) have merits of lower thresholds together with higher efficiencies through high intracavity intensities and multiple passes of the fundamental field inside the optical parametric oscillator (OPO) cavities. In the past decades, IOPOs driven by diode-end-pumped passively Q-switched (PQS) Nd-doped crystal lasers have proved an efficient and low-cost technique to generate high-repetition-rate and high-peak-power eye-safe lasers [1–11].

The progress of development is mainly owed to the growth of high-damage-threshold and high-nonlinear-coefficient nonlinear crystals such as $KTiOAsO_4$ (KTA) and $KTiOPO_4$ (KTP). The nonlinear crystal based OPO integrated with the well-developed Q-switched Nd-doped laser makes IOPO a robust and efficient technique. In addition, the OPO cavity design is a crucial issue. We have reported that the scheme of the shared OPO cavity [10] could achieve higher amplitude stability than the coupled cavity

* Corresponding author: e-mail: yfchen@cc.nctu.edu.tw

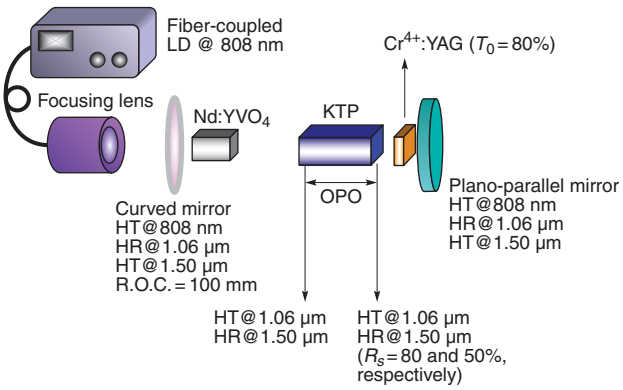

Figure 1 (online color at www.lasphys.com) The schematic diagram of the IOPO experimental setup. HT – high transmission, HR – high reflection, PR – partial reflection, and R.O.C. – radius of curvature

because more longitudinal modes could be simultaneously excited to reach OPO threshold. However, the shared cavity usually leads to lower conversion efficiency than the coupled cavity because of its longer cavity length [10]. The configuration of the coupled OPO cavity is usually designed to share the same output coupler with the fundamental cavity. In the coupled cavity configuration, the amplitude stability of the signal output is severely dependent on the OPO cavity alignment because the resonator length and the longitudinal-mode spacing are different for the fundamental and signal beams. However, it is not capable of aligning individually the IOPO cavity and the fundamental cavity of the coupled cavity. The output power is therefore very sensitive to the alignment of the shared output coupler and is difficult to optimize. The power instability and the diode-to-signal conversion efficiency were 1.72% and 3.70% for an Nd:YAG/KTA laser by Zhang et al. [1], 1.2 and 6.5% for an Nd:YAG/KTP/KTA laser by Huang et al. [6], and 4% together with 18% for an Nd:YVO_4/KTA laser by Zhu et al. [7]. It is practically important to improve the stability and attain high efficiency simultaneously in diode-pumped IOPOs.

In this work, we improve the stability and efficiency in a diode-pumped Q-switched Nd:YVO_4/Cr^{4+}:YAG IOPO laser by employing mirrors to be directly deposited on top of the KTP crystal to form an independent monolithic OPO cavity. We study the performance of this IOPO cavity with different reflectivity of the output coupler at 1.5 μm (R_s) of 80 and 50%. The average power of 1.5 μm was up to 3.3 W at the maximum pump power of 16.8 W for both cases with the instability of 0.2% for $R_s = 80\%$ and 1% for $R_s = 50\%$, respectively. The diode-to-signal conversion efficiency that defined by the ratio of the average power of the signal wavelength (1.5 μm) to the pump wavelength (808 nm) is up to 20%, which is the highest one for IOPOs to our best knowledge.

2. Experimental setup

Fig. 1 presents the schematic experimental setup. The 1064-nm resonator was formed by a plano-convex mirror with radius of curvature of 100 mm and a plano-parallel mirror. The curved mirror was coated with high-transmission coverage (HT, $T > 90\%$) at 1.5 μm, highly reflectivity coverage (HR, $R > 99.8\%$) at 1064 nm, and HT coverage at 808 nm. The end plano-parallel mirror was coated with HR coverage at 1064 nm and HT coverage at 808 nm together with 1.5 μm. The gain medium was a 12-mm-long a-cut 0.3 at.% Nd:YVO_4 crystal. Both end faces of the gain medium were deposited with an anti-reflectivity coverage (AR, $R < 0.2\%$) at 1064 nm. The Cr^{4+}:YAG crystal was 2.5-mm-long with initial transmission (T_0) of 80%. Both end facets of the Cr^{4+}:YAG crystal were also deposited with AR coverage at 1064 nm and 1.5 μm. The gain medium and the Cr^{4+}:YAG crystal were placed as close as possible to the curved mirror and the end plano-parallel mirror, respectively. The cavity length of the 1064-nm resonator was about 100 mm. Two KTP crystals deposited with coatings of different reflectivity at 1.5 μm ($R_s = 80\%$ and $R_s = 50\%$) were employed for comparison. Both of them were 20-mm-long and were deposited AR at 1064 nm and HR at 1.5 μm on one face. The remaining face was deposited with a HT coverage at 1064 nm and $R_s = 80\%$ and $R_s = 50\%$ at 1.5 μm, respectively. KTP crystals were used in a type II non-critical phase-matching (NCPM) configuration along the x-axis ($\theta = 90°$ and $\phi = 0°$). It is worth noting that the NCPM design is to have both a maximum effective nonlinear coefficient and no walk-off between the pump, signal, and idler beams. All the Nd:YVO_4, KTP, and Cr^{4+}:YAG crystals were wrapped with indium foil and mounted in water-cooled copper heat sinks. The water temperature was maintained at 20°C. Our former result [2] used a coupled cavity IOPO that consists of the front mirror of the signal wavelength (1.5 μm) deposited on one end facet of the KTP crystal, and the shared output coupler of the fundamental wavelength (1064 nm) together with the signal wavelength deposited on the Cr^{4+}:YAG. In comparison with our previous work, we use a monolithic KTP crystal alone served as the independent IOPO cavity and use another output coupler to form the fundamental cavity in this work. The pump source was an 808-nm and 18-W fiber-coupled laser diode. The fiber had an 800μm core in diameter and a numerical aperture of 0.2. A focusing lens with 25-mm focusing length and 95% coupling efficiency was used to re-image the pump beam into the gain medium.

3. Experimental results and discussion

There are two criterions required to be satisfied for realizing efficient and stable passively Q-switched Nd:YVO^4/Cr^{4+}:YAG lasers. One is the criterion of second Q-switching threshold that determines the quality and

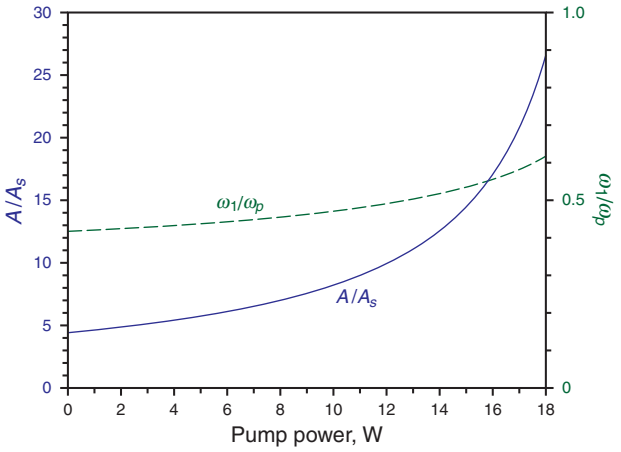

Figure 2 (online color at www.lasphys.com) Calculation results for the dependence of the mode size ratios ω_1/ω_p and A/A_s on the pump power for the present cavity configuration

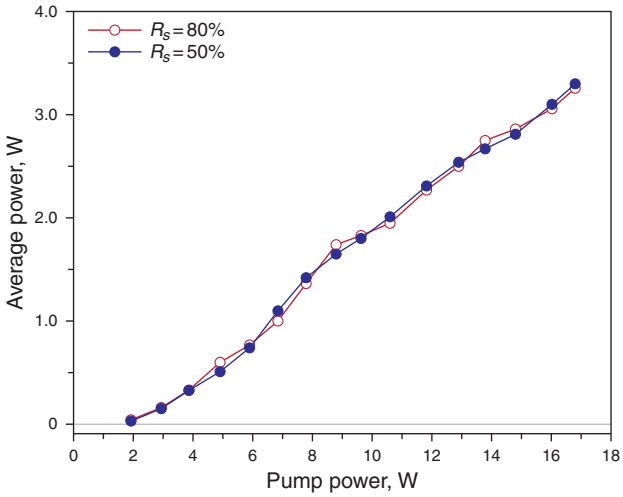

Figure 3 (online color at www.lasphys.com) Dependence of the average signal power at 1572 nm on the pump power for different KTPs with $R_s = 80\%$ (open symbol) and $R_s = 50\%$ (filled symbol)

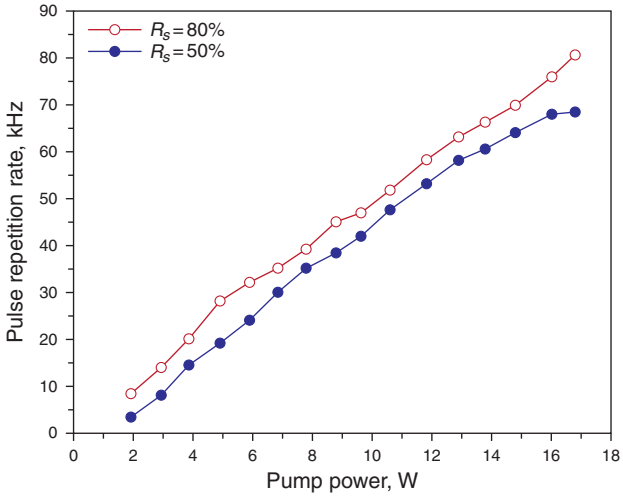

Figure 4 (online color at www.lasphys.com) Dependence of the pulse repetition rate at 1572 nm on the pump power for different KTPs with $R_s = 80\%$ (open symbol) and $R_s = 50\%$ (filled symbol)

stability of Q-switched pulses [12]. The difficulty of Q-switching a Nd:YVO_4 laser by a Cr^{4+}:YAG crystal is chiefly attributed to the cross section mismatch [11]. We have proposed that a hemispherical cavity design is a suggested solution because this cavity could increase the ratio of the effective mode area at Nd:YVO_4 (A) to that at Cr^{4+}:YAG crystals (A_s) to meet the second Q-switching criterion [11]. With the equation (14) in [12], the required value of A/A_s for the present setup was calculated to be higher than 3. The second one named mode-to-pump ratio is the ratio of the effective mode radius at gain medium (ω_1) and that of the pump laser (ω_p). This criterion decides the optical efficiency and the output power. The ratio of ω_1 to ω_p is demanded to be 0.6 – 1.0 for pump power higher than 10 W to reach good mode matching [13]. Fig. 2 depicts the values of ω_1/ω_p and A/A_s with respect to the pump power by use of the mode size calculation method [14], respectively. As seen in this figure, the value of ω_1/ω_p is higher than 0.6 and A/A_s is higher than 5 for all pump powers. Hence the pump-to-cavity mode matching and the second Q-switching criterion are satisfied simultaneously for this experimental setup.

Fig. 3 shows the average signal power at 1572 nm with respect to the pump power for different KTPs with $R_s = 80\%$ (open symbol) and $R_s = 50\%$ (filled symbol), respectively. The 808-nm pump thresholds were about 2 W. Maximum output powers were 3.3 W for both cases. There was no obvious power roll-off for both cases. The diode-to-signal optical conversion efficiency was about 20%, which is the highest conversion efficiency for IOPOs to our best knowledge. The improvement of average power as well as the conversion efficiency is very significant in comparison with our previous similar experiment [2]. Fig. 4 presents the pulse repetition rate (PRR) with respect to the pump power for different KTPs with $R_s = 80\%$ (open symbol) and $R_s = 50\%$ (filled symbol), respectively. Both PRRs increase nearly linearly with the pump power and reach 80 kHz for $R_s = 80\%$ and 68 kHz for $R_s = 50\%$ at the maximum pump power of 16.8 W, respectively. The pulse energy versus the pump power for different KTPs with $R_s = 80\%$ (open symbol) and $R_s = 50\%$ (filled symbol) is shown in Fig. 5. The pulse energy is obtained by calculating the value of the average power times the inverse of the PRR. Both pulse energies increase with the pump power initially and start to saturate at about 45 μJ

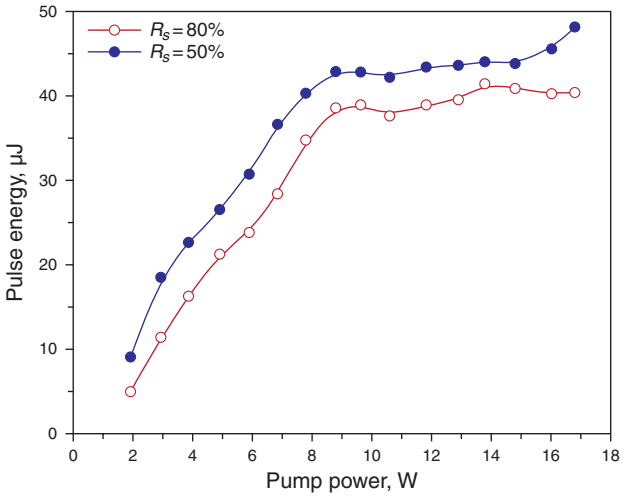

Figure 5 (online color at www.lasphys.com) Dependence of the pulse energy at 1572 nm on the pump power for different KTPs with $R_s = 80\%$ (open symbol) and $R_s = 50\%$ (filled symbol)

under a pump power of 9 W. The photodiode does not saturate because the PRR still increases with the pump power. The pulse energy saturation could be regarded as the satisfaction of the second Q-switching threshold.

Fig. 6 and Fig. 7 show the oscilloscope traces, those were recorded with a LeCroy digital oscilloscope (Wavepro 7100, 10 G samples/sec, 1 GHz bandwidth) with a fast InGaAs photodiode. Fig. 6 shows the typical oscilloscope traces of the Q-switched pulse train of both cases at the maximum pump power. The amplitude fluctuations in standard deviation are 2.6% for $R_s = 80\%$ and 4% for $R_s = 50\%$, respectively. Fig. 7 presents the oscilloscope traces of a single pulse of the fundamental (1064 nm) and signal (1572 nm) wave at various pump powers for (a) $R_s = 80\%$ and (b) $R_s = 50\%$, respectively. For the case of $R_s = 80\%$, the number of satellite pulses in signal wave increased with the escalating pump power. The ratio of the pulse energy of the major pulse to that of the entire pulses was calculated to be 10 – 15% for the pump power higher than 12 W, where the pulse width of the major pulse was 2 – 3 ns. Hence the maximum peak power was estimated to be 1 – 2 kW. On the other hand, for the case of $R_s = 50\%$, the satellite pulse is not obvious for all pump powers because the conversion threshold is increased by reducing the R_s [15,16]. Noticeably, the satellite pulse is absent at the maximum pump power. The pulse duration is about 1.2 ns for all pump powers and the highest peak power is thus estimated to be 43 kW. To study the average power stability of the two cases, an hour-long power fluctuation test was demonstrated. As shown in Fig. 8, the averaged output power was 3.34 W with a standard deviation of 6.9 mW for $R_s = 80\%$ and the averaged output power was 3.3 W with a standard deviation of 35 mW for $R_s = 50\%$. The corresponding fluctuations in standard deviation are 0.2 and 1.0% for $R_s = 80\%$ and $R_s = 50\%$, respectively.

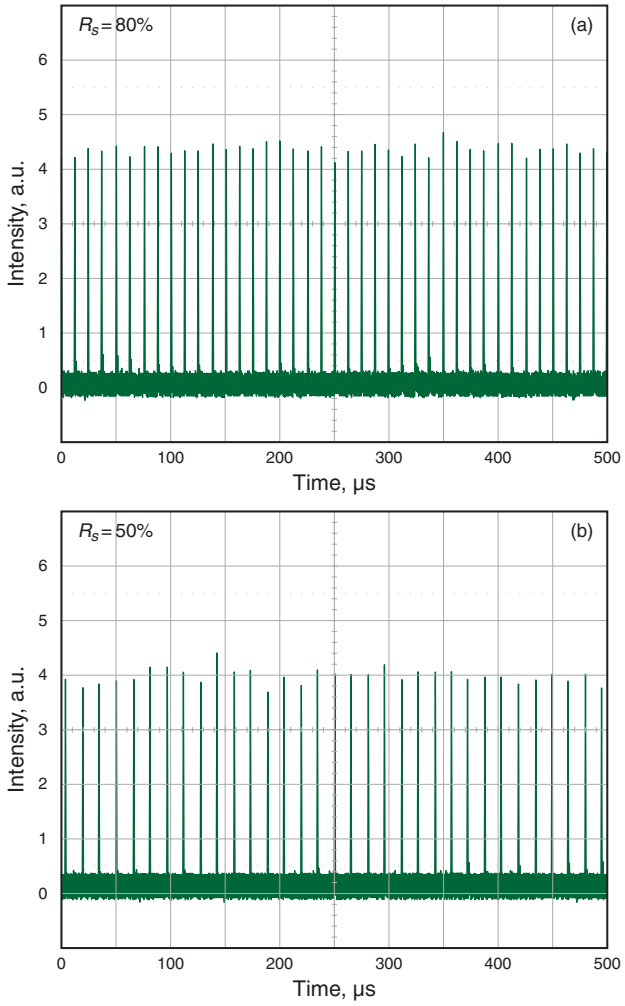

Figure 6 (online color at www.lasphys.com) The oscilloscope traces of a train of signal wave (1572 nm) for different KTPs with $R_s = 80\%$ (the left) and $R_s = 50\%$ (the right), respectively

4. Conclusions

We improve the stability and efficiency of IOPOs pumped by a diode-pumped Q-switched Nd:YVO_4/Cr^{4+}:YAG laser. The mirrors are directly deposited on top of the KTP crystal to form an independent monolithic IOPO cavity with stability and high conversion efficiency. The performances of IOPOs with different reflectivity of the output coupler at 1.5 μm (R_s) of 80 and 50% have been investigated. The average power of 1.5 μm was up to 3.3 W at the maximum pump power of 16.8 W for both cases with the instability of 0.2% for $R_s = 80\%$ and 1% for $R_s = 50\%$, respectively. The diode-to-signal conversion efficiency was

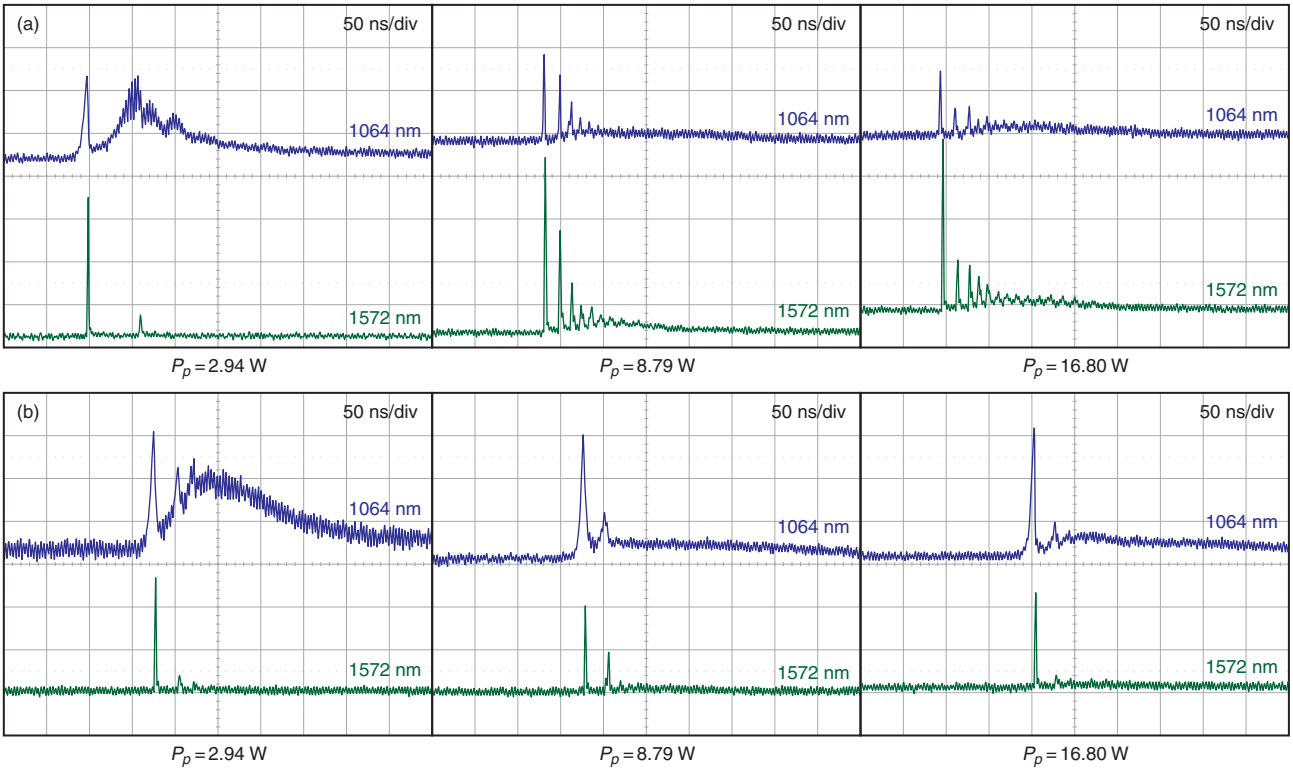

Figure 7 (online color at www.lasphys.com) The oscilloscope traces of a single pulse of fundamental (1064 nm) and signal wave (1572 nm) at various pump powers for (a) $R_s = 80\%$ and (b) $R_s = 50\%$, respectively

up to 20%, which is the highest one for IOPOs to our best knowledge. At the maximum pump power, pulse energies were 41 μJ at a PRR of 80 kHz for $R_s = 80\%$ and 51 μJ at a PRR of 65 kHz for $R_s = 50\%$, respectively. The temporal domain showed that several satellite pulses were observed behind a major pulse for the case of $R_s = 80\%$. Reducing the R_s to 50%, satellite pulses could be suppressed effectively without energy loss. The pulse train amplitude fluctuation in standard deviation was slightly larger with the lower R_s. However, the peak power was remarkably enhanced by employing the KTP crystal with lower reflectivity of the output coupler at 1.5 μm, which is advantageous to generate high peak power eye-safe light source. Besides, in comparison with our previous similar experiment using a coupled IOPO [2], performances such as average power, conversion efficiency, and pulse energy in this work are much better. It is believed that this high power and high efficiency eye-safe laser could be a promising light source in many applications.

Acknowledgements The authors acknowledge the National Science Council of Taiwan (NSCT) for their financial support of this research under contract NSC-100-2628-M-009-001-MY3.

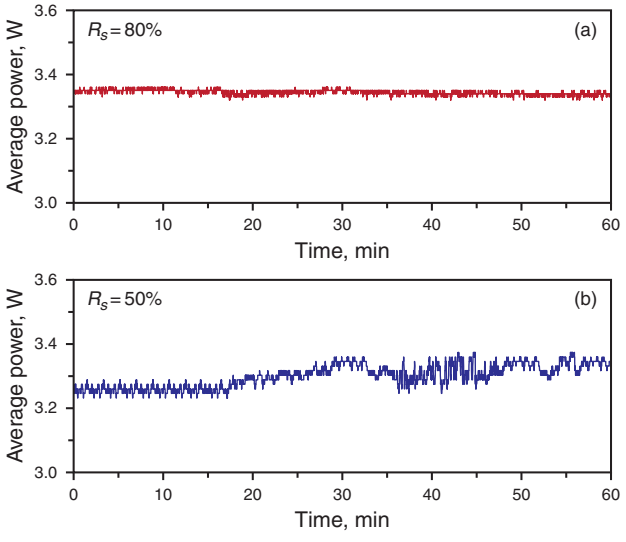

Figure 8 (online color at www.lasphys.com) The hour-long average power stability of the signal power of $R_s = 80\%$ (the top) and $R_s = 50\%$ (the bottom), respectively, at the maximum pump power

References

[1] B.T. Zhang, X.L. Dong, J.L. He, H.T. Huang, K.J. Yang, C.H. Zuo, J.L. Xu, and S. Zhao, Laser Phys. Lett. **5**, 869 (2008).
[2] Y.F. Chen, Y.C. Chen, S.W. Chen, and Y.P. Lan, Opt. Commun. **234**, 337 (2004).
[3] H.Y. Zhu, Y.M. Duan, G. Zhang, C.H. Huang, Y. Wei, W.D. Chen, H.Y. Wang, and G. Qiu, Laser Phys. Lett. **7**, 703 (2010).
[4] J.F. Yang, S.D. Liu, J.L. He, X.Q. Yang, F.Q. Liu, B.T. Zhang, J.L. Xu, H.W. Yang, and H.T. Huang, Laser Phys. Lett. **8**, 28 (2011).
[5] J. Wang, X. Chen, H. Zhang, S. Zhao, J. Liang, and P. Wang, Laser Phys. **22**, 120 (2012).
[6] H.T. Huang, J.L. He, S.D. Liu, F.Q. Liu, X.Q. Yang, H.W. Yang, Y. Yang, and H. Yang, Laser Phys. Lett. **8**, 358 (2011).
[7] H.Y. Zhu, G. Zhang, H.B. Chen, C.H. Huang, Y. Wei, Y.M. Duan, Y.D. Huang, H.Y. Wang, and G. Qiu, Opt. Express **17**, 20669 (2009).
[8] J.G. Miao, Y.Z. Pan, and G.J. Guo, Laser Phys. **21**, 1184 (2011).
[9] J. Wang, S.Z. Zhao, P.J. Wang, K.J. Yang, G.Q. Li, D.C. Li, and J. Liang, Laser Phys. **19**, 927 (2009).
[10] Y.F. Chen and L.Y. Tsai, Appl. Phys. B **82**, 403 (2006).
[11] Y.F. Chen, S.W. Chen, Y.C. Chen, Y.P. Lan, and S.W. Tsai, Appl. Phys. B **77**, 493 (2003).
[12] Y.F. Chen, Y.P. Lan, and H.L. Chang, IEEE J. Quantum Electron. **37**, 462 (2001).
[13] Y.F. Chen, T.M. Huang, C.F. Kao, C.L. Wang, and S.C. Wang, IEEE J. Quantum Electron. **33**, 1424 (1997).
[14] N. Hodgson and H. Weber, Laser Resonators and Beam Propagation, 2nd ed. (Springer, Berlin, 2005), chapter 8.
[15] S. Brosnan and R. Byer, IEEE J. Quantum Electron. **15**, 415 (1979).
[16] A. Agnesi, S. Dell'Acqua, and G. Reali, Appl. Phys. B **70**, 751 (2000).

Optics Communications 285 (2012) 59–63

Contents lists available at SciVerse ScienceDirect

Optics Communications

journal homepage: www.elsevier.com/locate/optcom

Efficient high-power UV laser generated by an optimized flat–flat actively Q-switched laser with extra-cavity harmonic generations

Y.J. Huang, P.Y. Chiang, H.C. Liang, K.W. Su, Y.F. Chen *

Department of Electrophysics, National Chiao Tung University, Hsinchu, Taiwan

ARTICLE INFO

Article history:
Received 30 June 2011
Accepted 2 September 2011
Available online 17 September 2011

Keywords:
Diode-pumped solid-state laser
Acousto-optically Q-switching
Parasitic lasing effect
Extra-cavity second and third harmonic generation

ABSTRACT

We investigate the parasitic lasing effect in the high-power actively Q-switched laser with a flat–flat resonator. The parasitic lasing effect in the low-Q stage is found to lead to long tails in the output pulses, corresponding to the peak-power reduction. We experimentally determine the shortest cavity length without the parasitic lasing effect to optimize the performance of the high-power actively Q-switched laser with a flat–flat cavity. We further use the optimized fundamental laser to generate green and UV lasers by extra-cavity harmonic generations. At a pump power of 44 W, the output powers at 355 nm and 532 nm as high as 6.65 W and 8.38 W are obtained at a pulse repetition rate of 40 kHz.

1. Introduction

In recent years, ultraviolet (UV) light sources have been rapidly developed because they are useful in many applications such as rapid prototyping, laser printing, laser processing, spectroscopy, optical data storage, medical treatment and so on. Compared with other UV lasers, diode-pumped all-solid-state lasers with extra-cavity harmonic generations intrinsically possess advantages of smaller focused size, higher efficiency, longer life time, higher stability, easier implement and smaller system size etc [1, 2]. The acousto-optic (AO) Q-switch is characterized by its low-insertion loss that is suitable for repetitively Q-switched lasers [3–10]. It can provide a high-stability, low timing jitter and large-peak-power laser operation with a continuously adjustable pulse repetition rate, which is beneficial for efficient extra-cavity harmonic generations.

The parasitic lasing means that there is residual lasing in the low-Q stage. The parasitic lasing effect is a critical issue for scaling up the output peak powers of the Q-switched lasers [3, 11–13]. The parasitic lasing effect of the AO Q-switched laser usually leads to a peak-power reduction that significantly deteriorates the performance of extra-cavity second and third harmonic generations (SHG and THG). Although lengthening the cavity length can effectively assist the diffraction loss of the AO device to suppress the parasitic lasing in the low-Q stage, a long cavity length usually needs an intricate design to obtain a stable resonator under the thermal lensing effect. More importantly, longer cavity lengths always lead to longer pulse widths that also reduce the output peak powers. Therefore, it is practically valuable to optimize the peak power by designing the shortest cavity length for the AO Q-switched laser without the parasitic lasing effect.

In this work, we firstly employ a Nd:YVO_4 crystal with dopant concentration as low as 0.1 atm.% in an actively Q-switched laser to explore the parasitic lasing effect in a flat–flat resonator. Experimental results reveal that the parasitic lasing leads to a long tail in the Q-switched pulse. We experimentally determine the critical cavity length without the parasitic lasing effect as a function of incident pump power. We also confirm that Nd:YVO_4 crystals with dopant concentration greater than 0.2 atm.% are hardly serviceable in designing the high-power Q-switched laser without parasitic lasing. Furthermore, we utilize the optimized laser to achieve highly efficient extra-cavity harmonic generations. At a pump power of 44 W, the output powers at 532 nm and 355 nm under a pulse repetition rate of 40 kHz reach 8.38 W and 6.65 W, respectively. The optical-to-optical conversion efficiencies from 1064 nm to 355 nm and from 808 nm to 355 nm are found to be up to 38.2% and 15.1%, respectively. To our knowledge, this is the highest conversion efficiency based on the AO Q-switched laser with a flat–flat cavity.

2. Optimization in the flat–flat AO Q-switched laser

The experimental setup is schematically shown in Fig. 1. The flat front mirror was antireflection (AR) coated at 808 nm on the entrance face, and was coated at 808 nm for high transmission as well as 1064 nm for high reflection on the second surface for lights with normal incidence. The flat folded mirror had the same coated characteristics as the flat front mirror except that the angle of the incident light was 45°. The gain medium was a 0.1 at.% Nd:YVO_4 crystal with

* Corresponding author at: Department of Electrophysics, National Chiao Tung University, 1001 TA Hsueh Road, Hsinchu, Taiwan, 30050. Fax: +886 35725230.
E-mail address: yfchen@cc.nctu.edu.tw (Y.F. Chen).

0030-4018/$ – see front matter © 2011 Elsevier B.V. All rights reserved.
doi:10.1016/j.optcom.2011.09.002

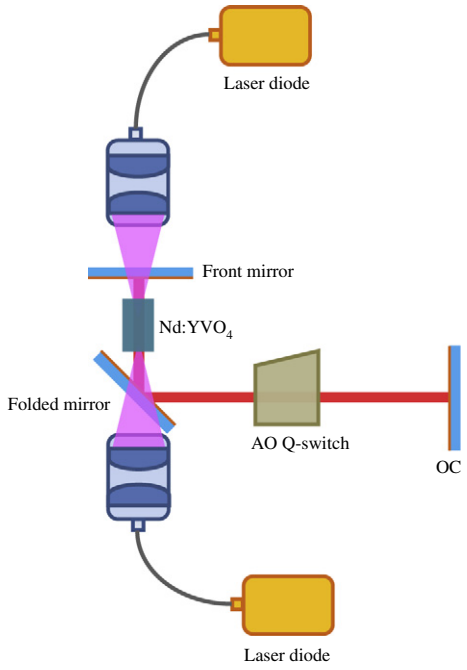

Fig. 1. Schematic of the cavity setup for a diode-pumped AO Q-switched Nd:YVO_4 laser.

dimensions of $3\times3\times14$ mm^3. Both facets of the laser crystal were AR coated at 808 nm and 1064 nm. The laser crystal was wrapped with indium foil and mounted in a water-cooled copper heat sink at 20 °C. A 20-mm-long AO Q-switch (NEOS technologies) with AR coating at 1064 nm on both faces was placed in the center of the cavity, and was driven at a central frequency of 41 MHz with RF power of 25 W. The pump sources were two 25-W 808-nm fiber-coupled laser diodes with a core diameter of 800 μm and a numerical aperture of 0.16. The pump beam was re-imaged into the laser crystal with a lens set that has the focal length of 25 mm with a magnification of unity and the coupling efficiency of 88%. As a result, the maximum pump power in our experiment is approximately 44 W. The flat output coupler with 50% transmission was employed during the experiment. The relatively low reflectance of the output coupler is practically helpful for the effective hold-off in the low-Q stage. The pulse temporal behaviors were recorded by a LeCroy digital oscilloscope (Wavepro 7100, 10 G samples/s, 1 GHz bandwidth) with a fast Si photodiode.

Since the parasitic lasing in the low-Q stage can be utterly suppressed with increasing the cavity length in a flat–flat cavity, we define the critical cavity length to be the shortest cavity length without parasitic lasing. Fig. 2 depicts experimental results for the critical

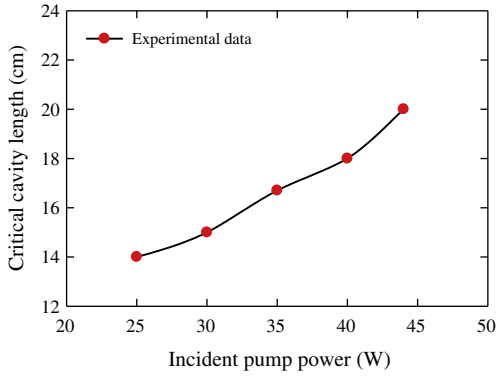

Fig. 2. Experimental results for the relationship between the critical cavity length and the incident pump power.

cavity length as a function of the pump power. The critical cavity length without parasitic lasing can be seen to increase with increasing the incident pump power. More importantly, we experimentally found that the parasitic lasing significantly affects the temporal shape of the Q-switched pulse. Fig. 3(a) and (b) shows the influence of parasitic lasing on the Q-switched pulse at the maximum pump power of 44 W for the cavity lengths of 16 cm and 18 cm, respectively. It can be seen that the Q-switched pulse is accompanied with a long tail or a satellite pulse. In contrast, the Q-switched pulse without parasitic lasing displays a short tail as well as no satellite pulse, as shown in Fig. 3(c) and (d) for the cavity lengths of 20 cm and 22 cm, respectively.

The long tail of Q-switched pulses induced by parasitic lasing implies the reduction of the peak power. The degree of the peak-power reduction can be simply analyzed with the rate equation. Assume the average photon density caused by parasitic lasing to be ϕ_b, the rate equation for the population inversion density n in the low-Q stage can be described as

$$\frac{dn}{dt}=R_p-\frac{n}{\tau}-c\sigma\phi_b n, \tag{1}$$

where R_p is the rate of the pump density, τ is the upper-state lifetime of laser crystal, c is the speed of light, σ is the stimulated emission cross section. With $\tau_b=1/c\sigma\phi_b$, Eq. (1) can be rewritten as

$$\frac{dn}{dt}=R_p-\frac{n}{\tau_e}, \tag{2}$$

where $1/\tau_e=1/\tau+1/\tau_b$ and τ_e represents the effective upper-state lifetime with parasitic lasing. τ_e is clear to be smaller than τ. Since the amount of the maximum stored energy is proportional to the upper-state lifetime, the parasitic lasing can be comprehended to cause a reduction in the pulse energy and peak power. To be brief, the parasitic lasing scarcely affects the average output power but has a detrimental effect on the peak power.

As shown in Fig. 2, the critical cavity length is approximately 20 cm for the maximum pump power of 44 W. With the ABCD-matrix theory, it can be derived that the cavity length L of a stable flat–flat resonator should be shorter than the thermal focal length f_{th},; namely, the criterion of $L\le f_{th}$ must be satisfied to maintain the cavity stable. Since the thermal focal length of the laser crystal can be verified to be inversely proportional to the dopant concentration, the criterion of $L\le f_{th}$ signifies the importance of using a Nd:YVO_4 crystal with extremely low dopant concentration. The effective focal length of thermal lens in the end-pumped laser crystal can be analyzed with the following equation [14]:

$$\frac{1}{f_{th}}=\frac{\xi P}{\pi K_c}\int_0^l\frac{\alpha e^{-\alpha z}}{1-e^{-\alpha l}}\frac{1}{\omega_p^2(z)}\left[\frac{1}{2}\frac{dn}{dT}+(n-1)\alpha_T\frac{\omega_p(z)}{l}\right]dz, \tag{3}$$

where ξ is the fraction of incident pump power that results in heat, P is the absorbed pump power, K_c is the thermal conductivity of laser crystal, α is the absorption coefficient, $\omega_p(z)$ is the variation of pump radius, dn/dT is the thermal-optic coefficient, n is the refractive index, α_T is the thermal expansion coefficient, and l is the length of gain medium. With the following parameters: $K_c=5.23$ W/m K, $\omega_{po}=400$ μm, $dn/dT=3\times10^{-6}$ K^{-1}, $n=2.1652$, $\alpha_T=4.43\times10^{-6}$ K^{-1}, we calculated the effective thermal focal length f_{th} as a function of the Nd dopant concentration of laser crystal at the incident pump power of 44 W. In the present calculation, the crystal length l is related to the absorption coefficient α with the condition of $\alpha l=4$ for pump absorption of 98%. Note that the relation between the absorption coefficient α and the Nd dopant concentration of laser crystal for a pump wavelength of 808 nm is given by $\alpha=2\cdot N_d$ mm^{-1} [15], where N_d is the Nd dopant concentration in units of atomic %. Fig. 4 depicts the calculated results ranging from $N_d=0.05\%$ to $N_d=1\%$ at

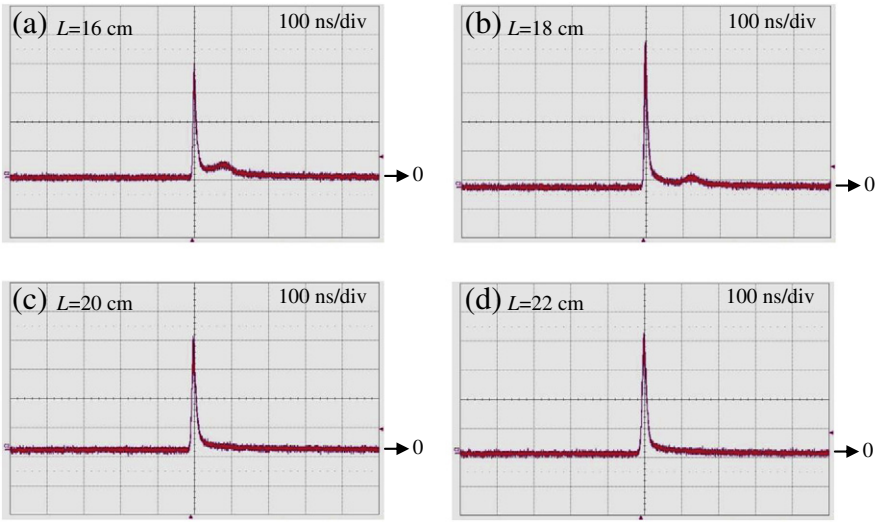

Fig. 3. Temporal behaviors of the Q-switched pulses with different cavity lengths L: (a) $L=16$ cm; (b) $L=18$ cm; (c) $L=20$ cm; (d) $L=22$ cm.

a pump power of 44 W. It can be seen that the smaller the Nd dopant concentration, the longer the thermal focal length. Moreover, the Nd:YVO_4 crystal with dopant concentration greater than 0.2 atm.% cannot comply with the requirement of $L \leq f_{th}$, where $L=20$ cm is employed to suppress the parasitic lasing at a pump power of 44 W. To sum up, using a Nd:YVO_4 crystal with extremely low dopant concentration is a promising way to simultaneously suppress the parasitic lasing and maintain a stable flat–flat resonator in high-power Q-switched lasers.

With the cavity length of 20 cm, we make a thorough evaluation for the performance of Q-switched operation. Fig. 5 shows the output power and pulse width as a function of the incident pump power at the pulse repetition rate of 40 kHz. At a pump power of 44 W, the average output power of 17.5 W was obtained without any signature of output power saturation, indicating the cavity to remain in a stable region. For the pump power increasing from 16 W to 44 W, the pulse width can be seen to decrease from 36 ns to 12 ns. Fig. 6(a) and (b) illustrates the dependences of average output power, pulse width, pulse energy and peak power on the pulse repetition rate at a pump power of 44 W. It can be seen that with increasing the pulse repetition rate from 20 kHz to 100 kHz, the average output power increases from 13 W to 19.4 W and the pulse duration smoothly varies from 8 ns to 24 ns. Accordingly, it can be found that when the pulse repetition rate increases from 20 kHz to 100 kHz, the pulse energy changes from 650 μJ to 194 μJ and the peak power varies from 81.5 kW to 8.1 kW. In the following section, we employ this compact high-power actively Q-switched laser to investigate the performance of the extra-cavity SHG and THG.

3. Performance of extra-cavity SHG and THG

Here lithium triborate (LBO) crystals are exploited as nonlinear frequency converters for SHG and THG since they have the advantages of high damage threshold, relatively large acceptance angle, and small walk-off angle. One LBO crystal with dimensions of $3\times3\times15$ mm^3 was cut at $\theta=90°$, $\varphi=10.4°$ for type-I phase-matched SHG at a temperature of 46.6 °C. Both facets of the SHG crystal were AR coated at 1064 nm and 532 nm. Another LBO crystal with dimensions of $3\times3\times10$ mm^3 was cut at $\theta=44°$, $\varphi=90°$ for type-II phase-matched THG at a temperature of 48 °C. Both facets of the THG crystal were AR coated at 1064 nm, 532 nm, and 355 nm. The temperatures of the SHG and THG nonlinear crystals were monitored by thermoelectric controllers with the precision of 0.1 °C. Two convex lenses were used to focus the laser beams into the SHG and THG nonlinear crystals for achieving efficient harmonic generations. The former one with focal length of 38 mm was AR coated at 1064 nm on both sides, the latter one with focal length of 19 mm was AR coated at 1064 nm and 532 nm on both sides. The optimized geometrical distances of L_1, L_2, L_3 and L_4 indicated in Fig. 7 were experimentally determined to be approximately 70 mm, 43 mm, 34 mm, and 21 mm, respectively.

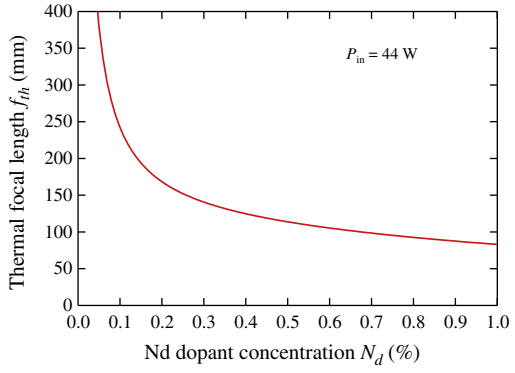

Fig. 4. Calculated results for the thermal focal length as a function of the Nd dopant concentration of laser crystal at a pump power of 44 W.

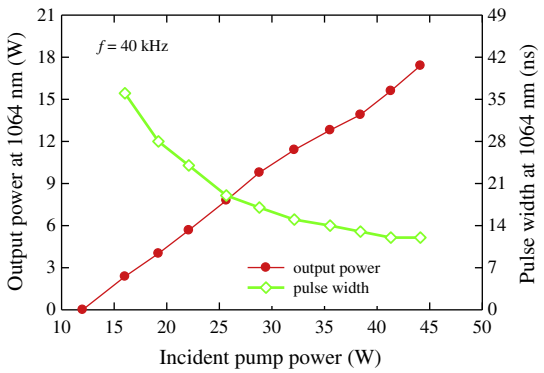

Fig. 5. Output power (red) and pulse width (green) versus the pump power at a pulse repetition rate of 40 kHz.

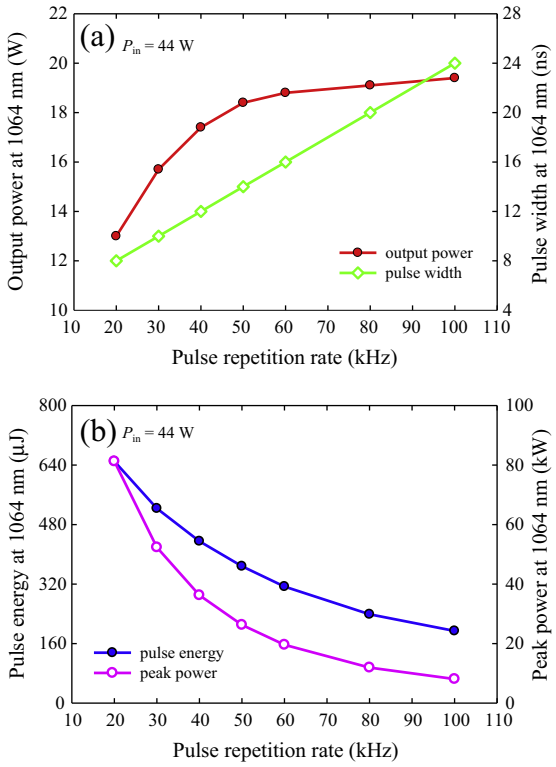

Fig. 6. (a) Dependences of the average output power (red) and the pulse width (green) on the pulse repetition rate at a pump power of 44 W; (b) dependences of the pulse energy (blue) and the peak power (pink) on the pulse repetition rate at a pump power of 44 W.

At a pump power of 44 W, the output power, the pulse energy, and the peak power at 532 nm and 355 nm versus the pulse repetition rate are shown in Fig. 8(a)–(c), respectively. Although the conversion efficiency of harmonic generations increases with decreasing the pulse repetition rate, the average output power at 1064 nm is proportional to the pulse repetition rate in the range of 20–50 kHz. As a result, the highest average output powers for extra-cavity SHG and THG are found to be approximately at a pulse repetition rate of 40 kHz and their values at 532 nm and 355 nm are 8.38 W and 6.65 W, respectively. The corresponding optical-to-optical conversion efficiencies from 808 nm to 355 nm and 1064 nm to 355 nm are up to 15.1% and 38.2%, respectively. On the other hand, at a pulse repetition rate of 20 kHz the largest pulse energy and the highest peak power at 532 nm are found to be 270 μJ and 30 kW, respectively. Similarly, at a pulse repetition rate of 20 kHz the largest pulse energy and the highest peak power at 355 nm are found to be 200 μJ and 22 kW, respectively. With a knife-edge method, the beam quality factors for orthogonal direction

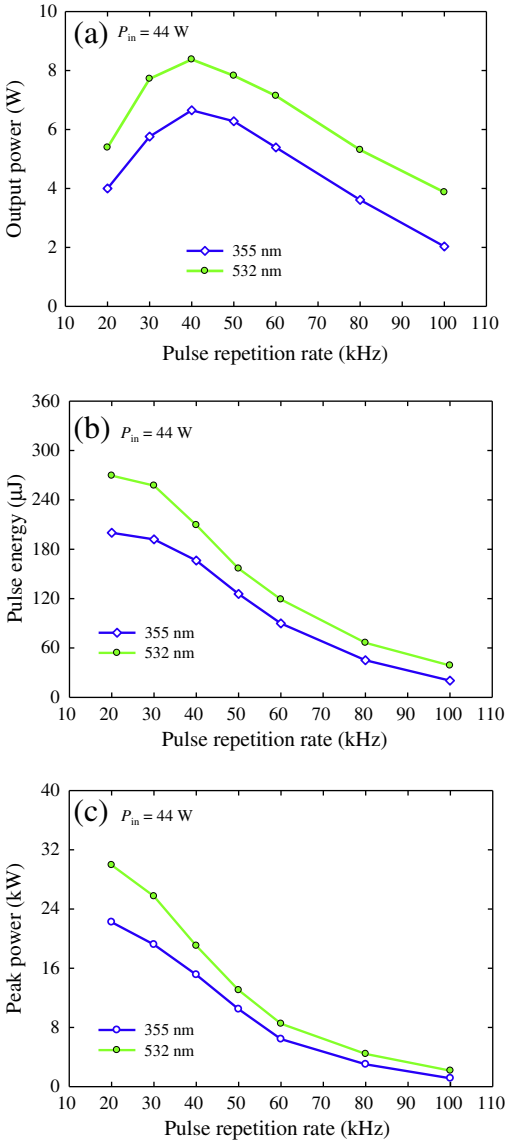

Fig. 8. Dependences of (a) the average output powers, (b) the pulse energies, and (c) the peak powers at 532 nm and 355 nm on the pulse repetition rate at a pump power of 44 W.

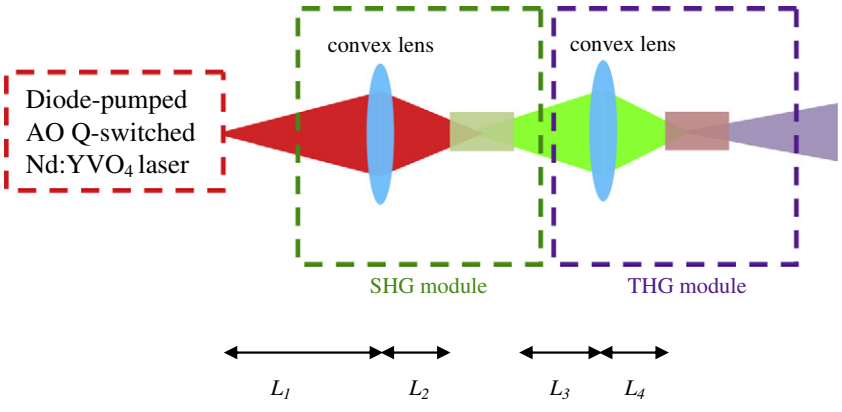

Fig. 7. Schematic of the experimental setup for the extra-cavity SHG and THG.

were measured to be $M_x^2 < 1.2$ and $M_y^2 < 1.3$. To manifest the influence of parasitic lasing on the extra-cavity harmonic generations, the Q-switched laser with $L = 16$ cm was also employed to perform the process of SHG and THG. Experimental results reveal that even though the average output power at 1064 nm obtained with $L = 16$ cm is nearly the same as that obtained with $L = 20$ cm, the average output powers at SHG and THG obtained with $L = 16$ cm were found to be 15–25% lower than the results obtained with $L = 20$ cm. The lower conversion efficiencies obtained with $L = 16$ cm confirm that the parasitic lasing effect leads to the peak-power reduction in Q-switched lasers.

4. Conclusion

In summary, we have explored the parasitic lasing effect in an actively Q-switched laser with a flat–flat resonator and a 0.1 atm.% Nd:YVO_4 crystal. Experimental results revealed that the critical cavity length without parasitic lasing was proportional to the pump power. The parasitic lasing effect was also found to lead to a long tail in the Q-switched pulse, corresponding to a reduction in the peak power. We manifestly disclosed that the combined effects of the parasitic lasing and the thermal lensing made Nd:YVO_4 crystals with dopant concentration greater than 0.2 atm.% to be problematical in designing the high-power Q-switched laser with a flat–flat cavity. We further employed the optimized high-power Q-switched laser without parasitic lasing to achieve highly efficient extra-cavity harmonic generations. At a pump power of 44 W, the output powers at 355 nm and 532 nm as high as 6.65 W and 8.38 W are obtained at the pulse repetition rate of 40 kHz. The optical-to-optical conversion efficiencies from 1064 nm to 355 nm and 808 nm to 355 nm are up to 38.2% and 15.1%, respectively.

Acknowledgments

The authors thank the National Science Council for their financial support of this research under contract no. NSC-97-2112-M-009-016-MY3.

References

[1] A.V. Hicks, C.X. Wang, G.Y. Wang, Proceedings of SPIE 5332 (2004) 120.
[2] C.X. Wang, G.Y. Wang, A.V. Hicks, D.R. Dudley, H.Y. Pang, N. Hodgson, Proceedings of SPIE 6100 (2006) 610019.
[3] P. Maak, L. Jakab, P. Richter, H.J. Eichler, B. Liu, Applied Optics 39 (2000) 3053.
[4] J. Liu, C. Wang, C. Du, L. Zhu, H. Zhang, X. Meng, J. Wang, Z. Shao, M. Jiang, Optics Communications 188 (2001) 155.
[5] J.H. García-López, V. Aboites, A.V. Kir'yanov, M.J. Damzen, A. Minassian, Optics Communications 218 (2003) 155.
[6] T. Ogawa, T. Imai, K. Onodera, H. Machida, M. Higuchi, Y. Urata, S. Wada, Applied Physics B 81 (2005) 521.
[7] Li Shutao, Zhang Xingyu, Wang Qingpu, Cong Zhenhua, Liu Zhaojun, Fan Shuzhen, Zhang Xiaolei, Journal of Physics D: Applied Physics 41 (2008) 055104.
[8] Su Fufang, Zhang Xingyu, Wang Qingpu, Ding Shuanghong, Jia Peng, Li Shutao, Fan Shuzhen, Zhang Chen, Liu Bo, Journal of Physics D: Applied Physics 39 (2006) 2090.
[9] F. He, L. Huang, M. Gong, Q. Liu, X. Yan, Laser Physics Letters 4 (2007) 511.
[10] X. Li, X. Yu, F. Chen, R. Yan, J. Gao, J. Yu, D. Chen, Optics Express 17 (2009) 9468.
[11] M.E. Storm, Journal of the Optical Society of America B 9 (1992) 1299.
[12] T. Crawford, C. Lowrie, J.R. Thompson, Applied Optics 35 (1996) 5861.
[13] P. Yan, M. Gong, T. Xie, X. Liu, Optical Engineering 42 (2003) 159.
[14] W. Koechner, Solid-State Laser Engineering, 6th ed. Spring-Verlag, Berlin, Germany, 2005 ch. 7.
[15] Y.F. Chen, IEEE Quantum Electronics 35 (1999) 234.

Appl Phys B (2011) 105:385–390
DOI 10.1007/s00340-011-4483-6

Applied Physics B
Lasers and Optics

High-power Q-switched laser with high-order Laguerre–Gaussian modes: application for extra-cavity harmonic generations

Y.J. Huang · P.Y. Chiang · H.C. Liang · K.W. Su · Y.F. Chen

Received: 14 January 2011 / Revised version: 14 February 2011 / Published online: 15 April 2011

Abstract We present a compact efficient scheme for generation of high-order Laguerre–Gaussian $TEM_{p,0}$ modes in a diode-pumped actively Q-switched Nd:YVO_4 laser. The resonator is composed of two plane mirrors with an intracavity concave lens to expand the cavity mode size for generating a high-power Laguerre–Gaussian $TEM_{5,0}$ mode. We further confirm that the $TEM_{5,0}$ mode is noticeably superior to the $TEM_{0,0}$ mode in the processes of second and third harmonic generations.

1 Introduction

In recent years, ultraviolet (UV) light sources have rapidly attracted a lot of interest because they are useful in numerous applications such as rapid prototyping, laser printing, laser processing, spectroscopy, optical data storage, medical treatment and so on. Compared with other UV lasers, diode-pumped all-solid-state lasers with extra-cavity nonlinear frequency conversion intrinsically possess advantages of smaller focused size, higher efficiency, longer life time, higher stability, easier implementation and smaller system size, etc. [1, 2]. Currently, the fundamental Gaussian modes are usually used in the processes of second and third harmonic generations (SHG and THG) because of the good spatial property [3, 4].

In cylindrical coordinates, the transverse modes can be expressed in terms of Laguerre–Gaussian modes with the label of $TEM_{p,l}$, where p and l represent the number of radial nodes and azimuthal nodes, respectively. In the past years, several investigations have been carried out to generate low- and higher-order $TEM_{p,l}$ modes in solid-state lasers [5–11]. Among these studies, $TEM_{p,l}$ modes with $p \neq 0$ and $l = 0$ have been demonstrated [5, 12] to be similar to the Bessel-like beam that possesses a central peak with a divergence considerably lower than that of the Gaussian beam with the same waist [13–17]. Bessel-like modes have already been utilized as light sources in lithographic patterning, laser machining, and nonlinear optics [18–22]. However, so far high-order Laguerre–Gaussian $TEM_{p,0}$ modes have not been employed in processes of SHG and THG.

In this work, we originally design a compact three-element resonator to excite high-order Laguerre–Gaussian $TEM_{p,0}$ modes in a diode-pumped actively Q-switched Nd:YVO_4 laser. We use flat-flat cavity with an intra-cavity concave lens to expand the cavity mode size for efficiently generating the Laguerre–Gaussian $TEM_{5,0}$ mode with the output power up to 8.52 W at a pulse repetition rate of 40 kHz. We experimentally confirm that the conversion efficiencies in the processes of SHG and THG obtained with the $TEM_{5,0}$ mode are noticeably higher than the results obtained with the $TEM_{0,0}$ mode. The optical-to-optical conversion efficiencies from 1064 nm to 355 nm are found to be 35.6% and 28.1% for the $TEM_{5,0}$ mode and $TEM_{0,0}$ mode, respectively.

2 Cavity configuration and analysis

The radial intensity of the Laguerre–Gaussian $TEM_{p,l}$ modes is given by

Y.J. Huang · P.Y. Chiang · H.C. Liang · K.W. Su · Y.F. Chen (✉)
Department of Electrophysics, National Chiao Tung University,
1001 TA Hsueh Road, Hsinchu 30050, Taiwan
e-mail: yfchen@cc.nctu.edu.tw
Fax: +886-35-725230

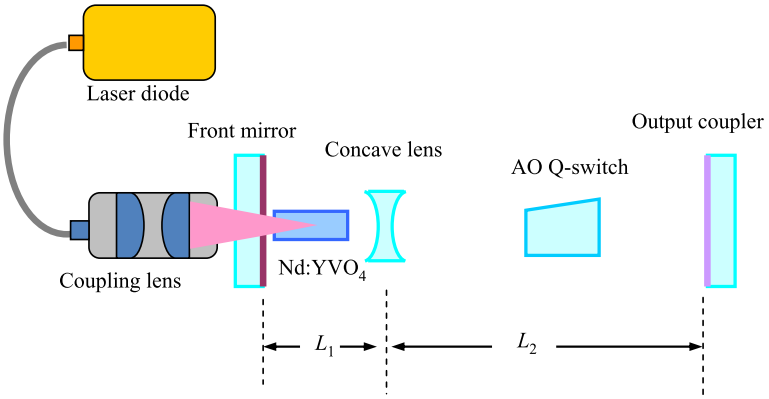

Fig. 1 Schematic of the cavity setup for a diode-pumped AO Q-switched Nd:YVO_4 laser

$$I_{p,l}(\rho,z)=\frac{2p!}{\pi(p+|l|)!}\frac{1}{w^2(z)}\left(\frac{2\rho^2}{w(z)^2}\right)^l L_p^l\left(\frac{2\rho^2}{w(z)^2}\right)\times\exp\left[-\frac{2\rho^2}{w(z)^2}\right], \quad (1)$$

where $w(z)=w_0\sqrt{1+(z/z_R)^2}$, w_0 is the beam radius at the waist, and $z_R=\pi w_0^2/\lambda$ is the Rayleigh range, and $L_p^l(\cdot)$ are the associated Laguerre polynomials. Flood et al. [5] demonstrated that high-order Laguerre–Gaussian $TEM_{p,0}$ modes could be generated in an end-pumped solid-state laser when the pump spot size ω_p was considerably smaller than the fundamental $TEM_{0,0}$-mode spot size ω_o of the cavity, i.e., $\omega_o/\omega_p \gg 1$. Although the pump beams can be tightly focused to reach the criterion of $\omega_o/\omega_p \gg 1$, the tight focusing of pump beam inevitably causes strong thermal effects such as thermal lensing, thermal fracture, etc., leading to the obstruction for the power scale-up. Therefore, a practical way is to expand the cavity mode size without tight focusing of the pump beam. Here, we design a compact efficient three-element resonator, consisting of a flat front mirror, a concave lens and a flat output coupler, to obtain large fundamental mode sizes.

Figure 1 shows the configuration of the three-element cavity for an end-pumped acousto-optic (AO) solid-state laser, where L_1 is the distance between the front mirror and the concave lens, L_2 is the distance between the concave lens and the flat output coupler, and f is the focal length of the concave lens. The flat front mirror was antireflection (AR) coated at 808 nm on the entrance face and was coated at 808 nm for high transmission as well as 1064 nm for high reflection (HR) on the second surface. The gain medium was a 0.1 at.% Nd:YVO_4 crystal with dimensions of $3\times3\times12$ mm^3 and was located to be adjacent the front mirror for convenience of end-pumping scheme. Both facets of the laser crystal were AR coated at 808 nm and 1064 nm. The laser crystal was wrapped with indium foil and mounted in a water-cooled copper heat sink at 20°C. Although using the laser crystal with the HR-AR coating is preferable for more compact configuration, we use a separate front mirror and the AR-AR coated laser crystal in the present setup because of the availability of experimental components. A concave lens with AR coating at 1064 nm on both faces was placed just behind the laser crystal. A 20-mm-long AO Q-switch (NEOS technologies) with AR coating at 1064 nm on both faces was placed in the center of the cavity and was driven at a central frequency of 41 MHz with RF power of 25 W. The pump source was a 30-W 808-nm fiber-coupled laser diode with a core diameter of 600 μm and a numerical aperture of 0.16. The pump beam was reimaged into the laser crystal with a lens set that has the focal length of 25 mm with a magnification of unity and the coupling efficiency of 90%. As mentioned earlier, the use of the relatively large pump radius is beneficial for power scaling with the avoidance of serious thermal problems. The flat output coupler with 50% transmission was employed during the experiment. For constructing a compact Q-switched laser, we set the optical cavity length to be $L_1=20$ mm and $L_2=120$ mm.

The effective focal length of the thermal lens in a Nd:YVO_4 crystal could be expressed as [23]:

$$\frac{1}{f_{\text{th}}}=\frac{\xi}{\pi K_c}\int_0^l\frac{\alpha e^{-\alpha z}}{1-e^{-\alpha l}}\frac{1}{\omega_p^2(z)}\times\left[\frac{1}{2}\frac{dn}{dT}+(n-1)\alpha_T\omega_p(z)/l\right]dz, \quad (2)$$

where ξ is the fraction of pump power that results in heat, K_c is the thermal conductivity of the laser material, α is the absorption coefficient, n is the refractive index, l is the length of the gain medium, dn/dT is the thermal-optic coefficient, α_T is the thermal expansion coefficient, and $\omega_p(z)$ is the variation of the pump radius. With the following parameters: $K_c=5.23$ W/m K, $\alpha=0.2$ mm^{-1}, $n=2.1652$, $l=12$ mm, $dn/dT=3\times10^{-6}$ K^{-1}, $\alpha_T=4.43\times10^{-6}$ K^{-1}, the effective focal length of thermal lens was estimated to be approximately $f_{\text{th}}=220$ mm at a pump power of 25 W. We then use the ABCD-matrix method to calculate the cavity mode size at the front mirror as a function of the effective

thermal focal length for a given focal length of the concave lens. Figure 2 depicts the calculated results for the four cases of $f = -200$ mm, -300 mm, -400 mm, and $-\infty$. Note that the case of $f = -\infty$ means the cavity without the concave lens. As seen in Fig. 2, the cavity mode size without a concave lens is approximately equal to the pump spot size. Although a concave lens can effectively enlarge the cavity mode size in some regime, the cavity needs an appropriate thermal focal length to step into the stable region. With the ABCD-matrix theory, we can find that the stable region is given by

$$(L_1 - f)\left[1 - \frac{f^2}{f^2 + L_1 L_2 - (L_1 + L_2)f}\right] \leq f_{\text{th}} \leq (L_1 - f). \quad (3)$$

The thermal focal length in the present setup approximately changes from 320 mm to 220 mm for the pump power increasing from 10 W to 25 W. As a result, we chose a concave lens with $f = -300$ mm to meet the range of the thermal focal length.

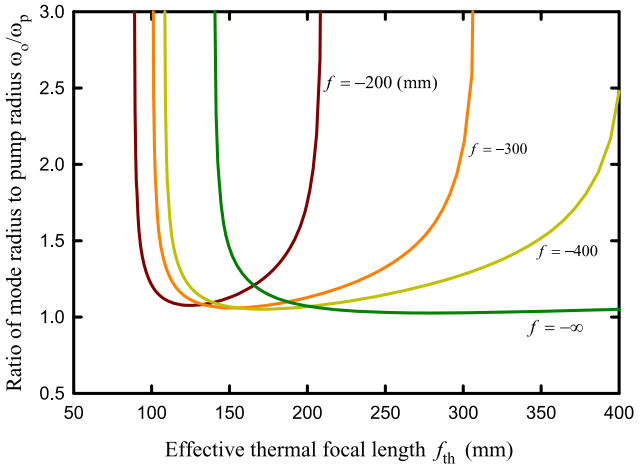

Fig. 2 Calculated results for the ratio of cavity mode size at the front mirror to pump size as a function of the effective thermal focal length for the cases of $f = -200$ mm, -300 mm, -400 mm, and $-\infty$

3 High-order Laguerre–Gaussian TEM$_{p,0}$ modes

First of all, the laser experiment for the standard flat-flat cavity without a concave lens was performed to measure the transverse pattern as a baseline for comparison. To record the transverse profiles of the different structure, the laser output was directly projected on a screen at a distance of approximately 1220 mm behind the output coupler and the scattered light was captured by a digital camera. As seen in Fig. 3(a), the transverse mode in the resonator without a concave lens is a pure fundamental TEM$_{0,0}$ mode. Figure 3(b) depicts the experimental transverse pattern observed in the laser cavity with a concave lens of $f = -300$ mm at a pump power of 25 W. It can be seen that the spatial distribution displays the lasing mode to be dominated by a Laguerre–Gaussian TEM$_{5,0}$ mode with negligible fundamental Gaussian mode. When the pump radius was changed from 300 μm to 100 μm, we found that the dominated transverse mode varied from TEM$_{5,0}$ mode to TEM$_{8,0}$ mode, as shown in Fig. 3(c). In short, we have experimentally confirmed the proportionality between the transverse order and the ratio ω_o/ω_p, but the detailed theoretical analysis of the dependence of the transverse order on the ratio ω_o/ω_p is beyond the scope of this work.

As found by Flood et al. [5], we confirmed that the experimental Laguerre–Gaussian TEM$_{5,0}$ mode has a central peak with a divergence considerably lower than that of a TEM$_{0,0}$ mode with the same waist. This observation indicates that the experimental TEM$_{5,0}$ mode might be beneficial for the achievement of the higher frequency conversion efficiency in processes of SHG and THG. Before investigating the conversion efficiency in nonlinear optics, we make

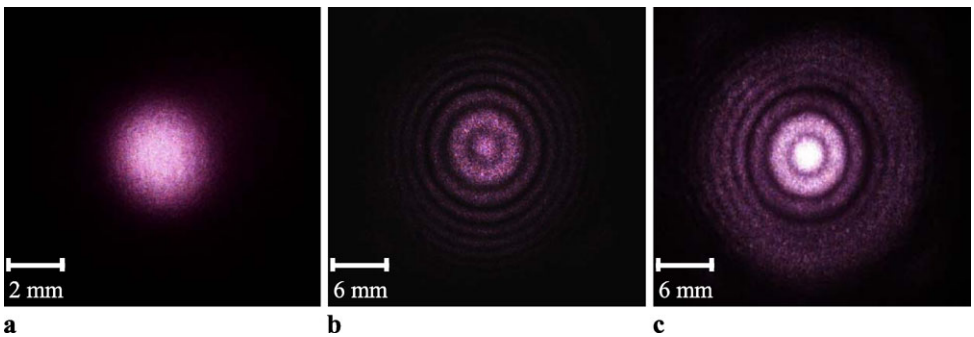

Fig. 3 Experimental transverse mode patterns of (**a**) TEM$_{00}$ mode without a concave lens at a pump power of 25 W; (**b**) TEM$_{5,0}$ mode with a concave lens ($f = -300$ mm) and a pump radius of 300 μm at a pump power of 25 W; (**c**) TEM$_{8,0}$ mode with a concave lens ($f = -300$ mm) and a pump radius of 100 μm at a pump power of 25 W. The patterns were measured at a distance of approximately 1220 mm behind the output coupler

a comparison of the laser performances of the cavities with and without the concave lens. Figure 4 shows the average output power as a function of the incident pump power for both configurations operating at a pulse repetition rate of 40 kHz. The cavity with the concave lens has a considerably lager pump threshold because the thermal focal power of the crystal should be greater than $(L_1 - f)^{-1}$ to result in the cavity to be stable. At a pump power of 25 W, the maximum average output powers at a repetition rate of 40 kHz were 8.52 W and 8.76 W for the cavities with and without concave lens. In other words, the difference of the maximum average output power between both cavity configurations was rather small. Figure 5 depicts the dependence of the average output powers, pulse energies and peak powers on the pulse repetition rate at a pump power of 25 W for both cavity configurations. On the whole, the average output power of the cavity with a concave lens was smaller than that of the cavity without a concave lens by approximately 5–10%, as shown in Fig. 5(a). The pulse temporal behavior was recorded by a LeCroy digital oscilloscope (Wavepro 7100, 10 G samples/s, 1 GHz bandwidth) with a fast Si photodiode. The pulse durations for both configurations were experimentally found nearly the same. With increasing the pulse repetition rate from 20 kHz to 80 kHz, the pulse duration was found to vary from 7 to 16 ns. As a result, the pulse energy and the peak power obtained with a concave lens were generally smaller than the results obtained without a concave lens, as shown in Fig. 5(b) and 5(c). In the following section, we make a comparison of the high-order $TEM_{5,0}$ mode and the fundamental $TEM_{0,0}$ mode in the processes of extra-cavity SHG and THG.

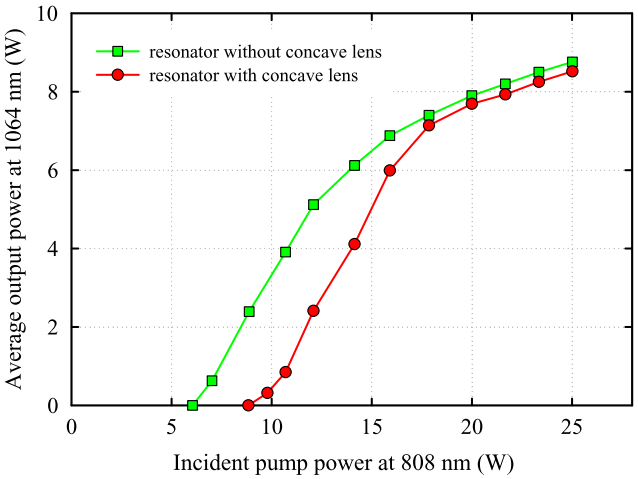

Fig. 4 Average output power at a repetition rate of 40 kHz as a function of the incident pump power for the cavities with and without the concave lens

4 Conversion efficiencies of extra-cavity SHG and THG

Here lithium triborate (LBO) crystals are exploited as nonlinear frequency converters for SHG and THG since they have the advantages of high damage threshold, relatively large acceptance angle, and small walk-off angle. One LBO crystal with dimensions of $3 \times 3 \times 15$ mm^3 was cut at $\theta = 90°$, $\varphi = 10.4°$ for type-I phase-matched SHG at temperature of 46.6°C. Both facets of the SHG crystal were AR coated at 1064 nm and 532 nm. Another LBO crystal with dimensions of $3 \times 3 \times 10$ mm^3 was cut at $\theta = 44°$, $\varphi = 90°$ for type-II phase-matched THG at temperature of 48°C. Both facets of the THG crystal were AR coated at 1064 nm, 532 nm, and 355 nm. The temperatures of the SHG and THG nonlinear crystals were monitored by thermoelectric controllers with the precision of 0.1°C. Two convex lenses were used to focus the laser beams into the SHG and THG nonlinear crystals for achieving efficient nonlinear conversion. The former one with focal length of 38 mm was AR coated at 1064 nm on both sides, the latter one with focal length of 19 mm was AR coated at 1064 nm and 532 nm on both sides. The optimized geometrical distances of L_3, L_4, L_5, and L_6 indicated in Fig. 6 were experimentally found to be approximately 70 mm, 30 mm, 25 mm, and 30 mm, respectively.

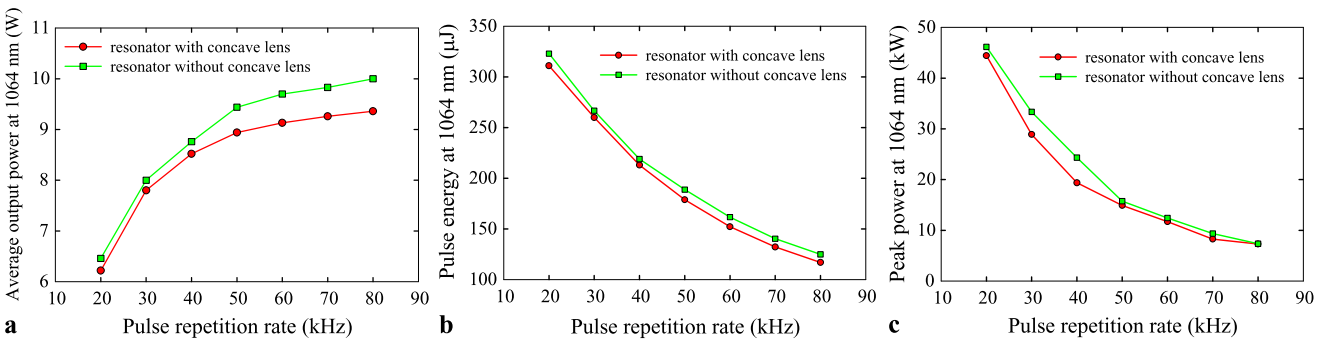

Fig. 5 Dependence of the (**a**) average output power, (**b**) pulse energy, and (**c**) peak power on the pulse repetition rate at a pump power of 25 W for the cavities with and without the concave lens

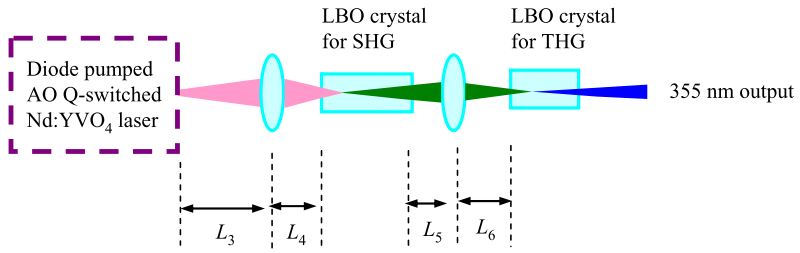

Fig. 6 Schematic of the experimental setup for extra-cavity SHG and THG

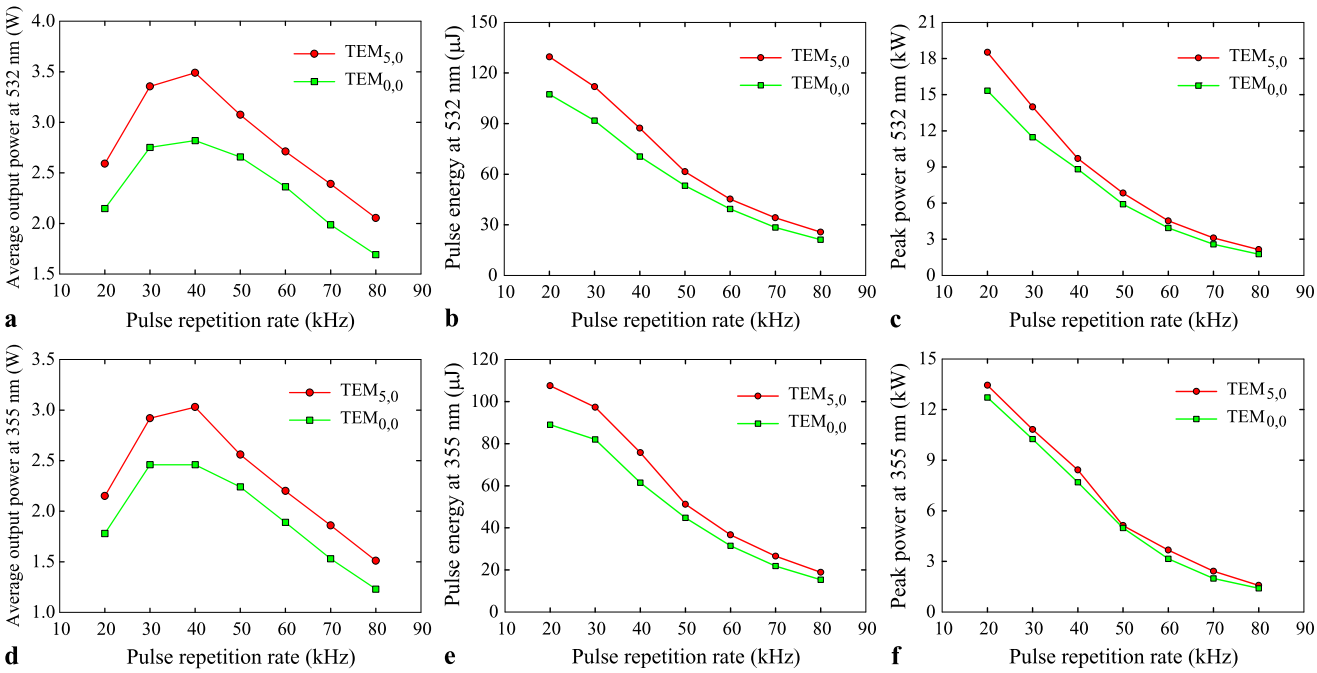

Fig. 7 Harmonic generation performances: (**a**) average output power, (**b**) pulse energy, (**c**) peak power at 532 nm; and (**d**) average output power, (**e**) pulse energy, (**f**) peak power at 355 nm versus the pulse repetition rate at a pump power of 25 W for the high-order $TEM_{5,0}$ mode and the fundamental $TEM_{0,0}$ mode

At a pump power of 25 W, the maximum output powers, pulse energies, and peak powers at 532 nm and 355 nm versus the pulse repetition rate for the high-order $TEM_{5,0}$ mode and the fundamental $TEM_{0,0}$ mode are shown in Fig. 7, respectively. Note that, as shown in Fig. 5, the average power at 1064 nm of the $TEM_{5,0}$ mode is 5–10% lower than that of the fundamental $TEM_{0,0}$ mode. However, it is intriguing that the conversion efficiencies in the processes of SHG and THG obtained with the $TEM_{5,0}$ mode are noticeably higher than the results obtained with the $TEM_{0,0}$ mode, as illustrated in Fig. 7(a) and (d). At a pulse repetition rate of 40 kHz, the maximum output power at 355 nm obtained with the $TEM_{5,0}$ mode was 3.1 W; the optical-to-optical conversion efficiencies were 35.6% (from 1064 nm to 355 nm) and 12.4% (from 808 nm to 355 nm), respectively. On the other hand, the maximum output power at 355 nm obtained with the $TEM_{0,0}$ mode was 2.45 W; the optical-to-optical conversion efficiencies were 28.1% (from 1064 nm to 355 nm) and 9.8% (from 808 nm to 355 nm), respectively. Based on the calculated results for the case of $f = -\infty$ in Fig. 2, the mode radius of the $TEM_{0,0}$ mode is about 300 μm. A Rayleigh range of such a $TEM_{0,0}$ beam is estimated to be 26.6 cm, so the divergence of the beam would be rather low. However, we experimentally found that the superiority of the $TEM_{5,0}$ mode over the fundamental $TEM_{0,0}$ mode in the processes of extra-cavity SHG and THG. This experimental observation is regard as a result of the considerable narrowness of the central peak of the high-order Laguerre–Gaussian $TEM_{p,0}$ mode than that of the Gaussian beam.

It is worthwhile to mention that although the generation of high-order Laguerre–Gaussian $TEM_{p,0}$ modes in a Q-switched laser has been reported with the other method [9], our experimental setup intrinsically owns the advantages of compactness, simplicity and is potentially beneficial for power scaling. In comparison with [5], expanding the cavity mode size instead of tight focusing of the pump beam can remarkably relieve the thermal problems under high-power operation. Furthermore, the application

of high-order Laguerre–Gaussian modes in the process of extra-cavity SHG and THG was investigated for the first time and we experimentally found the $TEM_{p,0}$ mode is noticeably superior to the $TEM_{0,0}$ mode in the harmonic generation process.

5 Conclusion

In summary, we have successfully designed a compact resonator to generate high-power Laguerre–Gaussian $TEM_{5,0}$ mode. The resonator is composed of two plane mirrors with an intra-cavity concave lens to expand the cavity mode size. At a pump power of 25 W, the average output power for the Laguerre–Gaussian $TEM_{5,0}$ mode was found to be up to 8.52 W at a pulse repetition rate of 40 kHz. Furthermore, we experimentally verify that the $TEM_{5,0}$ mode is conspicuously superior to the $TEM_{0,0}$ mode in the processes of SHG and THG. At an incident pump power of 25 W at 808 nm and a repetition rate of 40 kHz, the maximum output powers at 355 nm obtained with the $TEM_{5,0}$ mode and $TEM_{0,0}$ mode were 3.1 W and 2.45 W, respectively. The optical-to-optical conversion efficiencies from 1064 nm to 355 nm were found to be 35.6% and 28.1% for the $TEM_{5,0}$ mode and $TEM_{0,0}$ mode, respectively.

Acknowledgements The authors thank the National Science Council for their financial support of this research under Contract No. NSC-97-2112-M-009-016-MY3.

References

1. A.V. Hicks, C.X. Wang, G.Y. Wang, Proc. SPIE **5332**, 120 (2004)
2. C.X. Wang, G.Y. Wang, A.V. Hicks, D.R. Dudley, H.Y. Pang, N. Hodgson, Proc. SPIE **6100**, 610019 (2006)
3. X.P. Yan, Q. Liu, M. Gong, D.S. Wang, X. Fu, Laser Phys. Lett. **6**, 93 (2009)
4. B. Li, J. Yao, X. Ding, Q. Sheng, P. Wang, Opt. Commun. **283**, 3497 (2010)
5. C.J. Flood, G. Giuliani, H.M. van Driel, Opt. Lett. **15**, 215 (1990)
6. R. Oron, S. Blit, N. Davidson, A.A. Friesem, Z. Bomzon, E. Hasman, Appl. Phys. Lett. **77**, 3322 (2000)
7. Y.F. Chen, Y.P. Lan, S.C. Wang, Appl. Phys. B **72**, 167 (2001)
8. Y.F. Chen, Y.P. Lan, Phys. Rev. A **63**, 063807 (2001)
9. A.A. Ishaaya, N. Davidson, G. Machavariani, E. Hasman, A.A. Friesem, IEEE J. Quantum Electron. **39**, 74 (2003)
10. T. Moser, M.A. Ahmed, F. Pigeon, O. Parriaux, E. Wyss, Th. Graf, Laser Phys. Lett. **1**, 234 (2004)
11. J.F. Bisson, Yu. Senatsky, K.I. Ueda, Laser Phys. Lett. **2**, 327 (2005)
12. M.A. Porras, R. Borghi, M. Santarsiero, J. Opt. Soc. Am. A **18**, 177 (2001)
13. J. Durnin, J.J. Miceli, Jr., J.H. Eberly, Phys. Rev. Lett. **58**, 1499 (1987)
14. A. Hakola, A. Shevchenko, S.C. Buchter, M. Kaivola, N.V. Tabiryan, J. Opt. Soc. Am. B **23**, 637 (2006)
15. A. Hakola, T. Hakkarainen, R. Tommila, T. Kajava, J. Opt. Soc. Am. B **27**, 2342 (2010)
16. A.N. Khilo, E.G. Katranji, A.A. Ryzhevich, J. Opt. Soc. Am. A **18**, 1986 (2001)
17. F. Wu, Y. Chen, D. Guo, Appl. Opt. **46**, 4943 (2007)
18. Y. Matsuoka, Y. Kizuka, T. Inoue, Appl. Phys. A **84**, 423 (2006)
19. F. Courvoisier, P.-A. Lacourt, M. Jacquot, M.K. Bhuyan, L. Furfaro, J.M. Dudley, Opt. Lett. **34**, 3163 (2009)
20. T. Wulle, S. Herminghaus, Phys. Rev. Lett. **70**, 1401 (1993)
21. C. Altucci, R. Bruzzese, D. D'Antuoni, C. de Lisio, S. Solimeno, J. Opt. Soc. Am. B **17**, 34 (2000)
22. S. Orlov, A. Stabinis, V. Smilgevičius, G. Valiulis, A. Piskarskas, Opt. Lett. **32**, 68 (2007)
23. W. Koechner, *Solid-State Laser Engineering*, 6th edn. (Springer, Berlin, 2005)

ISSN 1054-660X, Laser Physics, 2011, Vol. 21, No. 10, pp. 1750–1754.

High-Power 10-GHz Self-Mode-Locked Nd:$LuVO_4$ Laser[1]

Y. J. Huang[a], H. C. Liang[a], Y. F. Chen[a, *], H. J. Zhang[b], J. Y. Wang[b], and M. H. Jiang[b]

[a] *Department of Electrophysics, National Chiao Tung University, Hsinchu, Taiwan*

[b] *State Key Laboratory of Crystal Materials and Institute of Crystal Materials, Shandong University, Jinan, PR China*

*e-mail: yfchen@cc.nctu.edu.tw

Received March 22, 2011; in final form, April 15, 2011; published online September 2, 2011

Abstract—We report on a high-power diode-end-pumped self-mode-locked Nd:$LuVO_4$ laser with the pulse repetition rate up to 9.52 GHz for the first time. The large third-order nonlinearity of the Nd:$LuVO_4$ crystal is exploited to efficiently achieve a fairly stable self-mode-locked operation without any additional components. The detailed characteristics of the compact efficient self-mode-locked laser are experimentally investigated and theoretically analyzed. With the incident pump power of 2.6 W, the average output power up to 0.54 W is generated with the pulse width of 7.9 ps at the pulse repetition rate of 9.52 GHz.

DOI: 10.1134/S1054660X11190169

1. INTRODUCTION

In recent years, high-repetition-rate laser sources have been rapidly developed since they are useful in a verity of applications that include optical frequency combs, low-noise microwave sources, high-speed optical sampling, optical clocking, ultrafast spectroscopy, particle accelerators, high-capacity telecommunication systems, frequency metrology, etc. [1–3]. In comparison with other techniques, diode-pumped mode-locked solid-state laser intrinsically possesses the advantages of high average output power, low cost, compactness, long-term stability, and excellent timing jitter that is favorable for accomplishing the high-repetition-rate operation. Among numerous mode-locked methods, the phenomenon of self mode locking in laser resonator is of greatly scientific interest because it does not need any additional nonlinearities except the gain medium to obtain the short pulses. According to several theoretical studies and experimental investigations, the origin of the self mode locking is regarded as a result of the combination tone of the third-order nonlinearity of the gain medium that could compensate for the dispersion effect caused by the multimode oscillation [4–11]. As a result, the relative compactness and simplicity of the self-mode-locked mechanism is potentially suitable for achieving the mode-locked lasers with high repetition rates.

Nd-doped vanadate crystals, such as Nd:YVO_4 and Nd:$GdVO_4$, are extensively studied owing to their high absorption coefficients for diode pumping, large stimulated emission cross sections, and constantly polarized outputs due to natural birefringence [12–15]. Previous studies also manifested that YVO_4 and $GdVO_4$ crystals have attractive $\chi^{(3)}$ nonlinear properties [16, 17] that have been exploited for efficient stimulated Raman scattering conversions [18–26]. Furthermore, it has also been demonstrated that the large third-order nonlinearities of the Nd vanadate crystals could be employed to achieve a fairly stable self-mode-locked operation with several gigahertz (GHz) repetition rates [27–30]. Recently, a new member of the vanadate family, known as Nd:$LuVO_4$, was proposed as a promising laser crystal for diode pumping [31–40]. Its absorption and emission cross section have been determined to be greater than those of other Nd vanadate crystals. More importantly, it has been proved to possess a large third-order nonlinearity [41] and diode-pumped Nd:$LuVO_4$ self-Raman lasers have been successfully demonstrated either in continuous-wave (CW) or pulsed operation [42, 43]. However, so far there is no any reports on the self-mode-locked performance of the Nd:$LuVO_4$ crystal to the best of our knowledge.

In this letter, we report on a high-power diode-end-pumped self-mode-locked Nd:$LuVO_4$ laser with the pulse repetition rate up to 9.52 GHz for the first time. The large third-order nonlinearity of the Nd:$LuVO_4$ crystal is exploited to efficiently achieve a fairly stable self-mode-locked operation without any additional components. The detailed characteristics of the compact efficient self-mode-locked laser are experimentally investigated and theoretically analyzed. With the incident pump power of 2.6 W, the average output power up to 0.54 W is generated with the pulse width of 7.9 ps at the pulse repetition rate of 9.52 GHz.

2. EXPERIMENTAL SETUP

The experimental setup is schematically shown in Fig. 1. The concave input mirror had a radius of curvature of 500 mm. It was antireflection (AR) coated at 808 nm on the entrance face, and was coated at 808 nm for high transmission as well as 1064 nm for high reflection on the second surface. The gain

[1] The article is published in the original.

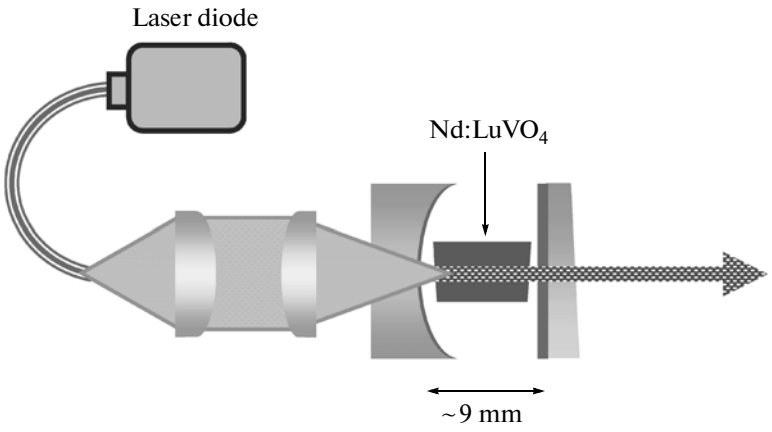

Fig. 1. Schematic of a diode-end-pumped self-mode-locked Nd:$LuVO_4$ laser.

medium was an a-cut 0.5 at % Nd:$LuVO_4$ crystal with dimensions of $3 \times 3 \times 8$ mm^3. Both facets of the laser crystal were AR coated at 808 nm as well as 1064 nm and wedged 1° to avoid the Fabry–Perot etalon effect. The laser crystal was wrapped with indium foil and mounted in a water-cooled copper heat sink at 20°C. A flat wedged output coupler with 15% transmission at 1064 nm was used during the experiment. The pump source was a 3-W 808-nm fiber-coupled laser diode with a core diameter of 100 μm and a numerical aperture of 0.16. The pump radius of 60 μm was re-imaged into the laser crystal by a lens unit, which has the focal length of 25 mm with the coupling efficiency of 90%. The optical cavity length l^*_{cav} was adjusted to be around 15 mm, corresponding to the free spectral range of 10 GHz. The fundamental mode radius on the laser crystal was calculated to be 150 μm by the use of ABCD matrix method.

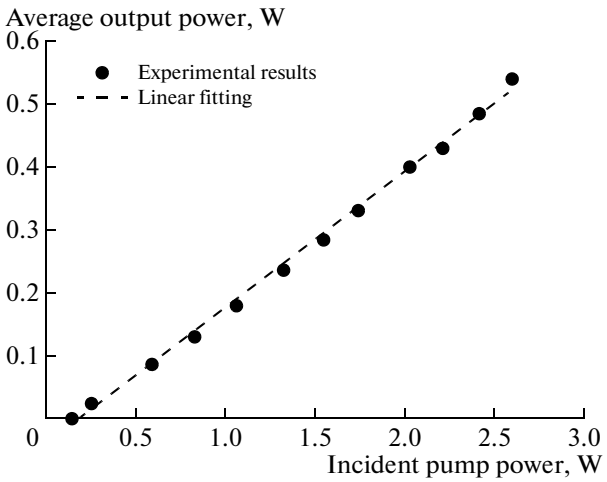

Fig. 2. The dependence of the average output power on the incident pump power for the self-mode-locked Nd:$LuVO_4$ laser.

A high-speed InGaAs photodetector with rise time of 35 ps and a digital oscilloscope (Agilent, DSO 80000) with electrical bandwidth of 12 GHz as well as sampling rate of 25 ps were employed to observe the real-time temporal dynamics. The photodetector was also connected to a radio-frequency (RF) spectrum analyzer (ROHDE & SCHWARZ, FSEK30) with bandwidth of 40 GHz to analyze the output signal. The spectral information of the laser was monitored by a Fourier optical spectrum analyzer (Advantest, Q8347) that is constructed with a Michelson interferometer with resolution of 0.003 nm. The fine structure of the mode-locked pulses was measured with the help of the commercial autocorrelator (APE pulse check, Angewandte Physik and Elektronik GmbH).

3. RESULTS AND DISCUSSIONS

First of all, the laser cavity was aligned to obtain the maximum output power. Under this circumstance, the pulse train was found to exhibit a spontaneous mode locking with small amplitude fluctuation and CW background. With the fine-tuning of the cavity alignment, the temporal behavior was transformed into a nearly perfect mode-locked state without any CW background. The observation of the present configuration is nearly the same as the recent investigations of the self mode locking on Nd-doped lasers and fiber lasers [11, 27–30]. The average output power of the stable mode locking was experimentally found to be approximately 90% of the maximum average output power. Figure 2 shows the dependence of the average output power on the incident pump power for the stable mode-locked operation at the pulse repetition rate of 9.52 GHz. The laser pump threshold is 0.14 W and the maximum output power reaches 0.54 W at the incident pump power of 2.6 W. Note that the stable mode-locked state could always be generated as long as the incident pump power was beyond the laser pump threshold. Figure 3 shows the temporal behav-

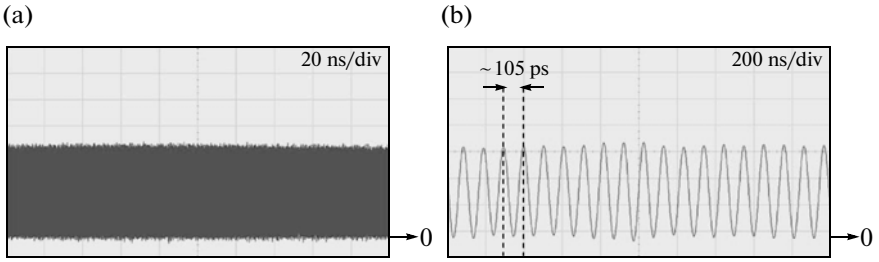

Fig. 3. Pulse trains on two different timescales: (a) time span of 200 ns, demonstrating amplitude stability; (b) time span of 2 ns, demonstrating the mode-locked pulses and the separation between neighboring pulses.

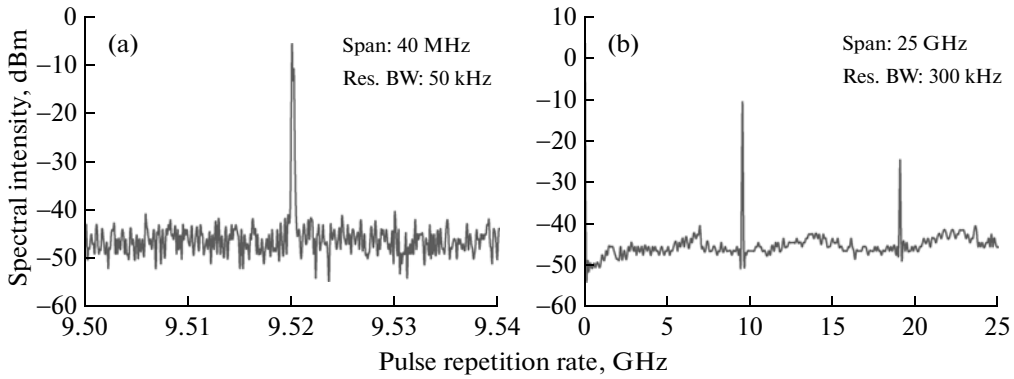

Fig. 4. RF spectrum for the self-mode-locked Nd:$LuVO_4$ laser: (a) span of 40 MHz, illustrating the fundamental harmonic at 9.52 GHz; (b) span of 25 GHz, illustrating the locations of the first two harmonics.

iors of the self-mode-locked laser with two different time scales at the incident pump power of 2.6 W and the pulse repetition rate of 9.52 GHz. The fluctuation of amplitude stability is found to be less than 3% during day-long operation, as shown in Fig. 3a with time span of 200 ns. Figure 3b illustrates the pulse shapes with time span of 2 ns, and the separation between two neighboring pulses is roughly 105 ps that corresponds to the roundtrip time of the resonator. However, it is obvious that the detailed pulse shape could not be clearly resolved due to the limited bandwidth of a digital oscilloscope.

To confirm the stability of the self-mode-locked Nd:$LuVO_4$ laser, the RF spectrum is measured in Fig. 4, in which the fundamental harmonic is located at 9.52 GHz and the second harmonic is found to be approximately 19 GHz. It can be seen that the peak of the fundamental harmonic is 40 dBm above the background level and the relaxation oscillation sidebands are negligibly observable, as shown in Fig. 4a. The relative frequency deviation of the fundamental harmonic, $\Delta\nu/\nu$, is approximately 10^{-5} over day-long operation, where ν is the center frequency of the fundamental harmonic and $\Delta\nu$ is the frequency deviation in terms of the full width at half maximum (FWHM) and is inferred from the beat note spectrum. The optical spectrum with the FWHM width of 0.271 nm and the central wavelength of 1065.83 nm is depicted in Fig. 5a, where the number of lasing longitudinal modes in the self-mode-locked Nd:$LuVO_4$ laser could be definitely determined to be nine. It is well known that the maximum number of lasing longitudinal modes $N_{\max}$ that can oscillate in a optical cavity is determined from the condition that the effective round-trip gain is not less than the round-trip loss. With mode-locked states as a basis, we have recently derived an analytical formula to precisely estimate the maximum number of longitudinal modes in terms of the cavity geometry and well-known material parameters, which is given by [44]:

$$\left(\frac{2}{l_{\text{cav}}}\right)\left[\frac{\alpha l_g}{(1-e^{-\alpha l_g})}\right]\int_d^{d+l_g}\cos^2(kz)g_N(z)e^{-\alpha(z-d)}dz \geq \left[\ln\left(\frac{1}{R}\right)+L\right]\frac{h\nu_p/(\sigma\tau)}{2P_{\text{abs}}/[\pi(\omega_l^2+\omega_p^2)]},$$

where $g_N(z) = e^{-[N\pi z/2l_{\text{cav}}]^2} + e^{-[N\pi(l_{\text{cav}}-z)/2l_{\text{cav}}]^2}$, l_{cav} is the geometrical cavity length, α is the absorption coefficient, l_g is the crystal length, d is the separation between the input mirror and the laser crystal, k is the wavenumber, R is the reflectivity of the output coupler, L is the round-trip loss, h is the planck constant, ν_p is the pump frequency, σ is the stimulated emission cross

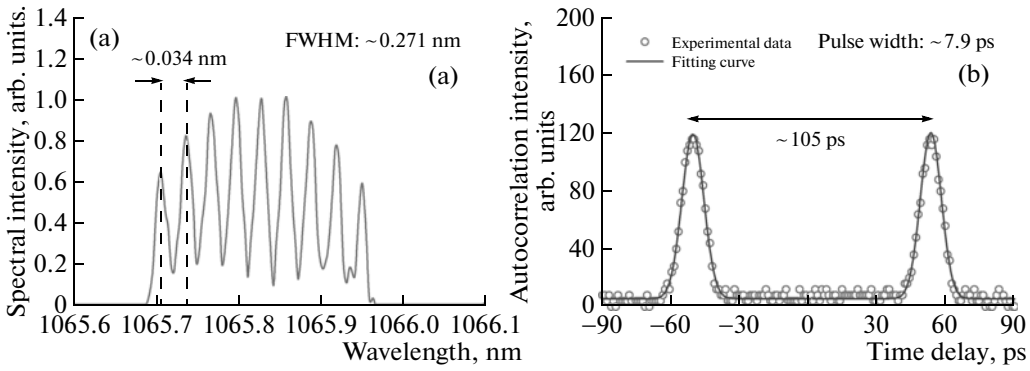

Fig. 5. (a) Optical spectrum of the output pulses for the self-mode-locked Nd:$LuVO_4$ laser; (b) corresponding autocorrelation trace.

section, τ is the emission lifetime, P_{abs} is the absorbed pump power, ω_l is the mode radius, and ω_p is the pump radius. For the present experimental configuration, the maximum number of longitudinal modes is calculated to be $N_{max} = 9-10$ with the following parameters: $l_{cav} = 9$ mm, $\alpha = 0.4$ mm^{-1}, $l_g = 8$ mm, $d = 0.5$ mm, $R = 0.85$, $L = 0.005$, $h\nu_p = 2.46 \times 10^{-19}$ J, $\sigma = 1.46 \times 10^{-18}$ cm^2, $\tau = 65$ μs, $P_{abs} = 2.6$ W, $\omega_l = 150$ μm, and $\omega_p = 60$ μm. The good agreement between the theoretical estimations and the experimental observations validates the usefulness of the model for our high-repetition-rate self-mode-locked Nd:$LuVO_4$ laser. On the other hand, the mode spacing $\Delta\lambda$ could be theoretically evaluated by the equation $\Delta\lambda = \lambda^2/2l^*_{cav}$ for a linear standing-wave resonator, where λ is the central lasing wavelength and the l^*_{cav} is the optical cavity length. For the present setup, the mode spacing $\Delta\lambda$ is calculated to be 0.036 nm, which is in excellent consistent with the experimental observation of 0.034 nm, as shown in Fig. 5a. The recorded autocorrelation trace of the stable CW mode-locked operation at the pulse repetition rate of 9.52 GHz is shown in Fig. 5b with time interval of 150 ps. Since the separation between the peaks of the autocorrelation trace is approximately equal to the roundtrip time of 105 ps, the pulse repetition rate could be determined to be 9.52 GHz. The FWHM width of the single pulse of the CW mode locking is measured to be 12 ps, and the pulse width is estimated to be 7.9 ps assuming the sech^2-shaped temporal profile. As a consequence, the time-bandwidth product of the mode-locked pulse is 0.565, indicating the pulses to be frequency chirped.

Finally, it is worthwhile to mention that the peak power of 7.2 W obtained from our self-mode-locked Nd:$LuVO_4$ laser is slightly better than the results obtained from other mode-locked Nd-doped laser with several GHz repetition rates [45–48], indicating that using self mode locking is a promising way for power scaling at high repetition rates. Currently, the semiconductor-based structure is the most popular saturable absorber for achieving mode-locked operation [49, 50]. Nevertheless, the main obstacle to fulfill the CW mode locking at high repetition rates with a semiconductor saturable absorber is the tendency of the laser to mode lock only under a Q-switched envelope due to the reduced intracavity pulse energy [51]. Comparative speaking, the self mode locking is believed to be a favorable approach for efficiently achieving a reliable mode-locked laser with high repetition rates.

4. CONCLUSIONS

In summary, we have reported on a high-power diode-end-pumped self-mode-locked Nd:$LuVO_4$ laser with the pulse repetition rate up to 9.52 GHz for the first time. The large third-order nonlinearity of the Nd:$LuVO_4$ crystal has been exploited to efficiently achieve a fairly stable self-mode-locked operation without any additional components. The detailed characteristics of the compact efficient self-mode-locked laser have been experimentally investigated and theoretically analyzed. With the incident pump power of 2.6 W, the average output power up to 0.54 W is generated with the pulse width of 7.9 ps at the pulse repetition rate of 9.52 GHz. We believe that the compact efficient self-mode-locked mechanism could provide a reliable high-repetition-rate laser source with high average output power in the future.

ACKNOWLEDGMENTS

The authors thank the National Science Council for their financial support of this research under Contract no. NSC-97-2112-M-009-016-MY3.

REFERENCES

1. U. Keller, Nature **424**, 831 (2003).
2. R. Paschotta, L. Krainer, S. Lecomte, G. J. Spühler, S. C. Zeller, A. Aschwanden, D. Lorenser, H. J. Unold,

K. J. Weingarten, and U. Keller, New J. Phys. **6**, 174 (2004).
3. U. Keller, Appl. Phys. B **100**, 15 (2010).
4. H. State, J. Appl. Phys. **38**, 4648 (1967).
5. F. R. Nash, IEEE J. Quantum Electron. **3**, 189 (1967).
6. M. A. Duguay, S. L. Shapiro, and P. M. Rentzepis, Phys. Rev. Lett. **19**, 1014 (1967).
7. M. Bass and D. Woodward, Appl. Phys. Lett. **12**, 275 (1968).
8. H. State and M. Bass, J. Appl. Phys. **40**, 377 (1969).
9. Ph. Brechignac and F. Legay, Appl. Phys. Lett. **18**, 424 (1971).
10. M. F. H. Tarroja, M. Sharafi, and L. W Casperson, J. Opt. Soc. Am. B **6**, 1564 (1989).
11. P. Glas, M. Naumann, A. Schirrmacher, L. Däweritz, and R. Hay, Opt. Commun. **161**, 345 (1999).
12. J. Yang, J. Liu, and J. He, Laser Phys. Lett. **2**, 171 (2005).
13. Y. Wang, L. Huang, H. Zhang, X. Yan, Q. Liu, and M. Gong, Laser Phys. Lett. **5**, 286 (2008).
14. A. Zhao, H. T. Huang, J. L. He, B. T. Zhang, J. F. Yang, J. L. Xu, and X. Q. Yang, Laser Phys. Lett. **6**, 571–574 (2009).
15. V. Kubeček, M. Jelínek, M. Čech, P. Hiršl, and J. C. Diels, Laser Phys. Lett. **7**, 130 (2010).
16. A. A. Kaminskii, K. Ueda, H. J. Eichler, Y. Kuwano, H. Kouta, S. N. Bagaev, T. H. Chyba, J. C. Barnes, G. M. A. Gad, T. Murai, and J. R. Lu, Opt. Commun. **194**, 201 (2001).
17. A. A. Kaminskii, H. J. Eichler, H. Rhee, and K. Ueda, Laser Phys. Lett. **5**, 804 (2008).
18. Y. F. Chen, Opt. Lett. **29**, 1251 (2004).
19. Y. F. Chen, Opt. Lett. **29**, 1915 (2004).
20. Y. F. Chen, Opt. Lett. **29**, 2172 (2004).
21. F. Su, X. Zhang, Q. Wang, S. Ding, P. Jia, S. Li, S. Fan, C. Zhang, and B. Liu, J. Phys. D: Appl. Phys. **39**, 2090 (2006).
22. S. Ding, X. Zhang, Q. Wang, F. Su, P. Jia, S. Li, S. Fan, J. Chang, S. Zhang, and Z. Liu, IEEE Quantum Electron. **42**, 927 (2006).
23. X. H. Chen, X. Y. Zhang, Q. P. Wang, P. Li, and Z. H. Cong, Laser Phys. Lett. **6**, 26(2009).
24. Y. F. Chen, Appl. Phys. B **78**, 685 (2004).
25. Y. F. Chen, Opt. Lett. **29**, 2632 (2004).
26. F. Su, X. Zhang, Q. Wang, F. Wu, S. Li, X. Zhang, and Z. Cong, Opt. Mater. **30**, 1895 (2008).
27. H. C. Liang, R. C. C. Chen, Y. J. Huang, K. W. Su, and Y. F. Chen, Opt. Express **16**, 21149 (2008).
28. H. C. Liang, H. L. Chang, W. C. Huang, K. W. Su, Y. F. Chen, and Y. T. Chen, Appl. Phys. B **97**, 451 (2009).
29. H. C. Liang, Y. J. Huang, Y. C. Lin, T. H. Lu, Y. F. Chen, and K. F. Huang, Opt. Lett. **34**, 3842 (2009).
30. H. C. Liang, Y. J. Huang, W. C. Huang, K. W. Su, and Y. F. Chen, Opt. Lett. **35**, 4 (2010).
31. C. Maunier, J. L. Doualan, R. Moncorge, A. Speghini, M. Bettinelli, and E. Cavalli, J. Opt. Soc. Am. B **19**, 1794 (2002).
32. Z. Wang, H. Zhang, F. Xu, D. Hu, X. Xu, J. Wang, and Z. Shao, Laser Phys. Lett. **5**, 25(2008).
33. K. Cheng, S. Z. Zhao, Y. F. Li, G. Q. Li, D. C. Li, K. J. Yang, J. An, G. Zhang, H. B. Ge, and Z. G. Yu, Laser Phys. Lett. **6**, 703 (2009).
34. H. Ge, S. Zhao, Y. Li, G. Li, D. Li, K. Yang, M. Li, G. Zhang, K. Cheng, and Z. Yu, Laser Phys. **19**, 1226(2009).
35. G. Zhang, S. Z. Zhao, Y. F. Li, G. Q. Li, D. C. Li, K. J. Yang, K. Cheng, H. B. Ge, and Z. G. Yu, Laser Phys. **19**, 2082 (2009).
36. F. Q. Liu, J. L. He, J. L. Xu, J. F. Yang, B. T. Zhang, H. T. Huang, C. Y. Gao, J. Q. Xu, and H. J. Zhang, Laser Phys. **20**, 786(2010).
37. J. H. Lin, C. C. Huang, and K. H. Lin, Laser Phys. **20**, 1881 (2010).
38. Y. F. Lü, X. H. Zhang, and J. Xia, Laser Phys. Lett. **7**, 487(2010).
39. Z. M. Jiang, W. Liang, D. R. Chen, and X. H. Zhang, Laser Phys. **21**, 90 (2011).
40. W. Liang, Z. L. Liang, Y. Q. Liu, and X. H. Zhang, Laser Phys. **21**, 108 (2011).
41. A. A. Kaminskii, H. Rhee, H. J. Eichler, K. Ueda, K. Oka, and H. Shibata, Appl. Phys. B **93**, 865 (2008).
42. A. A. Kaminskii, M. Bettinelli, J. Dong, D. Jaque, and K. Ueda, Laser Phys. Lett. **6**, 374 (2009).
43. Y. Lü, X. Zhang, S. Li, J. Xia, W. Cheng, and Z. Xiong, Opt. Lett. **35**, 2964 (2010).
44. Y. F. Chen, Y. J. Huang, P. Y. Chiang, Y. C. Lin, and H. C. Liang, Appl. Phys. B, DOI 10.1007/s00340-010-4293-2.
45. P. A. Schulz and S. R. Henion, Opt. Lett. **16**, 1502–1504 (1991).
46. L. Krainer, R. Paschotta, J. Aus der Au, C. Hönninger, U. Keller, M. Moser, D. Kopf, and K. J. Weingarten, Appl. Phys. B **69**, 245 (1999).
47. L. Krainer, D. Nodop, G. J. Spühler, S. Lecomte, M. Golling, R. Paschotta, D. Ebling, T. Ohgoh, T. Hayakawa, and U. Keller, Opt. Lett. **29**, 2629 (2004).
48. A. Agnesi, F. Pirzio, A. Tomaselli, G. Reali, and C. Braggio, Opt. Express **13**, 5302 (2005).
49. U. Keller, K. J. Weingarten, F. X. Kärtner, D. Kopf, B. Braun, I. D. Jung, R. Fluck, C. Hönninger, N. Matuschek, and J. Aus der Au, IEEE J. Sel. Top. Quantum Electron. **2**, 435(1996).
50. S. Tsuda, W. H. Knox, S. T. Cundiff, W. Y. Jan, and J. E. Cunningham, IEEE J. Sel. Top. Quantum Electron. **2**, 454(1996).
51. C. Hönninger, R. Paschotta, F. Morier-Genoud, M. Moser, and U. Keller, J. Opt. Soc. Am. B **16**, 46 (1999).

IOP Publishing Journal of Optics

J. Opt. **13** (2011) 075705 (7pp) doi:10.1088/2040-8978/13/7/075705

Non-paraxial contributions to the far-field pattern of surface-emitting lasers: a manifestation of the momentum-space wavefunctions of quantum billiards

Y T Yu, Y J Huang, P Y Chiang, Y C Lin, K F Huang and Y F Chen[1]

Department of Electrophysics, National Chiao Tung University, Hsinchu, Taiwan

E-mail: yfchen@cc.nctu.edu.tw

Received 5 January 2011, accepted for publication 19 April 2011
Published 12 May 2011
Online at stacks.iop.org/JOpt/13/075705

Abstract

We investigated experimentally non-paraxial contributions to the high-order far-field pattern of large-area vertical-cavity surface-emitting lasers in order to explore by analogy the momentum-space wave distributions of quantum billiards. Our results reveal that non-paraxial contributions significantly influence the morphology of the high-order far-field pattern. A fast reliable method is developed for transforming the experimental far-field patterns to the correct Fourier transform of the corresponding near-field lasing modes. In this way we visualize the momentum-space (p–q) wavefunctions of quantum billiards.

Keywords: surface-emitting laser, non-paraxial effect, far-field pattern, quantum billiards

(Some figures in this article are in colour only in the electronic version)

1. Introduction

The vertical-cavity surface-emitting laser (VCSEL) has been identified as a promising light source for applications in short distance communication, data transmission, and sensors [1, 2]. There has been intensive research on physical properties of the VCSEL, including the optical feedback dynamics, polarization, and transverse pattern formation [3–6]. Recently, the analogy between the Helmholtz equation and the time-independent Schrödinger equation has enables us to exploit the transverse near-field patterns of oxide-confined VCSELs to visualize the coordinate-space wavefunctions of 2D quantum billiards with the same lateral shapes [7–10]. Quantum billiard systems have been widely used to explore many striking mesoscopic phenomena such as electron transport [11], conductance fluctuations in quantum dots [12, 13], and the diffraction in time effect [14].

Since the far-field pattern is the Fourier transform of the near-field pattern based on the paraxial approximation, the momentum-space wavefunctions of 2D quantum billiards can also be analogously observed with the high-order lasing modes of VCSELs [8]. Generation of the higher-order transverse modes can provide more interesting perspectives for the exploration of the quantum–classical connection. However, during the free-space propagation of the higher-order lasing modes, non-paraxial contributions to the total wavevector k may significantly influence the far-field patterns. Therefore, it is essentially important to develop an appropriate correcting method for extracting the momentum-space wavefunctions from the experimental far-field patterns with the substantial non-paraxial contribution.

In this work, we first exploit square-shape large-aperture VCSELs to experimentally investigate the difference between the low-order and high-order far-field transverse patterns. Experimental results reveal that the high-order far-field patterns display significant bowing toward the center of the device. We define this effect as the pincushion curving of the Fourier transform of the near-field wavefunction and we refer to it as pincushion curving. We employ the stationary phase

[1] Address for correspondence: Department of Electrophysics, National Chiao Tung University, 1001 Ta Hsueh Road, Hsinchu 30050, Taiwan.

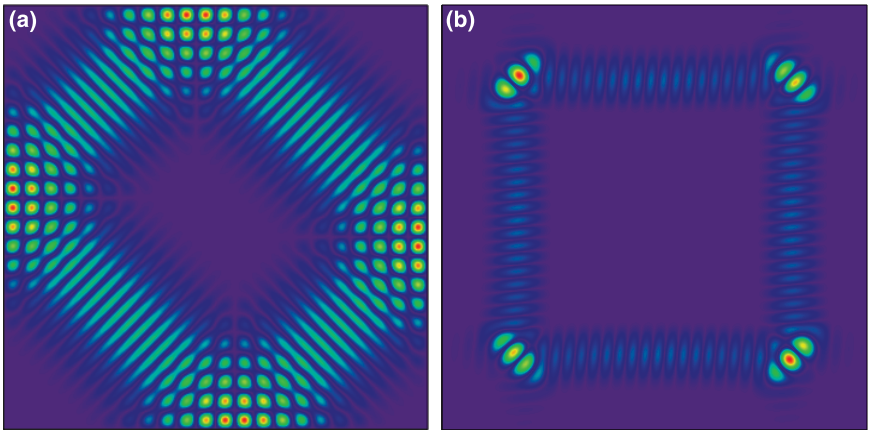

Figure 1. (a) Theoretically calculated coherent state $|S^{1,1,0.55\pi}_{22,5,+}(x, y)|^2$ in a 2D square billiard; (b) the correspondence momentum space.

method [15] to confirm that the curving feature arises from the non-paraxial contribution. Moreover, a useful mapping is developed to recover the momentum-space wave patterns of 2D quantum billiards from the experimental far-field lasing patterns. We further numerically explore the higher-order eigenstates of equilateral triangular VCSELs to demonstrate that the pincushion curving is a typical feature of the non-paraxial contribution to the far-field patterns.

From the viewpoint of experimental measurements, the motivation and significance of this research as well as relevant materials can be more clearly appreciated. The observation of near-field patterns of lasing modes inevitably requires a re-imaging optics with sufficiently high numerical aperture, whereas the far-field patterns can be directly measured without any re-imaging optics by simply using a screen. It is well known that the far-field pattern can be numerically obtained from the experimental near-field patterns with the diffraction theory. However, under the circumstances of a strong non-paraxial contribution, it is scientifically important to extract the information of the near-field pattern from the experimental far-field pattern. Our work is aimed at developing a straightforward procedure for mapping the experimental far-field lasing pattern into the accurate Fourier transform pattern of the near-field mode.

2. Coherent states in square quantum billiards

To begin with, we give a brief synopsis for the coordinate-space and momentum-space representations of the coherent states in a square billiard. The choice of the square-shape geometry is motivated by a recent experiment where the wavefunctions localized on classical periodic orbits were found not only to be the persistent states in open square quantum dots but also to be associated with the striking phenomena of conductance fluctuations [12, 13]. For a square billiard with the vertices at $(\pm a/2, \pm a/2)$ and $(\pm a/2, \mp a/2)$, the quantum eigenstates $\psi_{\tilde{m},\tilde{n}}(x, y)$ are given by [16]

$$\psi_{\tilde{m},\tilde{n}}(x, y) = (2/a)\sin\left[k_{\tilde{m}}\,(x + a/2)\right]\sin\left[k_{\tilde{n}}\,(y + a/2)\right], \quad (1)$$

where $k_n = n\pi/a$ $(n = 1, 2, 3, \ldots)$ and a is the length of the square boundary. On the other hand, each family of classical periodic orbits in a square billiard can be denoted by with three parameters (p, q, ϕ), where p and q are two positive integers describing the number of collisions with horizontal and vertical walls, and the phase factor ϕ is in the range of $-\pi$ to π that is related to the wall positions of specular reflection points [16]. It has been verified that with the Schwinger SU(2) representation the coherent states associated with periodic orbits (p, q, ϕ) can be analytically expressed as [16]

$$\Psi^{p,q,\phi}_{N,M}(x, y) = \sum_{K=-M}^{M} C_{M,K}\,\mathrm{e}^{\mathrm{i}K\phi}\psi_{qN+pK,pN-qK}(x, y), \quad (2)$$

where N represents the order of the coherent state, $C_{M,K} = \frac{1}{2^M}\binom{2M}{M+K}^{1/2}$ is the weighting coefficient, and $\binom{n}{k} = \frac{n!}{k!(n-k)!}$ represents the binomial coefficient. Note that the coherent states obtained as a linear superposition of a few nearly degenerate eigenstates have been verified to be the persistent stationary states in real mesoscopic systems and to display quantum interference features in the classical periodic orbits.

With the Fourier transform, the momentum-space representation of the coherent states $\Psi^{p,q,\phi}_{N,M}(x, y)$ is given by

$$\begin{aligned}\tilde{\Psi}^{p,q,\phi}_{N,M}(k_x, k_y) = &\sum_{K=-M}^{M} C_{M,K}\mathrm{e}^{\mathrm{i}K\phi}\\ &\times\{[F(k_x; k_{qN+pK}, a) - F(k_x; -k_{qN+pK}, a)]\\ &\times[F(k_y; k_{pN-qK}, a) - F(k_y; -k_{qN+pK}, a)]\} \quad (3)\end{aligned}$$

with

$$F(k_i; k_n, a) = \mathrm{e}^{\frac{\mathrm{i}k_n a}{2}}\frac{\sin[(k_i + k_n)\,a/2]}{(k_i + k_n)}, \quad (4)$$

where k_i $(i = x, y)$ are the wavevectors in the x-direction and y-direction, respectively. Note that the coherent states $\Psi^{p,q,\phi}_{N,M}(x, y)$ behave as traveling waves in the transverse plane. The standing-wave representation is given by $S^{p,q,\phi}_{N,M,\pm}(x, y) = [\Psi^{p,q,\phi}_{N,M}(x, y) \pm \Psi^{p,q,-\phi}_{N,M}(x, y)]/\sqrt{2}$. Consequently, the momentum-space representation of the coherent states $S^{p,q,\pm\phi}_{N,M}(x, y)$ is given by $\tilde{S}^{p,q,\phi}_{N,M,\pm}(k_x, k_y) = [\tilde{\Psi}^{p,q,\phi}_{N,M}(k_x, k_y) \pm \tilde{\Psi}^{p,q,-\phi}_{N,M}(k_x, k_y)]/\sqrt{2}$. Figures 1(a) and (b)

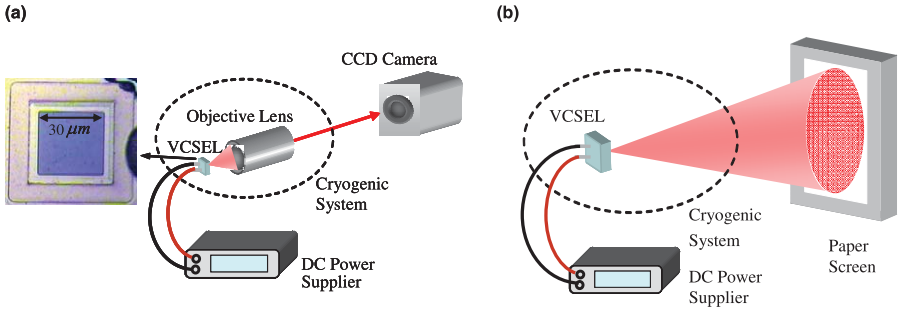

Figure 2. Schematics of the VCSEL device structure and the experimental setup: (a) measurement of the near-field pattern and (b) measurement of the far-field pattern.

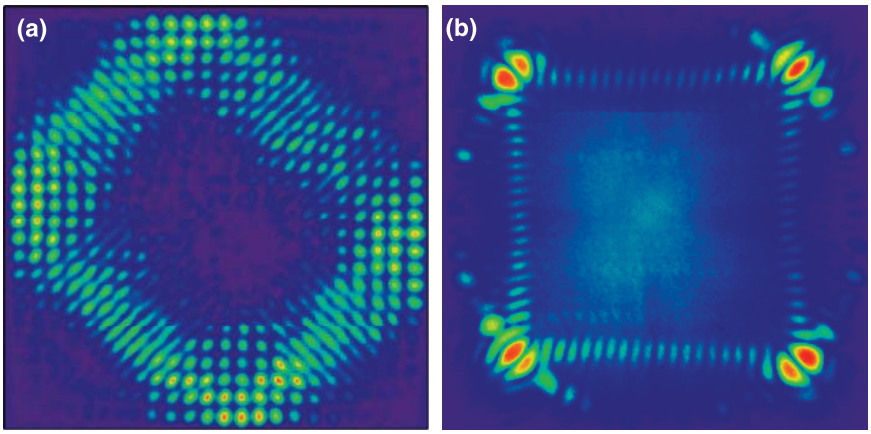

Figure 3. Experimental patterns of a square-shape VCSEL obtained with the detuning of $\Delta\omega/2\pi = 2.7$ THz: (a) near-field pattern; (b) far-field pattern.

illustrate the numerical patterns for the coordinate-space wave patterns $|S^{p,q,\phi}_{N,M,+}(x, y)|^2$ and the momentum-space wave patterns $|\tilde{S}^{p,q,\phi}_{N,M,+}(k_x, k_y)|^2$, respectively, with the parameters $(p, q) = (1, 1)$, $(N, M) = (22, 5)$, and $\phi = 0.55\pi$. It can be seen that the real-space wave pattern is concentrated along a diamond-shaped classical trajectory in the transverse plane $(x–y)$ and the corresponding momentum-space wavefunction exhibits high-intensity lobes at the corners of the aperture with flower-like structure and relatively weak stripes connecting them.

3. Experimental results

For VCSELs, the transverse order of the lasing mode depends on the frequency detuning $\Delta\omega = \omega - \omega_c$, where ω is the emission angular frequency and ω_c is the longitudinal cavity resonance. Experimentally, we fabricated several large-aperture square-shape VCSELs with different frequency detunings to explore the far-field transverse patterns of higher-order modes. Figure 2 depicts a top view of the VCSEL to show the square aperture and the experimental setup for near-field (figure 2(a)) and far-field (figure 2(b)) measurements. The size of the oxide aperture was 30×30 μm^2 and the emission wavelength was designed to be around 800 nm. The device structures of the oxide-confined VCSELs were similar to those described by [6]. The VCSELs were placed in a cryogenic system with a temperature stability of 0.1 K in the range of 80–300 K. A power supply providing current with a precision of 0.01 mA was utilized to drive the VCSEL. The near-field patterns were measured by a charge-coupled device (CCD) camera (Coherent, Beam-Code) with an objective lens (Mitsutoyo, numerical aperture 0.9). The far-field pattern was measured using a digital camera by directly projecting the laser beam on a scattering paper screen at a distance about 20–30 cm away from the VCSEL.

Figure 3 shows the near-field pattern and the corresponding far-field pattern for the experimental lasing mode obtained with the detuning of $\Delta\omega/2\pi = 2.7$ THz. It can be seen that the experimental patterns agree very well with the numerical results shown in figure 1 for the coordinate-space and momentum-space wavefunctions of a square quantum billiard. Next we generated a higher-order coherent state with a larger detuning. Figure 4 shows the experimental near-field pattern and the corresponding far-field pattern of the lasing mode obtained with the detuning of $\Delta\omega/2\pi = 6.9$ THz. The morphology of the near-field pattern (figure 4(a)) can be found to be in good agreement with the theoretical result; however, the far field (figure 4(b)) displays a significant pincushion curving when compared with a mode of lower transverse order (figure 3(b)). Experimental results reveal that the pincushion curving in the far-field distribution is independent of the pumping current in the range of 1.0–1.5 times the threshold

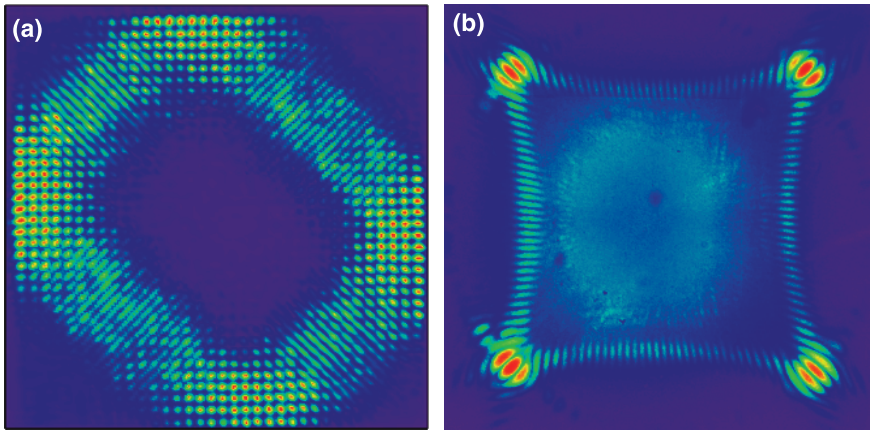

Figure 4. Experimental patterns of a square-shape VCSEL obtained with the detuning of $\Delta\omega/2\pi = 6.9$ THz: (a) near-field pattern; (b) far-field pattern.

level. Furthermore, the optical spectra indicate that the gray area in the central part of the far-field patterns in figures 3 and 4 arises from the amplified spontaneous emission. Consequently, the thermal lensing effect can be confirmed to be not the major mechanism in the formation of the pincushion curving. The origin of the present pincushion curving comes from the non-paraxial contribution because the transverse wavevector k_t is no longer much smaller than the longitudinal wavevector k_z for very high-order modes of VCSELs. Therefore, the non-paraxial contribution needs to be considered to obtain an accurate correspondence between the far-field pattern of high-order lasing modes of VCSELs and the momentum-space wavefunctions of quantum billiards. In section 4 we exploit the stationary phase method [15] to analyze the non-paraxial contribution and to develop a fast procedure for recovering the momentum-space wave patterns from the far-field patterns of high-order lasing modes of VCSELs.

4. Theoretical analysis and the recovery method

The propagation of a monochromatic near-field distribution $u_0(x, y)$ at $z = 0$ can be described in terms of a superposition of plane waves [17]:

$$u(x, y, z) = \int_{-\infty}^{\infty} \mathrm{d}k_x \int_{-\infty}^{\infty} \mathrm{d}k_y \, \tilde{u}_0(k_x, k_y) \mathrm{e}^{\mathrm{i}(k_x x + k_y y + k_z z)}, \quad (5)$$

where $k_z = \sqrt{k^2 - k_x^2 - k_y^2}$, and $\tilde{u}_0(k_x, k_y)$ is the Fourier transform of the near-field distribution $u_0(x, y)$. When the Fraunhofer approximation is valid, the far-field distribution with $kz \to \infty$ can be shown to be [17]

$$u(x, y, z) = \frac{2\pi k}{\mathrm{i}z} \mathrm{e}^{\mathrm{i}[k(x^2+y^2)/(2z)]} \mathrm{e}^{\mathrm{i}kz} \tilde{u}_0 \left(k\frac{x}{z}, k\frac{y}{z} \right). \quad (6)$$

Equation (6) indicates that the far-field pattern $|u(x, y, z)|$ is related to the Fourier transform pattern of the near-field distribution $|\tilde{u}_0(k_x, k_y)|$ with the arguments of $k_x = kx/z$ and $k_y = ky/z$. When the non-paraxial contribution is significant, the stationary phase method [15, 18–20] is usually employed to derive the far-field distribution and this results in

$$u(x, y, z) = \frac{2\pi k z}{\mathrm{i}r^2} \mathrm{e}^{\mathrm{i}kr} \tilde{u}_0 \left(k\frac{x}{r}, k\frac{y}{r} \right), \quad (7)$$

where $r = \sqrt{x^2 + y^2 + z^2}$. As a consequence, the accurate relationship between the far-field distribution and the Fourier transform of the near-field distribution is given by equation (7) instead of equation (6).

We used equations (2) and (7) to calculate the near-field and far-field VCSEL patterns and to show the analogy between them and the trajectories of the coherent states of square billiards with different orders N. Figure 5 shows the calculated results for the near-field patterns $|S^{p,q,\phi}_{N,M,+}(x, y)|^2$ with different orders of $N = 20$, 30, and 40 (figures 5(a)–(c)) and the corresponding far-field patterns (figures 5(a′)–(c′)). The values of the parameters used in the calculation are $(p, q) = (1, 1)$, $M = 5$, and $\phi = 0.55\pi$. It can be seen that the influence of the non-paraxial contribution leads to the pincushion curving in the far-field pattern with respect to the Fourier transform of the near-field distribution. The higher the transverse order is, the more curved the far-field pattern becomes. This result enables us to confirm the origin of the experimental patterns shown in figure 4. Since the far-field patterns of the VCSEL's lasing modes can be straightforwardly observed, it is practically useful to develop a transform procedure for recovering the momentum-space wave patterns from the experimental far-field patterns.

Equation (7) reveals that the far-field pattern $|u(x, y, z)|$ beyond the paraxial approximation is related to the Fourier transform pattern of the near-field distribution $|\tilde{u}_0(k_x, k_y)|$ with the arguments of $k_x = kx/r$ and $k_y = ky/r$. In other words, the experimental far-field pattern $|u(x, y, z)|$ can be used to obtain the Fourier transform pattern of the near-field distribution $|\tilde{u}_0(k_x, k_y)|$ via the change of the arguments of $x = k_x r/k$ and $y = k_y r/k$. However, since the variable r is a function of the variables x and y, the expressions $x = k_x r/k$ and $y = k_y r/k$ cannot be applied directly. For solving this problem, we use the asymptotic property of the free-space propagation to obtain the identity $r/k = z/k_z =$

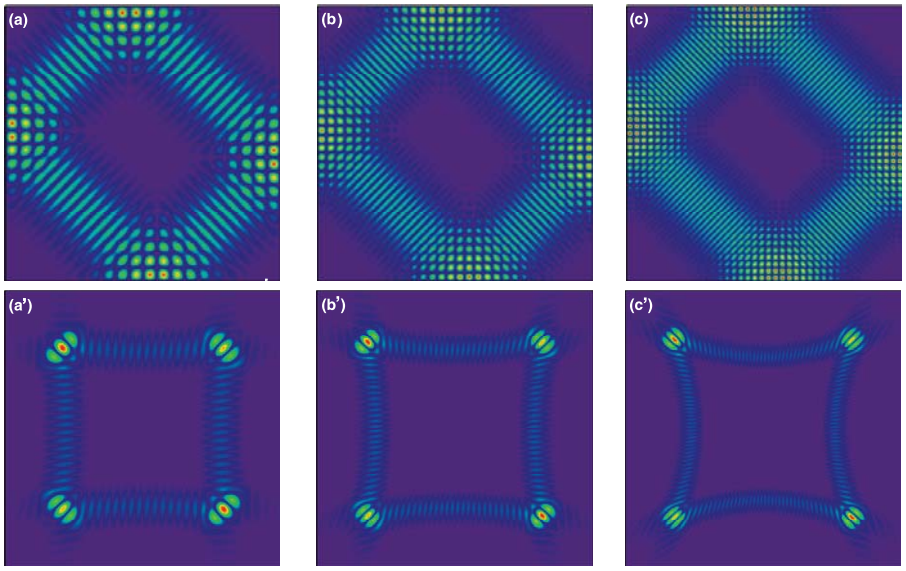

Figure 5. Numerically calculated near-field patterns of resonance modes with transverse order: (a) $N = 20$, (b) $N = 30$, (c) $N = 40$, and ((a′)–(c′)) the corresponding far-field patterns obtained by using the stationary phase method.

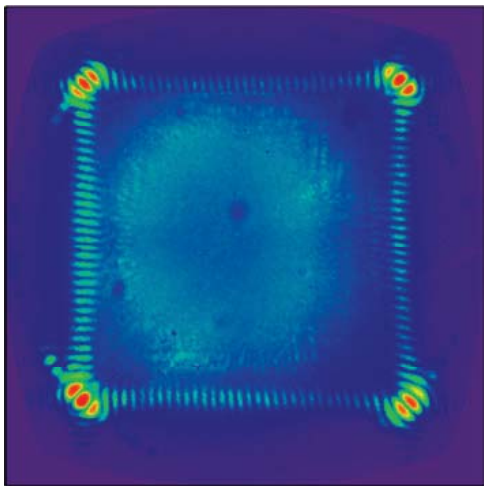

Figure 6. Reconstructed pattern for the far-field pattern shown in figure 4(b), to correspond to the Fourier transform pattern of the near-field distribution shown in figure 4(a).

$z/\sqrt{k^2 - k_x^2 - k_y^2}$. With this identity, the expressions $x = k_x r/k$ and $y = k_y r/k$ can be given as

$$x = k_x z \Big/ \sqrt{k^2 - k_x^2 - k_y^2} \tag{8}$$

and

$$y = k_y z \Big/ \sqrt{k^2 - k_x^2 - k_y^2}. \tag{9}$$

As a result, the Fourier transform pattern of the near-field distribution $|\tilde{u}_0(k_x, k_y)|$ can be straightforwardly obtained from the experimental far-field pattern $|u(x, y, z)|$ with the change of the arguments as in equations (8) and (9). Note that the far-field distribution intrinsically represents an angular field distribution that is essentially independent of the distance from the source. Equations (8) and (9) clearly reveal that the relationship between the transverse momentum (k_x, k_y) and the screen position (x, y) for recording the experimental far-field amplitude is not a linear mapping. It can be easily found that only when the non-paraxial contribution is negligible, i.e. $k^2 \gg k_{x,y}^2$, can the screen position (x, y) be linearly mapped to the specific transverse momentum (k_x, k_y). To the best of our knowledge, this is the first time that a useful mapping has been developed for obtaining the Fourier transform pattern of a near-field distribution from a corresponding far-field pattern that is subject to the influence of a non-paraxial contribution.

Applying the arguments of equations (8) and (9) to the experimental result shown in figure 4(b), the accurate Fourier transform pattern of the near-field distribution shown in figure 4(a) can be numerically reconstructed and it is depicted in figure 6. It can be seen that the pincushion curving of the original far-field pattern is almost completely eliminated. The morphology of the reconstructed pattern agrees very well with the momentum-space distribution of the coherent state shown in figure 1(b) with the transverse order of $N = 36$. In order to analyze quantitatively the correlation of these patterns, we calculate the spatial correlation function which is given by

$$g\,(\vec{\tau}) = \langle f_1\,(\vec{r} + \vec{\tau})\, f_2\,(\vec{r})\rangle\,, \tag{10}$$

where $f_1(\vec{r} + \vec{\tau})$ and $f_2(\vec{r})$ are normalized functions with the variable of position. Two functions are highly related to each other when $g(\vec{\tau})$ approaches the value of 1. Substituting the normalized reconstructed wave pattern and the momentum-space distribution of the coherent state with the transverse order of $N = 36$ into equation (8), we can obtain the value of 0.837. The calculated result reveals that the two patterns are highly correlated.

In addition to square billiards, the equilateral triangular structure is a classically non-separable but integrable system which also plays an important role in quantum billiards. Recently, various high-order modes of equilateral triangular

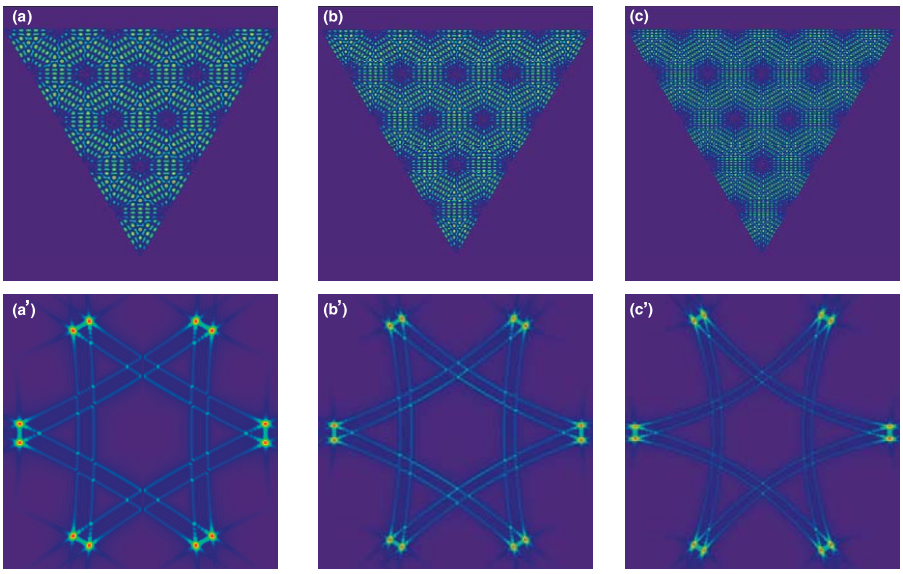

Figure 7. Numerically calculated wave patterns of eigenstates of an equilateral triangular VCSEL with transverse order: (a) $(m, n) = (5, 58)$, (b) $(m, n) = (5, 78)$, (c) $(m, n) = (5, 98)$, and ((a′)–(c′)) the corresponding far-field patterns obtained by using stationary phase method.

VCSELs have been investigated via controlling device temperatures [7]. It was confirmed that the near-field patterns of these high-order modes display the wavefunctions of equilateral triangular quantum billiards [7, 21]. Therefore, it is useful and pedagogical to elucidate the influence of the non-paraxial contribution to the high-order far-field pattern of VCSELs with optical apertures having an equilateral triangle shape.

For an equilateral triangular billiard with the vertices at $(0, 0)$, $(a/2, \sqrt{3}a/2)$, and $(-a/2, \sqrt{3}a/2)$, the quantum eigenstates $\Phi^{\pm}_{m,n}(x, y)$ are given by [21]

$$\Phi^{\pm}_{m,n}(x, y) = \sqrt{\frac{16}{a^2 3\sqrt{3}}}\left\{e^{\pm i(m+n)(2\pi/3a)x}\sin\left[(m-n)\frac{2\pi}{\sqrt{3}a}y\right] + e^{\mp i(2m-n)(2\pi/3a)x}\sin\left[n\frac{2\pi}{\sqrt{3}a}y\right] - e^{\mp i(2n-m)(2\pi/3a)x}\sin\left[m\frac{2\pi}{\sqrt{3}a}y\right]\right\} \quad (11)$$

with $2n \geqslant m$ $(m = 1, 2, 3, \ldots; n = 1, 2, 3, \ldots)$, where m and n represent the order of the eigenstates and a is the side length of the equilateral triangle. Equation (11) is the representation of the traveling-wave eigenstates. The standing-wave representation of the eigenstates can be given by $S^{\pm}_{m,n}(x, y) = \Phi^{+}_{m,n}(x, y) \pm \Phi^{-}_{m,n}(x, y)$. The wave patterns of the eigenstates are generally confirmed to display honeycomb patterns [7]. To explore the influence of the non-paraxial contribution, we used equations (2) and (7) to calculate the near-field and far-field patterns for the lasing modes $S^{\pm}_{m,n}(x, y)$ of VCSELs with different transverse orders. Figure 7 shows the numerical wave patterns $|S^{+}_{m,n}(x, y)|^2$ (figures 7(a)–(c)) and the corresponding far-field patterns (figures 7(a′)–(c′)) with the transverse order of $(m, n) = (5, 58)$, $(m, n) = (5, 78)$, and $(m, n) = (5, 98)$. As seen in figure 5 for the case of square billiards, the non-paraxial contribution causes the far-field patterns to display the feature of pincushion curving. To sum up, the characteristic of pincushion curving is a typical sign of a non-paraxial contribution to the far-field patterns.

5. Conclusion

In conclusion, we have experimentally investigated the difference between the low-order and high-order far-field transverse patterns of VCSELs with a square-shape aperture. It was experimentally found that the high-order far-field patterns displayed the feature of pincushion curving with respect to the Fourier transform of the near-field wavefunction. We have theoretically confirmed that the pincushion curving arises from the non-paraxial contribution. On the basis of the stationary phase method, we have developed a fast procedure for obtaining the Fourier transform of the near-field patterns from the experimental far-field patterns, for accurately visualizing the momentum-space wavefunction of 2D quantum billiards. Finally, we have also analyzed the influence of the non-paraxial contribution for equilateral triangular VCSELs to confirm that the pincushion curving of the far-field pattern is a typical feature in high-order transverse modes.

Acknowledgment

The authors thank the National Science Council for their financial support of this research under Contract No. NSC-97-2112-M-009-016-MY3.

References

[1] Chow W W, Choquette K D, Hagerot-Crowford M, Lear K L and Hadley G R 1997 *IEEE J. Quantum Electron.* **33** 1810–24
[2] Deppe D G, Huffaker D L, Oh T, Deng H and Deng Q 1997 *IEEE J. Sel. Top. Quantum Electron* 3 893–904

[3] Chang-Hasnain C J, Harbison J P, Hasnain G, Von Lehmen A C, Florez L T and Stoffel N G 1991 *IEEE J. Quantum Electron.* **27** 1402–9
[4] Cheng D L, Yen T C, Chang W, Kuo W C, Kao K S and Hsu C P 2007 *IEEE Photon. Technol. Lett.* **19** 1961–3
[5] Spencer P S, Mirasso C R, Volet P and Shore K A 1998 *IEEE J. Quantum Electron.* **34** 1673–9
[6] Hegarty S P, Huyet G, McInerney J G and Choquette K D 1999 *Phys. Rev. Lett.* **82** 1434–7
[7] Chen C C, Su K W, Chen Y F and Huang K F 2008 *Opt. Lett.* **33** 509–11
[8] Huang K F, Chen Y F, Lai H C and Lan Y P 2002 *Phys. Rev. Lett.* **89** 224102
[9] Chen C C, Liu C C, Su K W, Lu T H, Chen Y F and Huang K F 2007 *Phys. Rev.* E **75** 046202
[10] Gensty T, Becker K, Fischer I, Elsäßer W, Degen C, Debernardi P and Bava G P 2005 *Phys. Rev. Lett.* **94** 233901
[11] Berggren K F, Sadreev A F and Starikov A A 2002 *Phys. Rev.* E **66** 016218
[12] Zozoulenko I V, Schuster R, Berggren K F and Ensslin K 1997 *Phys. Rev.* B **55** R10209
[13] Zozoulenko I V and Berggren K F 1997 *Phys. Rev.* B **56** 6931
[14] Chen C C, Yu Y T, Chen R C C, Huang Y J, Su K W, Chen Y F and Huang K F 2009 *Phys. Rev. Lett.* **102** 044101
[15] Carter W H 1972 *J. Opt. Soc. Am.* **62** 1195–201
[16] Chen Y F, Huang K F and Lan Y P 2002 *Phys. Rev.* E **66** 046215
[17] Haus H A 1984 *Waves and Fields in Optoelectronics* (Englewood Cliffs, NJ: Prentice-Hall)
[18] Zhou G 2010 *J. Opt. Soc. Am.* A **27** 890–4
[19] Mei Z and Zhao D 2008 *J. Opt. Soc. Am.* A **25** 537–42
[20] Duan K and Lü B 2003 *Opt. Express* **11** 1474–80
[21] Chen Y F and Huang K F 2003 *Phys. Rev.* E **68** 066207

Appl Phys B (2011) 103:841–846
DOI 10.1007/s00340-010-4293-2

Applied Physics B
Lasers and Optics

Controlling number of lasing modes for designing short-cavity self-mode-locked Nd-doped vanadate lasers

Y.F. Chen · Y.J. Huang · P.Y. Chiang · Y.C. Lin · H.C. Liang

Received: 12 August 2010 / Revised version: 30 September 2010 / Published online: 23 November 2010

Abstract A short-cavity Nd:YVO_4 laser is employed to confirm that a spontaneous mode locking (SML) typically occurs without employing an extra nonlinearity. We further experimentally demonstrate that reducing the number of longitudinal lasing modes can diminish the phase fluctuation and effectively improve the SML pulse stability. Considering the spatial hole-burning (SHB) effect, an analytical expression is derived to accurately estimate the number of longitudinal lasing modes for a practical design guideline.

1 Introduction

The appearance of spontaneous mode locking (SML) in laser cavity without using additional nonlinearity except gain medium is an intriguing phenomenon of laser emission. During the early research on mode-locking, the SML phenomenon was observed on different types of lasers including He–Ne [1], ruby [2], Nd:glass [3], and argon ion [4] laser systems. In the mid-1960s, the SML was not considered to be a reliable approach for the generation of ultrashort pulses, partly because the mechanism for SML was not adequately understood. Recently, fairly stable SML pulses have been obtained in the experiments of Nd-doped vanadate miniature lasers [5] and Nd-doped double clad fiber lasers [6]. With the statistical analysis it has been shown that unless a systematic phase fluctuation over 2π is introduced, the mode-locked behavior will always be observed in a multimode laser [7, 8]. Although a systematic phase fluctuation is usually caused by dispersion effects, theoretical studies on the SML mechanism have confirmed that the combination tones of the third order nonlinear polarization terms can help in compensating the dispersion-induced phase shift [6, 9, 10]. As a result, the SML typically occurs in a multimode laser without employing an extra nonlinearity except the gain medium. However, the locking strength due to the nonlinear polarization terms is rather insubstantial. It is therefore crucial to precisely control the number of lasing modes for achieving relatively stable SML pulses.

Spatial hole burning (SHB) in the gain medium has been confirmed to be advantageously utilized for lasing mode selection [11–16]. In this work we first experimentally confirm that the separation between the gain medium and the end mirror in a standing-wave SML laser cavity can be employed to precisely control the number of longitudinal lasing modes via the SHB effect, leading to a stability improvement of the mode-locked pulses. With mode-locked states as a basis, we derive an analytical formula to analyze the number of longitudinal lasing modes. The predictions of the theoretical model have shown a fairly good agreement with experimental results.

2 Experimental results

We recently demonstrated that the large third-order nonlinearity of Nd-doped vanadate crystals could be used to achieve a short-cavity SML operation [5]. Here we employ the Nd:YVO_4 crystal to explore the influence of the number of longitudinal lasing modes on the stability of the SML performance. The cavity configuration is a linear concave-plano resonator, as shown in Fig. 1(a). The separation between the laser crystal and the input mirror, d, is freely adjusted in the range of 1–11 mm to control the number

Y.F. Chen (✉) · Y.J. Huang · P.Y. Chiang · Y.C. Lin · H.C. Liang
Department of Electrophysics, National Chiao Tung University,
1001 TA Hsueh Road, Hsinchu 30050, Taiwan
e-mail: yfchen@cc.nctu.edu.tw
Fax: +886-35-725230

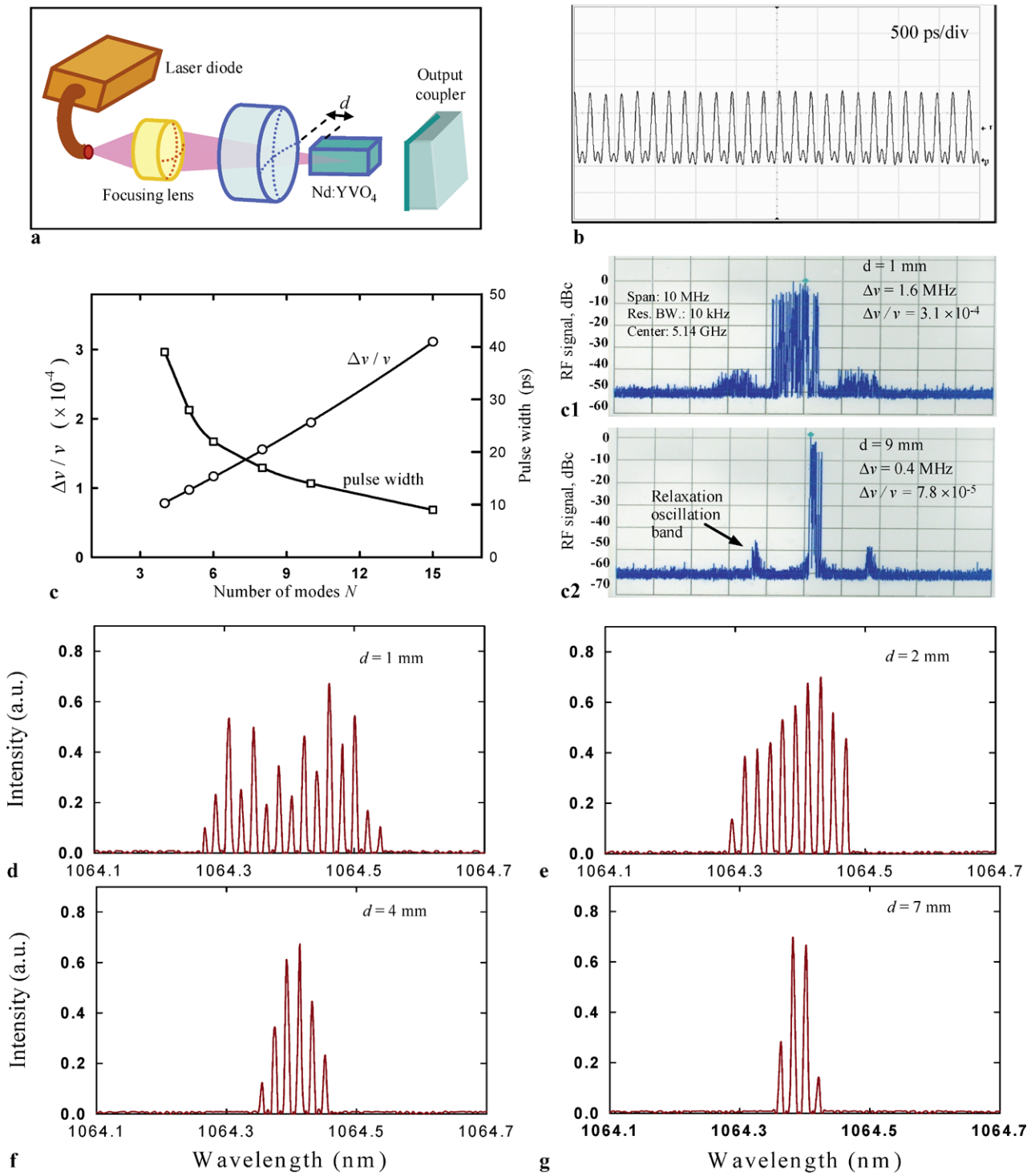

Fig. 1 (**a**) Cavity configuration. (**b**) Typical mode-locked pulse train. (**c**) Relative frequency deviation of the power spectra $\Delta\nu/\nu$ and pulse width versus number of longitudinal lasing modes. (**c1**) and (**c2**) Images of the measured RF power spectra for the cases of $d = 1$ mm and $d = 9$. (**d**)–(**g**) Experimental optical spectra for different crystal/mirror separations

of longitudinal lasing modes via the SHB effect. The gain medium is a-cut 0.5 at.% Nd:YVO_4 crystal with dimensions of $3 \times 3 \times 6$ mm^3. Both end surfaces of the Nd:YVO_4 crystal were antireflection coated at 1064 nm and wedged 2° to avoid the Fabry–Pérot etalon effect. The laser crystal was wrapped with indium foil and mounted in a water-cooled copper holder. The water temperature was maintained at around 20°C to ensure stable laser output. The input mirror

was a 20-cm radius-of-curvature concave mirror with antireflection coating at 808 nm on the entrance face and with high-reflectance coating at 1064 nm (>99.8%) and high transmittance coating at 808 nm on the second surface. A flat wedged output coupler with 10% transmission at 1064 nm was used throughout the experiment. The pump source was a 3-W 808-nm fiber-coupled laser diode with core diameter of 100 μm and numerical aperture of 0.20. Focusing lens with 25 mm focal length and 85% coupling efficiency was used to reimage the pump beam into the laser crystal. The average pump size was approximately 60 μm. The optical cavity length was set to be approximately 2.92 cm, corresponding to a free spectral range of 5.14 GHz. The mode-locked pulses were detected by a high-speed InGaAs photodetector with rise time 35 ps, whose output signal was connected to a digital oscilloscope (Agilent, DSO 80000) with 12 GHz electrical bandwidth and sampling interval of 25 ps. The output signal of the photodetector was also analyzed by an RF spectrum analyzer (Advantest, R3265A) with bandwidth of 8 GHz. The spectral information of the laser was monitored by a Fourier optical spectrum analyzer (Advantest, Q8347) that is constructed with a Michelson interferometer with resolution of 0.003 nm.

With the optimal alignment for $d = 1$ mm, the laser output had a slope efficiency of 31%; the output power reached 0.79 W at an incident pump power of 2.6 W. With the real-time dynamical temporal trace, the laser cavity can be easily adjusted to be in a SML operation with a pulse repetition rate of 5.14 GHz, as shown Fig. 1(b). We also found that the average output power is nearly independent of the crystal/mirror separation d in the range of 1–11 mm. Figures 1(d)–1(g) depict the measured optical spectra. The number of longitudinal lasing modes can be clearly seen to decrease with increasing the separation d. We also measured the radio-frequency (RF) spectrum of the output power to evaluate the stability of mode-locked pulse train. Figure 1(c) shows the experimental results for the relative frequency deviation of the power spectra, $\Delta\nu/\upsilon$, where υ is the center frequency of the power spectrum and $\Delta\nu$ is the frequency deviation of full width at half maximum and is inferred from the beat note spectrum. As shown in Fig. 1(c), the value of $\Delta\nu/\upsilon$ is significantly reduced with decreasing the number of longitudinal lasing modes. Figures 1(c1) and 1(c2) are the images of the measured RF power spectra for the cases of $d = 1$ mm and $d = 9$ mm, respectively. It can be seen that the relaxation oscillation sidebands is improved approximately from −40 dBc to −50 dBc. Since the relaxation oscillation frequencies for different lasing modes are somewhat different, the decrease of the number of lasing modes is found to be beneficial in reducing the frequency deviation for the mode-locked oscillation. The influence of the relaxation oscillation on the dynamics of multimode Nd-doped lasers can be referred to [17–19]. The pulse width was measured with the help of the commercial autocorrelator (APE pulse check, Angewandte physik & Elektronik GmbH) and assuming the sech^2-shaped temporal profile. As depicted in Fig. 1(c), the pulse width increases from 9 ps to 39 ps for the separation d being varied from 1 mm to 11 mm. The mode-locked pulses are nearly bandwidth-limited. Our experimental results manifestly reveal that the compromise between pulse stability and pulse width should be considered in designing an appropriate SML laser.

3 Theoretical analysis for number of lasing modes

Since the number of longitudinal modes play a critical role for the stability of the SML operation, it is useful to develop a method for estimating the number of lasing modes. Here we extend the early work of Zayhowski [16] to derive an analytical formula for estimating the maximum number of longitudinal modes in terms of the cavity geometry and well-known material parameters. Considering a standing-wave laser consisting of N oscillating modes and presuming that all modes have equal amplitude and phase, the normalized electric field can be given by

$$E_N(x,y,z,t) = \left[\frac{1}{\sqrt{N}}\sum_{m=0}^{N-1} e^{i\omega_m t}\sqrt{\frac{2}{l_{\mathrm{cav}}}}\sin(k_m z)\right]\psi(x,y,z), \tag{1}$$

where $\omega_m = (m_o + m)\pi c/l_{\mathrm{cav}}$, $k_m = \omega_m/c$, m_o is the resonant mode index, and l_{cav} is the effective cavity length. The transverse wave function $\psi(x,y,z)$ is given by

$$\psi(x,y,z) = \sqrt{2/\pi w_l^2}\exp\left[-\left(x^2+y^2\right)/w_l^2\right], \tag{2}$$

where w_l is the beam radius. Since the cavity length is much longer than the laser wavelength, the typical value of m_o is greater than 10^3. Thus always $N \ll m_o$ holds. After some algebra, the intensity $I_N(x,y,z,t) = |E_N(x,y,z,t)|^2$ can be expressed as

$$\begin{aligned} I_N(x,y,z,t) &= N/(2l_{\mathrm{cav}})\left\{\left[S_N\left(\pi(ct+z)/(2l_{\mathrm{cav}})\right)\right]^2\right. \\ &\quad + \left[S_N\left(\pi(ct-z)/(2l_{\mathrm{cav}})\right)\right]^2 \\ &\quad - 2S_N\left(\pi(ct+z)/(2l_{\mathrm{cav}})\right)S_N\left(\pi(ct-z)/(2l_{\mathrm{cav}})\right) \\ &\quad \left.\times\cos(2kz)\right\}\left|\psi(x,y,z)\right|^2, \end{aligned} \tag{3}$$

where $S_N(\theta) = \sin(N\theta)/N\sin\theta$ and $k = [m_o + (N-1)/2]\pi/l_{\mathrm{cav}} \approx \omega_o/c$. The intensity $I_N(x,y,z,t)$, averaged

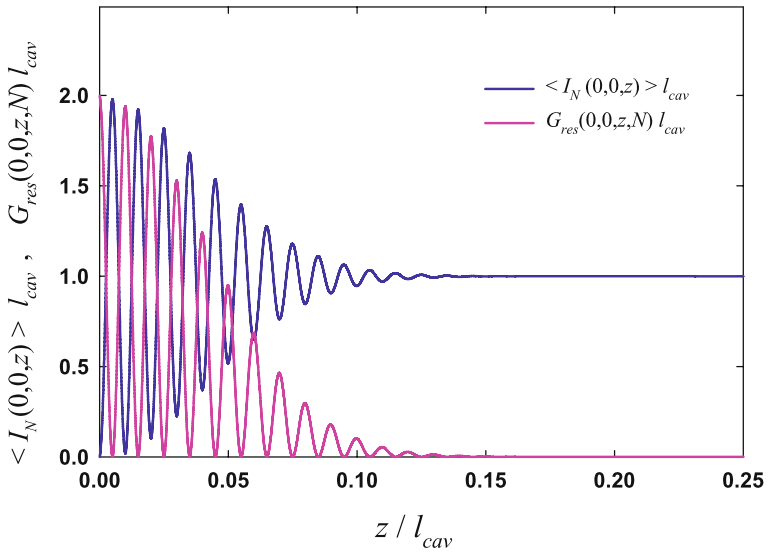

Fig. 2 Calculated results for $G_{res}(x, y, z; N)$ (*pink line*) and $\langle I_N(x, y, z)\rangle$ (*blue line*) as functions of z with $N = 11, x = y = 0$, and $m_o = 200$

over an round trip time $T = 2l_{\rm cav}/c$, becomes

$$\begin{aligned}&\big\langle I_N(x, y, z)\big\rangle\\ &\quad = (1/l_{\rm cav})\big[1 + S_N(\pi z/l_{\rm cav}) - 2S_N(\pi z/l_{\rm cav})\cos^2(kz)\big]\\ &\qquad \times \big|\psi(x, y, z)\big|^2. \end{aligned} \tag{4}$$

The function represents a standing-wave pattern which is fully modulated for the position near the reflecting mirrors and continuously loses contrast for the position away from the mirrors. Due to the standing-wave nature, superposition of the light fields of modes results in an envelope function for the total light intensity. The spatial variation of the envelope $S_N(\pi z/l_{\rm cav})$ occurs on the cavity-length scale to be much slower compared to rapid undulations of the intensities of individual modes. As N get larger, $S_N(\pi z/l_{\rm cav})$ becomes narrower such that it only has weight very close to the end mirrors, i.e., $z = 0$ and $z = l_{\rm cav}$. The envelope function $S_N(\pi z/l_{\rm cav})$ has a damping oscillation in the tail, causing some inconvenience in performing numerical integration. For a convenient numerical evaluation we use a Gaussian function

$$g_N(z) = e^{-[N\pi z/2l_{\rm cav}]^2} + e^{-[N\pi(l_{\rm cav}-z)/2l_{\rm cav}]^2} \tag{5}$$

to replace the envelope function $S_N(\pi z/l_{\rm cav})$. In terms of $g_N(z)$, the average intensity in (4) can be split into two terms:

$$\begin{aligned}&\big\langle I_N(x, y, z)\big\rangle\\ &\quad = \big|\psi(x, y, z)\big|^2\big[1 + g_N(z)\big]/l_{\rm cav} - G_{\rm res}(x, y, z; N), \end{aligned} \tag{6}$$

where the first term $|\psi(x, y, z)|^2[1 + g_N(z)]/l_{\rm cav}$ indicates the average intensity without the interference effect and the second term

$$G_{\rm res}(x, y, z; N) = (2/l_{\rm cav})\cos^2(kz)g_N(z)\big|\psi(x, y, z)\big|^2 \tag{7}$$

represents the residual gain distribution due to the interference term $\cos^2(kz)$ of the SHB effect. Figure 2 depicts the calculated results for $G_{\rm res}(x, y, z; N)$ and $\langle I_N(x, y, z)\rangle$ as functions of z, where we take $N = 11, x = y = 0$, and $m_o = 200$ for the convenience of presentation.

The maximum number of modes $N_{\rm max}$ that can oscillate in a standing-wave cavity is determined from the condition that the maximum value of N in $G_{\rm res}(x, y, z; N)$ leads to the effective round-trip gain not less than the round-trip losses, i.e.,

$$\begin{aligned}&2\sigma l_g(P_{\rm abs}\tau/hv_p)\\ &\qquad \times \iiint G_{\rm res}(x, y, z, N)r_p(x, y, z)\, dV\Big|_{N=N_{\rm max}}\\ &\quad \geq \ln(1/R) + L, \end{aligned} \tag{8}$$

where σ is the stimulated emission cross section, l_g is the length of the gain medium, $P_{\rm abs}$ is the absorbed pump power, v_p is the pump frequency, τ is the emission lifetime, L is the round-trip loss, R is the reflectivity of the output coupler, and $r_p(x, y, z)$ is the normalized pump intensity distribution. For a gain medium located between $z = d$ and $z = d + l_g$ and using a circular Gaussian beam to express the pump distribution, $r_p(x, y, z)$ is given by

$$\begin{aligned}&r_p(x, y, z)\\ &\quad = \big(2/\pi w_p^2\big)\big[\alpha e^{-\alpha(z-d)}/\big(1 - e^{-\alpha l_g}\big)\big]e^{-2(x^2+y^2)/w_p^2}\\ &\qquad \times \Theta(z - d)\Theta(d + l_g - z), \end{aligned} \tag{9}$$

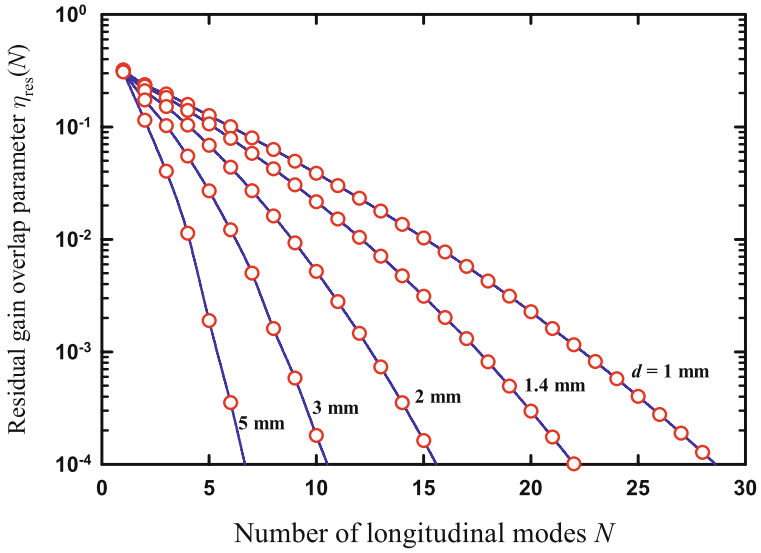

Fig. 3 Calculated results for $\eta_{\mathrm{res}}(N, d)$ as a function of N for several different values of d for the case of the Nd:YVO_4 laser

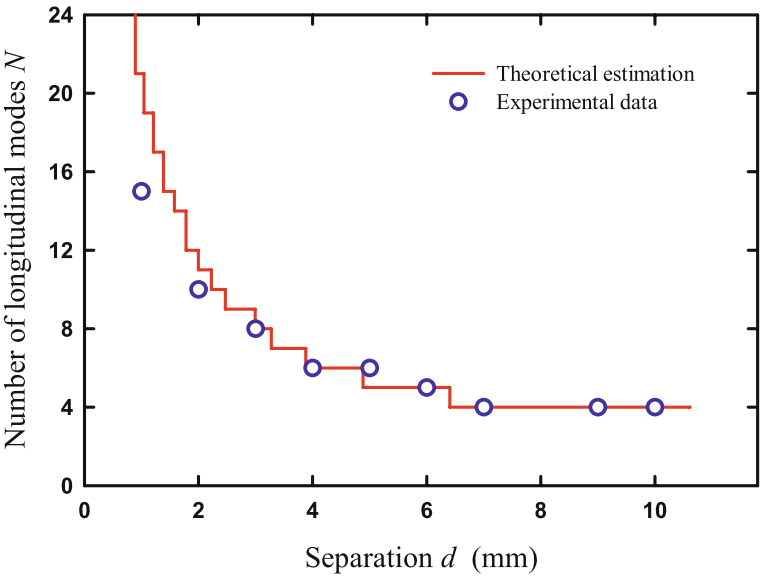

Fig. 4 Theoretical estimations and experimental data for the maximum number of modes $N_{\max}$ as a function of d

where α is the absorption coefficient at the pump wavelength, w_p is the pump radius, and $\Theta(\,)$ is the Heaviside step function. Note that the gain saturation effect is neglected because of low intensity levels. Substituting (7) and (9) into (8) and carrying out the integration in the transverse directions, we can obtain the relationship of $\eta_{\mathrm{res}}(N, d)|_{N=N_{\max}} \geq \zeta$, where the residual gain overlap parameter $\eta_{\mathrm{res}}(N, d)$ is defined as

$$\eta_{\mathrm{res}}(N, d) = (2/l_{\mathrm{cav}})\left[\alpha l_g/\left(1 - e^{-\alpha l_g}\right)\right] \times \int_d^{d+l_g} \cos^2(kz) g_N(z) e^{-\alpha(z-d)}\, dz \tag{10}$$

and the effective loss-to-pump factor ζ is defined as

$$\zeta = \frac{[\ln(1/R) + L]}{(I_p/I_s)}, \tag{11}$$

where $I_p = 2P_{\mathrm{abs}}/[\pi(w_l^2 + w_p^2)]$ and $I_s = h\upsilon_p/(\sigma\tau)$. The residual gain overlap parameter $\eta_{\mathrm{res}}(N, d)$ represents the overlap efficiency between the residual gain distribution and the pump absorption distribution in the longitudinal direction. The effective loss-to-pump factor ζ indicates the ratio of the cavity loss $\ln(1/R) + L$ to the transverse gain coefficient I_p/I_s. As a result, the maximum number of modes $N_{\max}$ can be determined with the criterion $\eta_{\mathrm{res}}(N, d)|_{N=N_{\max}} \geq \zeta$ and (10) and (11). Figure 3 shows the calculated results for $\eta_{\mathrm{res}}(N, d)$ as a function of N for several different values of d for the case of the Nd:YVO_4 laser: $l_{\mathrm{cav}} = 29$ mm, $l_g = 6$ mm, and $\alpha = 0.5$ mm^{-1}. From Fig. 3, it is clear that the maximum number of modes $N_{\max}$ is decreased with increasing d. For the experimental condition in Fig. 1, the effective loss-to-pump factor ζ can be found to be 3.1×10^{-3}, where the values of the parameters are as

follows: $\sigma = 2.5 \times 10^{-18}$ cm^2, $P_{\text{abs}} = 2.5$ W, $\tau = 100$ μs, $R = 0.9$, $L = 0.005$, $hv_p = 2.45 \times 10^{-19}$ J, $w_l = 0.06$ mm, and $w_p = 0.06$ mm. Applying $\zeta = 3.1 \times 10^{-3}$ into Fig. 3, the maximum number of modes N_{max} can be determined as a function of d, as depicted in Fig. 4. The good agreement between the theoretical estimations and the experimental data validate the usefulness of the present model.

4 Conclusions

In conclusion, we have experimentally confirmed that a SML can occur in short-cavity Nd:YVO_4 lasers without employing an extra nonlinearity. We further found that the stability of the SML pulses could be significantly improved by reducing the number of longitudinal lasing modes to diminish the phase fluctuation. Considering the SHB effect, we have derived an analytical formula to establish the relationship between the number of longitudinal lasing modes and the crystal/mirror separation. The theoretical estimations for the number of longitudinal lasing modes were shown to be in good agreement with experimental observations.

Acknowledgement This work is supported by the National Science Council of Taiwan (Contract No. NSC-97-2112-M-009-016-MY3).

References

1. M.H. Crowell, IEEE J. Quantum Electron. **1**, 12 (1965)
2. H. Statz, C.L. Tang, J. Appl. Phys. **36**, 3923 (1965)
3. M.A. Duguay, S.L. Shapiro, P.M. Rentzepis, Phys. Rev. Lett. **19**, 1014 (1967)
4. O.L. Gaddy, E.M. Schaefer, Appl. Phys. Lett. **9**, 281 (1966)
5. H.C. Liang, R.C.C. Chen, Y.J. Huang, K.W. Su, Y.F. Chen, Opt. Express **16**, 21149 (2008)
6. P. Glas, M. Naumann, A. Schirrmacher, L. Däweritz, R. Hey, Opt. Commun. **161**, 345 (1999)
7. A.A. Grütter, H.P. Weber, R. Dändliker, Phys. Rev. **185**, 629 (1969)
8. R. Dändliker, A.A. Grütter, H.P. Weber, IEEE J. Quantum Electron. **6**, 687 (1970)
9. H. Statz, J. Appl. Phys. **38**, 4648 (1967)
10. H. Statz, M. Bass, J. Appl. Phys. **40**, 377 (1969)
11. H. Fu, H. Haken, Phys. Rev. A **43**, 2446 (1991)
12. C.J. Flood, D.R. Walker, H.M. van Driel, Opt. Lett. **20**, 58 (1995)
13. H.S. Kim, S.K. Kim, B.Y. Kim, Opt. Lett. **21**, 1144 (1996)
14. L. Jiang, L.V. Asryan, IEEE Photonics Technol. Lett. **20**, 1661 (2008)
15. G.J. Kintz, T. Baer, IEEE J. Quantum Electron. **26**, 1457 (1990)
16. J.J. Zayhowski, Opt. Lett. **15**, 431 (1990)
17. T. Hill, M.W. Hamilton, D. Pieroux, P. Mandel, Phys. Rev. A **66**, 063803 (2002)
18. B. Peters, J. Hünkemeier, V.M. Baev, Y.I. Khanin, Phys. Rev. A **64**, 023816 (2001)
19. N.B. Abraham, L. Sekaric, L.L. Carson, V. Seccareccia, P.A. Khandokhin, Ya.I. Khanin, I.V. Koryukin, V.G. Zhislina, Phys. Rev. A **62**, 013810 (2000)

Appl Phys B (2011) 103:637–641
DOI 10.1007/s00340-010-4356-4

Applied Physics B
Lasers and Optics

Highly efficient Nd:$Gd_{0.6}Y_{0.4}VO_4$ laser by direct in-band pumping at 914 nm and observation of self-mode-locked operation

H.C. Liang · Y.J. Huang · P.Y. Chiang · Y.F. Chen

Received: 16 July 2010 / Revised version: 8 November 2010 / Published online: 12 January 2011

Abstract A highly efficient Nd:$Gd_{0.6}Y_{0.4}VO_4$ laser by direct in-band pumping at 914 nm is demonstrated for the first time. With an absorbed power of 3.7 W, a maximum output power of 2.65 W at 1064 nm was obtained, corresponding to an optical conversion efficiency of 72%. We also experimentally observed that the laser system could be efficiently operated in the self-mode-locked state in the range of 0.9–3.3 GHz. The pulse width was measured to be 16 ps at a repetition rate of 1.75 GHz.

1 Introduction

With the advance in growth of semiconductor technology, the diode-pumped solid-state lasers with high power are promising and attractive in various applications such as laser-video display, medicine, material processing, nonlinear wavelength conversion and so on. However, it is well known that the thermal effects in the laser cavity are the main challenges for developing high-power solid-state lasers. Several methods have been proposed to overcome the detrimental behaviors induced by thermal effects [1–6]. Nd-doped crystal lasers have been extensively studied and are conventionally pumped at 808 nm due to strongest absorption at $^4I_{9/2} \rightarrow {}^4F_{5/2}$ transition. Nevertheless, this pumping scheme produces significant heat thanks to the energy difference between pumping wavelength and lasing wavelength under four-level operation. Motivated by minimization of the Stokes factor loss together with maximization of quantum efficiency, direct in-band pumping in Nd-doped crystal lasers can basically eliminate the non-radiative transition to considerably reduce the thermal load and improve many laser parameters that include pump threshold as well as slope efficiency compared with the conventional 808-nm excitation [7–13]. These benefits make the direct in-band pumping one of the best methods for power scaling with high conversion efficiency. The use of the longest absorption wavelength from the highest sublevel of the ground state manifold to the emitting level can further enhance the laser performance. For example, several Nd-doped lasers by direct in-band pumping at their longest absorption wavelength have successfully been derived with a high-brightness laser diode as pump source [14–16].

Nd-doped vanadate crystals are characterized by their high absorption coefficient for diode pumping, large stimulated emission cross section, and moderate thermal conductivity that are suitable for achieving excellent laser performance. Previous studies also showed that vanadate crystals have attractive $\chi^{(3)}$ nonlinear properties [17], which are closely related to the stimulated Raman scattering process and self-mode-locked operation [18, 19]. In recent years, with Gd ions replacing a fraction of the Y ions in Nd:YVO_4 crystal, a new class of mixed vanadate crystal Nd:$Gd_xY_{1-x}VO_4$ has been successfully developed as an excellent gain medium in either continuous-wave operation or passively Q-switched operation [20–23]. More importantly, the broader fluorescence spectral width caused by the random distribution of the Gd and Y ions neighboring the Nd ions is favorable for the generation of the shorter pulses over the single-medium vanadate crystals in the mode-locked oscillation [24, 25]. Although Nd:$Gd_xY_{1-x}VO_4$ lasers pumped at 880 nm and 808 nm have been comparatively studied [26], direct in-band pumping at 914 nm has not been realized so far.

H.C. Liang · Y.J. Huang · P.Y. Chiang · Y.F. Chen (✉)
Department of Electrophysics, National Chiao Tung University,
1001 TA Hsueh Road, 30050 Hsinchu, Taiwan
e-mail: yfchen@cc.nctu.edu.tw
Fax: +886-35-725230

In this work, a highly efficient Nd:$Gd_{0.6}Y_{0.4}VO_4$ laser by direct in-band pumping at 914 nm is reported for the first time. With an absorbed power of 3.7 W, an average output power of 2.65 W at 1064 nm was obtained. The slope efficiency and optical conversion efficiency were up to 82% and 72%, respectively. Moreover, with the realization of large third-order nonlinearity of the Nd-doped vanadate crystal, the self-mode-locked operation was experimentally observed. Using an intracavity aperture to suppress high-order transverse mode and an wedged output coupler to eliminate the couple-cavity effect, a fairly stable fundamental mode-locked pulse train could be generated at repetition rates in the ranges of 0.9–3.3 GHz. The pulse width was measured to be 16 ps at a repetition rate of 1.75 GHz. This is also the first realization of a self-mode-locked laser under 914-nm pumping.

2 Experimental setup

Figure 1 shows the energy level diagram and measured absorption spectrum of a 1.0 at.% Nd:$Gd_{0.6}Y_{0.4}VO_4$ crystal with the length of 20 mm. The present laser crystal was cut about the a-axis, i.e. so-called a-cut, to use the larger stimulated emission cross section parallel to the c-axis for the purpose of lower pump threshold. The absorption spectrum was measured for non-polarized, σ-polarized and π-polarized incident light with resolution of 1 nm. It can clearly be seen that the crystal exhibits an attainable absorption at 914 nm, corresponding to its longest pump absorption wavelength. The overall absorption percentage of the crystal at 914 nm was experimentally evaluated to be approximately 20%, 18%, and 23% for non-polarized, σ-polarized and π-polarized incident light. In comparison with the traditional indirect pumping at 808 nm, which is related to the excitation $^4I_{9/2} \rightarrow {}^4F_{5/2}$ and the transition to $^4F_{3/2}$ via a non-radiative process, direct in-band pumping at 880 nm, which is in connection with the transition $^4I_{9/2} \rightarrow {}^4F_{3/2}$, can eliminate non-radiative process, leading to the reduction of thermal load by about 28% as well as the improvement of quantum defect ratio by around 9%. More importantly, the thermal load and the quantum defect ratio could be further ameliorated as much as 42% and 13% if the longest pump absorption wavelength of 914 nm is employed. Besides, differently from the traditional 808-nm indirect pumping, the absorption difference between σ-polarization and π-polarization at 914 nm is remarkably small, as indicated in Fig. 1. This polarization-insensitive absorption indicates the more homogeneous temperature distribution inside the crystal, thus being favorable for developing high-power laser [14].

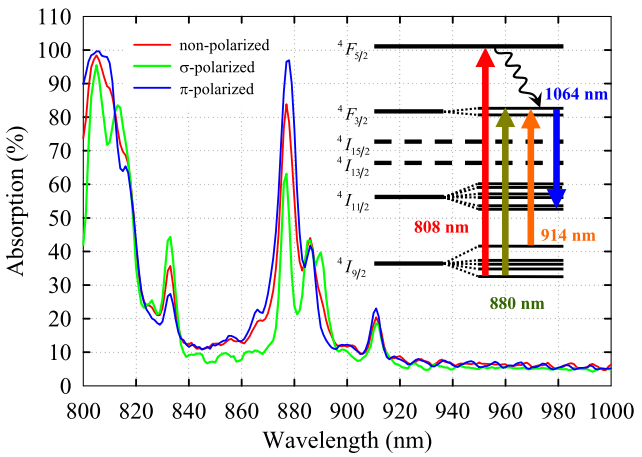

Fig. 1 Absorption spectrum for a 1.0 at.% Nd:$Gd_{0.6}Y_{0.4}VO_4$ crystal with a length of 20 mm. *Inset*: Energy level diagram of the pump-emission

The experimental setup was a simple concave-plano resonator. The gain medium with dimensions of $2 \times 5 \times 20$ mm^3 was an a-cut 1.0 at.% Nd:$Gd_{0.6}Y_{0.4}VO_4$ crystal purchased from CASTECH Inc. Both end facets were anti-reflection coated at 1064 nm and wedged 2° to avoid the couple-cavity effect. The laser crystal was wrapped with indium foil and mounted in a water-cooled copper heat sink at 20°C to ensure the stable laser output. The long crystal length is not only advantageous to enhance the absorption efficiency but also permits the thermal load to be spread over a larger volume leading to the minimization of stress and temperature rise etc., even though the overlapping between the pump beam and the laser beam might be problematic under diode pumping with so long a crystal. The input mirror with radius-of-curvature of 50 cm was coated at 914 nm for anti-reflection on the pump surface and at 1064 nm for high reflection as well as at 914 nm for high transmission on the second surface. An output coupler with transmission of 6% at 1064 nm was utilized throughout the experiment. The laser crystal was placed about 2–3 mm from the input mirror. The pump source was an 25-W 914-nm fiber-coupled laser diode with a core diameter of 800 μm and a numerical aperture of 0.16. The pump radius of 400 μm was re-imaged into the laser crystal with a lens set that has a focal length of 25 mm with a magnification of unity and a coupling efficiency of 85%. The geometrical cavity length was set as about 8.5 cm, and the fundamental mode radius inside the crystal was calculated to be 270 μm by the use of ABCD matrix method. To monitor the real-time temporal dynamics of the laser output, a high-speed InGaAs photodetector with rise time of 35 ps together with a digital oscilloscope (Agilent, DSO 80000) with electrical bandwidth of 12 GHz and sampling rate of 25 ps was employed.

3 Results and discussions

Figure 2 shows the average output power at 1064 nm with respect to the absorbed power at 914 nm. The pump threshold was about 0.8 W, and the maximum average output power was found to reach 2.65 W at an absorbed power of 3.7 W. The slope efficiency and optical conversion efficiency were up to 82% and 72%, respectively. Although the absorption at 914 nm is almost independent of the pump polarization, the laser output of an a-cut crystal is indeed π-polarized parallel to the c-axis of the crystal since its larger emission cross section will usually dominate the laser oscillation. The spatial distribution of the continuous-wave laser output was experimentally found to be multimode because the pump radius was much larger than the fundamental mode radius and will be discussed later. It was demonstrated that the highest slope efficiency of 74% and optical conversion efficiency 59% were achieved for Nd:$Gd_{0.18}Y_{0.82}VO_4$ crystal under direct 880-nm laser diode pumping in Ref. [26]. Consequently, our experimental results apparently reveal that the superior performance could be achieved by the use of direct in-band pumping at 914 nm.

The self-mode-locking is one of the intriguing phenomena during the early research on lasers. According to several theoretical studies and experimental investigations, the origin of the self-mode-locking is regarded as a result of the combination tones of the third-order nonlinearity of the gain medium, which could compensate for the dispersion effect [27–29]. Due to the large third-order nonlinearity of the vanadate crystal, the reliable self-mode-locked laser of present configuration is possibly fulfilled.

When monitoring the real-time temporal dynamics of the Nd:$Gd_{0.6}Y_{0.4}VO_4$ laser and finely tuning the cavity, we found that the laser output exhibited the self-mode-locked state with slightly lower output power, as shown in Fig. 2.

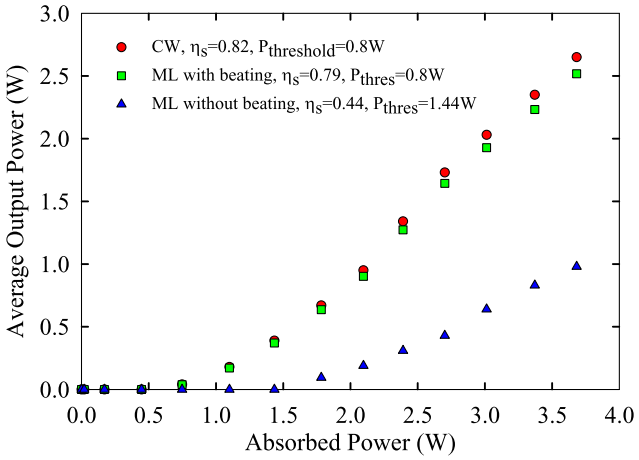

Fig. 2 The dependence of average output power on absorbed power. *Red points*: cw operation; *green points*: self-mode-locking with beat frequency; *blue points*: self-mode-locking without beat frequency

The separation between pulses was experimentally confirmed to correspond to the roundtrip time of the resonator, as demonstrated in Fig. 3(a) at a repetition rate of 1.75 GHz with time span of 20 ns. Nevertheless, the pulse train was modulated by the beat frequency between the transverse modes that resulted from the larger pump size of 400 μm compared with the fundamental mode size of 270 μm. The resonant frequency of an optical cavity could be expressed as [30]

$$f_{mnq} = q\Delta f_L + (m+n+1)\Delta f_T = q\frac{c}{2L} + (m+n+1)\frac{c}{2L}\frac{\cos^{-1}(\sqrt{g_1 g_2})}{\pi}$$

where $g_1 = 1 - \frac{L}{R_1}$, $g_2 = 1 - \frac{L}{R_2}$, m and n are the transverse mode number, q is the longitudinal mode number, L is the cavity length, R_1 and R_2 are the radius-of-curvature of the input mirror and the output coupler. With the experimental parameters, the transverse mode spacing Δf_T is evaluated as 230 MHz, which is in good agreement with the beat frequency between TEM_{00} mode and TEM_{01} mode.

An intracavity aperture was exploited to suppress the TEM_{01} mode in order to achieve a pure fundamental mode-locked state with single transverse mode, as shown in Fig. 3(b). However, the maximum output power was found to decrease to 1 W at an absorbed power of 3.7 W. This means that the overlapping between the pump mode and the laser mode was not good under single TEM_{00} mode operation at present. To overcome this problem, the mode-matching efficiency between the pump mode and the fundamental laser mode should be optimized in the future. On the other hand, the pulse train with noticeable amplitude fluctuation was observed, as displayed in Fig. 3(c) with time span of 500 ns. Previously, it was concluded that the wedged output coupler to avoid the couple-cavity effect plays a very important role in the achievement of the perfectly stable self-mode-locked Nd-doped vanadate laser [18, 19]. Therefore, we replaced the original output coupler by another 1°-wedged output coupler with transmission 6% at 1064 nm. The significantly improved stability of the pulse train was obtained, as displayed in Fig. 3(d). To confirm the reliable stability of self-mode-locked state, the radio-frequency (RF) spectrum analyzer was employed. The RF spectrum reveals that the relative frequency deviation of the power spectra $\Delta\nu/\nu$ is experimentally found to be smaller than 10^{-4} over day-long operation, where ν is the central frequency of the RF spectrum and $\Delta\nu$ is the full width at half maximum (FWHM) of the central frequency and is inferred from the beat note spectrum. The repetition rate of the reliable mode-locked laser could be steadily operated in the range of 0.9–3.3 GHz depending on the cavity length (16.7 cm–4.5 cm). With a commercial autocorrelator (APE, PulseCheck SM 250 IR), the pulse width under the stable cw mode-locked

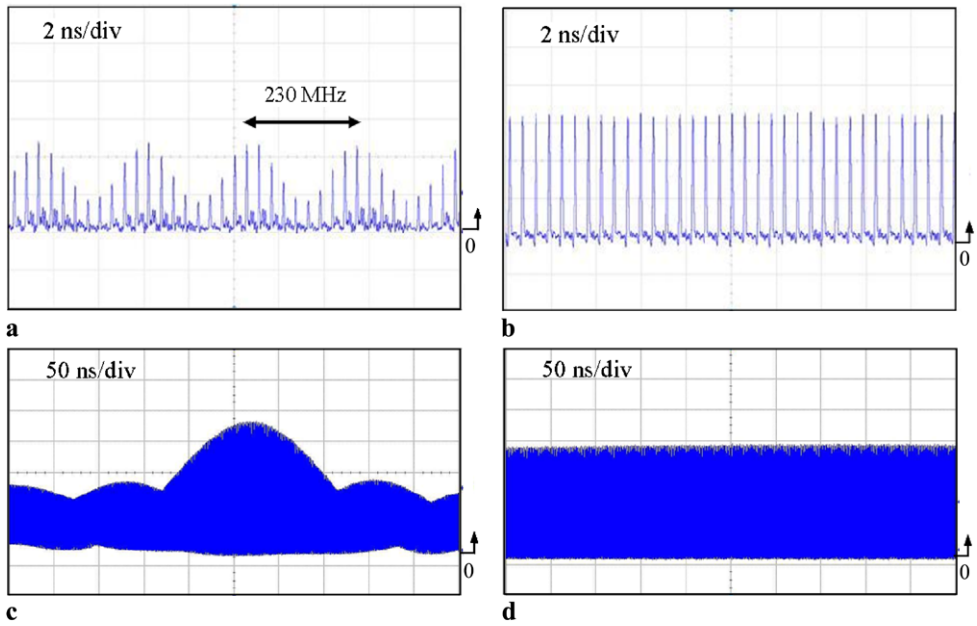

Fig. 3 (**a**) Pulse trains for the laser operated in a coherent superposition of TEM_{00} and TEM_{10} modes, time span of 20 ns; (**b**) pulse trains for the single transverse mode operation, time span of 20 ns; (**c**) pulse trains with the couple-cavity effect, time span of 500 ns; (**d**) pulse trains with the elimination of couple-cavity effect by the use of wedged output coupler, time span of 500 ns

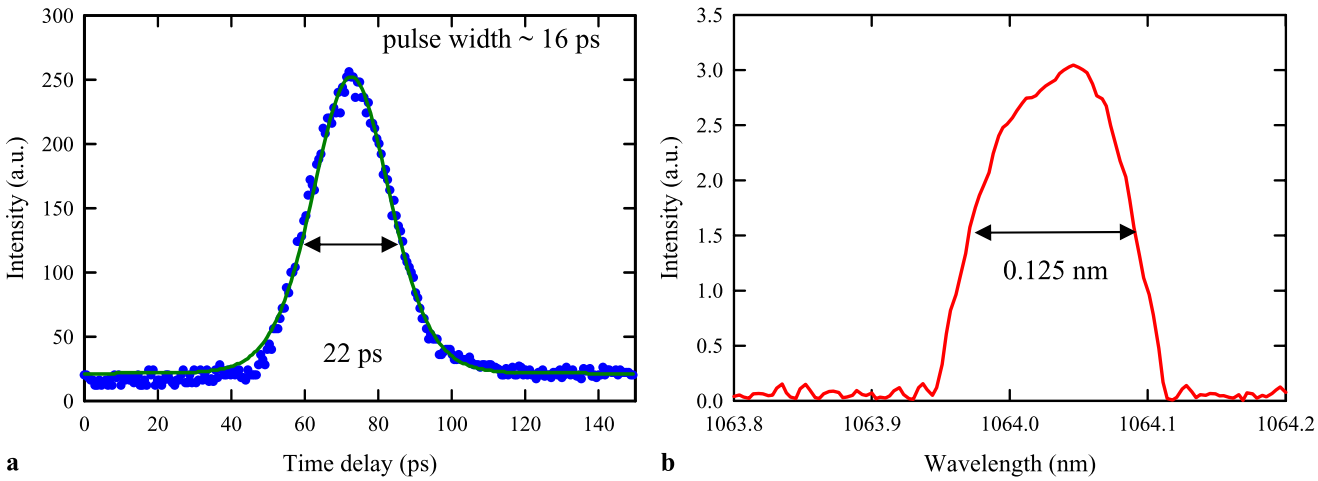

Fig. 4 (**a**) Autocorrelation trace of the output pulses from the cw mode-locked Nd:$Gd_{0.6}Y_{0.4}VO_4$ laser; (**b**) corresponding optical spectrum of the laser

operation was measured at a repetition rate of 1.75 GHz. The FWHM of the autocorrelation trace was measured to be 22 ps, as shown in Fig. 4(a). The pulse width was thus estimated to be 16 ps assuming the $sech^2$-shaped temporal profile. The spectral information of the laser was monitored by a Fourier optical spectrum analyzer (Advantest, Q8347) that is constructed with a Michelson interferometer with resolution of 0.003 nm. Figure 4(b) shows the FWHM width of the optical spectrum was 0.125 nm at the central wavelength of 1064.03 nm, giving the time-bandwidth product of the mode-locked pulse of 0.53 indicating the pulses to be frequency chirped and shorter pulse duration is possible under specific circumstance. As mentioned above, the inhomogeneous broadening of the emission spectrum of the Nd:$Gd_{0.6}Y_{0.4}VO_4$ is useful for producing shorter pulse duration over Nd:YVO_4 and Nd:$GdVO_4$. It is obvious that the pulse duration here is shorter than 23 ps, reported in Ref. [19] with the same experimental configuration, and we expect that a much shorter pulse duration could be obtained when the pump facet of Nd:$Gd_{0.6}Y_{0.4}VO_4$ is high-reflection coated at 1064 nm and acts as one cavity mirror of the resonator with the help of enhancement of spatial-hole-burning effect [18].

Finally, it should be pointed out that the enhanced absorption at 914 nm with optimum mode matching is very important to achieve high efficiency Nd-doped crystal laser in terms of incident pump power rather than absorbed power. Using a heavily Nd-doped laser crystal can essentially increase the absorption at 914 nm, but it suffers from some problems, such as the concentration quenching and the

degradation of optical quality etc. Lengthening the laser crystal can also increase the absorption at 914 nm; however, the mode matching needs to be considered for optimization. Comparatively speaking, the multi-pass end-pumping scheme seems to be a more practical way for improving the absorption at 914 nm.

4 Conclusion

In conclusion, we demonstrated a highly efficient Nd:$Gd_{0.6}Y_{0.4}VO_4$ laser by direct in-band pumping at 914 nm for the first time. With an absorbed power of 3.7 W, an average output power of 2.65 W at 1064 nm was obtained. The slope efficiency and optical conversion efficiency were up to 82% and 72%, respectively. We also found that the laser system could be efficiently operated in the self-mode-locked operation with the realization of large third-order nonlinearity of vanadate crystal. With an intracavity aperture to suppress the TEM_{10} mode as well as the wedged output coupler to eliminate the couple-cavity effect, a fairly stable mode-locked pulse train was obtained. The repetition rate of the mode-locked pulse train could be operated in the range of 0.9–3.3 GHz, depending on the cavity length. The pulse width was measured to be 16 ps at a repetition rate of 1.75 GHz. We believe that the reduction of thermal load and enhancement of laser efficiency with direct in-band pumping at 914 nm in combination with the self-mode-locked Nd:$Gd_{0.6}Y_{0.4}VO_4$ laser can provide an alternative choice for developing highly efficient mode-locked laser as long as the absorption at 914 nm is significantly improved.

The authors thank the National Science Council for their financial support of this research under Contract No. NSC-97-2112-M-009-016-MY3.

References

1. A. Giesen, H. Hügel, A. Voss, K. Wittig, U. Brauch, H. Opower, Appl. Phys. B **58**, 365 (1994)
2. A. Giesen, J. Speiser, IEEE J. Sel. Top. Quantum Electron. **13**, 598 (2007)
3. F. Hanson, Appl. Phys. Lett. **66**, 3549 (1995)
4. M. Tsunekane, N. Taguchi, T. Kasamastu, H. Inaba, IEEE J. Sel. Top. Quantum Electron. **3**, 9 (1997)
5. Z. Zhuo, T. Li, X. Li, H. Yang, Opt. Commun. **274**, 176 (2007)
6. Y.T. Chang, Y.P. Huang, K.W. Su, Y.F. Chen, Opt. Express **16**, 21155 (2008)
7. R. Lavi, S. Jackel, Y. Tzuk, M. Winik, E. Lebiush, M. Katz, I. Paiss, Appl. Opt. **38**, 7382 (1999)
8. V. Lupei, N. Pavel, Y. Sato, T. Taira, Opt. Lett. **28**, 2366 (2003)
9. N. Pavel, T. Taira, IEEE J. Sel. Top. Quantum Electron. **11**, 631 (2005)
10. L. McDonagh, R. Wallenstein, R. Knappe, A. Nebel, Opt. Lett. **31**, 3297 (2006)
11. X. Li, X. Yu, F. Chen, R. Yan, J. Gao, J. Yu, D. Chen, Opt. Express **17**, 9468 (2009)
12. X. Li, X. Yu, F. Chen, R. Yan, J. Yu, D. Chen, Opt. Express **17**, 12869 (2009)
13. L. McDonagh, R. Wallenstein, Opt. Lett. **32**, 1259 (2007)
14. D. Sangla, M. Castaing, F. Balembois, P. Georges, Opt. Lett. **34**, 2159 (2009)
15. D. Sangla, F. Balembois, P. Georges, Opt. Express **17**, 10091 (2009)
16. Y.F. Lü, X.H. Zhang, J. Xia, Laser Phys. Lett. **7**, 487 (2010)
17. A.A. Kaminskii, K. Ueda, H.J. Eichler, Y. Kuwano, H. Kouta, S.N. Bagaev, T.H. Chyba, J.C. Barnes, G.M.A. Gad, T. Murai, J. Lu, Opt. Commun. **194**, 201 (2001)
18. H.C. Liang, R.C.C. Chen, Y.J. Huang, K.W. Su, Y.F. Chen, Opt. Express **16**, 21149 (2008)
19. H.C. Liang, H.L. Chang, W.C. Huang, K.W. Su, Y.F. Chen, Y.T. Chen, Appl. Phys. B **97**, 451 (2009)
20. L. Qin, X. Meng, C. Du, L. Zhu, B. Xu, Z. Shao, Z. Liu, Q. Fang, R. Cheng, J. Alloys Compd. **354**, 259 (2003)
21. L.J. Qin, X.L. Meng, L. Zhu, J.H. Liu, B.C. Xu, H.Z. Xu, F.Y. Jiang, C.L. Du, X.Q. Wang, Z.S. Shao, Chem. Phys. Lett. **380**, 273 (2003)
22. J. Liu, Z. Wang, X. Meng, Z. Shao, B. Ozygus, A. Ding, H. Weber, Opt. Lett. **28**, 2330 (2003)
23. J. Liu, X. Meng, Z. Shao, M. Jiang, B. Ozygus, A. Ding, H. Weber, Appl. Phys. Lett. **83**, 1289 (2003)
24. J.L. He, Y.X. Fan, J. Du, Y.G. Wang, S. Liu, H.T. Wang, L.H. Zhang, Y. Hang, Opt. Lett. **29**, 2803 (2004)
25. Y.D. Zavartsev, A.I. Zagumennyi, Y.L. Kalachev, V.A. Mikhailov, A.A. Sirotkin, I.A. Shcherbakov, R. Renner-Erny, W. Lüthy, T. Feurer, Quantum Electron. **37**, 315 (2007)
26. N.C. Fernelius, X. Wang, Y. Tang, S. Tang, Proc. SPIE **7193**, 71930M-1 (2009)
27. H. Statz, J. Appl. Phys. **38**, 4648 (1967)
28. H. Statz, M. Bass, J. Appl. Phys. **40**, 377 (1969)
29. P. Glas, M. Naumann, A. Schirrmacher, L. Däweritz, R. Hay, Opt. Commun. **161**, 345 (1999)
30. J.P. Goldsborough, Appl. Opt. **3**, 267 (1964)

Appl Phys B (2011) 103: 291–294
DOI 10.1007/s00340-010-4189-1

Applied Physics B
Lasers and Optics

High-repetition-rate megawatt millijoule pulses from a Nd:YVO_4 laser passively Q-switched by a semiconductor saturable absorber

Y.P. Huang · P.Y. Chiang · Y.J. Huang · K.W. Su · Y.F. Chen · K.F. Huang

Received: 30 June 2010 / Revised version: 26 July 2010 / Published online: 15 September 2010

Abstract We exploit an AlGaInAs periodic quantum-well absorber with a large modulation strength to realize a multi-mJ passively Q-switched Nd:YVO_4 laser with a repetition rate up to 200 Hz. At a pump energy of 34 mJ, the output pulse energy and the peak power are found to be 3.5 mJ and 1.1 MW, respectively. The fluctuation of the output pulse energy is generally less than ±2%.

1 Introduction

Megawatt (MW) millijoule (mJ) laser pulses are practically useful for many applications, such as range finders, nonlinear optics, and medical systems. Q-switching is extensively exploited in producing high-peak-power and high-energy laser pulses. Compared with active Q-switching techniques, passive Q-switching methods that employ saturable absorbers can considerably enhance the compactness and simplify the operation. In earlier studies, the pulses with nanosecond durations and several tens of kilowatt peak power have been obtained in continuous-wave (CW) diode-pumped passively Q-switched lasers [1–4]. To produce pulses with larger energy and higher peak power, quasi-CW (QCW) laser diode bars or stacks have been often used as pump light sources [5–8]. Compared with conventional flash lamps, QCW diode stacks can be operated at higher pump repetition rates and introduce lower heat loads to gain media.

Y.P. Huang · P.Y. Chiang · Y.J. Huang · K.W. Su · Y.F. Chen (✉) · K.F. Huang
Department of Electrophysics, National Chiao Tung University, 1001 TA Hsueh Road, Hsinchu 30050, Taiwan
e-mail: yfchen@cc.nctu.edu.tw
Fax: +886-35-725230

Currently, Cr^{4+}:YAG crystal is the most widely used saturable absorber in the spectral region of 0.9–1.2 μm [9–11]. It has been recently demonstrated that several mJ of output pulse energies could be generated from QCW diode-pumped Nd:YAG lasers passively Q-switched by Cr^{4+}:YAG crystals with the optical-to-optical efficiency ranging from 4% to 7% [6, 8, 12]. The highest repetition rate achieved with QCW diode-pumped passively Q-switched Cr^{4+}:YAG/Nd:YAG lasers remains less than 100 Hz because the maximum duty factors of QCW diodes are generally less than 2%. There is consequently a need to use Nd-doped vanadate crystals with a shorter spontaneous lifetime (∼100 μs) for obtaining a higher repetition rate in a QCW pumped configuration. Moreover, Nd-doped vanadate crystals have a wider absorption band than Nd:YAG crystals. However, Cr^{4+}:YAG crystals are usually not appropriate to directly serve as saturable absorbers for Nd-doped vanadate crystal lasers because their absorption cross sections are not high enough for the good Q-switched criterion [13–16]. To the best of our knowledge, the single pulse energies generated from passively Q-switched Nd:YVO_4/Cr^{4+}:YAG lasers were normally not greater than 200 μJ [14–17]. Recently, an AlGaInAs semiconductor material with a periodic quantum-well (QW) structure grown on a Fe-doped InP structure has been successfully used as a saturable absorber in a CW diode-pumped Nd:YVO_4 laser to generate several tens of microjoule laser pulses [18]. More recently, the AlGaInAs periodic QW absorber has been applied in an Yb-doped fiber laser to produce pulse energy up to 300 μJ [19]. This result indicates that AlGaInAs QW absorbers have a potential to generate much higher pulse energies.

In this work we develop an AlGaInAs periodic QW device with a large modulation strength to severs as a saturable absorber in a QCW diode-pumped Nd:YVO_4 laser. Experimental results reveal that the efficient passively Q-switched

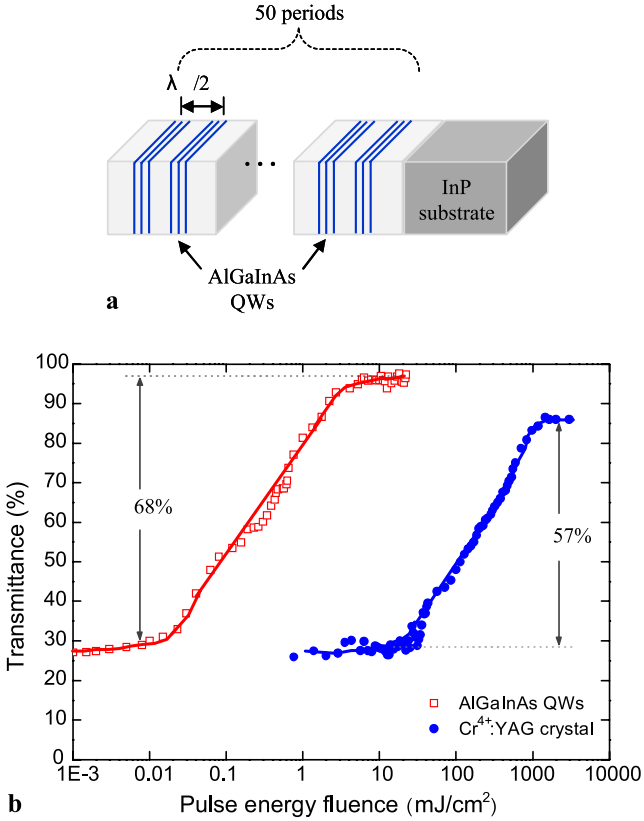

Fig. 1 (**a**) Structure of the present AlGaInAs material; (**b**) transmittance of AlGaInAs material and Cr^{4+}:YAG crystal as a function of the incident pulse energy fluence

$Nd:YVO_4$ laser is capable of generating 3.5 mJ of output pulse energy at 200 Hz repetition rate with a beam quality M^2 factor better than 1.5. The peak power is found to be greater than 1 MW and the fluctuation of the output pulse energy is generally less than ±2%.

2 Semiconductor QWs absorber

In our earlier work [18] we fabricated a saturable absorber that consisted of 30 groups of two QWs, spaced at half-wavelength intervals by InAlAs barrier layers with the band-gap wavelength around 806 nm and with the luminescence wavelength to be near 1064 nm. Here we use a similar device structure and enhance the modulation strength by increasing the number of QWs to be 50 groups of three QWs, as shown in Fig. 1(a). An InP window layer was deposited on the QW/barrier structure to avoid surface recombination and oxidation. The backside of the substrate was mechanically polished after growth. The both sides of the semiconductor saturable absorber were antireflection coated to reduce back reflections and the couple-cavity effects. The saturation transmission of the AlGaInAs QW saturable absorber was measured with a nanosecond 1064-nm Q-switched laser as

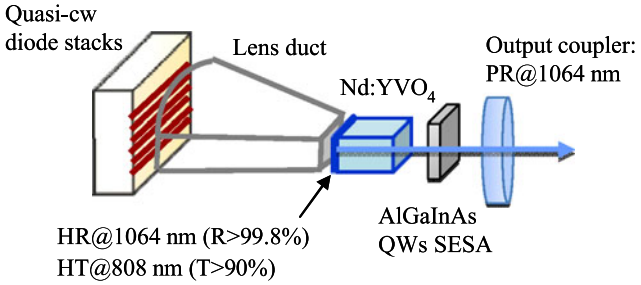

Fig. 2 Schematic of the laser experiment setup

the excitation source, as shown in Fig. 1(b). To make a comparison, we also measured the saturation transmission of a Cr^{4+}:YAG crystal and plotted the result in the same figure. The two sides of the Cr^{4+}:YAG crystal were coated for antireflection at 1064 nm ($R < 0.2\%$) and its initial transmission was nearly the same as that of the present AlGaInAs absorber. The saturation transmission of AlGaInAs QW absorber was observed to reach 95%, indicating a low non-saturable loss. An inferior final transmission (85%) of the Cr^{4+}:YAG crystal was mainly attributed to the excited-state absorption. With the values of the final transmission, the effective modulation strengths of AlGaInAs QW absorber and Cr^{4+}:YAG crystal were found to be 68% and 57%, respectively. The most important benefit of the AlGaInAs QW absorber is that its saturation fluence was two orders of magnitude smaller than that of Cr^{4+}:YAG crystal. This result indicates that AlGaInAs QW device has a much larger absorption cross section than that of Cr^{4+}:YAG crystal to be an appropriate absorber for passively Q-switching $Nd:YVO_4$ lasers. Employing the Frantz–Nodvik equation [20] to the saturation curve, the absorption cross section of the present AlGaInAs QW device was calculated to be 9×10^{-16} cm^2.

3 Laser experiment

Figure 2 depicts the experimental configuration of a QCW diode-pumped passively Q-switched $Nd:YVO_4$ laser with AlGaInAs QWs as a saturable absorber. The pump source was a QCW high-power diode stack (Coherent G-stack package, Santa Clara, Calif., USA) which consisted of six 10-mm-long diode bars with a maximum output power of 120 W per bar at the central wavelength of 808 nm. The diode stack was constructed with 400 μm spacing between the diode bars so the whole emission area was approximately 10×2.4 mm^2. The full divergence angles in the fast and slow axes are approximately 35° and 10°, respectively. The pump duration of QCW laser diode stack was 100 μs to match the upper-level lifetime of $Nd:YVO_4$ laser crystal. A lens duct, which was fabricated from BK7 glass, was utilized to efficiently deliver the pump radiation to the laser crystal [21–23]. Compared with ordinary coupling methods,

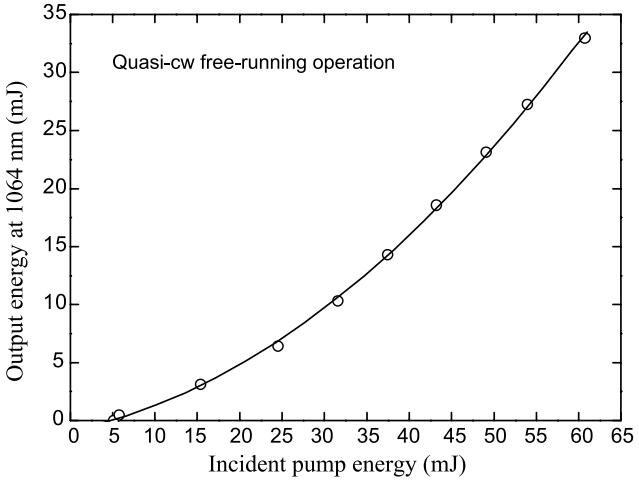

Fig. 3 Output energy at 1064 nm with respect to the incident pump energy at 808 nm for quasi-cw free-running operation

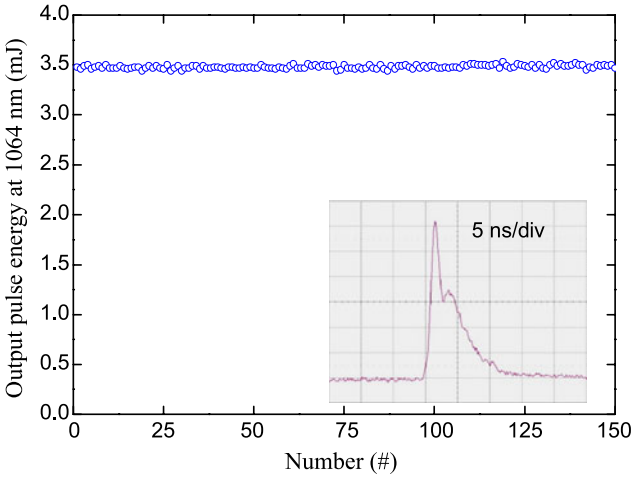

Fig. 4 Energy stability of the passively Q-switched Nd:YVO4 laser under a repetition rate of 200 Hz. Inset: temporal shape of a single pulse

the lens duct has the advantages of simple structure, optical coupling efficiency, and spatial homogeneity of the pump intensity distribution. In this experiment, the lens duct dimensions are as follows: radius of curvature of the input surface 10 mm, width of the input surface 12 mm, length of the duct 29 mm, and output aperture 3.8 mm × 3.8 mm. The lens duct with a large output aperture was used to enhance the laser mode volume in this plane-parallel cavity. The coupling efficiency of the lens duct was experimentally measured to be approximately 80%. The active medium was an a-cut 0.5 at% Nd^{3+}, 7-mm long Nd:YVO_4 crystal. The entrance surface of the laser crystal was coated with high reflection at 1064 nm ($R > 99.8\%$) and high transmission at 808 nm ($T > 90\%$). The other surface of the laser crystal was coated with antireflection at 1064 nm ($R < 0.2\%$). The laser crystal was wrapped with indium foil and mounted in a copper block. The output coupler was a flat mirror with partial reflection at 1064 nm. The overall laser cavity length was approximately 15 mm.

To begin with, we utilized a flat output coupler with 90% reflectivity at 1064 nm to evaluate the performance of free-running operation without saturable absorber. Figure 3 shows the experimental results of the output energy with respect to the pump energy in the free-running operation. At a pump energy of 59 mJ, the output energy at 1064 nm is approximately 33 mJ. The pump energy is defined as the energy delivered at the output of the lens duct. The good efficiency confirms the coupling function of the lens duct and the quality of the laser crystal.

We next placed the AlGaInAs QW absorber inside the cavity and exploited an output coupler with different reflectivity at 1064 nm to perform the passive Q-switching. Experimental results revealed that the maximum pulse energy could be obtained with an output coupler with 40–60% reflectivity at 1064 nm. Hereafter we present the experimental results obtained with an output reflectivity of 50%. The threshold energy for the stable Q-switched operation was measured to be approximately 34 mJ. At a pump energy of 34 mJ, the output pulse energy at 1064 nm was found to be 3.5 mJ, corresponding to an optical-to-optical efficiency of 10.3%. Note that the magnitude of thermal lensing in the laser rod was estimated to be approximately several meters during operation at 200 Hz. The beam quality M^2 factor was measured to be smaller than 1.5. When the pump energy exceeded 50 mJ, the cavity generated double pulses with nearly equal energies of 3.5 mJ.

Figure 4 shows the stability of the output pulse energy at a repetition rate of 200 Hz. The fluctuation of the output pulse energy can be seen to be less than ±2%. The pulse temporal behavior was recorded by a LeCroy digital oscilloscope (Wavepro 7100; 10 G samples/sec; 1 GHz bandwidth) with a fast InGaAs photodiode. A typical temporal shape of the laser pulse is shown in the inset of Fig. 4. Experimental results revealed that the tail of the pulse shape could not be improved by using an output coupler with a lower reflectivity. As a result, we speculated that the slightly long tail may come from the interaction between the QWs and laser light. However, the detailed mechanism is unclear and needs more study in the future. With the numerical integration for the measured temporal pulse profile, the peak power could be determined from the experimental pulse energy and its value was found to be 1.1 MW. These are to our knowledge the highest nanosecond pulse energies obtained by a passively Q-switched Nd:YVO_4 laser with a repetition rate up to 200 Hz. To make a comparison, we also employed a Cr^{4+}:YAG crystal with the initial transmission of 30% to Q-switch the present laser cavity. Experimental results revealed that the output emission consisted of a series of spikes with the overall pulse width longer than 200 ns and the pulse energy less than 1 mJ.

4 Summary

In conclusion, an AlGaInAs periodic QW device with a large modulation strength has been developed and employed to passively Q-switch a QCW diode-pumped Nd:YVO_4 laser at 1064 nm. Stable Q-switched pulses with a pulse energy of 3.5 mJ and a peak power of >1 MW were generated at a pump energy of 34 mJ. The optical-to-optical efficiency is considerably greater than the results obtained in QCW diode-pumped Nd:YAG/Cr^{4+}:YAG lasers. The fluctuation of the output pulse energy at a repetition rate of 200 Hz was found to be less than $\pm 2\%$. This compact efficient Q-switched laser is expected to be a useful light source for many applications.

Acknowledgements The authors gratefully acknowledge various AlGaInAs/InP chips from TrueLight Corporation. The authors also thank the National Science Council for their financial support of this research under Contract No. NSC-97-2112-M-009-016-MY3.

References

1. J.J. Zayhowski, C. Dill III, Opt. Lett. **19**, 1427 (1994)
2. Y. Shimony, Z. Burshtein, Y. Kalisky, IEEE J. Quantum Electron. **31**, 1738 (1995)
3. Y. Shimony, Z. Burshtein, A. Ben-AmarBaranga, Y. Kalisky, M. Strauss, IEEE J. Quantum Electron. **32**, 305 (1996)
4. A. Agnesi, S. Dell'Acqua, G.C. Reali, Opt. Commun. **133**, 211 (1997)
5. Th. Graf, J.E. Balmer, Opt. Lett. **18**, 1317 (1993)
6. R.S. Afzal, A.W. Yu, J.J. Zayhowski, T.Y. Fan, Opt. Lett. **22**, 1314 (1997)
7. A. Agnesi, F. Pirzio, G. Reali, G. Piccinno, Appl. Phys. Lett. **89**, 101120 (2006)
8. W. Zendzian, J.K. Jabczynski, J. Kwiatkowski, Laser Technol. **40**, 441 (2008)
9. Y. Kalisky, Prog. Quantum Electron. **28**, 249 (2004)
10. X. Zhang, S. Zhao, Q. Wang, Q. Zhang, L. Sun, S. Zhang, IEEE J. Quantum Electron. **33**, 2286 (1997)
11. A.R. Bijanzaden, R. Khordad, Opt. Commun. **282**, 2595 (2009)
12. Y. Wang, D. Xu, J. Xiong, Z. Wang, P. Wang, J. Yao, Chin. Phys. Lett. **25**, 2880 (2008)
13. Y.F. Chen, Y.P. Lan, H.L. Chang, IEEE J. Quantum Electron. **37**, 462 (2001)
14. Y.X. Bai, N. Wu, J. Zhang, J.Q. Li, S.Q. Li, J. Xu, P.Z. Deng, Appl. Opt. **36**, 2468 (1997)
15. H. Chen, E. Wu, H.P. Zeng, Opt. Commun. **230**, 175 (2004)
16. Y.F. Chen, S.W. Tsai, S.C. Wang, Opt. Lett. **25**, 1442 (2000)
17. J. Liu, J.M. Yang, J.L. He, Opt. Laser Technol. **35**, 431 (2003)
18. S.C. Huang, S.C. Liu, A. Li, K.W. Su, Y.F. Chen, K.F. Huang, Opt. Lett. **32**, 1480 (2007)
19. J.Y. Huang, W.C. Huang, W.Z. Zhuang, K.W. Su, Y.F. Chen, K.F. Huang, Opt. Lett. **34**, 2360 (2009)
20. L.M. Frantz, J.S. Nodvik, J. Appl. Phys. **34**, 2346 (1963)
21. G. Feugnet, C. Bussac, C. Larat, M. Schwarz, J.P. Pocholle, Opt. Lett. **20**, 157 (1995)
22. R.J. Beach, Appl. Opt. **35**, 2005 (1996)
23. R. Fu, G. Wang, Z. Wang, E. Ba, G. Mu, X. Hu, Appl. Opt. **37**, 4000 (1998)

ISSN 1054-660X, Laser Physics, 2011, Vol. 21, No. 3, pp. 480–484.

Simultaneous Self-Mode-Locking of $TEM_{0,0}$ and $TEM_{1,0}$ Modes in a Nd:YVO_4 Laser: Application for Measuring the Thermal Focal Length[1]

H. C. Liang, P. Y. Chiang, Y. J. Huang, Y. C. Lin, and Y. F. Chen*

Department of Electrophysics, National Chiao Tung University, Hsinchu, Taiwan

*e-mail: yfchen@cc.nctu.edu.tw

Received October 19, 2010; in final form, October 21, 2010; published online February 2, 2011

Abstract—We demonstrate that the simultaneous self-mode-locking of $TEM_{0,0}$ and $TEM_{1,0}$ modes can be achieved in a standard end-pumped Nd:YVO_4 laser. With this simultaneous self-mode-locking, the transverse beat frequency can be accurately measured as a function of the absorbed power. We employ the measured beat frequency and the cavity theory to precisely determine the effective focal length of the thermal lens in the gain medium.

DOI: 10.1134/S1054660X11050197

1. INTRODUCTION

During the early research on mode-locking, the self-mode-locked behavior was always observed in a multimode laser [1–4] without employing an extra nonlinearity except gain medium. Recently, it has been found that the self-mode-locking operation can be successfully achieved in diode-pumped Nd-doped vanadate crystal lasers without the need of any additional components [5]. It has been found that the wedge shape of the laser crystal is vital for obtaining a complete stable mode-locking operation. When a laser crystal without a wedge is used in a flat-flat cavity, the pulse train exhibit incomplete mode locking with CW background to a certain extent.

On the other hand, the unused pump power inside the gain medium gives rise to a thermal lens that occurs due to the combined effect of thermal expansion and thermally induced refractive index change [6, 7]. The pump-induced thermal lens can significantly influence the laser stability, the oscillation mode size, the maximum achievable average power, and the output beam quality [8–17]. To date, various experimental methods were developed to measure the focal length of the induced thermal lens, such as utilizing a second laser as probe laser [18–23], using the interferometric method [24–28], measuring the output beam parameters [29], employing the unstable-resonator method [30–32], and measuring the degenerate cavity length [33] or the beat frequency of the transverse modes [34]. Among these techniques, the transverse beat frequency method is of particular interest since it can be applied even for very weak thermal lensing.

In this work, we demonstrate for the first time that simultaneous self-mode-locked operation for $TEM_{0,0}$ and $TEM_{1,0}$ modes can be also realized with an off-axis pumping scheme [35–37]. We also employ the simultaneous self-mode-locking precisely to precisely measure the transverse beat frequency. With the measured transverse beat frequency and the cavity theory, the effective focal length of the thermal lensing can be precisely determined as a function of the absorbed power. Experimental results reveal that the effective focal power of the thermal lensing varies from 0.45 to 1.66 m^{-1} for the absorbed power increasing from 0.7 to 2.3 W in a 4.5-cm cavity with an average pump radius of 150 μm.

2. EXPERIMENTAL SETUP

Figure 1 depicts the experiment setup for the self-mode-locked laser. The cavity configuration is a simple concave-piano resonator. The gain medium is *a*-cut 0.2 at % Nd:YVO_4 crystal with a length of 10 mm. Both end surface of the Nd:YVO_4 crystal were antireflection coated at 1064 nm and wedge 0.5° to suppress the Fabry–Perot etalon effect. The laser crystal was wrapped with indium foil and mounted in a water-cooled copper holder with the water temperature to be maintained around 20°C for obtaining a stable laser output. The input mirror was a 50 cm radius-of-curvature concave mirror with antireflection coating at 808 nm on the entrance face and with high-reflectance coating at 1064 nm (>99.8%) and high transmittance coating at 808 nm on the second surface. A flat wedged output coupler with 15% transmission at 1064 nm was used throughout the experiment. The pump source was a 2.5-W 808-nm fiber-coupled laser diode with a core diameter of 100 μm and a numerical aperture of 0.16. Focusing lens with 25 mm focal length and 85% coupling efficiency was used to reimage the pump beam into the laser crystal. The average pump radius was approximately 150 μm. The opti-

[1] The article is published in the original.

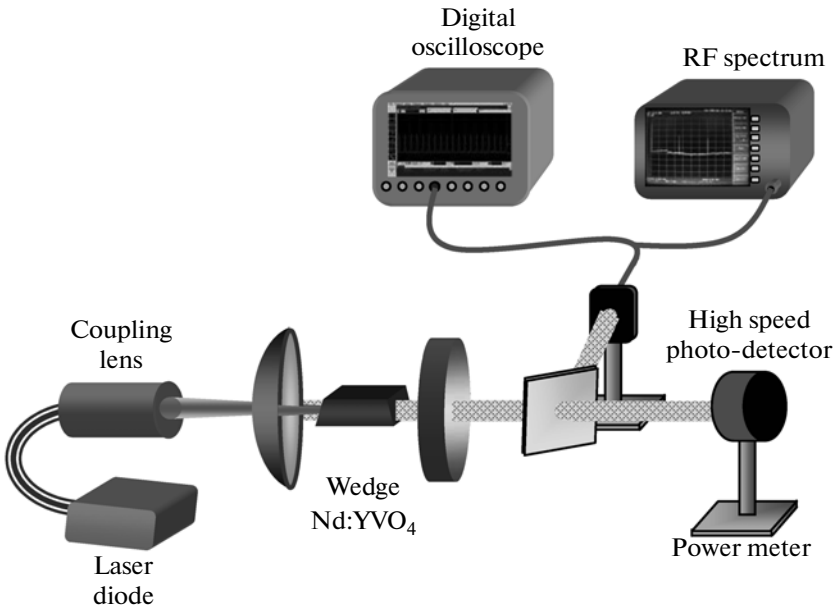

Fig. 1. Experimental setup of a self-mode-locked Nd:YVO_4 laser for measuring the focal length of thermal lens of the gain medium.

cal cavity length was set to be approximately 4.5 cm corresponding to free spectral range (FSR) of 3.3 GHz.

3. EXPERIMENTAL RESULTS

First of all, the pumping beam was focused right on the optical axis of laser cavity to obtain the maximum output power for fundamental mode. After finely adjusting the cavity alignment, the laser output can be found to display a stable self-mode-locked operation. Figure 2a shows the experimental lasing pattern measured with a CCD camera. The lasing mode can be clearly seen to be the $TEM_{0,0}$ mode. Note that once the pumped power reaches the lasing threshold, the system instantaneously steps into the stable mode-locked operation. The mode-locked pulses were detected by a high-speed InGaAs photodetector (Electro-optics Technology Inc. ET-3500 with rise time 35 ps), whose output signal was connected to a digital oscilloscope (Agilent, DSO 80000) with 12 GHz electrical bandwidth and sampling interval of 25 ps. Figure 2b shows the temporal trace of the self-mode-locked operation for the $TEM_{0,0}$ mode. Figure 2c depicts the average output power versus the absorbed power the self-mode-locked operation for the $TEM_{0,0}$ mode. The slope efficiency can be seen to be approximately up to 56% with respect to the incident pumped power, corresponding to an optical-optical efficiency of 50%. The pulse width was measured with the help of the commercial autocorrelator (APE pulse check, Angewandte physik & Elektronik GmbH) and assuming the $sech^2$-shaped temporal profile. As depicted in Fig. 2d, the pulse width was approximately 26 ps.

It has been shown that the off-axis pump scheme can be used to generate the high-order transverse modes [35–37]. Here we observed that the simultaneous self-mode-locking of the $TEM_{0,0}$ and $TEM_{1,0}$ modes could be achieved with a pump-beam displacement of several tens of microns off the axis of the cavity. Under the two mode self-mode-locked operation, the output power was found to decrease only a few percent relative to the pure $TEM_{0,0}$ output. Figures 3a and 3b show the spatial pattern and the temporal trace of pulse train obtained at a pump power of 1.1 W, respectively. It can be seen that the pulse train was modulated with a transverse beat frequency. The output signal was also analyzed with an RF spectrum analyzer (Advantest, R3265A) with bandwidth of 8 GHz. The corresponding RF power spectrum is depicted in Fig. 3c. The center frequency can be seen to be approximately 3.3 GHz which corresponds to the longitudinal mode spacing. In addition to the center frequency, the transverse beat frequency can be determined with the difference between the main peak and one of the secondary peaks in the RF power spectrum. As obtained in Fig. 3c, the transverse beat frequency was $228 \pm \Delta v$ MHz at a pump power of 1.1 W, where $\Delta v = 1$ MHz is the frequency deviation of full width at half maximum. Consequently, the transverse beat frequency can be precisely measured with the simultaneous self-mode-locking of $TEM_{0,0}$ and $TEM_{1,0}$ modes. The pulse width for the simultaneous self-mode-locking of $TEM_{0,0}$ and $TEM_{1,0}$ modes was

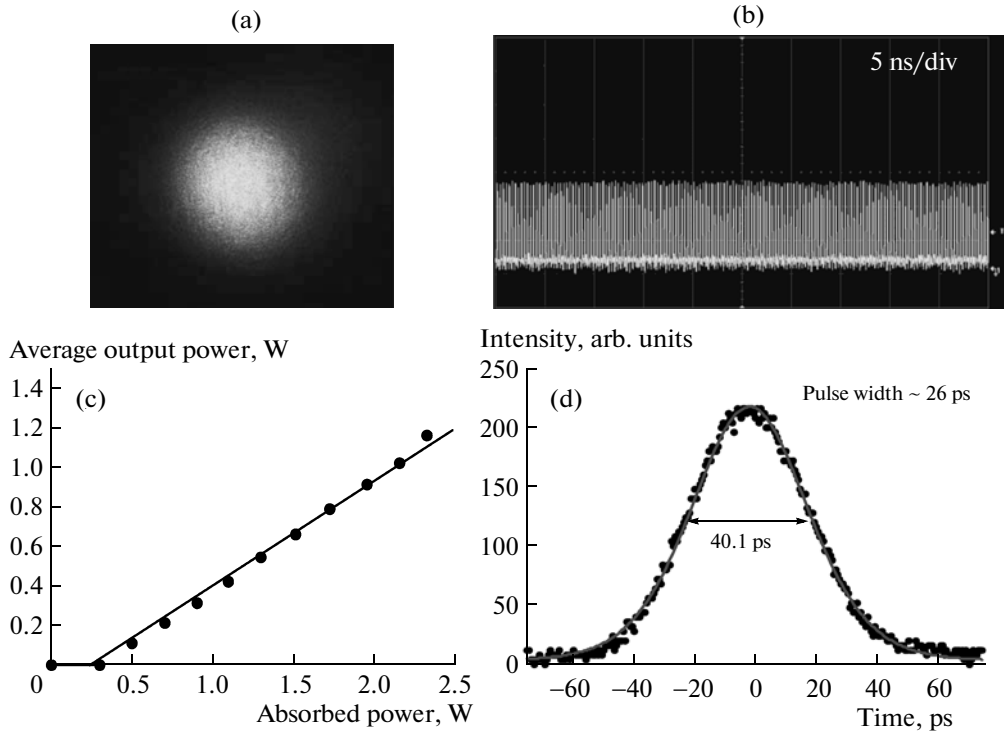

Fig. 2. (a) Experimental transverse pattern for the $TEM_{0,0}$ mode. (b) Temporal trace with the time span of 50 ns for demonstrating stable CW mode-locked pulses. (c) Average output powers versus the absorbed powers for the self-mode-locked operation. (d) Autocorrelation trace of the output pulses.

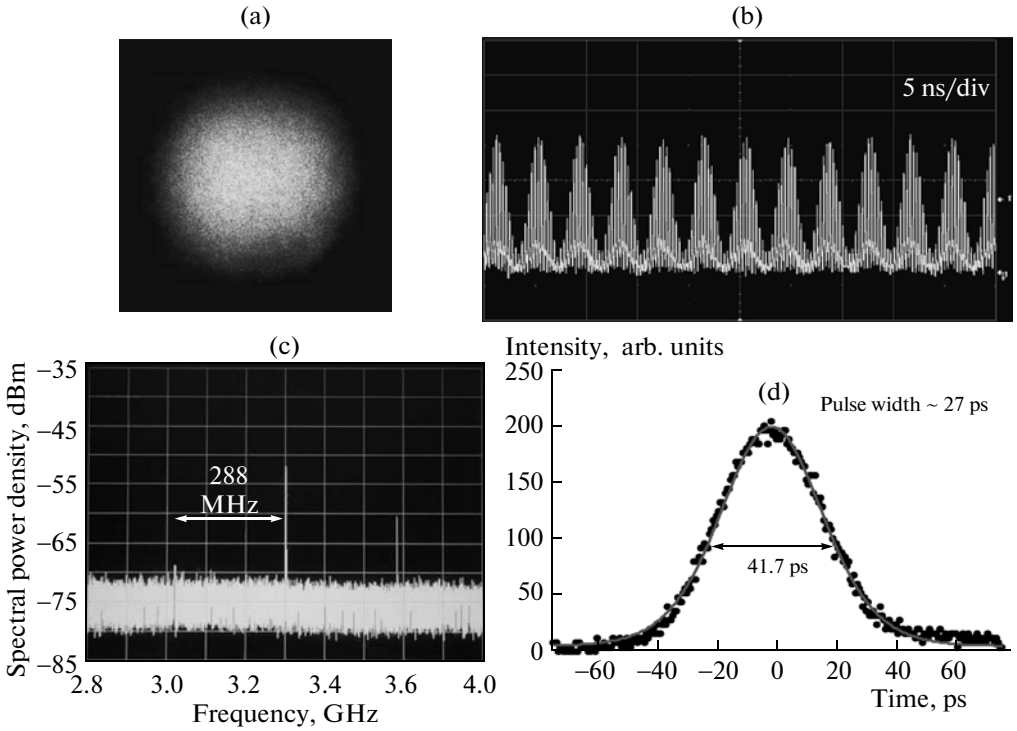

Fig. 3. (a) Experimental transverse pattern for a superposition of $TEM_{0,0}$ and $TEM_{1,0}$ modes. (b) Temporal trace with the time span of 50 ns for demonstrating the simultaneously self-mode-locked pulses. (c) Experimental RF Power spectrum for the simultaneously self-mode-locked operation. (d) Autocorrelation trace of the output pulses.

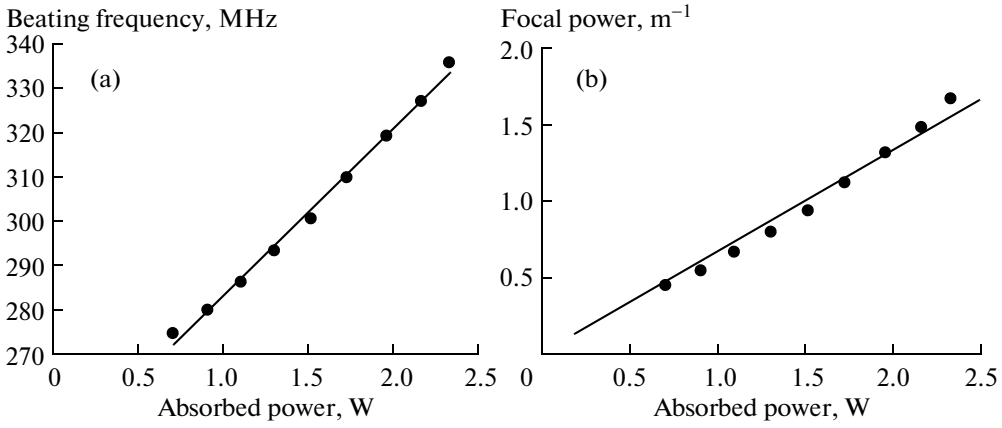

Fig. 4. (a) Transverse beat frequency versus the absorbed power in the simultaneously self-mode-locked operation. (b) The effective focal power of the thermal lensing versus the absorbed power calculated with the experimental data and Eq. (6).

found to be nearly the same as the result of the $TEM_{0,0}$ mode-locking, as depicted in Fig. 3d.

4. APPLICATION FOR MEASURING THE THERMAL FOCAL LENGTH

The thermal-lensing effect causes the transverse beat frequency to be strongly dependent on the pump power. Figure 4a shows the dependence of the transverse beat frequency on the absorbed power in the range of 0.7–2.3 W. It can be seen that the transverse beat frequency varies from 275 to 336 MHz with ±1 MHz frequency deviation for the pump power increasing from 0.7 to 2.3 W. With the experimental data for the transverse beat frequency, the effective focal length of the thermal lens can be determined by the formula of the equivalent *g*-parameters.

An optical resonator with an internal thermal lens can be replaced by a empty cavity with the equivalent *g*-parameters g^* and the equivalent cavity length L^* which are given by [38]

$$g_i^* = g_i - Dd_j\left(1 - \frac{d_i}{R_i}\right), \quad i,j = 1,2; \quad i \neq j, \tag{1}$$

$$L^* = d_1 + d_2 - Dd_1d_2, \tag{2}$$

$$g_i = 1 - \frac{d_1 + d_2}{R_i}, \tag{3}$$

where D is the effective focal power of the thermal lens, R_i is the radius of curvature of mirror, and d_1 and d_2 are the optical path length from the center of gain medium to the two mirrors. Because of the internal thermal lens, the Gaussian propagated with the wavelength λ in the cavity exhibits two waists whose position and radius are a function of the focal length of thermal lens. In terms of the equivalent cavity parameters, the beam waists and their positions are given by [38]

$$\omega_{oi} = \frac{\lambda L^*}{\pi}\frac{\sqrt{g_1^*g_2^*(1 - g_1^*g_2^*)}}{g_j^*(L^*/R_i) + g_i^*(1 - g_1^*g_2^*)}, \tag{4}$$

$$d_{oi} = L^*\frac{g_j^*(L^*/R_i)}{g_j^*(L^*/R_i)^2 + g_i^*(1 - g_1^*g_2^*)}. \tag{5}$$

Note that the beam waist i is located to the left of mirror i for $d_{oi} < 0$ and to the right for $d_{oi} > 0$. As a result, the Gouy phase function for each beam waist ω_{oi} is given by $\Theta_i(z) = \tan^{-1}(z/z_{oi})$, where $z_{oi} = \pi\omega_{oi}/\lambda$ is the Rayleigh range. With the Gouy phase function, the transverse beat frequency of the adjacent modes can be given as [39]

$$\Delta\nu_T = \frac{\Delta\nu_L}{\pi}[\Theta_1(d_1 - d_{o1}) + \Theta_1(d_{o1}) + \Theta_2(d_2 - d_{o2}) + \Theta_2(d_{o2})], \tag{6}$$

where $\Delta\nu_L$ is the longitudinal mode spacing. With Eq. (6), the effective focal power of the thermal lens can be solved as a function of the transverse beat frequency. Consequently, the dependence of the effective focal power of the thermal lens on the absorbed power can be obtained from the experimental results for the transverse beat frequency versus the absorbed power. Figure 4b shows the calculated results for the effective focal power as a function of the absorbed power with Eq. (6) and the experimental data shown in Fig. 4a, where the parameters used in the calculation are as follows: $d_1 = 14.3$ mm, $d_2 = 13.3$ mm, $R_1 = 500$ mm, and $R_2 \longrightarrow \infty$. Considering the linewidth of the transverse beat frequency, the uncertainty of the measured focal powers is calculated to be within 0.24–0.60% for the pump power increasing from 0.7 to 2.3 W. The small uncertainty indicates that this method can precisely determine the thermal lens of laser crystal. The

solid line shown in Fig. 4b is calculated with the empirical formula $D^{-1} = C\omega_p^2/P_{in}$, where P_{in} is the pump power in the unit of watts, ω_p is the average pump radius in the unit of mm, and C is the proportional constant in the unit of W/mm. The value of C for the best fitting to the experimental data was found to be 5.6×10^4 W/mm. This result is in good agreement with the values 4.14×10^4 and 4.9×10^4 W/mm which obtained by the unstable-resonator method described in [34, 35].

5. CONCLUSIONS

In summary, we have achieved the simultaneous self-mode-locking of $TEM_{0,0}$ and $TEM_{1,0}$ modes in a standard end-pumped Nd:YVO_4 laser. We employed this simultaneous self-mode-locking to accurately measure the transverse beat frequency as a function of the absorbed power. With the measured beat frequency and the cavity theory, we precisely determined the effective focal length of the thermal lens as a function of the absorbed power.

ACKNOWLEDGMENTS

The authors thank the National Science Council for their financial support of this research under Contract no. NSC-97-2112-M-009-016-MY3.

REFERENCES

1. A. Grütter, H. P. Weber, and R. Dändliker, Phys. Rev. **185**, 629 (1969).
2. R. Dändliker, A. A. Grütter, and H. P. Weber, IEEE J. Quantum Electron. **6**, 687 (1970).
3. H. Statz, J. Appl. Phys. **38**, 4648 (1967).
4. P. Glas, M. Naumann, A. Schirrmacher, L. Däweritz, and R. Hey, Opt. Commun. **161**, 345 (1999).
5. H. C. Liang, Ross C. C. Chen, Y. J. Huang, K. W. Su, and Y. F. Chen, Opt. Express **16**, 21149 (2008).
6. A. K. Cousins, IEEE J. Quantum Electron. **28**, 1057 (1992).
7. W. Koechner, *Solid-State Laser Engineering*, 6th ed. (Springer, New York, 2006), Ch. 7.
8. Y. F. Chen, T. M. Huang, C. F. Kao, C. L. Wang, and S. C. Wang, IEEE Quantum Electron. **33**, 1424 (1997).
9. Y. F. Chen, C. F. Kao, T. M. Huang, C. L. Wang, and S. C. Wang, IEEE J. Sel. Top. Quantum Electron. **3**, 29 (1997).
10. W. A. Clarkson, J. Phys. D **34**, 2381 (2001).
11. L. Sun, L. Zhang, H. J. Yu, L. Guo, J. L. Ma, J. Zhang, W. Hou, X. C. Lin, and J. M. Li, Laser Phys. Lett. **7**, 711 (2010).
12. J. Q. Zhao, Y. Z. Wang, B. Q. Yao, and Y. L. Ju, Laser Phys. Lett. **7**, 135 (2010).
13. X. P. Yan, Q. Liu, M. Gong, D. S. Wang, and X. Fu, Laser Phys. Lett. **6**, 93 (2009).
14. H. Chen, Q. Liu, X. Yan, and M. Gong, Laser Phys. **20**, 1594 (2010).
15. J. Ma, L. Guo, B. Xiong, X. Yan, S. Zhang, R. Chen, W. Zhao, X. Lin, J. Li, and Q. Duanmu, Laser Phys. **20**, 1350 (2010).
16. B. Song, C. Q. Li, A. G. Xie, Y. G. Wu, and T. B. Wang, Laser Phys. **20**, 197 (2010).
17. Z. Zhao, Y. Dong, C. Liu, M. Hu, Z. Xiang, J. Ge, and J. Chen, Laser Phys. **19**, 2069 (2009).
18. W. Koechner, Appl. Opt. **9**, 2548 (1970).
19. D. C. Burnham, Appl. Opt. **20**, 1727 (1970).
20. H. P. Kortz, R. Iffländer, and H. Weber, Appl. Opt. **20**, 4124 (1981).
21. K. P. Driedger, W. Krause, and H. Weber, Opt. Commun. **57**, 403 (1986).
22. D. S. Sumida, D. A. Rockwell, and M. S. Mangiv, IEEE J. Quantum Electron. **24**, 985 (1988).
23. R. Paugstadt and M. Bass, Opt. Laser Technol. **24**, 151 (1992).
24. T. S. Chen, V. L. Anderson, and O. Kahan, IEEE J. Quantum Electron. **26**, 6 (1990).
25. S. C. Tidwell, J. F. Seamans, M. S. Bowers, and A. K. Cousins, IEEE J. Quantum Electron. **28**, 997 (1992).
26. C. Phstner, R. Weber, H. P. Weber, S. Merazzi, and R. Gruber, IEEE J. Quantum Electron. **30**, 1605 (1994).
27. T. Omatsu, Y. Kato, M. Shimosegawa, A. Hasegawa, and I. Ogura, Opt. Commun. **118**, 302 (1995).
28. J. L. Blows, J. M. Dawes, and T. Omatsu, J. Appl. Phys. **83**, 2901 (1998).
29. B. Neuenschwander, R. Weber, and H. P. Weber, IEEE J. Quantum Electron. **31**, 1082 (1995).
30. D. G. Lancaster and J. M. Dawes, Opt. Laser Technol. **30**, 103 (1998).
31. F. Song, C. Zhang, X. Ding, J. Xu, G. Zhang, M. Leigh, and N. Peyghambarian, Appl. Phys. Lett. **81**, 2145 (2002).
32. Y. T. Chang, Y. P. Huang, K. W. Su, and Y. F. Chen, Opt. Express **16**, 21155 (2008).
33. B. Ozygus and Q. Zhang, Appl. Phys. Lett. **71**, 2590 (1997).
34. B. Ozygus and J. Erhard, Appl. Phys. Lett. **67**, 1361 (1995).
35. H. C. Liang, Y. J. Huang, Y. C. Lin, T. H. Lu, Y. F. Chen, and K. F. Huang, Opt. Lett. **34**, 3842 (2009).
36. Y. F. Chen, T. M. Huang, C. F. Kao, C. L. Wang, and S. C. Wang, IEEE J. Quantum Electron. **33**, 1025 (1997).
37. H. Laabs and B. Ozygus, Opt. Laser Technol. **28**, 213 (1996).
38. N. Hodgson and H. Weber, *Laser Resonators and Beam Propagation*, 2nd ed. (Springer, New York, 2005), Ch. 13.
39. A. E. Siegman, *Lasers* (Mill Valley, California, 1986), Ch. 19.

Manifestation of quantum-billiard eigenvalue statistics from subthreshold emission of vertical-cavity surface-emitting lasers

Y. F. Chen,* Y. T. Yu, P. Y. Chiang, P. H. Tuan, Y. J. Huang, H. C. Liang, and K. F. Huang
Department of Electrophysics, National Chiao Tung University, 1001 Ta-Huseh Road, Hsinchu 30050, Taiwan
(Received 4 October 2010; published 11 January 2011)

We report that the subthreshold emission spectra of vertical-cavity surface-emitting lasers (VCSELs) can be analogously used to manifest the quantum-billiard energy spectra. The Fourier-transformed distributions of the subthreshold emission spectra are demonstrated to display various peak structures that are in good agreement with the results of the quantum-billiard model. We also verify that the statistical analyses of the nearest-neighbor eigenvalue spacing distributions obey a Poisson distribution for an equilateral-triangular device and a Wigner distribution for a stadium-shaped device.

DOI: 10.1103/PhysRevE.83.016208 PACS number(s): 05.45.Mt, 42.65.Sf, 42.55.Sa

I. INTRODUCTION

Quantum manifestations of classical chaos recurrently attract much attention because the experimental techniques exploring the quantum classical correspondence have been continuously improved [1–4]. The two-dimensional (2D) billiard problem is particularly useful for studying the classical behaviors in the corresponding quantum regime due to their simplicity [5,6]. Ballistic-electron transport in quantum dots is often regarded as experimental realizations of quantum billiards [7–9]. The similarity between Schrödinger and Helmholtz equations has been widely used to develop electromagnetic wave resonators, ranging from 2D microwave cavities [10–12] to optical microdisk lasers [13–15], as another class of experimental and theoretical quantum-chaotic model systems.

Recently, the lateral oxide confinements of the vertical-cavity surface-emitting lasers (VCSELs) with a unique longitudinal wave vector k_z have been justified to be equivalent to 2D wave billiards with hard walls [16]. The special superiority of oxide-confined VCSELs is that the unique longitudinal wave vector k_z brings out the lasing transverse modes to be directly reimaged with simple optics for analogous observations of 2D quantum-billiard wave functions. More recently, Gensty *et al.* [17] utilized the emission spectra far above lasing threshold to analyze the eigenvalue spacing distribution and confirmed the oxide-confined VCSELs to be fascinating devices for wave chaos studies. However, the mode-competition phenomena usually induce mode-hopping instability and only several tens of cavity modes can be simultaneously lasing in the emission spectra far above lasing threshold. So far, the VCSEL devices have never been successfully employed to manifest the signatures of classical chaos and the role of periodic orbits in the quantum-billiard spectra.

Shortly after the invention of the semiconductor laser early in the 1960s, it was found that several hundreds to a thousand cavity modes could be clearly observed just below the lasing threshold in conventional edge-emitting semiconductor lasers [18,19]. In the same way, it was recently demonstrated that the oxide-confined VCSELs could emit several hundreds of transverse modes in the subthreshold emission spectra [20]. This result casts light on the prospect of using the VCSEL device to realize the experimental manifestations of classical chaos in the quantum-billiard spectra.

In this work we first employ a large-aperture equilateral-triangular VCSEL to explore the subthreshold emission spectrum and the Fourier transformed length spectrum. It is found that the experimental length spectrum agrees very well with the result of the quantum-billiard model to exhibit a series of sharp peaks at multiples of the lengths of the primitive periodic orbits. Furthermore, we use the subthreshold emission spectrum in a stadium-shaped VCSEL to investigate the signatures of wave chaos. Experimental results noticeably reveal that the isolated periodic orbits, corresponding to the so-called scar modes, play an essential role in the genuine chaotic wave resonators. We also confirm that the nearest-neighbor eigenvalue spacing distributions for the equilateral-triangular and stadium-shaped VCSELs obey a Poisson distribution and a Wigner distribution, respectively.

II. PERIODIC-ORBIT THEORY

Periodic-orbit theory developed by Gutzwiller [5] and Balian and Bloch [21] has been extensively used to analyze the long-range correlations in quantum spectra [22–24]. Here we give a brief synopsis for the application of periodic-orbit theory on the analysis of quantum-billiard spectra. Mathematically, the energy level density $\rho_o(E)$ can be split into a smoothly varying part $\rho(E)$ and a remaining oscillatory part. According to the Gutzwiller trace formula, the oscillatory part of the eigenvalue density is given by the actions of classical orbits, $S_\mu(E)$. Therefore the energy level density $\rho(E)$ can be expressed as

$$\rho(E) = \sum_{n=1}^{\infty} \delta(E - E_n) = \rho_o(E) + \sum_{\nu=1}^{\infty} \sum_{\mu} \rho_{\nu,\mu} \cos\left[\nu\left(\frac{S_\mu(E)}{\hbar} - \phi_\mu\right)\right], \quad (1)$$

where the index μ labels the periodic orbits and $\nu = 1,2,\ldots$ run over all recurrences of such orbits. For quantum-billiard systems, the action $S_\mu(E)/\hbar$ is given through the term kL_μ, where k is the wave number and L_μ is the path length of the periodic orbit. The eigenvalue density for the billiard

*Author to whom correspondence should be addressed. yfchen@cc.nctu.edu.tw

problem can be expressed as $\sum_{n=1}^{\infty}\delta(k-k_n)$, where k_n are the quantized wave numbers. As a result, the Fourier-transformed spectrum of the eigenvalue density is given by

$$\rho_{\mathrm{FT}}(L)=\sum_{n=1}^{\infty}\int_{-\infty}^{\infty}\delta(k-k_n)e^{ikL}=\sum_{n=1}^{\infty}e^{ik_nL}$$
$$=\sum_{\nu=1}^{\infty}\sum_{\mu}\rho_{\nu,\mu}\delta(L-\nu L_\mu). \quad (2)$$

Equation (2) indicates that the length spectrum $\rho_{\mathrm{FT}}(L)$ will display a series of intense peaks at multiples of the lengths of the periodic orbits, i.e., at $L=\nu L_\mu$. In other words, the character of classical periodic orbits can be revealed in the Fourier-transformed spectrum of the eigenvalue density. For numerical evaluation, the length spectrum can be written as $\rho_N(L)=\sum_{n=1}^{N}e^{ik_nL}$, where N should be large but finite.

III. EXPERIMENTAL RESULTS AND THEORETICAL ANALYSIS

The experimental VCSEL devices were grown with metal-organic chemical vapor deposition. Each device consists of a multiple quantum-well active region and a vertical cavity formed by two distributed Bragg reflector (DBR) mirrors. The active region comprises three $Al_{0.07}Ga_{0.93}As$-$Al_{0.36}Ga_{0.64}As$ quantum wells with well and barrier thickness of 70 and 100 Å, respectively. The spacers at both sides of quantum well were added to form a 1-λ cavity. The longitudinal wave number is given by $k_z=2\pi/\lambda_o$and the values of λ_o are designed to be approximately 782.6 nm for the experimental devices. The periods for the top and bottom DBR mirrors are 23 and 29, respectively. A high-Al composition $Al_{0.97}Ga_{0.03}As$ layer was placed at the first p-type doped DBR mirror and was oxidized to define an aperture for current confinement. This oxide aperture simultaneously induces an optical confinement because of the large difference of the refractive index between the semiconductor material and the oxide layer, thus forming an essentially rigid wall waveguide [16,17]. Here we fabricated two different shapes of oxide apertures, an equilateral-triangular shape and a stadium shape, to explore the signature of wave chaos in the subthreshold emission spectra. The optical microscope photographs of the experimental VCSELs are shown in Fig. 1.

The VCSEL device was placed in a temperature-controlled system with a stability of 0.1 °C near room temperature. We employed an optical spectrum analyzer based on a Michelson interferometer to measure the subthreshold emission spectra with a resolution up to 0.002 nm. With the relation of $k_z=2\pi/\lambda_o$, the subthreshold emission spectrum $\rho(\lambda)$can be changed from a function of the emission wavelength λ to a function of the transverse wave number k by using the relation $k=\sqrt{(2\pi/\lambda)^2-k_z^2}$. We first investigate the subthreshold emission spectrum of an equilateral-triangular VCSEL with the side length of $a=66\,\mu$m, as shown in Fig. 1(a). Figure 2(a) shows the experimental emission spectrum $\rho(k)$ of the equilateral-triangular VCSEL just below the lasing threshold. With the experimental data, the Fourier transform of the subthreshold spectrum $\rho_{\mathrm{FT}}(L)$ can be numerically calculated.

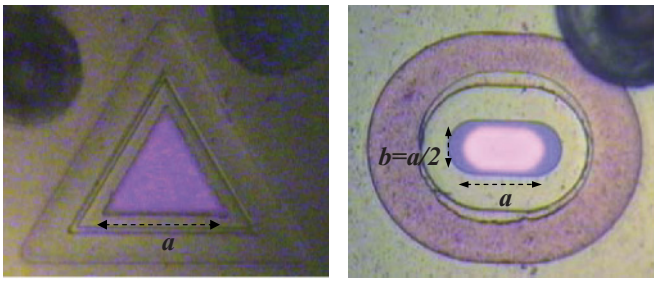

(a) (b)

FIG. 1. (Color online) Optical microscope photographs of the experimental VCSELs for (a) equilateral-triangular device with $a=66\,\mu$m and (b) stadium-shaped device with $a=42\,\mu$m and $b=21\,\mu$m.

Figure 2(b) depicts the calculated results for the path-length spectrum $|\rho_{\mathrm{FT}}(L)|^2$ corresponding to the experimental data shown in Fig. 2(a). We experimentally found that there was no obvious difference in the path-length spectra from sample to sample for device growth in the same batch. To make a comparison with the quantum-billiard spectrum, we calculated the Fourier transform of the density of states for an equilateral-triangular quantum billiard. The quantized wave numbers in an equilateral-triangular quantum billiard of side a can be analytically given by [25,26] $k_{m,n}=(4\pi/3a)\sqrt{m^2+n^2-mn}$ for integral values of m and n, with the restriction that $m\geqslant 2n$. The length spectrum was numerically calculated with the expression $\rho_N(L)=\sum_{n=1}^{N}\sum_{m=2n}^{2N}e^{ik_{m,n}L}$ and $N=15$. Figure 2(b) depicts the calculated results for the billiard model.

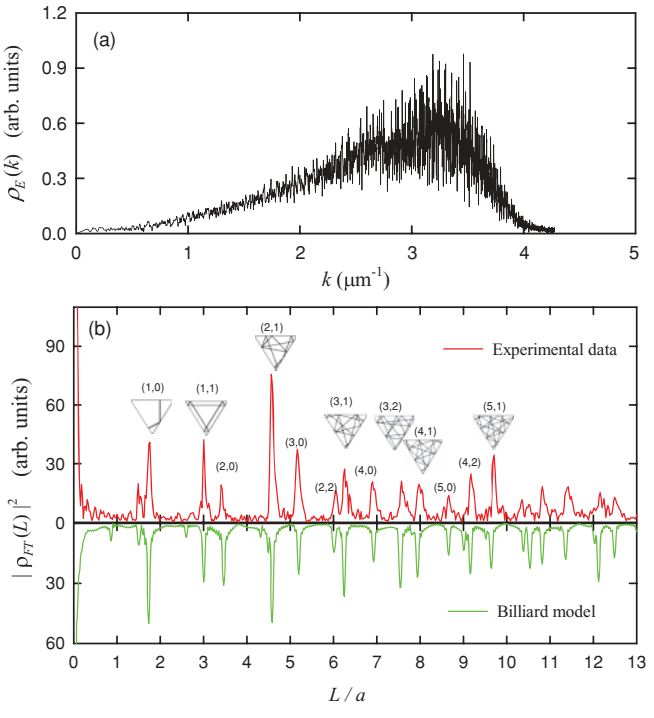

FIG. 2. (Color online) (a) Experimental emission spectrum $\rho(k)$ of the equilateral-triangular VCSEL just below the lasing threshold; (b) Fourier-transformed spectrum $|\rho_{\mathrm{FT}}(L)|^2$. The experimental and numerical results are displayed as mirror images.

Note that the path length of the periodic orbit (p,q) can be expressed as $L_{\mathrm{PO}}(p,q) = a\sqrt{3}\sqrt{p^2+pq+q^2}$. If p and q have common factors, such an orbit categorically corresponds to a recurrence of a simpler one in which the particle undergoes two or more periods. It can be seen that the experimental length spectrum agrees very well with the theoretical spectrum of the billiard model to exhibit a series of sharp peaks at multiples of the lengths of the primitive periodic orbits. This good agreement signifies the feasibility of exploiting the spontaneous emission spectra of large-aperture VCSELs to investigate the energy spectra of quantum billiards in an analogous way. In earlier times, the energy spectra of quantum billiards have been successfully studied by flat microwave resonators [4,10–12]. Here we manifest the quantum-billiard path-length spectra from the active devices in the optical regime. The observation of numerous cavity modes with narrow linewidth implies that the subthreshold emission spectra of VCSELs may be useful in developing wide-band tunable light sources for optical data communication.

Next, we fabricated a VCSEL, which has the shape of a Bunimovich stadium billiard, as shown in Fig. 1(b), with the dimensions $a = 42\,\mu$m and $b = 21\,\mu$m, corresponding to $\gamma = (a-b)/b = 1$. Figure 3(a) shows the experimental emission spectrum $\rho(k)$ of the stadium-shaped VCSEL just below the lasing threshold. Figure 3(b) depicts the calculated result for the Fourier-transformed spectrum $|\rho_{\mathrm{FT}}(L)|^2$ of the experimental data shown in Fig. 3(a). To make a comparison with the quantum-billiard spectrum, we employed the so-called expansion method [27] to calculate the theoretical eigenvalue density for the stadium billiard with the same geometry. The numerical result of the quantum-billiard model

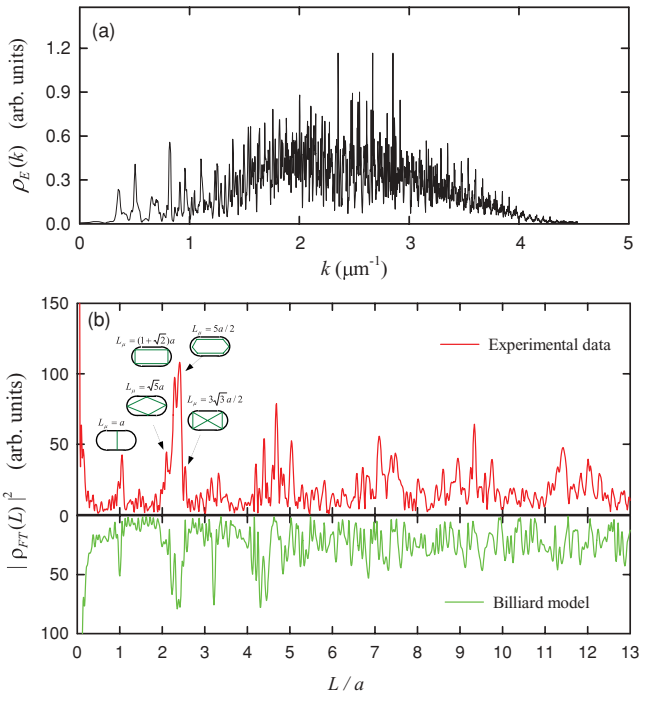

FIG. 3. (Color online) (a) Experimental emission spectrum $\rho(k)$ of the stadium-shaped VCSEL just below the lasing threshold; (b) Fourier-transformed spectrum $|\rho_{\mathrm{FT}}(L)|^2$. The experimental and numerical results are displayed as mirror images.

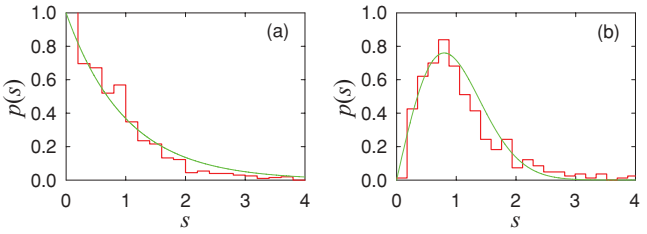

FIG. 4. (Color online) Experimental statistics for the nearest-neighbor eigenvalue spacing distribution $p(s)$ in form of histogram for (a) equilateral-triangular device and (b) stadium-shaped device. The curves represent (a) a Poisson distribution and (b) a Wigner distribution.

is shown in Fig. 3(b). It can be seen that the positions of the experimental peaks for the short-range periodic orbits, $(L/a) < 3.0$, agree well with the theoretical analysis. The short-range periodic orbits are associated with the scar modes that are numerically found to be rather insensitive to the geometry imperfection. For the long-range length distribution, the experimental spectrum comes close to the theoretical one to exhibit the complicated oscillations without conspicuous peaks. Numerical results indicate that the detailed structure in the long-range length distribution is more or less changed by the tiny perturbation, even though the salient feature of the complicated oscillations is quite similar. Therefore it is somewhat problematic to make a more quantitative comparison between the experimental and theoretical peaks for the long-range periodic orbits. Nevertheless, it is judiciously confirmed that the subthreshold emission spectra of the VCSELs with classically chaotic shape can manifest the path-length distributions to be in good agreement with the characteristics of the quantum-billiard model.

Finally, we employed the experimental emission spectra of the VCSELs to perform a statistical analysis. We searched all the peak positions in the experimental spectra and recorded these wave numbers as the sequence of eigenvalues $\{k_1,k_2,\ldots k_i,\ldots\}$. The spacings $s_i = (k_{i+1}-k_i)/\Delta k$ between adjacent eigenvalues were subsequently obtained by calculating the mean spacing Δk. We obtained 817 and 548 spacings of eigenmodes for the equilateral-triangular and stadium-shaped VCSELs, respectively. Figure 4 shows the experimental statistics for the nearest-neighbor eigenvalue spacing distribution $p(s)$ in the form of a histogram. It can be seen that the statistical results for the equilateral-triangular and stadium-shaped VCSELs are in good agreement with a Poisson distribution $p(s) = \exp(-s)$and a Wigner distribution $p(s) = (\pi s/2)\exp(-\pi s^2/4)$, respectively. The good consistency of the experimental statistics with the theoretical prediction further confirms that the subthreshold emission spectra of VCSELs can be analogously used to manifest the quantum-billiard spectra.

IV. CONCLUSIONS

In conclusion, we have investigated the manifestation of quantum-billiard energy spectra from the subthreshold emission spectra of equilateral-triangular and stadium-shaped VCSELs. The Fourier-transformed path length distribution for an equilateral-triangular VCSEL exhibits various peak

structures to be in good agreement with the results of the quantum-billiard model. We also employed a stadium-shaped VCSEL to manifest the path-length distribution corresponding to the characteristics of the quantum chaotic billiards. Furthermore, the statistical analyses of the nearest-neighbor eigenvalue spacing distributions have been verified to obey a Poisson distribution for the equilateral-triangular device and a Wigner distribution for the stadium-shaped device. The good agreement confirms that the subthreshold emission spectra of VCSELs can be analogously used to manifest the quantum-billiard spectra.

ACKNOWLEDGMENT

This work was supported by the National Science Council of Taiwan (Contract No. NSC-97-2112-M-009-016-MY3).

[1] H. J. Stöckmann, *Quantum Chaos—An Introduction* (University Press, Cambridge, England, 1999).
[2] T. Guhr, A. Müller-Groeling, and H. A. Weidenmüller, Phys. Rep. **299**, 189 (1998).
[3] *Quantum Chaos Y2K*—The 116th Nobel Symposium, edited by K.-F. Berggren, P. Omling, and S. Åberg [Physica Scripta, **T90**, 11 (2001).
[4] U. Kuhl, Eur. Phys. J. Special Topics **145**, 103 (2007).
[5] M. C. Guztwiller, *Chaos in Classical and Quantum Mechanics* (Springer-Verlag, New York, 1990).
[6] O. Bengtsson, J. Larsson, and K. F. Berggren, Phys. Rev. E **71**, 056206 (2005).
[7] C. M. Marcus, A. J. Rimberg, R. M. Westervelt, P. F. Hopkins, and A. C. Gossard, Phys. Rev. Lett. **69**, 506 (1992).
[8] K. F. Berggren and Z. L. Ji, Chaos **6**, 543 (1996).
[9] C. W. J. Beenakker, Rev. Mod. Phys. **69**, 731 (1997).
[10] H. J. Stöckmann and J. Stein, Phys. Rev. Lett. **64**, 2215 (1990).
[11] S. Sridhar, Phys. Rev. Lett. **67**, 785 (1991).
[12] A. Richter, Found. Phys. **31**, 327 (2001).
[13] J. U. Nöckel and D. Stone, Nature (London) **385**, 45 (1997).
[14] C. Gmachl, F. Capasso, E. E. Narimanov, J. U. Nöckel, A. D. Stone, J. Faist, D. L. Sivco, and A. Y. Cho, Science **280**, 1556 (1998).
[15] T. Harayama, P. Davis, and K. S. Ikeda, Phys. Rev. Lett. **90**, 063901 (2003).
[16] K. F. Huang, Y. F. Chen, H. C. Lai, and Y. P. Lan, Phys. Rev. Lett. **89**, 224102 (2002).
[17] T. Gensty, K. Becker, I. Fischer, W. Elsäßer, C. Degen, P. Debernardi, and G. P. Bava, Phys. Rev. Lett. **94**, 233901 (2005).
[18] M. I. Nathan, A. B. Flower, and G. Burns, Phys. Rev. Lett. **11**, 152 (1963).
[19] H. S. Sommers, J. Appl. Phys. **44**, 1263 (1973).
[20] Y. F. Chen, Y. T. Yu, Y. J. Huang, P. Y. Chiang, K. W. Su, and K. F. Huang, Opt. Lett. **35**, 2723 (2010).
[21] R. Balian and C. Bloch, Ann. Phys. (NY) **60**, 401 (1970); **64**, 271 (1971); **69**, 76 (1970); **85**, 514 (1974).
[22] D. Wintgen, Phys. Rev. Lett. **58**, 1589 (1987).
[23] I. V. Zozoulenko, A. S. Sachrajda, P. Zawadzki, K. F. Berggren, Y. Feng, and Z. Wasilewski, Semicond. Sci. Technol. **13**, A7 (1998).
[24] L. Christensson, H. Linke, P. Omling, P. E. Lindelof, I. V. Zozoulenko, and K. F. Berggren, Phys. Rev. B **57**, 12306 (1998).
[25] M. V. Berry and M. Wilkinson, Proc. R. Soc. London, Ser. A **392**, 15 (1984).
[26] M. Brack and R. K. Badhuri, *Semiclassical Physics* (Addison-Wesley, Reading, MA, 1997).
[27] D. L. Kaufman, I. Kosztin, and K. Schulten, Am. J. Phys. **67**, 133 (1999).

Extracting photon periodic orbits from spontaneous emission spectra in laterally confined vertically emitted cavities

Yung-Fu Chen,* Yan-Ting Yu, Yu-Jen Huang, Po-Yi Chiang, Kuan-Wei Su, and Kai-Feng Huang

Department of Electrophysics, National Chiao Tung University, Hsinchu, Taiwan
**Corresponding author: yfchen@cc.nctu.edu.tw*

Received March 22, 2010; revised June 21, 2010; accepted July 16, 2010;
posted July 21, 2010 (Doc. ID 125825); published August 10, 2010

We report our observation of the signature of photon periodic orbits in the spontaneous emission spectra of large-aperture vertical-cavity surface-emitting lasers (VCSELs). The high-resolution measurement clearly demonstrates that over a thousand cavity modes with a narrow linewidth can be perfectly exhibited in the spontaneous emission spectrum just below the lasing threshold. The Fourier-transformed spectrum is analyzed to confirm that the spontaneous emission spectra of large-aperture VCSELs can be exploited to analogously investigate the energy spectra of the 2D quantum billiards. © 2010 Optical Society of America

OCIS codes: 140.3410, 140.5960, 260.5740.

Optical microcavities have great potential for applications in miniature lasers, biological sensors, optical telecommunications, and basic research on modern physics [1–4]. Recently, large-aperture oxide-confined vertical-cavity surface-emitting lasers (VCSELs), serving as an analogous quantum billiard, have been employed to explore the quantum wave functions in mesoscopic systems [5–7]. An interesting phenomenon has been observed in that the electromagnetic field distributions of the lasing modes are mostly localized on the periodic ray trajectories, signifying the particle-wave duality [7]. Nowadays, periodic orbits are ubiquitously recognized as the most prominent feature in a wide range of systems, including particle accelerators [8], atomic spectra [9], and astronomy [10]. To the best of our knowledge, all studies to date related to photon periodic orbits have been restricted lasing spectra [2,5,6,11], and none has explored the role of photon periodic orbits from spontaneous emission spectra. As proposed by Purcell [12], the spontaneous emission rate of a radiating system can be significantly modified by using a cavity to tailor the coupling of an emitter with the vacuum field. This question naturally arises: would it be possible that photon periodic orbits play an important role in the spontaneous emission of an emitter in the large-aperture microcavity?

In this Letter we fabricate a large-aperture square-shape oxide-confined VCSEL to explore the spontaneous emission spectra in very high resolution. Experimental results clearly reveal that the coupling effects between the optical modes and the spontaneous emission increase with the increase of the injection current. We observed that several thousand cavity modes can be almost perfectly displayed in the spontaneous emission spectra. The Fourier transform of the spontaneous emission spectrum just below the lasing threshold reveals a recurrence spectrum in which each photon periodic orbit appears a peak in a plot of intensity versus length. This finding casts light on the new application of large-aperture VCSELs in studying the energy spectra of 2D quantum billiards with spontaneous emission spectra.

In this investigation, the VCSEL device, grown with metal–organic chemical vapor deposition, consists of a multiple quantum-well active region and doped semiconductor distributed Bragg reflector (DBR) mirrors to form the vertical cavity. The active region comprises three $Al_{0.07}Ga_{0.93}As$-$Al_{0.36}Ga_{0.64}As$ quantum wells with well and barrier thickness of 70 and 100 Å, respectively. The spacers at both sides of a quantum well were added to form a $1-\lambda$ cavity. For exploring the optical mode spectrum by electroluminescence spectroscopy, a large detuning between the quantum-well ground-state exciton and the fundamental cavity mode was designed. The detuning magnitude was approximately $\Delta\omega/2\pi = 2.7$ THz. The periods for the top and bottom DBR mirrors are 23 and 29, respectively. A high Al composition $Al_{0.97}Ga_{0.03}As$ layer is placed at the first positive-DBR mirror, which is oxidized for current and optical confinement. The device processing was carried out as follows. The wafers were wet oxidized at 425 °C, and the oxidation time is controlled to fabricate a 40 μm oxide square aperture in a 110 μm mesa structure.

Schematics of the laser device structure and the experimental setup are shown in Fig. 1. The VCSEL device was placed in a temperature-controlled system with a stability of 0.1 °C near room temperature. A current source with a precision of 0.01 mA was utilized to drive the VCSEL device. The emitted pattern was reimaged onto a CCD camera with a very-large-NA microscope objective lens (Mitutoyo, NA = 0.9) mounted on a translation stage. The spectral information of the radiation output

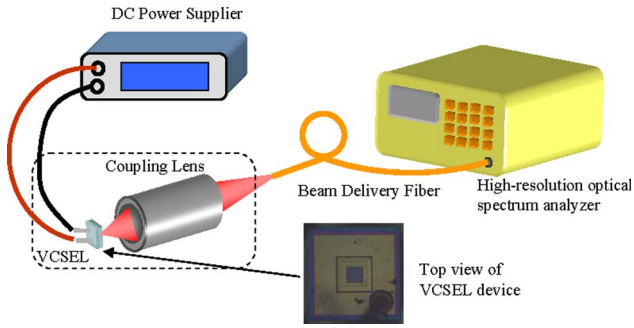

Fig. 1. (Color online) Schematics of the laser device structure and the experimental setup.

was measured by a high-resolution optical spectrum analyzer (Advantest Q8347). The present spectrum analyzer employs a Michelson interferometer with a Fourier spectrum system to reach a resolution of 0.002 nm; consequently, the cavity-mode spectral information can be resolved to a large extent.

Figures 2(a)–2(e) depict the emission spectra measured for several injection currents. Below the lasing threshold of 26 mA, the scale of the modulation depth in the emission spectra was clearly seen to deepen with an increase of the injection current, as shown in Figs. 2(a)–2(e). The presence of sharp emission peaks arises from the high-Q optical confinement and each peak at the injection current of 25 mA [Fig. 2(d)] is clearly resolved with less background. These peaks not only correspond to optical resonance modes but also signify the fact that transition probabilities are enhanced for emission wavelengths near the optical modes. As shown in the inset of Fig. 2(d), the linewidth of each isolated optical mode can be down to narrower than 0.01 nm. Because the linewidth of the quantum-well emitter is 10^3 – 10^4 wider than the average mode spacing of the cavity mode, there are several thousand cavity modes to be almost perfectly exhibited in the spontaneous emission spectra. More specifically, all the observed modes are the transverse modes of the cavity [13]. The change of cavity finesse with current indicates that the observed spectra should be referred to as the amplified spontaneous emission. When the injection current amounts to 26 mA, a few optical modes reach the lasing threshold and start to dominate the emission intensity, as seen in Fig. 2(e).

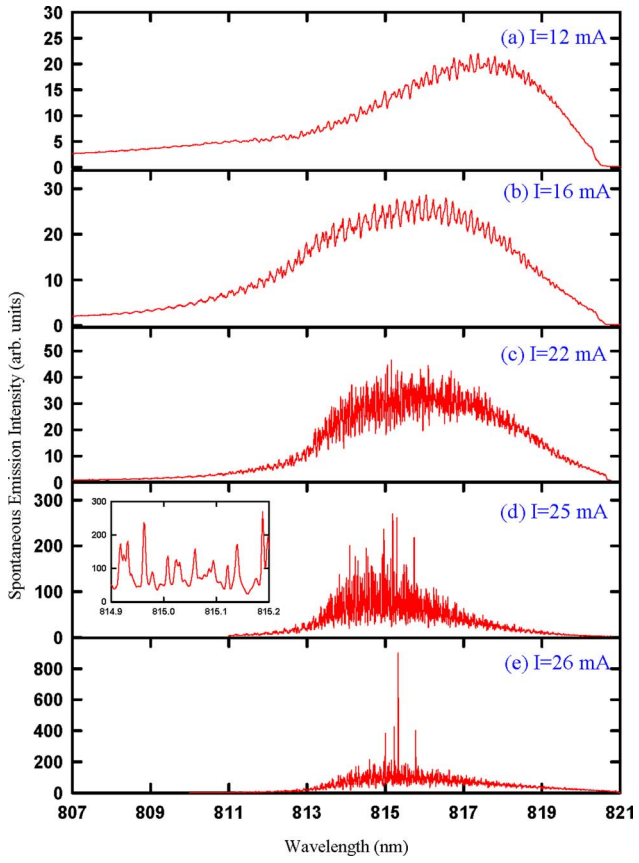

Fig. 2. (Color online) Emission spectra measured for several injection currents: (a)–(d) below lasing threshold and (e) just above lasing threshold.

It has been confirmed that the character of classical periodic orbits can be extracted from observed quantum spectra with a Fourier transform [14–16]. Analogously, the Fourier transform of the amplified spontaneous emission spectra should exhibit resonances corresponding to photon periodic orbits in VCSEL cavities. Because the longitudinal wavenumber in the VCSEL device is unique and given by $k_z = 2\pi/\lambda_o$, the experimental amplified spontaneous emission spectrum can be interpreted as the equivalent 2D density of state $\rho_{\mathrm{SE}}(K) = \sum_n \delta(K - K_n)$, where K is the variable for the transverse wavenumber, $K_n = \sqrt{k_n^2 - k_z^2}$, $k_n = 2\pi/\lambda_n$, and λ_n are the observed cavity modes. As a consequence, the Fourier transform of the amplified spontaneous emission spectrum with K as the variable is given by $\tilde{\rho}_{\mathrm{SE}}(L) = \int \mathrm{d}K \rho_{\mathrm{SE}}(K)\, e^{iKL} = \sum_n e^{iK_nL}$, where the sum is over all observed wavenumbers and L is the conjugate variable of the wavenumber. To be precise, $\tilde{\rho}_{\mathrm{SE}}(L)$ represents the autocorrelation function of the amplified spontaneous emission spectrum and each peak showing up in $|\tilde{\rho}_{\mathrm{SE}}(L)|$ is associated with the length of a resonant ray orbit. Note that the value of λ_o can be determined by the longest emission wavelength in the experimental spectrum. As shown in Fig. 2(a), the value of λ_o is approximately 820.8 nm. Numerical analysis reveals that the extracted resonant lengths were found to be almost unchanged for the value of λ_o varying within 820.8 ± 0.1 nm.

Figures 3(a)–3(e) depict the Fourier-transformed spectra $|\tilde{\rho}_{\mathrm{SE}}(L)|$, corresponding to the spontaneous emission spectra shown in Figs. 2(a)–2(e), respectively. It can be also seen that below the lasing threshold, the higher the current is injected, the more resonance peaks appear in $|\tilde{\rho}_{\mathrm{SE}}(L)|$. This result indicates that the coupling strength between the optical modes and the spontaneous emission spectra increase with increasing the injection current. The origin of the resonance peaks in $|\tilde{\rho}_{\mathrm{SE}}(L)|$ can be confirmed to be associated with the photon periodic orbits in the transverse plane. In a square lateral confinement, the formation of periodic orbits for photons undergoing specular reflection at each side wall is subject to the conditions of $k_x/k_y = p/q$, where p and q are two integers and k_x and k_y are the x component and y component of the transverse wavenumber, respectively. The path length of the periodic orbit $(p,\ q)$ is then given by $L(p,q) = 2a\sqrt{p^2 + q^2}$, where a is the length of the square boundary. Note that if p and q have common factors, such an orbit categorically corresponds to a recurrence of a simpler one in which the photon undergoes two or more periods. As seen in Figs. 3(a)–3(d), the resonance peaks in $|\tilde{\rho}_{\mathrm{SE}}(L)|$ are in good agreement with the results of the geometric orbits, which manifest the importance of the photon periodic orbits in spontaneous emission spectra. More intriguingly, the discernible orbits $(p,\ q)$ become more and more complex as the injection current increases. On the other hand, Fig. 3(e) illustrates that just above the lasing threshold, the stimulated emission significantly affects the interplay between the optical modes and the spontaneous emission, causing the elimination of the resonance peaks in $|\tilde{\rho}_{\mathrm{SE}}(L)|$. Recently,

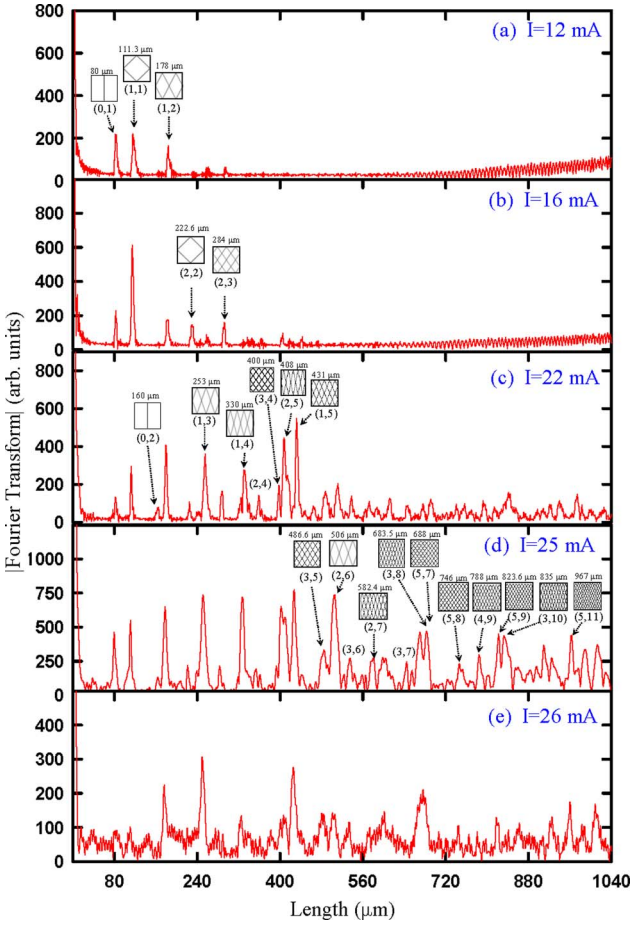

Fig. 3. (Color online) Fourier-transformed spectra $|\tilde{\rho}_{SE}(L)|$, corresponding to the spontaneous emission spectra shown in Figs. 2(a)–2(e), respectively.

Du *et al.* [17] theoretically found that the concept of periodic-orbit theory can be extended from electron to photon in analyzing the spontaneous emission rate of an atom near a dielectric interference. It is the first time, to our knowledge, to discover the significance of photon periodic orbits in the feature of the spontaneous emission spectra of large-aperture VCSELs, as found in the atomic absorption spectra [18]. More importantly, it is worth mentioning that there was no obvious difference in the spectra from sample to sample for devices growth in the same batch.

In conclusion, we have performed very-high-resolution measurement to demonstrate the signature of photon periodic orbits in the spontaneous emission spectra of large-aperture VCSELs. The coupling effects between the optical modes and the spontaneous emission are found to increase with an increase in the injection current. Just below the lasing threshold, we have observed that more than a thousand cavity modes with a narrow linewidth are precisely displayed in the spontaneous emission spectra. The resonant peaks that appeared in the Fourier-transformed spectrum are verified to excellently coincide with the theoretical ones obtained from the 2D square quantum-billiard model. Based on all the agreement, large-aperture VCSELs can be confirmed to function as "photonic billiards," and their spontaneous emission spectra can be employed to analogously investigate the energy spectra of quantum billiards.

This work is supported by the National Science Council of Taiwan (NSCT) (contract NSC-97-2112-M-009-016-MY3).

References

1. C. Gmachl, F. Capasso, E. E. Narimanov, J. U. Nöckel, A. D. Stone, J. Faist, D. L. Sivco, and A. Y. Cho, Science **280**, 1556 (1998).
2. M. Lebental, N. Djellali, C. Arnaud, J. S. Lauret, J. Zyss, R. Dubertrand, C. Schmit, and E. Bogomolny, Phys. Rev. A **76**, 023830 (2007).
3. T. Tanaka, M. Hentschel, T. Fukushima, and T. Harayama, Phys. Rev. Lett. **98**, 033902 (2007).
4. J. Wiersig and M. Hentschel, Phys. Rev. Lett. **100**, 033901 (2008).
5. K. F. Huang, Y. F. Chen, H. C. Lai, and Y. P. Lan, Phys. Rev. Lett. **89**, 224102 (2002).
6. T. Gensty, K. Becker, I. Fischer, W. Elsässer, C. Degen, P. Debernardi, and G. P. Bava, Phys. Rev. Lett. **94**, 233901 (2005).
7. Y. F. Chen, K. F. Huang, and Y. P. Lan, Phys. Rev. E **66**, 066210 (2002).
8. D. Robin, C. Steier, J. Laskar, and L. Nadolski, Phys. Rev. Lett. **85**, 558 (2000).
9. D. M. Wang and J. B. Delos, Phys. Rev. A **63**, 043409 (2001).
10. V. Szebehely, *Theory of Orbits* (Academic, 1967).
11. M. Schulz-Ruhtenberg, I. V. Babushkin, N. A. Loiko, T. Ackemann, and K. F. Huang, Appl. Phys. B **81**, 945 (2005).
12. E. M. Purcell, Phys. Rev. **69**, 37 (1946).
13. D. Wintgen, Phys. Rev. Lett. **58**, 1589 (1987).
14. M. Schulz-Ruhtenberg, I. V. Babushkin, N. A. Loiko, K. F. Huang, and T. Ackemann, Phys. Rev. A **81**, 023819 (2010).
15. I. V. Zozoulenko, A. S. Sachrajda, P. Zawadzki, K. F. Berggren, Y. Feng, and Z. Wasilewski, Semicond. Sci. Technol. **13**, A7 (1998).
16. K. F. Berggren, K. N. Pichugin, A. F. Sadreev, and A. Starikov, JETP Lett. **70**, 403 (1999).
17. M. L. Du, F. H. Wang, Y. P. Jin, Y. S. Zhou, X. H. Wang, and B. Y. Gu, Phys. Rev. A **71**, 065401 (2005).
18. M. L. Du and J. B. Delos, Phys. Rev. Lett. **58**, 1731 (1987).

Comparative study between conventional and diffusion-bonded Nd-doped vanadate crystals in the passively mode-locked operation

Y. J. Huang, Y. P. Huang, H. C. Liang, K. W. Su, Y. F. Chen*, and K. F. Huang

Department of Electrophysics, National Chiao Tung University, Hsinchu, Taiwan
**yfchen@cc.nctu.edu.tw*

Abstract: We design a reliable linear three-element cavity to make a comparative study between the conventional and diffusion-bonded Nd:$GdVO_4$ crystals in the passively mode-locked operation. Experimental investigations reveal that the mode-locked pulse width obtained with the diffusion-bonded crystal is considerably broader than that obtained with the conventional crystal, even though the diffusion-bonded crystal can significantly reduce the thermal effects. The pulse broadening is experimentally verified to come from the length of the undoped part that brings in a reduction of the spatial-hole-burning (SHB) effect.

OCIS codes: (140.3480) Lasers, diode-pumped; (140.3530) Lasers, neodymium; (140.4050) Mode-locked lasers; (140.6810) Thermal effects.

References and links

1. U. Keller, D. A. B. Miller, G. D. Boyd, T. H. Chiu, J. F. Ferguson, and M. T. Asom, "Solid-state low-loss intracavity saturable absorber for Nd:YLF lasers: an antiresonant semiconductor Fabry-Perot saturable absorber," Opt. Lett. **17**(7), 505–507 (1992).
2. U. Keller, K. J. Weingarten, F. X. Kärtner, D. Kopf, B. Braun, I. D. Jung, R. Fluck, C. Hönninger, N. Matuschek, and J. Aus Der Au, "Semiconductor saturable absorber mirrors (SESAM's) for femtosecond to nanosecond pulse generation in solid-state lasers," IEEE J. Sel. Top. Quantum Electron. **2**(3), 435–453 (1996).
3. U. Keller, "Recent developments in compact ultrafast lasers," Nature **424**(6950), 831–838 (2003).
4. G. J. Spühler, R. Paschotta, U. Keller, M. Moser, M. J. P. Dymott, D. Kopf, J. Meyer, K. J. Weingarten, J. D. Kmetec, J. Alexander, and G. Truong, "Diode-pumped passively mode-locked Nd:YAG laser with 10-W average power in a diffraction-limited beam," Opt. Lett. **24**(8), 528–530 (1999).
5. Y. F. Chen, S. W. Tsai, Y. P. Lan, S. C. Wang, and K. F. Huang, "Diode-end-pumped passively mode-locked high-power Nd:YVO_4 laser with a relaxed saturable Bragg reflector," Opt. Lett. **26**(4), 199–201 (2001).
6. L. McDonagh, R. Wallenstein, and A. Nebel, "111 W, 110 MHz repetition-rate, passively mode-locked TEM_{00}Nd:YVO_4 master oscillator power amplifier pumped at 888 nm," Opt. Lett. **32**(10), 1259–1261 (2007).
7. R. Paschotta, J. Aus der Au, G. J. Spühler, F. Morier-Genoud, R. Hövel, M. Moser, S. Erhard, M. Karszewski, A. Giesen, and U. Keller, "Diode-pumped passively mode-locked lasers with high average power," Appl. Phys. B **70**, S25–S31 (2000).
8. F. Hanson, "Improved laser performance at 946 and 473 nm from a composite Nd:$Y_3Al_5O_{12}$ rod," Appl. Phys. Lett. **66**(26), 3549–3551 (1995).
9. M. Tsunekane, N. Taguchi, T. Kasamatsu, and H. Inaba, "Analytical and experimental studies on the characteristics of composite solid-state laser rods in diode-end-pumped geometry," IEEE J. Sel. Top. Quantum Electron. **3**(1), 9–18 (1997).
10. Z. Zhuo, T. Li, X. Li, and H. Yang, "Investigation of Nd:YVO_4/YVO_4 composite crystal and its laser performance pumped by a fiber coupled diode laser," Opt. Commun. **274**(1), 176–181 (2007).
11. Y. T. Chang, Y. P. Huang, K. W. Su, and Y. F. Chen, "Comparison of thermal lensing effects between single-end and double-end diffusion-bonded Nd:YVO_4 crystals for $^4F_{3/2}\rightarrow{}^4I_{11/2}$ and $^4F_{3/2}\rightarrow{}^4I1_{3/2}$ transitions," Opt. Express **16**(25), 21155–21160 (2008).
12. T. Li, Z. Zhuo, S. Zhao, and Y. G. Wang, "Diode-pumped passively mode-locked YVO_4/Nd:YVO_4 composite crystal laser with LT-$In_{0.25}Ga_{0.75}As$ saturable absorber," Laser Phys. Lett. **5**(5), 350–352 (2008).
13. Z. Zhuo, T. Li, and Y. G. Wang, "Passively mode-locked YVO_4/Nd:YVO_4 composite crystal laser with a semiconductor saturable absorber as a high reflector," Laser Phys. Lett. **5**(6), 421–424 (2008).
14. B. E. Bouma, and J. G. Fujimoto, "Compact Kerr-lens mode-locked resonators," Opt. Lett. **21**(2), 134–136 (1996).
15. B. E. Bouma, M. Ramaswamy-Paye, and J. G. Fujimoto, "Compact resonator designs for mode-locked solid-state lasers," Appl. Phys. B **65**(2), 213–220 (1997).

#125744 - $15.00 USD Received 22 Mar 2010; revised 19 Apr 2010; accepted 20 Apr 2010; published 21 Apr 2010

16. B. Y. Zhang, G. Li, M. Chen, Z. G. Zhang, and Y. G. Wang, "Passive mode locking of a diode-end-pumped Nd:$GdVO_4$ laser with a semiconductor saturable absorber mirror," Opt. Lett. **28**(19), 1829–1831 (2003).
17. J. Kong, D. Y. Tang, S. P. Ng, B. Zhao, L. J. Qin, and X. L. Meng, "Diode-pumped passively mode-locked Nd:$GdVO_4$ laser with a GaAs saturable absorber mirror," Appl. Phys. B **79**(2), 203–206 (2004).
18. S. J. Zhang, E. Wu, H. F. Pan, and H. P. Zeng, "Passive mode locking in a diode-pumped Nd:$GdVO_4$ laser with a semiconductor saturable absorber mirror," IEEE J. Quantum Electron. **40**(5), 505–508 (2004).
19. G. J. Spühler, S. Reffert, M. Haiml, M. Moser, and U. Keller, "Output-coupling semiconductor saturable absorber mirror," Appl. Phys. Lett. **78**(18), 2733–2735 (2001).
20. Y. X. Fan, J. L. He, Y. G. Wang, S. Liu, H. T. Wang, and X. Y. Ma, "2-ps passively mode-locked Nd:YVO_4 laser using an output-coupling-type semiconductor saturable absorber mirror," Appl. Phys. Lett. **86**(10), 101103 (2005).
21. C. J. Flood, D. R. Walker, and H. M. van Driel, "Effect of spatial hole burning in a mode-locked diode end-pumped Nd:YAG laser," Opt. Lett. **20**(1), 58–60 (1995).
22. B. Braun, K. J. Weingarten, F. X. Kärtner, and U. Keller, "Continuous-wave mode-locked solid-state lasers with enhanced spatial hole burning," Appl. Phys. B **61**(5), 429–437 (1995).

1. Introduction

Diode-end-pumped passively mode-locked all-solid-state lasers with semiconductor saturable absorber mirrors (SESAMs) [1,2] have been extensively studied due to their short pulse duration, compactness, low insertion loss, flexibility, inexpensive, reliable operation, and wide bandgap ranging from visible to infrared etc. High-power mode-locked lasers are desirable because they are useful for numerous applications such as laser-video display, medicine, material processing, nonlinear wavelength conversion and so on [3]. Although several high-power passively mode-locked lasers have been proposed [4–6], thermal effects of the gain media are still the main challenge [7].

The composite crystal, which is fabricated by the diffusion bonding of a doped crystal to an undoped crystal as a heat sink for the pump surface, has been confirmed to be a superior method in reducing the thermal effects [8–11]. Recently, passively mode-locked composite crystal lasers have been reported with average output power greater than 10 W, indicating that the composite crystals are suitable for accomplishing high-power mode-locked laser [12,13]. Nevertheless, so far there is no systematic comparison between the conventional and composite crystals in the passively mode-locked performance.

In this work, we develop a linear three-element resonator to make a comparative study between the conventional crystal (Nd:$GdVO_4$) and the composite crystal ($GdVO_4$/Nd:$GdVO_4$) in the passively mode-locked performance. Compared to the conventional Nd:$GdVO_4$ crystal, the maximum output power with the diffusion-bonded Nd:$GdVO_4$ crystal can be enhanced by nearly 30% thanks to the reduction of thermal effects. However, the mode-locked pulse widths obtained with the diffusion-bonded crystal are found to be considerably broader than that obtained with the convenient crystal. We experimentally confirm that the undoped part of the diffusion-bonded crystal introduce a reduction of the spatial-hole-burning (SHB) effect to lead to the pulse broadening. Our experimental results reveal that the length of the undoped part needs to be taken into account in optimizing the pulse width of the mode-locked laser.

2. Cavity design and analysis

First of all we design a reliable cavity to evaluate the mode-locked laser performance between the conventional crystal and the composite crystal. In the past years, the three-element resonator, consisting of a flat rear mirror, a convex lens and a flat output coupler, has been identified to be an effective method for realizing the Kerr-lens mode-locked laser [14,15]. The linear three-element resonator is beneficial for easy assembly, mode-matching design, and insensitivity to misalignment. Moreover, the linear three-element resonator is also practically useful for the evaluation of thermal effects in the laser crystal. Therefore, here we employ the linear three-element resonator to design a passively mode-locked laser with SESAM as a saturable absorber for studying the performance between the conventional crystal and the composite crystal.

The configurations for a three-element cavity with and without the thermal-lensing effect are shown in Fig. 1(a) and 1(b), where L_1 is the distance between the front mirror and the convex lens, L_2 is the distance between the convex lens and the output coupler, and f is the

#125744 - $15.00 USD Received 22 Mar 2010; revised 19 Apr 2010; accepted 20 Apr 2010; published 21 Apr 2010

focal length of the convex lens. The laser crystal and the SESAM device are designed to be as close as to the front mirror and the output coupler, respectively. With a pump spot radius of 100 μm, the mode size at the front mirror ω_1 is aimed at 160 μm to lead to a good mode-size matching. On the other hand, the mode size at the output coupler ω_2 is aimed to be 50 μm to achieve a high-quality mode-locked operation. Consequently, the required mode-size ratio ω_1/ω_2 is approximately 3.2. The focal length of the convex lens is chosen to be f = 125 mm. The key issue for the cavity design is to determin the values of L_1 and L_2.

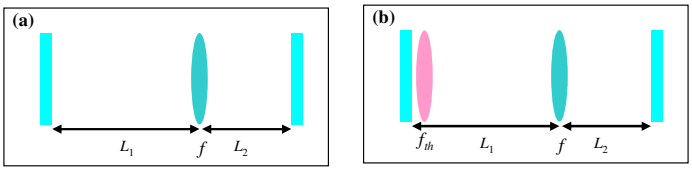

Fig. 1. The configurations for a three-element cavity (a) with and (b) without the thermal-lensing effect.

Using the ABCD-matrix method, the stable condition for a three-element cavity without the thermal-lensing effect is given by $0 \le (1-L_1/f)(1-L_2/f) \le 1$. For the purpose of presentation, we define the factor $\eta = 1/(1+\omega_1/\omega_2)$ and calculate η with f = 125 mm as a function of L_1 and L_2. In Fig. 2, a rainbow color bar is used to present the different value of the calculated η, whereas the unstable zone is displayed with a black color. The stable region can be clearly seen to be enclosed by three curves: $(1-L_1/f)(1-L_2/f)=1$, $L_1 = f$, and $L_2 = f$. For the required ratio of ω_1/ω_2 = 3.2, the corresponding η value is 0.238 that is characterized by a light pink in the color bar. With the representation of Fig. 2, the appropriate values of L_1 and L_2 can be found to approximately 500 mm and 166 mm, respectively, as the location of point P indicated in Fig. 2.

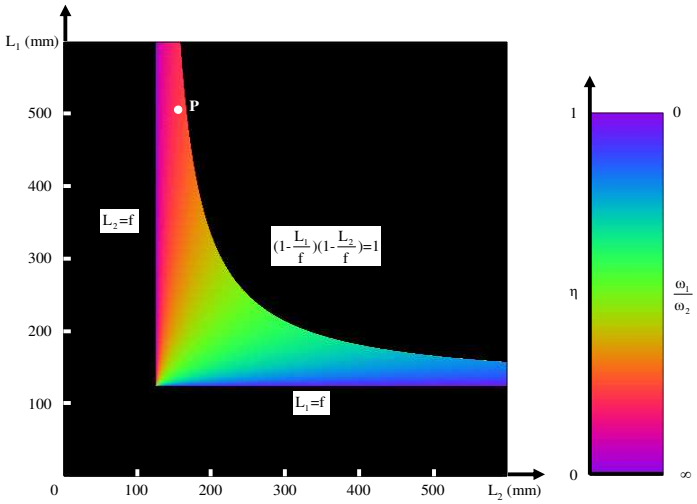

Fig. 2. Calculated results for the factor η as a function of L_1 and L_2 with f = 125 mm; the black color denotes the unstable zone.

Taking the thermal-lensing effect into account, we find that the effective focal power of the thermal lens in the laser crystal needs to be smaller than $2(L_1 - f)^{-1}$ to maintain the cavity stable. With $L_1 = 500$ mm and $f = 125$ mm, we can find that the critical focal length of the thermal lens is approximately 188 mm. The focal length of the thermal lens can be expressed as $f_{th} = C\omega_p^2 / P_{in}$ [11], where ω_p is the pump radius on the gain medium, P_{in} is the incident

#125744 - $15.00 USD Received 22 Mar 2010; revised 19 Apr 2010; accepted 20 Apr 2010; published 21 Apr 2010

pump power, and C is a proportional constant. As a result, we can calculate the critical pump power $P_{critical}$ beyond which the thermal-lensing effect will cause the cavity to be unstable. It is clear that the smaller thermal-lensing effect the laser crystal brings in, the higher critical pump power can be reached.

3. Experimental setup

The experimental setup is schematically shown in Fig. 3. The laser cavity contains a gain medium, a convex lens, and an output-coupling semiconductor saturable absorber mirror (SESAMOC). The gain medium is a Nd:$GdVO_4$ crystal that owns high absorption coefficient for diode pumping, large stimulated emission cross section, and high thermal conductivity along the <110> direction [16–18]. We prepared two types of gain media for the purpose of our experimental study. The one was a conventional 0.5 at.% Nd:$GdVO_4$ crystal with dimensions of 3 × 3 × 8 mm^3, the other one was a 3 × 3 × 10 mm^3 composite $GdVO_4$/Nd:$GdVO_4$ crystal with a 2-mm-long undoped $GdVO_4$ crystal diffusion bonded to a 0.5 at.% Nd:$GdVO_4$ crystal. The pump facets of two type of laser crystals were coated at 808 nm for high transmission as well as at 1064 nm for high reflection (HR) as rear mirrors, and the other sides of each were anti-reflection (AR) coated at 1064 nm and wedged 0.5° to suppress the Fabry-Perot etalon effect. The laser crystals were wrapped with indium foil and mounted in a copper holder with water-cooled at 20 °C. The pump source was a 10-W 808-nm fiber-coupled laser diode with a core radius of 100 μm and a numerical aperture of 0.16. The pump beam was re-imaged into the laser crystal with a lens set that has a focal length of 25 mm with a magnification of unity and a coupling efficiency of 85%. The convex lens with focal length of 125 mm was anti-reflective at 1064 nm on both sides.

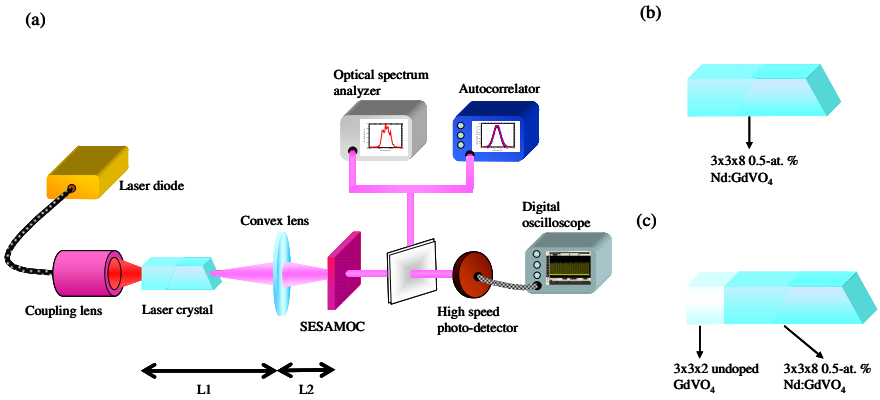

Fig. 3. (a) Schematic of a linear three-element diode-end-pumped passively mode-locked laser; (b) conventional Nd:$GdVO_4$ crystal; (c) composite $GdVO_4$/Nd:$GdVO_4$ crystal.

For passively mode-locked operation at 1064 nm, we fabricated a SESAM structure that was monolithically grown on an undoped GaAs substrate by metalorganic chemical vapor deposition (MOCVD). The present SESAM device was designed to simultaneously serve as an saturable absorber and an output coupler (SESAMOC) [19,20]. The saturable absorber was composed of two 8-nm $In_{0.34}Ga_{0.66}As$ quantum wells (QWs) with a modulation depth of 1.5% and a saturable fluence of 80 μJ/cm^2. The Bragg mirror structure comprised 10 AlAs/GaAs quarter-wavelength layers, designed for a reflectivity of 96.3% at 1064 nm. The back side of the 350-μm GaAs substrate was coated for anti-reflection at 1064 nm. The SESAMOC was surfaced mounted in a copper without any active cooling. As designed in Sec. 2, L_1 and L_2 were set at 500 mm and 166 mm, respectively, to implement the mode-locked operation. The total cavity length was then 666 mm, corresponding to repetition rates of 225 MHz. The mode radii on the laser crystal and the SESAMOC were approximately 160 μm and 50 μm, respectively. The cw mode-locked pulses were detected by a high-speed InGaAs photodetector (Electro-optics Technology Inc. ET-3500 with rise time 35 ps), whose output

#125744 - $15.00 USD Received 22 Mar 2010; revised 19 Apr 2010; accepted 20 Apr 2010; published 21 Apr 2010

signal was connected to a digital oscilloscope (Agilent, DSO 80000) with 12 GHz electrical bandwidth and the sampling rates of 25 ps. The spectral information of the laser was monitored by a Fourier optical spectrum analyzer (Advantest, Q8347) that is constructed with a Michelson interferometer with resolution of 0.003 nm.

4. Results and discussion

The dependence of average output power on the incident pump power is shown in Fig. 4(a). The slope efficiencies obtained with the conventional and composite gain media were found to be almost the same, approximately 35%. The threshold pump powers for the cw mode-locked operation were also very comparable for two types of gain media, approximately to be 1.7 W. When the pump power exceeded 1.7 W, the stable mode-locked pulses could be continuously generated, as shown in Fig. 4 (b). The thermal lensing effect leads to a critical pump power that restricts the maximum TEM_{00} output power in the cw mode-locked operation. When the pump power exceeded the critical pump power, the pulse train was found to be unstable, as revealed in Fig. 4(c). The critical pump powers were approximately 5.4 W and 7.8 W for the cavities with the conventional and composite gain media, respectively, as shown in Fig. 4(a). Limited by the thermal lensing effect, the maximum output powers were 1.75 W and 2.30 W for the cavities with the conventional and composite gain media, respectively. In short, the maximum output power with the diffusion-bonded crystal can be enhanced by nearly 30% thanks to the reduction of thermal effects.

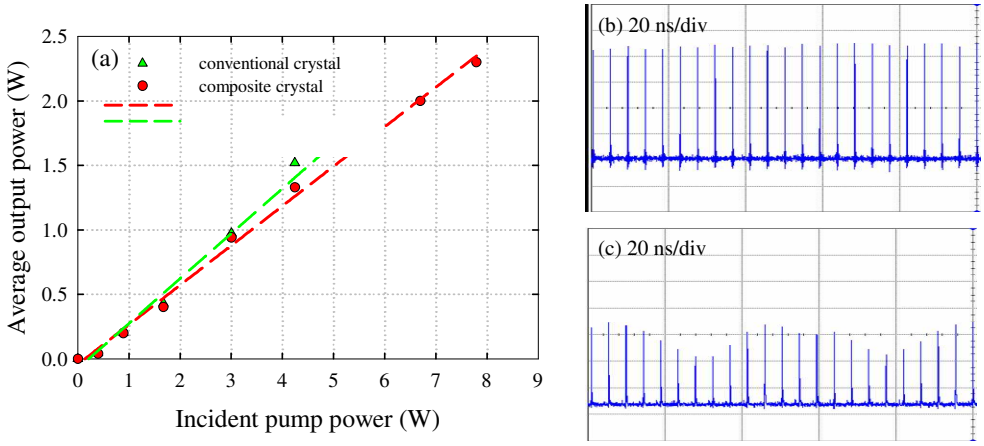

Fig. 4. (a) Average output power at 1064 nm versus incident pump power in cw mode-locked operations. And pulse trains on two circumstances with time span of 200 ns: (b) Stable cw mode-locked pulse train; (c) Modulation mode-locked pulse train with 24-MHz fluctuation.

With the help of the commercial autocorrelator (APE pulse check, Angewandte physik & Elektronik GmbH), we measured the full width at half maximum (FWHM) of the autocorrelation trace of the mode-locked pulse. Assuming the $sech^2$-shaped temporal profile, the pulse widths were found to be 8.0 ps and 24 ps for the cavities with the conventional and composite gain media, respectively, as shown in Fig. 5(a) and 5(b). We also measured the optical spectra for the mode-locked laser outputs. The FWHM of the optical spectra was found to be 0.17 nm and 0.07 nm for the cavities with the conventional and composite gain media, respectively, as shown in Fig. 6(a) and Fig. 6(b). It can be seen that the pulse broadening is consistent with the narrowing of the optical spectrum for the cavity with a composite crystal. Therefore, it is worthwhile to explore the origin of spectral narrowing in the cavity with a composite gain medium. In the following, we will verify that the undoped part of the diffusion-bonded crystal introduce a reduction of the SHB effect to lead to the spectral narrowing.

#125744 - $15.00 USD Received 22 Mar 2010; revised 19 Apr 2010; accepted 20 Apr 2010; published 21 Apr 2010

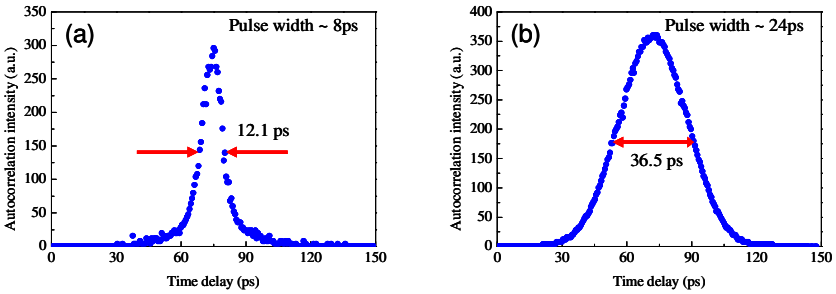

Fig. 5. Autocorrelation traces of the output pulses from (a) cw mode-locked Nd:$GdVO_4$ laser and (b) cw mode-locked $GdVO_4$/Nd:$GdVO_4$ laser;

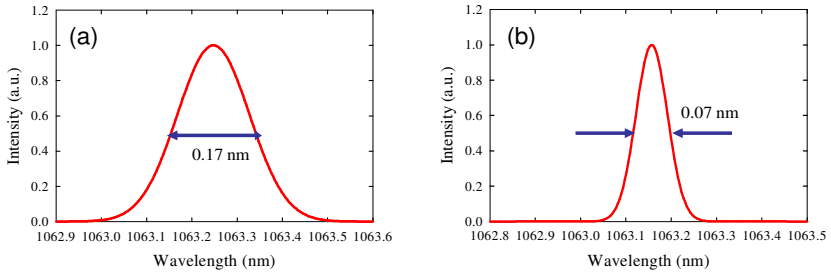

Fig. 6. Optical spectrum for (a) cw mode-locked Nd:$GdVO_4$ laser and (b) cw mode-locked $GdVO_4$/Nd:$GdVO_4$ laser.

The influence of the SHB effect on the performance of mode-locked solid-state lasers was previously studied for the cases of gain-at-the-end (GE), gain-in-the-middle (GM) as well as the intermediate transition between GE and GM [21,22]. It was found that thanks to the enhancement of the SHB effect, the pulse width in a GE mode-locked laser could be shorter than that in a GM mode-locked laser under the same cavity configuration. To investigate the SHB effect in the present three-element cavity, we replaced the HR-AR coated gain medium with a AR-AR coated Nd:$GdVO_4$ crystal and a flat front mirror. We then used a linear micro-stage to tailor the degree of the SHB effect by varying the separation d between the gain medium and the front mirror. With increasing the separation d from d = 0.2 mm to d = 10 mm, we found that the mode-locked pulse increased smoothly from 15.8 ps to 36.6 ps and the optical spectral FWHM changed from 0.085 nm to 0.048 nm, as shown in Fig. 7. In short, the pulse width strongly depends on the separation between the gain medium and the front mirror. The effective optical length of the undoped part in the diffusion-bonded crystal was approximately 4.5 mm. Referring to the results in Fig. 7, such a separation could cause the lasing spectral width to be significantly narrowed; consequently, the pulse width would be nearly doubled. This result is consistent with the experimental observation in the mode-locked laser with a composite crystal as a gain medium. Therefore, it is practically important in optimizing the mode-locked pulse width to consider the influence of the undoped length of the composite crystal.

#125744 - $15.00 USD Received 22 Mar 2010; revised 19 Apr 2010; accepted 20 Apr 2010; published 21 Apr 2010

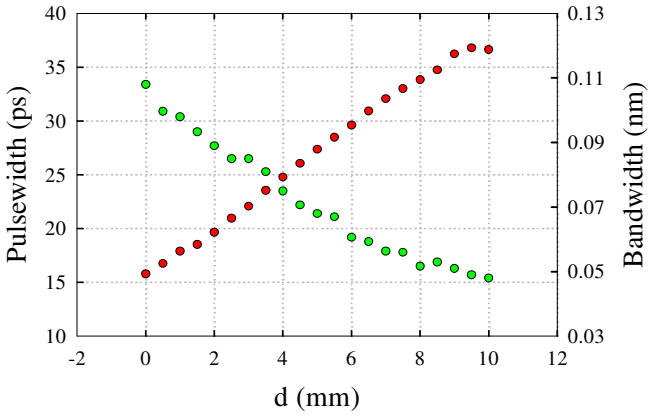

Fig. 7. Pulse width (red) and spectral FWHM (green) as a function of the Nd-doped gain medium/front mirror separation *d*.

5. Conclusion

In conclusion, a comparative study between the conventional and diffusion-bonded Nd:$GdVO_4$ crystals in the passively mode-locked operation has been performed by designing a reliable linear three-element cavity. We have found that although the diffusion-bonded crystal can usefully reduce the thermal effects, the mode-locked pulse width is usually broader than that obtained with the conventional crystal. To explain the experimental results, we have experimentally built the relationship between the degree of the SHB effect and the separation between the gain medium and the front mirror. With the developed relationship, we confirm the origin of the pulse broadening in the mode-locked laser with a composite crystal. Our investigations also indicate that the specification of the undoped length in the composite crystal needs to take into account for optimizing the mode-locked pulse width.

Acknowledgments

The authors thank the National Science Council for their financial support of this research under Contract No. NSC-97-2112-M-009-016-MY3.

#125744 - $15.00 USD Received 22 Mar 2010; revised 19 Apr 2010; accepted 20 Apr 2010; published 21 Apr 2010

Observation of lasing modes with exotic localized wave patterns from astigmatic large-Fresnel-number cavities

T. H. Lu,[2] Y. C. Lin,[1] H. C. Liang,[1] Y. J. Huang,[1] Y. F. Chen,[1,*] and K. F. Huang[1]

[1]*Department of Electrophysics, National Chiao Tung University, Hsinchu, Taiwan*
[2]*Department of Physics, National Taiwan Normal University, Taipei, Taiwan*
[*]*Corresponding author: yfchen@cc.nctu.edu.tw*

Received October 23, 2009; revised December 23, 2009; accepted December 28, 2009; posted January 7, 2010 (Doc. ID 118996); published January 26, 2010

We investigate the lasing modes in large-Fresnel-number laser systems with astigmatism effects. Experimental results reveal that numerous lasing modes are concentrated on exotic patterns corresponding to intriguing geometries. We theoretically use the quantum operator algebra to construct the wave representation for manifesting the origin of the localized wave patterns. © 2010 Optical Society of America

OCIS codes: 070.1675, 070.2580.

Laser resonators have been employed as analogous systems for generating high-order lasing modes to manifest the wave patterns of quantum coherent states, especially for mesoscopic and macroscopic regions [1–4]. Various laser systems are widely used to study optical pattern formation including, the Laguerre–Gaussian (LG) modes, Hermite–Gaussian (HG) modes, and the generalized coherent states that form a general family to comprise the HG and LG mode families as special cases [5,6]. Recently, we have employed a large-Fresnel-number laser system with an off-axis pumping scheme to visualize the coherent optical waves with localization related to the Lissajous and trochoidal curves [7,8]. This result signifies that exploring the transformation geometry of quantum coherent states plays a significant role in understanding the quantum-classical connection. More importantly, the investigation of high-order laser modes is useful for developing the idea for generating the coherent structured light that can carry orbital angular momentum or contain optical vortices for many applications [9,10].

In this Letter we experimentally performed a very large off-axis pumping for studying the lasing modes under the influence of considerable astigmatism. We observed that numerous lasing modes with exotic localized wave patterns correspond to the topological transformations. We used the quantum operator algebra to derive the generalized unitary operator for generating the eigenmodes for the spherical cavity subject to the astigmatism effects. With the generalized unitary operator and the quantum-classical connection, the geometries corresponding to the localized lasing patterns can be perfectly manifested.

The present laser cavity was composed of a spherical mirror and a large-aperture gain medium, as shown in Fig. 1. The gain medium was an a-cut 2.0 at. % $Nd:YVO_4$ crystal with a length of 2 mm and a cross section of 8×8 mm^2 to comply with the requirement of the extremely high transverse orders. The pump source was a 2 W, 809 nm fiber-coupled laser diode with a core diameter of 100 μm. A coupling lens was used to focus the pump beam to be approximately 25 μm in the laser crystal. The spherical mirror was a 10 mm radius-of-curvature concave mirror with antireflection coating at the pumping wavelength on the entrance face ($R<0.2\%$), high-reflection coating at lasing wavelength ($R>99.8\%$), and high-transmission coating at the pumping wavelength on the other surface ($T<95\%$). One planar surface of the laser crystal was coated for antireflection at the pumping and lasing wavelengths; the other surface was coated to be an output coupler with a reflectivity of 99%. To generate the high-order modes subject to considerable astigmatism, the pumping beam was focused into the crystal in the region with a large off-axis displacement along the c axis and a rather small displacement along the b axis. We experimentally find that more than 100 different laser modes related to distinct localized wave patterns can be generated at different degenerate cavities. In addition to Lissajous and trochoidal patterns [7,8] shown in Figs. 2(a) and 2(b), new findings of numerous lasing patterns corresponding to the topological transformations can be observed, as shown in Figs. 2(c)–2(e). These patterns propagate in the cavity with localization on 3D parametric surfaces, which is distinct from M mode and spiral beams. Since the laser cavity is an excellent analog system for studying the coherent waves, the understanding of these wave patterns should provide some useful insights into the fundamental behavior of wave functions at the border of the classical and quantum regimes.

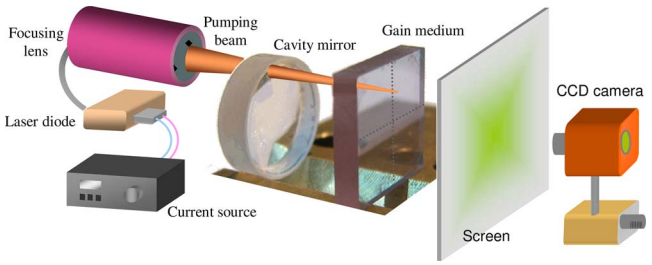

Fig. 1. (Color online) Experimental setup for the generation of high-order lasing modes in astigmatic cavities with an off-axis pumping scheme.

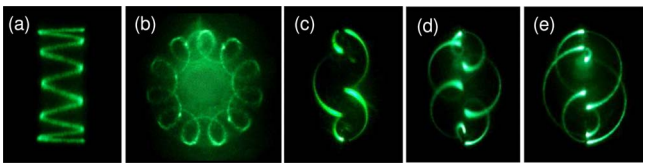

Fig. 2. (Color online) Experimental far-field patterns: (a) Lissajous pattern; (b) trochoidal pattern; (c), (d) other typical lasing patterns.

The paraxial eigenmodes of stable spherical cavities can be expressed as the normalized HG modes [11] $\Phi^{(\mathrm{HG})}_{m,n,l}(x,y,z)=\Phi^{(\mathrm{HG})}_{m,n}(x,y,z)e^{i(m+n+1)\theta_G(z)}e^{-i\zeta_{m,n,l}(x,y,z)}$, where

$$\Phi^{(\mathrm{HG})}_{m,n}(x,y,z)=\frac{1}{\sqrt{2^{m+n-1}\pi m!n!}}\frac{1}{w(z)}e^{-(x^2+y^2/w(z)^2)}\times H_m\left(\frac{\sqrt{2}}{w(z)}x\right)H_n\left(\frac{\sqrt{2}}{w(z)}y\right), \quad (1)$$

$w(z)=w_o\sqrt{1+(z/z_R)^2}$, $\zeta_{m,n,l}(x,y,z)=(\omega_{m,n,l}z/c)[1+(x^2+y^2)/2(z^2+z_R^2)]$, w_o is the beam waist, z_R is the Rayleigh range, $\omega_{m,n,l}$ is the resonance frequency, m and n are the transverse mode indices, l is the longitudinal mode index, and $\theta_G(z)=\tan^{-1}(z/z_R)$ is the Gouy phase. In the spherical cavity, $\omega_{m,n,l}$ is given by $\omega_{m,n,l}=[l\omega_L+(m+n+1)\omega_T)]$, where ω_L is the longitudinal mode spacing and ω_T is the transverse mode spacing. Since the paraxial wave equation can be exactly mapped on the time-dependent 2D quantum harmonic oscillator, the quantum operator algebra can be employed to explore the eigenmodes for the spherical cavity with the astigmatism effects [12,13]. The equivalent Hamiltonian for the HG modes can be expressed as $\hat{H}_o=\omega_T/2(\partial^2/\partial\tilde{x}^2+\partial^2/\partial\tilde{y}^2+\tilde{x}^2+\tilde{y}^2)$ with $\hat{H}_o|\Phi^{(\mathrm{HG})}_{m,n}\rangle=(m+n+1)\omega_T|\Phi^{(\mathrm{HG})}_{m,n}\rangle$, where $\tilde{x}=\sqrt{2}x/w$ and $\tilde{y}=\sqrt{2}y/w$ are dimensionless spatial variables. The operators for astigmatism and anisotropic effects can be expressed as $\hat{L}_1=\frac{1}{2}(\tilde{x}\tilde{y}+\partial/\partial\tilde{x}\partial/\partial\tilde{y})$, $\hat{L}_2=1/2i(\tilde{x}\partial/\partial\tilde{y}-\tilde{y}\partial/\partial\tilde{x})$, $\hat{L}_3=\frac{1}{4}(\tilde{x}^2+\partial^2/\partial\tilde{x}^2-\tilde{y}^2-\partial^2/\partial\tilde{y}^2)$ [12]. Without loss of generality, we model the 2D deformed harmonic oscillator as $\hat{H}_p=\hat{H}_0+A\cdot\hat{L}_1+B\cdot\hat{L}_2+C\cdot\hat{L}_3$ to consider the astigmatism and anisotropic effects, where A, B, and C are constants and usually significantly smaller than ω_T. The operators $\hat{L}_1$, $\hat{L}_2$ and $\hat{L}_3$ have been verified to satisfy the Lie commutator algebra $[\hat{L}_i,\hat{L}_j]=i\varepsilon_{i,j,k}\hat{L}_k$, where the Levi–Civita tensor $\varepsilon_{i,j,k}$ is equal to +1 and −1 for even and odd permutations of its indices, respectively, and zero otherwise [14]. With the SU(2) algebra, the eigenstates of $\hat{H}_p$ can be derived to be $|\Phi^{\alpha,\beta}_{m,n}\rangle=\hat{U}|\Phi^{(\mathrm{HG})}_{m,n}\rangle$ where $\hat{U}=e^{-i\alpha\hat{L}_3}e^{-i\beta\hat{L}_2}$, $\alpha=\tan^{-1}(B/A)$, and $\beta=\tan^{-1}(\sqrt{A^2+B^2}/C)$. This continuous transition between HG and LG modes is analogous to the transition between linear and circular polarization on the Poincaré sphere [15]. In terms of the Wigner d-matrix elements, the eigenstates $|\Phi^{\alpha,\beta}_{m,n}\rangle$ can be explicitly expressed as a linear combination of the states $|\Phi^{(\mathrm{HG})}_{m,n}\rangle$: $|\Phi^{\alpha,\beta}_{m,n}\rangle=\sum_{s=0}^{m+n}e^{-is\alpha}d^{m+n/2}_{s-m+n/2,m-n/2}(\beta)|\Phi^{(\mathrm{HG})}_{s,m+n-s}\rangle$, where

$$d^{m+n/2}_{s-(m+n)/2,m-n/2}(\beta)=\sqrt{s!(m+n-s)!m!n!}\sum_{\nu=\max[0,s-m]}^{\min[n,s]}\times\frac{(-1)^\nu(\cos(\beta/2))^{n+s-2\nu}(\sin(\beta/2))^{m-s+2\nu}}{\nu!(n-\nu)!(s-\nu)!(m-s+\nu)!}. \quad (2)$$

The state $|\Phi^{\alpha,\beta}_{m,n}\rangle$ for $\alpha=0$ can be viewed as a rotation of the HG mode $|\Phi^{(\mathrm{HG})}_{m,n}\rangle$ with an angle $\beta/2$ in the (x,y) plane [5]. Figures 3(a)–3(e) show the numerical wave patterns for the eigenstates $|\Phi^{\alpha,\beta}_{m,n}\rangle$ with $(m,n)=(18,55)$, $\alpha=\pi/2$ and five different β values. It can be seen that the states $|\Phi^{\alpha,\beta}_{m,n}\rangle$ for $\alpha=\pi/2$ with the parameter β changing from 0 to $\pi/2$ correspond to the astigmatic transformation from the HG mode to the LG mode [5,6].

Experimental results have evidenced that [7,8] that the longitudinal-transverse coupling in the large-Fresnel-number cavity usually forces the ratio ω_T/ω_L to be locked to a rational number P/Q. As a result, the group of the HG modes $\Phi^{(HG)}_{m_o+pk,n_o+qk,l_o+sk}$ with $k=0,1,2,3\cdots$ forms a family of frequency degenerate states, where the integers (p,q,s) obey the equation $s+(p+q)(P/Q)=0$. It has been verified [7] that the three-dimensional (3D) coherent states constructed by the family of $\Phi^{(\mathrm{HG})}_{m_o+pk,n_o+qk,l_o+sk}$ can be expressed as $|\Psi^{p,q,s}_{m_o,n_o,l_o}(\varphi)\rangle=\sum_{k=-M}^{M}C_{M,k}e^{ik\varphi}|\Phi^{(\mathrm{HG})}_{m_o+pk,n_o+qk,l_o+sk}\rangle$, where $C_{M,k}=2^{-M}\binom{2M}{M+k}^{1/2}$ is the weighting coefficient, $\binom{n}{k}=n!/k!(n-k)!$ represents the binomial coefficient, and the parameter φ is the relative phase between various HG modes at $z=0$. With the expression of Eq. (1), we can obtain $|\Psi^{p,q,s}_{m_o,n_o,l_o}(\varphi)\rangle=|\Psi^{p,q}_{m_o,n_o}(\varphi)\rangle e^{i(m_o+n_o+1)\theta_G(z)}e^{-i\zeta_{m_o,n_o,l_o}(x,y,z)}$ with $|\Psi^{p,q}_{m_o,n_o}(\varphi)\rangle=\sum_{k=-M}^{M}C_{M,k}e^{ik\phi(z)}e^{ik\varphi}|\Phi^{(\mathrm{HG})}_{m_o+pk,n_o+qk}\rangle$, where $\phi(z)=(p+q)\theta_G(z)$. Here, m_0 and n_0 indicate the order of the coherent state; M, the number of eigenstates involved in the superposition, is much smaller than m_0 and n_0. As discussed earlier, the astigmatism and anisotropic effects can be considered with the unitary operator $\hat{U}=e^{-i\alpha\hat{L}_3}e^{-i\beta\hat{L}_2}$. Consequently, the 3D coherent states subject to the astigmatism effect can be given by $\hat{U}|\Psi^{p,q,s}_{m_o,n_o,l_o}(\varphi)\rangle$, and their wave patterns are determined by the wave function $\hat{U}|\Psi^{p,q}_{m_o,n_o}(\varphi)\rangle=\sum_{k=-M}^{M}C_{M,k}e^{ik\phi(z)}e^{ik\varphi}|\Phi^{\alpha,\beta}_{m_o+pk,n_o+qk}\rangle$. The state $|\Psi^{p,q}_{n_o,m_o}(\varphi)\rangle$ has been verified to have the intensity lo-

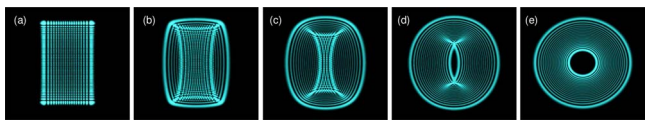

Fig. 3. (Color online) Numerical wave patterns for the intensity of eigenstates $|\Phi^{\alpha,\beta}_{m,n}\rangle$ with $(m,n)=(18,55)$, $\alpha=\pi/2$: (a) $\beta=0$, (b) $\beta=\pi/8$, (c) $\beta=\pi/4$, (d) $\beta=3\pi/8$, (e) $\beta=\pi/2$.

calized on the Lissajous parametric surface: $x=\mathrm{Re}[X(\vartheta,z)]$; $y=\mathrm{Re}[Y(\vartheta,z)]$, where $0\leqslant\vartheta\leqslant 2\pi$, $-\infty\leqslant z\leqslant\infty$, $X(\vartheta,z)=\sqrt{n_o}w(z)e^{i[q\vartheta+(\phi(z)+\varphi/p)]}$, and $Y(\vartheta,z)=\sqrt{m_o}w(z)e^{ip\vartheta}$ [7]. Using the isomorphic relation between SU(2) algebra and SO(3) algebra, the 3D coherent state $\hat{U}|\Psi^{p,q}_{m_o,n_o}(\varphi)\rangle$ can be deduced to be localized on the parametric surface: $x=\mathrm{Re}[\tilde{X}(\vartheta,z)]$; $y=\mathrm{Re}[\tilde{Y}(\vartheta,z)]$, where

$$\begin{bmatrix}\tilde{X}(\vartheta,z)\\ \tilde{Y}(\vartheta,z)\end{bmatrix}=\begin{bmatrix}e^{-i\alpha/2}\cos\left(\frac{\beta}{2}\right) & -e^{-i\alpha/2}\sin\left(\frac{\beta}{2}\right)\\ e^{i\alpha/2}\sin\left(\frac{\beta}{2}\right) & e^{i\alpha/2}\cos\left(\frac{\beta}{2}\right)\end{bmatrix}\times\begin{bmatrix}X(\vartheta,z)\\ Y(\vartheta,z)\end{bmatrix}. \quad (3)$$

Figures 4(a)–4(e) show the classical periodic orbits computed with the parametric curves in Eq. (3) to characterize the lasing patterns shown in Figs. 2(a)–2(e). The parameters are deduced from the best fit to the experimental patterns; where $(p,q)=(-1,10)$, $(m_o,n_o)=(40,200)$, $(\alpha,\beta)=(0,0)$ for Fig. 4(a); $(p,q)=(-1,10)$, $(m_o,n_o)=(50,500)$, $(\alpha,\beta)=(\pi/2,\pi/2)$ for Fig. 4(b); $(p,q)=(1,4)$, $(m_o,n_o)=(80,500)$, $(\alpha,\beta)=(\pi/2,\pi/3)$ for Fig. 4(c); $(p,q)=(1,6)$, $(m_o,n_o)=(80,500)$, $(\alpha,\beta)=(\pi/2,\pi/3)$ for Fig. 4(d); $(p,q)=(2,5)$, $(m_o,n_o)=(100,400)$, $(\alpha,\beta)=(\pi/2,\pi/3)$ for Fig. 4(e). The good agreement validates our quantum operator model and confirms the representation of the 3D coherent states $\hat{U}|\Psi^{p,q}_{m_o,n_o}(\varphi)\rangle$.

Finally, it is worth while mentioning that the transverse patterns of all experimental modes are position dependent during propagation. Figure 5(a) shows the variation of the experimental transverse patterns during propagation for the case corresponding to the far-field pattern in Fig. 2(c). We also use the 3D coherent state $\hat{U}|\Psi^{p,q}_{m_o,n_o}(\varphi)\rangle$ to mimic the experimental wave pattern [Fig. 5(b)] corresponding to Fig. 2(c) and to manifest the phase distribution for a small region, as shown in Fig. 5(c).

In summary, we have experimentally observed numerous lasing modes with exotic localized wave patterns from spherical cavities subject to considerable astigmatism. We have employed the quantum operator algebra to model the wave equation with the astigmatism effects and have derived a generalized unitary operator to obtain the eigenmodes. With the generalized unitary operator and the quantum-classical connection, we have perfectly manifested the geometries corresponding to the localized lasing patterns.

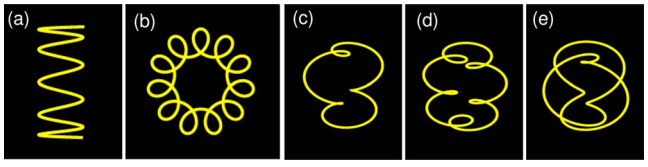

Fig. 4. (Color online) (a)–(e) Geometric curves with Eq. (3) corresponding to the experimental wave patterns shown in Fig. 1. Detailed description for the parameters; see text.

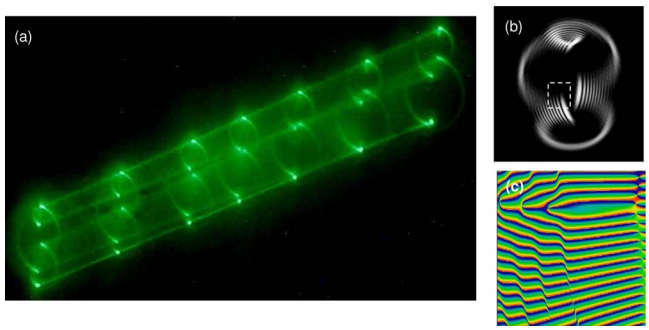

Fig. 5. (Color online) (a) Propagation-dependent experimental patterns of Fig. 2(a) from beam waist to 0.33 z_R; (b) numerical wave patterns corresponding to the experimental wave patterns shown in Fig. 2(c) with $(p,q)=(1,4)$, $(m_0,n_0)=(10,60)$; (c) phase distribution of the boxed region shown in (b).

This work is supported by the National Science Council of Taiwan (NSCT) (contract NSC-94-2112-M-009-034).

References

1. M. Brambilla, F. Battipede, L. A. Lugiato, V. Penna, F. Prati, C. Tamm, and C. O. Weiss, Phys. Rev. A **43**, 5090 (1991).
2. D. Dangoisse, D. Hennequin, C. Lepers, E. Louvergneaux, and P. Glorieux, Phys. Rev. A **46**, 5955 (1992).
3. E. Cabrera, O. G. Calderón, S. Melle, and J. M. Guerra, Phys. Rev. A **73**, 053820 (2006).
4. K. F. Huang, Y. F. Chen, H. C. Lai, and Y. P. Lan, Phys. Rev. Lett. **89**, 224102 (2002).
5. E. G. Abramochkin and V. G. Volostnikov, J. Opt. A **6**, S157 (2004).
6. L. E. Vicent and K. B. Wolf, J. Opt. Soc. Am. A **25**, 1875 (2008).
7. Y. F. Chen, T. H. Lu, K. W. Su, and K. F. Huang, Phys. Rev. Lett. **96**, 213902 (2006).
8. T. H. Lu, Y. C. Lin, Y. F. Chen, and K. F. Huang, Phys. Rev. Lett. **101**, 233901 (2008).
9. M. S. Soskin, V. N. Gorshkov, M. V. Vasnetsov, J. T. Malos, and N. R. Heckenberg, Phys. Rev. A **56**, 4064 (1997).
10. S. J. Van Enk and G. Nienhuis, J. Mod. Opt. **41**, 963 (1994).
11. G. Nienhuis and L. Allen, Phys. Rev. A **48**, 656 (1993).
12. S. J. van Enk and G. Nienhuis, Opt. Commun. **94**, 147 (1992).
13. G. Nienhuis and J. Visser, J. Opt. A **6**, 248 (2004).
14. J. Schwinger, in *Quantum Theory of Angular Momentum*, L. C. Biedenharn and H. van Dam, eds. (Academic, 1965), pp. 229–279.
15. J. Visser and G. Nienhuis, Phys. Rev. A **70**, 013809 (2004).

High-power, diode-end-pumped, multigigahertz self-mode-locked Nd:YVO_4 laser at 1342 nm

H. C. Liang, Y. J. Huang, W. C. Huang, K. W. Su, and Y. F. Chen*

Department of Electrophysics, National Chiao Tung University, 1001 TA Hsueh Rd., Hsinchu, Taiwan 30050
**Corresponding author: yfchen@cc.nctu.edu.tw*

Received August 6, 2009; revised November 13, 2009; accepted November 19, 2009;
posted November 30, 2009 (Doc. ID 115413); published December 17, 2009

We report on a high-power, diode-pumped, self-mode-locked laser at 1342 nm with the Kerr effect arising from large third-order nonlinearity of Nd:YVO_4 crystal. At the pump power of 10.2 W, the average output power of 1.2 W was generated with a repetition rate in the range of 2–6 GHz. The mode-locked pulse width can be smoothly varied from 11.5 to 37 ps by controlling the amount of spatial hole burning. © 2009 Optical Society of America

OCIS codes: 140.4050, 140.3580, 140.3480.

Numerous Nd-doped crystals have been developed for generating 1.3 μm lasers at cw or pulsed operation [1–5], because light sources at 1.3 μm have a wide variety of applications such as telecommunications, fiber sensing, range finding, and data storage. Nd-doped yttrium vanadate (Nd:YVO_4) has been identified as an excellent laser host material for diode-pumped solid-state lasers. Recent studies have further proved that YVO_4 crystals have a large value of third-order susceptibility [6] that has been exploited for efficient stimulated Raman scattering conversion [7–10]. More recently, it has also been demonstrated that the large third-order nonlinearity of Nd:YVO_4 crystals can be used to achieve an efficient self-starting Kerr-lens mode-locking operation at frequencies of several gigahertz [11]. This demonstration offers the promising prospect of developing a compact self-starting mode-locked Nd:YVO_4 laser at 1.34 μm.

In this Letter we report for the first time a compact multigigahertz, self-starting, mode-locked 1.34 μm Nd:YVO_4 laser without the need for any additional components. With an incident pump power of 10.2 W, the miniature linear laser cavity produces average output powers up to 1.2 W with repetition rates in the range of 2.0–6.0 GHz. The mode-locked pulse width can be varied smoothly from 11.5 to 37 ps by controlling the amount of spatial hole burning by moving the gain medium within the cavity [12].

An experimental setup is shown schematically in Fig. 1. The cavity configuration is a simple concave-plano resonator. The gain medium is a-cut 0.25 at. % Nd:YVO_4 crystal with dimensions of 3 mm × 3 mm × 10 mm. Both end surfaces of the Nd:YVO_4 crystal were antireflection coated at 1342 nm and wedged 2° to avoid the Fabry–Perot etalon effect. The laser crystal was wrapped with indium foil and mounted in a water-cooled copper holder. The water temperature was maintained at ≈20 °C to ensure stable laser output. The input mirror was a 50 cm radius-of-curvature concave mirror with antireflection coating at 808 nm on the entrance face and with high-reflectance coating at 1342 nm (>99.8%) and high-transmittance coating at 808 nm on the second surface. A flat wedged output coupler with 7% transmission at 1342 nm was used throughout the experiment. The pump source was a 12 W, 808 nm fiber-coupled laser diode with a core diameter of 200 μm and NA of 0.22. A focusing lens with 5 mm focal length and 85% coupling efficiency was used to reimage the pump beam into the laser crystal. The average pump size was approximately 130 μm. The optical cavity length was varied between 2.5 and 7.5 cm for a corresponding free spectral range of 6 to 2 GHz. The separation between the laser crystal and the input mirror d could be freely adjusted in the range of 1–10 mm. It has been verified that the crystal/mirror separation may be exploited to control the amount of spatial hole burning [12].

The mode-locked pulses were detected by a high-speed InGaAs photodetector (Electro-optics Technology Inc. ET-3500, with rise time of 35 ps) whose output signal was connected to a digital oscilloscope (Agilent, DSO 80000) with 12 GHz electrical bandwidth and sampling interval of 25 ps. The output signal of the photodetector was also analyzed by a radio frequency spectrum analyzer (Advantest, R3265A) with a bandwidth of 8 GHz. The spectral information of the laser was monitored by a Fourier optical spectrum analyzer (Advantest, Q8347) containing a Michelson interferometer with resolution of 0.003 nm.

The laser cavity was first aligned to obtain the maximum average output power. Under this circumstance, the laser output was found to exhibit a spontaneous mode locking with fairly small amplitude

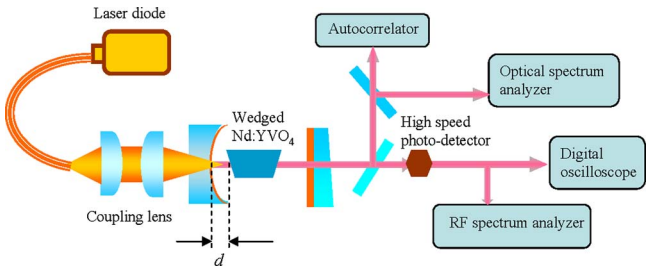

Fig. 1. (Color online) Schematic of a diode-pumped self-mode-locked Nd:YVO_4 laser at 1342 nm.

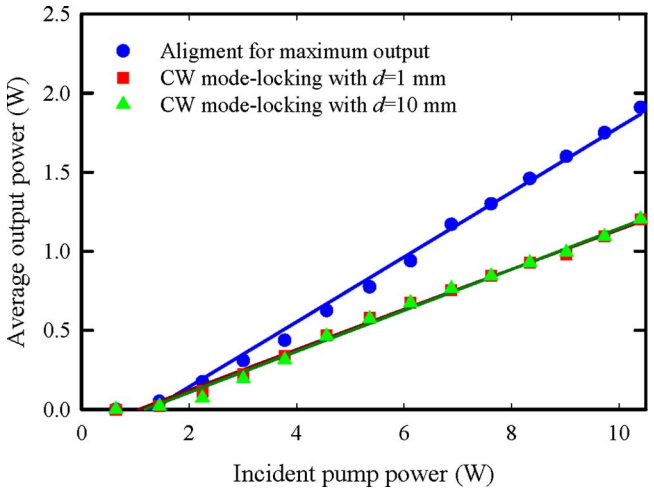

Fig. 2. (Color online) Average output power at 1342 nm versus incident pump power in cw and mode-locked operation.

fluctuations. With fine adjusting of the cavity, the amplitude instability was minimized to obtain a nearly perfect stable mode-locking operation. The average output power of the stable cw mode locking was found to be approximately 65% of the maximum average output power. Figure 2 depicts the average output power at 1342 nm with respect to the incident pump power in the optimum power-output operation and in the mode-locked operation with a frequency of 3.365 GHz. In the optimum power-output regime the laser had a slope efficiency of 20.1%; the output power reached 1.85 W at an incident pump power of 10.2 W. As shown in Fig. 2, the laser had a slope efficiency of 13%; the output power reached 1.2 W at an incident pump power of 10.2 W. It can also be seen that the average output power was nearly independent of the crystal/mirror separation d.

Note that once the pump power reaches the lasing threshold, the laser system instantaneously steps into a stable mode-locked operation, i.e., no threshold for the self-mode-locking. The thermal lens in the gain medium was estimated to be 20–30 cm at a pump power of 10 W. The mode sizes in the gain medium and on the output coupler were calculated to be $\approx$190 μm and 170 μm, respectively. The overall M^2 beam quality factor was found to be better than 1.4. The transverse beam profile did not reveal significant change between the optimum power output and the mode-locking regime. It is worth mentioning that the wedge shape of the output coupler is vital for obtaining a completely stable mode-locked operation. When an output coupler without a wedge is used in the laser cavity, the pulse trains exhibit incomplete mode-locking with cw background to a certain extent.

Figures 3(a) and 3(b) show the pulse trains on two different time scales, one with time span of 5 ns, demonstrating mode-locked pulses, and the other with time span of 5 μs, demonstrating the amplitude stability. It can be seen that the pulse trains display full modulation and complete mode-locking is achieved. The power spectrum reveals that the relative frequency deviation of the power spectra $\Delta\nu/\nu$ is experimentally found to be significantly smaller than 10^{-4} over day-long operation, where ν is the center frequency of the power spectrum and $\Delta\nu$ is the frequency deviation of FWHM. Experimental results reveal that the laser system can be stably operated in a single-pulse mode-locked state as long as the cavity length is shorter than $\approx$7.5 cm (mode-locked repetition rate $>$2 GHz). For cavity length longer than 8.5 cm, a single pulse per round trip was usually observed to split into several pulses. This characteristic is the same as the result in self-mode-locked lasers at 1.06 μm [11].

The pulse width during cw mode-locked operation was measured with an autocorrelator (APE Pulse Check, Angewandte Physik & Elektronik GmbH). For a crystal/mirror separation of $d=1$ mm, the FWHM of the autocorrelation trace was measured to be 17.3 ps, as shown in Fig. 4(a). Assuming a sech^2-shaped temporal profile, the pulse width was thus estimated to be 11.5 ps. Figure 4(b) shows the FWHM width of the optical spectrum to be approximately 0.22 nm at the central wavelength of 1342.1 nm. Consequently, the time–bandwidth product of the mode-locked pulse is 0.43, indicating the pulses to be frequency-chirped. Even though the pulse width is slightly longer than the 7.3 ps obtained in a passively mode-locked laser with semiconductor saturable absorber [13], the average output power of 1.2 W is significantly higher than the result in that case of 40 mW. More important, the self-mode-locked operation can be implemented without the need for any additional components. To confirm the peak power of the pulses, an experiment of the extra-cavity second-harmonic generation (SHG) was performed. The conversion efficiency for the average power was found to be enhanced by approximately 10 times, quite consistent with the theoretical simulation. The ratio of the peak to background for the SHG power was found to be increased by up to 2 orders of magnitude.

It was demonstrated [12] that the pulse width in diode-end-pumped actively mode-locked lasers can be

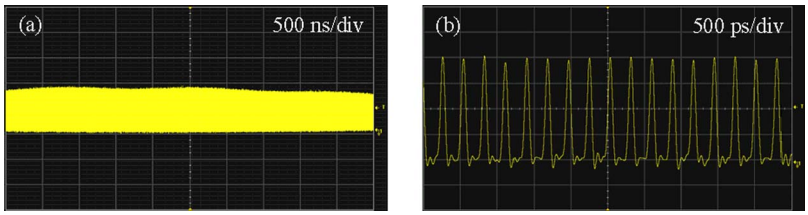

Fig. 3. (Color online) Pulse trains on two different time scales: (a) time span of 5 μs, demonstrating mode-locked pulses; (b) time span of 5 ns, demonstrating amplitude oscillation.

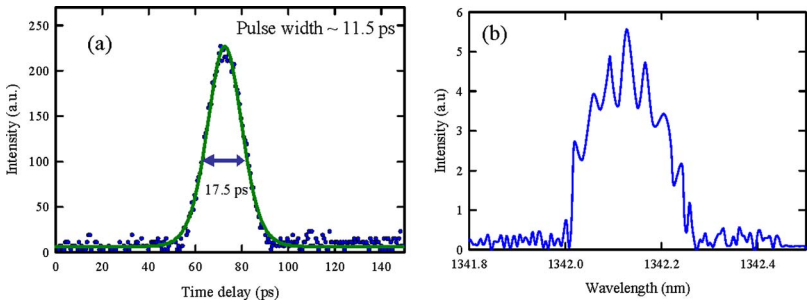

Fig. 4. (Color online) (a) Autocorrelation trace of the output pulses from the cw mode-locked Nd:YVO_4 laser; (b) corresponding optical spectrum of the laser.

adjusted by changing the crystal/mirror separation d to control the amount of spatial hole burning. This spatial-hole-burning effect is also speculated to be functioning in passively mode-locked lasers. We use the present simple linear cavity to investigate the pulse-width dependence on the crystal/mirror separation. With increasing crystal/mirror spacing up to 10 mm, the mode-locked pulse width varies smoothly from 11.5 to 37 ps, and the spectral bandwidth varies from 37 to 12 GHz, as shown in Fig. 5. This result confirms the speculation that spatial hole burning is also effective in passively mode-locked lasers [12].

In conclusion, we have realized a compact efficient self-mode-locked 1.34 μm Nd:YVO_4 laser in which the pulse repetition rate can be operated in the range of 2–6 GHz. The average output power was up to 1.2 W at an incident pump power of 10.2 W, which gives an optical conversion efficiency of 11.7%. The mode-locked pulse width could be smoothly varied from 11.5 to 37 ps by increasing the crystal/mirror separation from 1 mm to 10 mm to control the amount of spatial hole burning. We believe that a compact efficient GHz self-mode-locked Nd:YVO_4 laser at 1.34 μm can be a potential light source for many applications such as high-capacity telecommunication systems, photonic switching devices, optical interconnections, and optical clocking.

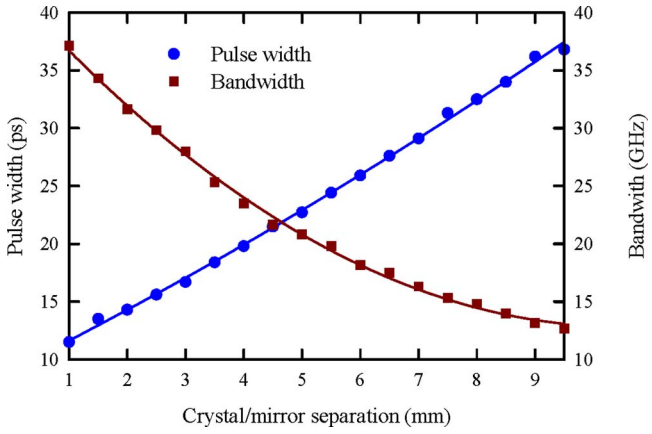

Fig. 5. (Color online) Mode-locked pulse width and bandwidth as functions of the crystal/mirror separation.

The authors thank the National Science Council of Taiwan (NSCT) for their financial support of this research under contract NSC-97-2112-M-009-016-MY3.

References

1. O. Musset and J. P. Boquillon, Appl. Phys. B **64**, 503 (1997).
2. H. J. Zhang, J. H. Liu, J. Y. Wang, X. G. Xu, and M. H. Jiang, Appl. Opt. **44**, 7439 (2005).
3. H. T. Huang, J. L. He, C. H. Zuo, H. J. Zhang, J. Y. Wang, and H. T. Wang, Appl. Phys. B **89**, 319 (2007).
4. Y. F. Chen, L. J. Lee, T. M. Huang, and C. L. Wang, Opt. Commun. **163**, 198 (1999).
5. R. Zhou, S. C. Ruan, C. L. Du, and J. Q. Yao, Opt. Commun. **282**, 605 (2009).
6. A. A. Kaminskii, K. Ueda, H. J. Eichler, Y. Kuwano, H. Kouta, S. N. Bagaev, T. H. Chyba, J. C. Barnes, G. M. A. Gad, T. Murai, and J. Lu, Opt. Commun. **194**, 201 (2001).
7. Y. F. Chen, Opt. Lett. **29**, 1251 (2004).
8. Y. F. Chen, Opt. Lett. **29**, 1915 (2004).
9. F. Su, X. Y. Zhang, Q. Wang, S. Ding, P. Jia, S. Li, S. Fan, C. Zhang, and B. Liu, J. Phys. D **39**, 2090 (2006).
10. X. H. Chen, X. Y. Zhang, Q. P. Wang, P. Li, and Z. H. Cong, Laser Phys. Lett. **6**, 26 (2009).
11. H. C. Liang, R. C. C. Chen, Y. J. Huang, K. W. Su, and Y. F. Chen, Opt. Express **16**, 21149 (2008).
12. C. J. Flood, D. R. Walker, and H. M. van Driel, Opt. Lett. **20**, 58 (1995).
13. G. J. Spühler, L. Krainer, V. Liverini, R. Grange, M. Haiml, S. Pawlik, B. Schmidt, S. Schön, and U. Keller, IEEE Photon. Technol. Lett. **17**, 1319 (2005).

Picosecond optical vortex converted from multigigahertz self-mode-locked high-order Hermite–Gaussian Nd:$GdVO_4$ lasers

H. C. Liang,[1] Y. J. Huang,[1] Y. C. Lin,[1] T. H. Lu,[2] Y. F. Chen,[1,*] and K. F. Huang[1]

[1]*Department of Electrophysics, National Chiao Tung University, Hsinchu, Taiwan*
[2]*Department of Physics, National Taiwan Normal University, Taipei, Taiwan*
[*]*Corresponding author: yfchen@cc.nctu.edu.tw*

Received August 19, 2009; revised November 4, 2009; accepted November 11, 2009;
posted November 17, 2009 (Doc. ID 115983); published December 9, 2009

We report on a gigahertz self-mode-locked high-order Hermite–Gaussian (HG) Nd:$GdVO_4$ laser. With a pump power of 2.2 W, the average output power for the $TEM_{0,m}$ modes from $m=9$ to $m=0$ are among 350–780 mW at a repetition rate of 3.5 GHz. The mode-locked pulse width is in the range of 20–25 ps for various HG $TEM_{0,m}$ modes. With a simple cylindrical-lens converter, the mode-locked HG beams are converted to generate picosecond optical vortex pulses. © 2009 Optical Society of America

OCIS codes: 140.4050, 140.3480, 080.4865.

Optical vortex beams [1,2] that possess orbital angular momentum because of a phase singularity have been extensively used in the study of optical tweezers [3–7], trapping and guiding of cold atoms [8–10], rotational frequency shift [11,12], and entanglement states of photons [13]. Several devices, including spiral phase plates [14], computer-generated holographic converters [15], and astigmatic mode converters (AMC) [16], have been successfully demonstrated to transform high-order Hermite–Gaussian (HG) modes into optical vortex beams.

Optical vortex pulses have recently been attracting great interest because they can open up various fields, including high-quality material processing [17], controllable specificity of chiral matter [18], and nonlinear frequency conversion [19]. Furthermore, optical vortex pulses in picosecond or femtosecond laser fields can be potentially utilized to investigate high-field laser physics [20–23]. However, AMC cannot be used directly, since conventional mode-locked lasers are usually designed to emit the fundamental TEM_{00} mode. Therefore, it is highly desirable to develop high-order HG mode-locked lasers for generating ultrafast vortex pulses.

Recently, the large third-order nonlinearities of Nd-doped vanadate crystals have been successfully exploited to achieve the self-starting self-mode-locking operation without the need of any additional components [24]. In this Letter we report for the first time (to our knowledge) on a multigigahertz self-mode-locked high-order HG Nd-doped $GdVO_4$ laser with an off-axis pumping scheme. With a pump power of 2.2 W, the average output powers for 3.5 GHz mode-locked HG modes vary in the range of 350–780 mW for the $TEM_{0,m}$ modes from $m=9$ to $m=0$. The mode-locked pulse width is found to be approximately 20–25 ps for various HG $TEM_{0,m}$ modes, with $m=0-9$. We also use simple AMC to convert the mode-locked HG $TEM_{0,m}$ beams into Laguerre–Gaussian (LG) modes for generating picosecond optical vortex pulses.

Figure 1 depicts the experimental setup for the self-mode-locked high-order HG $TEM_{0,m}$ laser with an off-axis pumping scheme [25,26]. The cavity configuration is a simple concave-plano resonator. The active medium is an a-cut 0.25 at. % Nd:$GdVO_4$ crystal with a length of 10 mm. Both end surfaces of the Nd:$GdVO_4$ crystal were antireflection coated at 1064 nm and wedged 2° to suppress the Fabry–Perot etalon effect. The laser crystal was wrapped with indium foil and mounted in a water-cooled copper holder. The water temperature was maintained around 20°C to ensure stable laser output. The laser crystal was placed very near (2–3 mm) the input mirror, which was a 50 cm radius-of-curvature concave mirror with antireflection coating at 808 nm on the entrance face and with high-reflectance coating at 1064 nm (>99.8%) and high transmittance coating at 808 nm on the second surface. A flat wedged output coupler with 15% transmission at 1064 nm was used throughout the experiment. The pump source was a 2.5 W, 808 nm fiber-coupled laser diode with a core diameter of 100 μm and an NA of 0.16. A focusing lens with 5 mm focal length and 85% coupling efficiency was used to reimage the pump beam into the laser crystal. The average pump size was approximately 70 μm. The optical cavity length was set

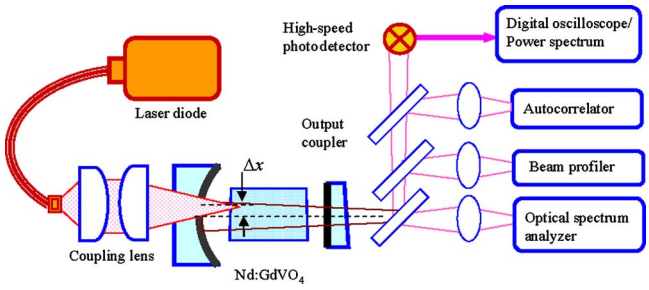

Fig. 1. (Color online) Schematic of a self-mode-locked high-order HG $TEM_{0,m}$ laser with an off-axis pumping scheme.

to be approximately 4.3 cm with the corresponding free spectral range (FSR) of 3.5 GHz.

First of all, the pumping beam was focused right on the optical axis of the laser cavity to obtain the maximum output power for the $TEM_{0,0}$ mode. After finely adjusting the cavity alignment, the laser output can be found to display a stable self-mode-locking operation. Subsequently the high-order HG $TEM_{0,m}$ mode-locked lasers can be generated with off-axis pumping [25,26]. The larger the off-axis displacement Δx is, the higher the HG $TEM_{0,m}$ order is. With varying Δx from 0 to 0.5 mm, the average output power was found to decrease gradually from 780 to 350 mW at a pump power of 2.2 W, as shown in Fig. 2. Ten HG $TEM_{0,m}$ modes were generated during the variation of off-axis displacement. The inset of Fig. 2 shows the experimental patterns that were measured using a CCD camera. All observed HG $TEM_{0,m}$ modes are found to be in the pure longitudinal mode-locking regime. Note that once the pump power reaches the lasing threshold, the laser system instantaneously steps into a stable mode-locked operation without any mechanical perturbation. The locking mechanism is presumed to be the Kerr effect. However, the laser system has high stability over day-long operation and is insensitive to mechanical vibrations and air current. As a result, some auxiliary mechanism seems to exist in the locking process. Bai *et al.* [27] proposed a novel self-mode-locking mechanism in narrowband lasers based on the analysis of the gain-line splitting induced by an intracavity laser field. Although the present experimental results are fairly consistent with this mechanism, further identification is still needed.

The mode-locked pulses were detected by a high-speed InGaAs photodetector (Electro-optics Technology, Inc. ET-3500 with rise time 35 ps), whose output signal was connected to a digital oscilloscope (Agilent DSO 80000) with 10 GHz electrical bandwidth and a sampling interval of 25 ps. Figures 3(a) and 3(b) show the pulse trains for the $TEM_{0,5}$ mode on two different time scales, one with time span of 5 ns, demonstrating mode-locked pulses, and the other with time span of 5 μs, demonstrating the amplitude stability. It can be seen that the pulse trains display full modulation, and the complete mode locking is achieved. The corresponding power spectrum is measured by an rf spectrum analyzer (Advantest, R3265A) with bandwidth of 8.0 GHz. Experiment results reveal that the relative frequency deviation of power spectrum, $\Delta\nu/\upsilon$, is smaller than 10^{-4} over day-long operation, where υ is the center frequency of the power spectrum and $\Delta\nu$ is the frequency deviation of FWHM. The laser was cw mode locked at 3.5 GHz with only weak noise at the relaxation oscillation frequency around 2 MHz, and the difference between the peak of mode-locked frequency and that of relaxation oscillation frequency was experimentally found to be larger than 55 dBm. The overall characteristics are almost the same as the results observed for the self-mode-locked fundamental $TEM_{0,0}$ mode [24]. The pulse width at the cw mode-locked operation was measured with an autocorrelator (APE pulse check, Angewandte physik & Elektronik GmbH). Assuming the sech^2-shaped temporal profile, the FWHM was measured to be in the range of 20–25 ps for HG $TEM_{0,m}$ modes with $m=0-9$. The result for the $TEM_{0,5}$ mode is shown in Fig. 3(c). The spectral information of the laser was monitored by a Fourier optical spectrum analyzer (Advantest, Q8347) that is constructed with a Michelson interferometer with resolution of 0.003 nm. Figure 3(d) shows the optical spectrum for the $TEM_{0,5}$ mode. It can be seen that the longitudinal mode with 3.5 GHz is clearly resolved and the FWHM of the spectrum is approximately 0.1 nm. Consequently, the time–bandwidth product of the mode-locked pulse is approximately 0.4, indicating the pulses to be frequency chirped. On the whole, there are no significant difference for the mode-locked performances of the HG $TEM_{0,m}$ modes with $m=0-9$.

The mode-locked HG $TEM_{0,m}$ beam was converted into the mode-locked LG $TEM_{0,m}$ beam with a

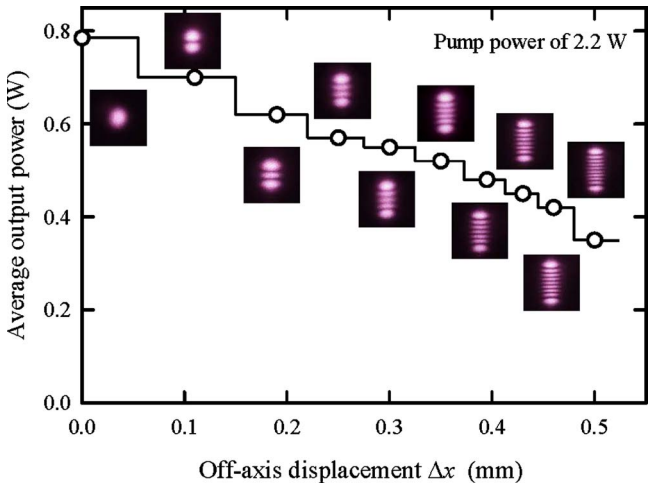

Fig. 2. (Color online) Dependence of the average output power on the variation off-axis displacement. Inset, transverse patterns observed in the mode-locked operation.

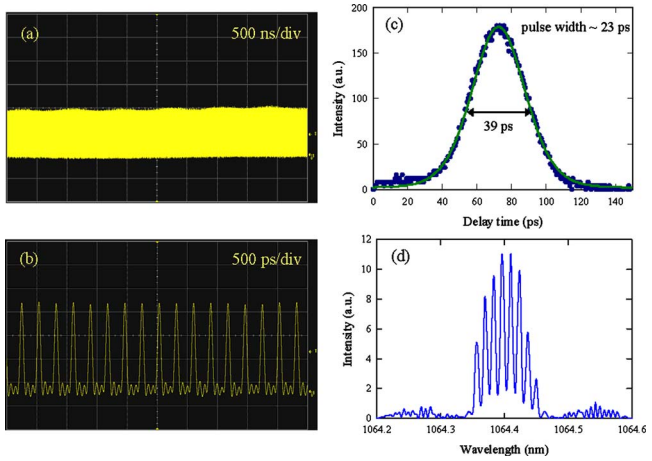

Fig. 3. (Color online) Pulse trains on two different time scales: (a) time span of 5 μs, demonstrating mode-locked pulses; (b) time span of 5 ns, demonstrating the amplitude oscillation. (c) Autocorrelation trace of the output pulses. (d) Corresponding optical spectrum. All results are for HG $TEM_{0,5}$ mode.

cylindrical-lens mode converter outside the laser resonator, as shown in Fig. 4(a). The focal length of the cylindrical lenses was $f=25$ mm, and the distance was precisely adjusted to be $\sqrt{2}f$ for the operation of the $\pi/2$ converter. Figure 4(b) depicts the results of the transformation of HG modes, shown in Fig. 2, to the corresponding LG modes. It can be seen that the mode-locked LG $TEM_{0,m}$ modes are successfully generated for azimuthal index from 0 to 9.

In conclusion, we have realized an efficient 3.5 GHz self-mode-locked $Nd:GdVO_4$ laser for HG $TEM_{0,m}$ modes with $m=0-9$. The average output powers for the $TEM_{0,m}$ modes from $m=9$ to $m=0$ were among 350–780 mW at a pump power of 2.2 W. The mode-locked pulse width was found to be in the range of 20–25 ps for various HG $TEM_{0,m}$ modes. With a simple cylindrical-lens converter, the picosecond optical vortex pulses have been generated by converting the mode-locked HG beams into LG modes. We believe that the generated picosecond optical vortices can be potentially beneficial to a number of applications.

The authors thank the National Science Council (NSC)for their financial support of this research under contract NSC-97-2112-M-009-016-MY3.

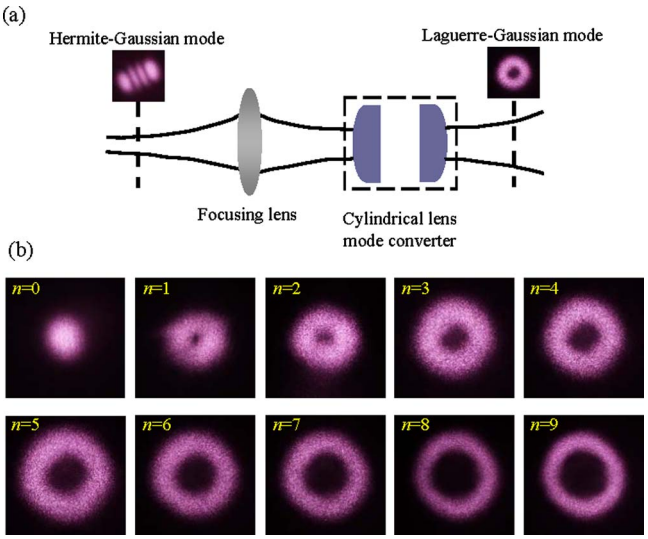

Fig. 4. (Color online) (a) Schematic of a cylindrical-lens mode converter. (b) Converted LG modes transformed from the HG modes shown in Fig. 2.

References

1. L. Allen, M. W. Beijersbergen, R. J. C. Spreeuw, and J. P. Woerdman, Phys. Rev. A **45**, 8185 (1992).
2. G. Indebetouw, J. Mod. Opt. **40**, 73 (1993).
3. N. B. Simpson, K. Dholakia, L. Allen, and M. J. Padgett, Opt. Lett. **22**, 52 (1997).
4. E. Santamato, A. Sasso, B. Piccirillo, and A. Vella, Opt. Express **10**, 871 (2002).
5. K. T. Gahagan and G. A. Swartzlander, Jr., Opt. Lett. **21**, 827 (1996).
6. L. Paterson, M. P. MacDonald, J. Arlt, W. Sibbett, P. E. Bryant, and K. Dholakia, Science **292**, 912 (2001).
7. M. P. MacDonald, Opt. Commun. **201**, 21 (2002).
8. Y. Song, D. Milam, and W. T. Hill, Opt. Lett. **24**, 1805 (1999).
9. X. Xu, K. Kim, W. Jhe, and N. Kwon, Phys. Rev. A **63**, 3401 (2001).
10. T. Kuga, Y. Torii, N. Shiokawa, T. Hirano, Y. Shimizu, and H. Sasada, Phys. Rev. Lett. **78**, 4713 (1997).
11. J. Courtial, D. A. Robertson, K. Dholakia, L. Allen, and M. J. Padgett, Phys. Rev. Lett. **81**, 4828 (1998).
12. J. Courtial, K. Dholakia, D. A. Robertson, L. Allen, and M. J. Padgett, Phys. Rev. Lett. **80**, 013601 (1998).
13. A. Mair, A. Vaziri, G. Weihs, and A. Zeilinger, Nature **412**, 313 (2001).
14. M. W. Beijersbergen, R. P. C. Coerwinkel, M. Kristensen, and J. P. Woerdman, Opt. Commun. **112**, 321 (1994).
15. N. R. Heckenberg, R. McDuff, C. P. Smith, and A. G. White, Opt. Lett. **17**, 221 (1992).
16. M. W. Beijersbergen, L. Allen, H. E. L. O. van der Veen, and J. P. Woerdman, Opt. Commun. **96**, 123 (1993).
17. J. Hamazaki, R. Morita, Y. Kobayashi, S. Tanda, and T. Omatsu, in *Proceedings of IEEE Conference on CLEO/Europe-EQEC* (IEEE, 2009), paper ThuCC1.5.
18. D. L. Andrews, L. C. Dávila Romero, and M. Babiker, Opt. Commun. **237**, 133 (2004).
19. K. Dholakia, N. B. Simpson, M. J. Padgett, and L. Allen, Phys. Rev. A **54**(5), R3742 (1996).
20. I. G. Mariyenko, J. Strohaber, and C. J. G. J. Uiterwaal, Opt. Express **13**, 7599 (2005).
21. K. Bezuhanov, A. Dreischuh, G. G. Paulus, M. G. Schatzel, and H. Walther, Opt. Lett. **15**, 1942 (2004).
22. G. B. Jung, K. Kanaya, and T. Omatsu, Opt. Express **14**, 2250 (2006).
23. Y. Tanaka, M. Okida, K. Miyamoto, and T. Omatsu, Opt. Express **17**, 14362 (2009).
24. H. C. Liang, Ross C. C. Chen, Y. J. Huang, K. W. Su, and Y. F. Chen, Opt. Express **16**, 21149 (2008).
25. Y. F. Chen, T. M. Huang, C. F. Kao, C. L. Wang, and S. C. Wang, IEEE J. Quantum Electron. **33**, 1025 (1997).
26. H. Laabs and B. Ozygus, Opt. Laser Technol. **28**, 213 (1996).
27. Y. Bai, S. Chen, Z. Wang, and G. Zhang, Appl. Phys. Lett. **63**, 2597 (1993).

Exploring the origin of the directional emission from a microcavity with a large-aperture surface-emitting laser

Ross C. C. Chen, Y. T. Yu, Y. J. Huang, C. C. Chen, Y. F. Chen,* and K. F. Huang

Department of Electrophysics, National Chiao Tung University, Hsinchu, Taiwan
**Corresponding author: yfchen@cc.nctu.edu.tw*

Received March 24, 2009; revised May 9, 2009; accepted May 10, 2009;
posted May 12, 2009 (Doc. ID 109194); published June 8, 2009

The origin of the direction emission from a microcavity is investigated with a large-aperture surface-emitting laser with an equilateral-triangular shape. Experimental results reveal that a wide-spread eigenmode and a localized superscar mode can display quite similar far-field directional emissions. This experimental finding is theoretically confirmed with the quantum-billiard wave function and the approximation of the paraxial propagation. © 2009 Optical Society of America

OCIS codes: 140.3410, 140.5960, 260.5740.

Optical microcavities, regarded as billiards for light, have great potential for applications in miniature lasers, optoelectronics, and biological sensors [1–3]. In the aspect of basic research on modern physics, microcavity lasers have been recently used to investigate the ray–wave correspondence in mesoscopic systems [4–6]. The directional emissions in chaotic microdisk lasers are usually interpreted with the concept of quantum scar effect that signifies the wave patterns to be localized on the isolated and unstable periodic orbits (POs) [7]. To be distinguishable, the resonant modes associated with the stable and nonisolated POs are called the superscar or quasi-scar modes [8–10]. The superscar modes have been theoretically studied in square [11], equilateral-triangular [12], and circular quantum billiards [13]. In experiments, microdisk lasers have been recently employed to explore the characteristics of resonant modes in square [14] and equilateral-triangular [15,16] cavities. Since the spatial morphologies of the lasing modes cannot be directly observed from the lateral radiation of microdisk lasers, the directional emission is often identified to originate from the superscar modes. However, the correspondence between the directional emission and the spatial localization in laser modes has not been investigated yet.

In contrast to two-dimensional (2D) microdisk lasers, the vertical-cavity surface-emitting lasers (VCSELs) are designed to have a dominant longitudinal wave vector k_z that can bring out the near-field patterns to be directly reimaged with simple optics. Recently, the transverse modes of the oxide-confined VCSELs have been verified to be analogous to the wave functions in the 2D quantum billiards with the shapes the same as the lateral confinements [17–19]. This analogy enables us to clarify the correspondence between the far-field emission and the near-field morphology in microcavity lasers. In this Letter we use a large-aperture equilateral-triangular VCSEL to explore the relationship between the far-field emission and the near-field morphology. Experimental results reveal that a wide-spread eigenmode can display a far-field directional emission quite similar to that emitted from a superscar mode. We also use the wave functions of the eigenstates and the coherent states to numerically confirm the experimental observation. Our finding indicates that the far-field directional emission from a microcavity is just a necessary not sufficient condition for the emergence of a superscar mode.

First of all, we present a brief synopsis for the near- and far-field characteristics of lasing modes emitted from an oxide-confined VCSEL. The separability of the wave function in the VCSEL device enables the wave vectors to be decomposed into k_z and k_t, where k_z is the wave-vector component along the direction of vertical emission and k_t is the transverse wave-vector component. Under the circumstance of paraxial optics, $k_t \ll k_z$, the longitudinal field is significantly small in comparison with the transverse field. Therefore, the electric field can be approximated to have only transverse components and no longitudinal component, i.e., the so-called quasi-TEM waves. After separating the z component in the wave equation, we are left with a 2D Helmholtz equation $(\nabla_t^2 + k_t^2)\psi(x,y) = 0$, where ∇_t^2 means the Laplacian operator operating on the coordinates in the transverse plane and $\psi(x,y)$ is a scalar wave function that describes the transverse distribution of the laser mode. Consequently, the transverse modes of the oxide-confined VCSEL device are equivalent to the eigenfunctions of the 2D Schrödinger equation with hard wall boundaries of the same geometry. Based on the paraxial approximation, the resonant mode $\psi_o(x,y)$ that emits from the cavity boundary $z=0$ to the surroundings in the direction of the $+z$ axis can be expressed as the Fresnel transformation,

$$\psi(x,y,z) = \frac{ie^{-ikz}}{\lambda z}\int dy' \int dx' \times \exp\left\{-\frac{ik[(x-x')^2 + (y-y')^2]}{2z}\right\}\psi_o(x',y'). \quad (1)$$

In the far-field region, $z \gg x'$ and $z \gg y'$, Eq. (1) can be reduced to be the Fraunhofer diffraction formula,

$$\psi(x,y,z) = \frac{ie^{-ikz}}{\lambda z}\exp\left[-\frac{ik(x^2+y^2)}{2z}\right]\int dy' \int dx' \times \exp\left[-\frac{ik(xx'+yy')}{z}\right]\psi_o(x',y'). \quad (2)$$

In this regime, $\psi(x,y,z)$ is just the 2D Fourier transform of $\psi_o(x',y')$ except for a multiplicative phase factor, which does not affect the intensity of the light. To be brief, the near- and far-field transverse patterns of an oxide-confined VCSEL represent the coordinate- and momentum-space wave functions of a 2D quantum billiard, respectively.

The schematics of the laser device structure and the experimental setup are shown in Fig. 1. The edge length of the oxide aperture was measured to be approximately 66.8 μm. The VCSEL device was placed in a cryogenic system with a temperature stability of 0.01 K in the range of 80–300 K. The near-field patterns were reimaged into a charge-coupled device (CCD) camera (Coherent, Beam Code) with an objective lens (Mitsutoyo, NA of 0.9). As found in our previous study, the typical lasing modes include the honeycomb eigenmode and the superscar mode. Here the far-field patterns are measured with a CCD placed behind a screen. Figure 2 shows the experimental near-field morphologies [Figs. 2(a)–2(c)] and the corresponding far-field patterns [Figs. 2(a′)–2(c′)] for the honeycomb eigenmode, the superscar mode, and the chaotic mode. It can be seen that the near-field patterns for the honeycomb eigenmode and the superscar mode are conspicuously different; however, their far-field patterns display fairly similar directional emission. The directional emission for a superscar mode can be easily traced from its localization in the near-field feature. It is demanding, however, to associate the directional emission with a honeycomb lasing mode. Therefore, this finding deserves to be confirmed with theoretical analysis.

Setting the three vertices to be at (0,0), $(a/2,\sqrt{3}a/2)$, and $(-a/2,\sqrt{3}a/2)$, where a is the side length, the eigenstates of the equilateral-triangular billiard are given by [19]

$$\Phi^{\pm}_{m,n}(x,y) = \sqrt{\frac{16}{a^2 3\sqrt{3}}}\left\{e^{\pm i(m+n)(2\pi x/3a)} \times \sin\left[(m-n)\frac{2\pi y}{\sqrt{3}a}\right] + e^{\mp(2m-n)(2\pi x/3a)}\sin\left[n\frac{2\pi y}{\sqrt{3}a}\right] - e^{\mp i(2n-m)(2\pi x/3a)}\sin\left[m\frac{2\pi y}{\sqrt{3}a}\right]\right\}, \quad (3)$$

with $2n \geq m$. The eigenstates $\Phi^{\pm}_{m,n}(x,y)$ embody the traveling waves. The eigenstates for the standing waves can be given by $S^{\pm}_{m,n}(x,y) = \Phi^{+}_{m,n}(x,y) \pm \Phi^{-}_{m,n}(x,y)$. In terms of $S^{-}_{m,n}(x,y)$, the experimental honeycomb pattern shown in Fig. 2(a) can be well reconstructed with $m=6$ and $n=60$, as depicted in Fig. 3(a).

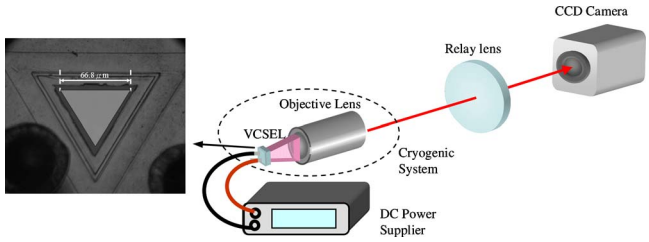

Fig. 1. (Color online) Schematics of the laser device structure and the experimental setup.

On the other hand, the wave functions for the superscar modes can be represented with the coherent states and given by [12,19]

$$\Psi^{\pm}_{N,M}(x,y;p,q,\varphi) = \frac{1}{\sqrt{M}}\sum_{K=0}^{M-1} e^{\pm iK\varphi}\Phi^{\pm}_{m_o+pK,n_o+q(M-1-K)}(x,y), \quad (4)$$

with $m_o=(p+2q)N$ and $n_o=(2p+q)N$, where m_o and n_o indicate the order of the coherent state and M stands for the number of eigenstates that are involved in the superposition. Note that the parameters (p,q,φ) are used to classify the POs in the equilateral-triangular billiard, where the parameters p and q are nonnegative integers with the restriction that $p \geq q$ and the parameter ϕ is in the range of $-\pi$ to π [12]. In the same way, the traveling-wave form $\Psi^{\pm}_{N,M}(x,y;p,q,\varphi)$ can be used to express the standing-wave representation as $C^{\pm}_{N,M}(x,y;p,q,\varphi) = \Psi^{+}_{N,M}(x,y;p,q,\varphi) \pm \Psi^{-}_{N,M}(x,y;p,q,\varphi)$. In terms of $C^{+}_{N,M}(x,y;p,q,\varphi)$, the experimental superscar pattern shown in Fig. 2(b) can be well reconstructed with $N=22$, $M=6$, and $(p,q,\varphi)=(1,1,0.3\pi)$, as depicted in Fig. 3(b).

With the theoretical wave functions $S^{-}_{6,60}(x,y)$ and $C^{+}_{22,6}(x,y;1,1,0.3\pi)$, we use Eq. (2) to calculate the corresponding far-field patterns. Figures 3(a′) and 3(b′) depict the calculated far-field patterns for the modes $S^{-}_{6,60}(x,y)$ and $C^{+}_{22,6}(x,y;1,1,0.3\pi)$, respectively. The far-field patterns for the modes $S^{-}_{6,60}(x,y)$

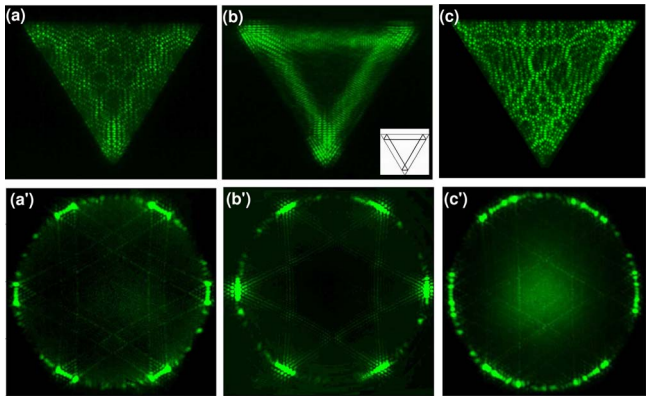

Fig. 2. (Color online) Experimental near-field morphologies: (a) honeycomb eigenmode, (b) superscar mode, (c) chaotic mode. The far-field patterns (a′), (b′), and (c′) correspond to (a), (b), and (c), respectively.

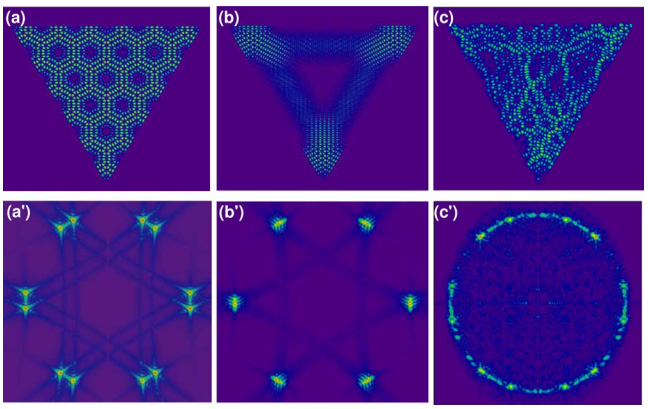

Fig. 3. (Color online) (a) Numerical wave pattern $|S^{-}_{6,60}(x,y)|^2$ corresponding to the experimental honeycomb pattern shown in Fig. 2(a). (b) Numerical wave pattern $|C^{+}_{22,6}(x,y;1,1,0.3\pi)|^2$ corresponding to the experimental patterns shown in Fig. 2(b). (c) Reconstructed wave pattern corresponding to the experimental patterns shown in Fig. 2(c). The far-field patterns (a′), (b′), and (c′) correspond to (a), (b), and (c), respectively.

and $C^{+}_{22,6}(x,y;1,1,0.3\pi)$ can be found to exhibit similar directional emissions, in good consistency with the experimental results shown in Figs. 2(a′) and 2(b′). As a consequence, we can confirm that the far-field directional emission is just a necessary not sufficient sign for the emergence of a superscar mode. Finally, we employed the method described in [20] to reconstruct the wave function for the experimental chaotic mode shown in Fig. 2(c). With the reconstructed wave function, the far-field pattern was calculated with Eq. (2). It can be seen that the numerical results depicted in Figs. 3(c) and 3(c′) agree very well with the experimental results shown in Figs. 2(c) and 2(c′), respectively. The excellent agreements between the experimental and reconstructed results both in near- and far-field patterns confirm our physical analyses and experimental observations.

In conclusion, we have experimentally investigated the relationship between the far-field emission and the near-field morphology with a large-aperture equilateral-triangular VCSEL. It was found that not only the localized superscar mode but also the widespread eigenmode may radiate very similar far-field directional emission. Based on the quantum-billiard wave function and the paraxial approximation, we have successfully confirmed the experimental finding that the far-field directional emission from a microcavity is just a necessary not sufficient condition for the emergence of a superscar mode. More importantly, the present result can provide what we believe to be a new prospect in designing a microcavity laser with directional emissions.

The authors acknowledge the National Science Council of Taiwan (NSCT) for their financial support of this research under contract NSC-95-2112-M-009-041-MY2.

References

1. C. Gmachl, F. Capasso, E. E. Narimanov, J. U. Nöckel, A. D. Stone, J. Faist, D. L. Sivco, and A. Y. Cho, Science **280**, 1556 (1998).
2. N. B. Rex, H. E. Tureci, H. G. L. Schwefel, R. K. Chang, and A. D. Stone, Phys. Rev. Lett. **88**, 094102 (2002).
3. M. Lebental, J. S. Lauret, J. Zyss, C. Schmit, and E. Bogomolny, Phys. Rev. A **75**, 033806 (2007).
4. S. Y. Lee, S. Rim, J. W. Ryu, T. Y. Kwon, M. Choi, and C. M. Kim, Phys. Rev. Lett. **93**, 164102 (2004).
5. T. Tanaka, M. Hentschel, T. Fukushima, and T. Harayama, Phys. Rev. Lett. **98**, 033902 (2007).
6. J. Wiersig and M. Hentschel, Phys. Rev. Lett. **100**, 033901 (2008).
7. E. J. Heller, Phys. Rev. Lett. **53**, 1515 (1984).
8. E. Bogomolny, B. Dietz, T. Friedrich, M. Miski-Oglu, A. Richter, F. Schäfer, and C. Schmit, Phys. Rev. Lett. **97**, 254102 (2006).
9. S. Aberg, T. Guhr, M. Miski-Oglu, and A. Richter, Phys. Rev. Lett. **100**, 204101 (2008).
10. J. Lee, S. Rim, J. Cho, and C. M. Kim, Phys. Rev. Lett. **101**, 064101 (2008).
11. Y. F. Chen, K. F. Huang, and Y. P. Lan, Phys. Rev. E **66**, 066210 (2002).
12. Y. F. Chen and K. F. Huang, Phys. Rev. E **68**, 066207 (2003).
13. C. C. Liu, T. H. Lu, Y. F. Chen, and K. F. Huang, Phys. Rev. E **74**, 046214 (2006).
14. A. W. Poon, F. Courvoisier, and R. K. Chang, Opt. Lett. **26**, 632 (2001).
15. H. C. Chang, G. Kioseoglou, E. H. Lee, J. Haetty, M. H. Na, Y. Xuan, H. Luo, and A. Petrou, Phys. Rev. A **62**, 013816 (2000).
16. J. Yoon, S.-J. An, K. Kim, J. K. Ku, and O. Kwon, Appl. Opt. **46**, 2969 (2007).
17. K. F. Huang, Y. F. Chen, H. C. Lai, and Y. P. Lan, Phys. Rev. Lett. **89**, 224102 (2002).
18. T. Gensty, K. Becker, I. Fischer, W. Elsäßer, C. Degen, P. Debernardi, and G. P. Bava, Phys. Rev. Lett. **94**, 233901 (2005).
19. C. C. Chen, K. W. Su, Y. F. Chen, and K. F. Huang, Opt. Lett. **33**, 509 (2008).
20. C. C. Chen, K. W. Su, T. H. Lu, C. C. Liu, Y. F. Chen, and K. F. Huang, Phys. Rev. E **76**, 026219 (2007).

Subnanosecond mJ eye-safe laser with an intracavity optical parametric oscillator in a shared resonator

Y. P. Huang[1], H. L. Chang[1], Y. J. Huang[1], Y. T. Chang[1], K. W. Su[1], W. C. Yen[2], and Y. F. Chen[1]*

[1]Department of Electrophysics, National Chiao Tung University, Hsinchu, Taiwan
[2]Chung-Shan Institute of Science & Technology, Lung-Tan, Tao-Yuan, Taiwan
**Corresponding author: yfchen@cc.nctu.edu.tw*

Abstract: We theoretically verify that the threshold of an intracavity optical parametric oscillator pumped by a passively Q-switched laser is entirely controlled by the bleach of the saturable absorber not by the signal output reflectivity. We use a series of different output couplers to optimize the output performance. With a signal output reflectivity of 15%, we experimentally achieve an efficient subnanosecond eye-safe laser with 3.3 mJ pulse energy and 1.5 MW peak power.

OCIS codes: (140.3540) Lasers, Q-switched; (190.4410) Nonlinear optics, parametric processes; (140.3480) Lasers, diode-pumped.

References and links

1. E. Gregor, D. E. Nieuwsma, and R. D. Stultz, "20 Hz eyesafe laser rangefinder for air defense," Proc. SPIE, **1207**, 124-134 (1990).
2. L. R. Marshall, A. D. Hays, and J. Kasinski, "Highly efficient optical parametric oscillators," Proc. SPIE **1419**, 141–152 (1991).
3. J. E. Nettleton, B. W. Schilling, D. N. Barr, and J. S. Lei, "Monoblock laser for a low-cost, eyesafe, microlaser range finder," Appl. Opt. **39**, 2428-2432 (2000).
4. T. Debuisschert, J. Raffy, J. P. Pocholle, and M. Papuchon, "Intracavity optical parametric oscillator: Study of the dynamics in pulsed regime," J. Opt. Soc. Am. **B 13**, 1569–1587 (1996).
5. Z. Liu, Q. Wang, X. Zhang, Z. Liu, J. Chang, H. Wang, S. Fan, W. Sun, G. Jin, X. Tao, S. Zhang, and H. Zhang, "Efficient acoustic-optically Q-switched intracavity Nd:YAG/ $KTiOAsO_4$ parametric oscillator," Appl. Phys. **B 92**, 37-41 (2008).
6. H. T. Huang, J. L. He, X. L. Dong, C. H. Zuo, B. T. Zhang, G. Qiu, and Z. K. Liu, "High-repetition-rate eye-safe intracavity KTA OPO driven by a diode-end-pumped Q-switched Nd:YVO_4 laser," Appl. Phys. **B 90**, 43-45 (2008).
7. Y. F. Chen, S. W. Chen, S. W. Tsai, and Y. P. Lan, "High repetition-rate eye-safe optical parametric oscillator intracavity pumped by a diode-pumped Q-switched Nd:YVO_4 laser," Appl. Phys. **B 76**, 263–266 (2003).
8. J. Miao, J. Peng, B. Wang, H. Tan, and H. Bian, "Compact low threshold Cr:YAG passively Q-switched intracavity optical parametric oscillator," Opt. Commun. **281**, 2265–2270 (2008).
9. Y. F. Chen, S. W. Chen, Y. C. Chen, Y. P. Lan, and S. W. Tsai, "Compact efficient intracavity optical parametric oscillator with a passively Q-switched Nd:YVO4/Cr^{4+}:YAG laser in a hemispherical cavity," Appl. Phys. **B 77**, 493-495 (2003).
10. Y. F. Chen, S. W. Chen, L. Y. Tsai, Y. C. Chen, and C. H. Chien,"Efficient subnanosecond intracavity optical parametric oscillator pumped with a passively Q-switched Nd:$GdVO_4$ laser," Appl. Phys. **B 79**, 823–825 (2004).
11. R. Dabu, C. Fenic, and A. Stratan, "Intracavity pumped nanosecond optical parametric oscillator emitting in the eye-safe range," Appl. Opt. **40**, 4334-4340 (2001).
12. Y. Yashkir and H. M. van Driel, "Passively Q-switched 1.57-μm intracavity optical parametric oscillator," Appl. Opt. **38**, 2554-2559 (1999).
13. A. Agnesi, S. Dell'Acqua, and G. Reali, "Diode-pumped quasi-cw intracavity optical parametric oscillator at 1.57 μm with efficient pulse shortening," Appl. Phys. B **70**, 751-753 (2000).
14. W. Zendzian, J. K. Jabczyński, and J. Kwiatkowski, "Intracavity optical parametric oscillator at 1572-nm wavelength pumped by passively Q-switched diode-pumped Nd:YAG laser," Appl. Phys. **B 76**, 355-358 (2003).

#104782 - $15.00 USD Received 1 Dec 2008; revised 18 Dec 2008; accepted 22 Dec 2008; published 26 Jan 2009

15. B. W. Schilling, S. R. Chinn, A. D. Hays, L. Goldberg, and C. W. Trussell, "End-pumped 1.5 μm monoblock laser for broad temperature operation," Appl. Opt. **45**, 6607-6615 (2006).
16. Y. F. Chen and L. Y. Tsai, "Comparison between shared and coupled resonators for passively Q-switched Nd:GdVO4 intracavity optical parametric oscillators," Appl. Phys. **B 82**, 403–406 (2006).
17. Y. F. Chen, K. W. Su, Y. T. Chang, and W. C. Yen, "Compact efficient eye-safe intracavity optical parametric oscillator with a shared cavity configuration," Appl. Opt. **46**, 3597-3601 (2007).
18. R. J. Beach, "Theory and optimization of lens ducts," Appl. Opt. **35**, 2005-2015 (1996).
19. R. Fu, G. Wang, Z. Wang, E. Ba, G. Mu, and X. Hu, "Design of efficient lens ducts," Appl. Opt. **37**, 4000-4003 (1998).
20. J. J. Degnan, "Optimization of passively Q-switched lasers," IEEE J. Quantum Electron., **vol. 31**, pp. 1890–1901, 1995.
21. S. J. Brosnan and R. L. Byer, "Optical parametric oscillator threshold and linewidth studies," IEEE J. Quantum Electron., **vol. 15**, pp. 415–431, 1979.

1. Introduction

Human exposure is usually inevitable in many applications such as laser radar, remote sensing, rangefinder, target designation, and laser countermeasures; consequently, protection again injury of the eye is one of the most important issues [1-3]. Since water absorption in eye tissue and the intraocular fluid prevents light in the spectral range of 1.4-1.8 μm from reaching the retina, there is a considerable interest in compact laser sources with wavelengths in this eye-safe regime. One of the most promising approaches for high-peak-power eye-safe laser sources is based on intracavity optical parametric oscillators (OPO) [4-15]. The advent of high damage threshold nonlinear crystals and diode-pumped Nd-doped lasers leads to a renaissance of interest in intracavity OPO's. In recent years, a number of efficient eye-safe intracavity OPOs pumped by actively [5-7] or passively [8-10] Q-switched Nd-doped lasers have been demonstrated to produce pulse energies of tens of μJ with pulse peak powers of 1-100 kW. Nevertheless, eye-safe laser systems with pulse energies in the mJ range and peak powers greater than MW are indispensable for the many long-distance applications [11-15].

The intracavity OPOs are mostly constructed with the coupled cavity configuration in which the resonators for the signal and fundamental wave fields are separate. Recently, it was found [16,17] that the shared cavity configuration in which the pump and signal beams share the same resonator provides a substantially superior amplitude stability, in comparison with the coupled cavity configuration. Even so, the maximum peak power in a shared cavity is usually several times lower than that in a coupled cavity under the circumstance of the same output coupler. Therefore, it is a practical interest to explore an intracavity OPO in a shared resonator in quest of optimal pulse energies and peak powers.

Here, for what is believed to be the first time, a subnanosecond mJ eye-safe laser is experimentally demonstrated with an intracavity OPO pumped in a shared resonator. We first confirm that the threshold of an intracavity OPO pumped by a passively Q-switched laser is essentially determined by the bleach of the saturable absorber not by the signal output reflectivity. As a result, a series of different output couplers are used to ascertain the design criteria for the output optimization. With a signal output reflectivity of 15%, we realize an efficient subnanosecond eye-safe laser with 3.3 mJ pulse energy and 1.5 MW peak power.

2. Experimental setup

Figure 1 shows the experimental setup for an intracavity OPO pumped by a high-power quasi-continuous-wave (QCW) diode-pumped passively Q-switched Nd:YAG laser in a shared resonator. The fundamental laser cavity was formed by a coated Nd:YAG crystal and an output coupler. The OPO cavity entirely overlapped with the fundamental laser cavity. The pump source is a high-power QCW diode stack (Quantel Laser Diodes) that consists of three 10-mm-long diode bars generating 130 W per bar, for a total of 390 W at the central wavelength of 808 nm. The diode stack is designed with 0.4 mm spacing between the diode bars so the overall area of emission is approximately 10 mm (slow axis) × 0.8 mm (fast axis). The full divergence angles in the fast and slow axes are approximately 35^{o} and 10^{o}, respectively. A lens duct was exploited to couple the pump light from the diode stack into the

#104782 - $15.00 USD Received 1 Dec 2008; revised 18 Dec 2008; accepted 22 Dec 2008; published 26 Jan 2009

laser crystal. The lens duct has the benefits of simple structure, high coupling efficiency, and unaffected by slight misalignment. The geometric parameters of a lens duct include r, L, H_1, H_2, and H_3, where r is the radius of the input surface, L is the length of the duct, H_1 is the width of the input surface, H_2 is the width of the output surface, and H_3 is the thickness of the duct [18, 19]. Here a lens duct with the parameters of r = 10 mm, L = 32 mm, H_1 = 12 mm, H_2 = 2.7 mm, and H_3 = 2.7 mm was manufactured and used in the experiment. The coupling efficiency of this lens duct is found to be approximately 85%.

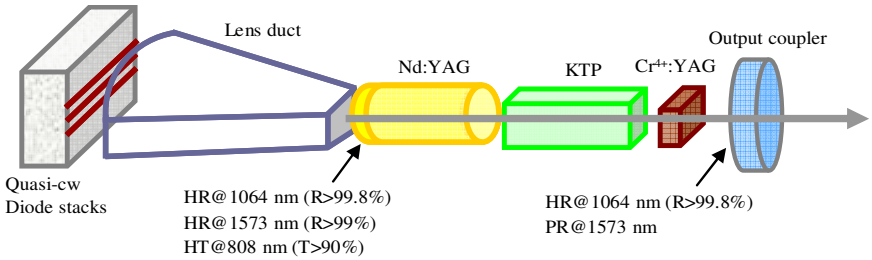

Fig. 1. Experimental setup for an intracavity OPO pumped by a high-power QCW diode-pumped passively Q-switched Nd:YAG laser in a shared resonator.

The gain medium was a 1.0 at. % Nd:YAG crystal with a diameter of 5 mm and a length of 10 mm. The incident surface of the laser crystal was coated to be highly reflective at 1064 nm and 1573 nm (R>99.8%) and highly transmitted at the pump wavelength of 808 nm (T>90%). The other surface of the laser crystal was coated to be antireflective at 1064 nm and 1573 nm (R<0.2%). The nonlinear material for the intracavity OPO was an x-cut KTP crystal with a size of 4×4×20 mm^3. The saturable absorber for the passive Q-switching was a Cr^{4+}:YAG crystal with a thickness of 3 mm and an initial transmission of 60% at 1064 nm. Both surfaces of the KTP and Cr^{4+}:YAG crystals were coated for antireflection at 1573 nm and 1064 nm. All crystals were wrapped with indium foil and mounted in conductively cooled copper blocks. The output coupler had a dichroic coating that was highly reflective at 1064 nm (R > 99.8%) and partially reflective at 1573 nm. Several output couplers with different reflectivities (10% ≤ Rs ≤ 70%) at 1573 nm were used in the experiment to investigate the output optimization. The total cavity length was approximately 5.5 cm. The pulse temporal behavior at 1063 nm and 1571 nm was recorded by a LeCroy digital oscilloscope (Wavepro 7100; 10 G samples/sec; 1 GHz bandwidth) with a fast InGaAs photodiode. The spectral information was monitored by an optical spectrum analyzer (Advantest Q8381A) that employs a diffraction grating monochromator to for measure high-speed light pulses with the resolution of 0.1 nm. In all investigations, the diode stack was driven to emit optical pulses 250 μs long, at a repetition rate less than 40 Hz, with a maximum duty cycle of 1%.

3. Theoretical analysis

The advantage of the intracavity OPO mainly consists in the exploit of high photon density of the fundamental wave. First of all, we analyze the maximum value of the intracavity photon density for the fundamental wave in a passively Q-switched laser. Next, we verify that the intracavity photon density of the present laser cavity can generally exceed the threshold of a singly resonant intracavity OPO by far, even though the reflectivity of the output mirror at the signal wavelength is nearly zero. In a passively Q-switched laser with a fast Q-switching condition, the maximum value of the intracavity photon density of the fundamental wave can be expressed as [20]

#104782 - $15.00 USD Received 1 Dec 2008; revised 18 Dec 2008; accepted 22 Dec 2008; published 26 Jan 2009

$$\phi_{f,\max} = \frac{l_{gm}}{l_{cav}}\left\{n_i - n_t\left[1+\ln\left(\frac{n_i}{n_t}\right)\right]\right\} \tag{1}$$

where $n_i = \frac{1}{2\sigma l_{gm}}\left[\ln\left(1/T_o^2\right)+\ln(1/R)+L\right]$; $n_t = \frac{1}{2\sigma l_{gm}}\left[\beta\ln\left(1/T_o^2\right)+\ln(1/R)+L\right]$; $\beta = \frac{\sigma_{es}}{\sigma_{gs}}$; n_i is the initial population density in the gain medium; σ is the stimulated emission cross section of the gain medium; l_{gm} is the length of the gain medium; l_{cav} is the cavity length; T_o is the initial transmission of the saturable absorber; σ_{gs} and σ_{es} are the ground-state and excited-state absorption cross sections in the saturable absorber, respectively; R is the reflectivity of the output mirror at the fundamental wavelength; and L is the nonsaturable intracavity round-trip loss. With the properties of the Nd:YAG and Cr^{4+}:YAG crystals and the typical cavity parameters: $\sigma = 2.8\times10^{-19}$ cm^2 , $\sigma_{gs} = 8.7\times10^{-19}$ cm^2, $\sigma_{es} = 2.2\times10^{-19}$ cm^2, $l_{cav} = 5.5$ cm, $R = 99.8\%$, $T_o = 0.6$, and $L = 0.01$, it can be found that $\phi_{f,\max}$ can be up to 1.56×10^{17} cm^{-3}.

With Brosnan and Byer's equation [21], the threshold photon density for the double-pass pumped, single resonant OPO is derived to be given by

$$\phi_{f,th}(R_s) = \frac{1.12}{G\, g_s\,(1+\gamma)^2}\left[33\frac{l_{cav}}{c\,\tau_p}+\ln\left(\frac{1}{\sqrt{R_s}}\right)+L_s+\ln 4\right]^2 \tag{2}$$

with the gain coefficient

$$G = \frac{2\hbar\omega_3\,\omega_1\,\omega_2\;d_{eff}^2\;l_{nl}^2}{n_3\,n_1\,n_2\,\varepsilon_0\,c^2} \tag{3}$$

where g_s is the mode coupling coefficient, γ is the ratio of backward to forward pump amplitude in the cavity; ω_1, ω_2 and ω_3 are the signal, idler and pump frequencies, respectively;, n_2 and n_3 are the refractive indices at the signal, idler and pump wavelengths, respectively; τ_p is the FWHM of the pump pulse; d_{eff} is the effective non-linear coefficient; ε_0 is the vacuum permittivity; c is the speed of light; l_{nl} is the length of the nonlinear crystal; L_s is the round-trip signal wave intensity loss in the cavity; and R_s is the output reflectivity at the signal wavelength.

Figure 2 depicts the calculated results for the dependence of the threshold photon density $\phi_{f,th}(R_s)$ on the output reflectivity R_s with the properties of the KTP crystal and the typical cavity parameters: $\omega_1 = 1.198\times10^{15}$ sec^{-1}, $\omega_2 = 5.712\times10^{14}$ sec^{-1}, $\hbar\omega_3 = 1.865\times10^{-19}$ J, $d_{eff} = 3.64$ pm/V, $l_{nl} = 20$ cm, $n_1 = 1.737$ $n_2 = 1.771$, $n_3 = 1.748$, $\varepsilon_0 = 8.854$ pF/m, $L_s = 0.01$, $\gamma = 0.9$, $g_s = 0.9$, $\tau_p = 10$ ns and c = 3×10^8 m/s. It can be seen that the threshold photon density $\phi_{f,th}$ increases from 6×10^{15} cm^{-3} to 6×10^{16} cm^{-3} for the reflectivity R_s varying from 99.9% to 0.1%. As analyzed earlier, the obtainable intracavity photon density of the fundamental wave generally exceeds 10^{17} cm^{-3}. Therefore, the intracavity OPO for any value of R_s can be promisingly generated in the shared cavity, as long as the pump energy can excite the fundamental wave to bleach the saturable absorber and to overcome the lasing threshold.

#104782 - $15.00 USD Received 1 Dec 2008; revised 18 Dec 2008; accepted 22 Dec 2008; published 26 Jan 2009

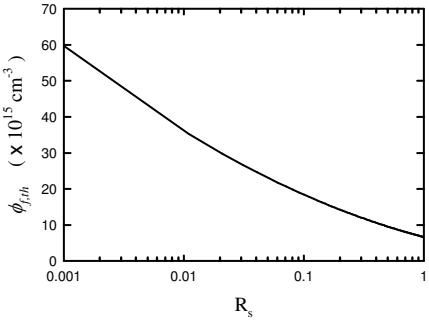

Fig. 2. Calculated results for the dependence of the threshold photon density on the output reflectivity R_s.

4. Experimental results and discussions

Figure 3 shows the experimental results for the threshold pump energy versus the OPO output reflectivity. Experimental results confirm that the threshold pump energy is determined by the bleach of the saturable absorber not by the signal output reflectivity. Consequently, a wide range of the signal output reflectivity can be used to optimize the output performance. Figure 4 depicts the experimental results for the pulse energy of the signal output versus the signal output reflectivity. The optimal output reflectivity for the output pulse energy can be found to be within R_s =40–50%. With the optimum output coupler, the conversion efficiency from the diode input energy to the signal output energy is approximately 7%, which is slightly superior to the efficiency of 4–6% obtained in a coupled cavity [15].

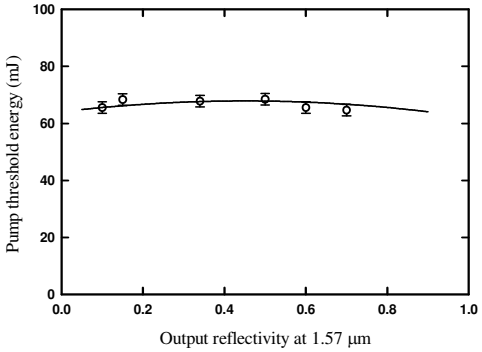

Fig. 3. Experimental results for the threshold pump energy versus the OPO output reflectivity.

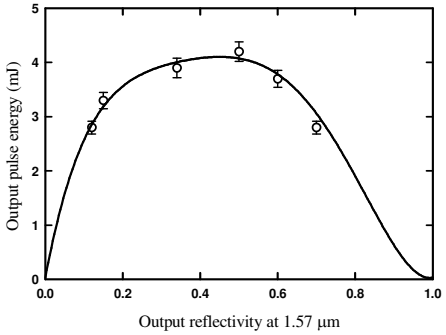

Fig. 4. Experimental results for the pulse energy of the signal output versus the OPO output reflectivity.

#104782 - $15.00 USD Received 1 Dec 2008; revised 18 Dec 2008; accepted 22 Dec 2008; published 26 Jan 2009

Figures 5(a)-(c) show the experimental results for the temporal shapes of the fundamental and the signal pulses obtained with three different output couplers. It can be seen that the pulse durations of the signal output are 4.4 ns, 2.1 ns, and 0.85 ns for R_s=60%, 50%, and 15%, respectively. The pulse width obtained with R_s = 15% is 2.4 times shorter than that obtained with R_s = 50%; however, the pulse energy is only 20% less than the maximum value. In other words, the peak power reached with R_s = 15% can be nearly two times higher than that obtained with R_s = 50%. To be more accurate, the output peak was calculated with the experimental pulse energy and the numerical integration of the measured temporal pulse profile. Figure 6 depicts the experimental results for the peak power of the signal output versus the OPO output reflectivity. The optimal output reflectivity for the output peak power can be found to be within R_s =10–20%. With the optimum output coupler, the maximum peak power can be up to 1.5 MW.

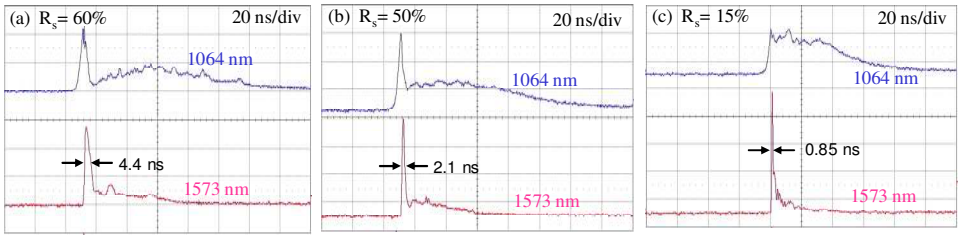

Fig. 5. Experimental results for the temporal shapes of the fundamental and the signal pulses.

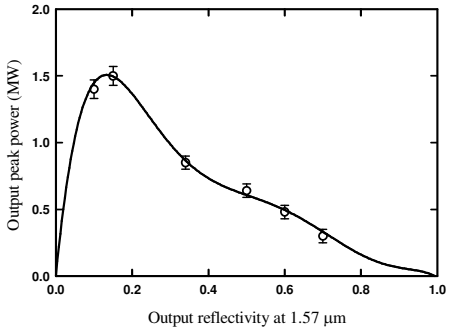

Fig. 6. experimental results for the peak power of the signal output versus the OPO output reflectivity.

5. Summary

In summary, we have theoretically and experimentally explored the output performance of an intracavity OPO in a shared cavity configuration. The threshold of an intracavity OPO pumped by a passively Q-switched Nd:YAG laser has been verified to be utterly controlled by the bleach of the saturable absorber not by the signal output reflectivity. Based on thorough experimental studies, we found that an efficient subnanosecond eye-safe laser with 3.3 mJ pulse energy and 1.5 MW peak power could be achieved with a signal output reflectivity of 15%.

Acknowledgments

The authors also thank the National Science Council for their financial support of this research under Contract No. NSC-97-2112-M-009-016-MY3.

#104782 - $15.00 USD Received 1 Dec 2008; revised 18 Dec 2008; accepted 22 Dec 2008; published 26 Jan 2009

Transient Dynamics of Coherent Waves Released from Quantum Billiards and Analogous Observation from Free-Space Propagation of Laser Modes

C. C. Chen, Y. T. Yu, Ross C. C. Chen, Y. J. Huang, K. W. Su, Y. F. Chen,* and K. F. Huang
Department of Electrophysics, National Chiao Tung University, 1001 Ta Hsueh Road, Hsinchu, Taiwan
(Received 2 October 2008; published 30 January 2009)

The transient dynamics of the eigenstates and coherent states released from a square quantum billiard is analytically and numerically investigated. It is experimentally verified that this transient dynamic can be analogously observed with the free-space propagation of the lasing modes emitted from the laterally confined, vertically emitted cavities. Furthermore, we exploit a chaotically shaped cavity to originally demonstrate the diffraction-in-time characteristics of the chaotic wave functions. It is found that the transient patterns of chaotic wave functions exhibit a striking feature of random branching behavior with the appearance of intricate interference fringes.

DOI: 10.1103/PhysRevLett.102.044101 PACS numbers: 05.45.Mt, 03.65.−w, 42.55.Px, 42.60.Jf

One of the most relevant quantum transient phenomena in matter waves is the diffraction-in-time effect for a suddenly released coherent beam, which appears to have first been introduced by Moshinsky in 1952 [1]. The hallmark feature of the diffraction-in-time effect is the temporal quantum interference patterns, by analogy with the spatial interference patterns of light diffracted by a sharp edge [2–5]. The experimental test for this effect was indeed hard to reach at the time of its first introduction. However, because of the development of an ultrafast laser [6], atom cooling, and optical trapping [7], the transient dynamics has been recently observed in a wide variety of systems including neutrons [8], ultracold atoms [9], electrons [10], and Bose-Einstein condensates [11].

Another physical connection to the diffraction-in-time effect would be the transient response to abrupt changes of the confined potential in semiconductor structures and quantum dots [12,13]. Semiconductor quantum dots, in which electronic motion is predominately ballistic in nature, have been widely used as two-dimensional (2D) quantum billiards to explore the properties of quantum chaos [14–16]. Understanding the time evolution of suddenly released quantum-billiard waves has some important applications, as it can provide the nanostructure transport properties for developing novel ultrahigh-speed semiconductor devices [12]. Moreover, it is closely related to atom laser dynamics from a tight waveguide whose boundary shape can be modified with the laser trapping beam [13,17]. Nevertheless, the investigation for the transient dynamics of 2D quantum-billiard coherent waves has not been performed as yet.

In this Letter we first theoretically investigate the diffraction-in-time effect of quantum eigenstates in square billiards. We further use the analytical result to explore the transient dynamics of the quantum coherent states that have intensities to concentrate on the classical periodic orbits. With the numerical visualization and experimental identification, we verify that the transient dynamics of coherent waves suddenly released from quantum billiards can be analogously observed with the free-space propagation of the lasing modes emitted from the laterally confined vertically emitted cavities. More importantly, we design a chaotically shaped laser cavity to experimentally demonstrate for the first time the characteristics of the diffraction in time of the chaotic billiard waves.

The 2D square billiard is one of the simplest billiards in classical mechanics [18,19]. The quantum eigenstates $\psi_{\tilde{m},\tilde{n}}(x, y)$ for the vertices are at $(\pm a/2, \pm a/2)$ and $(\pm a/2, \mp a/2)$ and are given by

$$\psi_{\tilde{m},\tilde{n}}(x, y) = (2/a)\sin[k_{\tilde{m}}(x + a/2)]\sin[k_{\tilde{n}}(y + a/2)], \quad (1)$$

where $k_n = n\pi/a$ $(n = 1, 2, 3, \ldots)$ and a is the length of the square boundary. In terms of the 2D free propagator, the free time evolution of the eigenstates $\psi_{\tilde{m},\tilde{n}}(x, y)$ suddenly released at time $t = 0$ is given by [1,2]

$$\psi_{\tilde{m},\tilde{n}}(x, y, t) = \frac{m}{2\pi i\hbar t}\int_{-a/2}^{a/2} dy' \int_{-a/2}^{a/2} dx' \psi_{\tilde{m},\tilde{n}}(x', y') \times \exp\left\{\frac{im}{2\hbar}\frac{[(x - x')^2 + (y - y')^2]}{t}\right\}. \quad (2)$$

Substituting Eq. (1) into (2), after some algebra, the wave function $\psi_{\tilde{m},\tilde{n}}(x, y, t)$ is given by

$$\psi_{\tilde{m},\tilde{n}}(x, y, t) = \frac{e^{-(i/\hbar)E_{\tilde{m},\tilde{n}}t}}{4i^3 a}[G(x, t; k_{\tilde{m}}, a) - G(x, t; -k_{\tilde{m}}, a)] \times [G(y, t; k_{\tilde{n}}, a) - G(y, t; -k_{\tilde{n}}, a)], \quad (3)$$

with

$$G(x, t; k_{\tilde{m}}, a) = e^{ik_{\tilde{m}}(x+a/2)}[F(\xi(x - a/2, t; k_{\tilde{m}})) - F(\xi(x + a/2, t; k_{\tilde{m}}))], \quad (4)$$

where $E_{\tilde{m},\tilde{n}} = \hbar^2(k_{\tilde{m}}^2 + k_{\tilde{n}}^2)(2m)$, $F(\xi)$ is the complex Fresnel integral, $F(\xi) = \int_0^{\xi} \exp(i\pi u^2/2)du$, and the integral's argument is given by $\xi(x, t; k) = \sqrt{m(\pi\hbar t)}[(\hbar k t/m) - x]$. Figures 1(a)–1(f) depict the numerical results calculated with Eq. (3) and the parameters of $(\tilde{m}, \tilde{n}) = (25, 25)$ to illustrate the wave patterns $|\psi_{\tilde{m},\tilde{n}}(x, y, t)|^2$ at $t = 0, 0.1T$,

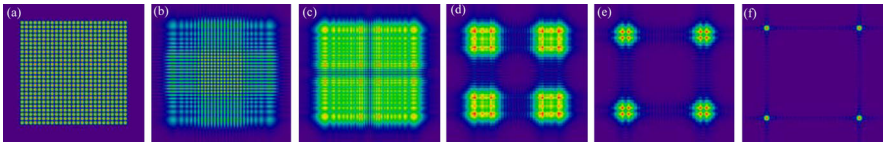

FIG. 1 (color online). Numerical patterns calculated with Eq. (3) and the parameters of $(\tilde{m}, \tilde{n}) = (25, 25)$ to illustrate the wave patterns $|\psi_{\tilde{m},\tilde{n}}(x, y, t)|^2$ at (a) $t = 0$, (b) $0.1T$, (c) $0.25T$, (d) $0.50T$, (e) $1.0T$, and (f) ∞, where T is defined in the text.

$0.25T$, $0.50T$, $1.0T$, and ∞, where $T = 2ma/\hbar k_{\tilde{m}}$ corresponds to the round trip time of the wave in the x direction. The time-evolution wave distributions clearly exhibit strong interference patterns in the time interval between $0.1T$ and T. Note that the wave function $\psi_{\tilde{m},\tilde{n}}(x, y, t)$ in an infinite time is just the Fourier transform of the initial wave function $\psi_{\tilde{m},\tilde{n}}(x, y)$, corresponding to the momentum-space representation. Therefore, the four-lobed beam pattern in Fig. 1(f) reveals the momentum distribution.

The results of recent studies of open square quantum dots show that the wave functions localized on classical periodic orbits are not only the persistent states but also are associated with the striking phenomena of conductance fluctuations [14–16]. The primitive periodic orbits in a 2D square billiard can be described with three parameters (p, q, ϕ), where p and q are two positive integers describing the number of collisions with the horizontal and vertical walls, and the phase factor ϕ is in the range of $-\pi$ to π that is related to the wall positions of specular reflection points [19]. Recently, we have employed the representation of SU(2) coherent states to analytically establish the relation between the quantum wave functions and the classical periodic orbits. As in the Schwinger SU(2) representation, the wave functions associated with periodic orbits (p, q, ϕ) is analytically expressed as $\Psi_{N,M}^{p,q,\phi}(x, y) = \sum_{K=-M}^{M} C_{M,K} e^{iK\phi} \psi_{qN+pK,pN-qK}(x, y)$, where N represents the order of the coherent state and

$$C_{M,K} = 2^{-M}\left[\frac{2M!}{(M-K)!(M+K)!}\right]^{1/2}$$

is the weighting coefficient. Note that the discussion for the asymptotic property of the coherent states can be found in Ref. [19].

The free time evolution of the coherent states $\Psi_{N,M}^{p,q,\phi}(x, y)$ suddenly released at time $t = 0$ can be expressed as $\Psi_{N,M}^{p,q,\phi}(x, y, t) = \sum_{K=-M}^{M} C_{M,K} e^{iK\phi} \times \psi_{qN+pK,pN-qK}(x, y, t)$. Note that the coherent states $\Psi_{N,M}^{p,q,\phi}(x, y)$ behave as the traveling waves in the transverse plane. The standing-wave representation is given by $S_{N,M}^{p,q,\pm\phi}(x, y) = [\Psi_{N,M}^{p,q,\phi}(x, y) \pm \Psi_{N,M}^{p,q,-\phi}(x, y)]/\sqrt{2}$. As a result, the time evolution of the coherent states $S_{N,M}^{p,q,\pm\phi}(x, y)$ suddenly released at time $t = 0$ can be expressed as $S_{N,M,\pm}^{p,q,\phi}(x, y, t) = [\Psi_{N,M}^{p,q,\phi}(x, y, t) \pm \Psi_{N,M}^{p,q,-\phi}(x, y, t)]/\sqrt{2}$. Figures 2(a)–2(f) illustrate the numerical patterns for the wave patterns $|S_{N,M,+}^{p,q,\phi}(x, y, t)|^2$ with the parameters of $(p, q) = (1, 1)$, $(N, M) = (42, 6)$, and $\phi = 0.6\pi$ at $t = 0$, $0.08T$, $0.15T$, $0.25T$, $0.5T$, and ∞, where $T = 2ma/\hbar k_N$ corresponds to the round trip time of the periodic orbit and $k_N = N\pi/a$. It can be seen that the transient dynamics of the coherent state displays not only the feature of classical flow but also the salient interference patterns.

Similarities between paraxial optics and nonrelativistic quantum mechanics have long been recognized and recently been used to make analog studies of quantum wave functions [20]. This correlation has been used to manifest the spatial morphology of wave functions [21] and energy-level statistics [22] in 2D quantum billiards with the oxide-confined vertical-cavity surface-emitting lasers (VCSELs). The literatures [23] revealed that the chessboardlike patterns of the eigenstates $\psi_{\tilde{m},\tilde{n}}(x, y)$ could be similarly generated with the lasing modes from phase-coupled VCSEL arrays or photonic resonator crystals. In addition to resonant stationary states, the free time evolution of quantum wave functions can be expressed as an analogous way to the free-space propagation of coherent lights. However, the free-space propagation of the lasing modes had not been investigated. Here we use the coherent lasing modes generated from the large-aperture VCSELs to experimentally investigate the time evolution of the coherent state.

Schematics of the laser device structure and the experimental setup are shown in Fig. 3. The separability of the wave function in the VCSEL device enables the wave vectors to be decomposed into k_z and k_t, where k_z is the wave-vector component along the direction of vertical emission and k_t is the transverse wave-vector component. Under the circumstance of paraxial optics, $k_t \ll k_z$, the longitudinal field is significantly small in comparison with the transverse field. Therefore, the electric field can be

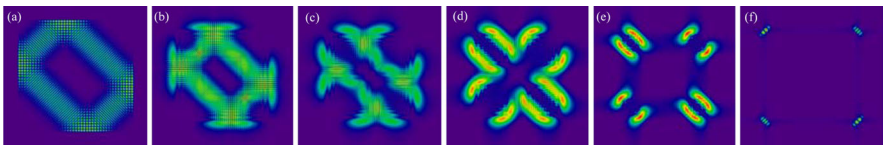

FIG. 2 (color online). Numerical patterns for the wave patterns $|S_{N,M,+}^{p,q,\phi}(x, y, t)|^2$ with the parameters of $(p, q) = (1, 1)$, $(N, M) = (42, 6)$, and $\phi = 0.6\pi$ at (a) $t = 0$, (b) $0.08T$, (c) $0.15T$, (d) $0.25T$, (e) $0.5T$, and (f) ∞, where T is defined in the text.

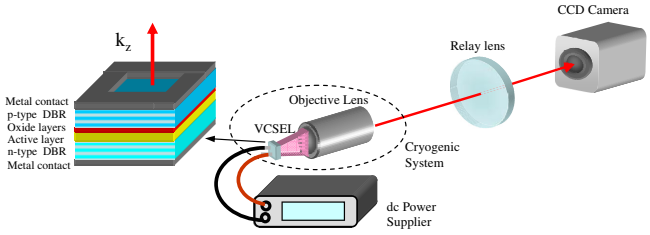

FIG. 3 (color online). Schematics of the laser device structure and the experimental setup. (DBR is distributed Bragg reflector.)

approximated to have only transverse components and no longitudinal component, i.e., so-called quasi-TEM waves. After separating the z component in the wave equation, we are left with a two-dimensional Helmholtz equation: $(\nabla_t^2 + k_t^2)\psi(x, y) = 0$, where ∇_t^2 means the Laplacian operator operating on the coordinates in the transverse plane and $\psi(x, y)$ is a scalar wave function that describes the transverse distribution of the laser mode. Consequently, the transverse modes of the oxide-confined VCSEL device are equivalent to the eigenfunctions of the 2D Schrödinger equation with hard wall boundaries of the same geometry. The vertical cavity is formed by two distributed Bragg reflectors and its optical length is designed to be nearly one wavelength. The resonant optical wave emitted from the cavity end $z = 0$ to the environment in the direction of the $+z$ axis can be expressed as the Fresnel transformation:

$$\psi(x, y, z) = \frac{ie^{-ikz}}{\lambda z} \int dy' \int dx' \exp\left\{-\frac{ik}{2} \times \frac{[(x - x')^2 + (y - y')^2]}{z}\right\} \psi(x', y'). \quad (5)$$

Comparing Eqs. (2) and (5) it is evident that the time evolution of a 2D quantum state is equivalent to the Fresnel transformation of a near-field optical wave with the substitution of $t \rightarrow z$ and $m/\hbar \rightarrow 2\pi/\lambda$, where λ is the lasing wavelength.

First we used square-shaped VCSELs with 40 μm oxide aperture to explore the free-space propagation of coherent modes. The VCSEL devices were placed in a cryogenic system with a temperature stability of 0.1 K at the range of 80–300 K. A current source with a precision of 0.01 mA was utilized to drive the VCSEL device. The transverse patterns at different propagation distances were reimaged onto a CCD camera with a very large numerical aperture (NA) microscope objective lens (Mitsutoyo, NA = 0.9) mounted on a translation stage.

Although an ideal 2D square billiard has many possible eigenstates, the coherent states related to classical periodic orbits with $(p, q) = (1, 1)$ are experimentally found to be the persistent states at the temperature below 260 K. Figure 4(a) shows the near-field pattern of the lasing mode at $T = 260$ K. The experimental transverse patterns for the free-space propagation are shown in Figs. 4(b)–4(e) measured at the positions of $z/z_d = 0.08$, 0.2, 0.35, and 0.70, respectively, where $z_d = 2ak_z/nk_t$ is the characteristic length and n is the refractive index of the semiconductor cavity. Note that the characteristic length of the optical diffraction is analogous to the characteristic time T of the quantum diffraction in time. With the properties that $k_z = 26.3\ \mu\text{m}^{-1}$, $a = 40\ \mu\text{m}^{-1}$, $n = 3.5$, and $k_t = 4.2\ \mu\text{m}^{-1}$, z_d can be found to be approximately 143 μm. Figure 4(f) depicts the far-field pattern which was measured by a digital camera for the direct projection of the laser beam on a paper screen at a distance of ~20 cm from the laser device. It can be seen that the experimental patterns agree quite well with the numerical results shown in Fig. 2. The good agreement validates the fact that the free-space propagation of coherent modes emitted from VCSELs can be employed as an analogous observation of the time evolution of quantum-billiard wave functions.

Next we exploit a deformed-square-shaped VCSEL with a ripple boundary to experimentally study the transient dynamics of the wave functions released from 2D chaotic billiard systems. With a ripple boundary, the experimental near-field patterns are found to be randomly distributed over the laser cavity, i.e., so-called chaotic wave modes. Note that rough billiards and related systems are also of considerable interest elsewhere [24]. Figures 5(a)–5(e) depict the experimental transverse patterns obtained at the near-field position and $z/z_d = 0.25$, 0.4, and 0.6, and the far-field regime, respectively. It can be seen that the transverse patterns in the propagation position between $0.1z_d$ and $1.0z_d$ display a striking feature of random branching behavior with the appearance of intricate interference fringes.

It has been shown that the universal features of stationary chaotic wave functions in quantum billiards can be manifested with a superposition of plane waves of fixed wave-vector magnitude with random amplitude, phase, and direction [25]. Therefore, the standing-wave chaotic wave functions in a deformed square-shaped quantum billiard

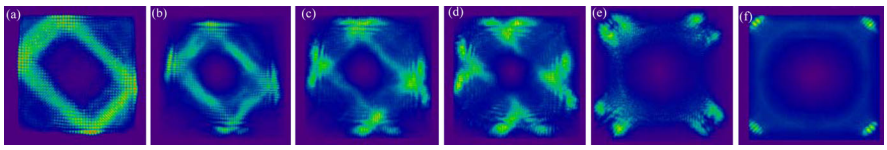

FIG. 4 (color online). Experimental transverse patterns for the free-space propagation of the coherent lasing mode measured at the positions of (a) near field, (b) $z/z_d = 0.08$, (c) $z/z_d = 0.2$, (d) $z/z_d = 0.35$, (e) $z/z_d = 0.70$, (f) far field, where z_d is defined in the text.

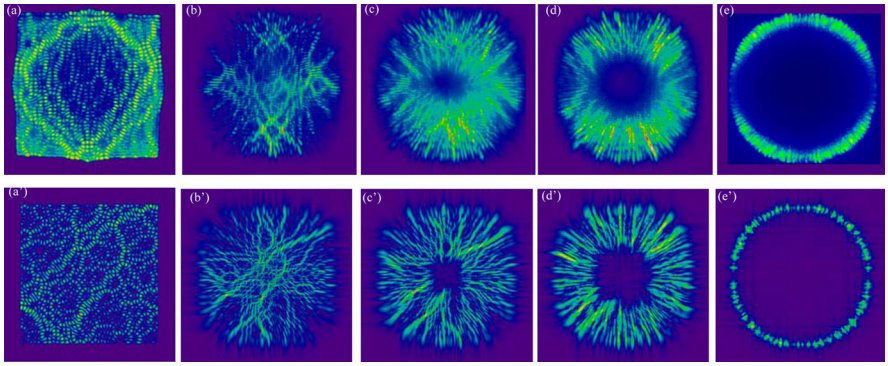

FIG. 5 (color online). Experimental transverse patterns for the free-space propagation of the chaotic mode measured at the positions of (a) near field, (b) $z/z_d = 0.25$, (c) $z/z_d = 0.4$, (d) $z/z_d = 0.6$, (e) far field, where z_d is defined in the text. (a′)–(e′) Numerical patterns calculated with $\Psi(x, y, t) = \sum_{\tilde{m},\tilde{n}} \cos(\phi_{\tilde{m},\tilde{n}}) \psi_{\tilde{m},\tilde{n}}(x, y, t)$ for the time at $t = 0$, $0.25T$, $0.4T$, $0.6T$, and ∞, respectively, where $49^2 < \tilde{m}^2 + \tilde{n}^2 < 51^2$ and $\phi_{\tilde{m},\tilde{n}}$ are random values.

can be described as $\Psi(x, y) = \sum_{\tilde{m},\tilde{n}} \cos(\phi_{\tilde{m},\tilde{n}}) \psi_{\tilde{m},\tilde{n}}(x, y)$, where the eigenstates $\psi_{\tilde{m},\tilde{n}}(x, y)$ in the summation are subject to the condition that the values $\sqrt{k_{\tilde{m}}^2 + k_{\tilde{n}}^2}$ are nearly constant and the phase factors $\phi_{\tilde{m},\tilde{n}}$ are random. With the superposition principle, the free time evolution of the chaotic wave $\Psi(x, y)$ is then given by $\Psi(x, y, t) = \sum_{\tilde{m},\tilde{n}} \cos(\phi_{\tilde{m},\tilde{n}}) \psi_{\tilde{m},\tilde{n}}(x, y, t)$. We use this expression for the states $\psi_{\tilde{m},\tilde{n}}(x, y, t)$ in the range of $49^2 < \tilde{m}^2 + \tilde{n}^2 < 51^2$ and random values for $\phi_{\tilde{m},\tilde{n}}$ to numerically generate typical wave patterns which are shown in Figs. 5(a′)–5(e′) at $t = 0$, $0.25T$, $0.4T$, and ∞. The general features of the numerical patterns are clearly similar to the experimental observation shown in Figs. 5(a)–5(e). Therefore, the free-space propagation of the chaotic modes emitted from VCSELs can be used to manifest the transient dynamics of the chaotic wave functions in quantum billiards.

In conclusion, we have analytically and numerically investigated the diffraction-in-time effect of the eigenstates and coherent states suddenly released from a square quantum billiard. We have utilized the large-aperture VCSEL devices to experimentally verify that the transient dynamics of quantum-billiard wave functions can be analogously observed with the free-space propagation of the coherent lasing modes. Moreover, we have exploited a chaotically shaped laser cavity to originally study the diffraction-in-time characteristics of the chaotic wave functions. The transient wave patterns of chaotic modes are found to display a striking feature of random branching interference fringes. We believe that the present investigation can provide an important insight into quantum physics and wave optics.

This work is supported by the National Science Council of Taiwan (Contract No. NSC-97-2112-M-009-016-MY3).

*yfchen@cc.nctu.edu.tw

[1] M. Moshinsky, Phys. Rev. **88**, 625 (1952).
[2] S. Godoy, Phys. Rev. A **65**, 042111 (2002); M. Kleber, Phys. Rep. **236**, 331 (1994).
[3] E. Granot and A. Marchewka, Europhys. Lett. **72**, 341 (2005).
[4] V. I. Man'ko, M. Moshinsky, and A. Sharma, Phys. Rev. A **59**, 1809 (1999).
[5] A. del Campo, J. G. Muga, and M. Moshinsky, J. Phys. B **40**, 975 (2007).
[6] G. G. Paulus, F. Lindner, H. Walther, A. Baltuška, E. Goulielmakis, M. Lezius, and F. Krausz, Phys. Rev. Lett. **91**, 253004 (2003).
[7] C. E. Wieman, D. E. Pritchard, and D. J. Wineland, Rev. Mod. Phys. **71**, S253 (1999), and references therein.
[8] T. Hils, J. Felber, R. Gähler, W. Gläser, R. Golub, K. Habicht, and P. Wille, Phys. Rev. A **58**, 4784 (1998).
[9] A. Steane, P. Szriftgiser, P. Desbiolles, and J. Dalibard, Phys. Rev. Lett. **74**, 4972 (1995).
[10] F. Lindner, M. G. Schätzel, H. Walther, A. Baltuška, E. Goulielmakis, F. Krausz, D. B. Milošević, D. Bauer, W. Becker, and G. G. Paulus, Phys. Rev. Lett. **95**, 040401 (2005).
[11] Y. Colombe, B. Mercier, H. Perrin, and V. Lorent, Phys. Rev. A **72**, 061601 (2005).
[12] F. Delgado, H. Cruz, and J. G. Muga, J. Phys. A **35**, 10 377 (2002).
[13] F. Delgado, J. G. Muga, D. G. Austing, and G. García-Calderón, J. Appl. Phys. **97**, 013705 (2005).
[14] R. Akis and D. K. Ferry, Phys. Rev. B **59**, 7529 (1999).
[15] I. V. Zozoulenko and K. F. Berggren, Phys. Rev. B **56**, 6931 (1997).
[16] J. P. Bird, R. Akis, D. K. Ferry, D. Vasikska, J. Cooper, Y. Aoyagi, and T. Sugano, Phys. Rev. Lett. **82**, 4691 (1999).
[17] A. del Campo, I. Lizuain, M. Pons, J. G. Muga, and M. Moshinsky, J. Phys. Conf. Ser. **99**, 012003 (2008).
[18] J. Wiersig, Phys. Rev. E **64**, 026212 (2001).
[19] Y. F. Chen, K. F. Huang, and Y. P. Lan, Phys. Rev. E **66**, 046215 (2002).
[20] D. Dragoman and M. Dragoman, *Quantum-Classical Analogies* (Springer-Verlag, Berlin, 2004), and references cited therein.
[21] K. F. Huang, Y. F. Chen, H. C. Lai, and Y. P. Lan, Phys. Rev. Lett. **89**, 224102 (2002); C. C. Chen, C. C. Liu, K. W. Su, T. H. Lu, Y. F. Chen, and K. F. Huang, Phys. Rev. E **75**, 046202 (2007).
[22] T. Gensty, K. Becker, I. Fischer, W. Elsäßer, C. Degen, P. Debernardi, and G. P. Bava, Phys. Rev. Lett. **94**, 233901 (2005).
[23] H. Pier, E. Kapon, and M. Moser, Nature (London) **407**, 880 (2000).
[24] Y. Hlushchuk, L. Sirko, U. Kuhl, M. Barth, and H. J. Stöckmann, Phys. Rev. E **63**, 046208 (2001); N. Savytskyy, O. Hul, and L. Sirko, *ibid.***70**, 056209 (2004).
[25] M. V. Berry, J. Phys. A **10**, 2083 (1977); P. O'Connor, J. Gehlen, and E. J. Heller, Phys. Rev. Lett. **58**, 1296 (1987).

Compact efficient multi-GHz Kerr-lens mode-locked diode-pumped Nd:YVO_4 laser

H. C. Liang, Ross C. C. Chen, Y. J. Huang, K. W. Su, and Y. F. Chen*

Department of Electrophysics, National Chiao Tung University, Hsinchu, Taiwan
yfchen@cc.nctu.edu.tw

Abstract: We demonstrate the compact efficient multi-GHz Kerr-lens mode locking in a diode-pumped Nd:YVO_4 laser with a simple linear cavity without the need of any additional components. Experimental results reveal that the laser system can be characterized in stable single-pulse and multiple-pulse mode-locked operations. With a pump power of 2.5 W, the compact laser cavity produces average output powers greater than 0.8 W with a pulse width less than 10 ps in the range of 2–6 GHz.

OCIS codes: (140.4050) Mode-locked lasers; (190.3270) Kerr effect; (140.3480) Lasers, diode-pumped.

References and links

1. A. García-Cortés, M. D. Serrano, C. Zaldo, C. Cascales, G. Strömqvist, and V. Pasiskevicius, "Nonlinear refractive indices of disordered $NaT(XO_4)_2$ T=Y, La, Gd, Lu and Bi, X=Mo, W femtosecond laser crystals," Appl. Phys. B **91**, 507-510 (2008).
2. A. A. Kaminskii, K. Ueda, H. J. Eichler, Y. Kuwano, H. Kouta, S. N. Bagaev, T. H. Chyba, J. C. Barnes, G. M. A. Gad, T. Murai, and J. Lu, "Tetragonal vanadates YVO_4 and $GdVO_4$ – new efficient $\chi^{(3)}$-materials for Raman lasers," Opt. Commun. **194**, 201-206 (2001).
3. A. A. Kaminskii, H. J. Eichler, H. Rhee, and K. Ueda, "New manifestations of nonlinear $\chi^{(3)}$-laser properties in tetragonal YVO_4 crystal: many-phonon SRS, cascaded self-frequency tripling, and self-sum-frequency generation in blue spectral range with the involving of Stokes components under one-micron picosecond pumping," Laser Phys. Lett. **5**, 804-811 (2008).
4. Y. F. Chen, "Efficient subnanosecond diode-pumped passively Q-switched Nd:YVO_4 self-stimulated Raman laser," Opt. Lett. **29**, 1251-1253 (2004).
5. Y. F. Chen, "High-power diode-pumped actively Q-switched Nd:YVO_4 self-Raman laser: influence of dopant concentration," Opt. Lett. **29**, 1915-1917 (2004).
6. F. Su, X. Y. Zhang, Q. Wang, S. Ding, P. Jia, S. Li, S. Fan, C. Zhang and B. Liu, "Diode pumped actively Q-switched Nd:YVO_4 self-Raman laser," J. Phys. D: Appl. Phys. **39**, 2090-2093 (2006).
7. X. H. Chen, X. Y. Zhang, Q. P. Wang, P. Li, and Z. H. Cong, "Diode-pumped actively Q-switched c-cut Nd:YVO_4 self-Raman laser," Laser Phys. Lett. 1–4 (2008) / DOI 10.1002/lapl.200810093.
8. N. Minkovski, G. I. Petrov, S. M. Saltiel, O. Albert, and J. Etchepare, "Nonlinear polarization rotation and orthogonal polarization generation experienced in a single-beam configuration," J. Opt. Soc. Am. B **21**, 1659-1664 (2004).
9. S. Kourtev, N. Minkovski, S. M. Saltiel, A. Jullien, O. Albert, and J. Etchepare, "Nonlinear mirror based on cross-polarized wave generation," Opt. Lett. **31**, 3143-3145 (2006).
10. A. G. Selivanov, I. A. Denisov, N. V. Kuleshov, and K. V. Yumashev, "Nonlinear refractive properties of Yb^{3+}-doped $KY(WO_4)_2$ and YVO_4 laser crystals," Appl. Phys. B **83**, 61-65 (2006).
11. D. E. Spence, P. N. Kean, and W. Sibbett, "60-fsec pulse generation from a self-mode-locked Ti:sapphire laser," Opt. Lett. **16**, 42-44 (1991).
12. G. P. A. Malcolm and A. I. Ferguson, "Self-mode locking of a diode-pumped Nd:YLF laser," Opt. Lett. **16**, 1967-1969 (1991).
13. K. X. Liu, C. J. Flood, D. R. Walker, and H. M. van Driel, "Kerr lens mode locking a diode-pumped Nd:YAG laser," Opt. Lett. **19**, 1361-1363 (1992).
14. A. Sennaroglu, C. R. Pollock, and H. Nathel, "Continuous wave self-mode-locked operation of a femtosecond Cr^{4+}:YAG laser," Opt. Lett. **19**, 390-392 (1994).
15. Y. Pang, V. Yanovsky, F. Wise, and B. I. Minkov, "Self mode-locked Cr:forsterite laser," Opt. Lett. **18**, 1168-1170 (1993).
16. P. M. W. French, R. Mellish, J. R. Teylor, P. J. Delfyett, and L. T. Florez, "Mode-locked all-solid-state diode-pumped Cr:LiSAF laser," Opt. Lett. **18**, 1934-1946 (1993).
17. P. Li Kam Wa, B. H. T. Chai, and A. Miller, "Self-mode locked Cr^{3+}:$LiCaAlF_6$ laser," Opt. Lett. **17**, 1438-1440 (1992).

#103268 - $15.00 USD Received 27 Oct 2008; revised 24 Nov 2008; accepted 28 Nov 2008; published 5 Dec 2008

18. G. Q. Xie, D. Y. Tang, L. M. Zhao, L. J. Qian, and K. Ueda, "High-power self-mode-locked Yb:Y_2O_3 ceramic laser," Opt. Lett. **32**, 2741–2743 (2007).
19. K. J. Weingarten, M. J. W. Rodwell, and D. M. Bloom, "Picosecond optical sampling of GaAs integrated circuits," IEEE J. Quantum Electron. **24**, 198–220 (1988).
20. R. Ramaswami and K. Sivarajan, *Optical Networks: A Practical Perspective*. (San Mateo, CA: Morgan Kaufmann, 1998).
21. A. Bartels, T. Dekorsky, and H. Kurz, "Femtosecond Ti:sapphire ring laser with 2-GHz repetition rate and its application in time-resolved spectroscopy," Opt. Lett. **24**, 996–998 (1999).
22. J. J. Zayhowski and A. Mooradian, "Single-frequency microchip Nd lasers," Opt. Lett. **14**, 24-26 (1989).
23. G. J. Dixon, L. S. Lingvay, and R. H. Jarman, "Properties of close coupled monolithic, lithium neodymium, tetraphosphate lasers," Proc. SPIE **1104**, 107 (1989).
24. Y. F. Chen, "High-power diode-pumped Q-switched intracavity frequency-doubled Nd:YVO4 laser with a sandwich-type resonator," Opt. Lett. **24**, 1032-1034 (1999).

1. Introduction

The third-order nonlinear optical responses are closely related to the stimulated Raman scattering (SRS) process and the Kerr-lensing effect [1]. Yttrium vanadate crystals (YVO_4) were recently predicted to be promising Raman-active materials for a wide range of pump pulse durations from picoseconds to nanoseconds [2,3]. More recently, diode-pumped passively and actively Q-switched Nd:YVO_4 self-stimulated Raman lasers have been efficiently demonstrated [4-7]. Realization of the self-SRS laser operation elucidates that the tetragonal YVO_4 crystal possesses a considerable nonlinear refractive index. Experimental results revealed that third-order nonlinearity of YVO_4 crystal is significantly larger than that of BaF_2 crystal by a factor of (8.2 ± 2.1) [8]. The magnitude of the nonlinear refractive index is directly proportional to the strength of self-focusing effect that determines the capability for efficient Kerr-lens mode locking (KLM). As a consequence, the YVO_4 crystal is possible to be a promising host crystal for efficient self-starting KLM operation [9,10].

In addition to Ti:sapphire [11], lasers with KLM have been reported in materials such as Nd:YLF [12], Nd:YAG [13], Cr:YAG [14], Cr:forsterite [15], Cr:LiSAF [16], Cr:LiCAF [17], and Yb:Y_2O_3 [18]. However, from a review of the available literature, it appears that so far there has been no work on self-mode locked lasers based on Nd:YVO_4 crystals. Here, for what is believed to be the first time, a continuous-wave (CW) self-sustained mode-locked operation in a Nd:YVO_4 laser is reported. We experimentally demonstrate that a CW self-mode locking with multi-gigahertz (GHz) oscillations can be straightforwardly achieved in a Nd:YVO_4 laser with a simple linear cavity without the need of any additional components. With an incident pump power of 2.5 W, the compact laser cavity, operating in the range of 2-6 GHz, produces average output powers greater than 0.8 W with a pulse width as short as 7.8 ps. When the mode-locked repetition rate is significantly lower than 2 GHz, a single pulse per round trip was usually observed to split into several pulses. Since there is increasing interesting in multi-GHz mode-locked lasers for many applications such as high-speed electro-optic sampling, telecommunications, and optical clocking [19-21], the prospect of high-frequency self-mode-locked Nd:YVO_4 lasers is practically desirable.

2. Experimental setup

A schematic of the laser experiment is shown in Fig. 1. The cavity configuration is a simple flat-flat resonator. This concept was found nearly simultaneously by Zayhowski and Mooradian [22] and by Dixon *et al* [23]. A linear flat–flat cavity is an attractive design because it reduces complexity and makes the system compact and rugged. The active medium is *a*-cut 0.2 at.% Nd:YVO_4 crystal with a length of 10 mm. One facet of the laser crystal was normal to the crystal axis and was high-reflection coated at 1064 nm (>99.8%) and high-transmission coated at 808 nm. The second facet was antireflection coated at 1064 nm and wedged 0.5^o to suppress the Fabry-Perot etalon effect. The laser crystal was wrapped with indium foil and mounted in a water-cooled copper holder. The water temperature was maintained around 20 °C to ensure stable laser output. A flat wedged output coupler with 15% transmission at 1064 nm was used throughout the experiment. The pump source was a 3-W

#103268 - $15.00 USD Received 27 Oct 2008; revised 24 Nov 2008; accepted 28 Nov 2008; published 5 Dec 2008

808-nm fiber-coupled laser diode with a core diameter of 100 μm and a numerical aperture of 0.16. Focusing lens with 5 mm focal length and 85% coupling efficiency was used to re-image the pump beam into the laser crystal. The average pump radius was approximately 70 μm.

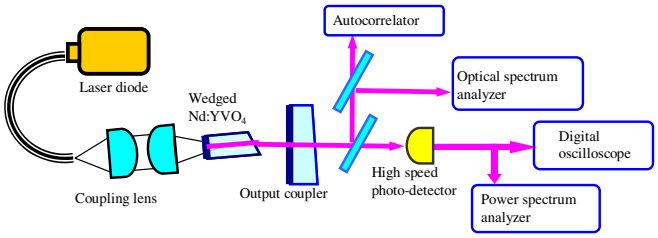

Fig. 1. Experimental setup for a diode-pumped self-mode locked Nd:YVO_4 laser.

The optical cavity length was varied between 16 cm and 2.5 cm with the corresponding free spectral range (FSR) between 0.935 GHz and 6.0 GHz. The mode-locked pulses were detected by a high-speed InGaAs photodetector (Electro-optics Technology Inc. ET-3500 with rise time 35 ps), whose output signal was connected to a digital oscilloscope (Agilent DSO 90000) with 10 GHz electrical bandwidth and a sampling interval of 25 ps. At the same time, the output signal of the photodetector was analyzed by an RF spectrum analyzer (Advantest, R3265A) with a bandwidth of 8.0 GHz. The spectral information of the laser was monitored by an optical spectrum analyzer (Advantest Q8381A). The spectrum analyzer, which employs a diffraction lattice monochromator, can be used for high-speed measurement of pulse light with a resolution of 0.1 nm.

The cavity mode size in the gain medium is given by [24]

$$\omega_l = \sqrt{\frac{\lambda}{\pi}} \frac{(L f_{th})^{1/4}}{(1 - L/f_{th})^{1/4}} \tag{1}$$

where f_{th} is the effective focal length of the thermal lens and L is the effective cavity length. Note that the difference between the effective cavity length L and the optical cavity length L_{opt} is given by $L_{opt} - L = l(n-1/n)$, where l is the length of the gain medium and n is the refractive index of the gain medium. The effective focal length for an end-pumped laser rod can be approximately expressed as $f_{th} = C\omega_p^2 / P_{in}$, where ω_p is the average pump radius in the unit of mm, P_{in} is the incident pump power in the unit of watt (W), and C is a proportional constant in the unit of W/mm. The effective focal length at a given pump power can be experimentally estimated from the longest cavity length with which a flat-flat cavity can sustain stable. Therefore, we perform the laser experiments to obtain the critical cavity lengths for different pump powers at a fixed pump size. We fitted the experimental results and found the constant C to be approximately 6.5×10^4 W/mm. Figure 2 shows the cavity mode size as a function of the optical cavity length for three different pump powers. The cavity mode sizes were calculated with the parameters of $C = 6.5\times10^4$ W/mm, $\omega_p = 0.07$ mm, n=2.18, and l = 10 mm. The cavity mode size can be seen to be generally smaller than 0.2 mm for the optical cavity length shorter than 70 mm. On the other hand, the cavity mode size begins to be greater than 0.3 mm for the optical cavity length longer than 150 mm.

Based on the assumption of a parabolic laser-intensity-dependent index variation, the effective Kerr-lens focal length can be given by $f_{kr} = \omega_1^2 / 4 n_2 I_o$, where n_2 is the nonlinear refractive index and I_o is the laser peak intensity. For the present laser cavity, f_{kr} was calculated to be several meters. The mode size change in the laser crystal due to the Kerr self-focusing was estimated to be 0.05–0.2 μm, which could lead to a round-trip diffraction-loss modulation of 10^{-4} –10^{-5}. This loss modulation is sufficient for self-starting of mode locking [18].

#103268 - $15.00 USD Received 27 Oct 2008; revised 24 Nov 2008; accepted 28 Nov 2008; published 5 Dec 2008

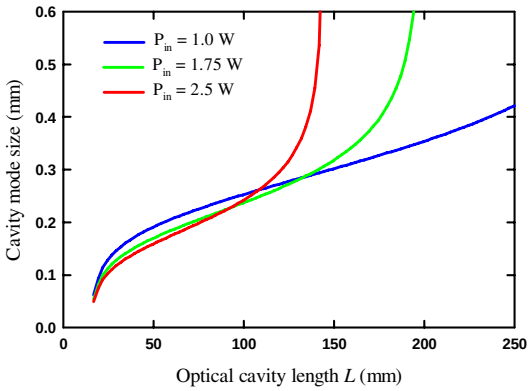

Fig. 2. Cavity mode size as a function of the optical cavity length for three different pump powers.

3. Experimental results and discussions

The optical cavity length was firstly set to be approximately 6.4 cm, corresponding to the FSR of 2.35 GHz. When the cavity alignment was optimized for generating the maximum average output power, the time trace of the output radiation revealed the laser to be in the spontaneous mode-locked state. Figures 3(a) and 3(b) show the pulse trains on two different timescales, one with time span of 10 ns, demonstrating mode-locked pulses, the other with time span of 5 μs, demonstrating the amplitude oscillation. The corresponding power spectrum is shown in Fig. 3(c). Although some amplitude fluctuation exists under the circumstance of the optimum output power, it can be definitely improved with the fine-tuning of the cavity alignment by monitoring the temporal behavior of the pulse train profile and the width of the power spectrum. Figures 4(a)-4(c) show the real-time traces and the power spectrum for the case of minimizing amplitude fluctuation. As shown in Figs. 4(a) and 4(b), the full modulation of pulse trains without any CW background indicates the realization of complete mode locking. Excellent performance on self-mode locking indicates that the YVO_4 crystal is a promising host medium for efficient self-starting KLM operation at GHz oscillations. Experimental results reveal that the relative frequency deviation of the power spectrum, $\Delta\nu/\nu$, is smaller than 5×10^{-5} over day-long operation, where ν is the center frequency of the power spectrum and $\Delta\nu$ is the frequency deviation of full width at half maximum. It is worthwhile to mention that the wedge shape of the laser crystal is vital for obtaining a complete stable mode-locked operation. When a laser crystal without a wedge is used in the flat-flat cavity, the pulse trains exhibit incomplete mode locking with CW background to a certain extent. On the other hand, when an oscilloscope with bandwidth less than 500 MHz is used to measure the present temporal characteristics, the result will display like a pure CW laser. Perhaps this is the reason why the phenomenon of self-mode locking in the range of GHz has not been discovered earlier.

Experimental results reveal that the average output power of the stable continuous-wave mode-locking is approximately 90% of the maximum average output power. Figure 5(a) shows the average output powers versus the incident pump power obtained at a mode-locked frequency of 5.32 GHz with the cavity alignments for maximum output and stable cw mode-locking, respectively. The slope efficiency for the stable mode-locked operation can be seen to be approximately up to 40% with respect to the incident pump power, corresponding to an optical-optical efficiency of 32%. As shown in Fig. 5(b), the FWHM width of the optical spectrum is approximately 0.21 nm around the central wavelength of 1064.3 nm. Figure 5(c) depicts the real-time traces with time span of 1 ns to measure the temporal duration of the mode-locked pulses. The pulse width can be clearly found to be approximately 50 ps (FWHM) from the real-time trace for the mode-locked frequency in the range of 2–6 GHz. However, the pulse duration was measured with a homemade autocorrelator and was found to

#103268 - $15.00 USD Received 27 Oct 2008; revised 24 Nov 2008; accepted 28 Nov 2008; published 5 Dec 2008

be as short as 7.8 ps assuming a Gaussian-shaped temporal intensity profile, as shown in Fig. 5(d). The discrepancy comes from the condition that the impulse response of the present detector has a FWHM of 40 ps and the sampling interval of the present digital oscilloscope is 25 ps. Even though the experimental data shown in Figs. 5(b)-5(c) were obtained at a pump power of 2.5 W, these results were found to be almost the same for the pump power in the range of 0.5–2.5 W. Based on thorough experiments, it was confirmed that the pulse width obtained with the present real-time trace is approximately 40 ps greater than that derived from autocorrelation trace for the ps pulses. Therefore, the present real-time trace is a quick useful estimation for the temporal behavior of the ps mode-locked laser.

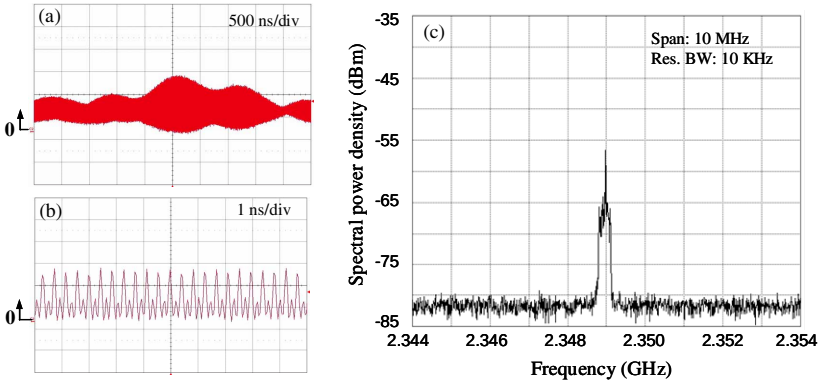

Fig. 3. Pulse trains on two different timescales. (a) time span of 10 ns, demonstrating mode-locked pulses; (b) time span of 5 μs, demonstrating the amplitude oscillation. (c) power spectrum.

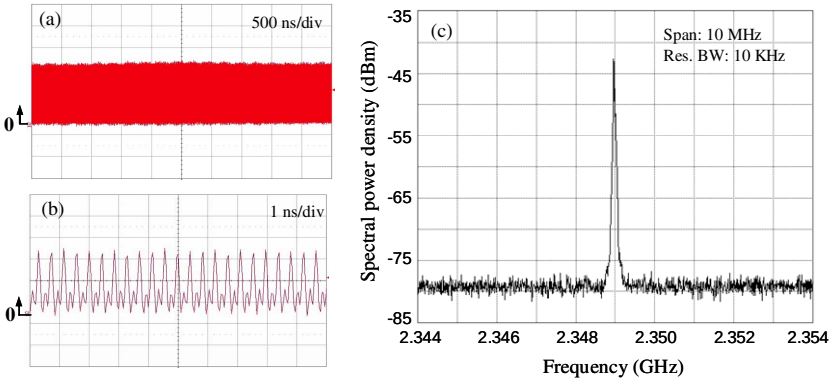

Fig. 4. Same as Fig. 3 for the stable CW mode-locked operation.

We performed the same experimental procedure for different cavity lengths to investigate the influence of the intracavity power intensity on the performance of the mode locking. We found that the laser system can be easily operated in a stable single-pulse mode-locked regime when the cavity length is approximately shorter than 7.5 cm (the mode-locked repetition rate >2 GHz). For the cavity length longer than 8.5 cm, a single pulse per round trip was usually observed to split into several pulses. Figure 6(a) shows the experimental time traces for the cavity length at 11.3 cm; the corresponding optical spectrum is depicted in Fig. 6(b). The interpulse spacing of the stable multiple-pulse state can be found to be associated with the spectral modulation. From Fig. 2, we can conclude that the cavity mode size needs to be smaller than 0.2 μm for a stable single-pulse mode-locked operation.

#103268 - $15.00 USD Received 27 Oct 2008; revised 24 Nov 2008; accepted 28 Nov 2008; published 5 Dec 2008

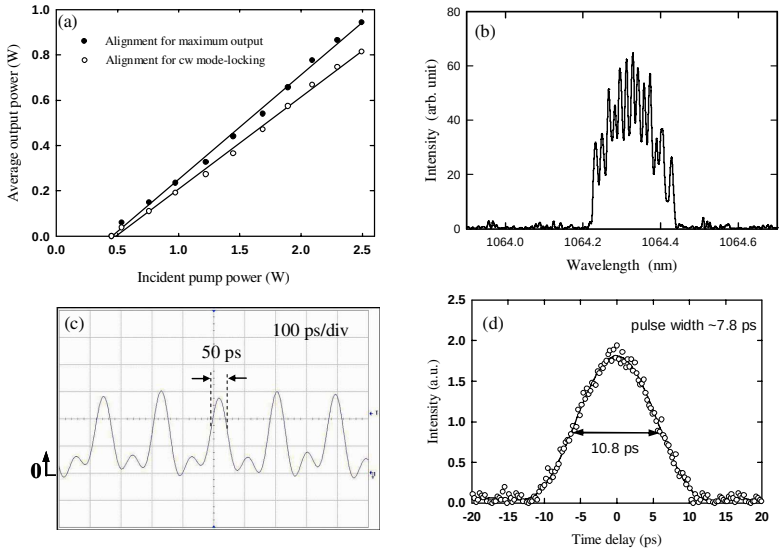

Fig. 5. (a). Average output powers versus incident pump power obtained with the cavity alignments for maximum output and stable CW mode-locking, respectively; (b). corresponding optical spectrum of the mode-locking; (c). mode-locked pulse trains in time span of 1 ns; (d). autocorrelation trace.

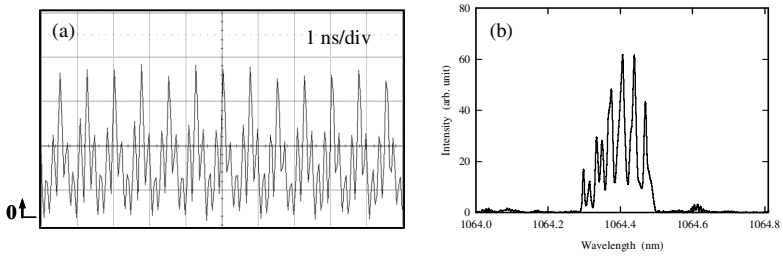

Fig. 6. (a). Experimental time traces for the multiple-pulse mode-locked operation at the cavity length of 11.3 cm (b) corresponding optical spectrum of the mode-locking.

4. Summary

In summary, we have demonstrated a compact efficient CW self-sustained mode-locked operation in the range of several GHz in a Nd:YVO_4 laser with a simple linear cavity without the need of any additional components. We found that the laser system can be operated in stable single-pulse and multiple-pulse mode-locked regimes for the cavity length shorter and longer than approximately 7.5 cm, respectively. At a pump power of 2.5 W, a maximum average output power of 0.8 W was obtained, which gives an optical conversion efficiency of 32%. The pulse width is generally less than 10 ps for the mode-locked frequency of 2-6 GHz. The present KLM performance confirms the large third-order nonlinearity of YVO_4 crystals found in the efficient self-Raman lasers [2-7].

Acknowledgments

The authors also thank the National Science Council for their financial support of this research under Contract No. NSC-97-2112-M-009-016-MY3.

#103268 - $15.00 USD Received 27 Oct 2008; revised 24 Nov 2008; accepted 28 Nov 2008; published 5 Dec 2008

高功率 Q-開關紫外固態雷射的優化與製作

Optimization and Fabrication of High-Power Ultraviolet Q-switched Solid-State Laser

黃郁仁、唐政猷、蘇冠暐、陳永富

Yu-Jen Huang, Cheng-Yu Tang, Kuan-Wei Su, Yung-Fu Chen

高功率紫外光雷射在基礎科學以及產業發展上占有不可或缺的角色。本文將針對高功率 Q-開關紫外固態雷射的優化與製作進行詳細的介紹與探討。我們發現當激發功率越高時，寄生雷射的產生會使得 Q-開關雷射的輸出性能明顯變差，為了有效抑制寄生雷射作用以及克服熱透鏡問題，利用摻釹濃度只有0.1% 的 Nd:YVO_4 晶體設計了一個輕巧簡便的高功率 Q-開關雷射。接著採用此優化的高功率 Q-開關雷射進行腔外二倍頻及三倍頻轉換，在脈衝重複率為 40 kHz 以及輸入功率 44 W 的情況下，532 nm 以及 355 nm 所得到的最高輸出功率分別為 8.38 W 以及 6.65 W。由 808 nm 到 355 nm 的光轉換效率達 15.1%；而由 1064 nm 到 355 nm 的光轉換效率則達 38.2%。

High-power ultraviolet laser plays an important role in a variety of scientific and industrial applications. In this report, optimization and fabrication of high-power ultraviolet Q-switched solid-state laser are introduced and investigated in detail. It is experimentally found that the parasitic lasing leads to the degradation of the actively Q-switched laser in high-power operation. We manifestly confirm that the combined effects of the parasitic lasing and the thermal lensing made Nd:YVO_4 crystals with 0.1% dopant concentration to be more appropriate in designing a high-power Q-switched laser with a flat-flat cavity. We further use the optimized high-power actively Q-switched laser to perform the extra-cavity harmonic generations. At an incident pump power of 44 W, the output powers at 355 nm and 532 nm as high as 6.65 W and 8.38 W are obtained at a pulse repetition rate of 40 kHz. The optical-to-optical conversion efficiencies from 808 nm to 355 nm and from 1064 nm to 355 nm are found to be up to 15.1% and 38.2%, respectively.

一、前言

近年來紫外 (ultraviolet, UV) 光源在快速成型技術 (rapid prototyping)、雷射列印 (laser printing)、雷射加工 (laser processing)、光譜學 (spectroscopy)、光資訊儲存 (optical data storage) 以及醫學治療 (medical treatment) 等基礎科學與產業應用上占有不可或缺的角色。相較於其他種類的 UV 雷射，利用雷射二極體激發固態雷射 (laser-diode-pumped solid-state laser) 進行腔外非線性頻率

轉換 (extra-cavity nonlinear frequency conversion) 的方式具有許多優點，例如：更小的聚焦尺寸、更高的轉換效率、更長的生命週期、更高的穩定性、更小的系統尺寸，以及易於操作的方便性等[1-2]。一般來說，要利用腔外非線性頻率轉換的方式來得到 UV 雷射，最常見的做法是將原本落在紅外波段的基頻光 (fundamental beam) 先進行二倍頻轉換 (second harmonic generation)，再由剩餘的基頻光與二倍頻光進行和頻作用 (sum frequency generation) 得到三倍頻光 (third harmonic generation)。以目前廣為流行的摻釹釩酸釔 (Nd:YVO_4) 為例，其基頻光波段為 1064 nm，進行二倍頻轉換後得到 532 nm 的二倍頻光，再將殘餘的 1064 nm 與 532 nm 利用和頻作用就可以得到 355 nm 的 UV 雷射光。而要有效率地完成非線性頻率轉換，通常空間上需藉由聚焦鏡將基頻光聚焦在非線性晶體 (nonlinear crystal) 裡；而時間上則需藉由時間調制元件 (time modulation) 得到相當高尖峰功率的基頻光。以後者而言，由於聲光 (acousto optic, AO) 晶體的損耗低 (low-insertion loss)、穩定性高 (high stability)、時序抖動低 (low timing jitter)，因此非常適合用於製造高脈衝重複率 (pulse repetition rate) 以及高尖峰功率的主動式 Q-開關固態雷射 (actively Q-switched solid-state laser)，完成高效率的腔外非線性頻率轉換。

本文將針對高功率 Q-開關紫外固態雷射的優化與製作進行詳細的介紹與探討。首先利用一顆雷射二極體作為激發光源，並且利用簡單的平平共振腔架構 (flat-flat cavity) 進行腔外三倍頻轉換，得到了 2.5 W 的 UV 雷射。接著利用兩顆雷射二極體作為激發光源，期望能得到更高且更有效率的 UV 雷射。然而，我們發現當激發功率越高時，寄生雷射 (parasitic lasing) 的產生會使得 Q-開關雷射的輸出性能明顯變差：寄生雷射使得 Q-開關脈衝波形帶有一條長長的尾巴，導致 Q-開關雷射的尖峰功率下降。我們發現在沒有寄生雷射作用下的臨界腔長隨著激發功率的增加而增加。同時實驗數據以及理論分析顯示，利用摻雜濃度高於 0.2% 的 Nd:YVO_4 很難完成一個沒有寄生雷射的 Q-開關雷射。因此使用 0.1% 的 Nd:YVO_4 設計了一個輕巧簡便的高功率 Q-開關雷射，並且利用此優化的高功率 Q-開關雷射進行腔外三倍頻轉換得到了高達 6.65 W 的 UV 雷射。由 808 nm 至 355 nm 以及 1064 nm 至 355 nm 的光轉換效率分別高達 15.1% 以及 38.2 %。

二、單端激發之 Q-開關紫外固態雷射

1. 實驗架構

圖 1 為單端激發 (single-end-pumped) Q-開關固態雷射的系統架構圖。前鏡 (front mirror) 的輸入面鍍有 808 nm 的抗反射膜 (antireflection)，而另一面則鍍有 808 nm 的高穿透膜 (high transmission) 以及 1064 nm 的高反射膜 (high reflection)。我們利用摻釹濃度為 0.1% 以及大小為 3 × 3 × 12 mm^3

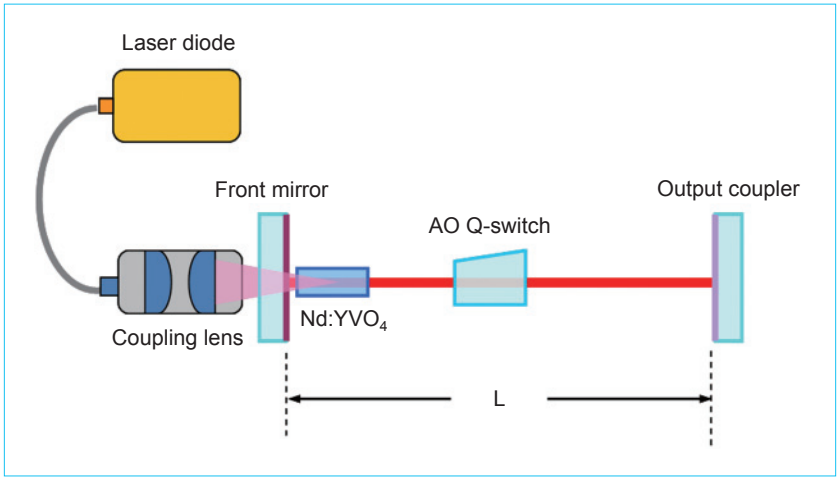

圖 1.
單端激發 Q-開關固態雷射的系統架構圖。

的 Nd:YVO_4 晶體作為增益介質 (gain medium)，並且放置於與前鏡相鄰的位置以方便作端面激發的設計。Nd:YVO_4 的兩面皆鍍有 808 nm 以及 1064 nm 的抗反射膜。為了將熱有效的散除，使用銦箔 (indium foil) 將晶體包裹並將其安裝於溫度為 20 °C 的水冷散熱銅座裡。在共振腔的中央處，放置一個 20 mm 長的聲光晶體，可產生 20 kHz 至 100 kHz 的脈衝重複率。聲光晶體的兩面皆鍍有 1064 nm 的抗反射膜，其中心頻率以及射頻 (radio frequency) 功率分別為 41 MHz 以及 25 W。激發光源的輸出功率為 30 W、中心波長為 808 nm 的光纖耦合雷射二極體 (fiber-coupled laser diode)，光纖的纖芯直徑 (core diameter) 為 600 μm，數值孔徑 (numerical aperture) 為 0.16。激發光束經由一個焦距長 25 mm、耦合效率為 90% 以及放大倍率為 1 的耦合透鏡 (coupling lens) 重新聚焦在晶體上。因此激發光束成像在晶體上的半徑大小約為 300 μm。在實驗中所用的輸出耦合鏡 (output coupler) 在 1064 nm 有著 50% 的穿透率。整個共振腔的腔長大約為 L = 14 cm。脈衝的動態行為是利用高速的矽光偵測器將雷射訊號送到 LeCroy 數位示波器 (WavePro 7100, 10 G samples/s, 1 GHz bandwidth) 進行分析。

2. 基頻光實驗結果

圖 2(a) 及 (b) 為基頻光在脈衝重複率為 40 kHz 時，其輸出功率 (output power)、脈衝寬度 (pulse width)、脈衝能量 (pulse energy) 以及尖峰功率 (peak power) 與激發功率 (incident pump power) 的關係圖。此基頻光雷射的臨界輸入閾值 (threshold) 約為 7 W；當激發功率為 25 W 時，輸出功率達 8.75 W，對應到的光轉換效率 (optical-to-optical conversion efficiency) 為 35%。同時，隨著激發功率由 9.5 W 增加至 25 W，脈衝寬度由 24 ns 縮短至 9 ns。利用下列的關係式：脈衝能量 = 輸出功率／脈衝重複率，尖峰功率 = 脈衝能量／脈衝寬度，可以發現當激發功率由 9.5 W 增加至 25 W 時，脈衝能量由 60 μJ 增加到 220 μJ，尖峰功率則由 2.5 kW 增加至 24.3 kW。圖 3(a) 及 (b) 為激發功率等於 25 W 時，基頻光的輸出功率、脈衝寬度、脈衝能量以及尖峰功率與脈衝重複率的關係圖。當脈衝重複率由 20 kHz 上升至 80 kHz 時，基頻光的輸出功率由 6.46 W 升至 10 W，脈衝寬度由 7 ns 增加至 17 ns，脈衝能量由 323 μJ 下降至 125 μJ，而尖峰功率也由 46.2 kW 變化至 7.35 kW。接下來，將運用此高功率 Q-開關雷射探討腔外二倍頻轉換與三倍頻轉換的效能。

3. 腔外二倍頻轉換及三倍頻轉換的實驗結果

使用三硼酸鋰 (lithium triborate, LBO) 作為二倍頻轉換與三倍頻轉換的非線性晶體，因其具有高損壞閾值 (damage threshold)、較大的容許接收角 (acceptance angle) 以及較小的走離角度 (walk-off angle) 等優點。二倍頻晶體的尺寸大小為 3 × 3 × 15 mm^3 的 LBO，其切角為 $\theta = 90°$、$\phi = 10.4°$，以符合在操作溫度為 46.6 °C 的情況下滿足第一類相位匹配條件 (type-I phase-matching)。二倍頻

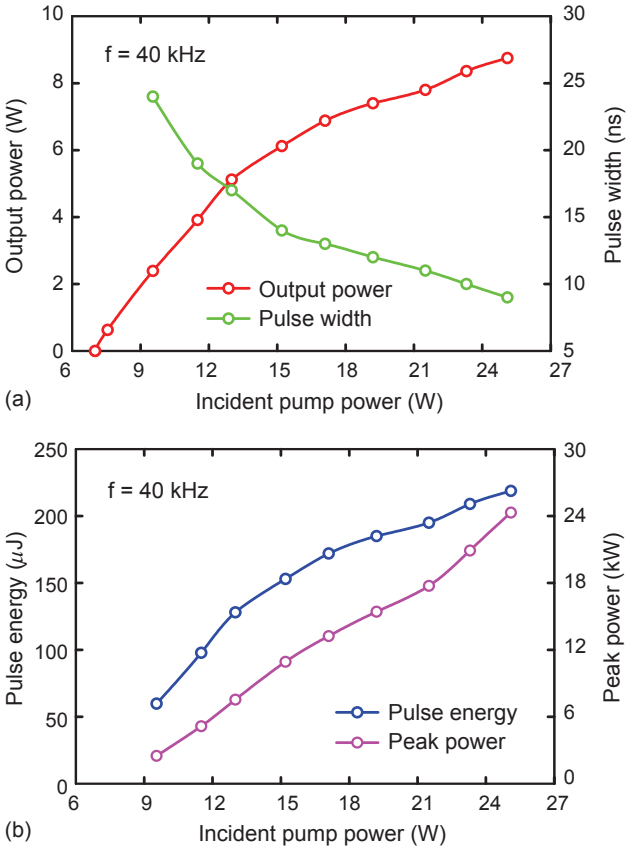

圖 2. 脈衝重複率為 40 kHz 時，其 (a) 輸出功率 (紅色)、脈衝寬度 (綠色)、(b) 脈衝能量 (藍色) 以及尖峰功率 (粉紅色) 與激發功率的關係圖。

晶體的兩端皆鍍有 1064 nm 與 532 nm 的抗反射膜。三倍頻晶體為尺寸大小為 3 × 3 × 10 mm^3 的 LBO，其切角為 $\theta = 44°$、$\phi = 90°$，以符合在操作溫度為 48 °C 的情況下滿足第二類相位匹配條件 (type-II phase-matching)。三倍頻晶體的兩端皆鍍有 1064 nm、532 nm 與 355 nm 的抗反射膜。此兩顆非線性晶體的溫度分別由精度為 0.1 °C 熱電致冷器 (thermoelectric controller) 精準地監控。為了進行有效的非線性頻率轉換過程，我們利用兩個聚焦鏡將雷射光束聚焦於二倍頻晶體以及三倍頻晶體，如圖 4 所示。第一個聚焦鏡的焦距為 38 mm，其兩端皆鍍有 1064 nm 的抗反射膜；而第二個聚焦鏡的焦距為 19 mm，其兩端皆鍍有 1064 nm 和 532 nm 的抗反射膜。實驗中發現 UV 功率最佳化的參數條件為 L_1 = 70 mm、L_2 = 30 mm、L_3 = 25 mm 以及 L_4 = 30 mm。

在激發功率為 25 W 的情況下，圖 5(a) 至 (c) 分別顯示了 532 nm 及 355 nm 的輸出功率、脈衝能量以及尖峰功率與脈衝重複率的關係。值得一提的是，雖然非線性頻率的轉換效率會隨著脈衝重複率的降低而提高，但也必須考慮到基頻光的輸出功率則是隨著頻率的增加而增加。在本實驗中，發現 532 nm及 355 nm 所得到的最大輸出功率是在脈衝重複率為 40 kHz 的情況下，而它們的值分別為 2.82 W 及 2.45 W。因此從 808 nm 到 355 nm 的光轉換效率為 9.8%；而由 1064 nm 至 355 nm 的光轉換效率則為 28.1%。另一方面，在脈衝重複率為 20 kHz 時，532 nm 的最大脈衝能量為 107.35 μJ，而最大尖峰功率則為 15.34 kW。同

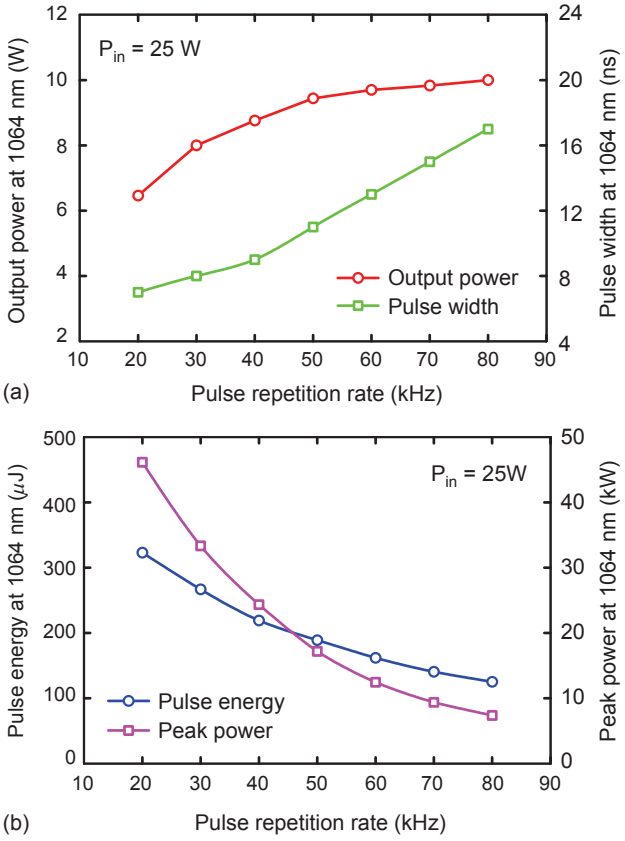

圖 3. 激發功率等於 25 W 時，其 (a) 輸出功率 (紅色)、脈衝寬度 (綠色)、(b) 脈衝能量 (藍色) 以及尖峰功率 (粉紅色) 與脈衝重複率的關係圖。

樣地，在脈衝重複率為 20 kHz 時，355 nm 的最大脈衝能量為 89 μJ，而最大尖峰功率則為 12.71 kW。雖然利用單端激發的架構已經可以得到相當大能量的 UV 雷射，然而工業上還是有許多應用是需要更高功率的 UV 光源。因此接下來將採用雙端激發 (dual-end-pumped) 的架構來提升 UV 雷射的輸出功率。

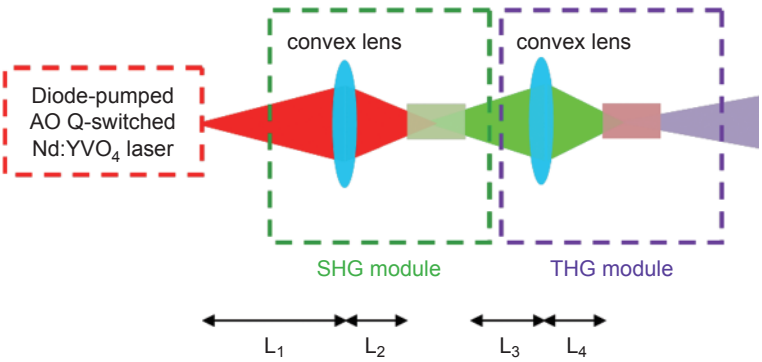

圖 4.
腔外二倍頻與三倍頻轉換的系統架構圖。

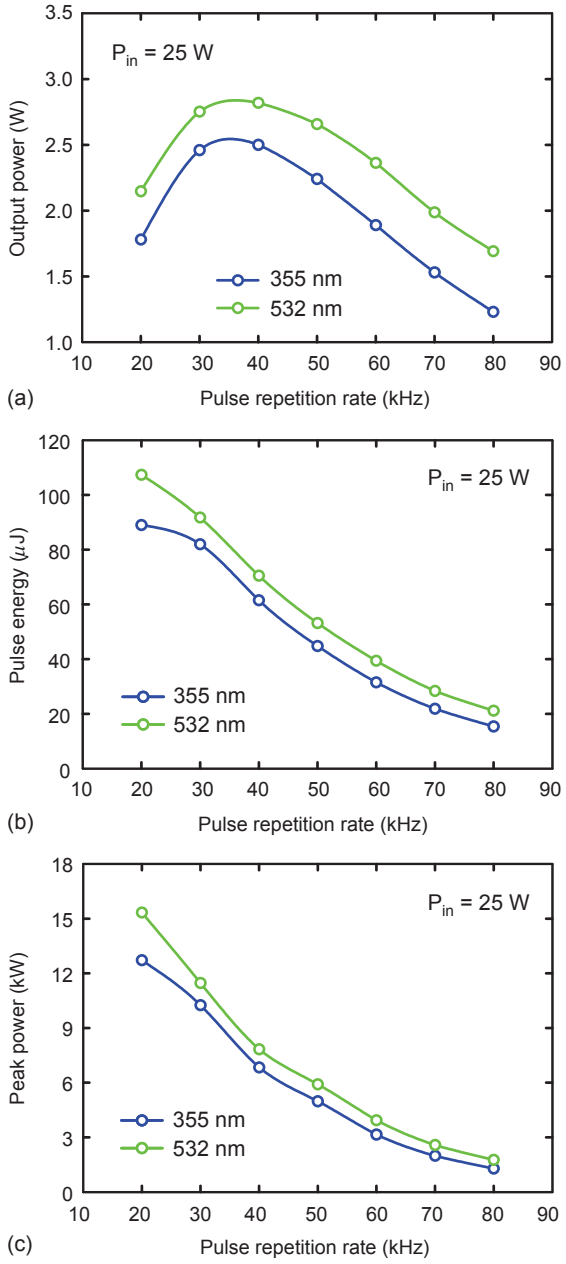

圖 5. 激發功率等於 25 W 時，532 nm (綠色) 與355 nm (藍色)，其 (a) 輸出功率、(b) 脈衝能量以及 (c) 尖峰功率與脈衝重複率的關係圖。

二、雙端激發之 Q-開關紫外固態雷射

1. 寄生雷射效應

雖然聲光晶體可以有效地應用在高脈衝重複率以及高尖峰功率的 Q-開關雷射。然而過去的研究發現，如何在高激發功率的操作下避免寄生雷射效應的產生是非常重要的[3-6]。寄生雷射效應意味著在低 Q 階段 (low-Q stage) 仍有殘餘的受激輻射光子，導致 Q-開關雷射的尖峰功率下降，並降低腔外非線性頻率轉換的輸出效率。雖然說增加共振腔的腔長可以有效地抑制寄生雷射效應，但是這將會導致脈衝寬度的增加；而且為了避免熱透鏡效應的影響，通常需要設計一個較為複雜的實驗架構來完成穩定的 Q-開關雷射操作。因此，如何設計一輕巧簡便的高功率 Q-開關雷射並且能夠有效地抑制寄生雷射效應是一個相當重要的研究課題。

2. 實驗架構

圖 6 為雙端激發 Q-開關固態雷射的系統架構圖。前鏡的輸入面鍍有 808 nm 的抗反射膜，而另一面則鍍有 808 nm 的高穿透膜以及 1064 nm 的高反射膜。轉折鏡 (folded mirror) 的鍍膜特性與前鏡相同，只是針對的入射光角度為 45°。我們利用摻釹濃度為 0.1% 及大小為 3 × 3 × 14 mm^3 的 Nd:YVO_4 晶體作為增益介質，其兩面皆鍍有 808 nm 及 1064 nm 的抗反射膜。為了將熱有效地散除，則使用銦箔將晶體包裹並將其安裝於溫度為

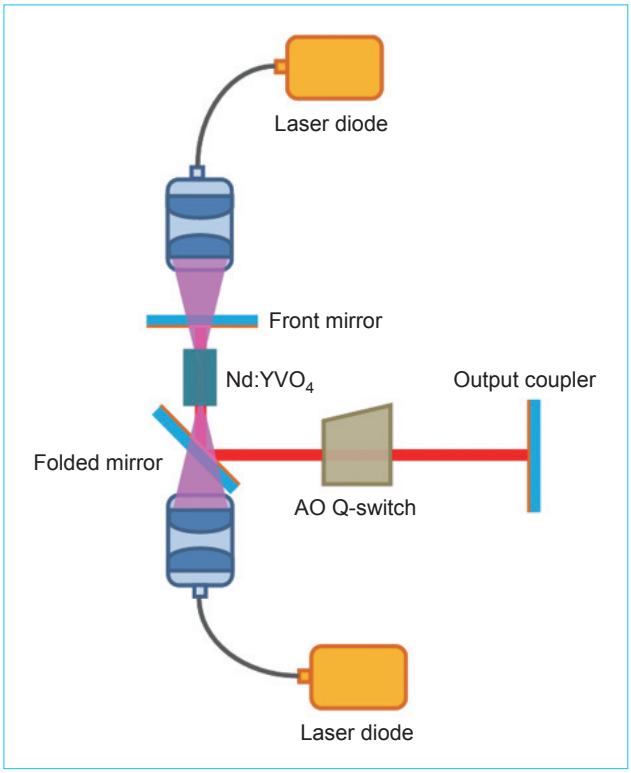

圖 6. 雙端激發 Q-開關固態雷射的系統架構圖。

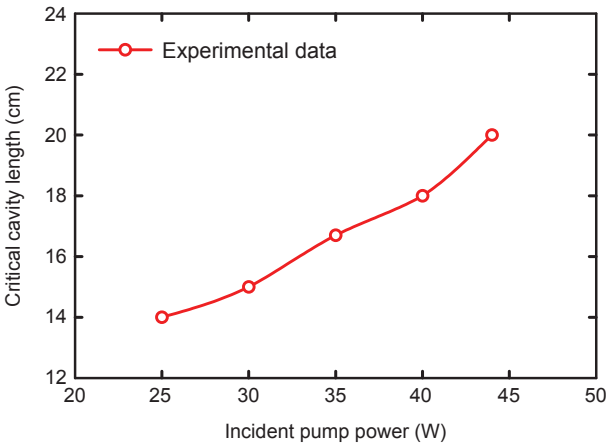

圖 7. 臨界腔長與激發功率的關係圖。

18 °C 的水冷散熱銅座裡。在共振腔的中央處，放置一個 20 mm 長的聲光晶體，其特性與單端激發架構中所用的皆相同。激發光源為兩顆輸出功率分別為 25 W、中心波長為 808 nm 的光纖耦合雷射二極體，光纖的纖芯直徑為 800 μm，數值孔徑為 0.16。激發光束分別經由一個焦距長 25 mm、耦合效率為 88 % ，以及放大倍率為 1 的耦合透鏡重新聚焦在晶體上。因此最大的激發光源功率大約為 44 W。在實驗中所用的輸出耦合鏡在 1064 nm 有著 50% 的穿透率。

3. 高功率 Q-開關雷射的優化：實驗結果與理論分析

由於寄生雷射效應在低 Q 階段可以利用共振腔長度的增加而完全抑制，所以定義了在無寄生雷射效應下的最短腔長為臨界腔長 (critical cavity length)。圖 7 為臨界腔長與隨不同激發功率的實驗關係圖。我們可以發現在無寄生雷射作用下的臨界腔長會因為激發功率的增加而增加。更重要的是，在實驗中發現寄生雷射效應嚴重地影響 Q-開關脈衝的動態行為。圖 8(a) 與 (b) 分別顯示當腔長為 16 cm 及 18 cm 的情況下，在最大輸入功率等於 44 W 時，寄生雷射作用對於 Q-開關脈衝波形的影響。可看出 Q-開關脈衝波形伴隨著一條長尾巴或是殘餘脈衝 (satellite pulse)。相反地，無寄生雷射作用下的 Q-開關脈衝波形，就只有一條短尾巴以及沒有殘餘脈衝的產生，如圖 8(c) 與 (d) 所示，其腔長分別等於 20 cm 與 22 cm。

Q-開關脈衝因寄生雷射效應而產生的長尾巴就意味著尖峰功率的降低。尖峰功率降低的程度可以簡單地由速率方程式 (rate equation) 來分析。假設由寄生雷射作用所造成的平均光子密度為 ϕ_b，則在低 Q 階段下，居量反轉密度 n (population inversion density) 的速率方程式可以表示成：

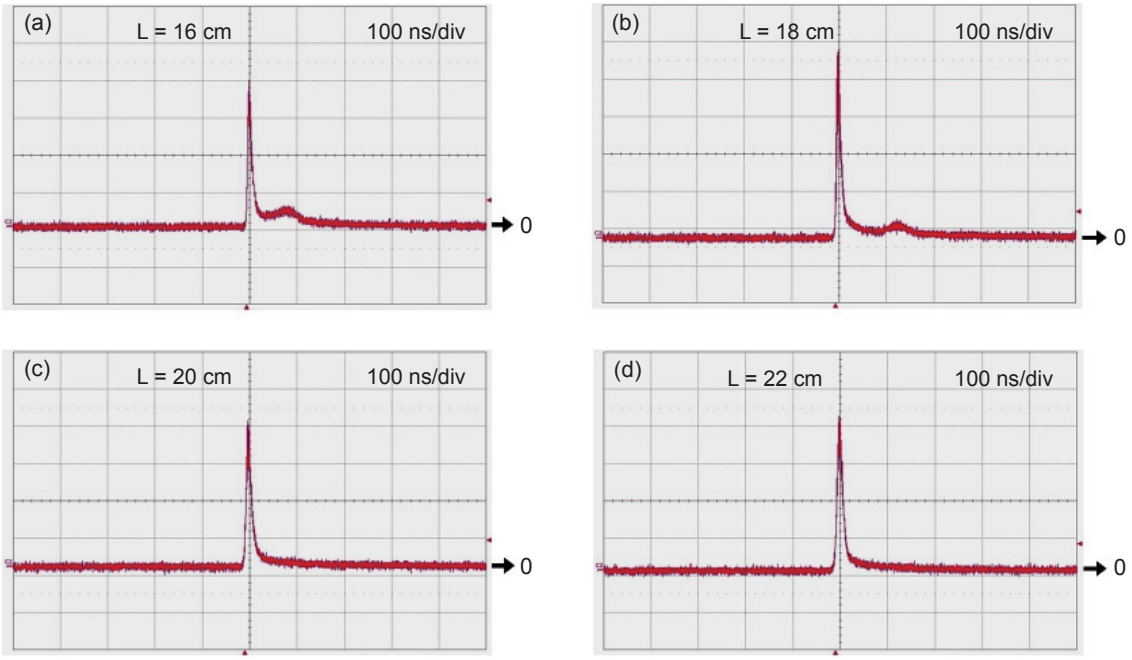

圖 8. Q-開關脈衝波形在：(a) L = 16 cm，(b) L = 18 cm，(c) L = 20 cm，(d) L = 22 cm 的情況。

$$\frac{dn}{dt} = R_p - \frac{n}{\tau} - c\sigma\phi_b n \tag{1}$$

其中 R_p 是激發光源密度的速率 (rate of the pump density)、τ 是增益介質雷射上能階的生命週期 (upper-state lifetime of gain medium)、c 是光速、σ 是受激輻射的截面積大小 (stimulated emission cross section)。利用 $\tau_b = 1/c\sigma\phi_b n$，(1) 式可改寫成：

$$\frac{dn}{dt} = R_p - \frac{n}{\tau_e} \tag{2}$$

其中 $1/\tau_e = 1/\tau_b + 1/\tau_b$，且 τ_e 代表寄生雷射作用下的有效上層能態生命週期，τ_e 很明顯地小於 τ。由於儲存能量的最大值與上能階的生命週期成比例關係，因此寄生雷射作用可以被理解為造成脈衝能量以及尖峰功率降低的主因。簡言之，雖然寄生雷射作用幾乎不影響輸出功率，但卻對尖峰功率的提升造成了不利的影響。

如圖 7 所示，在最高激發功率 44 W 時，臨界腔長大約為 20 cm。利用 ABCD-矩陣原理，可以推算出穩定平平共振腔的腔長 L 必須要比熱透鏡焦距 (thermal focal length) f_{th} 還要來得小；也就是說，為了維持雷射共振腔的穩定度，就必須滿足 $L \le f_{\text{th}}$。一般來說，雷射晶體的熱透鏡焦距與晶體的摻釹濃度成反比關係，因此不等式 $L \le f_{\text{th}}$ 凸顯出使用極低摻釹濃度 Nd:YVO_4 晶體的重要性。端面激發雷射晶體的等效熱透鏡焦距可由以下數學式作評估[7]：

$$\frac{1}{f_{th}} = \frac{\xi}{\pi K_c}\int_0^l \frac{\alpha e^{-\alpha z}}{1-e^{-\alpha l}}\frac{1}{\omega_p^2(z)}\left[\frac{1}{2}\frac{dn}{dT} + (n-1)\alpha_T\frac{\omega_p(z)}{l}\right]dz \tag{3}$$

其中 ξ 為激發光在晶體內部所產生的熱量，K_c 是雷射晶體的熱導率，α 是吸收係數，$\omega_p(z)$ 是激發光的半徑在晶體內部之變化，n 是折射率，l 是增益介質的長度，dn/Dt 是熱光係數，α_T 是熱膨脹係數。利用下列的參數：K_c = 5.23 W/m K，ω_{po} = 400 μm，$dn/dT = 3 \times 10^{-6}\ K^{-1}$，$n$ = 2.1652，$\alpha_T = 4.43 \times 10^{-6}\ \text{K}^{-1}$，可得到在激發功率為 44 W 下，熱透鏡焦距 f_{th} 隨雷射晶體中摻釹濃度的變化情形。在目前的計算中，假設晶體對激發功率有著 98% 的吸收率，因此晶體長度 l 和吸收係數 α 存在著 $\alpha l = 4$ 的關係。同時在激發光源波長為 808 nm 時，吸收係數 α 與雷射晶體中摻釹濃度的關係為 $\alpha = 2 \cdot N_d$ mm^{-1} [8]，其中 N_d 為雷射晶體中的摻釹濃度。在激發功率為 44 W 時，熱透鏡焦距隨著 N_d = 0.05% 到 N_d = 1% 的計算結果如圖 9 所示。由此可以看出，當摻釹濃度越小時，熱透鏡焦距越大。再者，摻釹濃度高於 0.2% 的 Nd:YVO_4 晶體不能滿足不等式 $L \le f_{\text{th}}$，其中已經從實驗上證明在激發功率為 44 W 時，腔長必須等於 20 cm，以完全抑制寄生雷射的作用。總結以上所述，在設計高功率的 Q-開關雷射時，使用極低摻釹濃度的 Nd:YVO_4 晶體對於同時抑制寄生雷射作用以及維持雷射共振穩定是一個非常有效的方法。

在腔長為 20 cm 的情形下，針對雙端激發的高功率 Q-開關雷射進行完整的探討。圖 10(a) 及 (b) 為基頻光在脈衝重複率為 40 kHz 時，其輸出功率、脈衝寬度、脈衝能量以及尖峰功率與激發功率的關係圖。當激發功率為 44 W 時，在沒有任何輸出功率飽和的情況下，平均輸出功率達 17.5 W，這也說明了共振腔維持在一個穩定的範圍內。同時，隨著激發功率由 16 W 增加至 44 W，脈衝寬度由 36 ns 縮短至 12 ns，脈衝能量由 60 μJ增加到 435 μJ，尖峰功率則由 1.6 kW 增加至 36.3 kW。圖 11 (a) 及 (b) 為激發功率等於 44 W 時，基頻光的

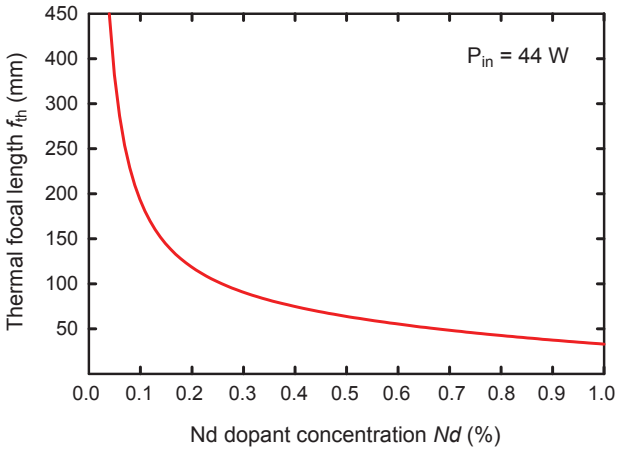

圖 9. 等效熱透鏡焦距在激發功率為 44 W 時隨不同摻釹濃度的關係圖。

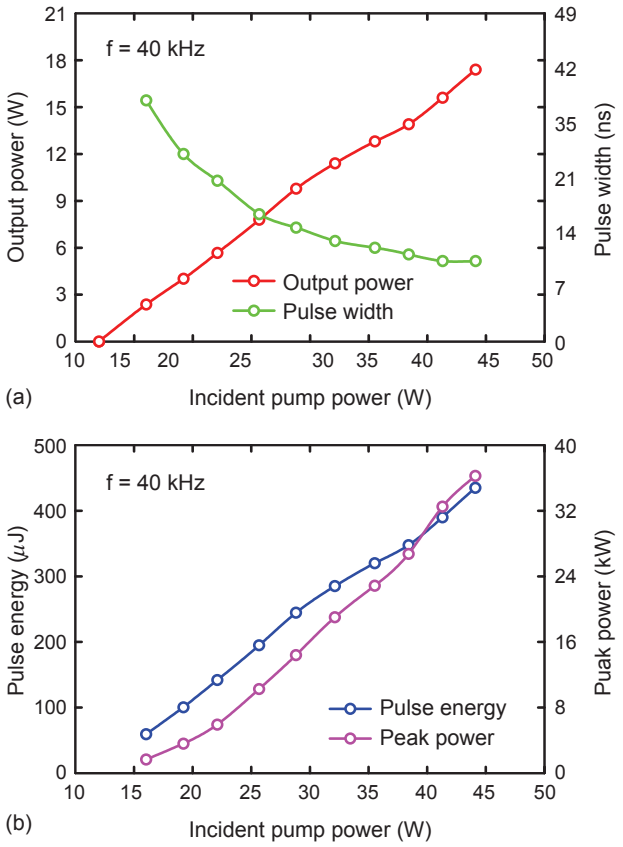

圖 10. 脈衝重複率為 40 kHz 時，其 (a) 輸出功率 (紅色)、脈衝寬度 (綠色)、(b) 脈衝能量 (藍色) 以及尖峰功率 (粉紅色) 與激發功率的關係圖。

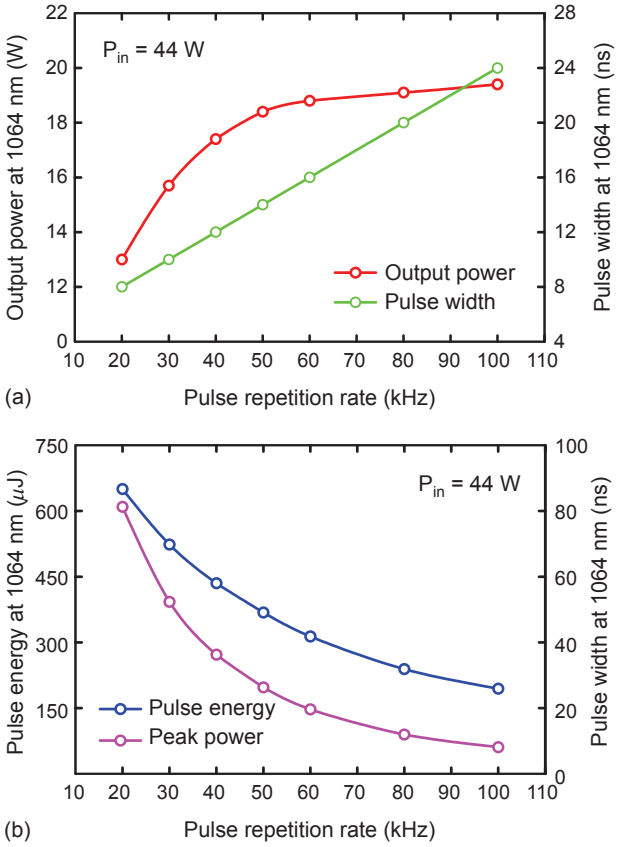

圖 11. 激發功率等於 44 W 時，其 (a) 輸出功率 (紅色)、脈衝寬度 (綠色)、(b) 脈衝能量 (藍色) 以及尖峰功率 (粉紅色) 與脈衝重複率的關係圖。

輸出功率、脈衝寬度、脈衝能量以及尖峰功率與脈衝重複率的關係圖。當脈衝重複率由 20 kHz 上升至 100 kHz 時，基頻光的輸出功率由 13 W 升至 19.4 W，脈衝寬度由 8 ns 增加至 24 ns，脈衝能量由 650 μJ 下降至 194 μJ，而尖峰功率也由 81.5 kW 變化至 8.1 kW。接下來，將運用此高功率Q-開關雷射探討腔外二倍頻轉換與三倍頻轉換的效能。

4. 腔外二倍頻轉換及三倍頻轉換的實驗結果

這裡所用腔外二倍頻轉換與三倍頻轉換的架構與單端激發的腔外倍頻架構相同，不同的是，在雙端激發的架構中，實驗上發現功率最佳化的參數條件為 L_1 = 70 mm、L_2 = 43 mm、L_3 = 34 mm，以及 L_4 = 21 mm。

在激發功率為 44 W 的情況下，圖 12(a) 至 (c) 分別顯示了 532 nm 及 355 nm 的輸出功率、脈衝能量、尖峰功率與脈衝重複率的關係。在雙端激發的架構中，腔外倍頻轉換的最佳脈衝重複率仍為 40 kHz，此時 532 nm 及 355 nm 所得到的最大輸出功率分別為 8.38 W 及 6.65 W。因此從 808 nm 到 355 nm 的光轉換效率為 15.1%；而由 1064 nm 到 355 nm 的光轉換效率則為 38.2%。另一方面，在脈衝重複率為 20 kHz 時，532 nm 的最大脈衝能量為 270 μJ，而最大尖峰功率則為 30 kW。同樣地，在脈衝重複率為 20 kHz 時，355 nm 的最大脈衝能量為 200 μJ，而最大尖峰功率則為 22 kW。利用刀口法 (knife-edge method)，此高功率 UV 雷射的光束品質係數 (beam quality factor) 分別為 $M_x^2 < 1.2$ 與

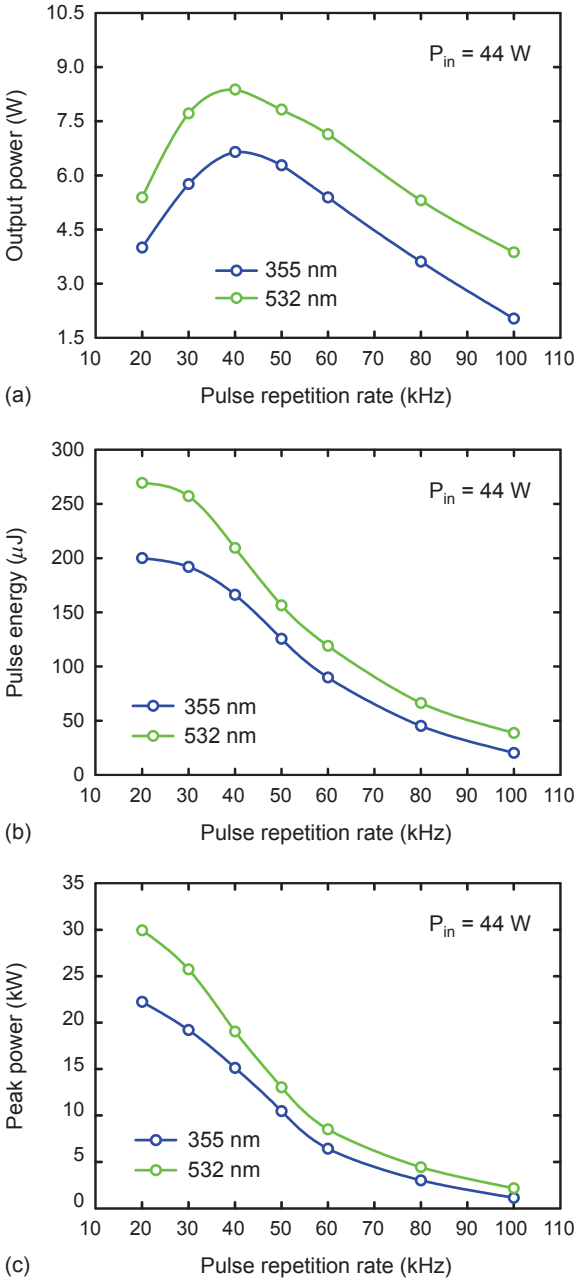

圖 12. 激發功率等於 44 W 時，532 nm (綠色) 與355 nm (藍色)，其 (a) 輸出功率、(b) 脈衝能量以及 (c) 尖峰功率與脈衝重複率的關係圖。

$M_y^2 < 1.3$。為了證明寄生雷射效應對於腔外倍頻的影響，也使用了 $L = 16$ cm 的Q-開關雷射進行腔外二倍頻與三倍頻的轉換。由實驗結果顯示，即使 $L = 16$ cm 與 $L = 20$ cm 的 Q-開關雷射所得到的 1064 nm 輸出功率幾乎一樣，但是利用 $L = 16$ cm 的 Q-開關雷射所得到的 532 nm 及 355 nm 的輸出功率卻比 $L = 20$ cm 的 Q-開關雷射所得到的結果還要低 15%－25%，證實了寄生雷射效應會導致尖峰功率的降低，使得 Q-開關雷射的性能變差。

四、結論

本文介紹了高功率 Q-開關紫外固態雷射的優化與製作過程。我們分別利用一顆以及兩顆雷射二極體作為激發光源，設計了高功率的 Q-開關雷射。實驗結果顯示，當激發功率越高時，寄生雷射的產生會使得 Q-開關雷射的輸出性能明顯變差。為了有效地抑制寄生雷射作用以及克服熱透鏡問題，利用摻釹濃度只有 0.1% 的 Nd:YVO_4 晶體設計了一個輕巧簡便的高功率 Q-開關雷射。接著採用此優化的高功率 Q-開關雷射進行腔外二倍頻及三倍頻轉換。在脈衝重複率為 40 kHz 及輸入功率 44 W 的情況下，532 nm 及 355 nm 所得到的最高輸出功率分別為 8.38 W 及 6.65 W。由 808 nm 到 355 nm 的光轉換效率為 15.1%；而由 1064 nm 到 355 nm 的光轉換效率則為 38.2%。未來若能將此技術產品化並推廣至工業界，相信能對台灣的雷射科技以及相關應用有很大的幫助。

誌謝

感謝國科會 (NSC-97-2112-M-009-016-MY3) 對於此研究所提供的財務支援。

參考文獻

1. V. Hicks, C. X. Wang, and G. Y. Wang, *Proc. of SPIE*, **5332**, 120 (2004).
2. C. X. Wang, G. Y. Wang, A. V. Hicks, D. R. Dudley, H. Y. Pang, and N. Hodgson, *Proc. of SPIE*, **6100**, 610019 (2006).
3. P. Maak, L. Jakab, P. Richter, H. J. Eichler, and B. Liu, *Appl. Opt.*, **39**, 3053 (2000).
4. M. E. Storm, *J. Opt. Soc. Am. B*, **9**, 1299 (1992).
5. T. Crawford, C. Lowrie, and J. R. Thompson, *Appl. Opt.*, **35**, 5861 (1996).
6. P. Yan, M. Gong, T. Xie, and X. Liu, *Opt. Eng.*, **42**, 159 (2003).
7. W. Koechner, *Solid-State Laser Engineering*, ch.7, 6th edn. Berlin:Springer (2005).
8. Y. F. Chen, *IEEE Quantum Electron.*, **35**, 234 (1999).

黃郁仁先生為國立交通大學電子物理研究所博士班學生。

Yu-Jen Huang is currently a Ph.D. student in the Institute of Electrophysics at National Chiao Tung University.

唐政猷先生為國立交通大學電子物理研究所碩士班學生。

Cheng-Yu Tang is currently a M.S. student in the Institute of Electrophysics at National Chiao Tung University.

蘇冠暐先生為國立交通大學電子物理博士，現任國立交通大學電子物理系助理教授。

Kuan-Wei Su received his Ph.D. in electrophysics from National Chiao Tung University. He is currently an assistant professor in the Department of Electrophysics at National Chiao Tung University.

陳永富先生為國立交通大學電子研究所博士，現任國立交通大學電子物理系教授。

Yung-Fu Chen received his Ph.D. in electronics from National Chiao Tung University. He is currently a professor in the Department of Electrophysics at National Chiao Tung University.